Physics of the Solid State, Vol. 44, No. 1, 2002, pp. 1–3. Translated from Fizika Tverdogo Tela, Vol. 44, No. 1, 2002, pp. 3–5.

A New Species of Information in Maxwell's Equations

A. G. Chirkov* and A. N. Ageev**

**St. Petersburg State Technical University, ul. Politekhnicheskaya 29, St. Petersburg, 195251 Russia*

***Ioffe Physicotechnical Institute, Russian Academy of Sciences, ul. Politekhnicheskaya 26, St. Petersburg, 194021 Russia*

Received May 21, 2001

Abstract—For the first time, it is demonstrated on a specific example that the traveling electromagnetic wave is characterized, generally speaking, not only by the magnitude of the electric and magnetic field vectors, but also by certain potentials whose existence can be experimentally detected through their action upon electron diffraction. The structure of the potentials in an electromagnetic wave depends on the emitter type and contains information on this type, being, thus, a new species of information media. © *2002 MAIK "Nauka/Interperiodica".*

One of the remarkable consequences of Schrödinger's equation is the so-called Aharonov–Bohm effect (ABE), which has a vector (magnetic) and a scalar (electric) form [1–5]. Already for more than 40 years, this effect has been investigated and the investigation results have been discussed (cf., e.g., [6, 7]). By the 1990s, it was understood that there was a definite need for extension of the ideas of Aharonov and Bohm and their followers [1–3] to the case of time-varying potentials and for the performance of the corresponding experiments. First attempts in this direction [8, 9], unfortunately, contained certain mistakes, which resulted in incorrect findings in the proposed experiments.

The investigations of the ABE in the dynamical regime undertaken by the present authors [10, 11] demonstrated that, in order to comprehend the ABE nature, it is extremely helpful to separate the field and zero components of the vector and scalar potentials:

$$\mathbf{A} = \mathbf{A}^f + \mathbf{A}^0 \text{ and } \varphi = \varphi^f + \varphi^0, \quad (1)$$

where the supercipt f designates electromagnetic-field components (field potentials) and the superscript 0 relates to the potentials that are necessary to satisfy Maxwell's equations with boundary conditions but that do not directly correspond to any electromagnetic field (potentials of zero fields or superfluous potentials).

It should be noted that in mathematical physics, an analog of zero-field potentials has been used for a long time, although, contrary to our consideration, no physical sense has been ascribed to it. For example, the vector potential of a zero field occurs in reconstructing a vector from its curl and divergence given in a finite region of space and is defined uniquely [12, 13].

Zero-field potentials can be represented in the form

$$\mathbf{A}^0 = \text{grad}\chi, \quad \varphi^0 = -\frac{1}{c}\frac{\partial\chi}{\partial t}, \quad (2)$$

where χ is a differentiable, though multivalued function.

We stress that it is zero-field potentials that are responsible for the ABE in all theoretical and experimental works published so far. The main problem was merely to create the conditions under which electrons would propagate in a region without fields but with nonzero potentials. For the better investigated magnetic ABE, such conditions could be obtained in the static case of electronic optics, which was proposed and put under consideration in the earliest papers [1–3]. However, the experimental difficulties encountered in carrying out static-regime experiments should be regarded as a disadvantage of this approach [14]. As far as technological applications of ABE are concerned, the static regime has altogether little prospects.

In the case of the dynamical regime, the main question is whether it is possible to create zero-field potentials in certain spatial regions. The question was discussed in [10, 11] considering the example of an infinitely long hollow continuous cylinder–solenoid with infinitely thin walls and with an alternating stationary current flowing along the circumferences in the cylinder and irradiating into the outer space. It was shown that in this case, there are zero-field potentials in the outer space and, therefore, *a priori*, one can assume they influence the electron diffraction pattern.

In the present paper, it is shown theoretically that a new effect caused by zero-field potentials is possible. This effect consists in the disappearance of interference fringes when a relatively weak electromagnetic wave having both electromagnetic and zero-field potentials is produced in the path of the de Broglie wave. For the existence of such an effect, the use of Lorentz's gauge is more preferable than Coulomb's gauge and the Schrödinger equation is valid.

1063-7834/02/4401-0001$22.00 © 2002 MAIK "Nauka/Interperiodica"

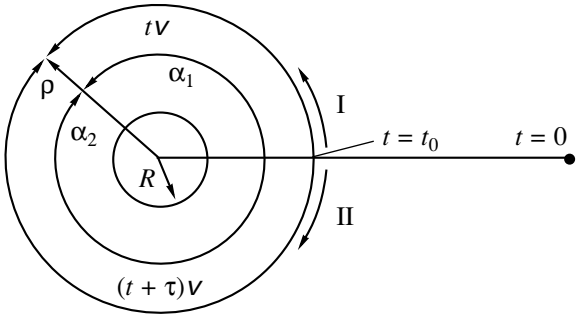

Fig. 1. Schematic representation of the experiment with electron emission at $t = 0$, its split into two de Broglie waves (I and II) at $t = t_0$, and the superposition of the waves on the circumference of radius ρ.

Let a cylindrical coordinate system (ρ, α, z) be chosen with the z axis along the solenoid axis. The space distribution of the current is assumed to be

$$j_\alpha(\rho, \alpha, z) = I_0\delta(\rho - R)\cos(\omega t), \quad j_\rho = j_z = 0, \quad (3)$$

where R is the solenoid radius, ω is the cyclic frequency of the current, and $I_0 = j/2\pi R$ is the current in the wall per unit length.

Solving the problem, we obtain the following expressions for the zero-field potentials outside the solenoid [10, 11]:

$$A_\alpha^0 = W\frac{2}{k\rho}\cos\omega t, \quad (4)$$

$$\varphi^0 = 2W\alpha\sin\omega t, \quad (5)$$

$$\chi = 2Wc\omega^{-1}\alpha\cos\omega t, \quad (6)$$

where $W = 2\pi I_0 R J_1(kR)/c$ and $k = \omega/c$.

Let us consider the influence of these potentials on de Broglie waves sweeping the solenoid along its circumference as shown in Fig. 1. Since our interest is only in the influence of zero-field potentials on electron interference, we will consider the case when there are no field potentials in the electron trajectories. Direct substitution into the Schrödinger equation shows that the alteration of the wave function reduces to the alternating wave function phase alone:

$$\Psi(\mathbf{l}, t) = \Psi_0\exp\left(-\frac{2\pi i}{\mu_0}\int d\chi\right), \quad (7)$$

where $\int d\chi = \int \mathbf{A}^0 d\mathbf{l} - c\int\varphi^0 dt$; $\mu_0 = ch/|e|$ is the magnetic flux quantum; the function Ψ_0 defines the motion of the electron in the absence of an electromagnetic field and is equal to $\Psi_0 = \exp(-i\int\omega_e dt)$, where ω_e is the cyclic de Broglie frequency for the electron; and $\mathbf{l}$ is a unit vector along an electron's trajectory.

Applying these solutions to the case of two de Broglie waves with wave functions $\Psi_i(\mathbf{l}_i, t)$ that propagate along two trajectories $i = 1, 2$ (Fig. 1), we find the magnitude of the interference effect:

$$P = \Psi_\Sigma\Psi_\Sigma^* = 0.5P_0\{1 + \cos[\omega_e\tau - 4\pi Wc\mu_0^{-1}f^{-1} \times \cos\omega(t_0 + \pi\rho v^{-1})]\}, \quad (8)$$

where $\Psi_\Sigma = \Psi_1 + \Psi_2$, $2\pi f = \omega$; t_0 is the instant of electron splitting, as shown in Fig. 1; v is the phase velocity of the electromagnetic wave; and P_0 is the magnitude of the effect at an interference maximum for $I_0 = 0$. We note that Eq. (8) gives the probability of finding an electron on the circumference with a given radius ρ if the electron leaves the emitter at the moment $t = 0$ and reaches the splitting point at the moment t_0. It is a matter of direct verification to prove that the displacement of the positions of interference maxima is entirely due to one part of the scalar potential, while the other part of the scalar potential fully compensates the displacement of the fringes caused by the vector potential.

Let us consider some particular cases of Eq. (8). At $\omega \longrightarrow 0$, we have

$$P(\omega \longrightarrow 0) = 0.5P_0\{1 + \cos[\omega_e\tau - 2\pi M\mu_0^{-1}]\}, \quad (9)$$

where $M = 4\pi^2 I_0 R^2 c^{-1}$ is the magnetic flux through the cross section of the solenoid. Thus, in the static case, Eq. (8) transforms into the well-known expression for the magnetic ABE. At $\omega t_0 = (2m + 1)\pi/2$, the electron reaches the splitting point at the moment when the current in the solenoid passes through zero and displacement will take place if $\omega\pi\rho/v \neq m\pi$. For electrons which reach the splitting point at the moment when $\omega t_0 = m\pi$, i.e., the current in the solenoid passes through a maximum, displacement will take place if $\omega\pi\rho/v \neq (2m + 1)\pi$.

Averaging the fringe pattern over all values of t_0, we get

$$\bar{P} = 0.5P_0\{1 + J_0(S)\cos[\omega_e\tau]\}, \quad (10)$$

where $S = 8\pi^2 I_0 R\mu_0^{-1} f^{-1} J_1(2\pi f c^{-1} R)$.

One can easily verify that the value of $S/I_0R^2 = 8\pi^2 \times R^{-1}\mu_0^{-1} f^{-1} J_1(2\pi f c^{-1} R)$ almost does not depend on the product fR throughout the radio-frequency range for all reasonable values of the solenoid radius (e.g., from 1 through 1000 μm). Therefore, the frequency in the experiment can be chosen on the basis of convenience.

In Fig. 2, the dependence of $\bar{P}/P_0$ on $\omega_e\tau$, given by Eq. (10), is shown for different values of the current in the solenoid wall I_0. The fringe pattern contrast is defined by the formula

$$K \equiv \frac{P_{\max} - P_{\min}}{P_{\max} + P_{\min}} = J_0(4\pi Wc\mu_0^{-1} f^{-1}). \quad (11)$$

Noteworthy is the independence of the fringe pattern contrast from the electron trajectory radius, which

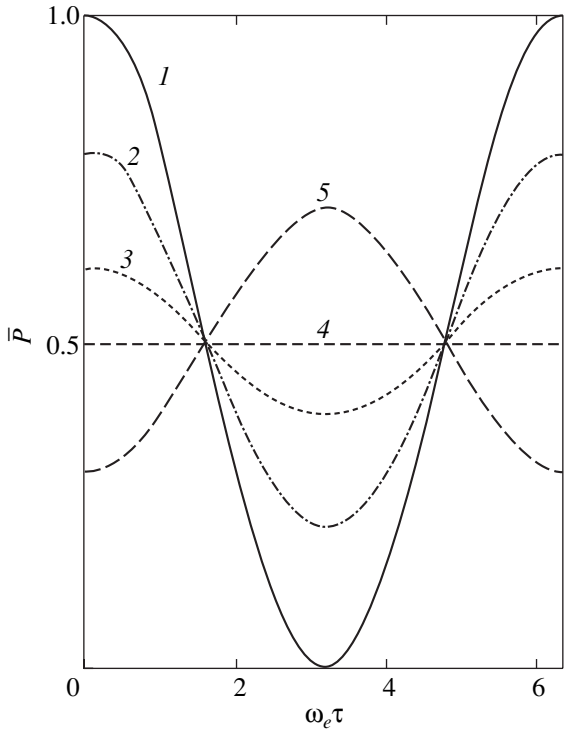

Fig. 2. Dependence of the magnitude of the interference effect $\bar{P}$ on $\omega_e\tau$ for $R = 10^{-2}$ cm, $f = 10^5$ Hz, and the current I_0 equal to (*1*) 0, (*2*) 0.2, (*3*) 0.3, (*4*) 0.4, and (*5*) 0.7 mA/cm.

is the consequence of the independence of the scalar potential from ρ.

As is evident from Eq. (11), the fringe pattern contrast is defined by a zero-order Bessel function of the first kind. Therefore, with increasing amplitude of the alternating current in the solenoid, the fringe pattern contrast will decrease. Let us consider the zero-order Bessel function in Eq. (10). Let the radius of the solenoid be, e.g., 10 μm. As indicated above, at the given radius, the argument of the Bessel function in Eq. (10) virtually does not depend on the solenoid radiation frequency up to 5×10^{10} Hz and is equal to $2 \times 10^{-6} I_0$. In order for the fringes to disappear as a result of the alternating current in the solenoid, the argument of the Bessel function in Eq. (10) has to be approximately 2.45, which is the case if the current in the solenoid equals 0.4 mA/cm.

Thus we may conclude that, first, the situation radically changes when one goes over from the static case to the case where an electromagnetic wave is present: the fringe pattern contrast changes. Second, the electromagnetic wave will be fully described if not only the fields but also the zero-field potentials are taken into account. Let us call the electromagnetic field together with the zero-field potentials the full Maxwell field. If an electromagnetic wave is generated using a different method, the structure of the full Maxwell field could prove different. For instance, the radiation of an infinitely thin metal rod does not produce a zero-field potential.

Thus, from the analysis of the full Maxwell field, information on the sources of the field can be obtained; therefore, zero-field potentials contain some additional information that is not available from analyzing the field alone.

Hence, the electromagnetic field is a more complex formation than a mere combination of an electric and a magnetic field. Its full description necessarily includes the electromagnetic potentials. The proposed experiment can substantially change the understanding of the nature of electromagnetic fields.

REFERENCES

1. W. Franz, Verh. Dtsch. Phys. Ges. **20**, 65 (1939).
2. W. Ehrenberg and R. E. Siday, Proc. Phys. Soc. London, Sect. B **62**, 8 (1949).
3. Y. Aharonov and D. Bohm, Phys. Rev. **115**, 485 (1959).
4. S. Olariu and I. I. Popesku, Rev. Mod. Phys. **57**, 339 (1985).
5. M. Peskin and A. Tonomura, Lect. Notes Phys. **340**, 115 (1989).
6. T. H. Boyer, Found. Phys. **30**, 893 (2000).
7. R. Blanco, Found. Phys. **29**, 693 (1999).
8. B. Lee, E. Yin, T. K. Gustafson, and R. Chiao, Phys. Rev. A **45**, 4319 (1992).
9. I. O. Kulik and A. S. Shumovsky, Appl. Phys. Lett. **69**, 2779 (1996).
10. A. G. Chirkov and A. N. Ageev, Pis'ma Zh. Tekh. Fiz. **26** (16), 103 (2000) [Tech. Phys. Lett. **26**, 747 (2000)].
11. A. G. Chirkov and A. N. Ageev, Zh. Tekh. Fiz. **71** (2), 16 (2001) [Tech. Phys. **46**, 147 (2001)].
12. N. E. Kochin, *Vector Calculus* (Izd. Akad. Nauk SSSR, Moscow, 1967).
13. V. I. Smirnov, *A Course of Higher Mathematics* (Nauka, Moscow, 1957; Addison-Wesley, Reading, 1964), Vol. 2.
14. A. Tonomura, N. Osakabe, T. Matsuda, *et al.*, Phys. Rev. Lett. **56**, 792 (1986).

Translated by D. Bayuk

Physics of the Solid State, Vol. 44, No. 1, 2002, pp. 102–110. Translated from Fizika Tverdogo Tela, Vol. 44, No. 1, 2002, pp. 97–105.

MAGNETISM AND FERROELECTRICITY

Spin Excitations in Granular Structures with Ferromagnetic Nanoparticles

L. V. Lutsev

Domen Research Institute, St. Petersburg, 196084 Russia

e-mail: lutsev@domen.ru

Received April 11, 2001

Abstract—Spin excitations and relaxation in a granular structure which contains metallic ferromagnetic nanoparticles in an insulating amorphous matrix are studied in the framework of the *s–d* exchange model. As the *d* system, we consider the granule spins, and the *s* system is represented by localized electrons in the amorphous matrix. In the one-loop approximation with respect to the *s–d* exchange interaction for a diagram expansion of the spin Green's function, the spin excitation spectrum is found, which consists of spin-wave excitations in the granules and of polarized spin excitations. In polarized spin excitations, a change in the granule spin direction is accompanied by an electron transition with a spin flip between two sublevels of a split localized state in the matrix. We considered polarized spin relaxation (relaxation of the granule spins occurring by means of polarized spin excitations) determined by localized deep energy states in the matrix and the thermally activated electronic cloud of the granule. It is found that polarized spin relaxation is efficient over a wide frequency range. Estimates made for structures with cobalt granules showed that this relaxation could be observed in centimetric, millimetric, and submillimetric wavelength ranges. *© 2002 MAIK "Nauka/Interperiodica".*

1. INTRODUCTION

Granular structures containing metallic ferromagnetic nanoparticles (granules) in an insulating amorphous matrix reveal various interesting magnetic properties, such as giant magnetoresistance, anomalous behavior of the magnetoresistance as a function of applied voltage and temperature (associated with the Coulomb blockade [1]), and the occurrence of additional modes in the FMR spectrum in a narrow range near the percolation threshold for which there is no correlation between the wavelength of spin waves and the film thickness [2–4]. However, the fundamental problem of magnetic relaxation in granular structures has not yet been investigated comprehensively.

Considerable broadening ΔH of the FMR spectrum of granular structures in comparison with bulk single-crystal samples was first observed in [5, 6]. Colloid structures which contain Fe, Co, or Ni particles in paraffin were investigated using the FMR method at wavelengths of 3.14 and 1.20 cm in magnetic fields at 3 and 8 kOe, respectively. The particle dimensions were 5–10 nm. The FMR line widths ΔH were, in effect, independent of temperature and frequency, and, for ferromagnetic powders prepared using different methods, they amounted to 500 (Ni), 450–3000 (Co), and 350–1100 Oe (Fe). After accounting for the anisotropy, random orientation of the particles in the ensemble, and spin–spin relaxation, a relatively large addition to the ΔH remained unexplained. A comparison with single-crystal samples shows that the FMR line widths for single crystals at the same frequencies have significantly lesser values, 110 (Co) and 32 Oe (Fe) [7].

The FMR investigations of the granular films also revealed a sharp increase in ΔH with decreasing concentration of ferromagnetic nanoparticles [2, 3]. For Fe–SiO_2 structures, with an Fe concentration of 0.4, $\Delta H \propto 800$ Oe at frequencies of 9.4 and 35.4 GHz [3]. At the same time, the FMR line width in pure Fe(100) sputtered films of the same thickness (16–24 nm) amounts to approximately 20 Oe at a frequency of 9.5 GHz [8]. The ΔH increase in [3] was explained in terms of shape anisotropy: the granules acquired a more elongated ellipsoidal form with decreasing concentration.

The magnetic relaxation in granular films has also been investigated using the spin-wave spectroscopy method in $Y_3Fe_5O_{12}$ (YIG)/(investigated granular film) structures at temperatures of 77 to 393 K and frequencies of 2.1 to 4.0 GHz [9–11]. From the changes in the characteristics of traveling spin waves in a YIG film, the spin relaxation was judged in the granular structures of amorphous hydrogenated carbon *a*-C : H with cobalt nanoparticles and amorphous SiO_2 with $Co_{86}Nb_{12}Ta_2$ nanoparticles. For the *a*-C : H–Co structures, in which the spacing Δ between the Fermi level of a metallic particle and the mobility edge of the matrix conduction band is small in comparison with kT, the observed magnetic relaxation was characterized by large values and a strong dependence on temperature. For the structures with a SiO_2 matrix and energy $\Delta \gg kT$, the relaxation also exhibited large values and was practically independent of temperature.

The purpose of the present work is to theoretically investigate spin excitations and relaxation in granular

1063-7834/02/4401-0102$22.00

structures containing metallic ferromagnetic nanoparticles in an insulating amorphous matrix. The study is done in the framework of the *s–d* exchange model in the one-loop approximation with respect to the *s–d* exchange interaction for a diagram expansion of the spin Green's function. The *d* system is represented by granule spins. As the *s* system, we consider the localized electrons of the amorphous matrix. It is found that the spin excitation spectrum consists of spin-wave excitations of the granules and polarized spin excitations. In polarized spin excitations, the change in the granule spin direction is accompanied by an electron transition between the two sublevels of a split localized state in the matrix. The polarized spin relaxation, i.e., the relaxation of the granule spins occurring by means of the polarized spin excitations, depends on the density of the localized states in the $2kT$-wide band near the Fermi level. Estimates of the density of states obtained from the conductivity temperature dependences of the granular structures [12] show that the polarized spin relaxation is quite efficient and that its contribution to the decay of spin excitations in a granule can significantly exceed the contributions from the spin–spin relaxation, spin–lattice relaxation, and the relaxation due to interaction between the spins and electrons of the granule [13]. The polarized spin relaxation allows one to explain the considerable increase in the damping observed in [2, 3, 5, 6, 9–11]. The process of polarized spin relaxation takes place over a wide frequency range. Estimates for structures with cobalt granules show that the frequency range where polarized spin relaxation can be observed corresponds to centimetric, millimetric, and submillimetric wavelength ranges. Therefore, using granular structures, one can produce coatings which efficiently absorb over a wide radio-frequency region.

2. DERIVATION OF THE BASIC EQUATION

Let us consider the interaction of the spin of a ferromagnetic granule with electrons of the matrix in the framework of the *s–d* exchange model [14]. We assume that the *d* system is formed by the localized electrons of the granule and its spin excitations are described in terms of the Heisenberg model. The granule size is assumed to be sufficiently large for the granule to be in a ferromagnetic state. For example, the *d* system can be represented by an ensemble of $3d$-electron spins of a Co granule in the case of structures with cobalt nanoparticles with dimensions larger than 1 nm. As the *s* system, we consider the localized electrons of the matrix. The *s* and *d* systems are connected to each other through the exchange interaction J. We assume that $J > 0$. We neglect the interaction between electrons of the *s* system. Under these assumptions, the Hamiltonian of the *s–d* model is written in the form

$$\mathcal{H} = \mathcal{H}_s^{(0)} + \mathcal{H}_d^{(0)} + \mathcal{H}_d^{(\mathrm{int})} + \mathcal{H}_{sd},$$

where

$$\mathcal{H}_s^{(0)} = \sum_{p,\lambda,\nu} \bar{\varepsilon}_\lambda^{(p)} a_{\lambda\nu}^{(p)+} a_{\lambda\nu}^{(p)} \tag{1}$$

is the Hamiltonian of the electrons of the *s* system not interacting with one another in the matrix crystal lattice and $a_{\lambda\nu}^{(p)+}$ and $a_{\lambda\nu}^{(p)}$ are the creation and annihilation operators, respectively, for an electron at the energy level λ of the one-particle state p with a spin ν; these operators obey the commutation relations $\{a_{\lambda\nu}^{(p)+}, a_{\lambda'\nu'}^{(p')}\} = \delta_{pp'}\delta_{\lambda\lambda'}\delta_{\nu\nu'}$. The summation in Eq. (1) is performed over the one-particle states p, the levels λ, and the electron spins $\nu = \uparrow, \downarrow$. The equation from which the wave functions $\varphi_\lambda^{(p)} \equiv |p, \lambda\rangle$, λ and the energy spectrum $\bar{\varepsilon}_\lambda^{(p)}$ of the one-particle states p are found is determined by the one-particle Hamiltonian $\mathcal{H}^{(p)}$ and has the form

$$(\mathcal{H}^{(p)} - \bar{\varepsilon}_\lambda^{(p)})\varphi_\lambda^{(p)} = 0. \tag{2}$$

The terms

$$\mathcal{H}_d^{(0)} = -g\mu_B H \sum_{\mathbf{l}} S_{\mathbf{l}}^z, \tag{3}$$

$$\mathcal{H}_d^{(\mathrm{int})} = -\frac{1}{2}\sum_{\mathbf{l}\neq\mathbf{l}'} I(\mathbf{l}-\mathbf{l}')(S_{\mathbf{l}}^z S_{\mathbf{l}'}^z + S_{\mathbf{l}}^- S_{\mathbf{l}'}^+) \tag{4}$$

describe the interaction between spins $\mathbf{S}$ of the *d* system and the external magnetic field H and the exchange interaction between the granule spins, respectively; g and μ_B are the Landé factor and the Bohr magneton, respectively; the summation in Eqs. (3) and (4) is performed over all sites ($\mathbf{l}$, $\mathbf{l}'$) of the crystal lattice of the granule;

$$\mathcal{H}_{sd} = -\sum_{\mathbf{l}} \int J(\mathbf{r}-\mathbf{l})\{\psi_\uparrow^+(\mathbf{r})\psi_\downarrow(\mathbf{r})S_{\mathbf{l}}^- + \psi_\downarrow^+(\mathbf{r})\psi_\uparrow(\mathbf{r})S_{\mathbf{l}}^+ + (\psi_\uparrow^+(\mathbf{r})\psi_\uparrow(\mathbf{r}) - \psi_\downarrow^+(\mathbf{r})\psi_\downarrow(\mathbf{r}))S_{\mathbf{l}}^z\}\,d\mathbf{r} \tag{5}$$

is the interaction Hamiltonian between the *s* and *d* systems; and $\psi_\nu(\mathbf{r}) = \sum_{p,\lambda}\varphi_\lambda^{(p)}(\mathbf{r})a_{\lambda\nu}^{(p)}$ is the second-quantized wave function of an electron in the *s* system. The summation and integration in Eq. (5) are carried out over the granule crystal lattice sites $\mathbf{l}$ and the electron positions $\mathbf{r}$ in the matrix, respectively.

To calculate the energies and decay constants of the granule spin excitations, we will find the temperature Green functions of electrons of the matrix and the granule spins:

$$G_{\nu\nu'}(\mathbf{r}\tau;\,\mathbf{r}'\tau') = \langle\sigma(\beta)\rangle_0^{-1}\langle T\psi_\nu^+(\mathbf{r}\tau)\psi_{\nu'}(\mathbf{r}'\tau')\sigma(\beta)\rangle_0,$$

$$K_{dd}^{\alpha\alpha'}(\mathbf{1}\tau;\,\mathbf{1}'\tau') = \langle\sigma(\beta)\rangle_0^{-1}\langle TS_{\mathbf{1}}^\alpha(\tau)S_{\mathbf{1}'}^{\alpha'}(\tau')\sigma(\beta)\rangle_0,$$

$$K_{ds}^{\alpha\alpha'}(\mathbf{1}\tau;\,\mathbf{r}'\tau') = \langle\sigma(\beta)\rangle_0^{-1}$$

$$\times \langle TS_{\mathbf{1}}^{\alpha}(\tau)\psi^{+}(\mathbf{r}'\tau')s^{\alpha'}\psi(\mathbf{r}'\tau')\sigma(\beta)\rangle_0,$$

$$K_{sd}^{\alpha\alpha'}(\mathbf{r}\tau;\mathbf{1}'\tau') = \langle\sigma(\beta)\rangle_0^{-1} \tag{6}$$

$$\times \langle T\psi^{+}(\mathbf{r}\tau)s^{\alpha}\psi(\mathbf{r}\tau)S_{\mathbf{1}'}^{\alpha'}(\tau')\sigma(\beta)\rangle_0,$$

$$K_{ss}^{\alpha\alpha'}(\mathbf{r}\tau;\mathbf{r}'\tau') = \langle\sigma(\beta)\rangle_0^{-1}$$

$$\times \langle T\psi^{+}(\mathbf{r}\tau)s^{\alpha}\psi(\mathbf{r}\tau)\psi^{+}(\mathbf{r}'\tau')s^{\alpha'}\psi(\mathbf{r}'\tau')\sigma(\beta)\rangle_0,$$

where $\sigma(\beta) = T\exp\{\int_0^\beta[\mathscr{H}_d^{(\mathrm{int})}(\tau) + \mathscr{H}_{sd}(\tau)]d\tau\}$ is the temperature scattering matrix, $\beta = 1/kT$, and all operators in Eq. (6) are defined in the interaction representation; i.e., $A(\tau) = \exp[(\mathscr{H}_s^{(0)} + \mathscr{H}_d^{(0)})\tau]A\exp[(-\mathscr{H}_s^{(0)} + \mathscr{H}_d^{(0)})\tau]$. In the Green's functions K_{ds}, K_{sd}, and K_{ss}, s^α is a vector operator whose components are Pauli matrices and

$$\psi(\mathbf{r}\tau) = \begin{pmatrix} \psi_\uparrow(\mathbf{r}\tau) \\ \psi_\downarrow(\mathbf{r}\tau) \end{pmatrix}.$$

Here, $\nu, \nu' = \{\uparrow, \downarrow\}$ are spin indices of electrons of the matrix and $\alpha, \alpha' = \{+, -, z\}$ are indices of the spin operators. The statistical averaging $\langle\ldots\rangle_0$ is performed over the states described by the Hamiltonian $\mathscr{H}_s^{(0)} + \mathscr{H}_d^{(0)}$.

The diagram technique for the Green's functions in Eq. (6) is described in [14]. We consider the diagram expansions of the Green's functions $G_{\nu\nu'}$ and K_{dd}^{-+}. In the self-consistent-field approximation in terms of the eigenfunctions $\varphi_\lambda^{(p)}$ of the Hamiltonian $\mathscr{H}_s^{(0)}$, the Fourier transform of the electronic Green's function with respect to the variables $\tau - \tau'$ has the form

$$G_{p,p',\lambda,\lambda',\nu,\nu'}^{(0)}(\omega_n) = \frac{\delta_{pp'}\delta_{\lambda\lambda'}\delta_{\nu\nu'}}{\beta(i\hbar\omega_n - \varepsilon_{\lambda,\nu}^{(p)})} \equiv G_{p,\lambda,\nu}^{(0)}(\omega_n)\delta_{pp'}\delta_{\lambda\lambda'}\delta_{\nu\nu'}, \tag{7}$$

where $\hbar\omega_n = (2n+1)\pi/\beta$, n is an integer,

$$\varepsilon_{\lambda,\nu}^{(p)} = \bar{\varepsilon}_\lambda^{(p)} \mp \left(\frac{1}{2}g\mu_B H + \sum_{\mathbf{1}}\langle S_{\mathbf{1}}^z\rangle_0\int\varphi_\lambda^{(p)*}(\mathbf{r})J(\mathbf{r}-1)\varphi_\lambda^{(p)}(\mathbf{r})d\mathbf{r}\right), \tag{8}$$

and the electron energy $\bar{\varepsilon}_\lambda^{(p)}$ in Eq. (8) is determined from Eq. (2) (this energy is reckoned from the Fermi level in the absence of the exchange interaction). The upper sign corresponds to $\nu = \uparrow$; the lower sign, to $\nu = \downarrow$. The *s*–*d* exchange interaction splits an electronic level into two.

The Fourier transform of the spin Green's function with respect to $\tau - \tau'$ in the self-consistent-field approximation has the form [14]

$$K_{dd}^{(0)-+}(\mathbf{1}, \mathbf{1}', \omega_n) = K^{(0)}(\mathbf{1}, \omega_n)\delta_{\mathbf{11}'}, \tag{9}$$

where

$$K^{(0)}(\mathbf{1}, \omega_n) = \frac{2\langle S_{\mathbf{1}}^z\rangle_0}{y - i\beta\hbar\omega_n},$$

$$y = \beta\left[g\mu_B H + \sum_{\mathbf{1}'} I(\mathbf{1}-\mathbf{1}')\langle S_{\mathbf{1}'}^z\rangle_0 + \int J(\mathbf{r}-\mathbf{1})\langle(\psi_\uparrow^+(\mathbf{r})\psi_\uparrow(\mathbf{r}) - \psi_\downarrow^+(\mathbf{r})\psi_\downarrow(\mathbf{r}))\rangle_0 d\mathbf{r}\right].$$

The quantity y is proportional to the sum of the magnetic field and the molecular field that is exerted on a spin at the site $\mathbf{l}$ by other granule spins and electrons of the matrix, $\hbar\omega_n = 2n\pi/\beta$, $\langle S_{\mathbf{1}}^z\rangle_0 = SB_S(Sy)$, and B_S is the Brillouin function for the spin S.

Equations (7) and (9) for the self-consistent-field approximation to the Green's functions are the zeroth-order terms in the expansion of these functions in a power series in the reciprocal radius of the exchange interaction. These bare Green's functions are represented by directed lines in diagrams (Fig. 1a). The next approximations to the Green's functions can be found form the Dyson equation; for the spin Green's functions (6)

$$\hat{K}^{\alpha\alpha'} = \begin{pmatrix} K_{dd}^{\alpha\alpha'} & K_{ds}^{\alpha\alpha'} \\ K_{sd}^{\alpha\alpha'} & K_{ss}^{\alpha\alpha'} \end{pmatrix},$$

this equation has the form

$$\hat{K}^{\alpha\alpha'} = \hat{\Sigma}^{\alpha\alpha'} + \hat{\Sigma}^{\alpha\alpha'}\hat{V}\hat{K}^{\alpha\alpha'}, \tag{10}$$

where

$$\hat{V} = \begin{pmatrix} V_{dd} & V_{ds} \\ V_{sd} & V_{ss} \end{pmatrix} = \beta\begin{pmatrix} \frac{1}{2}I(\mathbf{1}-\mathbf{1}') & J(\mathbf{1}-\mathbf{r}) \\ J(\mathbf{r}-\mathbf{1}) & 0 \end{pmatrix},$$

$$J(\mathbf{1}-\mathbf{r}) = J(\mathbf{r}-\mathbf{1})$$

and

$$\hat{\Sigma}^{\alpha\alpha'} = \begin{pmatrix} \Sigma_{dd}^{\alpha\alpha'}(\mathbf{1}\tau;\mathbf{1}'\tau') & \Sigma_{ds}^{\alpha\alpha'}(\mathbf{1}\tau;\mathbf{r}'\tau') \\ \Sigma_{sd}^{\alpha\alpha'}(\mathbf{r}\tau;\mathbf{1}'\tau') & \Sigma_{ss}^{\alpha\alpha'}(\mathbf{r}\tau;\mathbf{r}'\tau') \end{pmatrix}$$

is the self-energy, which is described by diagrams that cannot be divided into two parts through cutting an interaction line. According to their indices, the dia-

grams $\hat{\Sigma}^{\alpha\alpha'}$ have external spin vertices of the *d* system or external electron vertices of the *s* system. In Eq. (10), summation and integration is performed over the internal variables **l** and **r** of the matrices $\hat{\Sigma}^{\alpha\alpha'}$, $\hat{V}$, and $\hat{K}^{\alpha\alpha'}$ standing side by side.

To calculate $\hat{\Sigma}$ to the first order in the reciprocal radius of the exchange interaction, it is necessary to account for diagrams that contain no more than one loop [14]. We restrict ourselves to diagrams without loops with respect to the interaction *I* and to one-loop diagrams with respect to the exchange interaction *J* in $\hat{\Sigma}$. These approximations take into account spin waves in a granule and collective excitations of the granule spin and electrons of the matrix (polarized spin excitations). For $\alpha = -$ and $\alpha' = +$, the corresponding bare interaction lines and self-energy diagrams are shown in Figs. 1a and 1b in terms of the eigenfunctions $\varphi_\lambda^{(p)}(\mathbf{r})$ from Eq. (2). The *s*–*d* exchange interaction in $\varphi_\lambda^{(p)}(\mathbf{r})$ representation is approximated by

$$J(p, \lambda, \mathbf{1}) = \int \varphi_\lambda^{(p)*}(\mathbf{r}) J(\mathbf{r} - \mathbf{1}) \varphi_\lambda^{(p)}(\mathbf{r}) d\mathbf{r}.$$

Here, we disregard the transitions between the (p, λ) and (p', λ') levels that can be induced by the *s*–*d* exchange interaction through the terms $\int \varphi_{\lambda'}^{(p')*}(\mathbf{r}) J(\mathbf{r} - \mathbf{1}) \varphi_\lambda^{(p)}(\mathbf{r}) d\mathbf{r}$, with $\lambda \neq \lambda'$ and $p \neq p'$.

The Dyson equation (10) for $\alpha = -$ and $\alpha' = +$ in the chosen approximation is written in the form

$$\begin{aligned} K_{dd}^{(1)-+} &= \Sigma_{dd}^{(0)-+} + \Sigma_{dd}^{(0)-+} V_{dd} K_{dd}^{(1)-+} + \Sigma_{dd}^{(0)-+} V_{ds} K_{sd}^{(1)-+}, \\ K_{sd}^{(1)-+} &= \Sigma_{ss}^{(1)-+} V_{sd} K_{dd}^{(1)-+}, \\ K_{ds}^{(1)-+} &= \Sigma_{dd}^{(0)-+} V_{dd} K_{ds}^{(1)-+} + \Sigma_{dd}^{(0)-+} V_{ds} K_{ss}^{(1)-+}, \\ K_{ss}^{(1)-+} &= \Sigma_{ss}^{(1)-+} + \Sigma_{ss}^{(1)-+} V_{sd} K_{ds}^{(1)-+}. \end{aligned} \tag{11}$$

When the interactions V_{sd} and V_{ds} are nonzero, the spins of the *s* system are polarized by the *d* system and, vice versa, the electrons of the *s* system affect the spins of the *d* system. From Eq. (11), we obtain an integral equation for the spin Green's function describing spin excitations of the granular structure (Fig. 1c):

$$\begin{aligned} K_{dd}^{(1)-+}(\mathbf{1}, \mathbf{1}', \omega_n) &= \Sigma_{dd}^{(0)-+}(\mathbf{1}, \mathbf{1}', \omega_n) + \sum_{\mathbf{2}, \mathbf{3}} \Sigma_{dd}^{(0)-+}(\mathbf{1}, \mathbf{2}, \omega_n) \\ &\times \left[\frac{1}{2} \beta I(\mathbf{2} - \mathbf{3}) + \beta^2 \sum_{p, p', \lambda, \lambda'} J(p, \lambda, \mathbf{2}) \right. \\ &\left. \times \Sigma_{ss}^{(1)-+}(p, p', \lambda, \lambda', \omega_n) J(p', \lambda', \mathbf{3}) \right] K_{dd}^{(1)-+}(\mathbf{3}, \mathbf{1}', \omega_n), \end{aligned} \tag{12}$$

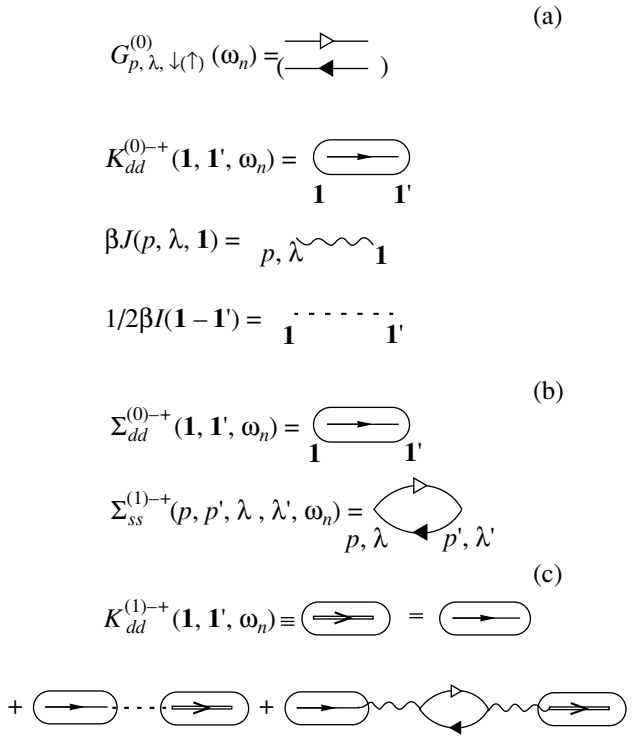

Fig. 1. (a) Bare Green's functions and the interaction lines, (b) self-energy diagrams corresponding to spin waves and polarized spin excitations, and (c) the equation describing spin excitations.

where

$$\Sigma_{dd}^{(0)-+}(\mathbf{1}, \mathbf{2}, \omega_n) = K_{dd}^{(0)-+}(\mathbf{1}, \mathbf{2}, \omega_n),$$

$$\begin{aligned} \Sigma_{ss}^{(1)-+}(p, p', \lambda, \lambda', \omega_n) &= -\delta_{pp'}\delta_{\lambda\lambda'} \\ &\times \sum_m G_{p,\lambda,\downarrow}^{(0)}(\omega_m) G_{p,\lambda,\uparrow}^{(0)}(\omega_m - \omega_n) \\ &= -\delta_{pp'}\delta_{\lambda\lambda'} \frac{n_F(\varepsilon_{\lambda,\uparrow}^{(p)}) - n_F(\varepsilon_{\lambda,\downarrow}^{(p)})}{\beta(i\hbar\omega_n - \varepsilon_{\lambda,\downarrow}^{(p)} + \varepsilon_{\lambda,\uparrow}^{(p)})}, \end{aligned}$$

$$n_F(x) = (e^x + 1)^{-1}.$$

3. SPIN EXCITATIONS IN THE GRANULAR STRUCTURE

We will solve Eq. (12) in the case when the exchange interaction between the spins of a granule is considerably stronger than the exchange interaction between a granule spin and electrons of the matrix ($I \gg J$). In this case, the spin excitation spectrum is divided into two parts: spin-wave excitations in a granule and collective excitations of a granule spin and electrons of the matrix, i.e., polarized spin excitations. In polarized spin excitations, the change in the granule spin direction is

accompanied by changes in the polarization of the neighboring localized electrons of the matrix.

3.1. Spin-Wave Excitations in Granules

We neglect the interaction J and convert the sum over the granule crystal lattice sites into an integral. Then, going over to the Fourier transform of $I(\mathbf{r}-\mathbf{r}')$ with respect to the spatial variables, Eq. (12) can be written in the form of an integral equation:

$$K_{dd}^{(1)-+}(\mathbf{r},\mathbf{r}',\omega_n) = K^{(0)}(\mathbf{r},\omega_n)\delta(\mathbf{r}-\mathbf{r}') + AK_{dd}^{(1)-+}(\mathbf{r},\mathbf{r}',\omega_n), \quad (13)$$

where

$$AK_{dd}^{(1)-+}(\mathbf{r},\mathbf{r}',\omega_n) = \frac{1}{(2\pi)^3}\iint a(\mathbf{r},\mathbf{r}'',\mathbf{q},\omega_n) \times \exp[i\mathbf{q}(\mathbf{r}-\mathbf{r}'')]K_{dd}^{(1)-+}(\mathbf{r}'',\mathbf{r}',\omega_n)d\mathbf{r}''d\mathbf{q},$$

$a(\mathbf{r},\mathbf{r}'',\mathbf{q},\omega_n) = \frac{1}{2}\beta K^{(0)}(\mathbf{r},\omega_n)I(\mathbf{q})\theta(\mathbf{r})\theta(\mathbf{r}'')$, and $I(\mathbf{q})$ is the Fourier transform of the interaction $I(\mathbf{r}-\mathbf{r}')$; $\theta(\mathbf{r}) = 1$ in the granule bulk and $\theta(\mathbf{r}) = 0$ outside the granule. Since the exchange interaction between the granule spins is a short-range interaction, we can restrict ourselves to the Fourier transform calculated to the second order in q:

$$I(\mathbf{q}) = I(0) - \kappa q^2.$$

In this approximation, the integral operator A in Eq. (13) is a second-order pseudodifferential operator [15] and Eq. (13) is reduced to a boundary-value problem. The spin-wave spectrum is determined by the poles of the spin Green's function obtained through analytic continuation $i\omega_n \longrightarrow \omega + i\delta\,\mathrm{sgn}\,\omega$ ($\delta \longrightarrow +0$). This is equivalent to solving an eigenvalue problem, i.e., to finding the distribution functions of the spin oscillations $\chi(\mathbf{r},\mathbf{q})$ in the granule:

$$(1-A)\chi(\mathbf{r},\mathbf{q}) = 0. \quad (14)$$

Assuming that the average magnetization in the granule is the same everywhere over the volume, i.e., $\langle S_1^z\rangle_0 = \langle S^z\rangle_0$, Eq. (14) in the granule bulk takes the form

$$\left[-\hbar\omega + g\mu_B H - \kappa\langle S^z\rangle_0\sum_{i=1}^{3}\partial^2/\partial r_i^2\right]\chi(\mathbf{r},\mathbf{q}) = 0.$$

The eigenvalues of Eq. (14) define the energy spectrum of stationary spin waves in the granule:

$$\varepsilon_{sw}(\mathbf{q}) = g\mu_B H + \langle S^z\rangle_0\kappa q^2, \quad (15)$$

where $q^2 \propto (\pi\mathbf{k}/d)^2$, d is the granule diameter, and $\mathbf{k} = (k_1, k_2, k_3)$ is a vector with integer components ($k_i = 0, 1, 2, \ldots$). The spin-wave spectrum given by Eq. (15) is limited from above by the energy excitation of a Stoner electron pair in the granule.

3.2. Polarized Spin Excitations

Now, we consider the case where Eq. (12) contains a term involving $\Sigma_{ss}^{(1)-+}$ and J; this term describes the interaction of the granule spins with electrons of the matrix:

$$K_{dd}^{(1)-+}(\mathbf{r},\mathbf{r}',\omega_n) = K^{(0)}(\mathbf{r},\omega_n)\delta(\mathbf{r}-\mathbf{r}') + (A+B)K_{dd}^{(1)-+}(\mathbf{r},\mathbf{r}',\omega_n), \quad (16)$$

where

$$BK_{dd}^{(1)-+}(\mathbf{r},\mathbf{r}',\omega_n) = \beta^2 K^{(0)}(\mathbf{r},\omega_n)\theta(\mathbf{r}) \times \sum_{p,\lambda}\frac{1}{V_a}\int_V J(p,\lambda,\mathbf{r})\Sigma_{ss}^{(1)-+}(p,p',\lambda,\lambda',\omega_n) \times J(p,\lambda,\mathbf{r}'')K_{dd}^{(1)-+}(\mathbf{r}'',\mathbf{r}',\omega_n)d\mathbf{r}'',$$

V_a is the granule unit-cell volume, and integration is performed over the granule volume V.

Since the pseudodifferential operator A is elliptic in the granule volume and $J \ll I$, one can divide Eq. (16) by A [15] and find the first several terms of the expansion in B/A. Performing the analytic continuation $i\omega_n \longrightarrow \omega + i\delta\,\mathrm{sgn}\,\omega$ and using the eigenfunctions of Eq. (14), we find that the spin-excitation spectrum in the first-order approximation in B/A is determined by the equation

$$\int_V \chi^*(\mathbf{r},\mathbf{q})(1-A-B)\chi(\mathbf{r},\mathbf{q})d\mathbf{r} = 0.$$

Neglecting the dependence of $\langle S_1^z\rangle_0$ on the spatial variable, we obtain

$$\hbar\omega = \varepsilon_{sw}(\mathbf{q}) + 2\sum_{p,\lambda} m_\lambda^{(p)}\left\{J(p,\lambda,\mathbf{q}) + \frac{2\langle S^z\rangle_0}{\hbar\omega - E_\lambda^{(p)}}|J(p,\lambda,\mathbf{q})|^2\right\}, \quad (17)$$

where $m_\lambda^{(p)} = (1/2)[n_F(\varepsilon_{\lambda,\uparrow}^{(p)}) - n_F(\varepsilon_{\lambda,\downarrow}^{(p)})]$ is the average spin of an electron at level λ of the localized state p, $J(p,\lambda,\mathbf{q}) = \int_V J(p,\lambda,\mathbf{r})\chi(\mathbf{r},\mathbf{q})d\mathbf{r}$, and $E_\lambda^{(p)} = \varepsilon_{\lambda,\downarrow}^{(p)} - \varepsilon_{\lambda,\uparrow}^{(p)} = g\mu_B H + 2\sum_{\mathbf{1}} J(p,\lambda,\mathbf{1})\langle S_1^z\rangle_0$.

If we take into account N levels (p,λ), then Eq. (17) will have $N+1$ roots for a fixed value of $\varepsilon_{sw}(\mathbf{q})$. The function $K_{dd}^{(1)-+}$ in Eq. (11) acquires N additional poles, which correspond to collective one-particle excitations

in the d and s systems. The same poles occur in the functions $K_{sd}^{(1)-+}$, $K_{ds}^{(1)-+}$, and $K_{ss}^{(1)-+}$. When $E_\lambda^{(p)} \ll kT$, the average electron spin is much less than the average granule spin ($m_\lambda^{(p)} \ll \langle S^z \rangle_0$) and the N roots of Eq. (17) will be close in value to the splitting values of the (p, λ) levels:

$$\hbar\omega_\lambda^{(p)}(\mathbf{q}) = E_\lambda^{(p)} + O(m_\lambda^{(p)}/\langle S^z \rangle_0).$$

When $\omega \longrightarrow \omega_\lambda^{(p)}(\mathbf{q})$, a change in the granule spin directions $\langle S^z \rangle_0$ will be accompanied by the transition of an electron between the spin sublevels $(p, \lambda, \uparrow)$ and $(p, \lambda, \downarrow)$ in the matrix and by a change in the (p, λ) level polarization. This gives grounds to refer to these excitations as polarized spin excitations. The upper limit of the frequency range of polarized spin excitations is determined by the strength of the s–d exchange interaction between the granule spins and an electron at the (p, λ) level in the case when the electron in the localized state p is near the granule boundary ∂V:

$$0 < \hbar\omega_\lambda^{(p)}(\mathbf{q}) - g\mu_B H < 2\sum_{\mathbf{1}} J(p, \lambda, \mathbf{1})\langle \mathbf{S}_\mathbf{1}^z \rangle_0\big|_{\partial V}. \quad (18)$$

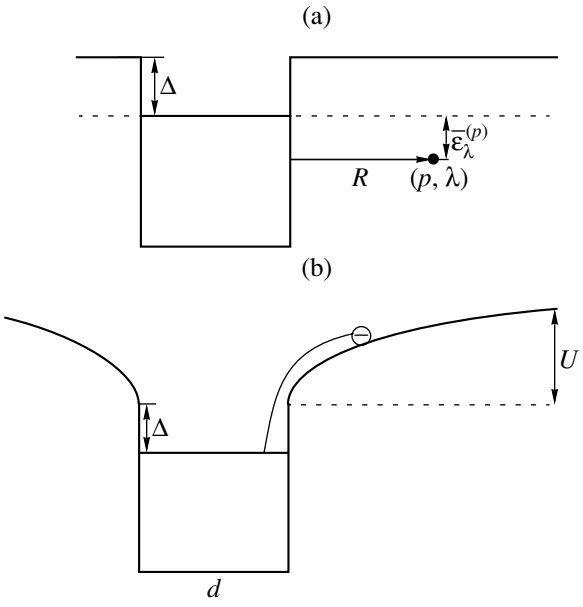

Fig. 2. (a) Position of a localized deep-energy state with respect to the Fermi level in the granule, and (b) the energy structure change due to excitation of an electron from the granule.

4. RELAXATION OF SPIN EXCITATIONS

Now, we study the relaxation of spin excitations in the granular structure. We write Eq. (16) for $K_{dd}^{(1)-+}(\mathbf{r}, \mathbf{r}', \omega_n)$ in terms of the granule spin-oscillation functions $\chi(\mathbf{r}, \mathbf{q})$. Then, the decay constant of spin excitations γ is determined by the imaginary part of the pole of the Green's function:

$$K_{dd}^{(1)-+}(\mathbf{q}, \omega_n)\delta(\mathbf{q} - \mathbf{q}')$$
$$= \iint_{VV} \chi^*(\mathbf{r}, \mathbf{q}) K_{dd}^{(1)-+}(\mathbf{r}, \mathbf{r}', \omega_n)\chi(\mathbf{r}', \mathbf{q}')d\mathbf{r}d\mathbf{r}',$$

which, after analytic continuation $i\omega_n \longrightarrow \omega + i\delta\,\mathrm{sgn}\,\omega$, is equal to

$$\mathrm{Im}\int_V \chi^*(\mathbf{r}, \mathbf{q})(1 - A - B)\chi(\mathbf{r}, \mathbf{q})d\mathbf{r}\big|_{i\omega_n \to \omega + i\delta\mathrm{sgn}\omega}.$$

Substituting the explicit expressions for the A and B operators, we obtain

$$\hbar\gamma(\omega, \mathbf{q}) = 2\beta\langle S^z \rangle_0 \sum_{p, \lambda} |J(p, \lambda, \mathbf{q})|^2$$
$$\times \mathrm{Im}\Sigma_{ss}^{(1)-+}(p, p, \lambda, \lambda, \omega_n)\big|_{i\omega_n \to \omega + i\delta\mathrm{sgn}\omega} \quad (19)$$
$$= 4\pi\langle S^z \rangle_0 \sum_{p, \lambda} |J(p, \lambda, \mathbf{q})|^2 m_\lambda^{(p)} \delta(\hbar\omega - E_\lambda^{(p)}).$$

We consider the relaxation of uniform granule spin excitations, i.e., the relaxation at small q values. In this case, due to the condition $J \ll I$, the decay of the granule spin excitations is determined by polarized spin excitations, in which the change in the granule spin direction occurs simultaneously with a spin flip transition of an electron in the matrix from one sublevel of the spin-split state (p, λ) to the other. The electronic states involved in these transitions can be localized deep energy states in the matrix (Fig. 2a) or states that are created through thermal excitation of electrons from the granule to the conduction band of the matrix (Fig. 2b). We study the decay of spin excitations in both these cases.

4.1. Relaxation due to Electron Transitions between Sublevels of Deep Localized States in the Matrix

To obtain an explicit expression describing relaxation in the granular structure, we make a number of assumptions.

(1) We assume that the energy distribution and spatial position of the localized states p in the granular structure can be characterized by the density of states per unit volume $\bar{g}(\bar{\varepsilon}_\lambda^{(p)}, \mathbf{r})$. The introduction of this quantity allows one to pass over from relaxation of spin excitations of a granule [Eq. (19)] to relaxation of spin excitations in the granular structure and to take an average over all granules. In this case, the sum over p and λ in Eq. (19) is converted into an integral over the matrix volume and the energies of the localized states weighted by $\bar{g}(\varepsilon, \mathbf{r})$. Because of the presence of the fac-

tor $m_\lambda^{(p)}$ in Eq. (19), the main contribution to the relaxation comes from the localized states with energies in a range $2kT$ wide near the Fermi level. We assume that the energy levels are uniformly distributed over this energy range and that the spatial distribution is also uniform; that is, the density $\bar{g}(\varepsilon, \mathbf{r}) = \bar{g} = \text{const}$.

(2) The exchange integral in Eq. (19) involves integration over the granule volume V and the matrix volume:

$$J(p, \lambda, \mathbf{q}) = \int_V d\mathbf{r}' \int d\mathbf{r} \varphi_\lambda^{(p)*}(\mathbf{r}) \times J(\mathbf{r} - \mathbf{r}') \varphi_\lambda^{(p)}(\mathbf{r}) \chi(\mathbf{r}', \mathbf{q}). \quad (20)$$

If the wave functions $\varphi_\lambda^{(p)}$ of the localized states are hydrogen-like [16], then, because of the short-range character of the interaction $J(\mathbf{r} - \mathbf{r}')$, the functions $J(p, \lambda, \mathbf{q})$ at $\mathbf{q} \longrightarrow 0$ decrease exponentially with distance:

$$J(p, \lambda, \mathbf{q}) = J_0 \exp(-\xi_\lambda^{(p)} R),$$

where $\xi_\lambda^{(p)}$ is the reciprocal radius of interaction of the granule spin with (p, λ) localized state and R is the distance from the center of the p hydrogen-like state to the granule boundary. In averaging over all energy levels of the N localized states, we assume that $J(p, \lambda, \mathbf{q})$ exponentially decreases with distance and that its decrease is characterized by an effective reciprocal radius $\xi = N^{-1} \sum_{p, \lambda} \xi_\lambda^{(p)}$.

(3) We will consider the case when the distance between the granules is $l \gg \zeta^{-1}$. Therefore, we can neglect the interaction between the granules and extend the upper limit of integration over the spatial variable in the matrix to infinity. We assume that the spacing between the bottom of the conduction band in the matrix and the Fermi level in the metallic particle is large, $\Delta \gg kT$ (Fig. 2a). Therefore, the upper limit of integration over the energy of the localized states can be extended to infinity. In this case, we will refer to the localized states with energies in a range $2kT$ wide near the Fermi level as deep energy states.

Under the above assumptions, the decay constant of spin excitations in the granular structure in the frequency range $0 < \hbar\omega - g\omega_B H < 2J_0 \langle S^z \rangle_0$ is given by

$$\hbar\gamma(\omega) = 2\pi \langle S^z \rangle_0 \int_{-\infty}^{\infty} d\varepsilon \int_0^\infty dr 4\pi r^2 \bar{g} J_0^2 \exp(-2\xi r) \times \left\{ \frac{1}{\exp[\beta(\varepsilon - E/2)] + 1} - \frac{1}{\exp[\beta(\varepsilon + E/2)] + 1} \right\} \quad (21)$$

$$\times \delta(\hbar\omega - E) = \frac{2\pi^2 \bar{g}(\hbar\omega - g\mu_B H)\hbar\omega}{\xi^3 \langle S^z \rangle_0} \ln^2 \frac{2J_0 \langle S^z \rangle_0}{\hbar\omega - g\mu_B H},$$

where $E = 2\langle S^z \rangle_0 J_0 \exp(-\xi r) + g\mu_B H$. For $\hbar\omega < g\mu_B H$ and $\hbar\omega > g\mu_B H + 2\langle S^z \rangle_0 J_0$, the decay constant is equal to zero. The ratio of the decay constant to the frequency is maximum at $\hbar\omega = g\mu_B H + 2\exp(-2)\langle S^z \rangle_0 J_0$, with the maximum being equal to

$$\max \frac{\gamma}{\omega} = \frac{16\pi^2 \bar{g} J_0}{\exp(2)\xi^3}.$$

As can be seen from Eq. (21), the decay constant determined by electron spin-flip transitions between the sublevels of the deep localized states in the matrix does not depend on temperature.

4.2. Relaxation due to Transitions between the Sublevels of a Thermally Excited Electron from the Granule

Let us consider the energy structure of a granule in the matrix in the case when the Fermi level of the metallic granule is located below the bottom of the conduction band of the matrix by an energy value Δ. Due to thermal activation, electrons overcome the energy barrier Δ and the granule acquires a charge which is equal to the total charge of the electrons leaving the granule. We assume that the granule has a spherical form with diameter d. Then, removing Z electrons from the granule will result in a decrease in the granule energy by $U = Ze^2/2C$ (Fig. 2b), where e is the electron charge and $C = \tilde{\varepsilon} d/2$ is the capacity of the granule in the matrix with dielectric permittivity $\tilde{\varepsilon}$. Some of the thermally activated electrons do not spread over infinitively large distances from the granule but instead form an electron cloud around the granule. The wave functions of the electrons in the cloud are determined by the Coulomb field of the granule; we will consider them to be hydrogen-like. Since the exchange interaction has approximately a contact character, namely, $J(\mathbf{r} - \mathbf{1}) \propto \delta(\mathbf{r} - \mathbf{1})$, we will allow for only the hydrogen-like s states among all (p, λ) levels of the cloud [16] whose wave functions are

$$\varphi_n(\mathbf{r}) = \pi^{-1/2} \left(\frac{Z}{n} \right)^{3/2} F(-n + 1, 2, 2Z\rho/n) \exp(-Z\rho/n),$$

where $\rho = me^2|\mathbf{r}|/\hbar^2$, m is the electron mass, F is the degenerated hypergeometric function, and the index (p, λ) is reduced to the index n. The function $J(p, \lambda, \mathbf{q}) = J(n, \mathbf{q})$ in Eqs. (19) and (20) is defined as an integral over the granule and the matrix volume. For the hydrogen-like s states, at large values of n and $\mathbf{q} \longrightarrow 0$, the main contribution comes from terms that can be written as

$$J(n, 0) = \frac{J_0 Z^3}{\pi n^3} + O(n^{-4}). \quad (22)$$

We convert the sum in Eq. (19) into an integral and take into account Eq. (22) to an accuracy of the order $O(n^{-4})$. Substituting $E_\lambda^{(p)} = E_n = \varepsilon_{n,\downarrow} - \varepsilon_{n,\uparrow} = g\mu_B H +$

$2J(n, 0)\langle S^z\rangle_0$ into Eq. (19), we write the decay constant of spin excitations at $\hbar\omega > g\mu_B H$ in the form

$$\hbar\gamma(\omega) = \frac{\pi(\hbar\omega - g\mu_B H)^2}{2\langle S^z\rangle_0}\sum_n\left\{\frac{1}{\exp[\beta(\Delta + f_n)] + 1}\right.$$
$$\left. - \frac{1}{\exp[\beta(\Delta + f_n + \hbar\omega)] + 1}\right\}\delta(\hbar\omega - E_n)$$
$$= \frac{\pi^{2/3} J_0 Z[\exp(\beta\hbar\omega) - 1]}{3[\exp(-\beta(\Delta + f)) + 1][\exp(\beta(\Delta + f + \hbar\omega)) + 1]} \quad (23)$$
$$\times\left(\frac{\hbar\omega - g\mu_B H}{2J_0\langle S^z\rangle_0}\right)^{2/3},$$

where $f_n = U - \zeta/n^2$ is the energy of an electron excited to the state n, reckoned from the conduction band bottom near the granule boundary; $\zeta = mZ^2e^4/2\hbar^2$; and

$$f = U - \frac{\zeta}{Z^2}\left[\frac{\pi(\hbar\omega - g\mu_B H)}{2J_0\langle S^z\rangle_0}\right]^{2/3}.$$

In deriving Eq. (23), we allowed for n values for which the energy f_n and, hence, f have positive values. This approximation is equivalent to an indirect account of the granule size. The condition $\hbar\omega = g\mu_B H$, or $f = U$ determines the lower limit for the decay constant. When $\hbar\omega < g\mu_B H$, the decay constant is equal to zero. The upper limit for the decay constant is determined by the condition $f = 0$:

$$\hbar\omega \le g\mu_B H + \left(\frac{U}{\zeta}\right)^{3/2}\frac{Z^3 J_0\langle S^z\rangle_0}{\pi}.$$

As can be seen from Eq. (23), the decay (relaxation) constant γ depends heavily on temperature.

5. RESULTS AND DISCUSSION

As can be seen from Eqs. (21) and (23), the decay of spin excitations in the granular structure is determined by the spacing Δbetween the Fermi level in the granule and the conduction band bottom in the matrix. Experimental investigations on damping have been carried out on granular structures of amorphous hydrogenated carbon a-C : H with Co nanoparticles and on amorphous SiO_2 with $Co_{86}Nb_{12}Ta_2$ granules [9–11]. Those studies verified the character of the temperature dependences of the decay constant determined from Eqs. (21) and (23). The activation energy $\Delta + U$ for the $(a\text{-C : H})_{1-x}Co_x$ structures with a small Co content x was determined from the temperature dependences of current in the geometry where the current was perpendicular to the plane and was found to be 0.22 eV. Taking into account that the Co particles were 2.0–2.2 nm in size, we estimated the mean capacity of the particles, the electrical energy U, and the energy Δ, which turned out to be small and comparable to the value of kT ($\sim$0.02 eV). For the a-SiO_2 structures with $Co_{86}Nb_{12}Ta_2$ granules, the energy Δ, by contrast, was large, $\Delta \gg kT$.

The decay constant of spin excitations in a granular structure was determined using the spin-wave spectroscopy method [9] on the YIG/(investigated granular film) structures at temperatures 77–393 K. Changes in the group velocity and in the damping of surface magnetostatic spin waves in the YIG film were studied in the frequency range 2.2–4.0 GHz. The coupling between a spin wave propagating in the YIG film and the granular film occurred through magnetic dipole interaction. The relaxation of spin excitations in the granular film resulted in a decrease in the group velocity and in an increase in the spin-wave damping in the YIG film. From these changes, we estimated the relaxation of spin excitations in the granular structure. For $(a\text{-C : H})_{1-x}Co_x$ granular films (250–550 nm thick) at $x < 0.45$, the relaxation drastically increased with increasing temperature. The temperature dependence of relaxation was similar to that given by Eq. (23) [9, 11]; this suggests that the relaxation is due to spin-flip electronic transitions between the sublevels of the thermally activated granule electron cloud. For a-SiO_2 granular films with $Co_{86}Nb_{12}Ta_2$ particles (the film thickness was of 2.7–5.1 μm) with cobalt concentrations of $x < 0.45$, the relaxation of spin excitations virtually did not depend on temperature [10, 11]. This lead to the conclusion that the relaxation of spin excitations in structures with an a-SiO_2 matrix is determined by polarized spin excitations at deeper energy levels of localized states in the matrix and is described by Eq. (21). Let us estimate the decay constant given by Eq. (21). The interatomic exchange interaction for the nearest neighbors is roughly $J_0 = 0.05$–0.10 eV [17, 18]. The density of localized states $\bar{g}$ can be estimated from the conductivity temperature dependences of the granular structure [12]. The temperature dependence in the in-plane-current geometry follows a power law. The index of the power law depends on the number of localized states in the matrix through which the process of inelastic resonant tunneling occurs between the granules in the energy range $2kT$ wide near the Fermi level. For the $(a\text{-C : H})_{1-x}Co_x$ structures, the mean number of localized states in the matrix varies from 1 ($x = 0.46$) to 2 ($x = 0.24$). This makes it possible to estimate $\bar{g}$ in the $2kT$ range. Putting $\bar{g} = 1$ eV^{-1} nm^{-3}, $J_0 = 0.1$ eV, $\langle S^z\rangle_0 = 1/2$, $\xi = 1$ nm^{-1}, $H = 0$, and $\omega/2\pi = 10$ GHz, we obtain $\gamma/\omega = 0.1$. Such high values allow one to explain the large magnitude of magnetic relaxation reported in [9, 11]. The initiation of polarized spin transitions can be responsible for the large ΔH values observed in [5, 6] and high electromagnetic-radiation absorption coefficients of the granular structures.

In [2, 3], an increase in ΔH with decreasing Fe concentration was observed. The model proposed above allows one to explain this effect. The relaxation observed in [2, 3] at frequencies of 9.4 and 35.4 GHz is

due to splitting of the levels disposed far away from the granules. With decreasing granule concentration, the density of such localized states (with a small amount of splitting) increases. The magnetic field H produced by the granules causes an additional increase in the splitting of the localized states. With decreasing granule concentration, the field H decreases. According to Eq. (21), these two factors cause the damping to increase.

The damping due to polarized spin excitations [see Eq. (21)] is characterized by a wide-range spectrum. The maximum damping is equal to

$$\hbar\omega_{max} = g\mu_B H + 2J_0\langle S^z\rangle_0.$$

In real granular structures, the demagnetizing magnetic field produced by the neighboring granules contributes to the field H. Taking, as an example, structures with cobalt granules and accounting for the fact that the demagnetizing field near the granule is determined by the magnetization ($4\pi M \propto 17.9$ kOe [13]), for $H = 4\pi M$, $J_0 = 0.1$ eV, and $\langle S^z\rangle_0 = 1/2$, we find that $\omega_{max}/2\pi = 25$ THz. Thus, we can conclude that, using structures with cobalt granules, one can create films that absorb electromagnetic radiation in the centimetric, millimetric, and submillimetric wavelength ranges. Estimates show that a granular structure with Co granules provides significantly more effective absorption (per unit volume) than ferrite films.

6. CONCLUSIONS

Our results obtained within the theoretical model constructed in this paper allow the following conclusions to be drawn:

(1) The spin excitation spectrum of a granular structure with ferromagnetic metallic nanoparticles embedded in an amorphous matrix consists of granule spin-wave excitations and polarized spin excitations. In polarized spin excitations, the change in the granule spin direction is accompanied by a transition of an electron between two sublevels of a split localized state in the matrix and by a change in the polarization of this localized state.

(2) The localized electron states in the matrix can be either deep energy levels or thermally activated states of the granule electron cloud. In the first case, the spin relaxation process in the granules, which occurs through polarized spin excitations (polarized spin relaxation), does not depend on temperature. In the second case, a strong temperature dependence is observed.

(3) Polarized spin relaxation can be observed over a wide frequency range. Estimates for granular structures with cobalt nanoparticles showed that polarized spin relaxation can occur in the centimetric, millimetric, and submillimetric wavelength ranges.

ACKNOWLEDGMENTS

The author is grateful to Yu.M. Yakovlev for useful discussions and remarks.

This study was supported by the Russian Foundation for Basic Research, project no. 99-02-17071a.

REFERENCES

1. S. Mitani, K. Takanashi, K. Yakushiji, and H. Fujimori, J. Appl. Phys. **83** (11), 6524 (1998).
2. Wen-Nai Wang, Zheng-Sheng Jiang, and You-Wei Du, J. Appl. Phys. **78** (11), 6679 (1995).
3. A. Butera, J. N. Zhou, and J. A. Barnard, Phys. Rev. B **60** (17), 12270 (1999).
4. A. Butera, J. N. Zhou, and J. A. Barnard, J. Appl. Phys. **87** (9), 5627 (2000).
5. D. M. S. Bagguley, Proc. Phys. Soc. London, Sect. A **66** (404A), 765 (1953).
6. D. M. S. Bagguley, Proc. R. Soc. London, Ser. A **228**, 549 (1955).
7. Yu. I. Petrov, *Clusters and Small Particles* (Nauka, Moscow, 1986).
8. J. R. Fermin, A. Azevedo, F. M. de Aguiar, *et al.*, J. Appl. Phys. **85** (10), 7316 (1999).
9. L. V. Lutsev and S. V. Yakovlev, in *Proceedings of the XVII International School-Workshop "Novel Magnetic Materials for Microelectronics," Moscow, 2000*, p. 524.
10. L. V. Lutsev, S. V. Yakovlev, Yu. E. Kalinin, *et al.*, in *Proceedings of the XVII International School-Workshop "Novel Magnetic Materials for Microelectronics," Moscow, 2000*, p. 544.
11. L. V. Lutsev, S. V. Yakovlev, Yu. E. Kalinin, *et al.*, in *Proceedings of the II International Conference "Amorphous and Microcrystalline Semiconductors," St. Petersburg, 2000*, p. 77.
12. L. V. Lutsev, T. K. Zvonareva, and V. M. Lebedev, Pis'ma Zh. Tekh. Fiz. **27** (15), 84 (2001) [Tech. Phys. Lett. **27**, 659 (2001)].
13. A. G. Gurevich and G. A. Melkov, *Magnetic Oscillations and Waves* (Nauka, Moscow, 1994).
14. Yu. A. Izyumov, F. A. Kassan-ogly, and Yu. N. Skryabin, *Field Methods in Theory of Ferromagnetism* (Nauka, Moscow, 1974).
15. F. Treves, *Introduction to Pseudodifferential and Fourier Integral Operators* (Plenum, New York, 1980; Mir, Moscow, 1984), Vol. 1.
16. A. S. Davydov, *Quantum Mechanics* (Nauka, Moscow, 1973; Pergamon, Oxford, 1976).
17. S. V. Vonsovskiĭ, *Magnetism* (Nauka, Moscow, 1971; Wiley, New York, 1974).
18. E. V. Kuz'min, G. A. Petrakovskiĭ, and É. A. Zavadskiĭ, *Physics of Magnetically Ordered Materials* (Nauka, Novosibirsk, 1976).

Translated by N. Kovaleva

Physics of the Solid State, Vol. 44, No. 1, 2002, pp. 111–116. Translated from Fizika Tverdogo Tela, Vol. 44, No. 1, 2002, pp. 106–111.

MAGNETISM AND FERROELECTRICITY

Stability of the One-Dimensional Precession Regime of a Domain Wall under a DC Magnetic Field in a Uniaxial Ferromagnet

G. E. Khodenkov

Institute of Electronic Control Machines, ul. Vavilova 24, Moscow, 117812 Russia

Received May 14, 2001

Abstract—The conditions for parametric excitation of flexural vibrations of a domain wall (DW) are determined in the case where the DW moves under the action of a uniform dc magnetic field whose strength exceeds the Walker critical value (in the spin precession regime). Vibrations are excited when uniform precession caused by the magnetic field during DW translational motion breaks down. Using numerical methods, it is shown that steady-state large-amplitude vibrations can occur and that these vibrations significantly affect the average DW velocity © *2002 MAIK "Nauka/Interperiodica".*

1. INTRODUCTION

The nonlinear dynamics of a domain wall (DW) in an external dc uniform magnetic field is characterized by two fundamentally different regimes. If the strength of the applied field is lower than a certain critical value, then the steady-state regime is stable; in this regime, the DW moves translationally and its internal structure does not change. As the field strength exceeds the critical value, the steady-state regime becomes unstable: spin precession occurs in the DW plane, and transverse (flexural) distortions and/or other changes are developed. At the present time, the steady-state regimes are the best theoretically studied regimes; the spin precession regimes are more complicated, and they and their stability have not been well investigated.

Investigation of the latter regimes is not only of academic interest; in many cases, spin precession occurs in weak fields, whose strength lies in the field range of practical importance. For example, for a one-dimensional 180° Bloch wall in a uniaxial ferromagnet, in the (most extensively studied) case where the DW plane contains the easy magnetization axis, the corresponding critical field strength H_W (Walker field, see [1] and references therein) is equal to $2\pi M\alpha$ (M is the magnetization, α is the dimensionless Gilbert damping parameter), which is equal to a few oersteds. If the DW plane is perpendicular to the easy axis, the critical field vanishes altogether and spin precession always occurs in such a DW [2] (this less well-understood case was investigated experimentally in [3]). It should also be mentioned that H_W may have greater values for fields in the basal plane [4] and that there are magnets (primarily, rare-earth orthoferrites) in which the DW motion remains stationary even in very high fields (a few kilogauss) [5–7].

In finite samples, the initial DW structure is not one-dimensional and the DW dynamics is more complicated. As a rule, even the determination of the ground state of such DWs (to say nothing of the investigation of its stability) is an intricate numerical problem. In this case, the DW dynamics is also characterized by the two regimes mentioned above, but the critical fields can differ significantly from their values in the one-dimensional case and the spin precession regimes may vary more widely (for example, chaotic motion can occur [8, 9]). Here, the best understood cases are the twisted DW [4] and the vortex DW (see, e.g., [10, 11]), which are formed in perpendicularly and in-plane magnetized films, respectively.

In this paper, we consider the simple case of a 180° DW in a uniaxial ferromagnet with a quality factor $Q \equiv H_a/4\pi M > 1$ (H_a is the uniaxial-anisotropy field). The one-dimensional precession regime in a uniform dc magnetic field $H > H_W$ has been well studied for this type of DW [4, 12]. We investigate the stability of this DW with respect to transverse small-amplitude distortions localized in the DW plane, i.e., with respect to flexural vibrations. The one-dimensional regime becomes unstable if the field strength and the wavenumber of the flexural vibration mode are in the ranges where parametric excitation occurs. It is shown in this paper, that these ranges depend critically on the damping parameter α. Due to the nonlinear mechanism, the DW spin precession under a dc magnetic field gives rise to parametric excitation of pairs of surface magnons. Numerical nonlinear simulations show that the parametric amplification can be significant. It should be noted that, although the parametric resonance of flexural DW vibrations has been being investigated for a relatively long time (one of the first publications on this subject is [3]), only ac external magnetic fields have been used for resonant excitation.

1063-7834/02/4401-0111$22.00 © 2002 MAIK "Nauka/Interperiodica"

In this paper, we also consider the influence of flexural vibrations excited parametrically by uniform spin precession on the average DW velocity. This mechanism was proposed in [14, 15], where order-of-magnitude estimates of the effect were made. Using numerical methods, we show in this paper that this mechanism can be highly efficient in the case of low damping ($\alpha \ll 1$).

2. LINEARIZED STABILITY EQUATIONS AND PARAMETRIC EXCITATION

Flexural vibrations of the 180° DW are a spatial modification of its lowest energy (translational) mode. In uniaxial ferromagnets with quality factors $Q \gg 1$, the corresponding frequencies lie below the ferromagnetic resonance frequency. In an approximation where terms of the order of $1/Q$ are neglected, the coordinate along the normal to the DW plane can be eliminated and, therefore, the spatial dimensionality of the problem is lowered. In this case, the DW dynamics is described by the Slonczewski equations [4, 12], which take into account only the translational mode in the nonlinear approximation. The DW surface $q(x, t)$ and the azimuth angle of the magnetization vector $\psi(x, t)$ at the DW center are governed by the nonlinear set of equations

$$\dot{\psi} - H + \alpha\dot{q} = q'', \tag{1a}$$

$$\dot{q} - \alpha\dot{\psi} = -\psi'' + \sin\psi\cos\psi. \tag{1b}$$

The superscript dots and primes on the dependent variables indicate derivatives with respect to time t and the spatial coordinate x in the DW plane, respectively, and $H > 0$ is a dc external drive magnetic field parallel to the magnetization vector in one of the domains. Equations (1) involve dimensionless variables

$$\begin{aligned} x &\longrightarrow \Lambda x, \quad t \longrightarrow 4\pi\gamma M t, \\ H &\longrightarrow 4\pi M H, \quad q \longrightarrow \Delta q, \end{aligned} \tag{2}$$

where $\Lambda = \sqrt{Q}\,\Delta$ is the width parameter of a Bloch line ($\Delta = \sqrt{A/K}$ is the DW width; A and K are the exchange-stiffness and uniaxial anisotropy constants, respectively; $Q = H_a/4\pi M > 1$; $H_a = 2K/M$ is the effective anisotropy field) and $\gamma > 0$ is the gyromagnetic ratio.

First, we present some known results [1, 4, 12] for one-dimensional DW motion which will be used later. From Eqs. (1), it is seen that if $\dot{q}$ and H do not exceed the Walker limiting values $\dot{q}_W = 1/2$ and $H_W = \alpha/2$, then the translational DW motion is steady: $\dot{q}_0 = H/\alpha$ and $\psi_0 = \arcsin(2\dot{q}_0)/2$. In higher fields, a periodic spin-precession regime is established [12]:

$$\dot{\psi}_0(t) = \omega\cos\psi_H/(1 + \sin\psi_H\sin 2\omega t), \tag{3}$$

$$\cos 2\psi_0(t) = \frac{-(1+\alpha^2)\ddot{\psi}_0(t)}{\alpha\dot{\psi}_0(t)} \equiv \frac{\cos\psi_H\cos 2\omega t}{1 + \sin\psi_H\sin 2\omega t}. \tag{4}$$

Here,

$$\omega = \frac{\sqrt{H^2 - (\alpha/2)^2}}{1+\alpha^2} \tag{5}$$

is the fundamental precession frequency, equal to the time average of the quantity given by Eq. (3); $\overline{\dot{\psi}_0(t)} = \omega$; and $\sin\psi_H = \alpha/2H$ ($0 < \psi_H < \pi/2$). The time dependence of the DW velocity can be found by substituting Eq. (3) into Eq. (1a). Averaging Eqs. (1) over time and using Eqs. (3) and (4), we obtain

$$\omega - H + \alpha\bar{\dot{q}}_0 = 0, \tag{6a}$$

$$\bar{\dot{q}}_0 - \alpha\omega = \overline{\sin\psi_0\cos\psi_0}, \tag{6b}$$

where $\overline{\sin\psi_0\cos\psi_0} = H(1 - \cos\psi_H)/\alpha$ and the average DW velocity $\bar{\dot{q}}_0$ is

$$\bar{\dot{q}}_0 = \frac{H}{\alpha}\left(1 - \frac{\omega}{H}\right). \tag{7}$$

It is interesting that this velocity has a minimum at $H_m = (1 + \alpha^2)/2\sqrt{2+\alpha^2}$; this minimum equals $\bar{\dot{q}} = \alpha\sqrt{2+\alpha^2}/2(1+\alpha^2)$. In high fields, the DW motion becomes simpler:

$$\begin{aligned} q_0(t) &= \frac{\alpha H t}{1+\alpha^2} - \frac{1}{4H}\cos\frac{2Ht}{1+\alpha^2}, \\ \psi_0(t) &= \frac{Ht}{1+\alpha^2} + \frac{\alpha}{4H}\cos\frac{2Ht}{1+\alpha^2}. \end{aligned} \tag{8}$$

We are now in a position to investigate the stability of the various modes of DW motion. Substituting $\psi = \psi_0(t) + \delta\psi(x, t)$ and $q = q_0(x) + \delta q(x, t)$ into Eqs. (1) and expanding the result in powers of small amplitudes $\delta\psi$ and δq about the unperturbed solution, we write the perturbations in the form of plane waves $\delta\psi, \delta q \sim \exp(ikx)$ and obtain the linearized stability equations

$$\delta\dot{\psi} + a\delta\dot{q} = -k^2\delta q, \tag{9a}$$

$$\delta\dot{q} - \alpha\delta\dot{\psi} = k^2\delta\psi + \cos 2\psi_0\delta\psi. \tag{9b}$$

In the steady DW translation regime below the Walker limit H_W, we can put $\delta\psi, \delta q \sim \exp(-i\omega t)$ because $\cos 2\psi_0$ is time-independent. It can be shown that in this case, $\mathrm{Im}(\omega) < 0$; that is, the steady DW motion is stable. We note that above H_W, the spin precession regime is also stable but with respect to perturbations with $k = 0$. Indeed, differentiating Eqs. (1) with respect to time, we find that $\delta\psi = C\dot{\psi}_0(t)$ and $\delta q = -C\dot{\psi}_0(t)/\alpha$, where C is a constant and $\dot{\psi}_0(t)$ is a finite function, as seen from Eq. (3).

In the general case of $k \neq 0$, Eqs. (9) with periodic coefficients are Floquet-type equations and, in the limit of $\alpha \longrightarrow 0$, they are reduced to the Mathieu equation

$$\delta\ddot{\psi} + (a - 2b\cos 2\tau)\delta\psi = 0, \qquad (10)$$

where $\tau = t/H$, $a = k^4/H^2$, and $b = k^2/2H^2$. It is well known that in the (a, b) plane, the boundaries of the regions of parametric instability (specified by index $i = 1, 2, \ldots$) leave the points with coordinates $a_i = 1^2, 2^2, \ldots$ and $b = 0$ and go to the $a < 0$ region as b increases. In the (H, k) plane, these instability regions have the form shown in Fig. 1, where the corresponding periodic solutions (Mathieu functions) are also indicated on the boundaries of these regions. Near the boundary points a_i, the Mathieu functions are closely approximated by the first few harmonics in their expansion into a Fourier series. In the (H, k) plane, these points go to infinity, whereas the intersection points of the boundaries and the b axis go to the origin of coordinates. It is significant that if damping is taken into account in Eq. (10), then the boundary points on the a axis are shifted from this axis by an amount proportional to α. In this case, the regions of parametric instability in the (H, k) plane are limited by maximum values H_M and k_M, which are the higher, the smaller the value of α [see Eq. (15)]. Near these maximum values, the Mathieu functions can be approximated (for small α) by the first few Fourier harmonics; this property will be used in what follows.

Now, we investigate Eqs. (9). For this purpose, we first estimate the relative contribution from the first few harmonics to the expansion of $\cos 2\psi_0(t)$ into a Fourier series:

$$\cos 2\psi_0(t) = a_2\cos 2\omega t + a_6\cos 6\omega t + \ldots + b_4\sin 4\omega t + b_8\sin 8\omega t + \ldots, \qquad (11a)$$

where

$$a_2 = 2\cos\psi_H/(1 + \cos\psi_H) > 0,$$
$$a_6 = -16\cos\psi_H\sin^6(\psi_H/2)/\sin^4\psi_H < 0, \qquad (11b)$$
$$b_4 = -2\cos\psi_H(1 - \cos\psi_H)^2/\sin^3\psi_H < 0.$$

At $H = \alpha/2$, all expansion coefficients vanish. As $H \longrightarrow \infty$, all expansion coefficients also vanish except $a_2 \longrightarrow 1$, which increases monotonically and tends to unity. The higher coefficients are not greater than a_2 (in absolute value) and have extrema in the range of low fields of the order of $\sim\alpha(\ll 1)$. Therefore, for $\alpha \ll 1$ and sufficiently high fields, one can replace $\cos 2\psi_0(t)$ with $a_2\cos 2\omega t$ in Eqs. (9).

From the above discussion, it follows that one can keep only two Fourier harmonics in the solution to Eqs. (9) near the boundaries of the first region of parametric instability:

$$(\delta\psi, \delta q) = (F_1, Q_1)\cos\omega t + (F_2, Q_2)\sin\omega t, \qquad (12)$$

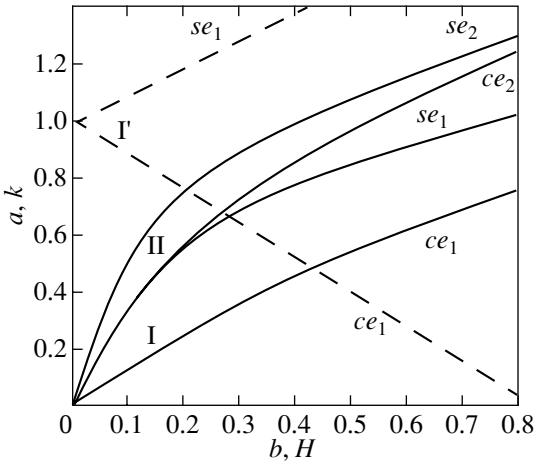

Fig. 1. Parametric instability regions for solutions to the Mathieu equation in the (b, a) plane (region I, bounded by dashed lines) and in the (H, k) plane (regions I and II, bounded by solid curves).

where the amplitudes $F_{1,2}$ and $Q_{1,2}$ are slowly varying functions of time. Substituting Eq. (12) into Eqs. (9) and equating the coefficients of like harmonics on the left- and right-hand sides, we arrive at a set of four differential equations with constant coefficients:

$$\dot{F}_{1,2} \pm \omega F_{2,1} + \alpha(\dot{Q}_{1,2} \pm \omega Q_{2,1}) = -k^2 Q_{1,2},$$
$$\dot{Q}_{1,2} \pm \omega Q_{2,1} - \alpha(\dot{F}_{1,2} \pm \omega F_{2,1}) = k^2 Q_{1,2} \pm \frac{1}{2}a_2 F_{1,2}, \qquad (13)$$

where the frequency ω is given by Eq. (5) and a_2 is given by Eq. (11b). Solutions to Eq. (13) are proportional to $\exp(st)$, and the boundaries of their stability region are defined by the condition $s = 0$. The characteristic equation of Eq. (13),

$$k^8 + 2(-1 + \alpha^2)\omega^2 k^4 - \frac{1}{4}a_2^2(k^4 + \alpha^2\omega^2) + (1 + \alpha^2)^2\omega^4 = 0, \qquad (14)$$

determines the boundaries of region I. It follows from Eq. (14) that, for small α, this region is limited above by

$$H_M \approx 1/4\alpha, \quad k_M \approx 1/2\sqrt{\alpha}, \qquad (15)$$

with its middle width (for $\alpha = 0$) being $\Delta k \approx 1/4\sqrt{H}$ (Fig. 2).

The boundaries of region II can be found in a similar way. However, instead of Eq. (12), one should use the approximation [16]

$$(\delta\psi, \delta q) = (F_0, Q_0) + (F_1, Q_1)\cos 2\omega t + (F_2, Q_2)\sin 2\omega t + (F_3, Q_3)\cos 4\omega t + (F_4, Q_4)\sin 4\omega t. \qquad (16)$$

Solution of the corresponding characteristic tenth-degree equation determines the boundaries of region II

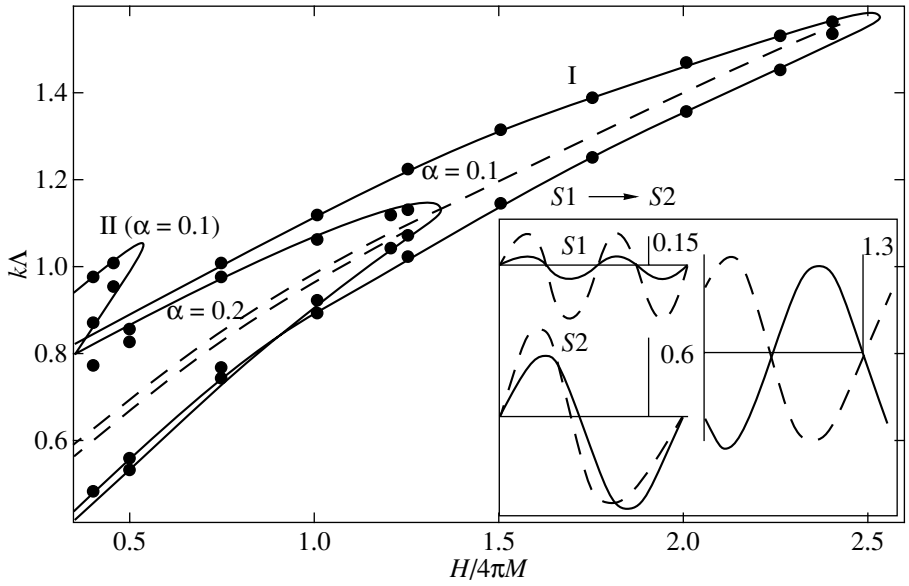

Fig. 2. Parametric excitation regions I and II for different values of the damping parameter α. The DW velocity reaches its maximum (Fig. 3) on the dashed curves inside these regions. The dots near the boundaries of the regions are calculated from nonlinear equations (1). The inset shows the behavior of the solution when passing through the boundary of region I along a horizontal line segment $S1 \longrightarrow S2$ ($k = 1.2$): the period of vibrations is doubled; the time dependence of the solution at point $S1$ outside the region ($H = 1.65$, $T = 1.92$) is shown on the upper left and that at point $S2$ inside the region ($H = 1.6$, $T = 3.98$) is shown on the lower left; the same dependence at a point on the curve corresponding to the maximum values of the DW velocity ($H = 1.5$, $T = 4.27$) is shown at the right of the inset; dashed curves are the oscillatory component of $q(x = 0; t)$, and solid curves are the oscillatory component of $\psi(x = 0, t)$; the values of the amplitudes are indicated near the vertical bars; the time on the horizontal axes is measured in units of the period T.

(Fig. 2). This region is limited above by $H_M \sim 1/\sqrt{\alpha}$ and $k_M \sim 1/\sqrt[4]{\alpha}$. These values are smaller than those in Eq. (15), and region II is smaller in size, such that in the case of $\alpha = 0.2$, this region is beyond the limits of Fig. 2.

The lower limits of the H and k ranges of parametric instability in Fig. 2 are due to the fact that, as numerical integration of the linearized stability equations (9) shows, higher harmonics in expansion (11a) become important for smaller values of H and k and the simple approximations in Eqs. (12) and (16) become inadequate. These approximations are the better, the smaller the damping parameter α and, hence, the higher H_M and k_M. In this case, in Eqs. (1), one can take into account only quadratic exchange dispersion and local magnetostatic contributions proportional to $\sim\cos 2\psi_0(t)$. The contributions from nonlocal magnetostatic interactions proportional to k (see [17]), when incorporated into Eqs. (1), will lead to terms of the order of $\sim 1/\sqrt{Q}$ for $1/Q \ll 1$.

3. NONLINEAR EQUATIONS AND NUMERICAL CALCULATIONS

In this section, we present a numerical solution to the Cauchy problem for a nonlinear partial differential equation (1) with periodic boundary conditions in x. This problem corresponds to the experimental situation where initial periodic perturbations of $q(x)$ and $\psi(x)$ characterized by a certain wavenumber k are produced at $t = 0$ and then, after a constant magnetic field H is applied, the system response is monitored. The amplitudes of the initial perturbations were taken to be small enough (~0.1) for the nonlinear effects to be insignificant at the initial stage. The numerical calculation was carried out by means of a standard computer code using the well-known method of lines. The time interval was taken long enough for a solution to become stationary. It was assumed that in a stationary regime at the boundaries of the instability regions, a solution to Eqs. (1) has the form

$$q(x, t) = \bar{\dot{q}}t + \sum_{n = 0, 1, 2\ldots}^{\infty} [q_{1n}(x)\cos n\omega t + q_{2n}(x)\sin n\omega t], \quad (17)$$

where $q_{1n}(x)$ and $q_{2n}(x)$ are periodic functions of x; the function $\psi(x, t)$ had a similar form.

From the calculated stationary functions $q(x, t)$ and $\psi(x, t)$, we determined the fundamental frequency ω and the average DW velocity $\bar{\dot{q}}$, which are different from those given by Eqs. (5) and (7), because they are functions of the wavenumber k dictated by the initial conditions. However, Eqs. (6) hold in this case, if the averaging is performed not only over time but also over a spatial period of vibrations. The self-consistency of

solutions was checked independently by averaging $\sin\psi\cos\psi$ numerically and substituting the result into Eq. (6). In some cases, we used another checking technique, which is based on the energy balance equation following from Eqs. (1),

$$\frac{\partial}{\partial t}\overline{(\psi'^2 + q'^2 + \sin^2\psi - 2Hq)} + 2\alpha\overline{(\dot{q}^2 + \dot{\psi}^2)} = 0. \quad (18)$$

The relation that was directly checked follows from Eq. (18) and has the form

$$\bar{\dot{q}} = \alpha(\omega^2 + \overline{\dot{q}^2} + \overline{\Delta\Omega^2})/H, \quad (19)$$

where $\overline{\Delta\Omega^2} = \overline{\Delta\dot{q}^2} + \overline{\Delta\dot{\psi}^2} \equiv (\omega/\alpha)\overline{\sin\psi\cos\psi}$; Δq and $\Delta\psi$ are the oscillatory components of solutions $q(x, t)$ and $\psi(x, t)$, respectively; and the overscribed bar denotes double averaging (over a temporal and a spatial period).

For H and k lying outside the parametric-excitation regions, the solutions were found to be very similar to the one-dimensional solution given by Eq. (4). As the boundary of one of the regions was approached (see the typical example of crossing the boundary shown in the inset to Fig. 2, $S1 \longrightarrow S2$), the amplitude and the spatial modulation depth of the solution increased. When passing through the boundary, the period $T = 2\pi/\omega$ doubled and parametric vibrations arose, their wavenumber k being dictated by the initial conditions. The boundaries of the regions were determined as a locus (dots in Fig. 2) at which the $n = 1$ harmonics in Eq. (17) became dominant. For this purpose, the numerical solutions were expanded in a Fourier series and the Parseval equality was used.

In the parametric-excitation regions, the system response increased with distance away from the boundary (the effect being weaker in region II) and became maximal on the extremum curves (dashed curves in the regions shown in Fig. 2). On these curves, the average DW velocity reached its maximum values (dots in Fig. 3) for fixed values of H; the corresponding values of k can be found from Fig. 2. The average frequency ω decreased only slightly; its values can be determined from Eq. (6a) using the values of the average DW velocity and the field H presented in Fig. 3. Figure 4 shows the typical oscillatory components of the $q(x, t)$ and $\psi(x, t)$ functions at a point on the extremum curve. All effects become more pronounced and greater with decreasing damping parameter α.

4. DISCUSSION OF RESULTS

In this paper, we have investigated uniaxial ferromagnets with $Q \gg 1$; among them are perpendicularly magnetized rare-earth garnet-ferrite films, which are believed to be of considerable promise in information processing. However, even for optimal values of the parameters of these materials (M = 15 Oe, A = 10^{-7} erg/cm, $\alpha = 10^{-3}$), the propagation length of free flexural DW vibrations (approximately equal to $\sim 2\Lambda/\alpha$) is ≥ 0.025 cm [7].

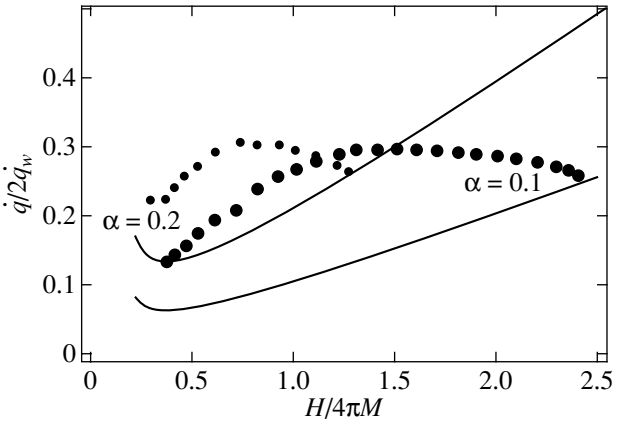

Fig. 3. Dependence of the maximum DW velocity (dots) on the external magnetic field in parametric-excitation region I (dashed curves inside regions I in Fig. 2) for two different values of α. Solid curves are the DW velocity calculated from Eq. (7) derived within the one-dimensional approximation.

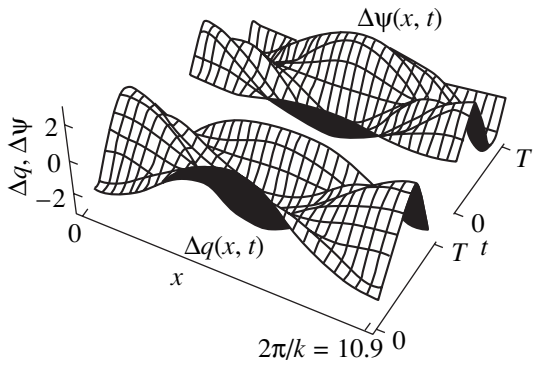

Fig. 4. Typical oscillatory components of the DW coordinate $\Delta q(x, t)$ and of the azimuth angle $\Delta\psi(x = 0, t)$; the dimensionless period is $4\pi\gamma MT$, $\alpha = 0.1$, $H/4\pi M = 0.35$, and $k\Lambda = 0.575$.

Therefore, investigation of the possible mechanisms of excitation and enhancement of localized DW vibrations is of considerable interest. The distinctive feature of internal parametric excitation [14, 15] investigated in this paper, in comparison with another more familiar method (see, e.g., [13]), is that pumping with a dc magnetic field is employed. We note that there are also other parametric mechanisms of flexural DW vibration excitation which involve bulk spin waves [18, 19] and nonparametric excitation of bulk waves by a dc magnetic field acting on a DW [15, 20].

The intensity of parametrically excited stationary DW vibrations in the corresponding regions can be fairly high: the double amplitude $\psi(x, t)$ can be larger than the π "power" of an isolated Bloch line (Fig. 4).

These vibrations significantly affect the average DW velocity (Fig. 3). In this connection, it should be noted that the expression in Eq. (17) is not the most general, because it does not take into account subharmonics, vibrations with incommensurate periods, chaotic regimes, etc. Investigation of the stability of parametric vibrations and various DW translation regimes is beyond the scope of this paper. As for the occurrence of parametric instability of DW spin precession, this phenomenon is fairly universal.

In closing, we point out experimental situations to which our findings are relevant. It was shown in [21] that in a perpendicularly magnetized film whose thickness h is such that $\Delta < h < \Delta\sqrt{Q}$, the DW is twisted only slightly and its spin precession dynamics is very close to the one-dimensional DW dynamics investigated in this paper. Another case is that of films with $Q > 1$ and an in-plane easy magnetization axis. In these two cases, long-range magnetostatic effects characteristic of films (see [22, 23], respectively) are significant only for small wavenumbers, $hk < 1$. The approximations made in this paper will be adequate for films with low damping and for the range of wavenumbers k near the maximum value given by Eq. (15).

REFERENCES

1. N. L. Shryer and L. R. Walker, J. Appl. Phys. **45** (12), 5406 (1990).
2. H. Ye. Khodenkov, Phys. Status Solidi A **53** (2), K103 (1979).
3. D. Ĭorgov, O. S. Kolotov, and V. A. Pogozhev, Fiz. Tverd. Tela (Leningrad) **32** (2), 602 (1990) [Sov. Phys. Solid State **32**, 352 (1990)].
4. A. P. Malozemoff and J. C. Slonczewski, *Magnetic Domain Walls in Bubble Materials* (Academic, New York, 1979; Mir, Moscow, 1982).
5. A. K. Zvezdin, Pis'ma Zh. Éksp. Teor. Fiz. **29** (10), 605 (1979) [JETP Lett. **29**, 553 (1979)].
6. V. G. Bar'yakhtar, B. A. Ivanov, and A. L. Sukstanskiĭ, Pis'ma Zh. Tekh. Fiz. **5** (4), 853 (1979) [Sov. Tech. Phys. Lett. **5**, 351 (1979)].
7. V. G. Bar'yakhtar, M. V. Chetkin, B. A. Ivanov, and S. N. Gaidetskii, *Dynamics of Topological Magnetic Solitons* (Springer-Verlag, Berlin, 1994).
8. R. A. Kosinskii, Phys. Rev. B **50** (10), 6751 (1994).
9. E. E. Kotova and V. M. Chetverikov, Fiz. Tverd. Tela (Leningrad) **32** (4), 1269 (1990) [Sov. Phys. Solid State **32**, 748 (1990)].
10. S. W. Yuan and H. N. Bertram, Phys. Rev. B **44** (22), 12395 (1991).
11. B. N. Filippov and L. G. Korzukhin, Fiz. Tverd. Tela (St. Petersburg) **38** (8), 2442 (1996) [Phys. Solid State **38**, 1343 (1996)].
12. J. C. Slonczewski, Int. J. Magn. **2** (2), 85 (1972).
13. J. H. Spreen and B. E. Argyle, Appl. Phys. Lett. **38** (8), 930 (1981).
14. Yu. V. Ivanov and G. S. Kandaurova, Fiz. Tverd. Tela (Leningrad) **21** (1), 294 (1979).
15. Yu. V. Ivanov, Zh. Éksp. Teor. Fiz. **81** (2), 612 (1981) [Sov. Phys. JETP **54**, 327 (1981)].
16. L. D. Landau and E. M. Lifshitz, *Course of Theoretical Physics*, Vol. 1: *Mechanics* (Fizmatgiz, Moscow, 1958; Pergamon, New York, 1988).
17. I. A. Gilinskiĭ, Zh. Éksp. Teor. Fiz. **68** (3), 1032 (1975) [Sov. Phys. JETP **41**, 511 (1975)].
18. G. E. Khodenkov, Fiz. Tverd. Tela (Leningrad) **16** (4), 1000 (1974) [Sov. Phys. Solid State **16**, 646 (1974)].
19. B. N. Filippov, V. P. Lucomskii, and Yu. G. Lebedev, Phys. Status Solidi B **65** (1), 111 (1974).
20. G. E. Khodenkov, Fiz. Met. Metalloved. **39** (2), 466 (1975).
21. G. E. Khodenkov, Fiz. Met. Metalloved. **81** (1), 43 (1996).
22. E. Schloemann, IEEE Trans. Magn. **MAG-10** (1), 11 (1974).
23. A. V. Nikiforov, Fiz. Tverd. Tela (Leningrad) **29** (7), 2036 (1987) [Sov. Phys. Solid State **29**, 1171 (1987)].

Translated by Yu. Epifanov

Physics of the Solid State, Vol. 44, No. 1, 2002, pp. 117–123. Translated from Fizika Tverdogo Tela, Vol. 44, No. 1, 2002, pp. 112–118.

MAGNETISM AND FERROELECTRICITY

An Effective-Medium Method: The Phonon Mechanism of Anomaly Formation in the Magnon Spectrum of a Finite Magnetic Superlattice

S. V. Tarasenko

Donetsk Physicotechnical Institute, National Academy of Sciences of Ukraine, Donetsk, 83114 Ukraine

Received May 17, 2001

Abstract—An effective-medium method is developed and applied to calculate the effect of dynamic magnetoelastic interaction on the spin dynamics of a finite magnetic thin-layer superlattice in the long-wavelength approximation. It is shown that if the intra- and interlayer spin–spin interactions are predominantly due to indirect coupling via the long-range field of quasi-static magnetoelastic strains, then the magnon spectrum of such a superlattice exhibits anomalies which are absent in the usually considered case where collective spin-wave excitations are formed through magnetodipole interaction. *© 2002 MAIK "Nauka/Interperiodica".*

1. INTRODUCTION

Many papers have been dedicated to theoretical investigation of the conditions under which spin waves can arise and propagate in magnetic superlattices of the magnet–nonmagnet type. However, in most of those papers, only the magnetodipole mechanism of both intra- and interlayer spin–spin interaction was taken into account [1–3]. Using this approach, it has been shown that a magnetic superlattice of the magnet–superconductor type cannot support collective exchangeless spin waves if the thickness of the superconductor layers exceeds the London penetration depth.

However, in general, a consistent theory of real magnets (among them magnetic superlattices) should take into account interaction between the spin and elastic subsystems. Since the spectrum of collective spin-wave excitations of an infinite magnet–nonmagnet superlattice is a result of hybridization of the magnon spectra of individual magnetic layers of the superlattice, the main manifestations of the influence of the elastic subsystem on the spin dynamics of the magnetic superlattice away from magnetoacoustic resonance are commonly believed to be the same as in the case of an isolated magnetic layer. These manifestations are (i) the change in the magnon activation energy associated with renormalization of the magnetic anisotropy energy of the magnet caused by spontaneous elastic strains that exist in the crystal in the ground state [4]; (ii) the appearance of a magnetoelastic energy gap in the spectrum of the soft magnon mode when the specified magnetic state becomes unstable [5]; and (iii) the occurrence of an additional spatially inhomogeneous magnetic-anisotropy field associated with inhomogeneous elastic strains in the case where the boundary between a magnetic and a nonmagnetic medium is not coherent [6].

At the same time, it was first shown in [7–9] that if the lattice dynamics can be described in terms of the elastostatics equations [10] (in the corresponding ranges of frequencies ω and wave vectors $\mathbf{k}$ of spin waves)

$$\partial\sigma_{ik}/\partial x_k = 0 \qquad (1)$$

($\hat{\sigma}$ is the elastic strain tensor), then a finite magnet can support a new type of propagating exchangeless magnon, namely, elastostatic spin waves. The physical mechanism responsible for the occurrence of these exchangeless spin waves in the case where Eq. (1) holds is the indirect spin–spin coupling via the long-range field of quasi-static magnetoelastic strains. If indirect interlayer spin–spin coupling via the magnetodipole field is impossible (e.g., in the magnet–superconductor superlattices mentioned above, with superconductor layer thicknesses larger than the London penetration depth), only the phonon mechanism of interlayer interaction can lead to the occurrence of collective exchangeless spin waves in such structures. In magnetic single crystals, this mechanism of exchangeless magnon dispersion can also be more efficient than the magnetodipole mechanism. In particular, the spin-wave spectra of antiferromagnets simultaneously show exchange-enhanced magnetoelastic effects and exchange-weakened magnetodipole effects. The capability of antiferromagnet–nonmagnet superlattices to support propagating surface and bulk exchangeless magnons of this new type through the phonon mechanism of intra- and interlayer spin–spin coupling was first demonstrated in [11, 12]. In those papers, calculations were performed using the *T*-matrix method without regard for magnetodipole and inhomogeneous

1063-7834/02/4401-0117$22.00

exchange interactions. However, in a real magnetic metallic superlattice under the condition of Eq. (1), the above-mentioned intra- and interlayer spin–spin coupling mechanisms all operate simultaneously and the *T*-matrix method is not appropriate for analytical calculation of the magnon spectrum.

In [13, 14], the spectrum of collective magnetostatic spin waves (MSSW) was considered in a magnet–nonmagnet superlattice and it was shown that analytical calculation of the exchangeless magnon spectrum could be significantly simplified if one restricted his or her consideration to the wavenumber range in which the dynamics of any of the layers composing the superlattice unit cell could be treated in the thin-layer approximation. A magnetic thin-layer superlattice can be considered a spatially homogeneous magnetic medium characterized by an effective magnetic susceptibility tensor. This effective-medium method allows analytical calculations to be significantly simplified in some cases of practical importance. In particular, using this method, the dispersion relation of MSSW traveling along a finite magnetic superlattice (layered waveguide) can be reduced to the dispersion relation of MSSW in a homogeneously magnetized layer of the corresponding effective medium. One would expect this method to be highly efficient in analytical calculation of the magnon spectrum of a finite magnetic metallic superlattice in which the magnetodipole and phonon mechanisms of intra- and interlayer spin–spin coupling operate simultaneously. In order to solve this problem, one should use the results of [13, 14] and adapt the effective-medium method to describing the exchangeless magnon spectrum of a superlattice in the case where the magnons are formed solely through the phonon mechanism of intra- and interlayer spin–spin coupling (elastostatic spin waves); this has not yet been accomplished to date.

In this paper, the effective-medium method is used to calculate the spectrum of surface and bulk exchangeless magnons in a finite magnetic superlattice of the magnet–nonmagnet type. The thicknesses of the magnetic and nonmagnetic layers composing a superlattice unit cell are d_1 and d_2, respectively. Collective spin-wave excitations are assumed to be formed solely through the phonon mechanism of intra- and interlayer spin–spin coupling.

2. BASIC RELATIONS

As the magnetic medium, we consider a two-sublattice antiferromagnet (AFM) of the easy-axis type in the collinear phase with $\mathbf{l} \parallel z$ and $|\mathbf{m}| = 0$, where $\mathbf{l} = (\mathbf{M}_1 - \mathbf{M}_2)/2M_0$ is the antiferromagnetism vector, $\mathbf{m} = (\mathbf{M}_1 + \mathbf{M}_2)/2M_0$ is the ferromagnetism vector, $\mathbf{M}_1$ and $\mathbf{M}_2$ are the magnetizations of the sublattices ($|\mathbf{M}_1| = |\mathbf{M}_2| = M_0$) [15], and the easy axis is along the z axis. It is assumed that (i) in a sufficiently weak external magnetic field $\mathbf{H}$, the electrostatics equations (1) describe the coupling of the elastic and spin subsystems for both branches of the magnon spectrum of the two-sublattice AFM at hand and that (ii) the ferromagnetism and antiferromagnetism vectors are subject to the condition

$$|\mathbf{m}| \ll |\mathbf{l}|. \tag{2}$$

As in [12], we restrict our consideration to spin waves propagating in the plane perpendicular to the easy axis (z axis) of the AFM and, for the sake of simplicity, assume that the magnetic and nonmagnetic layers are isotropic elastic (and magnetoelastic, in the former case) media (for example, crystals of hexagonal symmetry). In this case, the energy density W of the uniaxial two-sublattice AFM crystal (medium 1), including the interaction energy between the elastic and spin subsystems, can be written as [5]

$$W = W_\mathrm{m} + W_\mathrm{me} + W_\mathrm{e},$$
$$W_\mathrm{m} = 0.5\delta\mathbf{m}^2 + 0.5\delta_1(\nabla\mathbf{l})^2 - 0.5bl_z^2 - \mathbf{mH}, \tag{3}$$
$$W_\mathrm{me} = Bl_il_ku_{ik}, \quad W_\mathrm{e} = 0.5\lambda_1u_{ii}^2 + \mu_1u_{ik}^2,$$

where δ, δ_1, b, and B are the uniform and nonuniform exchange constants and the uniaxial-anisotropy and magnetoelastic coupling constants, respectively; $\mathbf{H}$ is an external magnetic field; λ_1 and μ_1 are the Lamé coefficients for the magnetic medium; and u_{ik} is the elastic strain tensor.

Under assumptions (i) and (ii), the set of dynamic equations describing the coupling between the elastic and spin subsystems in medium 1 consists of the elastostatics equations (1) for the lattice displacement vector $\mathbf{u}$ and the effective equation of motion for the antiferromagnetism vector $\mathbf{l}$. As for the nonmagnetic medium (medium 2, with Lamé coefficients λ_2, μ_2) of the magnetic superlattice under study, we assume that its shear modulus is subject to the condition $\mu_2 > \mu_1$ and, therefore, the elastic dynamics of both the magnetic and nonmagnetic media can be described by Eq. (1) in the frequency range under study. The superlattice is assumed to be acoustically continuous; therefore, at the interfaces between magnetic and nonmagnetic layers, we have [16]

$$\mathbf{u}^{(1)} = \mathbf{u}^{(2)}, \quad \sigma_{ik}^{(1)}n_k^{(1)} = \sigma_{ik}^{(2)}n_k^{(2)}. \tag{4}$$

If $\mathbf{k} \in xy$, then, without loss of generality, we can assume that the normal to the interfaces between layers is $\mathbf{n} \parallel y$, because the magnetic medium is isotropic in the xy plane.

3. ELASTOSTATIC SPIN WAVES IN AN INFINITE AND A SEMI-INFINITE SUPERLATTICE

The description of wave processes in a superlattice within the effective-medium approximation is adequate only in the long-wavelength range. Therefore, it is assumed that in the two unit-cell layers (1, 2), the components q_1 and q_2 of the wave vector $\mathbf{k}$ along the normal

to the interface are much smaller than the inverse thicknesses of the respective layers (d_1, d_2). For the two-layer (magnet–nonmagnet) superlattice under study, this condition can be written as

$$q_1 d_1 \ll 1, \quad q_2 d_2 \ll 1. \tag{5}$$

Thus, we treat the superlattice as a spatially homogeneous effective medium. In the case of the phonon mechanism of intra- and interlayer spin–spin coupling, this medium is characterized by the averaged components (over the superlattice period $d = d_1 + d_2$) of elastic stress tensor $\langle \sigma_i \rangle$ and elastic strain tensor $\langle u_i \rangle$. The relation between these averaged tensors is determined by the effective elastic moduli $\bar{c}_{ik}$. In terms of the relative thicknesses of the magnetic and nonmagnetic layers being expressed as

$$f_1 = \frac{d_1}{d_1 + d_2}, \quad f_2 = \frac{d_2}{d_1 + d_2}, \tag{6}$$

the components $\langle \sigma_i \rangle$ and $\langle u_i \rangle$ in the geometry under study ($\mathbf{H} \parallel \mathbf{u} \parallel z$, $\mathbf{k} \in xy$, $\mathbf{l} \parallel z$, $\mathbf{n} \parallel y$) can be written as

$$\begin{aligned} \langle \sigma_5 \rangle &= f_1 \sigma_5^{(1)} + f_2 \sigma_5^{(2)}, \quad \langle \sigma_4 \rangle = \sigma_4^{(1)} = \sigma_4^{(2)}, \\ \langle u_5 \rangle &= u_5^{(1)} = u_5^{(2)}, \quad \langle u_4 \rangle = f_1 u_4^{(1)} + f_2 u_4^{(2)}. \end{aligned} \tag{7}$$

In deriving Eq. (7), we have taken into account that the superlattice is acoustically continuous at each interface between layers, which means that, for $\mathbf{n} \parallel y$, $\mathbf{k} \in xy$, and $\mathbf{u} \parallel z$, the normal component σ_4 of the elastic stress tensor and the lattice displacement $\mathbf{u}$ are continuous. In terms of linear elasticity theory, the effective elastic moduli $\bar{c}_{44}$, $\bar{c}_{55}$, and $\bar{c}_{45}$ (for the geometry under study) can be written as

$$\begin{aligned} \langle \sigma_4 \rangle &= \bar{c}_{44} \langle u_4 \rangle + i \bar{c}_{45} \langle u_5 \rangle, \\ \langle \sigma_5 \rangle &= \bar{c}_{55} \langle u_5 \rangle - i \bar{c}_{54} \langle u_4 \rangle. \end{aligned} \tag{8}$$

For the isotropic elastic nonmagnetic medium 2, $c_{44}^{(2)} = c_{55}^{(2)} = \mu_2$ and $c_{45}^{(2)} = c_{54}^{(2)} = 0$, while in the magnetic medium 1, for $\mathbf{k} \in xy$, we have

$$\begin{aligned} c_{44}^{(1)} &= c_{55}^{(1)} = \mu, \quad c_{45}^{(1)} = \mu_*, \\ \mu &\equiv \mu_1 [(\omega_0^2 - \omega_H^2 + \omega_{\text{me}}^2 - \omega^2)(\omega_0^2 - \omega_H^2 - \omega^2) \\ &\quad - 4\omega^2 \omega_H^2 / \varphi], \\ \varphi &\equiv (\omega_0^2 - \omega_H^2 + \omega_{\text{me}}^2 - \omega^2)^2 - 4\omega^2 \omega_H^2, \\ \mu_* &\equiv \mu_1 2\omega \omega_H \omega_{\text{me}}^2 / \varphi. \end{aligned} \tag{9}$$

It follows from Eqs. (7)–(9) that, in the effective-medium approximation, the magnet–nonmagnet superlattice in which the intra- and interlayer spin–spin coupling occurs solely via phonons is characterized by the following effective elastic moduli depending on layer thickness ($\mathbf{H} \parallel \mathbf{u} \parallel z$, $\mathbf{k} \in xy$, $\mathbf{l} \parallel z$, $\mathbf{n} \parallel y$):

$$\begin{aligned} \bar{c}_{44} &= c_{44}^{(1)} c_{44}^{(2)} (\Delta f_2)^{-1}, \quad \Delta \equiv c_{44}^{(1)} + c_{44}^{(2)} f_1 f_2^{-1}, \\ \bar{c}_{45} &= c_{44}^{(2)} c_{45}^{(1)} f_1 f_2^{-1} \Delta^{-1}, \\ \bar{c}_{55} &= f_1 c_{55}^{(1)} + f_2 c_{55}^{(2)} - f_1 (c_{45}^{(1)})^2 \Delta^{-1}. \end{aligned} \tag{10}$$

It is easy to verify that in the absence of magnetoelastic interaction [$B \longrightarrow 0$ in Eqs. (9), (10)], the effective elastic moduli in Eq. (10) are identical to the corresponding elastic moduli of a nonmagnetic two-layer superlattice (see, e.g., [17]).

As before, we assume that the spin oscillation frequency ω is such that the dynamics of the elastic subsystem is described by the elastostatics equations (1). In this case, using Eqs. (9) and (10), it is easily shown that, within the effective-medium approximation characterized by Eqs. (5), the spectrum of exchangeless elastostatic spin waves in the infinite magnetic superlattice under study ($\mathbf{H} \parallel \mathbf{u} \parallel z$, $\mathbf{k} \in xy$, $\mathbf{l} \parallel z$) is determined from the equation

$$\frac{\partial \langle \sigma_4 \rangle}{\partial y} + \frac{\partial \langle \sigma_5 \rangle}{\partial x} = 0. \tag{11}$$

In the effective medium, the component u_z is represented in the form

$$u_z = A \exp(i\mathbf{k}\mathbf{r}_\perp - i\omega t), \quad \mathbf{r}_\perp \in xy \tag{12}$$

and Eq. (11) is reduced to the dispersion relation

$$\begin{aligned} &\omega^4 - M_{1*}\omega^2 + M_{2*} = 0, \\ &M_{1*} = \bar{R}[2 f_1 f_2 (\mu_1^2 \mu_2^{-2} (\omega_0^2 + 3\omega_H^2) \\ &\quad + 2(\omega_0^2 + 3\omega_H^2 + \omega_{\text{me}}^2)) \\ &\quad + \mu_1 \mu_2^{-1} (f_1^2 + f_2^2 + k_x^2 k_y^{-2})(2\omega_0^2 + 3\omega_H^2 + \omega_{\text{me}}^2)], \\ &M_{2*} = \bar{R} f_1 f_2 [\mu_1^2 \mu_2^{-2} (\omega_0^2 + \omega_H^2)^2 + (\omega_0^2 + \omega_H^2 + \omega_{\text{me}}^2)^2] \\ &\quad + \mu_1 \mu_2^{-1} (f_1^2 + f_2^2 + k_x^2 k_y^{-2})(\omega_0^2 + \omega_H^2)(\omega_0^2 + \omega_H^2 + \omega_{\text{me}}^2), \\ &\bar{R} \equiv (f_1 f_2 \mu_1^2 \mu_2^{-2} + f_1 f_2 + \mu_1 \mu_2^{-1} (f_1^2 + f_2^2 + k_x^2 k_y^{-2}))^{-1}. \end{aligned} \tag{13}$$

Equation (13) becomes identical to the exact solution obtained using the *T*-matrix method given by Eqs. (A1) and (A2) if the latter equations are written in the thin-layer approximation (5). Thus, in the ranges of wave vectors $\mathbf{k}_\perp$ and frequencies ω under study, the bulk elastostatic spin waves in the magnetic superlattice can be described in terms of the effective-medium approximation.

Now, we will show that the spectrum of elastostatic surface magnons in the magnetic superlattice is also adequately described in terms of the effective elastic moduli (10) if conditions (5) are fulfilled. For this purpose, we compare the spectrum of collective surface elastostatic spin waves in a semi-infinite magnetic

superlattice calculated using the *T*-matrix method given by Eqs. (A3) and (A4) and the spectrum of the same waves in the same geometry ($\mathbf{H} \parallel \mathbf{u} \parallel z$, $\mathbf{k} \in xy$, $\mathbf{l} \parallel z$) in a semi-infinite ($y > 0$) spatially homogeneous elastic medium characterized by the effective elastic moduli given by Eqs. (9) and (10) and whose dynamics is described by Eqs. (1). At the $y = 0$ interface between the nonmagnetic medium ($y < 0$) and the effective medium with the elastic moduli given by Eq. (10), the condition of acoustic continuity has the form

$$u_z = u_z^{(a)}, \quad \sigma_4^{(a)} = \langle \sigma_4 \rangle, \quad y = 0. \tag{14}$$

An exchangeless elastostatic spin wave will be localized near the $y = 0$ surface of the magnetic superlattice if the following conditions are fulfilled in addition to Eqs. (1), (9), (10), and (14):

$$u_z^{(a)}(y \longrightarrow -\infty) \longrightarrow 0, \quad u_z(y \longrightarrow \infty) \longrightarrow 0. \tag{15}$$

For such exchangeless surface magnons, the dispersion relation takes the form

$$\bar{c}_{44}\alpha + s\bar{c}_{45} = \mu_a, \tag{16}$$

where $\alpha^2 \equiv \bar{c}_{55}/\bar{c}_{44}$, $s \equiv \mathbf{k}_\perp/|\mathbf{k}_\perp| = \pm 1$, and μ_a is the shear modulus of the nonmagnetic medium in the $y < 0$ half-space. A comparison of Eq. (16) with the corresponding exact solution found using the *T*-matrix method shows that the spectrum of both bulk and surface long-wavelength exchangeless elastostatic magnons in the magnetic superlattice is adequately described in terms of the effective elastic moduli if the conditions of Eq. (5) are fulfilled. The spectrum of these exchangeless surface magnons is dispersionless (in the approximations described above) and nonreciprocal [$\omega(\mathbf{k}_\perp) \neq \omega(-\mathbf{k}_\perp)$] for $H_z \neq 0$. At $\mu_a = \mu_2$, this spectrum will not change if the magnetic superlattice occupying the upper ($y > 0$) half-space is replaced by the AFM of the easy-axis type described by Eq. (3) ($\mathbf{H} \parallel \mathbf{l}$, $\mathbf{k} \in xy$).

Although the dispersion relation given by Eq. (16) does not depend on the relationship between the thicknesses of the magnetic (d_1) and nonmagnetic (d_2) layers, analysis shows that this type of collective exchangeless surface spin waves is supported by the superlattice only in the case of $d_2 < d_1$.

In the framework of the *T*-matrix approach, analytical calculation of the spectrum of collective exchangeless elastostatic magnons becomes much more complicated if the magnetic superlattice is finite: $0 < y < D$, where $D = N(d_1 + d_2)$ is the thickness of the acoustically continuous superlattice (N is the number of unit cells). However, if the finite number N is large ($N \gg 1$, $D \gg d = d_1 + d_2$) and, as before, Eqs. (1) and (5) are simultaneously true, then the spectrum of exchangeless elastostatic magnons of the finite magnetic superlattice can be calculated using the effective-medium method developed above. The results of these calculations are presented in the next section. The layers near the surface of the superlattice and those in the bulk of it are assumed to be identical.

4. ELASTOSTATIC SPIN WAVES IN THE FINITE MAGNETIC SUPERLATTICE

The finite superlattice occupies the region $0 < y < D$ and the geometry is the same as before: $\mathbf{H} \parallel \mathbf{u} \parallel z$, $\mathbf{k} \in xy$, $\mathbf{l} \parallel z$. At the outer surfaces $y = 0$ and $y = D$, the superlattice is in acoustic contact with an isotropic nonmagnetic medium, which is the same above ($y > D$) and below ($y < 0$) the superlattice and whose shear modulus is μ_a. The thickness of the $y > D$ overlayer is t, the thickness of the $y < 0$ overlayer is f, and the surfaces at $y = D + t$ and $y = -f$ are assumed to be mechanically free. In this case, using the effective-medium approximation [Eqs. (7), (8) and the effective elastic moduli in Eq. (10)], the boundary conditions can be written as

$$\begin{aligned} \langle \sigma_4 \rangle = \sigma_4^{(a)}, \quad u_z = u_z^{(a)}, \quad y = 0, D, \\ \sigma_4^{(a)} = 0, \quad y = D + t, \\ \sigma_4^{(a)} = 0, \quad y = -f. \end{aligned} \tag{17}$$

The dispersion relation for elastostatic magnons with $\mathbf{k} \in xy$ for $\mathbf{H} \parallel \mathbf{u} \parallel z$ and $\mathbf{l} \parallel y$ has the form ($\alpha^2 \equiv \bar{c}_{55}/\bar{c}_{44}$)

$$\begin{aligned} \bar{c}_{44}^2\alpha^2 + \bar{c}_{44}\alpha\mu_a[\tanh(k_\perp t) + \tanh(k_\perp f)]\coth(\alpha k_\perp D) \\ + \bar{c}_{45}s\mu_a[\tanh(k_\perp t) - \tanh(k_\perp f)] - \bar{c}_{45}^2 \\ + \mu_a^2\tanh(k_\perp t)\tanh(k_\perp f) = 0. \end{aligned} \tag{18}$$

It is easy to verify that, in the particular cases considered above, Eq. (18) reduced to the expressions derived using the effective-medium method for the spectrum of normal vibration modes of an infinite magnetic superlattice [Eq. (13)] ($\mu_a \longrightarrow 0$, $k_\perp t \longrightarrow 0$, $k_\perp f \longrightarrow 0$, $k_\perp D \longrightarrow \infty$ and for the spectrum of exchangeless surface elastostatic magnons [Eq. (16)] in a semi-infinite magnetic superlattice in acoustic contact with a nonmagnetic medium with shear modulus μ_a. Solutions to Eq. (18) cannot be represented in an explicit form for an arbitrary value of the wavenumber $k_\perp$ and arbitrary relative thicknesses of the nonmagnetic overlayers t/D and f/D. In the specific case of t/D, $f/D \longrightarrow \infty$, the dispersion relation of elastostatic magnons in the finite magnetic superlattice can be represented in the form $k_\perp = k_\perp(\omega)$ as

$$k_\perp = (\alpha D)^{-1}\operatorname{arccoth}\frac{\bar{c}_{45}^2 - \bar{c}_{44}^2 - \mu_a^2}{2\bar{c}_{44}\alpha\mu_a}. \tag{19}$$

In the case of $t/D = f/D = 0$, Eq. (18) takes the form

$$(\bar{c}_{44}^2\alpha^2 - \bar{c}_{45}^2)\tanh(\alpha k_\perp D) = 0. \tag{20}$$

If t/D, $f/D \neq 0$, $\mathbf{k} \in xy$, $t \neq f$ and $H_z \neq 0$ ($\mathbf{H} \parallel \mathbf{l}$), then the spectrum of both surface and bulk exchangeless magnons given by Eq. (18) is nonreciprocal with respect to

the reversal of the spin-wave propagation direction ($s = \pm 1$), $\omega(\mathbf{k}_\perp) \neq \omega(-\mathbf{k}_\perp)$ for any sign of α^2. In particular, at $t \longrightarrow \infty$ and $f = 0$, the dispersion relation (18) has the form

$$k_\perp = (\alpha D)^{-1} \operatorname{arccoth} \frac{\bar{c}_{45}^2 - \bar{c}_{44}^2 + \bar{c}_{45} s \mu_a}{\bar{c}_{44} \alpha \mu_a}. \qquad (21)$$

The function $k_\perp(\omega, s)$ described by Eqs. (19)–(21) possesses the following property. Let us designate $k_\perp(\omega)$ in Eq. (19) as $k_0(\omega)$ and the functions $k_\perp(\omega, s = 1)$ and $k_\perp(\omega, s = -1)$ in Eq. (21) as $k_+(\omega)$ and $k_-(\omega)$, respectively. Then, for all values of ω such that $\alpha^2 > 0$, we have $k_+(\omega) + k_-(\omega) = k_0(\omega)$. It follows from Eqs. (18)–(21) that, depending on the sign of $\alpha^2 = \alpha^2(\omega)$, the superlattice can support either bulk ($\alpha^2 < 0$) or surface ($\alpha^2 > 0$) propagating exchangeless elastostatic spin waves. The number of bulk exchangeless magnon modes is finite. For any value of the wavenumber $k_\perp$, these modes form two nondegenerate (higher and lower) frequency bands, the band widths being independent of the wavenumber $k_\perp$ (in the approximation used here). The positions of the band edges can be found from Eq. (18) by putting $\alpha^2 = 0$ and $\alpha^2 = \infty$; we designate the corresponding frequencies as ω_i, with $\omega_i < \omega_{i+1}$ for $1 \leq i \leq 3$. At a given mode index ν and an arbitrary value of $k_\perp$, each band has a corresponding branch of bulk elastostatic magnons. For both bands, the dispersion curves of elastostatic magnons have a long-wavelength and a short-wavelength condensation point. In other words, in each band, for any two modes ν and ρ characterized by $\Omega_\nu(k_\perp)$ and $\Omega_\rho(k_\perp)$ dispersion relations, we have $|\Omega_\nu(k_\perp) - \Omega_\rho(k_\perp)| \longrightarrow 0$ as $k_\perp \longrightarrow 0$ and $k_\perp \longrightarrow \infty$. For the magnetic superlattice and geometry under study, we have $\Omega_\nu(k_\perp \longrightarrow 0) \longrightarrow \omega_2$ and $\Omega_\nu(k_\perp \longrightarrow \infty) \longrightarrow \omega_1$ in the lower frequency band of elastostatic magnons and $\Omega_\nu(k_\perp \longrightarrow 0) \longrightarrow \omega_3$ and $\Omega_\nu(k_\perp \longrightarrow \infty) \longrightarrow \omega_4$ in the higher frequency band for any mode index ν. For a fixed mutual orientation of the vectors $\mathbf{k}_\perp$, $\mathbf{H}$, $\mathbf{l}$, and $\mathbf{n}$, the dispersion curves of bulk elastostatic magnons for each frequency band correspond to waves of the same type, direct ($\partial\Omega_\nu/\partial k_\perp > 0$) or back ($\partial\Omega_\nu/\partial k_\perp < 0$) waves. For modes of the direct-wave type, the long-wavelength condensation point of the frequency spectrum is positioned above the short-wavelength condensation point; the opposite situation occurs for modes of the back-wave type.

Taking into account the effect of the thicknesses t and f on the spectrum of bulk elastostatic magnons in the superlattice, it is easy to show that, for the bulk spin-wave modes that have nodes of zero amplitude in the $0 < y < D$ region, the spectrum virtually does not depend on the boundary conditions and is nearly identical to the spectrum given by Eq. (20) for a finite magnetic superlattice with mechanically free outer surfaces ($y = D$ and $y = 0$).

The situation is different for a bulk mode that is quasi-uniform over the thickness of a superlattice with nonmagnetic overlayers (the spectrum of such a mode consists of two branches, as is the case with the spectrum of all other bulk elastostatic magnons in the geometry $\mathbf{H} \parallel \mathbf{l} \parallel z$, $\mathbf{k} \in xy$, $\mathbf{n} \parallel y$). Analysis of Eq. (18) reveals that the dispersion of such a mode depends critically on whether or not the finite superlattice is covered with nonmagnetic overlayers. In the long-wavelength limit, for example, as follows from Eq. (18), for sufficiently small values of the wavenumber $k_\perp$ ($k_\perp \ll 1/\alpha D$, $k_\perp t \longrightarrow 0$, $k_\perp f \longrightarrow 0$), the dispersion relation of these modes has the form

$$\bar{c}_{44}^2 \alpha^2 + \bar{c}_{44} \mu_a (t + f)/D - \bar{c}_{45}^2 = 0; \qquad (22)$$

thus, the long-wavelength limit of these branches depends crucially on the relative thicknesses of the nonmagnetic overlayers t/D and f/D of the finite magnetic superlattice. Therefore, this limiting point of the dispersion curve of a quasi-uniform mode of bulk exchangeless magnons in the superlattice under study does not have to coincide with the long-wavelength condensation point for the other modes of bulk elastostatic magnons in both the lower and higher frequency bands. Furthermore, comparison of Eqs. (18) and (22) shows that the presence of nonmagnetic overlayers can drastically affect the shape of the dispersion curves of the quasi-uniform bulk spin waves. In particular, in the case of a finite magnetic superlattice, with both its outer surfaces ($y = 0, D$) being mechanically free [$\mu_a = 0$ in Eq. (17)], the spectrum of quasi-uniform bulk modes can be entirely dispersionless.

It follows from Eq. (18) that, at a given value of the wavenumber $k_\perp$, the magnon spectrum of the finite superlattice under study ($\mathbf{l} \perp \mathbf{n}$, $\mathbf{k}_\perp \perp \mathbf{l}$) can contain not only the two-band spectrum of bulk elastostatic spin waves ($\alpha^2 < 0$) but also, in principle, two branches of surface elastostatic magnons ($\alpha^2 > 0$). Their dispersion curves lie in the gap between the higher and lower frequency bands of bulk elastostatic magnons. One of the conditions that define the positions of the frequency band edges of bulk magnons for any value of $k_\perp$ is $\alpha^2 = 0$ (which is equivalent to $\bar{c}_{44} = 0$ for the geometry in question). It follows from Eq. (18) that, in addition to $\bar{c}_{44} = 0$, the following inequality must be satisfied for exchangeless surface magnons to occur in the magnetic superlattice in the case of $t = f \longrightarrow \infty$:

$$\bar{c}_{45} > \mu_a. \qquad (23)$$

Thus, at $k_\perp \neq 0$, the dispersion curve of a quasi-uniform mode of bulk spin waves can continuously transform into that of a surface mode. This transformation will occur if the corresponding dispersion curve is of the direct-wave type ($\partial\Omega_\nu/\partial k_\perp > 0$) in the lower frequency band of bulk magnons or of the back-wave type ($\partial\Omega_\nu/\partial k_\perp < 0$) in the higher frequency band. For the

geometry in question ($\mathbf{n} \parallel y$, $\mathbf{H} \parallel \mathbf{u} \parallel \mathbf{l} \parallel z$), the corresponding wavenumber $k_* \neq 0$ is determined from Eq. (19), where one puts $\bar{c}_{44} = 0$. Calculations show that there is an analogy between the dispersion properties of collective spin waves under study (which are solely due to the phonon mechanism of intra- and interlayer spin–spin coupling in the magnetic superlattice) and the properties of collective magnetostatic spin waves [1–3]. In the case of magnetodipole spin waves, a role similar to that played by a nonmagnetic overlayer of thickness t in the formation of the spectrum of elastostatic magnons in a magnetic superlattice is played by a metallic screen situated at a distance t from the surface of the magnetic superstructure under study. Calculations show that if both types of exchangeless spin waves can occur simultaneously in the magnetic superlattice, then the analogy indicated above also takes place between the magnetic *TE* polariton and the magnetoelastic *SH* wave propagating along the magnetic superstructure under study (these statements are true only for the geometry considered in this paper). Indeed, the spectrum of magnetostatic spin waves is the quasi-static limit ($\omega/ck_\perp \longrightarrow 0$, c is the speed of light) of the low-frequency branch of the spectrum of electromagnetic spin vibrations of the superlattice which involve a *TE*-type electromagnetic wave. For elastostatic magnons ($\mathbf{u} \perp \mathbf{k}_\perp$, $\mathbf{u} \perp \mathbf{n}$), these are the quasi-static limit of magnetoelastic vibrations of the magnetic superlattice which involve *SH*-type acoustic phonons, as follows from calculations taking into account acoustic retardation ($\omega/c_{\text{ph}}k_\perp < \infty$, where c_{ph} is the minimum velocity of elastic waves in an infinite crystal).

5. CONCLUSIONS

In this paper, we developed a version of the effective-medium method which allows one to significantly simplify (in comparison with the *T*-matrix method) analytical calculations of the long-wavelength magnon spectrum of a finite magnetic superlattice in the case where the basic mechanism of formation of collective spin waves is indirect intra- and interlayer spin–spin coupling via the long-range field of quasi-static magnetoelastic strains. By analogy with magnetostatics, these exchangeless spin waves can be referred to as elastostatic spin waves. The method developed here was used to calculate the spectrum of (bulk and surface) magnons of this type in infinite, semi-infinite, and finite magnetic superlattices of the antiferromagnet–nonmagnetic-metal type and to investigate the effect of the following factors on this spectrum and on the conditions of its formation: (1) nonmagnetic overlayers (elastic substrate), (2) magnetic growth anisotropy, and (3) an external magnetic field.

In terms of the effective-medium approximation, the effect of phonons on the spin dynamics of magnetic superlattices of the AFM–ideal metal and AFM–nonmagnetic insulator types was considered in this paper with allowance for the magnetoelastic intralayer spin–spin coupling alone. However, the calculation method used here is also appropriate for investigating the spectrum of elastostatic magnons in a metallic magnetic superlattice in which the phonon mechanism of intra- and interlayer spin–spin coupling operates and, in addition, in which indirect spin–spin interaction between adjacent magnetic layers (of thickness d_1) occurs through the conduction electrons of a nonmagnetic spacer (of thickness d_2) separating the layers. Analysis of the magnon spectrum of a finite metallic superlattice performed using the effective-medium method, in which the elastostatic, magnetodipole, and Heisenberg mechanisms of intra- and interlayer spin–spin coupling are consistently taken into account, will be published elsewhere.

ACKNOWLEDGMENTS

The author is grateful to E.P. Stefanovskiĭ, I.E. Dragunov, and T.N. Tarasenko for their encouragement and helpful discussions.

APPENDIX

$$\omega^4 - M_1\omega^2 + M_2 = 0,$$

$$M_1 = R[2\mu_1^2\mu_2^{-2}(\omega_0^2 + 3\omega_H^2) + 2(\omega_0^2 + 3\omega_H^2 + \omega_{\text{me}}^2) - \mu_1\mu_2^{-1}F_\kappa(2\omega_0^2 + 3\omega_H^2 + \omega_{\text{me}}^2)],$$

$$M_2 = R[\mu_1^2\mu_2^{-2}(\omega_0^2 + \omega_H^2)^2 + (\omega_0^2 + \omega_H^2 + \omega_{\text{me}}^2)^2 - \mu_1\mu_2^{-1}F_\kappa(\omega_0^2 + \omega_H^2)(\omega_0^2 + \omega_H^2 + \omega_{\text{me}}^2)], \quad \text{(A.1)}$$

$$R \equiv (1 + \mu_1^2\mu_2^{-2} - \mu_1\mu_2^{-1}F_\kappa)^{-1},$$

$$d = d_1 + d_2, \quad 0 < \kappa < \pi/d,$$

$$F_\kappa = 2[\cos(\kappa d)\cosh(k_\perp(d_1 - d_2))] \times [\sinh(k_\perp d_1)\sinh(k_\perp d_2)]^{-1}. \quad \text{(A.2)}$$

$$T_{11} - T_{22} + T_{12}(B_0/A_0) - T_{21}(B_0/A_0) = 0. \quad \text{(A.3)}$$

$$B_0/A_0 \equiv -f_-R_{-+}/R_{--}, \quad e_\pm \equiv \exp(\pm k_\perp d_2),$$
$$\Delta \equiv R_{++}R_{--} - R_{+-}R_{-+}, \quad f_\pm \equiv \exp(\pm k_\perp d_1),$$
$$T_{11} \equiv [f_+(e_+R_{++}R_{--} - R_{+-}R_{-+}e_-)]/\Delta,$$

$$T_{22} \equiv [f_-(e_-R_{++}R_{--} - R_{+-}R_{-+}e_+)]/\Delta, \quad \text{(A.4)}$$

$$T_{12} \equiv 2R_{--}R_{+-}/\Delta, \quad T_{21} \equiv 2R_{++}R_{-+}/\Delta.$$
$$R_{--} \equiv (-\mu - \mu_* + \mu_2)k_\perp, \quad R_{+-} \equiv (\mu - \mu_* + \mu_2)k_\perp,$$
$$R_{-+} \equiv (-\mu + \mu_* + \mu_2)k_\perp, \quad R_{++} \equiv (\mu + \mu_* + \mu_2)k_\perp.$$

REFERENCES

1. M. G. Cottam and D. R. Tilley, *Introduction to Surface and Superlattice Excitations* (Cambridge Univ. Press, Cambridge, 1989).
2. M. G. Cottam and D. J. Lockwood, *Light Scattering in Magnet Solids* (Wiley, New York, 1986; Nauka, Moscow, 1991).
3. R. E. Camley and R. L. Stamps, J. Phys.: Condens. Matter **5** (25), 3727 (1993).
4. A. G. Gurevich, *Magnetic Resonance in Ferrites and Antiferromagnets* (Nauka, Moscow, 1973).
5. E. A. Turov and V. G. Shavrov, Usp. Fiz. Nauk **140** (3), 429 (1983) [Sov. Phys. Usp. **26**, 593 (1983)].
6. A. N. Prokhorov, G. A. Smolenskiĭ, and A. N. Ageev, Usp. Fiz. Nauk **143** (1), 33 (1984) [Sov. Phys. Usp. **27**, 339 (1984)].
7. S. V. Tarasenko, Pis'ma Zh. Tekh. Fiz. **14** (22), 2041 (1988) [Sov. Tech. Phys. Lett. **14**, 885 (1988)].
8. S. V. Tarasenko, Fiz. Tverd. Tela (Leningrad) **33** (10), 3021 (1991) [Sov. Phys. Solid State **33**, 1705 (1991)].
9. A. L. Sukstanskiĭ and S. V. Tarasenko, Zh. Éksp. Teor. Fiz. **105** (4), 928 (1994) [JETP **78**, 498 (1994)].
10. Yu. I. Sirotin and M. P. Shaskol'skaya, *Fundamentals of Crystal Physics* (Nauka, Moscow, 1979; Mir, Moscow, 1982).
11. S. V. Tarasenko, Fiz. Tverd. Tela (St. Petersburg) **36** (9), 2554 (1994) [Phys. Solid State **36**, 1390 (1994)].
12. S. V. Tarasenko, Fiz. Tverd. Tela (St. Petersburg) **37** (9), 2659 (1995) [Phys. Solid State **37**, 1462 (1995)].
13. N. Raj and P. R. Tilley, Phys. Rev. B **36** (13), 7003 (1987).
14. N. S. Almeida and D. L. Mills, Phys. Rev. B **38** (12), 6698 (1988).
15. E. A. Turov, *Physical Properties of Magnetically Ordered Crystals* (Akad. Nauk SSSR, Moscow, 1963; Academic, New York, 1965).
16. V. A. Krasil'nikov and V. V. Krylov, *Introduction to Physical Acoustics* (Nauka, Moscow, 1984).
17. S. M. Rytov, Akust. Zh. **2** (1), 72 (1956) [Sov. Phys. Acoust. **2**, 68 (1956)].

Translated by Yu. Epifanov

Physics of the Solid State, Vol. 44, No. 1, 2002, pp. 124–132. Translated from Fizika Tverdogo Tela, Vol. 44, No. 1, 2002, pp. 119–127.

MAGNETISM AND FERROELECTRICITY

Distribution of Cations in Magnetite Prepared by Mechanochemical Synthesis

S. I. Novikov*, E. M. Lebedeva, A. K. Schtoltz***, L. I. Yurchenko*, V. A. Tsurin*, and V. A. Barinov***

** Institute of Metal Physics, Ural Division, Russian Academy of Sciences, ul. S. Kovalevskoĭ 18, Yekaterinburg, 620219 Russia*

*** Institute of Solid-State Chemistry, Ural Division, Russian Academy of Sciences, Pervomaĭskaya ul. 91, Yekaterinburg, 620219 Russia*

**** Ural State Technical University, ul. Mira 19, Yekaterinburg, 620002 Russia*

e-mail: novikov@imp.uran.ru

e-mail: barinov@imp.uran.ru

Received January 10, 2001; in final form, May 18, 2001

Abstract—The distribution of iron cations in the crystal lattice of the $Fe_{3-\nu}O_4$ ($\nu = 0.153$) cation-deficient spinel produced by mechanical dispersion of α-Fe_2O_3 hematite in water is investigated using x-ray diffraction and Mössbauer spectroscopy. Analysis of the Mössbauer data shows that the $Fe_{2.847}O_4$ magnetite prepared by mechanochemical synthesis is a chemically heterogeneous compound. The crystal structure of $Fe_{2.847}O_4$ is characterized by local environments of the $(Fe^{2.5+})_0$ cations at $\nu_0 \le 0.1$, $\nu_1 \cong 0.12$, $\nu_2 \cong 0.18$, and $\nu_3 \cong 0.26$, which are responsible for a broad distribution of magnetic hyperfine fields with the $P(H)$ probability maxima near 37.0, 36.0, 34.0, and 30.0 MA m^{-1}. © *2002 MAIK "Nauka/Interperiodica".*

1. INTRODUCTION

In 1939, Verwey [1] assumed that bivalent iron cations Fe^{2+} play the decisive role in the mechanism of electron conduction in magnetite and other compounds of the general formula $Fe_{3-\nu}O_4$ ($0 \le \nu \le 1.3$). This idea was confirmed in the 1970s [2–4] and received unexpected development in the investigation into the nature of the instability of α-Fe_2O_3 hematite under the mechanical action [5].

It is known [6–8] that iron oxides with a spinel structure ($Fd3m$) belong to the subtraction-type compounds. The structure of these oxides is stable over a wide composition range from the stoichiometric magnetite Fe_3O_4, which contains 8 Fe^{3+} cations at tetrahedral (8*a*) or *A* sites and 16 cations ($8Fe^{3+} + 8Fe^{2+}$) at octahedral (16*d*) or *B* sites, to the $Fe_{2.67}O_4$ compound known as γ-Fe_2O_3. In a unit cell of the $Fe_{2.67}O_4$ compound, a 1/9 fraction of all the regular lattice sites of iron atoms is vacant due to a deficit of Fe^{2+} cations ($8Fe^{3+}$ cations occupy the *A* sites and $13^{1/3}Fe^{3+}$ cations are located at the *B* sites). It is this feature of compounds in the Fe–O system that, at one time, determined the choice of the physical model advanced in [5, 9–11] for the mechanism of the hematite ⟶ magnetite transformation observed in α-Fe_2O_3 under mechanical actions.

However, the elucidation of the nature and mechanisms of transformations occurring in solids in the course of milling calls for detailed consideration of the interactions between the milling medium, the material subjected to milling, and the material of the vessel. As is known [12–14], a deficit of Fe^{2+} cations in the $Fe_{3-\nu}O_4$ compounds over the entire range $0 \le \nu \le 1/3$ can be rather easily attained using chemical methods (for example, redox reactions under the appropriate conditions). In our recent works [15, 16], we investigated the instability of hematite under mechanical actions and analyzed, in detail, the correlations between the degree and type of contamination of the treated material and the kinetics and direction of the mechanochemical reactions involved. It was established that the hematite ⟶ magnetite transformation observed upon milling has a chemical nature and is associated with the appearance of iron impurities (formed during attrition of milling fittings) in treated powders.

Moreover, by virtue of the specific features of the procedure used for preparing magnetite, we cannot rule out the possibility that the spinels prepared by mechanochemical synthesis will differ in the number of parameters from their analogs obtained using a chemical method under equilibrium conditions. In the present work, we investigated the features in the distribution of iron cations in the structure of spinels produced under the mechanical treatment of hematite in water.

2. EXPERIMENTAL TECHNIQUE

A powder of chemically pure hematite α-Fe_2O_3 with an iron content of 69.0 wt % and a mean particle size of 20 μm was used as the object of investigation. Distilled water (15–50 ml) served as the milling medium.

Hematite (m_p = 2 g) was mechanically treated in a Pulverisette-5 (Fritisch GMBH) centrifugal planetary mill in tight vessels (80 ml) fabricated from low-carbon steel. The diameter d_b of the milling balls was 10 mm. The ball-to-powder mass ratio m_b/m_p was equal to 50. The rate of rotation Ω_p of a carrying platform of the mill was constant and equal to 47.1 s^{-1} (N_p = 450 rpm), and the rate of rotation ω_v of the vessels was 89 s^{-1} (n_v = 850 rpm).

The content of iron cations in treated α-Fe_2O_3 was checked against a chemical analysis. The concentration of Fe^{3+} cations in the magnetite synthesized was measured using volume complexometry with sulfosalicylic acid as an indicator. Cations Fe^{2+} were fixed in the form of iron monooxide, and their content was determined by titrating with potassium bichromate in phenylatropic acid. The error in determination of iron cations was ±0.1 wt %. The chemical analysis data for hematite after milling in water (30 ml) for 30 h are presented in Table 1.

The structure and the phase state of hematite powders in different milling stages was studied by x-ray diffraction (filtered CuK_α radiation) and ^{57}Fe Mössbauer spectroscopy in a transmission geometry. The identification of the crystalline phases formed in hematite in the course of mechanochemical reactions and calculations of the structure parameters were carried out using the entire set of diffraction lines obtained. The theoretical diffraction patterns and the I_{hkl} intensities of individual reflections *hkl* were calculated with due regard for the coordinates of iron cations in the corresponding positions in the spinel lattice [8].

The ^{57}Fe Mössbauer spectra of the α-Fe_2O_3 powders obtained at different stages of mechanical treatment were recorded at 300 K on a spectrometer with the use of a ^{57}Co(Cr) source. The gamma-ray radiation was measured using a resonance scintillation detector. The model calculations of the experimental spectra and the reconstruction of the hyperfine-field distribution functions $P(H)$ were performed according to the algorithm described earlier in [17]. In some cases, the $P(H)$ functions were calculated using the regularization method [18].

3. EXPERIMENTAL RESULTS

3.1. Structural investigations. Hematite α-Fe_2O_3 is one of the most widespread metal oxides in nature. The crystal structure of α-Fe_2O_3 has been thoroughly investigated and described in the literature [7, 8, 19, 20].

Figure 1 shows fragments of x-ray diffraction patterns that illustrate the evolution of the hematite structure in the course of mechanical dispersion in water (30 ml). It can be seen from Fig. 1 that the mechanical treatment leads to the disappearance of a set of reflections typical of the α-Fe_2O_3 compound (Fig. 1a), which is characterized by the rhombohedral unit cell with the parameters a = 0.5424 nm and $\alpha = 55°17'$ [19], and the formation of a new set of lines (Figs. 1b, 1c) whose number and location indicate a face-centered cubic spinel structure ($Fd3m$) [18]. The lattice parameters a for hematite powders milled for 10 and 30 h are equal to 0.838 and 0.837 nm, respectively. These values are close to the lattice parameters available in the literature for Fe_3O_4 [3–8]. Upon annealing of the hematite powders (Fig. 1d), the a parameter increases to 0.84 nm (with a simultaneous decrease in the width of diffraction lines) and coincides with the corresponding parameter measured for a magnetite single crystal.

Analysis of the x-ray diffraction data demonstrates that the lattice parameters of the spinels produced by mechanochemical synthesis for different times are close to one another in the given milling experiment and weakly depend on the experimental conditions. A decrease in the water volume to 15 ml (all other milling conditions being the same) results in a change in the lattice parameter of the synthesized magnetite from 0.837 to 0.839 nm for powders subjected to milling for 10 and 30 h. The lattice parameters of the spinels prepared in water (50 ml) also turn out to be close to the above values, even though the reduction rate of hematite in this case decreases considerably.

The last circumstance and the absence of reflections from the planes characteristic of γ-Fe_2O_3 in the x-ray diffraction patterns confirm the assumption that the mechanical dispersion makes the dominant contribution to the hematite ⟶ magnetite transformation and the formation of $Fe_{3-v}O_4$ cation-deficient compounds

Table 1. Chemical analysis data for the magnetite prepared by mechanochemical synthesis

Sample	Fe_{tot}, wt %	Fe^{2+}, wt %	Fe^{3+}, wt %	Stoichiometry
$Fe_{3-v}O_4$ (v = 0)	72.37	24.12	48.25	Fe_3O_4
Mechanochemically synthesized	71.31	13.53	57.78	$Fe_{2.847}O_4$
Fe_3O_4-F [2]	70.60	17.84	–	$(Fe_2O_3)(FeO)_{0.068}$
γ-Fe_2O_3	69.90	–	69.90	$Fe_{2.66}O_4$

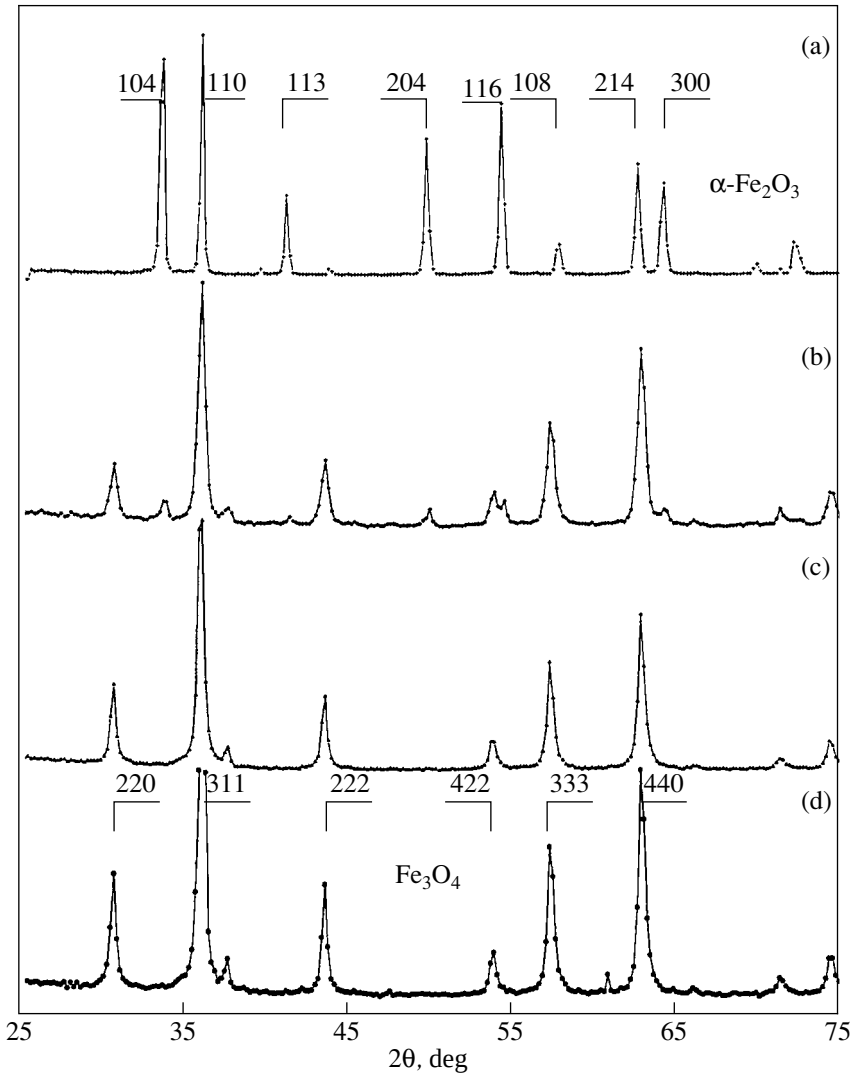

Fig. 1. Fragments of the x-ray diffraction patterns of the hematite in (a) the initial state (α-Fe_2O_3) and after milling in water (30 ml) for (b) 10 and (c) 30 h and (d) after milling in water (30 ml) for 30 h followed by annealing at 1075 K.

with a vacancy concentration in the range $0.06 < v < 0.16$ [2–4].

The specific features of the occupation of crystal lattice planes in the $Fe_{3-v}O_4$ compounds synthesized were determined by comparing the calculated and experimental ratios $I_{h_1k_1l_1}/I_{h_2k_2l_2}$ of the diffraction line intensities for the same vacancy concentration v. The diffraction line intensities were calculated from the structure amplitudes F_{hkl} of iron cations at the 8*a* and 16*d* positions in the spinel structure. Figure 2 displays typical dependences of the relative intensity of structure reflections for the (*hkl*) planes on the degree of occupation of the *A* and *B* sites with vacancies in the $Fe_{2.847}O_4$ spinel structure. The solid lines in Fig. 2 correspond to the theoretical dependences of the relative intensity $I_{h_1k_1l_1}/I_{h_2k_2l_2}$ at the vacancy concentration v = 0.153, which were calculated for the case when all the vacancies occupy either the *A* sites or the *B* sites in the unit cell. The experimental reduced intensities for the corresponding planes (*hkl*) in the lattice of $Fe_{2.847}O_4$ are indicated by arrows in Fig. 2.

As can be seen from Fig. 2, the distribution of vacancies over the sites allowed in the structure of the spinels produced by mechanochemical synthesis is not equally probable. The vacancies predominantly occupy octahedral sites of the crystal lattice with a probability of 0.69–0.80 for crystallographic planes differing in type and degree of occupation with ions. It should be noted that the accuracy of measuring the intensity in the x-ray diffraction patterns of the synthesized compounds did not exceed 10–15% due to a considerable increase in the background intensity I_b and broadening of the diffraction maxima. Therefore, it can be assumed

that, on the average, 74 ± 12% of the total amount of vacancies in the structure of the $Fe_{2.847}O_4$ compound are located at the octahedral sites. For comparison, we note that, according to the neutron diffraction data obtained for cation-deficient spinels prepared through low-power mechanical dispersion of hematite [21, 22], about 75% of the vacancies in the crystal lattice of the $Fe_{2.818}O_4$ compound occupy more energetically favorable octahedral sites. Unfortunately, the available data on the distribution of iron cations in the spinels synthesized by chemical methods under equilibrium conditions are rather contradictory. In particular, it was found that the distribution of vacancies in γ-Fe_2O_3 samples prepared through the oxidation of the stoichiometric magnetite Fe_3O_4 at low temperatures is similar to a statistical distribution [1, 4, 6]. However, according to other authors [14, 23], more than 90% of the vacancies are located at the octahedral sites of the spinel structure.

The discrepancy in the available data on the location of iron cations in the spinel lattice can be associated with different scales of inhomogeneities in the cation distribution and the possibility of identifying these inhomogeneities by using a particular technique rather than with the specific features of the procedure used for synthesizing the $Fe_{3-\nu}O_4$ compounds. Note that the reliability of the data obtained by diffraction techniques increases with both a rise in the degree of homogeneity of the solid solutions under investigation and an increase in the volume of precipitates in many-phase materials. Therefore, these techniques, as applied to analysis of chemical inhomogeneities in dispersed powders of $Fe_{3-\nu}O_4$ cation-deficient spinels, can provide merely the characteristics averaged over the volume of the studied sample.

3.2. Mössbauer data. The Mössbauer spectra of the hematite powders at T = 300 K after treatment in water (15 ml) for different times are displayed in Fig. 3. For comparison, Fig. 3 shows the spectra of α-Fe_2O_3 in the initial state (Fig. 3a) and after milling for 30 h and subsequent annealing at 1075 K under vacuum for 1 h (Fig. 3e). The Mössbauer spectrum of α-Fe_2O_3 in the initial state is represented by a single sextet that corresponds to Fe^{3+} cations at the 4*a* positions in the corundum rhombohedral unit cell [19]. It is seen from Fig. 3 that, in the course of mechanical treatment, this spectrum transforms into a spectrum (Fig. 3d) that can be considered a superposition of at least two Zeeman sextets. However, the least-squares calculations demonstrate that the experimental spectra of hematite milled for 30 h are best described by a superposition of the three sextets *A*, *B*, and *C* with mean magnetic hyperfine fields $\langle H_{hf} \rangle$ = 38.61, 36.54, and 33.43 MA m^{-1}, respectively. The hyperfine fields $\langle H_{hf} \rangle$ for the *A* and *B* components are independent of both the milling time (up to 30 h) and the annealing temperature and slightly differ from those for Fe_3O_4 [2–4]. Moreover, it can be seen from Figs. 3d and 3e that, unlike the x-ray diffraction

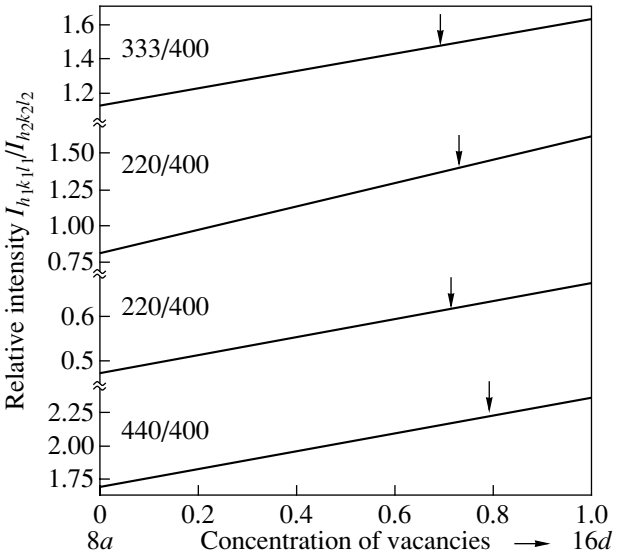

Fig. 2. Dependences of the relative intensity $I_{h_1k_1l_2}/I_{h_2k_2l_2}$ of the structure reflections for magnetite prepared by mechanochemical synthesis in water (30 ml) for 30 h.

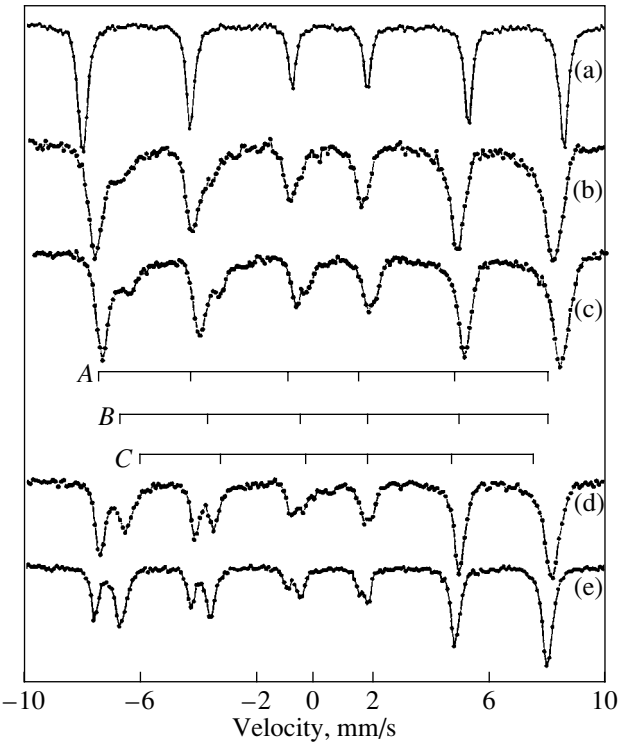

Fig. 3. Mössbauer spectra of the hematite in (a) the initial state (α-Fe_2O_3) and after milling in water (15 ml) for (b) 5, (c) 10, and (d) 30 h and (e) after milling in water (15 ml) for 30 h followed by annealing at 1075 K. The *A*, *B*, and *C* sextets are components of the ^{57}Fe Mössbauer spectrum. The *B* and *C* sextets correspond to iron cations in the 8*a* and 16*d* positions in the spinel structure. T = 300 K.

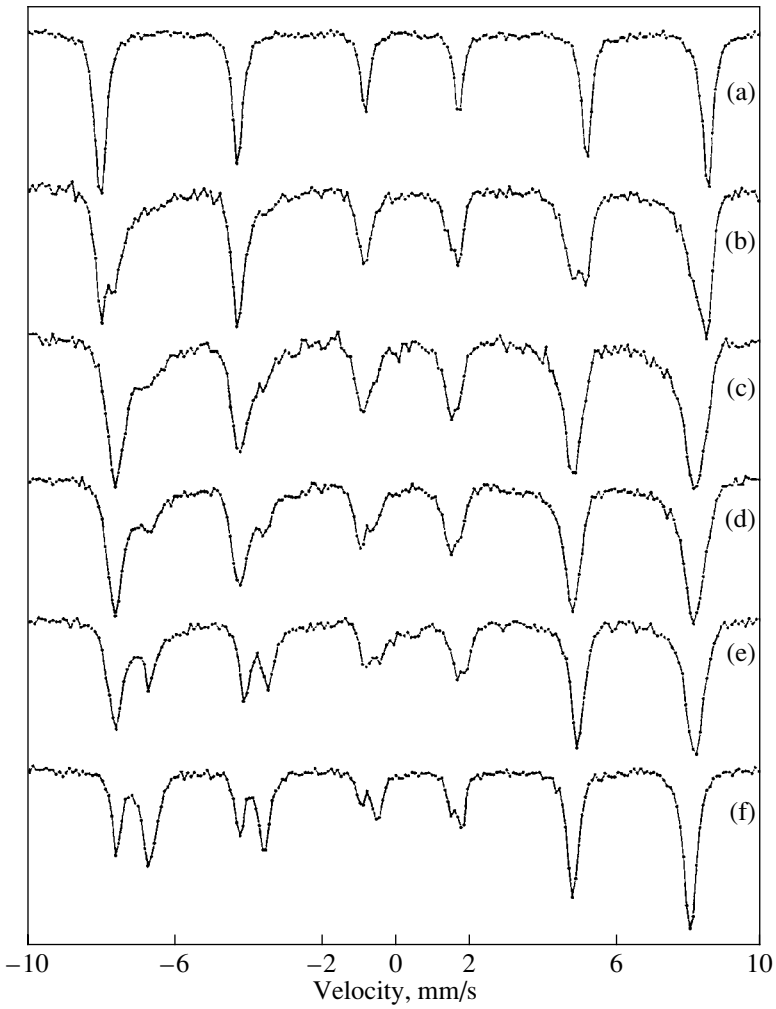

Fig. 4. Mössbauer spectra of the hematite in (a) the initial state (α-Fe_2O_3) and after milling in water (30 ml) for (b) 5, (c) 10, (d) 15, and (e) 30 h and (f) after milling in water (30 ml) for 30 h followed by annealing at 1075 K. T = 300 K.

patterns (Fig. 1), the spectra of $Fe_{3-v}O_4$ powders subjected to annealing change considerably owing primarily to the change in the area ratio of the Mössbauer components. The ratios S_{B+C}/S_A for the spectra of hematite milled for 10 and 30 h are equal to 1.17 and 1.27, respectively. After the annealing, this ratio increases to 1.63. This indicates that the occupation of nonequivalent sites becomes similar to an equilibrium occupation characteristic of cations in the structure of perfect spinel.

Mössbauer spectra similar in shape to those shown in Figs. 3c and 3d were observed earlier for $Fe_{3-v}O_4$ ($0 \le v \le 0.33$) cation-deficient spinels. These spectra should correspond to either an ordered solid solution of γ-Fe_2O_3 in the Fe_3O_4 matrix [4], a mixture of stoichiometric magnetite with the γ-Fe_2O_3 metastable phase [3], or a nonstoichiometric magnetite with a deviation in composition within the range $0.10 < v < 0.33$ [2]. However, the fact that the (321), (421), and (500) reflections typical of γ-Fe_2O_3 [4, 6] are absent in the x-ray diffraction patterns of the hematite powders prepared by mechanochemical synthesis counts in favor of the last model.

As in the case of annealing (Fig. 3e), the Mössbauer spectra of the synthesized $Fe_{3-v}O_4$ compounds substantially depend on the mechanical treatment conditions. Figure 4 displays the Mössbauer spectra of hematite powders at T = 300 K after treatment in water (30 ml) for different times. For comparison, this figure shows the spectra of α-Fe_2O_3 in the initial state (Fig. 4a) and after milling for 30 h followed by annealing at 1075 K under vacuum for 1 h (Fig. 4f). The calculations performed demonstrate that the area ratio S_B/S_A of the Mössbauer components assigned to iron cations at the octahedral and tetrahedral sites does not exceed 0.5 for the powder milled for 30 h under the given conditions of mechanical treatment. However, as in the preceding case (Fig. 3e), the S_B/S_A ratio also increases upon annealing and approaches the equilibrium value. It should be noted that the spectrum shown in Fig. 4e only

slightly differs in its parameters from the spectrum of the $Fe_{2.818}O_4$ compound prepared by low-power milling over 200 h [22].

4. DISCUSSION

The structure of spinels in the Fe–O system is stable over a wide range of concentrations [6–8]. This suggests that, although the parameters of the local environment of iron cations change considerably, the spatial scale of these changes can appear to be inadequate to provide all the necessary diffraction conditions of formation of the corresponding structure reflections. It is quite possible that, owing to the scale limitations on the degree of resolution of chemical inhomogeneities, the parameters characterizing the distribution of vacancies in the $Fe_{3-\nu}O_4$ spinels produced by mechanochemical synthesis can turn out to be close to one another over a wide range irrespective of the milling conditions and sizes of microcrystallites [21, 22]. On the other hand, the discrepancy in the available data on the location of iron cations in the γ-Fe_2O_3 compounds synthesized by chemical methods under equilibrium conditions can also be associated with the different degrees of dispersion of the prepared powders [6, 12, 14].

It should be noted that, in resonance methods, unlike diffraction methods, the resolution limit of features in the nearest atomic environment is determined primarily by the natural width of the absorption line of a resonant nucleus [24]. However, although the information comes from a local level, it is averaged over the volume of the studied sample; consequently, it is impossible to determine the true scale of the spatial localization of identical atomic environments.

Reasoning from the results of investigations performed with different compounds in the Fe_3O_4–γ-Fe_2O_3 system, which were synthesized using chemical methods under equilibrium conditions, it is believed that cations are distributed over both the tetrahedral and octahedral sites allowed in the structure of the $Fe_{3-\nu}O_4$ spinels [2–4, 6, 12]. According to the charge neutrality of the unit cell, the distribution of cations can be formally written in the form

$$Fe_{3-\nu}O_4 \longrightarrow [Fe^{3+}_{1-\tau}\square_\tau]_{tetr}[(Fe^{2.5+}_{2(1-3\nu)})Fe^{3+}_{6\nu-\omega}\square_\omega]_{oct}O_4^{2-}. \quad (1)$$

Here, ν is the total number of vacancies, τ is the fraction of vacancies at the tetrahedral sites of the lattice, and ω is the fraction of vacancies at the octahedral sites ($\nu = \tau + \omega$). This notation implies that each of the bivalent Fe^{2+} cations at the octahedral sites can be involved in an ideal pair ($Fe^{2+} + Fe^{3+}$), which can be considered a $Fe^{2.5+}$ cation with a mean valence of 2.5+. The homogeneous magnetite is described by the sole distribution (1). In the general case, the number of distributions is determined by the number of local environments of iron cations.

The description of the hyperfine interactions in the stoichiometric magnetite Fe_3O_4 ($\nu = 0$) presents no problems within the pair-localized model of distribution of Fe^{3+} and $Fe^{2.5+}$ magnetically active cations that are coupled through negative exchange interaction to the parameter $T_c = 858$ K [20, 25, 26]. Qualitatively, the Mössbauer spectra of $Fe_{3-\nu}O_4$ ($\nu \neq 0$) cation-deficient compounds can be interpreted rather easily provided that the deviation of the area ratio of spectral components for magnetite from the theoretical value $S_A/S_B = 8/16$ (to within the Lamb–Mössbauer factor) is determined not only by the small occupation of octahedral sites with iron cations [21] but also by the superposition of hyperfine fields of $(Fe^{3+})_t$ cations at the tetrahedral sites and $(Fe^{3+})_o$ octahedral cations unpaired due to the deficit of Fe^{2+} cations [2]. The appearance of the components with low hyperfine fields in the Mössbauer spectra indicates a deviation of the magnetite composition from stoichiometry. The larger the difference between the S_A/S_B ratio and 1/2, the greater the deviation from the stoichiometry (Figs. 3d, 4d). The asymmetry of spectral lines with respect to zero velocity can also indicate an increase in the number of environments of $Fe^{2.5+}$ cations with a small number of Fe^{2+}/Fe^{3+} pairs at the octahedral sites or the formation of a continuous distribution of iron cations over the sites allowed in the spinel structure.

Since the iron cations in the $Fe_{3-\nu}O_4$ structure can be distributed in different ways, we can argue that the unimodal distribution in cation-deficient spinels is an exception rather than the rule and is especially improbable in compounds produced by mechanical dispersion.

As was noted above, the spectrum of the $Fe_{2.847}O_4$ spinel (Fig. 4d) only slightly differs in its parameters from that of the $Fe_{2.818}O_4$ compound synthesized by low-power milling over 200 h [21]. However, as follows from the concentration dependence of the hyperfine field for iron cations in the B sublattice [4], the mean field $\langle H_{hf}(Fe^{2.5+})\rangle$ for the $Fe_{2.818}O_4$ spinel ($\tau = 0.044$ and $\omega = 0.138$) cannot exceed 33.43 MA m^{-1}. Correspondingly, the ν value should be no more than 0.12 for a field of 36.62 MA m^{-1}.

The required data on the number of vacancies in the structure of $Fe_{3-\nu}O_4$ compounds can be obtained from the concentration dependence of $\langle H_{hf}(Fe^{2.5+})\rangle$ [4], calculated from the neutron diffraction data (0.182) [22], and be determined from chemical analysis (0.153). Analysis shows that the scatter in the data is not accidental and can be explained in terms of the polymodal distribution of iron cations in spinels produced by mechanochemical synthesis. In this case, a considerable part of the iron cations corresponds to $\nu_i < 0.1$ and cannot be identified by Mössbauer spectroscopy.

Making allowance for the fact that all iron cations with different local environments contribute to the spectrum, we attempt to determine the number of dis-

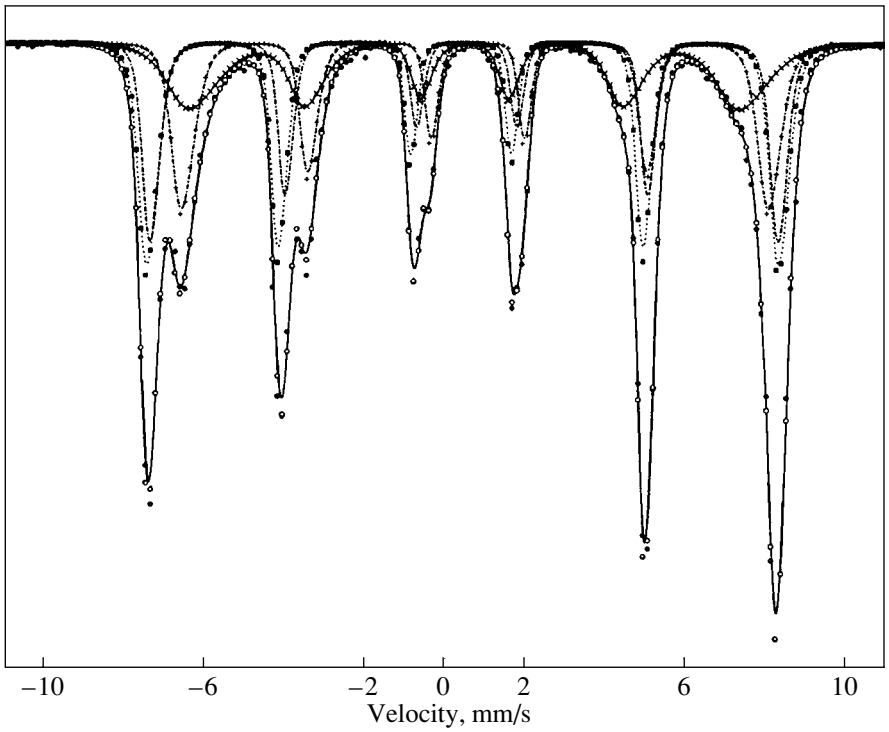

Fig. 5. Simulation of the Mössbauer spectrum of the $Fe_{2.847}O_4$ magnetite with inclusion of the four Mössbauer components.

tributions and the concentration of environments of a particular type from the corresponding partial contributions. It follows from formula (1) that, in the case when the spinel lattice contains ν vacancies ($\nu = \tau + \omega$), the partial Mössbauer components $S(Fe^{3+})_t$ (for tetrahedral iron cations in the *A* sublattice), $S(Fe^{3+})_o$ (for unpaired octahedral cations in the *B* sublattice), and $S(Fe^{2.5+})_o$ (for paired octahedral cations in the *B* sublattice) are determined by the relationships

$$S(Fe^{3+})_t = (1-\tau)/(3-\nu), \quad (2a)$$

$$S(Fe^{3+})_o = (6\nu-\omega)/(3-\nu), \quad (2b)$$

$$S(Fe^{2.5+})_o = 2(1-3\nu)/(3-\nu). \quad (2c)$$

Let us now assume that iron cations in the crystal lattice of the $Fe_{2.847}$ spinel (Fig. 4e) have a unimodal distribution with environments $(Fe^{2.5+})_o$ and $(Fe^{3+})_t$. From relationship (2c), we obtain $S(Fe^{2.5+})_o = 0.327$ and the number of vacancies $\nu = 0.18$. This value coincides with the above ν value for $Fe_{2.818}O_4$ [21] but exceeds the number of vacancies $\nu_c = 0.153$ obtained from the chemical analysis. The inclusion of three types of cation environments leads to a decrease in ν to 0.165 ($\tau = 0.0845$ and $\omega = 0.0805$). Thus, the simulation of the experimental spectrum with the above parameters results in a uniform distribution of vacancies over the *A* and *B* sublattices of the spinel prepared by mechanochemical synthesis. Moreover, the fulfillment of the inequality $\nu/\nu_c > 1$ (where $\nu_c \sim \Sigma c_i V_i$ is the weighted mean number of vacancies per mole of the analyzed compound and c_i is the partial concentration of vacancies in the volume V_i) for two and three types of cation environments in the spinel structure implies that the distribution of vacancies in $Fe_{2.847}O_4$ is not unimodal.

Table 2. Calculated hyperfine parameters of $Fe_{2.847}O_4$ magnetite for four Mössbauer components

Type and localization of Fe cations	Hyperfine field $\langle H_{hf}\rangle$, (MA m^{-1})/kOe	Isomer shift *IS*,* mm/s	Linewidth Γ_{1-6}, mm/s	Area, %
$(Fe^{2.5+})_{o1}$	36.31/456.20	0.67	0.536	24.493
$(Fe^{2.5+})_{o2}$	34.11/428.51	0.38	1.122	22.318
$(Fe^{3+})_{t1} + (Fe^{3+})_{t2}$	39.07/490.87	0.30	0.481	30.386
$(Fe^{3+})_{o1} + (Fe^{3+})_{o2}$	38.85/488.11	0.40	0.443	22.803

* Relative to α-Fe.

As was already mentioned, the experimental spectrum of the $Fe_{3-\nu}O_4$ magnetite prepared by mechanochemical synthesis is best described by the superposition of three Mössbauer sextets *A*, *B*, and *C* (Fig. 3d). Analysis of the hyperfine interaction parameters for the sextets shows that the *C* component in the spectrum is associated with the iron cations that occupy the octahedral sites of the lattice and whose environments are similar to those of paired iron cations in $Fe_{3-\nu}O_4$ ($\nu \cong 0.18$) cation-deficient spinels [4]. Since the spectrum of the $Fe_{2.847}O_4$ compound contains two sextets with effective magnetic fields $\langle H_{hf}(Fe^{2.5+})_o\rangle$ = 36.31 and 34.11 MA m^{-1} (Fig. 4d), the distribution of iron cations over the *A* and *B* sites in the spinel structure can be described by at least two expressions (1) at $\nu_1 \cong 0.12$ and $\nu_2 \cong 0.18$. Consequently, the experimental spectrum of the magnetite prepared through mechanochemical synthesis ($\nu_c = 0.153$) can be represented by the superposition of six Mössbauer components for $Fe^{2.5+}$ and Fe^{3+} cations at the octahedral and tetrahedral sites of the crystal lattice. However, simulation of the spectrum of $Fe_{2.847}O_4$ demonstrates that the values of τ_i and ω_i for a particular distribution cannot be determined from the $S_i(Fe^{3+})_t$ and $S_i(Fe^{3+})_o$ partial contributions, because the parameters of the corresponding sextets for ν_1 and ν_2 coincide to within the limits of resolution of the Mössbauer experiment. The decomposition of the spectrum of the spinel into four components is shown in Fig. 5. As in the preceding cases, the spectrum was calculated with freely variable parameters. The parameters available in the literature [2–4] were used as the zeroth approximation. The calculated parameters of the sextets are listed in Table 2. Note that $S(Fe^{3+})_t$ and $S(Fe^{3+})_o$ correspond to the sums $S_1 + S_2$ of the partial contributions from tetrahedral and octahedral Fe^{3+} cations in the corresponding distributions.

The experimental spectrum of the magnetite prepared by mechanochemical synthesis is quantitatively described well within the discrete approximation. However, in the qualitative sense, the results obtained seem to be insufficiently adequate, because the simulation of the spectrum ignored the contributions from cations with the environment characterized by small values $\nu_i < 0.1$, whose fraction can appear to be rather large. The occurrence of local environments of this type most clearly manifests itself when comparing the magnetic-hyperfine-field distribution functions $P(H)$ for the Mössbauer spectra of the cation-deficient spinel $Fe_{2.847}O_4$ and the stoichiometric magnetite Fe_3O_4 (Figs. 6b, 6c). As a first approximation, the $P(H)$ functions were reconstructed only for the $(Fe^{3+})_t$ and $(Fe^{2.5+})_o$ cations that occupy the tetrahedral and octahedral sites in the spinel lattice and are characterized by substantially different isomer shifts (Table 2). The correlations of the hyperfine parameters were determined in the following form: $\delta_j(A, B) = a_jH_n + b_j$ and $\varepsilon_j(A, B) = c_jH_h + d$, where $\delta_j(A, B)$ and $\varepsilon_j(A, B)$ are the isomer shifts and the quadrupole splittings for the *A* and *B* sublattices, respectively; and *a*, *b*, *c*, and *d* are the correlation parameters for each kernel of the distribution [17]. As can be seen from Fig. 6, the deficit of Fe^{2+} cations in the spinel structure actually leads to a broad distribution of magnetic hyperfine fields with the $P(H)$ probability maxima near 37.0, 36.0, 34.0, and 30.0 MA m^{-1}, which correspond to local environments of the $(Fe^{2.5+})_o$ cations at $\nu_0 < 0.1$, $\nu_1 \cong 0.12$, $\nu_2 \cong 0.18$, and $\nu_3 \cong 0.26$.

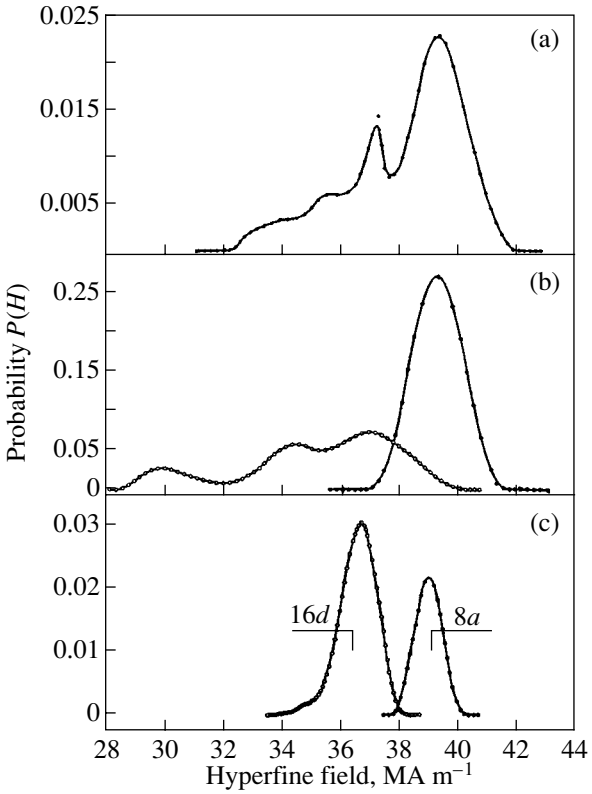

Fig. 6. Distribution functions $P(H)$ for the Mössbauer spectra of (a, b) the $Fe_{2.847}O_4$ compound and (c) magnetite. The $P(H)$ functions are reconstructed using (a) the regularization method and (b) two correlations.

5. CONCLUSION

It should be noted that, although the problems concerning the distribution of iron cations in the structure of $Fe_{3-\nu}O_4$ spinels are the most interesting problems in magnetochemistry [2–4, 13, 20], a number of questions remain open [5, 9, 15, 16, 22, 25]. Analysis of the x-ray diffraction and Mössbauer data obtained in the present work has demonstrated that the discrepancies in the available data on the cation distribution in cation-deficient compounds can be associated with the structural features of $Fe_{3-\nu}O_4$ compounds, on the one hand, and the failure to resolve chemical inhomogeneities formed in the spinel lattice under the given conditions of syn-

thesis, on the other. In this respect, attempts to describe the iron cation distribution in mechanochemically synthesized $Fe_{3-\nu}O_4$ compounds in terms of mean parameters are as justified as the parameters characterizing the homogeneous solid solution are applicable to adequate description of its heterogeneous analog. A more constructive approach to solving the problems associated with the characterization of the inhomogeneous state of material systems should involve (in addition to improvements in the technical potentialities of the methods used for investigating short-range atomic orders) a detailed analysis of experimental data on the basis of the appropriate mathematical apparatus in order to obtain information regarding local atomic environments on a qualitatively higher level, for example, on the level of polymodal distribution functions.

ACKNOWLEDGMENTS

We are grateful to G.N. Konygin and V.S. Rusakov for supplying the data on the reconstruction of the magnetic-hyperfine-field distribution functions for Mössbauer spectra of the $Fe_{3-\nu}O_4$ compounds prepared by mechanochemical synthesis.

REFERENCES

1. E. J. W. Verwey, Nature **144**, 327 (1939).
2. J. M. Daniels and A. Rosencwaig, J. Phys. Chem. Solids **30**, 1561 (1969).
3. H. P. Weber and S. S. Hafner, Z. Kristallogr. **133**, 327 (1971).
4. H. Annersten and S. S. Hafner, Z. Kristallogr. **137**, 321 (1973).
5. W. A. Kaczmarek and B. W. Ninham, IEEE Trans. Magn. **MAG-30**, 732 (1994).
6. G. Hägg, Z. Phys. Chem. Abt. B **29**, 95 (1935).
7. G. B. Bokiĭ, *Introduction to Crystal Chemistry* (Moscow Gos. Univ., Moscow, 1954).
8. K. Schubert, *Kristallstrukturen Zweikomponentiger Phasen* (Springer-Verlag, Heidelberg, 1964; Metallurgiya, Moscow, 1971).
9. W. A. Kaczmarek, I. Onyszkiewicz, and B. W. Ninham, IEEE Trans. Magn. **MAG-30**, 4725 (1994).
10. S. I. Campbell, W. A. Kaczmarek, and G. M. Wang, Nanostruct. Mater. **6**, 735 (1995).
11. S. I. Campbell and W. A. Kaczmarek, in *Mössbauer Spectroscopy Applied to Materials and Magnetism*, Ed. by G. J. Long and F. Grandjean (Plenum, New York, 1996), Vol. 2.
12. E. J. W. Verwey, Z. Kristallogr. **91**, 65 (1935).
13. P. W. Selwood, *Magnetochemistry* (Interscience, New York, 1956).
14. G. Kullerud, G. Donnay, and J. D. H. Donnay, Z. Kristallogr. **128**, 1 (1969).
15. S. I. Novikov and V. A. Barinov, in *Proceedings of the V All-Russia Scientific Conference on Oxides, Yekaterinburg, 2000*, p. 345.
16. S. I. Novikov and V. A. Barinov, in *Proceedings of the V All-Russia Scientific Conference on Oxides, Yekaterinburg, 2000*, p. 349.
17. V. I. Nikolaev and V. S. Rusakov, *Mössbauer Investigations of Ferrites* (Moscow Gos. Univ., Moscow, 1985), p. 21.
18. E. V. Voronina, N. V. Ershov, A. L. Ageev, and Yu. A. Babanov, Phys. Status Solidi B **160**, 625 (1990).
19. L. I. Mirkin, *Handbook of X-ray Analysis of Polycrystalline Materials* (Fizmatgiz, Moscow, 1961; Plenum, New York, 1964).
20. S. Krupichka, *Physik der Ferrite* (Verlag der Tschechoslowakischen Akademie der Wissenschaften, Prague, 1973).
21. M. Hofmann, S. J. Campbell, and W. A. Kaczmarek, Mater. Sci. Forum **228–231**, 607 (1996).
22. E. Wu, S. J. Campbell, W. A. Kaczmarek, *et al.*, Mater. Sci. Forum **312–314**, 121 (1999).
23. J. M. D. Coey and A. H. Morrish, J. Phys. (Paris) **32**, C1-271 (1971).
24. *Chemical Applications of Mössbauer Spectroscopy*, Ed. by V. I. Goldanskii and R. H. Herber (Academic, New York, 1962; Mir, Moscow, 1970).
25. B. N. Goshchitskiĭ, A. N. Men', I. A. Sinitskiĭ, and Yu. G. Chukalkin, *Structure and Magnetic Properties of Oxide Magnets Irradiated by Fast Neutrons* (Nauka, Moscow, 1986).
26. J. B. Goodenough, *Magnetism and the Chemical Bond* (Interscience, New York, 1963; Mir, Moscow, 1969), Chap. 1.

Translated by O. Borovik-Romanova

Physics of the Solid State, Vol. 44, No. 1, 2002, pp. 133–139. Translated from Fizika Tverdogo Tela, Vol. 44, No. 1, 2002, pp. 128–134.

MAGNETISM AND FERROELECTRICITY

Unidirectional Anisotropy and the Roughness of the Ferromagnet–Antiferromagnet Interface

V. D. Levchenko*, A. I. Morozov, and A. S. Sigov****

**Keldysh Institute of Applied Mathematics, Russian Academy of Sciences, Miusskaya pl. 4, Moscow, 125047 Russia*

***Moscow State Institute of Radio Engineering, Electronics, and Automation (Technical University), pr. Vernadskogo 78, Moscow, 117454 Russia*

e-mail: morosov@eot.mirea.ru

Received May 18, 2001

Abstract—Magnetization curves of a ferromagnetic film on an antiferromagnetic substrate are investigated with allowance for the frustration caused by roughness of the interface. The conditions for unidirectional anisotropy are determined, and its dependence on the degree of roughness of the film–substrate interface is found.

1. INTRODUCTION

Unidirectional anisotropy is manifested in a bias of the magnetization curve of a ferromagnetic film deposited on the surface of an antiferromagnet (AFM); examples are NiFe/FeMn, NiFe/CoO, Ni/NiO, Fe/FeF_2, and Fe/Cr. A great number of papers have been devoted to studying the unidirectional-anisotropy effect (see, e.g., review [1]).

We first consider the case where the spins of the AFM are not compensated in an atomic plane parallel to the ferromagnet–AFM interface. In a simple model where the interface is assumed to be perfectly smooth, the exchange interaction between spins of the film and substrate leads to the emergence of a preferential direction for the magnetization of the film. Magnetization reversal of the film gives rise to the formation of a domain wall (DW) in the antiferromagnetic substrate [2, 3].

Since the formation of a DW requires some energy, the magnetization curve is biased relative to its symmetric position along the magnetic-field axis by the amount

$$B_E \sim \frac{(A_{af}K_{af})^{1/2}S_{af}^2}{Ma}, \qquad (1)$$

where B_E is the bias magnetic induction, A_{af} is the exchange stiffness of the AFM, K_{af} is the AFM anisotropy constant in a plane parallel to the film–substrate interface, M is the magnetization of the ferromagnetic film, and a is the thickness of the film.

A real interface is not, of course, perfectly smooth; it contains atomic steps, each of which changes the substrate thickness by one atomic layer. The spin orientation is different on opposite sides of a step in the outer atomic layer of the AFM. Therefore, the presence of steps at the interface leads to frustration, irrespective of the sign of the exchange integral $J_{f,\,af}$ between spins of the film and substrate. We investigated the phase diagram of such a frustrated system in [4] within a continuum model.

Unidirectional anisotropy in an imperfect interface was considered in [5], where the AFM was assumed to consist of noninteracting grains.

In [2, 6], the mechanisms of unidirectional anisotropy were investigated in the case where the spins in an AFM atomic plane parallel to the interface are compensated. In [2], unidirectional anisotropy was assumed to be due to fluctuations of the exchange field at the interface, which are caused by roughness of the interface and, in turn, lead to the formation of microdomains (with dimensions as small as the DW width) in the interfacial region of the AFM.

In the model proposed in [6], unidirectional anisotropy is associated not with roughness of the interface but with a phenomenon which is similar to the spin-flop transition in an AFM and occurs under the action of an exchange field at the interface.

This paper is devoted to studying the magnetization process and determining the dependence of the strength of unidirectional anisotropy on the roughness of the interface in a frustrated system composed of a ferromagnetic film and an antiferromagnetic substrate.

2. MODEL

When studying the spatial distributions of the order parameters over the film and substrate, it was assumed that the magnetization and antiferromagnetism vectors lie in a plane parallel to the interface and are characterized by the angles θ_i ($i = f, af$) that these vectors make with the preferential direction in that plane. Minimizing

the exchange energy in the film–substrate system gives the equations

$$\Delta\theta_i = 0, \tag{2}$$

which should be supplemented by the boundary conditions

$$\tilde{\Delta}\theta_f - \frac{\partial\theta_f}{\partial n} = 0 \tag{3}$$

at the free surface of the film ($\tilde{\Delta}$ is the two-dimensional Laplacian in the film plane, $\frac{\partial}{\partial n}$ is the derivative in the direction of the outward normal to the surface of the layer),

$$\tilde{\Delta}\theta_i - \frac{\partial\theta_i}{\partial n} = \pm\frac{J_{f,af}S_{i+1}}{J_iS_i}\sin(\theta_i - \theta_{i+1}) \tag{4}$$

at the film–substrate interface (J_i is the exchange integral between spins, S_i is the average spin in the ith layer), and $\theta_{af} = 0$ in the bulk of the substrate, far from the interface. All distances are measured in units of the lattice parameter b, which is assumed to be relatively the same for both materials.

Solving the set of equations (2) with boundary conditions (3) gives the spatial distributions of the order parameters in the system under study. A solution was sought using numerical methods for the case where the steps form a set of periodically arranged parallel straight lines. The x axis of the coordinate frame was parallel to the film plane and perpendicular to the edges of the steps, while the z axis was normal to the film plane (two-dimensional case). The functions $\theta_i(x, z)$ were subject to periodic boundary conditions in the region $|x| < L$ and were calculated through expansion in a Fourier series in x. As the result of computer simulation, a phase diagram in the film thickness–roughness plane was obtained.

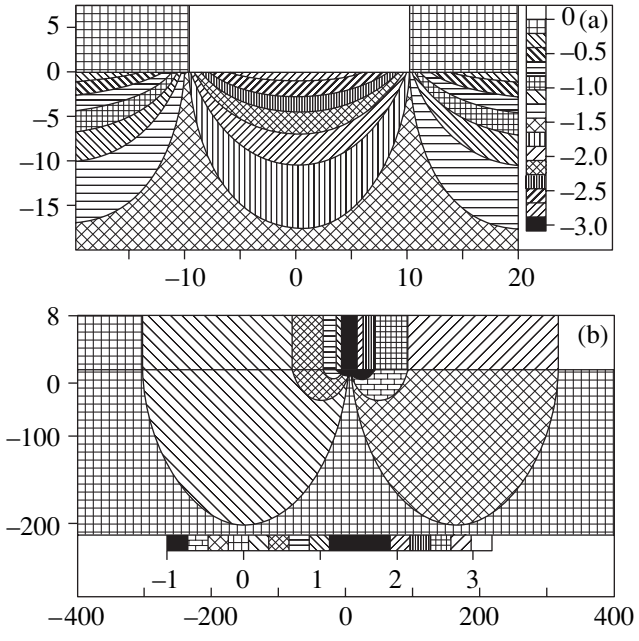

Fig. 1. Distributions of the order parameters in (a) the vortex phase and (b) the domain wall. The zero ordinate corresponds to the film–substrate interface. All distances are measured in units of the lattice parameter. The correspondence between the differently hatched regions and the values of θ_i (in radians) is indicated in the insets.

3. PHASE DIAGRAM

The film–substrate interface is partitioned by steps into regions of two types. In regions of the first type, the interface energy is a minimum when the ferromagnetic and antiferromagnetic vector order parameters are parallel to each other, while in regions of the second type, the energy is minimum when these two vectors are antiparallel.

If the characteristic distance R between steps on the interface is smaller than a certain critical value

$$R_c = \delta_f \approx \gamma a, \tag{5}$$

where

$$\gamma = \frac{J_fS_f^2}{J_{af}S_{af}^2} \gg 1, \tag{6}$$

then the film remains in a single-domain state but static spin vortices appear in the substrate near the interface (Fig. 1a).

A vortex is characterized by two spatial scales. There is a region around a step within which the angle $\theta_f - \theta_{af}$ at the interface is not equal to its optimum value that minimizes the interface energy; this angle is zero on one side of the step and π on the other. The width of this region is

$$\delta_0^{af} \approx \frac{(1+\alpha)b}{\alpha} \sim b, \tag{7}$$

where

$$\alpha = \frac{J_{f,af}S_f}{J_{af}S_{af}}. \tag{8}$$

In the remainder of the interface (the region of width $R \gg \delta_0^{af}$), the angle $\theta_f - \theta_{af}$ equals its optimum value. If the value of θ_{af} is nonzero at the interface, then θ_{af} varies gradually from its interface value to zero over a characteristic depth R in the substrate.

If the characteristic distance R between steps exceeds its critical value ($R > R_c$), then the film is divided into microdomains, with their boundaries coinciding with the edges of the atomic steps. The magnetization directions in the neighboring domains are opposite and correspond to a minimum interface energy. It is significant that the domain wall width δ_f in the case of

$a \sim 10$–100 Å is much smaller than the width of an ordinary DW, because the width δ_f is dictated by the balance of the exchange interactions rather than by that of the exchange and anisotropy energies.

It is seen from Fig. 1b that the DW has a complicated structure: in addition to magnetization rotations, there are vortex distortions of the antiferromagnetic order parameter with a characteristic size of δ_f. As in the case of $R < R_c$, the angle $\theta_f - \theta_{af}$ at the interface is not equal to its optimum value in the region of a width of δ_0^{af} around a step.

Next, we consider the magnetization reversal in each of these two phases.

4. THE SINGLE-DOMAIN PHASE

Let ψ be the angle between the magnetization vector of the film and the antiferromagnetism vector in the bulk of the substrate. Then, in the regions of the first type, far from the steps, we have $\theta_{af} = \psi$ at the interface and the antiferromagnetism vector rotates with distance away from the interface in the substrate at an angle $-\psi$. In the regions of the second type, the angle θ_{af} is equal to $\psi - \pi$ at the interface and the antiferromagnetism vector rotates at an angle $\pi - \psi$.

As in the magnetic-proximity model of Slonczewski [7], the film–substrate interaction energy can be written as

$$W_1 = [C_1\psi^2 + C_2(\pi - \psi)^2]/2, \quad (9)$$

where

$$C_j \equiv C\sigma_j \approx \frac{J_{af}S_{af}^2\sigma_j}{Rb} \quad (10)$$

and σ_j is the area of the regions of jth type ($j = 1, 2$). It should be noted that the estimation of the quantities C_j in [4, Eq. (13)] is incorrect. The point is that the contribution from the region near the edges of a step to the vortex energy involves the large parameter $\ln\left(\frac{R}{\delta_0^{af}}\right)$, which, however, is independent of ψ.

If $\sigma_1 = \sigma_2$, then the energy is minimal at $\psi = \frac{\pi}{2}$ in the absence of an external magnetic field [4]. The same conclusion was drawn in [6] for the case of an AFM with compensated spins at its surface. If an external magnetic field of induction B_0 is applied to the film plane at an angle φ to the preferential direction, then the total energy of the film–substrate system (per unit area of the film) is

$$w = \frac{C}{2}\left[\frac{(\pi - \psi)^2}{2} + \frac{\psi^2}{2}\right] - B_0aM\cos(\psi - \varphi). \quad (11)$$

The value of φ, at which the energy is minimal and, therefore, the quantities $M_\parallel = M\cos(\psi - \varphi)$ and $M_\perp = M\sin(\psi - \varphi)$, can be found from the equation

$$\psi = \frac{\pi}{2} = \eta\sin(\varphi - \psi), \quad (12)$$

where the dimensionless parameter η is

$$\eta = \frac{B_0Ma}{C} \approx \frac{B_0MaRb}{J_{af}S_{af}^2}. \quad (13)$$

If the external magnetic field is perpendicular to the spontaneous magnetization of the film ($\varphi = 0$), the magnetization curve is symmetric (Fig. 2a) and magnetization reversal occurs at a characteristic magnetic induction (corresponding to $\eta \sim 1$)

$$B^* \approx \frac{J_{af}S_{af}^2}{MaRb}. \quad (14)$$

It is easy to see that the induction B^* depends crucially on the parameter R characterizing the interface roughness.

In the range of fields $B_0 \gg B^*$, we have $\psi \propto B_0^{-1}$ up to the value B_{sf} at which the antiferromagnetic substrate undergoes the spin-flop transition. What occurs thereafter is dictated by the sign of $J_{f,af}$. If ferromagnetic exchange takes place between spins of the film and sub-

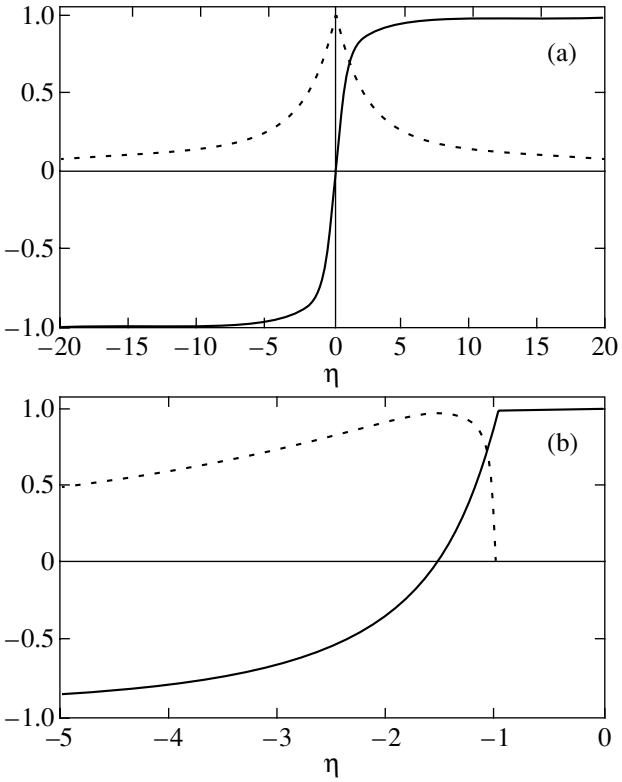

Fig. 2. Magnetization curves for the single-domain phase in the cases where the applied magnetic field is (a) perpendicular and (b) parallel to the spontaneous magnetization of the film. Solid curves are $M_\parallel/M$, and dotted curves are $M_\perp/M$.

strate, then ψ changes its value to zero or π in a jump (depending on the sign of B_0) and the film becomes magnetized to saturation, while the magnetization of the system is increased further through the magnetization of the substrate. If the exchange integral is of the opposite sign, two competing effects occur: the exchange interaction tends to align the magnetization vector of the film in opposition to that of the substrate, whereas under the action of the external magnetic field, both the magnetization vectors are forced to be aligned with this field. These effects may be the reason for the positive bias of magnetization curves of FeF_2/Fe films cooled in the presence of high magnetic fields [1]. In what follows, we restrict our consideration to the range of fields $B_0 < B_{sf}$ and neglect the magnetization of the substrate.

If the external magnetic field is parallel to the spontaneous magnetization $\left(\varphi = \frac{\pi}{2}\right)$, then, at $\eta \geq -1$, we have $\psi = \frac{\pi}{2}$ and $M_\parallel = M$. For $\eta < -1$ and $|\eta| - 1 \ll 1$, a square root singularity takes place: $\frac{\pi}{2} - \psi = [6(|\eta| - 1)]^{1/2}$. The magnetization $M_\parallel$ vanishes at $\eta = -\frac{\pi}{2}$; therefore, the magnetization curve is biased to the range of negative fields (Fig. 2b). The bias magnetic induction (unidirectional-anisotropy field) is equal to

$$B_E = \frac{\pi C}{2Ma} \sim B^*. \tag{15}$$

As in the case of $\varphi = 0$, the magnetization $M_\parallel$ reaches its saturation value ($-M$) when $|\eta| \gg 1$, $\eta < 0$ (deviation from this value decreases as $|B_0|^{-1}$).

The shape of the magnetization curves shown in Fig. 2b is qualitatively similar to that of experimental hysteresis loops for CoO/Co [8], permalloy/FeMn [9, 10], and CoNi/FeMn [11] bilayers. Furthermore, it follows from Eq. (15) that $B_E \propto R^{-1}$. This dependence allows one to understand the varying of B_E in inverse proportion to the CoO crystallite size in a permalloy/CoO system [12].

In the state which is established after magnetization reversal, the antiferromagnetism vector rotates with distance away from the interface through an angle of $\frac{\pi}{2}$ in the regions of one type and through an angle of $\frac{3\pi}{2}$ in the regions of the other type. This state is metastable. In order to pass over to the ground state in the regions where the rotation angle is $\frac{3\pi}{2}$, the antiferromagnetism vector must be rotated through one complete revolution (from $\frac{3\pi}{2}$ and $-\frac{3\pi}{2}$). However, this rotation involves virtual destruction of the magnetic order in the interface (which can be called a phase slip plane, by analogy with superconductors); that is, the system must overcome an energy barrier in a classical or a quantum-mechanical way.

The difference in energy between the metastable and stable states at saturation is greater than the energy of formation of a domain wall. Therefore, a DW parallel to the interface can appear in the AFM, owing to which the antiferromagnetism vector will rotate through an angle π near the interface and the vortex energy will decrease.

The above analysis was performed for the case of $\gamma \gg 1$. If $\gamma \ll 1$, the distribution of the antiferromagnetic order parameter is virtually uniform over the substrate and the frustration gives rise to distortions of the order parameter distribution in the ferromagnetic film [13]. In this case, a single-domain state occurs for $a \gg R$ and vortices appear near the interface in the film. The magnetization curves are similar to those discussed above, and their characteristic parameters are given by Eq. (10) with J_f in place of J_{af} and S_f replacing S_{af}.

In contrast to the case of $\gamma \gg 1$, where the interfacial energy is independent of the film magnetization, this energy is proportional to M^2 if $\gamma \ll 1$. At $\gamma \sim 1$, crossover occurs between these two cases and the spin vortex is displaced from the substrate to the film. We note that the dependence of the interfacial energy $\sigma \propto M^{1/2}$ observed in a Co–Ni/FeMn bilayer in [11] can be explained by the fact that $\gamma \sim 1$ for that sample.

5. THE POLYDOMAIN PHASE

In this phase, in the absence of an external magnetic field, distortions occur only in the region of a DW near a step (Fig. 1b), the width of this region being approximately δ_f. In an external magnetic field, the magnetization vector of a domain is tilted by an angle β from its initial direction and the antiferromagnetism vector at the interface follows it. Thus, a static vortex is formed in the substrate, with the antiferromagnetism vector rotating through an angle β in this vortex. The vortex energy (per unit of film area) equals (with logarithmic accuracy)

$$w_1 = \frac{J_{af} S_{af}^2 |\beta|}{2Rb} \ln \frac{R}{\delta_f}, \tag{16}$$

where $R \gg \delta_f$.

Taking into account that the concentration of DWs is roughly $\sim R^{-1}$, the DW energy per unit area is found to be

$$w_2 \approx \frac{\zeta^2 J_f S_f^2 a}{2\delta_f Rb} + \frac{\pi}{2} \frac{J_{af} S_{af}^2}{bR} \ln \frac{\delta_f}{\delta_0^{af}}, \tag{17}$$

where ζ is the rotation angle of magnetization within a DW.

In an external magnetic field, the angle between the magnetization vectors in adjacent domains decreases and the value of ζ tends either to zero (type 1 DW) or to 2π (type 2 DW), depending on the initial sense of magnetization rotation in the DW (Fig. 3).

If the magnetic field reverses its direction, the magnetization rotation angle tends to 2π in DWs of the first type and to zero in DWs of the second type.

In general, the shape of a magnetization curve depends on the type of DWs.

As an example, we consider an array of parallel equidistant steps on an interface. In this case, domains of the two types alternate with one another. First, we will discuss the situation where all DWs are of one type, which may take place if the ferromagnetic film is grown in an external magnetic field.

The energy surface density of the system of domains in an external field B_0 is

$$\tilde{w} = \frac{J_{af}S_{af}^2}{2Rb}\left\{\frac{(\pi-\beta_1-\beta_2)^2\gamma a}{\delta_f} + \pi\ln\frac{\delta_f}{\delta_0^{af}} + (|\beta_1|+|\beta_2|)\ln\frac{R}{\delta_f} - \eta[\cos(\beta_1-\varphi)-\cos(\beta_2+\varphi)]\right\}, \quad (18)$$

where the magnetization rotation angles in domains are reckoned as shown in Fig. 3b.

Minimizing $\tilde{w}$ with respect to δ_f gives

$$\delta_f = \gamma a\frac{(\pi-\beta_1-\beta_2)^2}{\pi-|\beta_1|-|\beta_2|}. \quad (19)$$

It is seen from Eq. (19) that the DW width decreases as the magnetization rotation angle in the DW tends to zero. When the rotation angle tends to 2π, the DW width increases up to the domain width R. Here, we assume that the distance R is smaller than the width of an ordinary DW in the AFM $\delta^* = (A_{af}/K_{af})^{1/2}$. Otherwise (at $\delta \gtrsim \delta^*$), one has to take into account the anisotropy energy in the film plane. As δ_f tends to zero, the DW structure is changed, but this leaves the magnetization curve unaffected, because the contribution of the DW energy to $\tilde{w}$ is insignificant in this case.

The behavior of the system in a magnetic field depends critically on the field direction. At $\varphi = \frac{\pi}{2}$, we have $\beta_1 = \beta_2$ (by symmetry) and the energy density $\tilde{w}$ takes the form

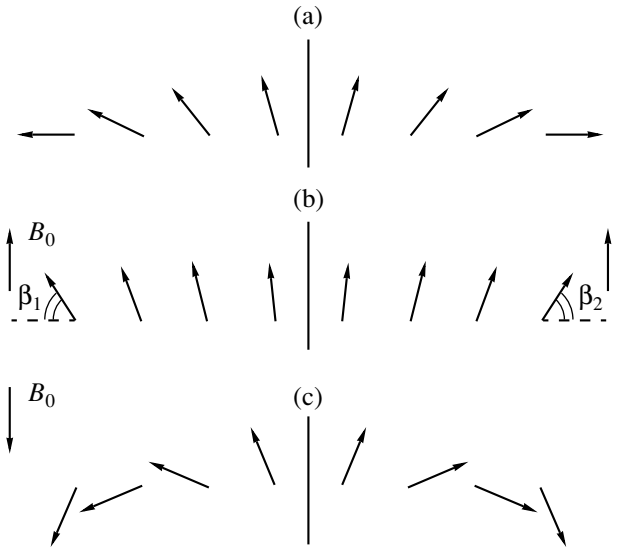

Fig. 3. Rotation of the magnetization vector in the domain wall (a) in the absence and (b, c) in the presence of an external magnetic field applied perpendicular to the magnetization vectors in the domains.

$$\tilde{w}(\beta) = \frac{J_{af}S_{af}^2}{2Rb}\left\{\frac{(\pi-2\beta)^2}{\pi-2|\beta|} + \pi\ln\frac{R}{\delta_0^{af}} - (\pi-2|\beta|)\ln\left[\frac{A(\pi-2|\beta|)}{(\pi-2\beta)^2}\right] - 2\eta\sin\beta\right\}, \quad (20)$$

where $A = R/a\gamma \gg 1$.

The $\beta(\eta)$ dependence for a fixed value of A can be easily found by minimizing $\tilde{w}(\beta)$, and it is presented in Fig. 4. It is easy to verify that there are two phases. In the range $\eta_-^* < \eta < \eta_+^*$, where

$$\eta_+^* = \ln\left(\frac{A}{\pi}\right) - 2, \quad (21)$$

$$\eta_-^* = -\ln\left(\frac{A}{\pi}\right) - 6, \quad (22)$$

we have $\beta = 0$. (A more correct calculation shows that β increases in proportion to B_0 in this range, $\beta \approx \eta b/R \ll 1$; there are no vortices in the substrate, but the angle $\theta_f - \theta_{af}$ at the interface is different from its optimum value.) At $\eta > \eta_+^*$ and $\eta < \eta_-^*$, the angle β increases linearly and then reaches saturation, following the law $\beta(\infty) - \beta(\eta) \propto \eta^{-1} \propto B_0^{-1}$ for $\eta \gg 1$.

Another distinctive feature of the magnetization curve is that it is asymmetric, because DWs of one type

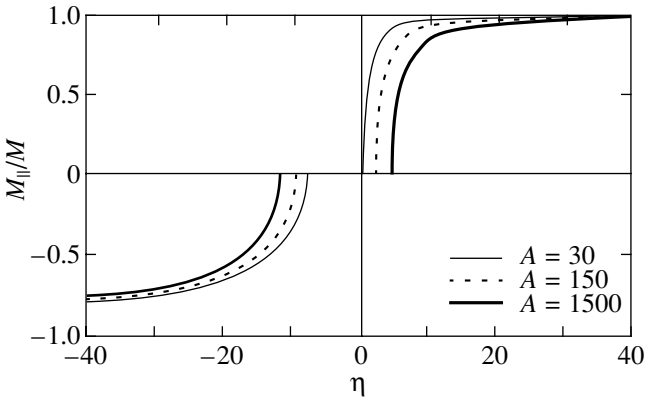

Fig. 4. Magnetization curves for a polydomain phase. The magnetic field is applied at right angles to the magnetization vectors in the domains.

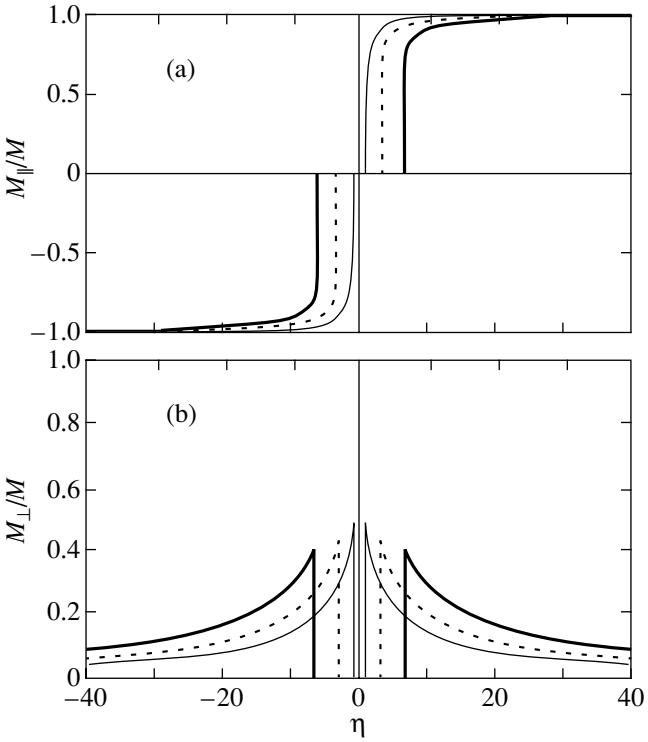

Fig. 5. Magnetization curves for a polydomain phase for different values of *A*: 30 (thin solid curves), 150 (dotted curves), and 1500 (heavy solid curves). The external magnetic field is parallel to the magnetization vectors in the domains.

are dominant. The center of the curve corresponds to $\eta_0 = -4$, and the film is magnetized much more easily for positive values of η than for negative ones, because in the former case, the DW energy decreases, while in the latter, it increases.

At $\varphi = 0$, the magnetization remains unchanged in the domains where it is parallel to the external field ($\beta_1 = 0$). This follows from the fact that the energy surface density of domains in Eq. (18) increases with increasing β_1 for a fixed value of $\beta_1 + \beta_2$. In the domains where the magnetization is antiparallel to the external field ($\beta_2 = 0$), it remains unchanged as η is increased up to a value $\eta_{cr} \sim \ln A$; at $\eta = \eta_{cr}$, β_2 is changed discontinuously to a value β_2^*. The values η_{cr} and β_2^* are found from the equation

$$\tilde{w}(\beta_2^*) = \frac{J_{af}S_{af}^2}{2Rb}\left\{\pi - \beta_2^* + \pi\ln\frac{R}{\delta_0^{af}} - (\pi - \beta_2^*)\ln\frac{A}{\pi - \beta_2^*} - \eta(1 - \cos\beta_2^*)\right\} = \tilde{w}(0) \quad (23)$$

and from the condition of minimum $\tilde{w}(\beta_2^*)$. At $\eta \gg 1$, β_2 reaches saturation, with its variation decreasing as $\propto B_0^{-1}$.

The B_0 dependences of the magnetization components $M_{\parallel}$ and $M_{\perp}$ parallel and perpendicular to the field, respectively, are shown in Fig. 5. After B_0 reverses its sign, β_2 remains equal to zero while β_1 varies; that is, the magnetization curves are symmetric.

Thus, unidirectional anisotropy in the polydomain phase is due to a predominance of DWs of one type. If DWs of both types occur with equal probabilities, the magnetization curve presented in Fig. 4 becomes symmetric and $M_{\perp}$ vanishes in the case of $\varphi = 0$ (Fig. 5b).

In order to calculate the magnetization curve in the case where DWs of different types alternate at random, one needs to solve a set of coupled equations for β_i in each domain.

6. THE CASE OF A COMPENSATED INTERFACE

Now, we consider the case where the surface of the AFM is compensated. It was shown in [2] that roughness leads to the occurrence of local random fields conjugate to the antiferromagnetic order parameter. In that paper, a random field $\pm h_0$ ($h_0 \approx J_{f,\,af}$) was assumed to arise in each unit cell at the interface.

However, generally speaking, this assumption is incorrect. Indeed, let atomic steps on the interface be arranged along two mutually perpendicular directions (the *x* and *y* axes). In this case, the interface is partitioned by steps into polygons whose angles are all right angles. By extending one of the two sides (e.g., that parallel to the *x* axis) of each internal angle whose magnitude is $3\pi/2$, one can divide a polygon into rectangles. If the dimensions of such a rectangle (L_x, L_y) are odd numbers when measured in units of the lattice parameter (that is, the rectangle consists of an odd number of unit cells), then the fields produced by the spins of the

atomic surface layer of the film within the rectangle are not compensated. Therefore, a random field arises only on the characteristic area $S_0 = 4\langle L_x^{-1} L_y^{-1}\rangle^{-1}$ (and not in each unit cell), where angular brackets signify averaging over the interface and the factor of 4 occurs under the assumption that, for $R \gg b$, the length of a step can measure an even or an odd number of lattice parameters with equal probabilities. Using the formula [14]

$$P(L) = A\exp\left(-\frac{2L}{R}\right)L \tag{24}$$

for the probability that the length of a step is L, we obtain $S_0 = R^2$.

In a region with linear dimensions l, the characteristic field fluctuation per unit cell is equal to

$$\langle h\rangle \sim h_0\left(\frac{l}{R}\right)\frac{b^2}{l^2} \sim \frac{h_0 b^2}{Rl}, \tag{25}$$

which is smaller than that assumed in [2] by a factor of R/b.

It was shown in [2] that the optimum size of domains into which the surface of a substrate can be partitioned, in principle, is of the order of δ^* ($l = \delta^*$). In this case, the energy (per unit cell) required to produce the corresponding nonuniform distribution of the antiferromagnetic order parameter equals [2] $(A_{\text{af}} K_{af})^{1/2} S_{\text{af}}^2 b^2$.

However, even in the case where the gain in the film–substrate interface energy due to the formation of domains in the substrate is overestimated by a factor of R/b, the total energy of the system with $J_{af} \approx J_{f,\,af}$ is higher than that in the case of uniform distribution of the ferromagnetic and antiferromagnetic order parameters. In other words, the phase with domains in the substrate is metastable. This conclusion is all the more valid when drawn from a correct estimate of the gain in the interface energy.

Thus, in the case where the surface of the AFM is compensated, the mechanism of unidirectional anisotropy proposed in [2] is inefficient.

7. CONCLUSIONS

Thus, the results of this paper allow the following conclusions to be made:

(1) Unidirectional anisotropy of a ferromagnetic single-domain film on the uncompensated surface of an antiferromagnet is due to spin vortices formed on the film–substrate rough interface; the strength of this anisotropy is inversely proportional to the spacing between steps on the interface.

(2) If the film is in a polydomain state, unidirectional anisotropy occurs, because the domain walls of one of the two possible types are dominant; the strength of this anisotropy is proportional to the difference in the concentration of DWs of two types; i.e., it is again inversely proportional to the spacing between the steps.

(3) If the surface of the AFM is compensated, the partition of the substrate into antiferromagnetic domains is energetically unfavorable and unidirectional anisotropy is due to the mechanism proposed in [6].

ACKNOWLEDGMENTS

This study was supported by the Russian Foundation for Basic Research (project no. 00-02-17162) and the Ministry of Education of the Russian Federation ("Universities of Russia" Program).

REFERENCES

1. J. Nogues and I. K. Schuller, J. Magn. Magn. Mater. **192** (2), 203 (1999).
2. A. P. Malozemoff, Phys. Rev. B **35** (7), 3679 (1987).
3. D. Mauri, H. C. Siegmann, P. S. Bagus, and E. Kag, J. Appl. Phys. **62** (7), 3047 (1987).
4. V. D. Levchenko, A. I. Morozov, and A. S. Sigov, Pis'ma Zh. Éksp. Teor. Fiz. **71** (9), 544 (2000) [JETP Lett. **71**, 373 (2000)].
5. M. D. Stiles and R. D. McMichael, Phys. Rev. B **59** (5), 3722 (1999).
6. N. C. Koon, Phys. Rev. Lett. **78** (25), 4865 (1997).
7. J. C. Slonczewski, J. Magn. Magn. Mater. **150** (1), 13 (1995).
8. M. Gruyters and D. Riegel, Phys. Rev. B **63**, 052401 (2001).
9. K. Liu, S. M. Zhou, C. L. Chien, *et al.*, J. Appl. Phys. **87** (9), 5052 (2000).
10. V. I. Nikitenko, V. S. Gornakov, A. J. Shapiro, *et al.*, Phys. Rev. Lett. **84** (4), 765 (2000).
11. S. M. Zhou and C. L. Chien, Phys. Rev. B **63**, 104406 (2001).
12. K. Takano, R. H. Kodama, A. E. Berkowitz, *et al.*, Phys. Rev. Lett. **79** (6), 1130 (1997).
13. V. D. Levchenko, A. I. Morozov, A. S. Sigov, and Yu. S. Sigov, Zh. Éksp. Teor. Fiz. **114** (11), 1817 (1998) [JETP **87**, 985 (1998)].
14. P. R. Pukite, C. S. Lent, and P. I. Cohen, Surf. Sci. **161** (1), 39 (1985).

Translated by Yu. Epifanov

Physics of the Solid State, Vol. 44, No. 1, 2002, pp. 140–144. Translated from Fizika Tverdogo Tela, Vol. 44, No. 1, 2002, pp. 135–139.

MAGNETISM AND FERROELECTRICITY

Thermal and Quantum Fluctuations of a Domain Wall in a Fine Magnetic Wire

A. F. Popkov

Lukin Scientific Research Institute of Physical Problems, Zelenograd, Moscow, 103460 Russia

e-mail: popkov@nonlin.msk.ru

Received February 23, 2001; in final form, April 17, 2001

Abstract—The effect of thermal fluctuations on the structure of a domain wall (DW) in a fine magnetic wire is analyzed. It is shown that the polarization of a DW in a magnetic nanowire is changed spontaneously as a result of thermal and quantum fluctuations. There is a critical diameter of the wire below which a transformation analogous to the superparamagnetic transition occurs, with the result that the Néel wall is transformed into a Ginzburg–Bulaevskiĭ wall. © *2002 MAIK "Nauka/Interperiodica".*

1. INTRODUCTION

A domain wall (DW) in a fine magnetic wire is a mesoscopic object. Its study is of interest for the following reasons. First, DWs in a nanocontact and a nanowire significantly affect spin-transport properties, which depend crucially on the relationship between the DW size and the wavelength of the conduction electrons [1–5]. Second, a DW in a nanowire is of interest for use in studying spontaneous magnetization reversal due to quantum fluctuations. In this connection, the paper by Bruno [6] should be cited, wherein an attempt was made to consider the micromagnetic structure of a DW in a small magnetic bridge between two magnetized bars and the effect of the strong spatial inhomogeneity in the microbridge cross section on this structure. The thermal effects were not taken into account in that paper. However, as the size of a wire is decreased, spin fluctuations not only blur the DW but also distort its structure. In this case, fluctuations associated with collective excitations, i.e., macroscopic modes having the lowest excitation energy, will be of primary importance. Therefore, one might expect mesoscopic repolarization of DWs to occur under fluctuations. To date, papers have been published on the effects of thermal DW creep [7], quantum tunneling through a defect, and flexural fluctuations of a DW as a macroscopic object [8, 9]. In this paper, we investigate mesoscopic repolarization of a DW under thermal fluctuations and the transformation of a polarized DW, having a certain plane in which the magnetic moments exhibit a screw rotation, into an unpolarized DW of the Ginzburg–Bulaevskiĭ type [10, 11], in which the magnetization varies only in magnitude, exhibiting no screw rotation and passing through zero at the DW midplane between the adjacent domains.

2. THE ORIGINAL HAMILTONIAN AND THE DYNAMIC EQUATIONS

We consider a magnetic wire with weak magnetic anisotropy in its cross section ($K_\perp \ll 2\pi M^2$); the diameter of the wire is assumed to be less than the exchange length, $D \le l_{ex} = \sqrt{A/\pi M^2}$, where A is the inhomogeneous-exchange energy and M is the magnetization. In such a fine wire, spins are collinear in the cross section. The Hamiltonian of the system under study has the form

$$\hat{H} = A(d\mathbf{m}/dz)^2 - \pi M^2 m_z^2 - K_\perp m_x^2 - H_z(z) M m_z, \quad (1)$$

where $\mathbf{m} = \mathbf{M}/M = (\sin\theta\cos\Phi, \sin\theta\sin\Phi, \cos\theta)$ and $H_z(z)$is a gradient magnetic field that pins the DW at the point $z = 0$.

We employ a zeroth approximation with respect to the small parameter $K_\perp/\pi M^2 \ll 1$ and a self-similar approximation in which the DW structure is determined by the balance of the exchange and demagnetization energies:

$$\Phi = \text{const},$$
$$d\theta/dz = l_{ex}^{-1}\sin\theta \longrightarrow \theta = 2\arctan[\exp((z-\Delta)/l_{ex})]. \quad (2)$$

Then, the Lagrangian of the system, when integrated over the volume of the wire with a cross section S_0, has the form[1]

[1] The Lagrangian L and the dissipative function R of the system can be expressed through the angular variables in the form (see, e.g., [11]) $L = (M/\gamma)(1 - \cos\theta)\partial_t\Phi - W(\theta, \Phi)$; $R = (\alpha M/2\gamma)[(\partial_t\Phi)^2\sin^2\theta + (\partial_t\theta)^2]$, where $W(\theta, \Phi)$ is the energy of the system corresponding to its Hamiltonian. In the self-similar approximation, the Lagrangian and dissipative function of the DW can be found through averaging over the spatial variables. The averaging procedure for a self-similar approximation to the dynamic equations similar to Eq. (2) is described, e.g., in [12].

$$\hat{L} = v[(2M/\gamma)(d\Phi/dt)(\Delta/l_{ex} - 1) - 2K_\perp \sin^2\Phi - |H_z'| l_{ex} M(\Delta/l_{ex})^2] + h_\Delta^{fluc}(\Delta/l_{ex}) + h_\Phi^{fluc}\Phi, \quad (3)$$

where $v = S_0 l_{ex}$ and h_Φ^{fluc} and h_Δ^{fluc} are the thermal-fluctuation fields corresponding to the variables Φ and Δ, respectively. The dissipative function of the system has the form

$$\hat{R} = (\alpha M/\gamma) l_{ex} S_0 [(d\Phi/dt)^2 + (d\Delta/dt)/l_{ex}^2]. \quad (4)$$

By calculating variations of the Lagrangian and dissipative function, we find the dynamic equations

$$\begin{cases} (d\Delta/dt)/l_{ex} + \alpha(d\Phi/dt) + (\gamma K_\perp/M)\sin 2\Phi \\ = (\gamma/2Mv) h_\Phi^{fluc}, \\ -(d\Phi/dt) + \alpha(d\Delta/dt) l_{ex} + \gamma|H_z'|\Delta \\ = (\gamma/2Mv) h_\Delta^{fluc}. \end{cases} \quad (5)$$

These equations have the form of nonlinear Langevin equations with a random right-hand side.

3. THERMAL BLURRING AND FLUCTUATIONAL REPOLARIZATION OF THE DOMAIN WALL

Let us calculate the correlation characteristics of fluctuations of the deviation angle and the position of the DW center. By solving the linearized equations (5), one can find the harmonic variations $\delta\Phi, \Delta \sim \exp(-i\omega t)$ of the angular variable and of the displacement of the DW center relative to their equilibrium values $\Phi = 0$ and $\Delta = 0$:

$$\delta\Phi = \chi_{\Phi\Phi} h_{\Phi\omega}^{fluc} + \chi_{\Phi\Delta} h_{\Delta\omega}^{fluc}, \qquad \Delta/l_{ex} = \chi_{\Delta\Phi} h_{\Phi\omega}^{fluc} + \chi_{\Delta\Delta} h_{\Delta\omega}^{fluc}, \quad (6)$$

where the magnetic susceptibilities χ_{ij} are given by

$$\chi_{\Phi\Phi} = \frac{\gamma}{2Mv} \frac{(\omega_D - i\omega\alpha)}{[\omega_\rho^2 - \omega^2(1+\alpha^2) - i\alpha\omega(\omega_A + \omega_D)]},$$

$$\chi_{\Delta\Delta} = \frac{\gamma}{2Mv} \frac{(\omega_A - i\omega\alpha)}{[\omega_\rho^2 - \omega^2(1+\alpha^2) - i\alpha\omega(\omega_A + \omega_D)]}, \quad (7)$$

$$\chi_{\Delta\Phi} = -\chi_{\Phi\Delta} = \frac{\gamma}{2Mv} \frac{i\omega}{[\omega_\rho^2 - \omega^2(1+\alpha^2) - i\alpha\omega(\omega_A + \omega_D)]},$$

with $\omega_A = \gamma 2K_\perp/M$, $\omega_\rho = \sqrt{\omega_D \omega_A}$, and $\omega_D = \gamma|H_z'| l_{ex}$.

According to the fluctuation–dissipation theorem (FDT) [13], we can write

$$\langle \delta x_i \delta x_j \rangle_\omega = (\hbar/2\pi)(\mathrm{Im}\chi_{ij}) \coth(\hbar\omega/2k_B T), \quad (8)$$

where $x_i, x_j = \Phi, \Delta$. If the frequencies are such that $\hbar\omega \ll k_B T$, then the spectral density of the square of the fluctuational angular deviation of the DW magnetization rotation plane is found from the above formulas to be

$$\langle \delta\Phi^2 \rangle_\omega = \frac{\alpha\gamma k_B T[\omega^2(1+\alpha^2) + \omega_D^2]}{4\pi M l_{ex} S_0 [(\omega^2(1+\alpha^2) - \omega_\rho^2)^2 + \omega^2\alpha^2(\omega_A + \omega_D)^2]}. \quad (9)$$

The average square of fluctuations of the angle Φ is

$$\langle \delta\Phi^2 \rangle = \int_{-\infty}^{\infty} \langle \delta\Phi^2 \rangle_\omega d\omega = \frac{k_B T}{4MS_0 l_{ex}} \frac{\gamma}{\omega_A}. \quad (10)$$

In a similar manner, one can find the average square of thermal fluctuations of the DW width:

$$\langle \Delta^2 \rangle / l_{ex}^2 = \frac{k_B T}{4MS_0 l_{ex}} \frac{\gamma}{\omega_D}. \quad (11)$$

Putting $\langle \delta\Phi^2 \rangle \sim (\pi/2)^2$, we find the critical cross-sectional area of the wire at which thermal fluctuations overcome the anisotropic barrier to delocalization of the plane of the DW magnetization rotation, $S_0^{cr} \sim k_B T/2\pi^2 K_\perp l_{ex}$. Therefore, the critical radius of the wire is $a_{cr} \sim (k_B T/2\pi^3 K_\perp l_{ex})^{1/2}$.

We will make an estimate for a wire of NiFe. Putting $T = 300$ K, $K_\perp \sim 10^5$ erg/cm^3, and $l_{ex} \sim 5$ nm, we obtain $a_{cr} \sim 1$ nm. The calculations performed above give rough estimates of the critical parameters for the transformation of a polarized DW into an unpolarized charged DW of the Ginzburg–Bulaevskiĭ type. A more detailed description of the dynamics of this transformation can be given using the Fokker–Planck equation for the probability density $P(\Phi, \Delta)$ of the DW state characterized by a certain orientation of the DW magnetization rotation plane (DW polarization) and the displacement of the DW center.

4. THE FOKKER–PLANCK EQUATION

An equation that describes the evolution of the probability density of DW states can be derived using the method developed by Brown [14] for describing thermal fluctuational magnetization reversal of a magnetic particle. According to the FDT, the spectral density of the random-field correlation function is given by

$$\langle h_i h_j \rangle_\omega = \frac{i\hbar}{4\pi}(\chi_{ij}^{-1} - \chi_{ji}^{-1*}) \coth\frac{\hbar\omega}{2k_B T}, \quad (12)$$

where χ_{ij}^{-1} are the inverse susceptibilities. Let us calculate the spectral density given by Eq. (12) at the point

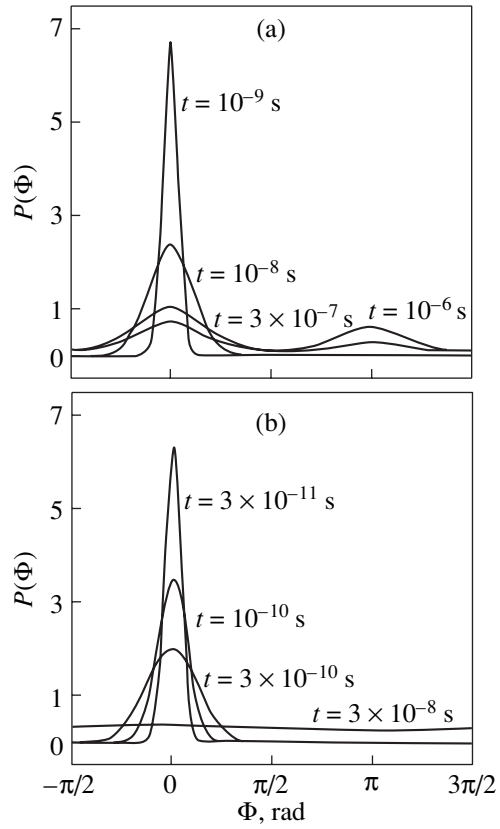

Fig. 1. Evolution of the probability density of the polarization state of a DW in a fine magnetic wire of diameter D = (a) 60 nm ($\nu = 9.9$) and (b) 10 nm ($\nu = 0.275$).

$\Phi = 0$, $\Delta = 0$. From the linearized set of equations (5), we find

$$\chi_{\Phi\Phi}^{-1} = \frac{2Mv}{\gamma}(\omega_A - i\omega\alpha), \quad \chi_{\Delta\Delta}^{-1} = \frac{2Mv}{\gamma}(\omega_D - i\omega\alpha), \qquad \chi_{\Phi\delta}^{-1} = -\chi_{\delta\Phi}^{-1} = \frac{2Mv}{\gamma}i\omega. \tag{13}$$

Substituting these expressions into Eq. (12) yields

$$\langle h_\Phi^2 \rangle_\omega = \langle h_\Delta^2 \rangle_\omega = \frac{\alpha M v}{\pi\gamma}\hbar\omega\coth\frac{\hbar\omega}{2k_BT}, \qquad \langle h_\Phi h_\Delta \rangle_\omega = 0. \tag{14}$$

In the case of high temperatures, we have $k_BT \gg \hbar\omega$ and, as follows from Eq. (14), the spectral density of thermal-fluctuation fields is characterized by a white noise spectrum, $\langle h_\Phi^2 \rangle_\omega = \langle h_\Delta^2 \rangle_\omega = (\alpha M v/\pi\gamma)2k_BT$. In this case, when describing the evolution of the probability density $P(\Phi, \Delta)$ of the DW states, one can employ a well-known method for deriving the Fokker–Planck equation from the nonlinear Langevin equations [12]. The common procedure for averaging the correlation moments $A_i = \lim_{dt\to 0}\langle dx_i\rangle/dt$ and $B_{ij} = \lim_{dt\to 0}\langle dx_i dx_j\rangle/dt$ yields the Fokker–Planck equation

$$\frac{\partial P(x_i, x_j)}{\partial t} = -\frac{\partial}{\partial x_i}A_iP(x_i, x_j) + \frac{1}{2}B_{ij}\frac{\partial^2 P(x_i, x_j)}{\partial x_i \partial x_j}. \tag{15}$$

In our case, this equation takes the form

$$\frac{\partial P}{\partial t} = \frac{\alpha\gamma K_\perp}{(1+\alpha^2)M}\frac{\partial P\sin 2\Phi}{\partial\Phi} + \frac{k_BT}{2K_\perp v}\frac{\partial^2 P}{\partial\Phi^2} + \frac{\gamma K_\perp l_{ex}}{(1+\alpha^2)M}\frac{\partial P\sin 2\Phi}{\partial\Delta} + \frac{k_BTl_{ex}^2}{2K_\perp v}\frac{\partial^2 P}{\partial\Delta^2}. \tag{16}$$

For the one-dimensional distribution $P(\Phi) = \int_{-\infty}^{\infty} P(\Phi, \Delta)d\Delta$, the equation is simplified:

$$\frac{1+\alpha^2}{\alpha\omega_A}\frac{\partial P}{\partial t} = \frac{\partial P\sin\Phi\cos\Phi}{\partial\Phi} + \frac{k_BT}{4K_\perp v}\frac{\partial^2 P}{\partial\Phi^2}. \tag{17}$$

This equation has an obvious steady-state solution $P(\Phi)|_{t=+\infty} = A\exp(-2K_\perp\sin^2\Phi/k_BT)$, where the normalization factor is given by

$$A = 1/\int_0^{2\pi}\exp(-2K_\perp\sin^2\Phi/k_BT)d\Phi = \exp(K_\perp/k_BT)/4\pi I_0(K_\perp/k_BT),$$

$I_0(x)$ is a Bessel function of imaginary argument. Any originally localized state $P(\Phi) = \delta(\Phi - \Phi_0)$ relaxes to this equilibrium distribution. The relaxation time characterizing the diffusive broadening of this distribution is determined by the parameter $\nu = k_BT/4K_\perp v$. The time scale that is associated with the Fokker–Planck equation (17) depends on the magnetic parameters and the expected angular broadening $\Delta\Phi$: $[t] \sim ((1 + \alpha^2)/\alpha\omega_A)(1 + k_BT/4K_\perp v\Delta\Phi^2)$. It can be seen that, if the parameter ν is large, the time of diffusive broadening varies in inverse proportion to the temperature: $[t] \sim vM/\gamma k_BT$. The evolution of the initially localized distribution is exemplified in Fig. 1 for two cases, $\nu \ll 1$ (Fig. 1a) and $\nu \gg 1$ (Fig. 1b). The calculations are performed for the following parameters of the wire: M = 1500 G, $K_\perp = 10^4$ erg/cm^3, $\alpha = 0.1$, T = 300 K, and diameter D = 60 (Fig. 1a) and 10 nm (Fig. 1b).

At low temperatures $k_BT \ll \hbar\omega_p$, a quantum-fluctuation limit is realized in which thermal fluctuations cannot be classified as white noise and the method employed above is inadequate. In the low-temperature limit, we have $\nu \longrightarrow 0$; however, the evolution of the initial DW state can be considered in the framework of the macroscopic quantum tunneling theory based on path integrals [15].

5. QUANTUM REPOLARIZATION OF THE DOMAIN WALL AT LOW TEMPERATURES

At $T = 0$, the DW is predominantly in the polarization states $\Phi = 0$ and π. For the sake of definiteness, we consider the case where the initial state of the DW is $\Omega(t = -\infty) = (\Phi = 0, \Delta = 0)$. The conditional-probability amplitude of the transition to the state $\mathbf{\Omega}(t = +\infty) = (\Phi = \pm\pi, \Delta = 0)$is expressed as an integral over instanton paths $\mathbf{\Omega}(\tau)$in imaginary time $\tau = it$ according to the formula $K_{\Omega(-\infty)\to\Omega(+\infty)} = \int \exp[-S_E(\mathbf{\Omega}(\tau))/\hbar]d\mathbf{\Omega}$, where the action S_E is defined as an integral over imaginary time, $S_E = \int L d\tau$. In the Lagrangian in Eq. (3), we discard the terms that involve random thermal-fluctuation fields; in addition, we include the field term $2MH\Delta$, which is responsible for the DW displacement, with an eye to treating quantum interference effects associated with the topological properties of instanton paths. The quadratic form in the variable Δ in the Lagrangian describes the DW motion and can be excluded by carrying out the integration over this variable in the expression for the tunneling probability amplitude. As a result, we obtain an effective Lagrangian of the system which depends on the angular variable Φ alone and has the form

$$L(\tau) = 4\nu K_\perp\left(\frac{(\partial_\tau\Phi)^2}{2\omega_\rho^2} + i\frac{\partial_\tau\Phi}{\omega_A}\left(1 + \frac{H}{H'l_{ex}}\right) + \frac{1}{2}\sin^2\Phi\right). \quad (18)$$

A similar Lagrangian is often used in the magnetic-instanton theory (see, e.g., [16, 17]); therefore, we drop the details of the mathematical treatment and present only the main formulas for the tunneling probability. The tunneling rate Γ is the sum of the transition probability amplitudes from the initial state $\Phi = 0$ to the final states $\Phi = \pm\pi$ along two topologically different instanton paths $\Phi = \pm 2\arctan\exp(\omega_\rho\tau)$, which correspond to clockwise and counterclockwise rotations of the DW polarization plane:

$$\frac{\Gamma}{2} = K_{0,+\pi} + K_{0,-\pi} = A_{0,+\pi}\exp(-S_{0,+\pi}) + A_{0,-\pi}\exp(-S_{0,-\pi}) = 2\omega_\rho\sqrt{\frac{S_{cl}}{2\pi\hbar}}\exp\left(-\frac{S_{cl}}{\hbar}\right)\cos\left[\frac{2M\nu}{\gamma}\left(1 + \frac{H}{H'l_{ex}}\right)\right], \quad (19)$$

where $A_{\Omega_\pm} = \int \exp(-\delta^2 S(\mathbf{\Omega})/\hbar)d(\mathbf{\Omega} - \mathbf{\Omega}_\pm)$ is the preexponential factor of the corresponding probability amplitude and $S_{cl} = 8\nu K_\perp/\omega_\rho$ is the classical part of the action along the instanton path $\mathbf{\Omega}_\pm$.

It follows from Eq. (19) that the tunneling rate can oscillate under the magnetic field of the displaced DW because of the macroscopic quantum interference of the two tunneling amplitudes along the two topologically different paths. This effect is very sensitive to the interaction of the spins with the dissipative environment (phonons and nuclear spins [18, 19]); this interaction destroys the phase coherence of tunneling instantons and smooths out the field oscillations.

An analysis of Eq. (19) shows that, in order to observe quantum DW repolarization experimentally, one has to meet rather stringent requirements, because the pinning magnetic field gradient has to be very strong. For example, if $M = 1500$ G, $K_\perp = 10^3$ erg/cm^3, $\gamma = 2\times10^7$ Oe^{-1} s^{-1}, and $A = 10^{-6}$ erg/cm, then, in a wire a nanometer in diameter, the tunneling rate has an observable value of $\Gamma \sim 1$ s^{-1} when the natural DW oscillation frequency is $\omega_\rho = 10^9$ s^{-1}. Natural DW oscillations of such a high frequency can occur in the case of artificial DW pinning at an exchange defect in the magnetic channel.

6. CONCLUSIONS

The analysis performed in this paper shows that the DW in the magnetic nanowire is subjected to strong thermal structural distortions at room temperature due to thermal fluctuations being in the orientation of the DW magnetization rotation plane and in the position of the DW center. There is a critical temperature (related to the height of the energy barrier to DW repolarization) above which the DW becomes unpolarized. The transition of the DW from the polarized to the unpolarized state, which occurs when the diameter of the magnetic wire decreases, is similar to the thermal deblocking effect observed in magnetic nanoparticles when the threshold for the Néel–Brown superparamagnetism is reached.

In essence, the DW in the nanowire is a magnetic vortex. In [20], quantum repolarization of a Bloch line in a thin film was considered; this effect is similar to the behavior of a DW in a magnetic nanowire. However, in our case, the mesoscopic volume involved in the tunneling process is smaller due to the smallness of the diameter of the nanowire and, therefore, the probability of quantum repolarization of the vortex is greater. An analysis of the macroscopic tunneling of the DW polarization plane reveals that, at zero temperature, the DW polarization can persist for a fairly long time and the quantum repolarization of the DW can be observed if the DW pinning in the magnetic channel is sufficiently strong.

The strong spatial inhomogeneity in the cross section of the magnetic bridge and near the exchange defect (the region of smaller exchange energy in the DW) causes the quantum DW repolarization rate to increase, because this inhomogeneity leads to a decrease in the DW width (see [6]) and strengthens the DW pinning.

The results obtained in this paper and, in particular, the features of the fluctuational transition of the DW to an unpolarized state should be taken into account when analyzing the spin transport in magnetic nanocontacts and nanowires controlled by an external magnetic field.

ACKNOWLEDGMENTS

The author is grateful to A.K. Zvezdin for helpful discussions.

This study was supported by the Russian Foundation for Basic Research, project no. 00-02-17240-a, and MNTTs, project no. 1522.

REFERENCES

1. N. Garcia, M. Munoz, and Y.-W. Zhao, Phys. Rev. Lett. **82**, 2923 (1999).
2. G. Tatara, Y.-W. Zhao, M. Munoz, and N. Garcia, Phys. Rev. Lett. **83** (10), 2030 (1999).
3. H. Imamura, N. Kobayashi, S. Takahashi, and S. Maekawa, Phys. Rev. Lett. **84** (5), 1003 (2000).
4. A. K. Zvezdin and A. F. Popkov, Pis'ma Zh. Éksp. Teor. Fiz. **71** (5), 304 (2000) [JETP Lett. **71**, 209 (2000)].
5. P. M. Levy and Sh. Zhang, Phys. Rev. Lett. **79** (25), 5110 (1997).
6. P. Bruno, Phys. Rev. Lett. **83** (12), 2425 (1999).
7. L. Neel, Ann. Univ. Grenoble **22**, 299 (1946).
8. T. Egami, Phys. Status Solidi B **57**, 211 (1973).
9. P. C. E. Stamp, Phys. Rev. Lett. **66** (21), 2802 (1991); E. M. Chudnovsky, O. Iglesias, and P. C. E. Stamp, Phys. Rev. B **46** (9), 5392 (1992); V. V. Dobrovitskiĭ and A. K. Zvezdin, Zh. Éksp. Teor. Fiz. **109** (4), 1420 (1996) [JETP **82**, 766 (1996)].
10. A. Hubert, *Theorie der Domanenwande in Geordneten Medien* (Springer-Verlag, Berlin, 1974; Mir, Moscow, 1977).
11. A. M. Kosevich, B. A. Ivanov, and A. S. Kovalev, *Nonlinear Waves of Magnetization. Dynamic and Topological Solitons* (Naukova Dumka, Kiev, 1988), p. 19; A. Hubert, *Theorie der Domanenwande in Geordneten Medien* (Springer-Verlag, Berlin, 1974; Mir, Moscow, 1977).
12. A. P. Malozemoff and J. C. Slonczewski, *Magnetic Domain Walls in Bubble Materials* (Academic, New York, 1979; Mir, Moscow, 1982).
13. L. D. Landau and E. M. Lifshitz, *Course of Theoretical Physics*, Vol. 5: *Statistical Physics* (Nauka, Moscow, 1964; Pergamon, Oxford, 1980).
14. W. F. Brown, Jr., Phys. Rev. **130** (5), 1677 (1963).
15. E. M. Chudnovsky, J. Appl. Phys. **73** (10), 6697 (1993).
16. A. Garg and G.-H. Kim, Phys. Rev. B **45** (22), 12921 (1992).
17. V. Yu. Golyshev and A. F. Popkov, Zh. Éksp. Teor. Fiz. **108**, 1755 (1995) [JETP **81**, 962 (1995)].
18. A. Garg, Phys. Rev. B **51** (21), 15161 (1995).
19. V. Yu. Golyshev and A. F. Popkov, Phys. Rev. B **56** (5), 2712 (1997).
20. V. V. Dobrovitskii and A. K. Zvezdin, J. Magn. Magn. Mater. **156**, 205 (1996).

Translated by Yu. Epifanov

Physics of the Solid State, Vol. 44, No. 1, 2002, pp. 145–148. Translated from Fizika Tverdogo Tela, Vol. 44, No. 1, 2002, pp. 140–143.

MAGNETISM AND FERROELECTRICITY

Magnetoelectric Effect in Samarium Molybdate

B. K. Ponomarev*, B. S. Red'kin*, E. Stiep, H. Wiegelmann**, A. G. M. Jansen**, and P. Wyder****

** Institute of Solid State Physics, Russian Academy of Sciences, Chernogolovka, Moscow oblast, 142432 Russia*

*** Grenoble High Magnetic Field Laboratory, B.P. 166, Grenoble Cedex 9, F-38042 France*

Received April 5, 2001

Abstract—This paper reports on the nonlinear magnetoelectric effect (MEE) in the orthorhombic ferroelectric ferroelastic β' phase of samarium molybdate $Sm_2(MoO_4)_3$ observed in magnetic fields up to 20 T and temperatures from 4.4 to 0.43 K. The magnetic-field-induced electric polarization in $Sm_2(MoO_4)_3$ is an order of magnitude larger than that in isomorphic $Gd_2(MoO_4)_3$. This provides support for the magnetostriction mechanism proposed by us for the MEE in rare-earth molybdates. The polarization in $Sm_2(MoO_4)_3$ was found to fall off with time. The relaxation time constant τ increases with decreasing temperature from $\tau = 10^2$ s at $T = 4.4$ K to $\tau \approx 10^3$ s at $T = 0.43$ K. © *2002 MAIK "Nauka/Interperiodica".*

1. INTRODUCTION

The metastable orthorhombic ferroelectric ferroelastic phase of samarium molybdate, β'-$Sm_2(MoO_4)_3$, exists at temperatures below 197°C [1]. The magnetoelectric effect (MEE) in $Tb_2(MoO_4)_3$ and $Gd_2(MoO_4)_3$ compounds isomorphic to samarium molybdate was studied experimentally in [2–5]. At liquid-helium temperatures, the magnetoinduced electric polarization (MEP) in $Tb_2(MoO_4)_3$ is two orders of magnitude larger than that in $Gd_2(MoO_4)_3$. This result provides supportive evidence for the magnetostriction mechanism of the MEE in rare-earth molybdates, which is described in [2–5]. It seemed important to check whether this mechanism of the MEE operates in other rare-earth molybdates. This stimulated the present experimental study of the MEE in $Sm_2(MoO_4)_3$. The measurements were carried out at temperatures varying from 4.4 to 0.43 K and magnetic fields of up to 20 T for two magnetic field orientations, along the [010] and [100] axes.

2. SAMPLES AND EXPERIMENT

An $Sm_2(MoO_4)_3$ single crystal was grown in accordance with the Czochralski method [6]. The larger face of a single-domain sample measuring $7 \times 7 \times 1$ mm was oriented parallel to the (001) plane. The technique employed to prepare single-domain samples was described in [7–9]; the measurement technique, in [10]. The MEP was measured along the [001] axis. The potential difference between the (001) sample faces was measured with a Keithley-617 electrometer. The input capacitance of the electrometer was C_{em} = 435.5 pF, and the capacitance of the sample was C_{sample} = 3.93 pF. A capacitor with C_{add} = 291 pF was connected in parallel with the sample. The electrometer input time constant was $\tau_{em} > 10^4$ s. The measurement error was ~5%.

3. RESULTS

Figure 1 presents a cycle of the MEP variation (*ABCD*) observed in a single-domain $Sm_2(MoO_4)_3$ sample at $T = 1.4$ K in a [010]-oriented magnetic field. The arrows indicate the direction followed in the *ABCD* cycle in the measurements. The magnetic field was increased at a rate $dH/dt = 0.0755$ T s^{-1}. The magnetic field dependence of the MEP, $P_{e\uparrow}(H)$, obtained with the field increasing from 0 to 20 T is represented graphically in Fig. 1 as the *AB* curve. This curve was measured in 265 s. At the *B* point, the MEP is 5.46×10^{-9} C cm^{-2}. At point *B* ($H = 20$ T), the magnetic field was fixed and remained constant for 232 s. During this time, the MEP changed to -3.01×10^{-9} C cm^{-2} (point *C*). At *C*, the magnetic field started to decrease at a rate $dH/dt = -0.0755$ T s^{-1}. Curve *CD* in Fig. 1 depicts the dependence of the MEP on the magnetic field, $P_{e\downarrow}(H)$, measured with the field reduced from 20 T to zero. At point *D*, the magnetic field reached zero and was fixed. The MEP was found to be 3.12×10^{-9} C cm^{-2} at this point. After fixing the magnetic field at zero, the MEP was measured for 338 s. During this time, it decreased to 1.4×10^{-9} C cm^{-2}. This variation of the MEP is plotted as the *DE* section in Fig. 1. Thus, the MEP in samarium molybdate relaxes in a fixed magnetic field. This relaxation is not due to charge leakage through the electrometer input circuit, because the measurement times at a fixed field, 232 and 338 s, are two orders of magnitude shorter than $\tau_{em} > 10^4$ s. Similar MEP measurement cycles were performed for other magnetic field orientations and temperatures.

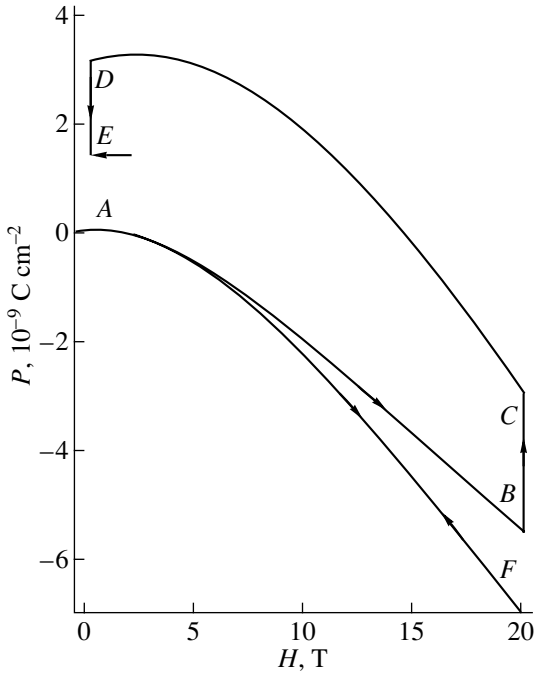

Fig. 1. Field dependences of MEP in $Sm_2(MoO_4)_3$. T = 1.4 K, field along [010]. Curves *AB* and *CD* are experimental $P_e\uparrow\downarrow(H)$ dependences obtained in an increasing and a decreasing field, respectively. Curves *BC* and *DE* are the variations of MEP with time at H = 20 T and 0, respectively. Curves *AF* and *FA* are $P\uparrow\downarrow(H)$ relations calculated from curves *AB* and *CD* using Eqs. (2) and (3), accordingly.

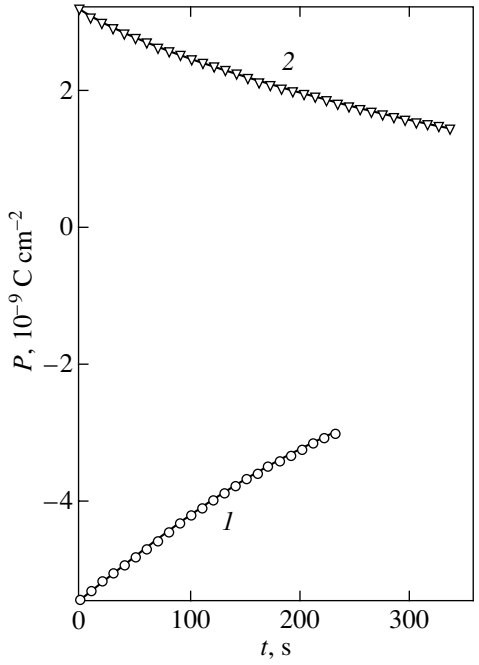

Fig. 2. Time evolution of MEP in $Sm_2(MoO_4)_3$ at T = 1.4 K. Curve *1* corresponds to section *BC* in Fig. 1 and H = 20 T along the [010] axis; curve *2* corresponds to section *DE* in Fig. 1 and H = 0 (after the *ABCD* cycle in Fig. 1; the field in the cycle was [010]-oriented).

Figure 2 displays the time evolution of the MEP, $P_e(H = \text{const}, t)$, at T = 1.4 K and fixed values of the magnetic field. The symbols identify the experimental values of the MEP, and the solid curves are plots calculated using Eq. (1) (see below). Curve *1* was obtained in a magnetic field H = 20 T directed along the [010] axis. This curve corresponds to section *BC* in Fig. 1. Curve *2* in Fig. 2 was measured in a zero magnetic field; it corresponds to section *DE* in Fig. 1 and was obtained immediately after the curves *AB*, *BC*, and *CD* in Fig. 1 were measured. Similar MEP dependences on time, $P_e(H = \text{const}, t)$, were obtained in the fields H = 20 T and H = 0 at all other temperatures and magnetic field orientations used. As seen from Fig. 2, the $P_e(H = \text{const}, t)$ relations are fitted well by the expression

$$P_e(H = \text{cons}, t) = P_0 \exp\left(-\frac{t}{\tau}\right) + P_R. \qquad (1)$$

The remanent polarization P_R depends only weakly on the magnetic field and is always small compared to P_0 ($P_R < 0.1P_0$). The magnitude of P_R apparently depends on the sample prehistory. To determine the exact form of this relationship, one should measure the time evolution of MEP until its complete relaxation at constant fields H = 20 T and H = 0 in each *ABCD*-type cycle. Such measurements would be time-consuming and, therefore, are difficult to realize. The MEP relaxation time constant τ also depends on the magnetic field only weakly. The table presents the values of τ obtained at different temperatures and orientations of the 20-T magnetic field. We readily see that the MEP relaxation time increases by an order of magnitude with a temperature decrease from 4.4 to 0.43 K. MEP relaxation noticeably affects the MEP field dependence, because the measurement time 265 s is comparable to τ. As a result of the relaxation, the measured $P_e(H)$ dependence contains a time-dependent contribution and differs markedly from the true $P(H)$ relation. As follows from our measurements, the relation connecting P_0 with P_R can be approximately described by the expression $P_R = \beta P_0$, where $\beta \ll 1$ is a constant. In this case, the time-dependent contribution can be eliminated using the relations

$$P\uparrow(H) = P_e\uparrow(H) + \int_0^H \frac{P_e\uparrow(H)}{a\tau(1+\beta)} dH, \qquad (2)$$

$$P\downarrow(H) = P_e\downarrow(H) - \int_{H_m}^H P_e\downarrow(H) \frac{dH}{a\tau(1+\beta)} + P\uparrow(H_m) - P_e\downarrow(H_m). \qquad (3)$$

Here, $P\uparrow\downarrow(H)$ does not depend on time. The $\uparrow$ and $\downarrow$ arrows denote the values obtained under increasing and

decreasing field, respectively; H_m is the maximum field reached in the measurements; $a = dH/dt$ is the rate of magnetic field variation with time; $P_{\uparrow}(H_m)$ is the true MEP at the maximum field calculated from the experimental curve $P_{e\uparrow}(H)$ using Eq. (2); and $P_{e\uparrow}(H_m)$ is the experimental value of MEP at the start of the decrease in the field (point *C* in the cycle in Fig. 1). As seen from Eqs. (2) and (3), the $P(H)$ and $P_e(H)$ relations coincide at sufficiently high dH/dt. Curves *A*B and *CD* were used to obtain the *AF* and *FA* curves (Fig. 1) by means of Eqs. (2) and (3), respectively. We readily see that elimination of the time-dependent contribution from the experimental $P_{e\uparrow\downarrow}(H)$ dependences yields a hysteresis-free $P(H)$ relation. Similar results were obtained when relaxation was taken into account at 0.9 and 0.43 K. At 4.4 and 2.6 K, the calculated $P(H)$ relations exhibit a slight hysteresis, which, in a zero magnetic field, is ≈5% of the maximum value of the MEP for a given curve and decreases down to zero with the field raised to its maximum level. Figure 3 displays the $P_{\uparrow}(H)$ relations obtained for $Sm_2(MoO_4)_3$ at different temperatures and magnetic-field orientations after the time-dependent contribution was subtracted from the $P_{e\uparrow}(H)$ dependences (curves *1–10*). The MEP grows in magnitude with decreasing temperature. The *1* and *6* dependences, obtained at 4.4 K, are fitted well in the weak-field region, $H < 5$ T, by a relation that is quadratic in the field. At higher fields and lower temperatures, this relation fails. The inset to Fig. 3 presents the field dependences of the MEP in $Gd_2(MoO_4)_3$ taken from [5].

4. DISCUSSION

A magnetostriction mechanism of the MEP in ferroelectric rare-earth molybdates was proposed in [3]. This mechanism is based on the assumption that magnetostriction affects the electric polarization of these ferroelectric compounds. A comparison of the field dependences of the MEP, $P(H)$, obtained in this work for $Sm_2(MoO_4)_3$ (Fig. 3) with the results quoted from [5] for $Gd_2(MoO_4)_3$ (inset to Fig. 3) qualitatively supports the applicability of the magnetostriction mechanism to the MEP in $Sm_2(MoO_4)_3$. As seen from Fig. 3, the MEP in $Sm_2(MoO_4)_3$ is twenty times that in $Gd_2(MoO_4)_3$. One should take into account that the effective magnetic moment of the Sm^{3+} ion ($\mu_{eff} = g\mu_B\sqrt{J(J+1)} = 0.845\mu_B$) is an order of magnitude smaller than that for Gd^{3+} ($\mu_{eff} = 7.94\mu_B$). Here, g is the magnetomechanical ratio ($g = 2/7$ for Sm^{3+}, and $g = 2$ for Gd^{3+}), $\mu_B = 0.9273 \times 10^{-20}$ G cm^3 is the Bohr magneton, and J is the total angular momentum ($J = 5/2$ for Sm^{3+} and 7/2 for Gd^{3+}). The values of g and J for the rare-earth ions were taken from [11]. The $P(H)$ relations for $Gd_2(MoO_4)_3$ show a tendency to saturation in relatively weak fields. At $T = 4.2$ K (curves *1* and *2* in the inset to Fig. 3), the tendency to saturation is seen in a field $H = 10$ T, while at $T = 0.4$ K (curves *3* and *4* in the inset), it is seen already in a field of about 2 T. The corresponding relations obtained for $Sm_2(MoO_4)_3$ do not exhibit any sign of saturation even at 20 T. These findings agree qualitatively with the magnetostriction mechanism. The orbital angular momentum of the Sm^{3+} ion in samarium molybdate is nonzero ($L = 5$). This implies that the charge cloud of the outer 4*f* electrons of the Sm^{3+} ion is spatially anisotropic. An external magnetic field changes the orientation of the Sm^{3+} magnetic moment. Spin–orbit coupling in rare-earth ions is considerably stronger than the 4*f*-electron interaction with

Relaxation time τ of the magnetoinduced electric polarization in $Sm_2(MoO_4)_3$ measured at different temperatures in a field of 20 T. Column 2: field along the [010] axis; column 3: field along [100]

T, K	τ, s; [010]	τ, s; [100]
4.4	127	128
2.6	279	192
1.4	337	403
0.9	490	490
0.43	534	828

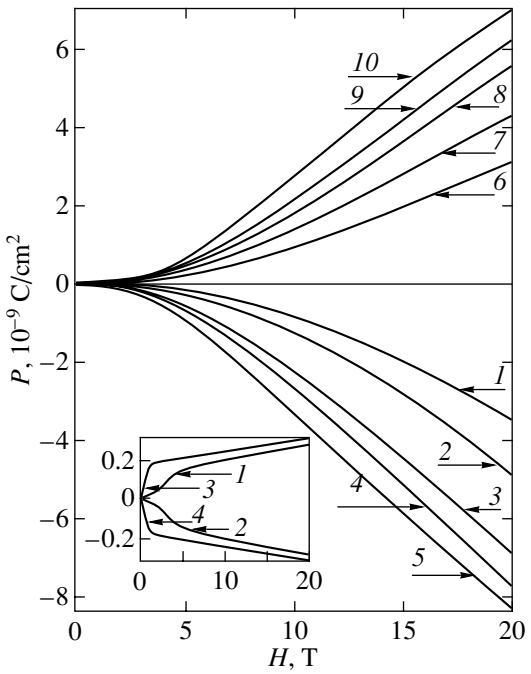

Fig. 3. Field dependences of the MEP in $Sm_2(MoO_4)_3$ after elimination of the time-dependent contribution. Curves *1–5* correspond to the field parallel to the [010] axis and curves *6–10* correspond to the [100]-oriented field. *T* (K): (*1*, *6*) 4.4, (*2*, *7*) 2.6, (*3*, *8*) 1.4, (*4*, *9*) 0.9, and (*5*, *10*) 0.43. Inset shows the field dependences of MEP in $Gd_2(MoO_4)_3$. Units of measurement are the same as in the main figure. Curve *1*: $T = 4.2$ K, H along [010]; (*2*) $T = 4.2$ K, H along [100]; (*3*) $T = 0.4$ K, H along [010]; and (*4*) $T = 0.4$ K, H along [100].

the crystal field. Therefore, the Sm^{3+} charge cloud also changes its orientation together with the magnetic moment. The rotation of the spatially anisotropic charge cloud acted upon by the external magnetic field deforms the crystal environment of the Sm^{3+} ion (such deformations are called single-ion magnetostriction), with the result that the electric polarization of the samarium molybdate changes. The Gd^{3+} ion has a zero orbital angular momentum. This means that the charge cloud around the Gd^{3+} ion is spherically symmetric. Therefore, its rotation driven by the magnetic field does not cause the crystal-field environment to deform. The magnetostriction deformation in gadolinium molybdate originates from the magnetic dipole–dipole interaction. The magnetostriction created by dipole–dipole interaction is known to be several orders of magnitude lower than single-ion magnetostriction. This is what accounts for the observed relation between the magnitudes of the MEP and μ_{eff} in $Sm_2(MoO_4)_3$ and $Gd_2(MoO_4)_3$. The presence of $P(H)$ saturation in $Gd_2(MoO_4)_3$ and its absence in $Sm_2(MoO_4)_3$ are likewise explained as being due to the values of the orbital angular momenta of the Gd^{3+} and Sm^{3+} ions. The nonzero orbital angular momentum of the Sm^{3+} ion accounts for the considerably higher effective field of magnetocrystalline anisotropy in $Sm_2(MoO_4)_3$ compared to $Gd_2(MoO_4)_3$, where the Gd^{3+} ion has a zero orbital angular momentum. This is explained by the fact that rotation of the nonspherical 4*f*-electron charge cloud of the Sm^{3+} ion brings about an increase in the energy of the 4*f*-electron interaction with the crystal field, whereas rotation of the spherically symmetric charge cloud of Gd^{3+} does not change the energy of this interaction. Therefore, the saturation of the magnetization, and, hence, of the $P(H)$ dependences in $Gd_2(MoO_4)_3$, occurs in weaker fields than in $Sm_2(MoO_4)_3$. As seen from Fig. 3 (curves *1–10*), the values of MEP in $Sm_2(MoO_4)_3$ measured in magnetic fields oriented along the [010] and [100] directions are different. For instance, at a temperature $T = 0.43$ K and magnetic field $H = 20$ T, the MEP is -8.35×10^{-9} C cm^{-2} in a [010]-oriented field (curve *5* in Fig. 3) and 6.93×10^{-9} C cm^{-2} for a field directed along the [100] axis (curve *10* in Fig. 3). These differences are observed throughout the field and temperature ranges studied. Similar measurements made on $Gd_2(MoO_4)_3$ (curves *1–4* in the inset to Fig. 3) yield practically the same absolute values of the MEP for the [010]- and [100]-oriented fields. The theory of MEE [12] gives the following relation for the MEP:

$$P(H) = -(1/2)\xi H^2 \sin 2\varphi. \quad (4)$$

Here, φ is the angle specifying the field direction in the basal plane and ξ is a constant. Equation (4) predicts the same absolute value of the MEP for a φ angle changed by 90°. This prediction does not agree with the experimental data obtained for $Sm_2(MoO_4)_3$. The quadratic field dependence of the MEP predicted by this theory is observed to hold for $Sm_2(MoO_4)_3$ only at $T = 4.2$ K and $H < 5$ T. In [13], another expression was derived for the MEP,

$$P(m) = \Gamma_1 m_x^2 + \Gamma_2 m_y^2. \quad (5)$$

Here, m_x, m_y are the magnetization components and Γ_1 and Γ_2 are constants. Equation (5) is capable of accounting for the asymmetry in the absolute values of the MEP in $Sm_2(MoO_4)_3$. A more comprehensive comparison of the theory of [13] with the behavior of the MEP in $Sm_2(MoO_4)_3$ would require magnetization measurements to be carried out.

The MEP relaxation in $Sm_2(MoO_4)_3$ is apparently caused by the screening of electric polarization, the effects considered in [14].

ACKNOWLEDGMENTS

This study was supported by the Russian Foundation for Basic Research, project no. 98-02-16635.

REFERENCES

1. L. H. Brixner and J. R. Barkley, *Handbook on the Physics and Chemistry of Rare Earths* (North-Holland, Amsterdam, 1979), p. 610.
2. S. A. Ivanov, V. N. Kurlov, B. K. Ponomarev, and B. S. Red'kin, Pis'ma Zh. Éksp. Teor. Fiz. **52** (7), 1003 (1990) [JETP Lett. **52**, 394 (1990)].
3. B. K. Ponomarev, S. A. Ivanov, B. S. Red'kin, and V. N. Kurlov, Physica B (Amsterdam) **177**, 327 (1992).
4. B. K. Ponomarev, B. S. Red'kin, H. Wiegelmann, *et al.*, Ferroelectr. Lett. **18** (3/4), 394 (1994).
5. B. K. Ponomarev, E. Stiep, H. Wiegelmann, *et al.*, Fiz. Tverd. Tela (St. Petersburg) **43** (4), 716 (2000) [Phys. Solid State **43**, 734 (2000)].
6. B. S. Red'kin, V. N. Kurlov, I. S. Pet'kov, and S. N. Rossolenko, J. Cryst. Growth **104** (1), 77 (1990).
7. B. K. Ponomarev, S. A. Ivanov, B. S. Red'kin, and V. N. Kurlov, Pis'ma Zh. Éksp. Teor. Fiz. **55** (6), 353 (1992) [JETP Lett. **55**, 356 (1992)].
8. B. K. Ponomarev, V. D. Negrii, B. S. Red'kin, and Yu. F. Popov, J. Phys. D **27**, 1995 (1994).
9. B. K. Ponomarev, S. A. Ivanov, Yu. F. Popov, *et al.*, Ferroelectrics **161**, 43 (1994).
10. H. Wiegelmann, B. K. Ponomarev, J. van Tol, *et al.*, Ferroelectrics **183**, 195 (1997).
11. K. P. Belov, M. A. Belyanchikova, R. Z. Levitin, and S. A. Nikitin, *Rare-Earth Ferromagnets and Antiferromagnets* (Nauka, Moscow, 1965), p. 15; p. 22.
12. S. L. Hou and N. Bloembergen, Phys. Rev. **138** (4A), A1218 (1965).
13. I. E. Chupis, Fiz. Nizk. Temp. **21** (9), 941 (1995) [Low Temp. Phys. **21**, 724 (1995)].
14. V. M. Fridkin, *Photoferroelectrics* (Nauka, Moscow, 1979), p. 66.

Translated by G. Skrebtsov

Physics of the Solid State, Vol. 44, No. 1, 2002, pp. 149–152. Translated from Fizika Tverdogo Tela, Vol. 44, No. 1, 2002, pp. 144–146.

MAGNETISM AND FERROELECTRICITY

Relaxation of Piezobirefringence in Triglycine Sulfate Crystals

N. M. Dem'yanishin and B. G. Mytsyk

Lviv Center, Space Research Institute, National Academy of Sciences of Ukraine and National Space Agency of Ukraine, Lviv, 79000 Ukraine

e-mail: mytsyk@mail.lviv.ua

Received April 16, 2001

Abstract—The effect of photoelastic relaxation is investigated using triglycine sulfate ferroelectric crystals as an example. The optical and deformation contributions to the photoelastic relaxation are described, and their percentage in the combined effect is determined. Consideration is given to the temperature dependences of the relaxation amplitudes of the path difference and birefringence, which are induced by mechanical stress. © *2002 MAIK "Nauka/Interperiodica".*

1. INTRODUCTION

Photoelastic (piezooptic) relaxation can be considered to be a change in the optical parameters of a sample with time under the action of constant mechanical stress. Earlier [1, 2], we proved the piezocaloric mechanism of relaxation changes in the path difference $\delta\Delta_{km}$ under the mechanical stress σ_m for triglycine sulfate crystals. Romanyuk *et al.* [3] noted that the relaxation change in the path difference $\delta\Delta^r_{km}$ is determined by two contributions, namely, the optical and deformation contributions. The optical contribution is due to the relaxation change in birefringence $\delta\Delta n^r_{km}$. The deformation contribution is associated with the relaxation change in the crystal thickness δd^r_{km} along the direction of light propagation. However, two problems remain unclear: (1) the magnitude of each of the contributions to the combined effect of relaxation of the path difference and (2) the reasons for the different signs of the quantities $\delta\Delta^r_{km}$, which can also be governed by the different signs of the two contributions to $\delta\Delta^r_{km}$.

In this paper, we analyze the temperature dependences of the relaxation amplitudes of the birefringence $\delta\Delta n^r_{km}$ for a purely piezooptic effect, which accounts for the change in birefringence (rather than in the path difference) under the mechanical stress σ_m.

2. THEORETICAL BACKGROUND

The two-index notation for $\delta\Delta^r_{km}$, $\delta\Delta n^r_{km}$, and δd^r_{km} is not an indication of the tensor character of these quantities (they are not tensors). The lower indices refer to the experimental conditions: k = 1, 2, and 3 are the subscripts indicating the directions of light propagation and m = 1, 2, and 3 stand for the directions of pressure action.

The optical and deformation contributions to the photoelastic relaxation effect are related to the relaxation change in the path difference by the following expression:

$$\delta\Delta^r_{km} = \delta(\Delta n_k d_k)^r_m = \delta\Delta n^r_{km} d_k + \Delta n_k \delta d^r_{km}, \quad (1)$$

where d_k is the sample dimension along the direction of propagation of the light beam and Δn_k is the birefringence.

Knowing δd^r_{km} and substituting the experimental values of $\delta\Delta^r_{km}$ into relationship (1), we can determine the pure piezooptic relaxation $\delta\Delta n^r_{km}$.

It should be emphasized that the relaxation of the linear dimensions δd^r_{km} of the sample has a purely piezocaloric nature, because the possible deformation relaxation due to plastic effects is absent. This is explained by the fact that the acting mechanical stresses are rather small: they are more than one order of magnitude less than the mechanical strength of triglycine sulfate crystals (in our experiments, we used the mechanical stress σ_m = 10–50 × 10^5 N/m^2). Moreover, the lack of plastic deformations is confirmed by the fact that residual effects are also absent after removal of the mechanical stresses and completion of the relaxation change in the path difference $\delta\Delta^r_{km}(\tau)$, where τ is the relaxation time.

The relationship for calculating δd^r_{km} can be obtained from the following considerations. Rapid action of the mechanical stress σ_m results in an adiabatic change in temperature δT^r_m, which can be determined from the formula [4]

$$\delta T^r_m = -(T_0/C_p)\alpha_m\sigma_m, \quad (2)$$

where the subscript m indicates the direction of pressure action, α_m is the coefficient of linear expansion along the direction of the pressure action, C_p is the heat capacity at a constant pressure per unit volume, and T_0 is the ambient temperature.

The temperature of the sample regains its initial value for a relaxation time τ due to heat exchange with the environment. The relaxation change in temperature $(-\delta T^r_m)$ causes the relaxation change in the sample dimension δd^r_{km} that is proportional to the thermal expansion coefficient α_k and the change in temperature, that is,

$$\delta d^r_{km} = d_k \alpha_k (-\delta T^r_m). \quad (3)$$

Here, the subscript m indicates the dependences of the relaxation temperature change and the deformation relaxation on the direction of pressure action. Relationship (3) will be used for calculating the deformation relaxation and, taking into account expression (1), the deformation contribution to $\delta\Delta^r_{km}$ (the second term).

In order to determine the relaxation of birefringence, we rewrite relationship (1) with allowance made for relationships (2) and (3) in the following form:

$$\delta\Delta^r_{km} = \delta\Delta n^r_{km} d_k + \Delta n_k d_k \alpha_k (T_0/C_p)\alpha_m \sigma_m. \quad (4)$$

By substituting the known values of α_k, α_m [5], and Δn_k [6] for triglycine sulfate crystals and our experimental values of $\delta\Delta^r_{km}$ into relationship (4), we calculated the relaxation changes in birefringence $\delta\Delta n^r_{km}$ after applying and relieving the mechanical stress σ_m. The sign of the experimental $\delta\Delta^r_{km}$ value with respect to the natural path difference Δ_k was determined using standard compensation techniques with the following criterion: if the relaxation change in the path difference $\delta\Delta^r_{km}$ increases or decreases the natural path difference Δ_k, the value of $\delta\Delta^r_{km}$ is positive or negative, respectively.

The relaxation change in birefringence $\delta\Delta n^r_{km}$ can also be calculated in a different way. By subtracting the deformation contribution (the second term) from the temperature changes in the path difference $\delta\Delta_k(T) = \delta\Delta n_k(T) d_k + \Delta n_k \delta d_k(T)$ we derive, as was done by Ivanov *et al.* [7], the temperature dependences of the relaxation change in birefringence $\delta\Delta n_k(T)$ and, correspondingly, the temperature derivative $d\Delta n_k(T)/dT$. Knowing this derivative and the relaxation temperature change $-\delta T^r_m$, we determine the relaxation of birefringence at each temperature T_0:

$$\delta\Delta n^r_{km}(T) = (d\Delta n_k(T)/dT)(-\delta T^r_m) \quad (5)$$

or, taking into account relationship (2),

$$\delta\Delta n^r_{km}(T) = (d\Delta n_k(T)/dT)(T_0/C_p)\alpha_m \sigma_m. \quad (6)$$

Both calculation techniques lead to identical results, to within the limits of experimental error in measuring $\delta\Delta^r_{km}(T)$ and $\delta\Delta_k(T)$.

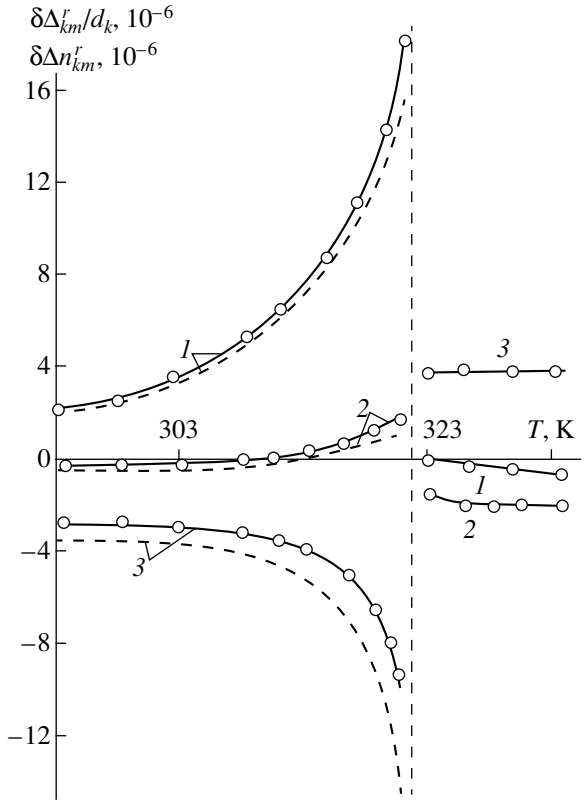

Temperature dependences of the relaxation amplitudes of the stress-induced path difference $\delta\Delta^r_{km}/d_k$ (solid line, experiment) and birefringence $\delta\Delta n^r_{km}$ (dashed line, calculation) for the triglycine sulfate crystal: (*1*) $\delta\Delta^r_{13}/d_1$ and $\delta\Delta n^r_{13}$, (*2*) $\delta\Delta^r_{23}/d_2$ and $\delta\Delta n^r_{23}$, and (*3*) $\delta\Delta^r_{31}/d_3$ and $\delta\Delta n^r_{31}$ ($\sigma_m = 50 \times 10^5$ N/m^2).

3. RESULTS AND DISCUSSION

The figure shows temperature dependences of the absolute amplitude of relaxation changes in the path difference $\delta\Delta^r_{km}$ per unit length (solid line) for triglycine sulfate crystals. The calculated temperature dependences of the relaxation change in birefringence $\delta\Delta n^r_{km}$ (dashed line) for experimental configurations, which provide relatively high values of the relaxation change in $\delta\Delta^r_{km}$, are also depicted in the same figure. The indi-

Optical and deformation contributions (calculated per unit length) and relaxation changes in the path difference $\delta\Delta^r_{km}/d_k$ for triglycine sulfate crystals at different temperatures and $\sigma_m = 50 \times 10^5$ N/m^2

Geometry of the experiment	T_0 = 293 K			T_0 = 321 K			T_0 = 327 K		
	$\delta\Delta^r_{km}/d_k \times 10^{-6}$	optical contribution, %	deformation contribution, %	$\delta\Delta^r_{km}/d_k \times 10^{-6}$	optical contribution, %	deformation contribution, %	$\delta\Delta^r_{km}/d_k \times 10^{-6}$	optical contribution, %	deformation contribution, %
$k = 1$ $m = 3$	2.2	96.1	3.9	17.3	91.0	9.0	–1.7	100.3	–0.3
$k = 2$ $m = 3$	–0.2	103.5	–3.5	1.7	70.0	30.0	–0.1	101.0	–1.0
$k = 3$ $m = 1$	3.0	117.0	–17.0	–8.6	166.0	–66.0	3.8	99.4	0.6

ces k, m = 1, 2, and 3 correspond to the directions coinciding with the axes X_1, X_2, and X_3 of the optical indicatrix of the crystal.

The comparative data on optical and deformation contributions [the first and second terms in relationship (1)] to the relaxation of the path difference at different temperatures are given in the table.

Analysis of the data presented in the table and the figure revealed the following features.

(I) The deformation contribution to $\delta\Delta^r_{km}$ has opposite signs at different experimental configurations; i.e., under certain conditions, the deformation contribution decreases the relaxation change in the path difference $\delta\Delta^r_{km}$ (for example, at $k = 3$, $m = 1$, and $T < T_c$ and at $k = 1$, $m = 3$, and $T > T_c$), and, under other conditions, the deformation leads to an increase in $\delta\Delta^r_{km}$ (for example, at $k = 1$, $m = 3$, and $T < T_c$ and at $k = 3$, $m = 1$, and $T > T_c$).

(II) Upon passing through T_c, the deformation contribution at $k = 1$, $m = 3$ and $k = 3$, $m = 1$ changes sign.

(III) In all cases, an increase in the temperature to T_c is accompanied by an increase in the magnitude of the deformation contribution. At $T > T_c$, the deformation contribution is small in magnitude (≤1%; hence, it is not shown in the figure) and is virtually temperature independent. The small magnitude of the deformation contribution in the paraelectric phase is determined primarily by the small magnitude of δd^r_{km}. The smallness of the latter quantity results from small coefficients α_k in relationship (3) at $T > T_c$ [5].

(IV) The relaxation changes in birefringence are very small compared to the natural changes (Δn_1 = 0.075, Δn_2 = 0.028, and Δn_3 = 0.103). This is confirmed by the following values (T = 273 K): $\delta\Delta n^r_{13}/\Delta n_1 \approx \delta\Delta n^r_{31}/\Delta n_3 \approx 3 \times 10^{-5}$ (0.003%) and $\delta\Delta n^r_{32}/\Delta n_2 \approx 1.4 \times 10^{-5}$ (0.0014%). However, compared to the piezooptic changes, the relaxation changes are rather large. For example, at T = 293 K, we have the following values: $\delta\Delta n^r_{13}/\delta\Delta n_{13} \approx 5.7\%$, $\delta\Delta n^r_{31}/\delta\Delta n_{31} \approx 3.0\%$, and $\delta\Delta n^r_{23}/\delta\Delta n_{23} \approx 1.5\%$. At $T \approx T_c$, these ratios are as follows: $\delta\Delta n^r_{13}/\delta\Delta n_{13} \approx 16.4\%$, $\delta\Delta n^r_{31}/\delta\Delta n_{31} \approx 16.6\%$, and $\delta\Delta n^r_{23}/\delta\Delta n_{23} \approx 7.0\%$. Here, $\delta\Delta n_{km}$ are the piezooptic changes, which were determined from the experimental piezooptic changes in the path difference $\delta\Delta_{km}$ with inclusion of the elastic contribution according to the procedure described in [8].

(V) The magnitude of the deformation contribution is smaller than that of the optical contribution over the entire temperature range covered. However, the deformation contribution near T_c reaches high values and, at $k = 3$ and $m = 1$, constitutes 66% of the combined effect.

As follows from item V, the opposite signs of the optical and deformation contributions to the relaxation change in the path difference are not responsible for the opposite signs of the $\delta\Delta^r_{km}$ quantities and the sign reversal upon passing through T_c, because the deformation contribution is universally smaller. The opposite signs of $\delta\Delta^r_{km}$ are determined by the signs of thermooptic (the path difference) and piezocaloric effects in the piezocaloric model of the $\delta\Delta^r_{km}$ relaxation, which was described earlier in [1–3].

In conclusion, we note that the sign reversal observed for relaxation of the path difference $\delta\Delta^r_{23}$ and the birefringence $\delta\Delta^r_{23}$ at T = 308 K (curve *2* in the figure) is nothing more than the piezocaloric reflection of the thermooptic effect. The sign reversal is characteristic of the thermooptic effect in the case of light propagation along the X_2 axis [7].

REFERENCES

1. B. G. Mytsyk and N. M. Dem'yanishin, Fiz. Tverd. Tela (St. Petersburg) **40** (2), 318 (1998) [Phys. Solid State **40**, 290 (1998)].
2. B. G. Mytsyk and N. M. Dem'yanishin, Ukr. Fiz. Zh. **43** (4), 479 (1998).
3. N. A. Romanyuk, B. H. Mytsyk, and N. M. Demyanyshyn, Ferroelectrics **203**, 101 (1997).
4. Yu. I. Sirotin and M. P. Shaskolskaya, *Fundamentals of Crystal Physics* (Nauka, Moscow, 1979; Mir, Moscow, 1982).
5. J. Stankowski and W. Malinowski, Acta Phys. Pol. A **58** (6), 773 (1980).
6. N. R. Ivanov and V. F. Zotov, Kristallografiya **11** (6), 924 (1966) [Sov. Phys. Crystallogr. **11**, 781 (1966)].
7. N. R. Ivanov, S. Ya. Benderskiĭ, and I. O. Tukhtasunov, Izv. Akad. Nauk SSSR, Ser. Fiz. **39** (4), 798 (1975).
8. N. A. Romanyuk and B. G. Mytsyk, *Optics of Anisotropic Media* (Moscow, 1985).

Translated by N. Korovin

Physics of the Solid State, Vol. 44, No. 1, 2002, pp. 153–156. Translated from Fizika Tverdogo Tela, Vol. 44, No. 1, 2002, pp. 147–149.

MAGNETISM AND FERROELECTRICITY

Physical Aspects of the Shape of Electron Emission Spectra for Ferroelectric Electrets

V. V. Kolesnikov and A. T. Kozakov

Research Institute of Physics, Rostov State University, pr. Stachki 194, Rostov-on-Don, 344090 Russia

e-mail: kozakov@iphys.rnd.runnet.ru

Received January 25, 2001; in final form, May 8, 2001

Abstract—A correlation between the specific features of the electron emission spectrum of a ferroelectric electret and the behavior of the potential at the surface of the sample is determined within the theoretical approach proposed. The physical nature of the main features in experimental emission spectra is interpreted in terms of the behavior of the potential relief. It is revealed that the electret charge relaxation affects the spectrum shape due to the bifurcation (branching) of singularities in the spectrum. © *2002 MAIK "Nauka/Interperiodica".*

1. INTRODUCTION

The distribution of the electric field in a ferroelectric plays an important role in the processes of electron emission from cold cathodes [1, 2] and ferroelectric electrets exposed to x-ray radiation [3–6]. In the latter case, as was noted in [5], the problem involves two aspects concerned with the behavior of tangential- and normal-to-surface components of the electric field. The normal component has a maximum in the surface layer owing to the injected electron charge [3], whose proximity to the surface of a solid determines the emission intensity [6]. The behavior of the tangential component is governed by the stability of the homogeneous state along the sample surface and can exhibit an oscillating character [5], resulting in a complex pattern of the observed emission spectrum $I(\varepsilon)$. In the present work, we theoretically proved a direct correlation between the singularities in the spectrum shape and the behavior of the potential along the surface of a ferroelectric electret. Formal aspects of this correlation are considered below.

2. THEORETICAL ANALYSIS

The proposed approach is a generalization of the approximation technique described earlier in [7] and, in essence, consists in the following. We assume that $j_0(\varepsilon)$ is the spectral density of the emission current from the neutral surface. In this case, the contribution to the current dI from the segment dS in the vicinity of the point with coordinates (x, y) and a potential $\varphi(\rho)$ (ρ is the radius-vector of the point) is determined from the expression

$$dI = j_0(\varepsilon - \varphi)dS. \quad (1)$$

The electron energy ε and potential φ are measured from the standard energy level, which is specified by the measuring system of the spectrometer (hereafter, the potential will be taken to mean the potential energy of an electron). Integration of expression (1) over the surface of the sample is performed in two stages: first, along the equipotential lines l and, then, over all physically possible values of the potential φ from the standpoint of recording the emission. The result for $I(\varepsilon)$ can be represented as the convolution of $j_0(\varepsilon)$ and function $n(\varphi)$:

$$I(\varepsilon) = \int j_0(\varepsilon - \varphi)n(\varphi)d\varphi. \quad (2)$$

The function $n(\varphi)$ is determined by the electric field $E = -\nabla\varphi(\rho)$at the surface of the sample, that is,

$$n(\varphi) = \int_l \frac{dl}{|\nabla\varphi(\rho)|}, \quad (2a)$$

and formally coincides with the definition of the density of electron states for a two-dimensional lattice, which, under certain conditions, exhibits specific features known as van Hove singularities [8]. In our case, as follows from expression (2a), these features are associated with the regions characterized by a low field E at the surface of the electret and should give rise to singularities in the shape of the spectrum $I(\varepsilon)$. Reasoning from the general behavior of the $n(\varphi)$ function [8] in these regions, the sharpest singularities in $I(\varepsilon)$ should be expected in the one-dimensional case. Physically, this situation corresponds to the formation of surface anisotropic band structures in the distributions of the electric field and polarization. The potential differences along one of the directions in these structures are small, and the problem under consideration can be treated as a one-dimensional case. The change-over to more symmetric two-dimensional distributions should lead to a smoothing of the singularities in $I(\varepsilon)$. Similar qualitative changes in the spectra are actually observed in experiments during ageing of the electrets: the shape of

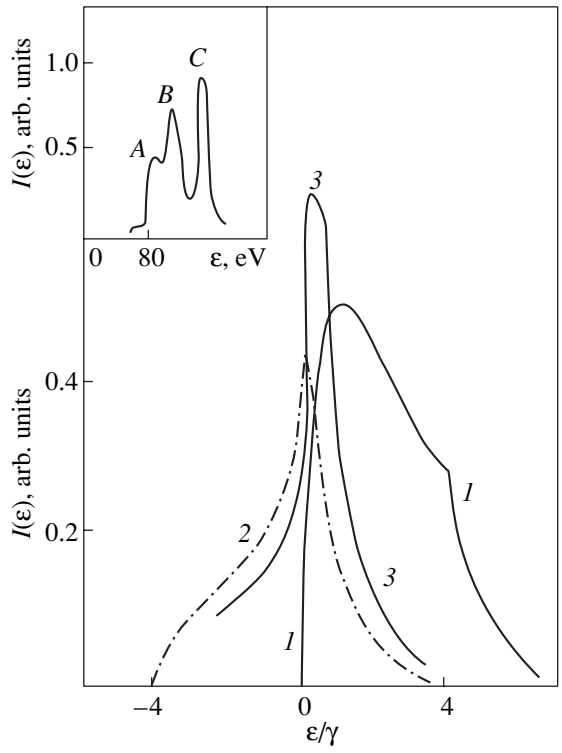

Fig. 1. Theoretical shape of the electron emission spectrum $I(\varepsilon)$ in the vicinity of the (*1*) minimum, (*2*) maximum, and (*3*) horizontal step of the potential. The electron energy ε is measured from the singularity. The inset shows the experimental emission spectrum of lead magnesium niobate [3].

the $I(\varepsilon)$spectra changes from a set of sharp δ-shaped maxima to broad distributions whose width can be as large as several hundred electron-volts and whose structure is weakly pronounced [3, 4]. Let us now begin our theoretical analysis of the changes in the shape of $I(\varepsilon)$with the one-dimensional case.

In the one-dimensional case, $n(\varphi) = 1/|E(\varphi)|$. We consider three types of characteristic points in the potential $\varphi(x)$ that can give rise to singularities in the $n(\varphi)$ function and the $I(\varepsilon)$ spectrum. These are the extrema (minimum or maximum) and an inflection point. We can write the following equations in the vicinity of these characteristic points:

$$\varphi(x) = ax^2, \quad a \gtrless 0, \tag{3}$$

$$\varphi = -\lambda x + bx^3. \tag{4}$$

For $j_0(\varepsilon)$, we accept a simple approximation of the form

$$j_0(\varepsilon) \sim \exp(-\varepsilon/\gamma)\theta(\varepsilon), \tag{5}$$

where $\theta(\varepsilon) = 0$ (at $\varepsilon < 0$) and 1 (at $\varepsilon > 0$).

Expression (5) corresponds to a spectrum in the form of a cascade maximum, which is typical of the neutral surface [9, 10]. The parameter γ characterizes the width of this maximum; as a rule, it is approximately equal to ~10 eV.

By using relationships (2) and (2a) with due regard for relationship (5), the intensity $I(\varepsilon)$ in the vicinity of the potential extrema can be expressed through the probability integrals [11]. Specifically, for a minimum ($a > 0$), the expression for $I(\varepsilon)$ has the form

$$I(\varepsilon) \sim l\exp(-s^2)\int_0^s \exp(t^2)dt, \quad \varphi_c > \bar{\varepsilon} > 0, \tag{6}$$

where $s = \sqrt{\bar{\varepsilon}}$ and $\bar{\varepsilon} = \varepsilon/\gamma$ is the dimensionless electron energy.

The parameter φ_c characterizes the potential difference in the vicinity of the singularity. For the region $\bar{\varepsilon} > \varphi_c$ in expression (6), the upper limit of integration should be fixed. In our case, it is taken as $s = s_c = \sqrt{\varphi_c}$ and $I(\varepsilon)$ decays exponentially. At $\varepsilon < 0$, we have the intensity $I(\varepsilon) = 0$ in the accepted approximation (5) for $j_0(\varepsilon)$.

According to relationship (6), the intensity $I(\varepsilon)$ is proportional to the characteristic length $l = (\gamma/|a|)^{1/2}$, which is specified by the curvature of the potential in expression (3). As the curvature of the potential decreases, the intensity $I(\varepsilon)$ increases.

The shape of the spectra, which correspond to the extrema in the potential at identical values of l, is shown in Fig. 1 (for the convenience of graphical representation, the $I(\varepsilon)$ intensity at the maximum is diminished by a factor of two). At $\varepsilon \sim 0$, the spectra are characterized by a singularity of the type

$$I(\varepsilon) \sim C|\varepsilon|^{\alpha} + I_0 \tag{7}$$

(where $\alpha = 0.5$ and C and I_0 are constants) to the right and to the left of this point for minimum and maximum, respectively. In the former case, $I_0 = 0$.

Now, we consider the evolution of the spectrum in the vicinity of the inflection point in $\varphi(x)$. At $\lambda < 0$ in formula (4) (for definiteness, we assume that $b > 0$), the function $n(\varphi)$ in expression (2) has no singularities, whereas $I(\varepsilon)$ exhibits a single structureless maximum whose intensity decreases with a decrease in λ. However, the situation reverses with an increase in λ. Indeed, at $\lambda = 0$, the potential is characterized by a horizontal step and the spectrum shows a maximum. The shape of the maximum is displayed in Fig. 1 (curve *2*). In the vicinity of $\varepsilon \lesssim 0$, the spectrum has a singularity of type (7) but with $\alpha = 1/3$. With a further increase in λ, this maximum splits into two maxima. Their energy positions $\varepsilon_{B,A}$, depending on λ (see the inset (b) in Fig. 2), are determined by zero values of the electric field as a function of φ. With allowance made for expression (4), this leads to the relationships $\varepsilon_{B,A} \sim \pm(\lambda/3b)^{3/2}$. The splitting of the lines is due to branching (bifurcation) of the singularities in the function $n(\varphi)$.

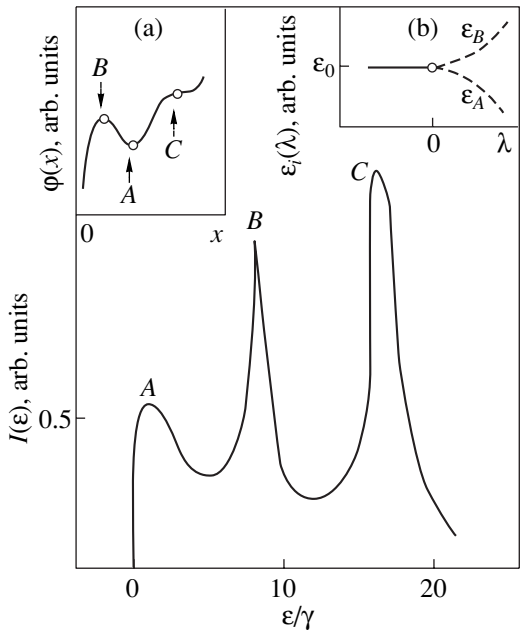

Fig. 2. Theoretical shape of the emission spectrum $I(\varepsilon)$ for the potential relief $\varphi(x)$ shown in the inset (a): the maxima *A*, *B*, and *C* in the spectrum correspond to the points *A*, *B*, and *C* in the potential relief $\varphi(x)$ in the vicinity of the side electrode of the electret. The inset (b) shows the energy location of lines *A* and *B* in the spectrum at different parameters λ in the course of bifurcation (branching) of singularities in the spectrum.

This function has no singularities to the left of the bifurcation point $\lambda = 0$ and exhibits two root singularities to the right of this point, namely, at the points $\varepsilon_{B,A}$: $n(\varphi) \sim |\varphi - \varepsilon_{B,A}|^{-1/2}$. The reverse change in the parameter λ is accompanied by the confluence of two maxima in the spectrum.

Let us illustrate the aforesaid with a fragment of the spectrum for lead magnesium niobate electret (see the inset in Fig. 1). The main features in the experimental spectrum can be explained in terms of quasi-one-dimensional (band) distributions of the electric field and polarization in the sample with the potential relief in the vicinity of the side electrode, which is shown in the inset (a) in Fig. 2. (The behavior of the potential relief agrees with the inferences made in [5] on the possible oscillating behavior of the potential on the surface of the ferroelectric electret.) The spectrum can be represented as the superposition of the contributions from the singularities *A*, *B*, and *C* in the potential. By using the data shown in Fig. 1 and choosing the appropriate energy position of the lines, we can obtain the spectrum $I(\varepsilon)$ shown in Fig. 2, which is in qualitative agreement with the experimental spectrum. Maxima *A*, *B*, and *C* in the spectrum correspond to contributions from the neighborhood of the corresponding points in $\varphi(x)$. The structure with two extrema (*A*, *B*) in $\varphi(x)$ corresponds to potential (4) with $\lambda > 0$ and $b > 0$. As is the case with the bifurcation effect, a decrease in the parameter λ results in convergence of the extrema (*A* and *B*) in the potential and lines *A* and *B* in the spectrum (see the inset (b) to Fig. 2) and their confluence at $\lambda = 0$. Subsequently, at $\lambda < 0$, there remains only a single line in the $I(\varepsilon)$ spectrum at the energy $\varepsilon = \varepsilon_0$. Similarly, the maximum *C* in Fig. 2 can split with an increase in λ.

The change in the spectrum shape when going over to two-dimensional distributions of the electric field can be considered using extrema in the potential φ as an example. In this case, the potential is determined by two values of the curvature $a_\pm$ in expression (3) and two values of the length $l_\pm = (\gamma/|a_\pm|)^{1/2}$ [see expression (6)]. The intensity $I(\varepsilon)$ is characterized by their average value $\bar{l} = (l_+ l_-)^{1/2}$. If one of the parameters $l_\pm$ (for example, l_+) exceeds the sample dimension *L*, we have the quasi-one-dimensional case discussed above. As the l_+ parameter decreases to $l_+ \lesssim L$, the potential in the immediate vicinity of the extremum becomes essentially two-dimensional and the function $n(\varphi)$ is constant in this region, as can easily be shown using relationship (2a). This lead to the truncation of vertices of the *A* and *B* maxima shown in Fig. 2 and the appearance of horizontal plateaus in the spectrum. With a further decrease in l_+, their width increases. In this energy range, the $I(\varepsilon)$ spectrum has the shape of a broad maximum with a weakly pronounced structure, as was noted above.

3. CONCLUSION

It was demonstrated that the complex shape of the energy spectra $I(\varepsilon)$ of electron emission from ferroelectric electrets is determined by the singularities in the distributions of the electric field and polarization over their surface. The character of $I(\varepsilon)$ is qualitatively different for a quasi-one-dimensional (band) distribution and a more symmetric two-dimensional distribution of the electric field. This circumstance can be used in analyzing the dynamics of the domain structure and elucidation of the physical mechanisms of electron emission from ferroelectric electrets.

ACKNOWLEDGMENTS

We are grateful to V.P. Sakhnenko for his support of this work.

This work was supported by the Government Budget of the Research Institute of Physics, Rostov State University.

REFERENCES

1. V. F. Puchkarev and G. A. Mesyats, J. Appl. Phys. **78** (9), 5633 (1995).
2. L. Schachter, J. D. Ivers, J. A. Nation, and G. S. Kerslich, J. Appl. Phys. **73** (12), 8097 (1993).
3. A. T. Kozakov, V. V. Kolesnikov, V. P. Sakhnenko, *et al.*, Fiz. Tverd. Tela (St. Petersburg) **38** (8), 2524 (1996) [Phys. Solid State **38**, 1385 (1996)].

4. A. T. Kozakov, V. V. Kolesnikov, A. V. Nikol'skiĭ, and V. P. Sakhnenko, Fiz. Tverd. Tela (St. Petersburg) **39** (4), 679 (1997) [Phys. Solid State **39**, 594 (1997)].
5. V. V. Kolesnikov, A. T. Kozakov, and A. V. Nikol'skiĭ, Fiz. Tverd. Tela (St. Petersburg) **42** (1), 141 (2000) [Phys. Solid State **42**, 146 (2000)].
6. V. V. Kolesnikov and A. T. Kozakov, Fiz. Tverd. Tela (St. Petersburg) **42** (11), 2085 (2000) [Phys. Solid State **42**, 2148 (2000)].
7. A. T. Kozakov, V. V. Kolesnikov, A. V. Nikol'skiĭ, and V. P. Sakhnenko, *Physical Aspects of Anomalies in X-ray Photoelectron Spectra and Electrophysical Properties of Coals*, Preprint, Sev.-Kavk. Nauchn. Tsentr Vyssh. Shk. (Rostov-on-Don, 1993).
8. I. M. Lifshits, M. Ya. Azbel', and M. I. Kaganov, *Electron Theory of Metals* (Nauka, Moscow, 1971; Consultants Bureau, New York, 1973).
9. A. T. Kozakov, V. V. Kolesnikov, A. V. Nikol'skiĭ, and V. P. Sakhnenko, Fiz. Tverd. Tela (St. Petersburg) **36** (2), 317 (1994) [Phys. Solid State **36**, 173 (1994)].
10. V. V. Kolesnikov, A. T. Kozakov, A. V. Nikol'skiĭ, and V. P. Sakhnenko, Poverkhnost', No. 3, 915 (2000).
11. *Handbook of Mathematical Functions*, Ed. by M. Abramowitz and I. A. Stegun (Dover, New York, 1971; Nauka, Moscow, 1979).

Translated by N. Korovin

Physics of the Solid State, Vol. 44, No. 1, 2002, pp. 157–161. Translated from Fizika Tverdogo Tela, Vol. 44, No. 1, 2002, pp. 150–154.

LOW-DIMENSIONAL SYSTEMS AND SURFACE PHYSICS

Low-Temperature Conduction of a System of Tunnel-Coupled Quantum Dots in YBaCuO and LaSrMnO Dielectric Films

V. D. Okunev*, N. N. Pafomov*, V. A. Isaev*, T. A. D'yachenko*, A. Klimov, and S. J. Lewandowski****

** Donetsk Physicotechnical Institute, National Academy of Sciences of Ukraine, Donetsk, 83114 Ukraine*

*** Instytut Fizyki PAN, 02-668 Warsaw, Poland*

e-mail: okunev@host.dipt.donetsk.ua

Received March 19, 2001

Abstract—This paper reports on new results of experimental investigations into the nature of the electrical resistivity $\rho(T) \cong$ const at $T < T_{crit}$ for YBaCuO and LaSrMnO dielectric films. The films are prepared by pulsed laser deposition and contain nanocrystalline clusters with metallic conductivity. Dependences of the electrical resistivity $\rho(T) \cong$ const are observed for the epitaxial films YBaCuO (T_{crit} = 10 K) with a tetragonal structure after exposure to KrF excimer laser radiation and for the as-prepared amorphous films LaSrMnO ($T_{crit} \cong$ 160 K). The effect of interest ($\rho(T) \cong$ const) manifests itself in the case when the optical spectra of the studied samples contain portions attributed to absorption by free charge carriers. The inference is made that this effect can be associated with tunneling conduction in a system of quantum dots. *© 2002 MAIK "Nauka/Interperiodica".*

1. INTRODUCTION

Rapid progress in nanoelectronics has stimulated a continuously increasing interest expressed by researchers in systems with different-type disordered structures containing crystalline or crystal-like nanoclusters (from several nanometers to several tens of nanometers in size) [1–13]. A specific feature of these systems is that they are hard to produce in materials with a perfect long-range order. From the practical standpoint, a randomly inhomogeneous medium—a dielectric matrix (in an amorphous or crystalline state) containing clusters with metallic conductivity—holds considerable promise. In this regard, metallic oxides (high-temperature superconductors and manganates), in which the mechanisms of formation of structural inhomogeneities are associated with the nature of these compounds [14–20], appear to be beyond comparison. This inhomogeneous medium is sometimes referred to as a foggy or droplet phase [17]. When the electrical conductivities of inhomogeneous regions differ considerably, the total electrical conductivity of the system is generally limited by two main channels: electron tunneling between neighboring clusters and tunneling between particular localized states formed by impurity atoms or point defects in the dielectric material. In the latter case, hopping conduction with a varying hopping length, as a rule, is realized at low temperatures and the temperature dependences of the electrical conductivity for the samples obey the Mott law:

$$\sigma \sim \exp[-(T_0/T)^{1/4}]. \quad (1)$$

In both cases, the tunneling depends on temperature and proceeds with the participation of phonons. For nonmetallic low-resistance inclusions, the former mechanism does not differ radically from the latter mechanism. Actually, we are dealing here with two different channels of hopping conduction. In the presence of clusters with metallic conductivity, dielectric films acquire the characteristic properties of granular metals. Intensive investigations performed over the last decades revealed that the electrical conductivity of these films changes with temperature according to the so-called one-half power law [1, 11],

$$\sigma \sim \exp[-(T_1/T)^{1/2}], \quad (2)$$

which is primarily related to the size distribution of the metallic grains involved [11].

However, experiments carried out for three systems (YBaCuO, LaSrMnO, and PrCaMnO) with the use of a planar geometry of electrodes demonstrated that, in the case when the dielectric films contain small-sized clusters with metallic conductivity, the temperature dependences of the electrical resistivity ρ exhibit portions with $\rho(T) \cong$ const [18, 21, 22]. For YBaCuO amorphous films, similar data were obtained for sandwich-type structures (Ag-*a*-YBaCuO–Cr–glass) [21]. This provides strong evidence that the phenomenon observed is related to neither surface contamination of high-resistance films nor to instrumental limitations in the course of measurements. In all the above cases, the films were prepared through pulsed laser deposition when the cluster formation was especially pronounced.

1063-7834/02/4401-0157$22.00

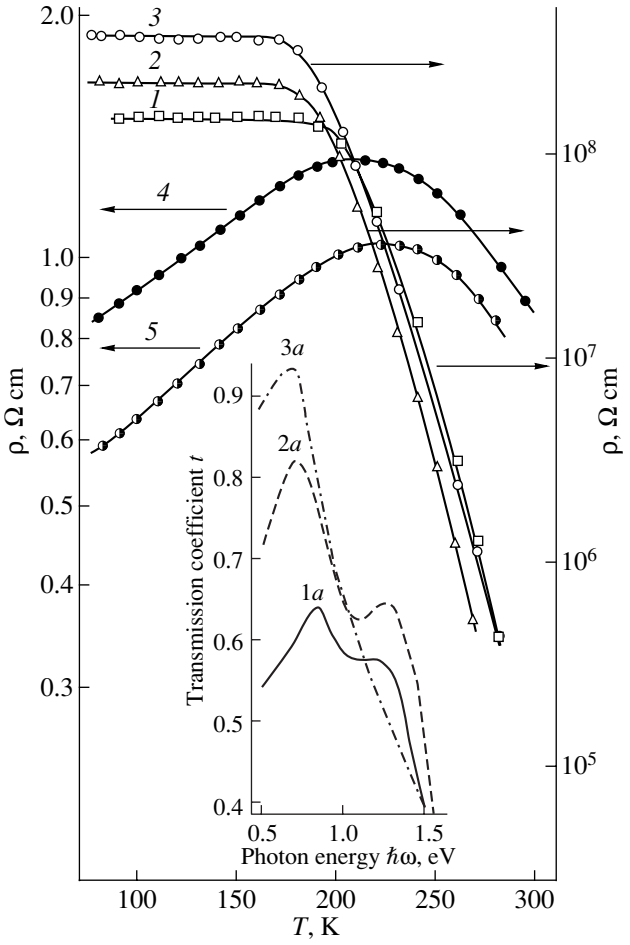

Fig. 1. Temperature dependences of the electrical resistivity for (*1–3*) amorphous and (*4*, *5*) crystalline $La_{0.6}Sr_{0.2}Mn_{1.2}O_3$ samples with a planar geometry of electrodes. Film growth temperature T_S, °C: (*1*) 450, (*2*) 550, (*3*) 600, (*4*) 650, and (*5*) 700. The film thickness l is 1×10^{-5} cm, and the interelectrode spacing is 0.3 cm. The dc electric field strength used in resistivity measurements is equal to (*1–3*) 1×10^3 and (*4*, *5*) 3.3 V/cm. The inset shows the optical transmission spectra of amorphous films at $T = 300$ K. T_S, °C: (*1a*) 450, (*2a*) 550, and (*3a*) 600.

In our recent work [21], this specific feature of dielectric systems with a disordered structure was interpreted in terms of the transformation of grains with extremely small sizes (of the order of several nanometers) into quantum dots. It is evident that analysis of the electrical conductivity in this system should account for the quantum-confinement effects. As is known from quantum mechanics, the electrical resistivity upon electron tunneling between two discrete levels can be characterized by the dependence $\rho(T) = \text{const}$.

The spacing Δ between the quantum-confinement levels is determined by the cluster size R and the density of states at the Fermi level $N(E_F)$ and can be represented by the relationship

$$\Delta \approx [R^3 N(E_F)]^{-1} \cong [R^3 p/E_F]^{-1}, \quad (3)$$

where p is the free charge carrier concentration, which depends on the density of states $N(E_F)$.

The electron tunneling between quantum dots is governed by the relationship between Δ, kT, and the charge energy

$$U = q_{2c}^2 \quad (4)$$

($c = \chi R/2$ is the capacitance of a spherical cluster of radius $R/2$). When solving this problem, the main difficulties are associated with the spread in grain size and free charge carrier concentration. According to Smirnov [13], the cluster plasma technique makes it possible to obtain materials with grains of identical size (in this case, nonactivation tunneling becomes possible [11]). However, in our opinion, this is highly improbable. Among theoretical investigations concerned with electron tunneling between two quantum dots, special mention should be made of the recent work by Burdov [23]. Burdov proved that, despite the Coulomb blockade limiting the electron tunneling between grains, the electron density can oscillate between quantum dots and a charge equal to the elementary charge periodically flows from one quantum dot to another [23]. A similar problem for granular systems still remains unsolved. However, it seems likely that the results obtained in [23] can be easily applied to granular systems, because this special case can be reduced to the problem of a resistance grating formed by neighboring grains.

In the present paper, we report new experimental data concerning the problem of the electrical resistivity $\rho(T) = \text{const}$ in YBaCuO and LaSrMnO films. As in our previous works [12, 18, 19], the films were prepared by pulsed laser deposition onto $SrLaGaO_4$ and $Nd_3Ga_5O_{12}$ substrates with the use of a KrF excimer laser ($\tau \approx 25$ ns and $\Phi \cong 1.5$–2.5 J/cm^2 at a target).

2. RESULTS AND DISCUSSION

First, let us consider the situation with amorphous films containing crystalline clusters, as is the case with the films studied earlier in [18, 21]. Figure 1 shows the temperature dependences of the electrical resistivity $\rho(T)$ for LaSrMnO amorphous films prepared by the sputtering of an $La_{0.6}Sr_{0.2}Mn_{1.2}O_3$ target at different temperatures T_S of the $Nd_3Ga_5O_{12}$ substrates. The portions $\rho(T) = \text{const}$ ($T_{crit} \cong 160$ K) are observed at deposition temperatures $T_S < 650$°C. At higher temperatures ($T_S \geq 650$°C), there occurs an amorphous–crystalline transition and the temperature dependences of the resistance $\rho(T)$ exhibit a maximum (typical of this state) at temperatures near the Curie point [15, 22]. In this case, the electrical conductivity of the studied films increases by five or nine orders of magnitude. The positive temperature coefficient of resistances, which is characteristic of metals, manifests itself in the temperature dependence of $\rho = \rho(T)$ at high electrical resistivities ρ (~1 Ω cm). This is an important indication that the sam-

ples involve inhomogeneities [17]. The occurrence of clusters with metallic conductivity can be judged from the fact that the optical transmission spectra at $\hbar\omega < 0.7$–0.9 eV contain certain portions attributable to absorption by free holes in the clusters upon interband optical transitions [19]. (The boundary value of $\hbar\omega$ decreases from 0.9 to 0.7 eV as the temperature T_S increases from 450 to 600°C.) Earlier [18], we observed similar portions in the spectra of YBaCuO amorphous films containing nanocrystalline clusters with metallic conductivity. It is worth noting that the increase in transmission of the films (and, correspondingly, the decrease in optical conductivity) in this $\hbar\omega$ range with an increase in the temperature T_S, which is caused by the decrease in volume of the metallic clusters, agrees well with the increase in the electrical resistivity ρ of the samples in the portion $\rho(T) = \text{const}$. By analyzing the function $(1/t)\partial t/\partial(\hbar\omega)$ (where t is the transmission coefficient) in the long-wavelength spectral range, we determine the product of the metal phase content C_m by the hole concentration p as follows [12, 18, 19]:

$$\frac{1}{t}\frac{\partial t}{\partial(\hbar\omega)} \approx C_m p. \tag{5}$$

Analysis of the transmission spectra of LaSrMnO films makes it possible not only to determine the concentration of metallic clusters but also to evaluate their size R with the use of the formula [15]

$$R^3 = \frac{135\pi^2\xi(1+X)^{1/3}}{32m^2e^2E_F f(X)}. \tag{6}$$

Here, ξ is the effective permittivity, $f(X) = [2X + 3 - 3(1 + X)^{2/3}]$, and $X = V_A/V_F$ is the volume ratio of the antiferromagnetic to ferromagnetic phase. It is assumed that $X \cong 1/C_m$. For $C_m = 0.02$–0.05, we obtain $R = 20$–50 Å, which corresponds to the sizes of the clusters formed in the amorphous films upon pulsed laser deposition [18]. In the case when the hole concentration p is approximately equal to $p \sim 3 \times 10^{21}$ cm^{-3}, the spacing Δ ranges from 10^{-2} to 10^{-1} eV. This provides an explanation of the critical temperature $T_{crit} = 160$ K.

In our experiments with YBaCuO epitaxial films, we hoped first of all to reveal the portions with $\rho(T) = \text{const}$ or portions with a nearly zero temperature coefficient of resistance in the temperature dependences of the electrical resistivity of films with a tetragonal structure. These films are of particular interest because they are characterized by a low oxygen concentration and a high probability of forming clusters with metallic conductivity. A typical optical transmission spectrum for these samples is depicted in Fig. 2 (curve *1*). Without going into detail on the short-wavelength spectral range, we should note that the spectrum contains no portion corresponding to absorption by free charge carriers at $\hbar\omega < 1.2$ eV. This portion is always observed in the spectra of YBaCuO epitaxial superconducting layers (Fig. 2, curve 5) [19]. The high resistance of the samples makes electrical measurements at low temperatures impossible; for this reason, the dependence $\rho(T) \cong \text{const}$ was not revealed. The portion that corresponds to absorption by free charge carriers and indicates the presence of metallic clusters appears after high-energy pulsed laser irradiation (Fig. 2, curve *2*), which promotes the formation of inhomogeneities [12]. Unfortunately, precision measurements at low temperatures failed due to the higher resistance of the samples (at $T \cong 300$ K, the electrical resistance increases by a factor of five or ten). Note that, even after exposure of the film to laser radiation, the content C_m of the metal phase did not exceed 2%.

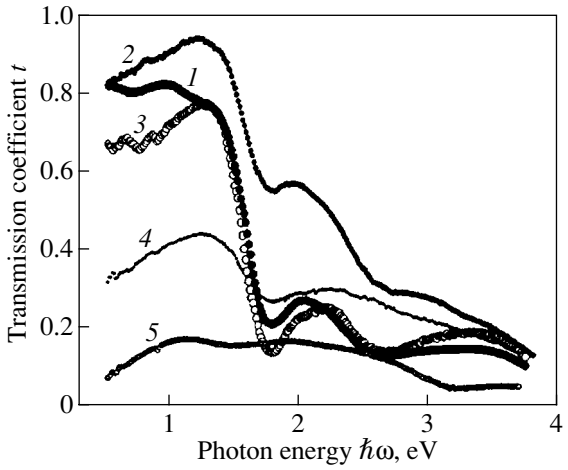

Fig. 2. Optical transmission spectra of $YBa_2Cu_3O_{6+x}$ crystalline films with a tetragonal structure ($\rho \cong 1.2 \times 10^4$ Ω cm at $T = 300$ K) (*1*) prior to and (*2*) after laser irradiation (20 pulses, $\tau \cong 25$ ns, $J = 0.1$ J/cm^2) and with a tetragonal structure and increased oxygen concentration ($\rho \cong 3 \times 10^2$ Ω cm at $T = 300$ K) (*3*) prior to and (*4*) after laser irradiation (10 pulses, $\tau \cong 25$ ns, $J = 0.1$ J/cm^2). (*5*) Optical transmission spectrum of the epitaxial superconducting film ($T_C = 90.3$ K).

Success was achieved with an increase in the oxygen content in the films with a tetragonal structure and a decrease (by approximately one order of magnitude at $T = 300$ K) in the electrical resistance of the samples. The decrease in the sample resistance favorably affected the measuring technique and permitted us to use conventional instruments for low-temperature measurements. No indications of a superconducting transition in the samples were observed at $T \geq 4.2$ K. However, as can be seen from Fig. 2 (curve *3*), the portions corresponding to absorption by free charge carriers appear even in the spectra of the initial samples.

The temperature dependences of the electrical resistivity of the samples (Fig. 3, curve *3*) differ qualitatively from those described by the Mott law (1) and relationship (2). At low temperatures, the local activation energies $\delta\varepsilon$, which we defined earlier in [10] as

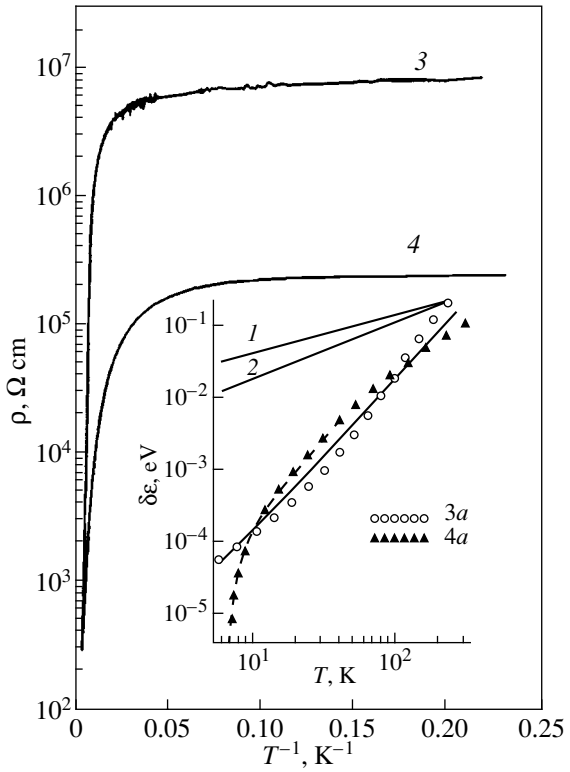

Fig. 3. Temperature dependences of the electrical resistivity for the film with a tetragonal structure and increased oxygen content (*3*) prior to and (*4*) after laser irradiation. The film thickness l is 1×10^{-5} cm, the interelectrode spacing L is 3×10^{-3} cm (planar geometry), and the dc electric field strength F used in the resistivity measurements is 3.5×10^4 V/cm. The numbering of the curves corresponds to that in Fig. 2. The inset shows the experimental temperature dependences of the local activation energy $\delta\varepsilon = \partial\ln\rho/\partial(kT)^{-1}$ for the film (*3a*) prior to and (*4a*) after laser irradiation and the calculated dependences (*1*) $\delta\varepsilon \sim T^{3/4}$ and (*2*) $\delta\varepsilon \sim T^{1/2}$ [corresponding to the Mott law (1) and relationship (2), respectively].

$\delta\varepsilon = \partial\ln\rho/\partial(kT)^{-1}$, are close to zero. As the temperature decreases further, the local energy $\delta\varepsilon$ decreases rather rapidly and becomes equal to 1.65×10^{-4} eV at $T = 10$ K, which is five times less than kT. However, the equality $\rho(T) = \text{const}$ does not hold. A virtually exact equality $\rho(T) = \text{const}$ (at $T < 10$ K) was achieved only after laser irradiation of the samples (Fig. 3, curve *4*). In the range 100 K < T < 300 K, the electrical resistivity of the samples increases by a factor of 1.5–5. At lower temperatures (T < 20 K), when the system of tunnel-coupled quantum dots makes the dominant contribution to the conduction, the electrical resistivity decreases by one or two orders of magnitude (almost by a factor of 40 in Fig. 3) as compared to the initial samples. An increase in the inhomogeneity of the samples under irradiation can be judged from the changes in the transmission spectra (Fig. 2). Indeed, considerable bleaching is observed in the short-wavelength range, whereas the transmission decreases in the long-wavelength spectral range in the portions associated with absorption by free charge carriers due to an increase in the amount of clusters with metallic conductivity. Under the assumption that the hole concentration in clusters with metallic conductivity corresponds to the carrier concentration in epitaxial layers with the Curie temperature T_C = 90–91 K (the spectrum of this film is represented by curve *5* in Fig. 2), the content C_m of the metal phase does not exceed 2–3% in the initial films and increases to ~5–7% after irradiation. Making allowance for the tendency toward a decrease in the size of clusters and the hole concentration in them, we find that, after laser irradiation of the samples, the amount of clusters with metallic conductivity in the film bulk can increase by a factor of four or five. The above estimates were made with due regard for the influence of the dielectric phase on the parameters of epitaxial layers [19]. In our opinion, the most important result obtained in this work is that the laser irradiation of films leads to a decrease in the distance between metallic clusters and, hence, to an exponential increase in the electron transition probability.

It remains unclear whether relationship (6) can be used to determine the size of nonferromagnetic clusters in YBaCuO films. Nonetheless, we performed the appropriate calculations with the use of the experimental results obtained. It was found that the cluster size is slightly larger and the T_{crit} temperature is slightly less than those for the LaSrMnO amorphous samples. However, the situation with YBaCuO films is complicated by the specific features of interaction between the laser radiation and the material [12]: a decrease in the cluster size and hole concentration is accompanied by the generation of new clusters. Therefore, the decrease in the inhomogeneity size does not necessarily occur with a decrease in the C_m content. In this case, the method proposed in [15] is inapplicable to determination of the cluster size.

Let us now assume that the electrical resistivity ρ and the temperature T are related by expression (2). It follows that the temperature dependence of the local activation energy can be represented by the expression $\delta\varepsilon = \partial\ln\rho/\partial(kT)^{-1} = (1/2)kT_1^{1/2}T^{1/2}$ (straight line *2* in the inset to Fig. 3). For the Mott law (1), this dependence is more pronounced: $\delta\varepsilon = (1/4)kT_0^{1/4}T^{3/4}$ (straight line *1* in the inset to Fig. 3). The experimental data are also represented by points in the inset to Fig. 3. If the experimental temperature dependence of $\delta\varepsilon$ is approximated by the power function $\delta\varepsilon \sim T^n$, we obtain n = 2.1. This value is three times larger than n = 3/4, which corresponds to the Mott law. After irradiation of the sample, the temperature dependence of $\delta\varepsilon$ falls off steeply at low temperatures. At T = 7 K, the quantity $kT = 6 \times 10^{-4}$ eV is more than two orders of magnitude greater than the local activation energy $\delta\varepsilon \cong 5 \times 10^{-6}$ eV. Lacking a satisfactory theory, the nature of these low energies $\delta\varepsilon$ remains unclear. In order to trace how the

energy $\delta\varepsilon$ approaches zero, it is necessary to decrease the experimental error, which can be achieved with lower resistance samples.

ACKNOWLEDGMENTS

This work was supported in part by the Polish Government, grant no. PBZ-KBN-013/T08/19.

REFERENCES

1. Ping Sheng and J. Klafter, Phys. Rev. B **27** (4), 2583 (1983).
2. A. G. Aronov, M. E. Gershenzon, and E. Yu. Zhuravlev, Zh. Éksp. Teor. Fiz. **87** (3), 971 (1984) [Sov. Phys. JETP **60**, 554 (1984)].
3. A. G. Zabrodskiĭ and K. N. Zinov'eva, Zh. Éksp. Teor. Fiz. **86** (2), 727 (1984) [Sov. Phys. JETP **59**, 425 (1984)].
4. A. M. Glukhov, N. Ya. Fogel', and A. A. Shablo, Fiz. Tverd. Tela (Leningrad) **28** (4), 1043 (1986) [Sov. Phys. Solid State **28**, 583 (1986)].
5. A. N. Aleshin, Z. A. Guts, A. N. Ionov, and I. S. Shlimak, Fiz. Tekh. Poluprovodn. (Leningrad) **20** (3), 490 (1986) [Sov. Phys. Semicond. **20**, 307 (1986)].
6. V. D. Okunev and Z. A. Samoĭlenko, Pis'ma Zh. Éksp. Teor. Fiz. **43** (1), 24 (1986) [JETP Lett. **43**, 28 (1986)].
7. V. D. Okunev and Z. A. Samoĭlenko, Pis'ma Zh. Éksp. Teor. Fiz. **53** (1), 42 (1991) [JETP Lett. **53**, 44 (1991)].
8. V. F. Gantmakher, V. N. Zverev, V. M. Teplinskiĭ, and O. I. Barkalov, Zh. Éksp. Teor. Fiz. **103** (4), 1460 (1993) [JETP **76**, 714 (1993)].
9. Yu. F. Komnik, Fiz. Nizk. Temp. **8** (2), 115 (1982) [Sov. J. Low Temp. Phys. **8**, 57 (1982)].
10. V. D. Okunev and N. N. Pafomov, Zh. Éksp. Teor. Fiz. **116** (1), 276 (1999) [JETP **89**, 151 (1999)].
11. E. Z. Meĭlikhov, Zh. Éksp. Teor. Fiz. **115** (4), 1484 (1999) [JETP **88**, 819 (1999)].
12. V. D. Okunev, Z. A. Samoilenko, A. Abal'oshev, *et al.*, Phys. Rev. B **62** (1), 696 (2000).
13. B. M. Smirnov, Usp. Fiz. Nauk **170** (5), 495 (2000).
14. G. Yu and A. J. Heeger, Int. J. Mod. Phys. B **7** (22), 3751 (1993).
15. É. L. Nagaev, Fiz. Tverd. Tela (St. Petersburg) **40** (11), 2069 (1998) [Phys. Solid State **40**, 1873 (1998)].
16. A. A. Abrikosov, Usp. Fiz. Nauk **168** (6), 683 (1998) [Phys. Usp. **41**, 605 (1998)].
17. L. P. Gor'kov, Usp. Fiz. Nauk **168** (6), 665 (1998) [Phys. Usp. **41**, 589 (1998)].
18. V. D. Okunev, Z. A. Samoilenko, V. M. Svistunov, *et al.*, J. Appl. Phys. **85** (10), 7282 (1999).
19. V. D. Okunev, Z. A. Samoilenko, A. Abal'oshev, *et al.*, Appl. Phys. Lett. **75** (13), 1949 (1999).
20. M. A. Ivanov and V. M. Loktev, Fiz. Nizk. Temp. **25** (12), 1325 (1999) [Low Temp. Phys. **25**, 996 (1999)].
21. V. D. Okunev, N. N. Pafomov, A. Abaleshev, *et al.*, Pis'ma Zh. Tekh. Fiz. **26** (20), 20 (2000) [Tech. Phys. Lett. **26**, 903 (2000)].
22. V. G. Prokhorov, G. G. Kaminsky, V. S. Flis, and Yong Pak Lee, Fiz. Nizk. Temp. **25** (10), 1060 (1999) [Low Temp. Phys. **25**, 792 (1999)].
23. V. A. Burdov, Pis'ma Zh. Éksp. Teor. Fiz. **71** (9), 570 (2000) [JETP Lett. **71**, 391 (2000)].

Translated by O. Borovik-Romanova

Physics of the Solid State, Vol. 44, No. 1, 2002, pp. 16–21. Translated from Fizika Tverdogo Tela, Vol. 44, No. 1, 2002, pp. 17–21.

METALS AND SUPERCONDUCTORS

On the Stability of the Critical State in Hard Superconductors with a Heterogeneous Temperature Profile

N. A. Taĭlanov and U. T. Yakhshiev

Scientific Research Institute for Applied Physics, Uzbekistan National University, Tashkent, 700174 Uzbekistan

Received March 27, 2001

Abstract—The problem of the thermal and magnetic destruction of the critical state in hard superconductors is investigated. The initial distributions of temperature and electromagnetic field are assumed to be essentially inhomogeneous. The limit of the thermomagnetic instability in quasi-stationary approximation is determined. The obtained integral criterion, unlike the analogous criterion for a homogeneous temperature profile, is shown to take into account the influence of any part of the superconductor on the threshold for critical-state instability.

While dealing with instabilities of the critical state in hard superconductors, the character of the temperature distribution $T(x, t)$ and that of the electromagnetic field $\mathbf{E}(x, t)$ are of substantial practical interest [1]. This derives from the fact that thermal and magnetic destructions of the critical state caused by Joule self-heating are defined by the initial temperature and electromagnetic-field distributions. Hence, the form of the temperature profile may noticeably influence the criteria of critical-state stability with respect to jumps in the magnetic flux in a superconductor. Earlier (cf., e.g., [2]), in dealing with this problem, it was usually assumed that the spatial distributions of temperature and field were either homogeneous or slightly inhomogeneous. However, in reality, physical parameters of superconductors may be inhomogeneous along the sample as well as in its cross-sectional plane. Such inhomogeneities can appear due to different physical reasons. First, the vortex structure pinning can be inhomogeneous due to the existence of weak bonds in the superconductor. Second, inhomogeneity of the properties may be caused by their dependence on the magnetic field **H**. Indeed, the field **H** influences many physical quantities, such as the critical current density $\mathbf{j}_c$, the differential conductivity σ_d, and the heat conductivity κ.

In the present paper, the temperature distribution in the critical state is investigated in the quasi-stationary approximation. It is shown that the temperature profile can be essentially inhomogeneous, which affects the conditions of initiation of a magnetic flux jump.

The evolution of thermal (T) and electromagnetic ($\mathbf{E}$, $\mathbf{H}$) perturbations in superconductors is described by a nonlinear heat conduction equation [3, 4],

$$\nu(T)\frac{dT}{dt} = \nabla[\kappa(T)\nabla T] + \mathbf{jE}; \quad (1)$$

a system of Maxwell's equations,

$$\mathrm{curl}\mathbf{E} = -\frac{1}{c}\frac{d\mathbf{H}}{dt}, \quad (2)$$

$$\mathrm{curl}\mathbf{H} = \frac{4\pi}{c}\mathbf{j}; \quad (3)$$

and a critical-state equation,

$$\mathbf{j} = \mathbf{j}_c(T, \mathbf{H}) + \mathbf{j}_r(\mathbf{E}). \quad (4)$$

Here, ν is the specific heat, $\mathbf{j}_c$ is the critical current density, and $\mathbf{j}_r$ is the active current density.

We use the Bean–London critical state model to describe the $\mathbf{j}_c(T, \mathbf{H})$ dependence, according to which $j = j_0 - a(T - T_0)$ [5], where the parameter a characterizes thermally activated weakening of Abrikosov vortex pinning on crystal lattice defects [3], j_0 is the equilibrium current density, and T_0 is the temperature of the superconductor.

The $j_r(E)$ dependence in the region of sufficiently strong electric fields $E \geq E_f$ can be approximated by a piecewise-linear function $j_r \approx \sigma_f E$, where σ_f is the effective conductivity in the regime of viscous flow and E_f is the limit of the linear region of the current–voltage characteristic of the sample. In the region of weak fields $E \leq E_f$, the function $j_r(T)$ is nonlinear. This nonlinearity is associated with thermally activated creep of the magnetic flux [6].

Let us consider a superconducting sample placed into an external magnetic field $\mathbf{H} = (0, 0, H_e)$ increasing at a constant rate $d\mathbf{H}/dt = \dot{\mathbf{H}} = \mathrm{const}$. According to the Maxwell equation (2), a vortex electric field $\mathbf{E} = (0, E_e, 0)$ is present. Here, H_e is the magnitude of the external magnetic field and E_e is the magnitude of the background electric field. In accordance with the concept of

the critical state, the current density and the electric field must be parallel: **j** || **E**.

The thermal and electromagnetic boundary conditions for Eqs. (1)–(4) have the form

$$\left(\kappa\frac{dT}{dx}\right)_0 + w_0(T(0)-T_0) = 0, \quad T(L) = T_0,$$
$$\left(\frac{dE}{dx}\right)_0 = 0, \quad E(L) = 0. \tag{5}$$

For the plane geometry (Fig. 1) and the boundary conditions $H(0) = H_e$, $H(L) = 0$, the magnetic field distribution is $H(x) = H_e(L - x)$, where $L = cH_e/4\pi j_c$ is the depth of magnetic flux penetration into the sample and w_0 is the coefficient of heat transfer to the cooler at the equilibrium temperature T_0.

The conditions of applicability of Eqs. (1)–(4) to the description of the dynamics of evolution of thermomagnetic perturbations are discussed at length in [1].

In the quasi-stationary approximation, terms with time derivatives can be neglected in Eqs. (1)–(4). This means that the heat transfer from the sample surface compensates the energy dissipation arising in the viscous flow of magnetic flux in the medium with an effective conductivity σ_f. In this approximation, the solution to Eq. (2) has the form

$$E = \frac{\dot{H}}{c}(L-x). \tag{6}$$

Upon substituting this expression into Eq. (1), we get an inhomogeneous equation for the temperature distribution $T(x, t)$,

$$\frac{d^2\Theta}{d\rho^2} - \rho\Theta = f(\rho). \tag{7}$$

Here, we introduced the dimensionless variables

$$f(\rho) = -[1 + r\omega\rho]\frac{j_0}{aT_0}, \quad \Theta = \frac{T-T_0}{T_0}, \quad \rho = \frac{L-x}{r}$$

and the dimensionless parameters $\omega = \sigma_f\dot{H}/cj_0$ and $r = (c\kappa/a\dot{H}L^2)^{1/3}$, where r characterizes the spatial scale of the temperature profile inhomogeneity in the sample.

Solutions to Eq. (7) are Airy functions, which can be expressed through Bessel functions of the order 1/3 [7]:

$$\Theta(\rho) = C_1\rho^{1/2}K_{1/3}\left(\frac{2}{3}\rho^{3/2}\right) + C_2\rho^{1/2}I_{1/3}\left(\frac{2}{3}\rho^{3/2}\right) + \Theta_0(\rho),$$
$$\Theta_0(\rho) = \rho^{1/2}K_{1/3}\left(\frac{2}{3}\rho^{3/2}\right) \tag{8}$$

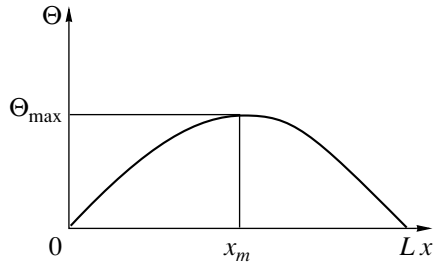

Fig. 1. Temperature distribution for the isothermal case.

$$\times\int_0^\rho [1 + r\omega\rho_1]\rho_1^{3/2}I_{1/3}\left(\frac{2}{3}\rho_1^{3/2}\right)d\rho_1 - \rho^{1/2}I_{1/3}\left(\frac{2}{3}\rho^{3/2}\right)$$
$$\times\int_0^\rho [1 + r\omega\rho_1]\rho_1^{3/2}K_{1/3}\left(\frac{2}{3}\rho_1^{3/2}\right)d\rho_1,$$

where C_1 and C_2 are integration constants, which are determined by the boundary conditions to be

$$C_1 = 0,$$
$$C_2 = \frac{-w_0L\Theta(0) + \kappa\left.\frac{d\Theta}{d\rho}\right|_{\rho = L/r}}{\left[w_0\left(\frac{L}{r}\right)^{1/2}I_{1/3}\left(\frac{2}{3}\rho^{-3/2}\right) - 2\frac{d}{d\rho}\left(\rho^{1/2}I_{1/3}\left(\frac{2}{3}\rho^{3/2}\right)\right)\right]\Big|_{\rho = L/r}}.$$

From the Maxwell equation (2), the temperature inhomogeneity parameter can be expressed in the form

$$\alpha = \frac{r}{L} = \left[\frac{4\pi\nu j_0}{aH_e^2}\frac{H_e}{\dot{H}t_\kappa}\right]^{1/3}. \tag{9}$$

It is evident that $\alpha \sim 1$ near the threshold for a flux jump, when $aH_e^2/4\pi\nu j_0 \sim 1$, even under the quasi-stationary heating condition $\dot{H}t_\kappa/H_e \ll 1$; $t_\kappa = \nu L^2/\kappa$ is the characteristic time of the heat conduction problem.

Let us estimate the maximum heating temperature Θ_m in the isothermal case $w_0 = \kappa/L \geq 1$. The solution to Eq. (7) can be represented in the form

$$\Theta(x) = \Theta_m - \rho_0\frac{(x-x_m)^2}{2} \tag{10}$$

near the point at which the temperature is a maximum, $x = x_m$ (Fig. 1).

With solution (10) being approximated near the point $x_m = L/2$ with the help of the thermal boundary

conditions, the coefficient ρ_0 can be easily determined to be $(8/L^2)\Theta_m$ and the temperature can be written as

$$\Theta(x) = \Theta_m\left[1 - \frac{4}{L^2}\left(x - \frac{L}{2}\right)^2\right]. \quad (11)$$

Substituting this solution into Eq. (7), the superconductor maximum heating temperature due to magnetic flux jumps can be estimated as

$$\Theta_m = \frac{\left[j_0 + \frac{\sigma_f \dot{H}}{c}(L - x_m)\right]\frac{\dot{H}}{c\kappa T_0}(L - x_m)}{\frac{\gamma}{L^2} - \frac{a\dot{H}}{c\kappa}(L - x_m)}. \quad (12)$$

For a typical situation when $\gamma/L^2 \ll (a\dot{H}/c\kappa)(L - x_m)$, the estimation for Θ_m is

$$\Theta_m \approx \left[j_0 + \frac{\sigma_f \dot{H}}{c}(L - x_m)\right]\frac{\dot{H}L^2}{c\kappa T_0}(L - x_m). \quad (13)$$

Here, the parameter $\gamma \sim 1$ (for a parabolic temperature profile, $\gamma \sim 8$). It is easy to verify that for typical values of $j_0 = 10^6$ A/cm^2, $\dot{H} = 10^4$ G/s, and $L = 0.1$ cm, the heating is sufficiently low: $\Theta_m \ll 1$. In the case of poor sample cooling, $w_0 = 1$–10 erg/(cm^2 s K), the Θ_m is

$$\Theta_m \approx \frac{\dot{H} j_0 L^2}{c w_0 T_0} \approx 0.5;$$

i.e., the heating temperature can be as high as $\delta T_m = T_0\Theta_m \sim 2$ K. One can see that in the case of poor sample cooling, the heating can be rather noticeable and influence the conditions of the thermomagnetic instability of the critical state in the superconductor.

Let us investigate the stability of the critical state with respect to small thermal (δT) and electromagnetic (δE) fluctuations in the quasi-stationary approximation. We represent solutions to Eqs. (1)–(4) in the form

$$T(x, t) = T(x) + \exp\left(\frac{\lambda t}{t_\kappa}\right)\delta T\left(\frac{x}{L}\right),$$
$$E(x, t) = E(x) + \exp\left(\frac{\lambda t}{t_\kappa}\right)\delta E\left(\frac{x}{L}\right), \quad (14)$$

where $T(x)$ and $E(x)$ are solutions to the unperturbed equations obtained in the quasi-stationary approximation describing the background distributions of temperature and electric field in the sample and λ is a parameter to be determined. The instability region is determined by the condition that $\mathrm{Re}\,\lambda \geq 0$. From solution (14), one can see that the characteristic time of thermal and electromagnetic perturbations t_j is of the order of t_κ/λ. Linearizing Eqs. (1)–(4) for small perturbations $[\delta T/T(x), \delta E/E(x) \ll 1]$, we obtain the following equations in the quasi-stationary approximation:

$$\nu\frac{\lambda}{t_\kappa}\delta T = \frac{\kappa}{L^2}\frac{d^2\delta T}{dx^2} + [j(x) + \sigma_f E(x)]\delta E - aE(x)\delta T,$$
$$\frac{1}{L^2}\frac{d^2\delta E}{dx^2} = \frac{4\pi\lambda}{c^2 t_\kappa}[\sigma_f \delta E - a\delta T]. \quad (15)$$

Eliminating the variable δT between Eqs. (15), we obtain a fourth-order differential equation with variable coefficients for the electromagnetic field δE:

$$\frac{d^4\delta E}{dz^4} - \left[\lambda(1 + \tau) + \frac{E(z)}{E_\kappa}\right]\frac{d^2\delta E}{dz^2} + [\lambda\tau - B(z)]\delta E = 0. \quad (16)$$

Here, we introduced the following dimensionless variables:

$$z = x/L, \quad B(z) = (4\pi a L^2/c^2\nu)j(z),$$
$$j(z) = \sigma_f E(z) - a[T(z) - T_0], \quad E(z) = (\dot{H}L/c)(1 - z),$$
$$\tau = 4\pi\sigma_f\kappa/c^2\nu, \quad E_\kappa = \kappa/aL^2,$$
$$\nu = \nu_0(T/T_0)^3, \quad \kappa = \kappa_0(T/T_0).$$

One should keep in mind that the variables $T(z)$ and $E(z)$ are given by Eq. (8), in which $\rho = (L/r)(1 - z)$. Using the relation between δE and δT given by Eqs. (15), we write the boundary conditions to Eq. (16) in the form

$$\left.\frac{d^2\delta E}{dz^2}\right|_{z=1} = 0, \quad \left.\frac{d^3\delta E}{dz^3}\right|_{z=0} = -W\left.\left[\frac{d^2\delta E}{dz^2} - \lambda\tau\delta E\right]\right|_{z=0},$$
$$\delta E|_{z=1} = 0, \quad \left.\frac{d\delta E}{dz}\right|_{z=0} = 0, \quad (17)$$

where $W = w_0 L/\kappa$ is the dimensionless thermal impedance.

The condition for the existence of a nontrivial solution to Eq. (16) subject to boundary conditions (17) allows one to determine the boundary of the critical-state thermomagnetic instability in a superconducting sample. This problem is complicated, and its analytical solution cannot be found in a closed form. We will consider the development of thermomagnetic instability in the adiabatic approximation, which is valid for hard superconductors with low heat conductivity. The adiabatic character of the instability development leads to the predominance of magnetic flux diffusion over heat diffusion in the sample: $\tau = D_t/D_m \ll 1$ [1], where $D_t = \kappa/\nu$ and $D_m = c^2/4\pi\sigma_f$ are the coefficients of the thermal and magnetic diffusion, respectively. In this case, as seen from Eq. (14), the characteristic times of temperature (t_j) and electromagnetic field perturbations have to satisfy the inequalities $t_j \ll t_\kappa$ ($\lambda \gg 1$) and $t_j \gg t_m$

($\lambda\tau \ll 1$), where $t_\kappa = L^2/D_t$ and $t_m = L^2/D_m$ are the characteristic times of the thermal and magnetic diffusion, respectively.

In this approximation ($\tau \ll 1$, $\lambda\tau \ll 1$, $\lambda \gg 1$), Eq. (16) is reduced to a lower order differential equation:

$$\frac{d^2\delta E}{dz^2} + \left[\left(\lambda - \frac{E(z)}{E_\kappa}\right)\tau - \left(1 - \tau - \frac{E(z)}{\lambda E_\kappa}\right)B(z)\right]\delta E = 0. \quad (18)$$

It is worth noting that while going over to Eq. (18), we kept only terms of the order of $\tau^{1/2}$, because $\lambda\tau \sim \tau^{1/2}$.

In the case of $\tau \ll 1$, the instability threshold depends on the thermal boundary conditions at the surface of the sample only slightly. Therefore, the thermal boundary conditions at the boundaries of the current-carrying layer ($z = 0$, $z = 1$) can be neglected and one can keep only the electrodynamic boundary conditions to Eq. (18),

$$\delta E|_{z=1} = 0, \quad \left.\frac{d\delta E}{dz}\right|_{z=0} = 0,$$

because under the condition of adiabatic instability development in a hard superconductor, the instability threshold depends on the conditions of heat removal on the sample surface only weakly [1].

Multiplying Eq. (18) by δE and integrating the result with respect to z over the interval $0 < z < 1$, we obtain

$$(1-\tau)\int_0^1 B(z)\delta E^2 dz + \tau\int_0^1 E_\kappa^{-1}E(z)\delta E^2 dz + \int_0^1\left(\frac{d\delta E}{dz}\right)^2 dz = \lambda\tau\int_0^1\delta E^2 dz + \frac{1}{\lambda}\int_0^1 E_\kappa^{-1}B(z)E(z)\delta E^2 dz, \quad (19)$$

where we use the equality

$$\int_0^1\frac{d^2\delta E}{dz^2}\delta E dz = \delta E(z)\left(\frac{d\delta E}{dz}\right) - \int_0^1\left(\frac{\delta E}{dz}\right)^2 dz = -\int_0^1\left(\frac{\delta E}{dz}\right)^2 dz$$

and the boundary conditions. The right-hand side of Eq. (19) has a minimum at $\lambda = \lambda_c$:

$$\lambda_c = \tau^{-1/2}\left[\frac{\int_0^1 E_\kappa^{-1}B(z)E(z)\delta E^2 dz}{\int_0^1\delta E^2 dz}\right]^{1/2}.$$

Therefore, Eq. (19) can be written in the form

$$(1-\tau)\int_0^1 B(z)n_E^2 dz + \tau\int_0^1 E_\kappa^{-1}E(z)n_E^2 dz + \frac{\int_0^1\left(\frac{d\delta E}{dz}\right)^2 dz}{\int_0^1\delta E^2 dz} = 2\left[\int_0^1 E_\kappa^{-1}B(z)E(z)n_E^2 dz\right]^{1/2}, \quad (20)$$

where

$$n_E^2 = \frac{\delta E^2}{\int_0^1\delta E^2 dz}, \quad \int_0^1 n_E^2 dz = 1.$$

Since we do not know the function $\delta E(z)$, we try, following [8], to obtain an integral estimation of the instability growth increment and the low boundary of its occurrence. The behavior of the integrand in Eq. (20) is basically determined by the factor $E = (\dot{H}L/c)(1 - z)$, which is equal to zero at $z = 1$ (the other factors change more smoothly). Hence, the integrand reaches its maximum at $z = 0$ and the upper estimate for λ_c is

$$\lambda_c \le \frac{B(0)E(0)}{E_\kappa}\times 1. \quad (21)$$

It is evident that $\lambda_c \gg 1$ and $\lambda_c\tau \ll 1$ at $\tau \ll 1$. Numerical evaluation gives $\lambda_c \approx 10$–10^2 at $\tau = 10^{-3}$. It should be noticed that in determining the critical-state instability boundary from Eq. (20), terms of the order of $\tau^{1/2} \ll 1$ can be omitted because the influence of normal currents is negligible in hard superconductors; i.e., $\sigma_f E(z) \ll j_c(T(z))$.

Equations (20) and (21) enable one to write the instability occurrence criterion in the form

$$\int_0^1 B(z)n_E^2 dz \ge \frac{\int_0^1\left(\frac{d\delta E}{dz}\right)^2 dz}{\int_0^1\delta E^2 dz}. \quad (22)$$

This criterion essentially depends on the boundary conditions and the functions $j(z)$, $E(z)$, $T(z)$, and $n_E^2(z)$. Figure 2 presents graphs of the functions $T(z)$ and

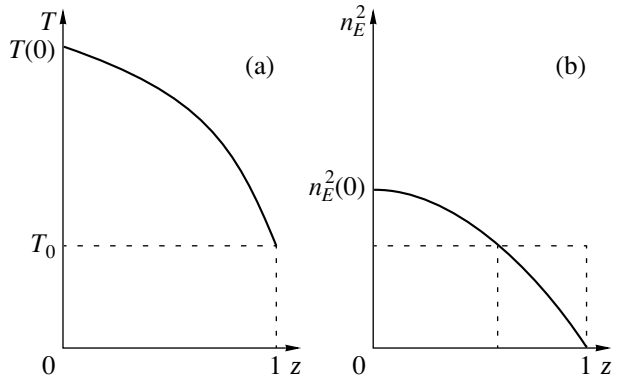

Fig. 2. Plots of the functions (a) $T(z)$ and (b) $n_E^2(z)$.

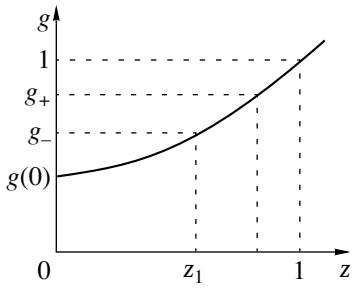

Fig. 3. Plot of the function $g(z)$.

$n_E^2(z)$. Inequality (22) can be strengthened by means of an evaluation,

$$\int_0^1 \left(\frac{d\delta E}{dz}\right)^2 dz \geq \frac{\pi^2}{4}\tau \int_0^1 \delta E^2 dz, \qquad (23)$$

which can be easily verified by expanding the function $\delta E(z)$ in a Fourier series:

$$\delta E(z) = A_m \cos\frac{\pi z(2m+1)}{2}.$$

Let us now try to strengthen inequality (22) further. For this purpose, we consider the integral

$$\int_0^1 g(z)(n_E^2 - 1)dz = \int_0^{z_1} g(z)(n_E^2 - 1)dz + \int_{z_1}^1 g(z)(n_E^2 - 1)dz.$$

The last term can be represented in the form

$$\int_0^1 g(z)(n_E^2 - 1)dz = (g_+ - g_-)\int_0^1 g(z)(n_E^2 - 1)dz,$$

taking intermediate values of the g_- in the range $z < z_1$ and $g > g_-$ in the range $z_1 < z < 1$ outside the integral. It is evident (Fig. 3) that

$$\int_0^1 g(z)(n_E^2 - 1)dz \leq 0$$

or

$$\int_0^1 g(z)n_E^2 dz \leq \int_0^1 g(z)dz. \qquad (24)$$

With inequality (24), the instability occurrence criterion can be represented in the form

$$\int_0^1 B(z)dz \geq \frac{\pi^2}{4}\tau. \qquad (25)$$

Inequality (25), unlike the analogous criterion for a homogeneous temperature profile, has an integral character and takes into account the influence of each part of the superconductor on the threshold for the superconducting-state instability. If condition (25) is satisfied, then small fluctuations of temperature δT and electric field δE in the superconductor will exponentially increase with time. The most probable result of the development of such an instability would be a transition from a critical state to a resistive one.

In conclusion, we note that the description of the critical state applied in this paper is based on the BCS microscopic theory. Then, a continual approximation is used and the physical parameters are assumed to vary slowly at distances of the order of the average distance d between vortices. The continuity condition is, therefore, $L \gg d$.

One more limitation occurs from possible superconductor overheating above the critical temperature T_c, where Eqs. (1)–(4) are not valid. This case is realized if the condition $j_c(T_0, E_e) \geq a(T_c - T_0)$ is fulfilled.

The quasi-stationary approximation is applicable if

$$\nu\frac{dT}{dt}\left(\kappa\frac{d^2T}{dx^2}\right)^{-1} = \frac{\dot{H}t_\kappa}{H_e} \ll \frac{\gamma}{3}.$$

Using this criterion, one can easily evaluate the rates of change of the electric field

$$\frac{dE}{dt} = \left(\frac{\dot{H}t_\kappa}{H_e}\right)^2 \frac{LH_e}{ct_\kappa^2},$$

temperature

$$\frac{dT}{dt} = \left(\frac{\dot{H}t_\kappa}{H_e}\right)^2 \frac{T_0}{t_\kappa},$$

and current density

$$\frac{dj}{dt} = \left(\frac{\dot{H}t_\kappa}{H_e}\right)^2 \frac{j_0}{t_\kappa}.$$

One can see that these quantities are small, because they are of the second order in the quasi-stationary parameter, and can be omitted.

REFERENCES

1. R. G. Mints and A. L. Rakhmanov, *Instabilities in Superconductors* (Nauka, Moscow, 1984).
2. A. M. Campbell and J. E. Evetts, *Critical Currents in Superconductors* (Taylor and Francis, London, 1972; Mir, Moscow, 1975).
3. I. L. Maksimov, Yu. N. Mastakov, and N. A. Taĭlanov, Fiz. Tverd. Tela (Leningrad) **28** (8), 2323 (1986) [Sov. Phys. Solid State **28**, 1300 (1986)].
4. N. A. Taĭlanov and U. T. Yakhshiev, Pis'ma Zh. Tekh. Fiz. **26** (20), 8 (2000) [Tech. Phys. Lett. **26**, 897 (2000)].
5. C. P. Bean, Phys. Rev. Lett. **8** (6), 250 (1962).
6. A. N. Larkin and Yu. N. Ovchinnikov, Zh. Éksp. Teor. Fiz. **80**, 2334 (1981) [Sov. Phys. JETP **53**, 1221 (1981)].
7. D. S. Kuznetsov, *Special Functions* (Nauka, Moscow, 1965).
8. Yu. N. Makov and Yu. A. Stepanyants, Okeanologiya **23** (2), 63 (1983).

Translated by D. Bayuk

Physics of the Solid State, Vol. 44, No. 1, 2002, pp. 162–163. Translated from Fizika Tverdogo Tela, Vol. 44, No. 1, 2002, pp. 155–156.

LOW-DIMENSIONAL SYSTEMS AND SURFACE PHYSICS

The Kane Oscillator

F. M. Gashimzade and A. M. Babaev

Institute of Physics, Academy of Sciences of Azerbaijan, pr. Dzhavida 33, Baku, 370143 Azerbaijan

Received March 26, 2001

Abstract—The energy spectrum and wave functions of the Kane oscillator are determined. The Kane oscillator equation describes the energy spectrum of electrons, light holes, and a spin–orbit split-off band of holes in a quantum dot with a parabolic confining potential. © *2002 MAIK "Nauka/Interperiodica".*

As is known [1], the energy spectrum of quantum dots can be described in the framework of the rigid wall model or the model of parabolic confining potential. It is established that the model of parabolic potential adequately describes small quantum dots. This model, as applied to the standard law of electron dispersion, was used in solving some problems of quantum dot physics, including the quantum crystallization of electrons in an external magnetic field [2].

Semiconductor compounds III–V (InAs, GaAs, InSb, etc.) with quantum dots exhibit a complex energy spectrum that can be described well by a multiband Hamiltonian. Specifically, the nonparabolicity of the energy spectrum can be accounted for in the Kane eight-band model [3]. This approach was applied by Darnhofer and Rössler [3]. However, the equation derived within this approach was very complicated and the analysis of its solution was performed using rather specific approximations.

The aforementioned complexity of the equation arises with the use of the standard procedure of introducing the parabolic confining potential through the scalar potential. However, the parabolic confining potential can be introduced through the so-called minimal substitution [4]:

$$\mathbf{p} = \mathbf{p} - \iota\lambda\beta\mathbf{r}, \tag{1}$$

where β is the diagonal matrix with the elements ± 1. In this case, as was shown earlier in [4–7], we obtain the oscillatory equation for the Dirac Hamiltonian with an extra constant term whose nature is associated with the spin–orbit interaction.

Here, we applied the above approach in deriving the oscillatory equation from the Kane eight-band Hamiltonian, in which the interaction between the valence and conduction bands is taken into account through a single matrix element of the Kane parameter *P*.

We referred to the obtained equation as the Kane oscillator by analogy with the Dirac oscillator. The Kane oscillator equation and its solutions are given below. The system of Kane equations, which also include the dispersionless bands of heavy holes, has the following form [8, 9]:

$$(-E)C_1 - \frac{PK}{\sqrt{2}}C_3 + \sqrt{\frac{2}{3}}PK_zC_4 + \frac{PK}{\sqrt{6}}C_5 + \frac{PK}{\sqrt{3}}C_7 + \frac{PK}{\sqrt{3}}C_8 = 0, \tag{2}$$

$$(-E)C_2 - \frac{PK}{\sqrt{6}}C_4 + \sqrt{\frac{2}{3}}PK_zC_5 + \frac{PK_+}{\sqrt{2}}C_6 + \frac{PK}{\sqrt{3}}C_7 - \frac{PK_z}{\sqrt{3}}C_8 = 0, \tag{3}$$

$$-\frac{PK_+}{\sqrt{2}}C_1 - (E + E_g)C_3 = 0, \tag{4}$$

$$\sqrt{\frac{2}{3}}PK_zC_1 - \frac{PK_+}{\sqrt{6}}C_2 - (E + E_g)C_4 = 0, \tag{5}$$

$$\sqrt{\frac{2}{3}}PK_zC_2 + \frac{PK_+}{\sqrt{6}}C_1 - (E + E_g)C_5 = 0, \tag{6}$$

$$\frac{PK_-}{\sqrt{2}}C_2 - (E + E_g)C_6 = 0, \tag{7}$$

$$\frac{PK_z}{\sqrt{3}}C_1 + \frac{PK_+}{\sqrt{3}}C_2 - (\Delta + E + E_g)C_7 = 0, \tag{8}$$

$$\frac{PK_-}{\sqrt{3}}C_1 - \frac{PK_z}{\sqrt{3}}C_2 - (\Delta + E + E_g)C_8 = 0. \tag{9}$$

Here, P is the Kane parameter, E_g is the band gap, Δ is the spin-orbit splitting, and

$$K_\pm = K_x \pm K_y,$$
$$\mathbf{K} = -\iota\nabla.$$

Let us carry out the substitution $\mathbf{K} \longrightarrow \mathbf{K} - \iota\lambda\beta r$, where $\beta_{ij} = 0$, $i \neq j$, $\beta_{11} = \beta_{33} = \beta_{66} = 1$, and $\beta_{44} = \beta_{55} = \beta_{77} = \beta_{88} = -1$.

1063-7834/02/4401-0162$22.00 © 2002 MAIK "Nauka/Interperiodica"

Substituting expressions (4)–(9) into formulas (2) and (3), we obtain

$$(A - BL_z)C_1 - BM_+C_2 = 0, \quad (10)$$

$$(A - BL_z)C_2 - BM_-C_1 = 0, \quad (11)$$

where $A = -E + \dfrac{P^2\left(E_g + E + \frac{2}{3}\Delta\right)}{(E_g + \Delta + E)(E_g + E)}(-\nabla^2 + \lambda^2 r^2 + 3\lambda)$; $A = -E + \dfrac{P^2\left(E_g + E + \frac{2}{3}\Delta\right)}{(E_g + \Delta + E)(E_g + E)}(-\nabla^2 + \lambda^2 r^2 + 3\lambda)$, and L_z are the components of the angular momentum operator. Since the problem has a spherical symmetry, we seek a solution to the differential equation in the form $F(r)Y_{l,m}(\theta, \varphi)$.

By acting upon the second equation through the operator L_+ and using commutation relationships for the operators ($[L_z, L_+] = L_+$, $[\hat{L}, L^2] = 0$), we obtain L_+C_2. After substituting this quantity into expression (10), we derive two equations for $F(r)$:

$$\left(A + \frac{B}{2} \mp B\left(l + \frac{1}{2}\right)F(r) = 0\right). \quad (12)$$

The eigenvalues and eigenfunctions take the following form:

$$f(E) = \hbar\omega\left[2n + l + \frac{1}{2}\right], \quad (13)$$

$$C_1 = A_{nl}r^l \exp\left(-\frac{\lambda}{2}r^2\right)L_n^{l+1/2}(\lambda r^2)Y_{l,m}(\theta, \varphi). \quad (14)$$

Here, $L_n^{l+1/2}(\lambda r^2)$ are the generalized Laguerre's polynomials and A_{nl} is the multiplier of normalization:

$$A_{nl} = \left[\frac{2\lambda^{l+3/2}}{n!\Gamma(n + l + 3/2)}\right]^{1/2}\frac{1}{\Gamma(l + 3/2)}, \quad (15)$$

$$f(E) = \frac{(E_g + E)(E_g + \Delta + E)}{\left(E_g + E + \frac{2}{3}\Delta\right)}\frac{E_g + \frac{2}{3}\Delta}{E_g(E_g + \Delta)}$$

$$+ \frac{2}{3}\frac{\Delta}{E + E_g + \frac{2}{3}\Delta}\frac{\hbar\omega}{2}\left\{-\frac{1}{2} \pm \left[l + \frac{1}{2}\right]\right\} - \frac{3}{2}\hbar\omega, \quad (16)$$

$$\omega = \frac{\hbar\lambda}{m}, \quad m = \frac{\hbar^2}{P^2}\frac{E_g(E_g + \Delta)}{E_g + \frac{2}{3}\Delta}.$$

Equation (13) determines the energies of electrons, light holes, and the spin–orbit split-off band of holes.

As for the Dirac oscillator, the zero energy for the Kane oscillator in the limit $\dfrac{E}{E_g} \leq 1$ exceeds the zero energy for the oscillator of the standard Schrödinger equation by a factor of two.

Equation (13) can be useful for analyzing the influence of nonparabolicity on the energy spectrum of electrons in a quantum dot. Earlier [10, 11], this problem was considered in the framework of the rigid wall model. The advantage of this approach lies in the simplicity of treating analytical expressions as compared to numerical calculations [10, 11].

ACKNOWLEDGMENTS

We are grateful to É. Dzhafarov, who called our attention to studies on the Dirac oscillator.

REFERENCES

1. N. E. Kaputkina and Yu. E. Lozovik, Fiz. Tverd. Tela (St. Petersburg) **40** (11), 1753 (1998) [Phys. Solid State **40**, 1594 (1998)].
2. N. E. Kaputkina and Yu. E. Lozovik, Fiz. Tverd. Tela (St. Petersburg) **40** (9), 2134 (1998) [Phys. Solid State **40**, 1935 (1998)].
3. T. Darnhofer and U. Rössler, Phys. Rev. B **47** (23), 16020 (1993).
4. J. P. Crawford, J. Math. Phys. **34** (10), 4428 (1993).
5. J. Benítez, R. P. Martínez y Romero, and H. N. A. L. Salas-Brito, Phys. Rev. Lett. **64** (14), 1643 (1990).
6. M. Moshinsky and A. Szezepanik, J. Phys. A **22**, L817 (1989).
7. P. A. Cook, Lett. Nuovo Cimento **1**, 419 (1971).
8. B. M. Askerov, *Kinetic Effects in Semiconductors* (Nauka, Leningrad, 1970).
9. A. I. Anselm, *Introduction to Semiconductor Theory* (Nauka, Moscow, 1978; Prentice-Hall, Englewood Cliffs, 1981).
10. Al. L. Efros and M. Rosen, Phys. Rev. B **58**, 7120 (1998).
11. F. M. Gashimzade, A. M. Babaev, and M. A. Bagirov, J. Phys.: Condens. Matter **12**, 7923 (2000).

Translated by N. Korovin

Physics of the Solid State, Vol. 44, No. 1, 2002, pp. 164–170. Translated from Fizika Tverdogo Tela, Vol. 44, No. 1, 2002, pp. 157–164.

LOW-DIMENSIONAL SYSTEMS AND SURFACE PHYSICS

Quantum-Well States and Resonances in Thin Single-Crystal Layers of Noble Metals on W(110) Substrates

D. V. Vyalykh[1, 2], A. M. Shikin[1], G. V. Prudnikova[1], A. Yu. Grigor'ev[1, 2], A. G. Starodubov[1], and V. K. Adamchuk[1]

[1] *Institute of Physics (Petrodvorets Branch), St. Petersburg State University, ul. Pervogo maya 100, Petrodvorets, 198904 Russia*

e-mail: vyalikh@paloma.spbu.ru

e-mail: prudnikg@paloma.spbu.ru

[2] *Free University of Berlin, Arnimalle 14, 14195 Berlin-Dahlem, Federal Republic of Germany*

Received March 15, 2001; in final form, May 7, 2001

Abstract—This paper reports on the first experimental observation of quantum-well states and *sp*-type resonances in thin single-crystal gold, silver, and copper layers formed on single-crystal W(110) surfaces, which result from spatial localization of Bloch-type electronic wave functions in a quantum well with potential barriers at the vacuum/metal and metal/W(110) interfaces. The quantization of the valence-band electronic structure in Au/W(110), Ag/W(110), and Cu/W(110) systems was studied experimentally using angle-resolved photoelectron spectroscopy. *© 2002 MAIK "Nauka/Interperiodica".*

1. INTRODUCTION

Research in modern solid-state physics focuses considerable attention on the experimental study and theoretical analysis of the electronic structure in low-dimensional systems. This interest is accounted for, on the one hand, by the lack of information on such structures compared, e.g., to bulk crystals and, on the other, by the broad application potential of low-dimensional systems in micro- and nanoelectronics. In thin layers, the motion of electrons perpendicular to the surface of a solid is substantially constrained, with the scale of this limitation being comparable to the coherence length of the electron wave function. As a result of the electron motion being constrained in this direction, the energy spectrum becomes modified and the continuum typical of a bulk crystal is replaced by a set of quantum-well states (QWSs). A QWS standing wave is produced through the interference of Bloch electronic waves, which are multiply reflected from the walls of the potential well formed by the vacuum/metal and metal/substrate interfaces. Note that the actual energy position of the QWS depends on the potential well width, i.e., on the thickness of the quasi-two-dimensional structure [1]. Therefore, dispersion in the spectral features of the thin-film system under study with variation of its thickness serves as evidence of the existence of the QWS. The quantization of the electronic energy bands of a bulk single crystal occurring as one crosses over to thin single-crystal films offers a unique possibility of using angle-resolved photoelectron spectroscopy (ARPES) to experimentally study the quantum electronic states created in thin metal layers [1, 2]. The most essential goal of these experimental studies was to obtain thin single-crystal films of noble metals with a perfect crystal structure, because any defects at the vacuum/metal and metal/W(110) interfaces, as well as film inhomogeneities, produce electron scattering and, as a consequence, weaken the effect to be observed. In our experiments, thin single-crystal films were prepared through thermal deposition of noble metals on an atomically clean W(110) surface. The crystal structure of the layers thus produced was analyzed using low-energy electron diffraction (LEED).

Earlier experiments showed [3–7] that the surface of the closely packed (111) face of a thin fcc metal layer formed on the (110) surface of a bcc metal can have two

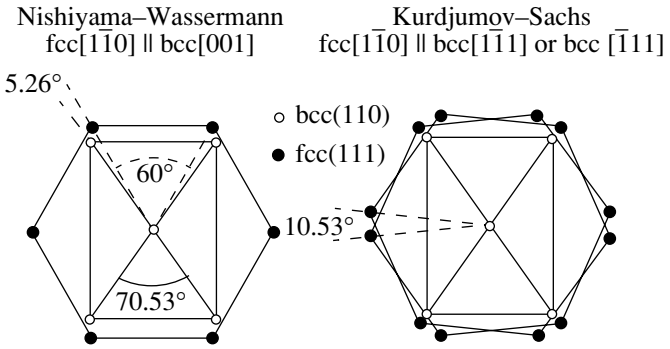

Fig. 1. Two possible (Nishiyama–Wassermann and Kurdjumov–Sachs [7]) orientations of the (111) surface of an fcc metal on the (110) surface of a bcc metal.

1063-7834/02/4401-0164$22.00 © 2002 MAIK "Nauka/Interperiodica"

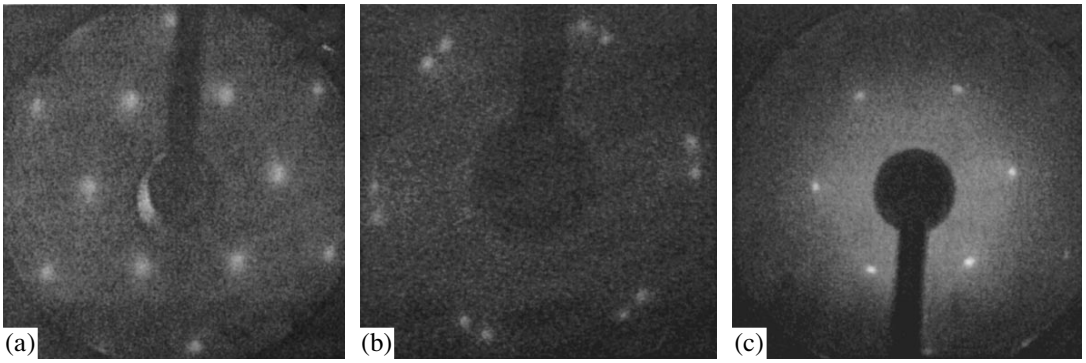

Fig. 2. LEEDS patterns obtained for (a) Au/W(110), E_p = 141 eV; (b) Ag/W(110), E_p = 121 eV; and (c) Cu/W(110), E_p = 173 eV.

types of orientation, Nishiyama–Wassermann (NW) or Kurdjumov–Sachs (KS) [5–7] (Fig. 1), depending on certain conditions (the relative magnitudes of the substrate and adsorbate interatomic distances, film thickness, temperature, etc. [3, 4]). The LEED patterns obtained for the Au/W(110), Ag/W(110), and Cu/W(110) systems (Fig. 2) confirm the formation of thin single-crystal films of Au, Ag, and Cu on the single-crystal W(110) surface. The LEED patterns permit one to conclude that thin Au and Cu layers form through the NW mechanism and Ag layers form through the KS mechanism, which is in agreement with [8].

Our photoemission studies showed that quantum states and resonances of the *sp* type indeed form in Au/W(110), Ag/W(110), and Cu/W(110) structures. It was demonstrated that the photoelectron (PE) spectra observed in the Ag/W(110) system can be employed to monitor the thickness of the deposited layers. The dispersion relation $E(\mathbf{k}_\perp)$ was obtained experimentally for the Cu/W(110) system in the [111] direction.

2. EXPERIMENTAL TECHNIQUE

The studies were carried out at the BESSY-I and BESSY-II synchrotron centers (Berlin, Germany), with output channels TGM3 and U125, respectively, using a WSW ARIES-type angle-resolved electron spectrometer equipped with a diffractometer to measure LEED patterns. Laboratory studies were performed on an SES 200 SCIENTA electron spectrometer with a gas-discharge helium lamp providing $h\nu$ = 21.2 and 40.8 eV photons for ARPES experiments. The total energy resolution reached in the ARPES experiments was ≈150 and ≈50 meV for the ARIES and SCIENTA electron spectrometers, respectively.

The atomically clean W(110) single-crystal surface was obtained through a series of short heatings of the crystal to 2300°C, with subsequent annealing at 1300°C in an oxygen environment in a vacuum of no worse than 5×10^{-8} Torr. The heating in oxygen resulted in a chemical reaction of the oxygen with the carbon evolved onto the W(110) surface from the bulk of the crystal, and the CO_2 thus formed escaped from the surface and was pumped out. This procedure produced an atomically clean W(110) surface, whose quality was monitored using ARPES and LEED. Figure 3 presents a PE spectrum and a LEED pattern characteristic of a perfectly clean W(110) single-crystal surface, which demonstrate the absence of any foreign inclusions on the surface.

Thin single-crystal layers of Au, Ag, and Cu on W(110) substrates were prepared through thermal evaporation of a small piece of the corresponding metal (a sphere ~2–3 mm in diameter, metal purity 99.999%) spot welded to a 0.25-mm diameter wire of W75-Re25 alloy. The wire with the metal was heated to the metal evaporation temperature by passing a dc current through it (~2.7 A for Ag, and ~3.8 A for Au and Cu). The Au, Ag, and Cu single-crystal layers were found to have the best quality when the deposition on a W(110) substrate was made at room temperature at a rate of no more than 2 Å per minute. The thickness of the deposited Au, Ag, and Cu layers was determined from the change in the frequency of a quartz resonator maintained inside the vacuum chamber under the same conditions as the sample. On reaching the base vacuum in the chamber, each source was outgassed to achieve cleanness of the source components, for which the pressure during the evaporator operation increased only to 2×10^{-10} Torr. The base pressure in the chamber in each experiment was kept below 1×10^{-10} Torr.

3. EXPERIMENTAL RESULTS AND DISCUSSION

3.1. Quantum Resonance States in the Au(111)/W(110) System

Figure 4 presents the photoemission spectrum obtained at a photon energy $h\nu$ = 50 eV under normal electron emission from the Au/W(110) system with a gold layer 22 Å thick. This spectrum exhibits several features (denoted by the symbols *2–6*, D_1–D_3, and *S*) that were observed earlier [9, 10]. The feature at 0.4 eV below the Fermi level, which is denoted by S_1, is a Shockley-type surface state located in the relative

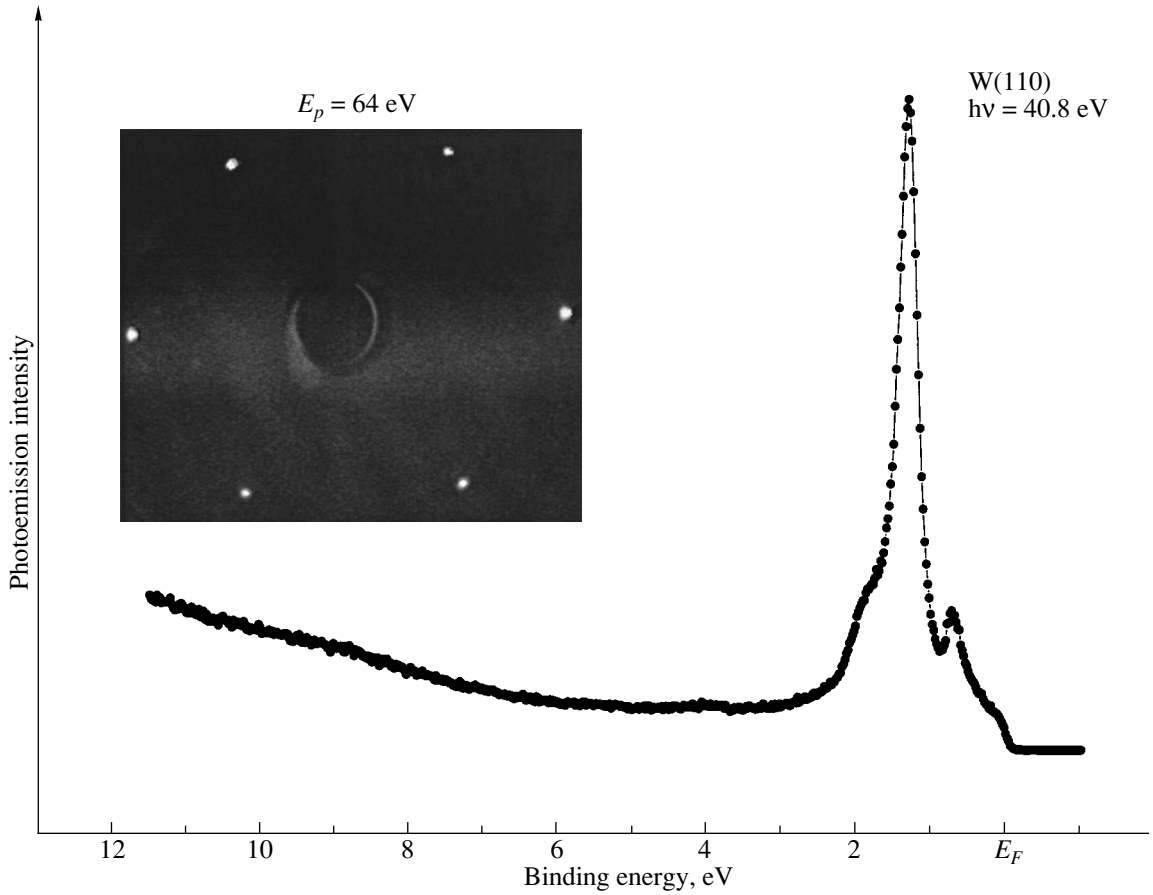

Fig. 3. Photoelectron valence-band spectrum of W(110) measured under normal photoelectron emission and incident photon energy $h\nu$ = 40.8 eV. Inset: LEED pattern for the W(110) single-crystal surface.

energy gap at the L point [10, 11]: $E_F < E_{SS} < 1.1$ eV. The S_2 feature is also assigned to a Shockley-type surface state. This feature was observed earlier in [11] and is in agreement with the surface-state calculations performed for Au(111) in [12]. The symmetric shape of the surface-state peaks and their high intensity argues for the high quality of the Au film. The *2–6* features result from direct transitions between the volume electronic states along the ΓL direction. The D_1–D_3 features were shown [9] to be surface resonances, because their energy does not change with varying the photon energy and they exhibit resonance properties at photon energies from 18.6 to 26.5 eV [9]. The *S* feature in the PE spectrum is accounted for by the variation in the potential at the surface [9]. In addition, the PE spectrum also has two new features lying at ≈1.3 and ≈2.0 eV below the Fermi level (denoted by QWR_1 and QWR_2, respectively) that were not observed earlier in the PE spectra obtained when studying bulk single-crystal Au(111) [10]. To establish the nature of these electronic states, we measured PE spectra for different gold layer thicknesses and photon energies. Figure 5 presents PE spectra for the Au/W(110) system obtained at a photon energy $h\nu$ = 60 eV. The gold layer thickness was varied from 8 to 30 Å. Note that at gold layer thicknesses in excess of 8 Å, a QWR_1 feature appears in the spectrum that shifts toward lower binding energies (toward the Fermi level) with increasing layer thickness. At a gold layer thickness of 18 Å, a QWR_2 feature is seen to appear in the PE spectrum that also changes its energy with increasing film thickness. Note that the QWR_1 and QWR_2 features for the gold layer thickness of 22 Å lie at binding energies of ~1.3 and ~2.0 eV, respectively, which coincide with the positions of similar features in the PE spectrum for the same system measured at a photon energy $h\nu$ = 50 eV. It should be pointed out that, as the gold layer thickness increases, the QWR_1 and QWR_2 features are observed in the PE spectra at energies down to an energy of ~1.1 eV below the Fermi level (the Au valence-band top in the [111] direction), but their intensities decrease noticeably as one approaches this energy. At binding energies of less than ~1.1 eV, these features are not seen.

The QWR_1 and QWR_2 features observed in the PE spectra cannot be due to surface resonance states, because although their positions are seen to be independent of the photon energy, they change with varying

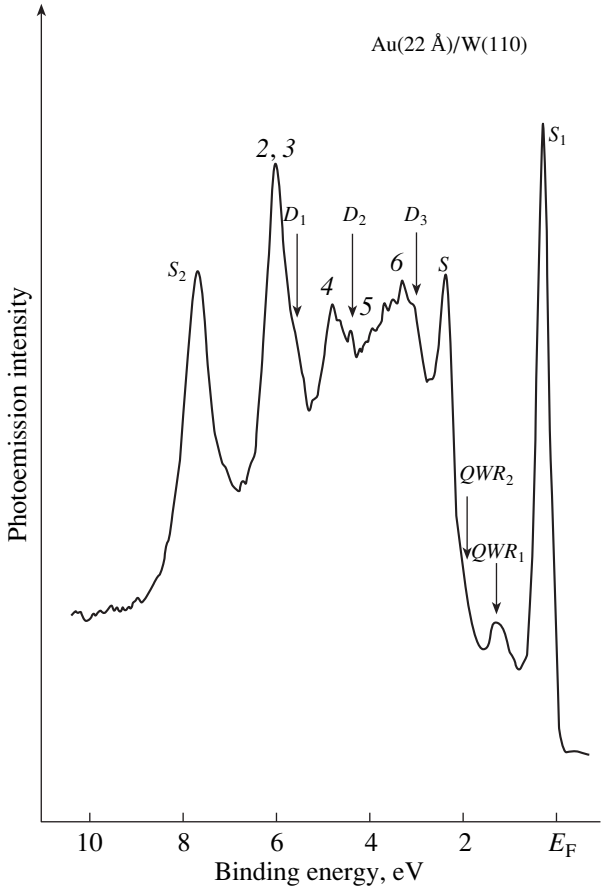

Fig. 4. Photoelectron valence-band spectrum of the Au/W(110) system measured under normal photoelectron emission and incident photon energy $h\nu = 50$ eV. Gold layer thickness 22 Å.

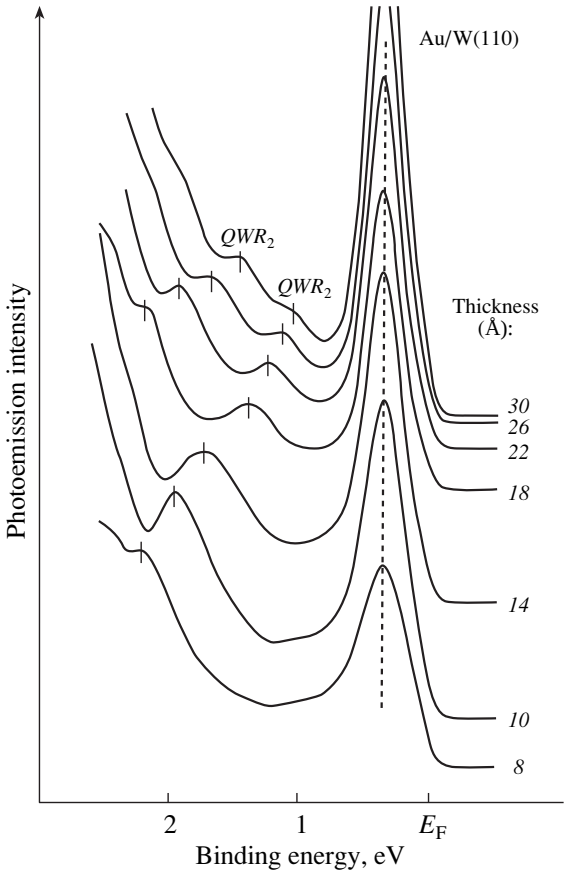

Fig. 5. Photoelectron valence-band spectra of the Au/W(110) system measured for different gold layer thicknesses. The spectra were obtained under normal photoelectron emission and incident photon energy $h\nu = 60$ eV. Dashed line specifies the position of the surface state.

gold layer thickness. For the same reason, QWR_1 and QWR_2 cannot result from hybridization of the Au and W electronic states. We believe that these specific features in the PE spectrum [compared to the PE spectrum of a bulk Au(111) single crystal] can be only a signature of *sp*-type quantum electronic states due to *sp* electrons being spatially confined to a thin single-crystal layer of gold by potential barriers at the Au/vacuum and Au/W interfaces. Tungsten has a relative gap extending from 3.5 to 6.2 eV below the Fermi level in the Γ*N* direction perpendicular to the surface [13, 14]. Because the energy bands Λ_6^1 and Σ_5^2 of gold and tungsten, respectively, have different crystal symmetries [15], the wave functions of the electronic *sp* states in gold will experience practically total reflection from the Au/W interface at energies from 2.0 to 6.2 eV. However, the wave functions of the Au *sp* electrons at binding energies of less than 2.0 eV can penetrate through the effective Au/W potential barrier to interact with the Σ_5^1 electronic states of tungsten [16, 17]. This means that the Au *sp* electron wave functions in this energy region are not totally localized in a thin single-crystal Au layer. Thus, the semiconfined electronic states observed in the PE spectra are *sp*-type quantum resonance states of Au. In the description of quantum resonance states [1], one observes a certain analogy to surface resonance states [9, 18].

Thus, the above analysis gives one grounds to conclude that thin epitaxial Au layers produced on single-crystal W(110) exhibit, in addition to known features, *sp*-type quantum resonance states. Note that the electronic structures of ultrathin gold layers on W(110) substrates were already studied in [17] and *d*-type quantum states were observed at energies from 2 to 4 eV, i.e., in the region of the W energy gap for electronic states in the Γ*N* direction of the Brillouin zone that exhibit Σ_5^1 crystal symmetry.

Note that when the Au/W(110) system is excited by photons of energy $h\nu = 21.2$ eV, the QWR_1 and QWR_2 quantum resonance states are not observed in the PE spectrum, because the electron photoionization cross section is considerably smaller in this case than that for

$h\nu$ = 60 eV. For this reason, quantum resonance states of the *sp* type were not observed in the studies in [17].

3.2. Quantum-Well States and Resonances in the Ag/W(110) System

Figure 6 displays a series of PE spectra measured at a photon energy $h\nu$ = 50 eV in a system prepared by depositing thin silver layers of various thicknesses onto a W(110) single crystal. For a layer thickness of 2 Å, the PE spectrum exhibits a feature in the region of the *sp* electron binding energy of ≈3.2 eV that can be associated with electron emission from a quantum state characteristic of a monolayer Ag film. As the silver thickness is increased gradually, a new feature appears in the PE spectrum at a binding energy of ≈2.4 eV, which signals the formation of a second monolayer. After the silver coating thickness reaches 7 Å, a feature with a binding energy of ≈2.0 eV is seen to appear in the spectrum, thus indicating the formation of the third monolayer.

Note that at silver film thicknesses above three monolayers, the film growth was shown to be accompanied by island formation on the surface [8]. This observation is supported by the considerable decrease in intensity of the spectral features originating from quantum states in thicker Ag layers. As a result of the presence of Ag surface imperfections in such films, electrons scatter from surface defects in reflection from the Ag/vacuum interface, thus giving rise to a blurred structure of the PE spectra associated with size quantization.

As in the Au/W(110) system, at binding energies of less than 2 eV, electron wave functions of silver can penetrate through the effective barrier into the substrate. Therefore, the quantum states of silver in this energy region should be considered to be *sp*-type resonance quantum states. Figure 7 plots the typical dependence of the energy positions of the quantum states and resonances on the silver layer thickness.

As seen from Fig. 6, the thickness of a silver layer can be derived from the position of the quantum electronic states in the PE spectra. This experimental observation offers the possibility of using QWSs to determine

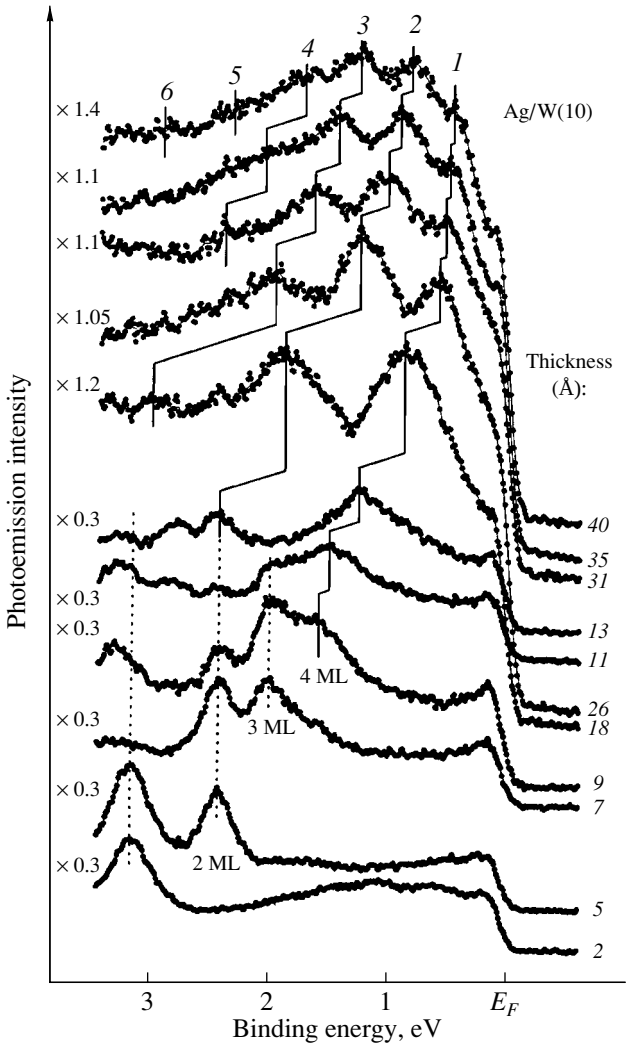

Fig. 6. Photoelectron valence-band spectra of the Ag/W(110) system measured for different silver layer thicknesses. The spectra were obtained under normal photoelectron emission and incident photon energy, $h\nu$ = 50 eV.

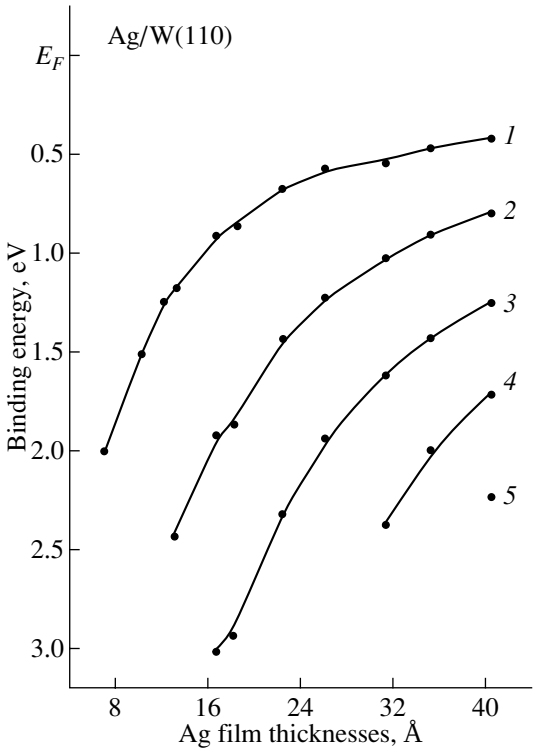

Fig. 7. Energy position of the peaks of quantum states vs. silver film thickness for the Ag/W(110) system derived from the photoelectron spectra in Fig. 6.

the thickness of very thin metal layers in addition to evaporator calibration.

3.3. Quantum Resonance States in the Cu/W(110) System

Interest in this system has been stimulated, on the one hand, by studies of the quantum effects in such systems as, for instance, Cu/Ni(100) [19] and Cu/Co(100) [20], and, on the other, by observations arguing for the existence of *sp*-type quantum resonance states in thin copper layers on W(110), namely, by the possibility of growing thin epitaxial single-crystal copper layers on W(110) substrates [21], by the similarity of the electronic band structures in Au, Ag, and Cu in the [111] direction [15], and by the existence of an effective potential barrier at the Cu/W interface.

Figure 8a displays a series of PE spectra of epitaxial copper films of various thicknesses on W(110) substrates measured at a photon energy $h\nu$ = 21.2 eV. At this photon energy, one observes the maximum intensity of the Shockley-type surface state on Cu(110), which provides a possibility of monitoring the surface quality of thin single-crystal copper layers. The feature corresponding to a surface state in the PE spectra shown is observed at a binding energy of ≈0.3 eV below the Fermi level and lies in the energy gap ($E_F < E_{SS} <$ 0.75 eV) at the *L* point. In addition to the surface state, the PE spectrum exhibits a number of features (denoted by *1–4*) not seen in the PE spectra of bulk Cu(110) sin-

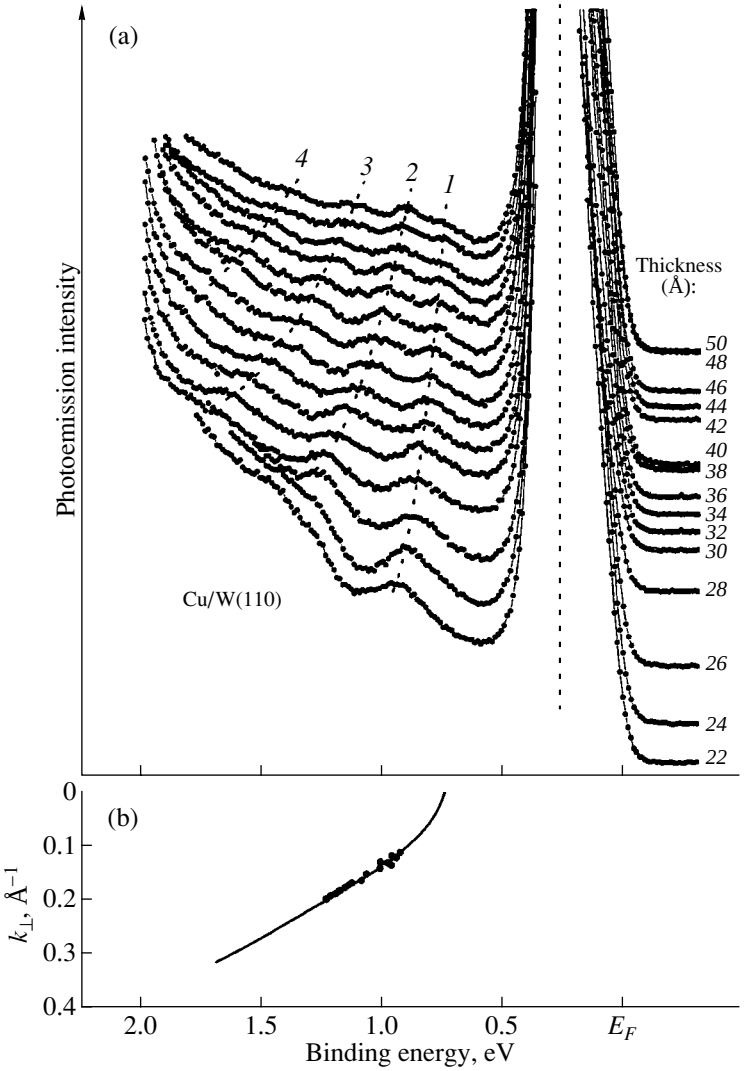

Fig. 8. (a) Valence-band photoelectron spectra of the Cu/W(110) system measured for various copper layer thicknesses; the spectra were obtained under normal photoelectron emission and incident photon energy, $h\nu$ = 21.2 eV; the Cu layer thickness is varied from 22 to 50 Å; the dashed line identifies the position of the surface state. (b) Dispersion relation $E(\mathbf{k}_\perp)$ along the [111] direction perpendicular to the Cu(111) surface; points are experimental data extracted from the PE spectra; the solid curve represents a fitting function calculated from the two-band model [25].

gle crystals [22]. Increasing the copper thickness shifts these features toward the Fermi level. These features can be accounted for in terms of the quantization of the Cu *sp* band in the Γ*L* direction through the formation of quantum electronic states. In the Cu/W(110) system, the wave functions of copper electrons with energies in the range $0.75 < E < 2$ eV are capable of penetrating through the effective Cu/W barrier into the substrate to form semiconfined resonance quantum states.

The quasi-wave vector $\mathbf{k}_\perp$ in the direction perpendicular to the surface for a quantum state with a given energy can be calculated from the condition of quantization of $\mathbf{k}_\perp$, which is based on the finite thickness of a thin layer [1, 23, 24]. Thus, experimental PE spectra can be used to calculate the dispersion relation $E(\mathbf{k}_\perp)$ along the [111] direction. The $E(\mathbf{k}_\perp)$ dispersion for the Cu(111)/W(110) system is presented in Fig. 8b as a set of experimental dots and a curve representing the fitting function $E(\mathbf{k}_\perp)$ calculated in [23] in terms of the two-band model [1, 25]. The best fit to the experimental data was obtained with the following parameters: a copper valence-band top in the given direction of 0.75 eV and an effective mass $m^* = 0.66m_e$, where m_e is the free-electron mass.

4. CONCLUSIONS

Thus, the results of our study of thin single-crystal Au, Ag, and Cu layers formed at room temperature on atomically clean W(110) single-crystal surfaces permit one to conclude that localization of the *sp* electron wave functions gives rise to the formation of quantum-well states and resonances, which reveal characteristic variations of the energy position with metal layer thickness. The quantum states observed in the PE spectra of thin uniform Ag layers on W(110) are a signature of the layer-by-layer film growth, which can be used to measure the thickness of a deposited coating. It should be pointed out that quantum-well states and resonances were observed in the Au/W(110), Ag/W(110), and Cu/W(110) systems for the first time.

ACKNOWLEDGMENTS

The authors express their gratitude to the administration and personnel of the BESSY-I and BESSY-II Synchrotron Radiation Centers for the opportunity to carry out photoemission studies with the use of synchrotron radiation. The authors warmly thank Prof. G. Kaindl and E. Weschke of the *Free* University of Berlin, as well as O. Rader of BESSY-II, for the possibility of using their equipment in the photoemission experiments and for useful discussions.

This study was supported by the State Program "Topical Problems in Condensed-Matter Physics" (Subprogram "Surface Atomic Structures," project no. 2.1-99), the Russian Foundation for Basic Research (project no. 01-02-17287), and also by the DFG (grant Sfb-290/TPA06) and BMBF (grant 05 SF8 KEC8) (Germany).

REFERENCES

1. T. C. Chiang, Surf. Sci. Rep. **39**, 181 (2000).
2. F. J. Himpsel, J. E. Ortega, G. J. Mankey, and R. F. Willis, Adv. Phys. **47** (4), 511 (1998).
3. Y. Goth, M. Uwaha, and I. Arai, Appl. Surf. Sci. **33/34**, 443 (1988).
4. E. Bauer and J. van der Werwe, Phys. Rev. B **33**, 3657 (1986).
5. Z. Nishiyma, Sci. Rep. Tohoku Univ. **23**, 658 (1934).
6. G. Kurdjumov and G. Shachs, Z. Phys. **64**, 325 (1930).
7. O. Hellwig, K. Theis-Brohl, G. Wihelmi, and H. Zabel, Surf. Sci. **410**, 362 (1998).
8. E. Bauer, H. Poppa, G. Todd, and P. R. Davis, J. Appl. Phys. **48**, 3773 (1977).
9. H. G. Zimmer and A. Goldmann, Surf. Sci. **176**, 115 (1986).
10. S. D. Kevan and R. Gaylord, Phys. Rev. B **36**, 5809 (1987).
11. R. Courths, H. Wern, U. Hau, *et al.*, J. Phys. F **14**, 1559 (1984).
12. S. H. Liu, C. Hinnen, C. C. Nguyen van Huong, *et al.*, J. Electronanal. Chem. **176**, 325 (1984).
13. D. Li, P. A. Dowben, J. E. Ortega, and F. J. Himpsel, Phys. Rev. B **47**, 12895 (1993).
14. J. Feydt, A. Elbe, H. Engelhard, *et al.*, Phys. Rev. B **58**, 14007 (1998).
15. H. Eckardt, L. Fritsche, and J. Noffke, J. Phys. F **14**, 97 (1984).
16. R. H. Gaylord and S. D. Kevan, Phys. Rev. B **36**, 9337 (1987).
17. H. Knoppe and E. Bauer, Phys. Rev. B **48**, 5621 (1993).
18. R. Courths, H.-G. Zimmer, A. Goldmann, and H. Saalfeld, Phys. Rev. B **34**, 33585 (1986).
19. H. Iwasaki, B. T. Jonker, and R. L. Park, Phys. Rev. B **32**, 643 (1985).
20. J. E. Ortega, F. J. Himpsel, G. J. Mankey, and R. F. Willis, Phys. Rev. B **47**, 1540 (1993).
21. K. Reshoft, C. Jensen, and U. Kohler, Surf. Sci. **421**, 320 (1999).
22. S. D. Kevan and R. G. Gaylord, Phys. Rev. Lett. **57**, 2975 (1986).
23. M. A. Mueller, T. Miller, and T.-G. Chiang, Phys. Rev. B **41**, 5214 (1990).
24. A. M. Shikin, D. V. Vyalikh, Yu. S. Dedkov, *et al.*, Phys. Rev. B **62**, R2303 (2000).
25. N. V. Smith, Phys. Rev. B **32**, 3549 (1985).

Translated by G. Skrebtsov

Physics of the Solid State, Vol. 44, No. 1, 2002, pp. 171–175. Translated from Fizika Tverdogo Tela, Vol. 44, No. 1, 2002, pp. 165–169.

LOW-DIMENSIONAL SYSTEMS AND SURFACE PHYSICS

Modification of the Al_2O_3 Surface by High-Energy Bismuth Ions

V. A. Skuratov, A. E. Efimov, and D. L. Zagorskiĭ

Joint Institute for Nuclear Research, Dubna, Moscow oblast, 141980 Russia

e-mail: skuratov@cv.jinr.ru

Received April 12, 2001

Abstract—This paper reports on an atomic-force microscopy study of the surface of α-Al_2O_3 single crystals irradiated by Bi ions with energies of 710, 557, 269, and 151 MeV. The shape of the radiation defects produced by single ions was established to depend on the ionization energy loss. The threshold ionization density above which the surface topography is observed to change lies in the 27–35 keV/nm interval. Possible mechanisms of defect formation in the thermal-spike model, namely, a phase transition and the creation of thermoelastic stresses in the high-energy ion track, are considered. © *2002 MAIK "Nauka/Interperiodica".*

1. INTRODUCTION

Irradiation by high-energy heavy ions may produce specific radiation damage on the surface of a solid. This damage is associated with the effect of single ions and observed to appear starting from a certain threshold level of the ionization energy losses $(dE/dx)_{ion}$. Depending on the actual conditions of irradiation and the type of material, the damage can take the form of craters or hillocks ranging in characteristic size from a few nanometers to a few tens of nanometers. Investigation of the mechanisms of formation of such defects and of their relation to structural distortions in the bulk appears to be of interest for predicting the behavior of materials whose radiation strength is determined by defects produced by fission fragments, i.e., atoms varying in atomic weight from 80 to 155 and having an energy of about 100 MeV, under conditions of high and superhigh (above 10 keV/nm) ionization losses and a high rate of defect formation. Of particular interest is the investigation of the surface topography and microstructure of a number of ceramics and oxides (which are candidate materials for use as inert nuclear-fuel matrices, such as MgO, Al_2O_3, $MgAl_2O_4$, SiC, TiC, AlN, and Si_3N_4) irradiated by heavy ions with energies above 1 MeV/nucleon to simulate the effect of actinide fission products.

Being one of the most radiation-stable dielectrics, Al_2O_3 is the most promising and widely used material in various nuclear power installations. This is due, to a large measure, to the fact that ionization, as an independent source of structural distortions in aluminum oxide, manifests itself only at ultrahigh energy losses observed under irradiation by high-energy heavy ions [1, 2]. The threshold value $(dE/dx)_{ion}$ = 21 keV/nm, starting from which the formation of both point and extended radiation defects can be assigned to inelastic energy losses, was estimated [2] by analyzing experimental Rutherford backscattering data for sapphire single crystals irradiated by uranium ions with energies ranging from 115 to 809 MeV. The research reported in [1, 2] was continued in the discovery of latent tracks in sapphire after its bombardment by 20-MeV fullerenes [3, 4]. Direct electron microscopic structural studies made determination of the track diameter possible; this diameter was found to be 13 nm for a given ionization energy loss level of 76.2 keV/nm. An atomic-force microscopy (AFM) study [4] of the surface topography of sapphire irradiated by 30-MeV fullerenes was also made, which showed that each latent track on the sample surface could be identified with a hillock about 20 nm in diameter and 4.5 ± 0.5 nm in height. The observed correlation between structural changes in the bulk and on the surface of irradiated crystals is of great interest, because it considerably broadens experimental possibilities through the use of such a powerful tool as AFM. Although AFM techniques are employed to advantage in similar experiments on other materials, the above study [4] is, in our opinion, the only example of an investigation into Al_2O_3 surface modification by high-energy heavy ions that stimulates systematic research over a broad range of ion energies and masses. Our previous paper [5] contains the first data on radiation defects on the surface of differently oriented α-Al_2O_3 crystals irradiated by 160–710 MeV bismuth ions. The present work represents a continuation of the AFM study of structural surface modifications of sapphire single crystals bombarded by high-energy bismuth ions.

2. EXPERIMENTAL TECHNIQUE

Irradiation by high-energy bismuth ions was carried out in the applied-research channel of a U-400 cyclotron of LNR, JINR [6]. Al_2O_3 single crystals, represent-

Conditions of sapphire single crystal irradiation

Absorber thickness, μm	Bismuth ion energy, MeV	$(dE/dx)_{ion}$, keV/nm	$(dE/dx)_{el}$, keV/nm
0	710	41	0.08
6	557	40	0.12
18	269	35	0.19
24	151	27	0.35
36			

ing 20 × 10 × 0.5-mm platelets oriented with (**c**){0001}, (**m**){$10\bar{1}0$}, and (**a**){$11\bar{2}0$}, were attached with heat- and electrically conducting carbon paste to a water-cooled target holder. To preclude the irradiated targets from overheating, the ion flux density was set to 2×10^8 cm^{-2} s^{-1}. Under these irradiation conditions, the heat power dissipated by the ion beam did not exceed a few tenths of a watt. The irradiation parameters, such as the ion energy, specific ionization energy losses, and energy losses to elastic scattering in the target surface layer (calculated using the SRIM-2000 code) are listed in the table. The ion energy was varied by means of aluminum absorbers screening different parts of the same sample, thus providing adequate comparison with experimental data. The samples were irradiated to a fluence of 10^{10} ion/cm^2. Uniform beam distribution over the surface of the irradiated targets was achieved by scanning the beam vertically and horizontally.

The AFM study of the irradiated samples was performed with a SOLVER P47-SPM-MDT microscope (Lukin SRIPP, Zelenograd, Moscow, Russia). The surface topography was studied in the resonant tapping mode at a cantilever frequency of 350 ± 50 kHz, with the idle and operating cantilever frequency, as well as the feedback gain, maintained constant when probing the parts of samples of a given orientation bombarded by ions of different energies. The data obtained are real three-dimensional images of the surface topography investigated.

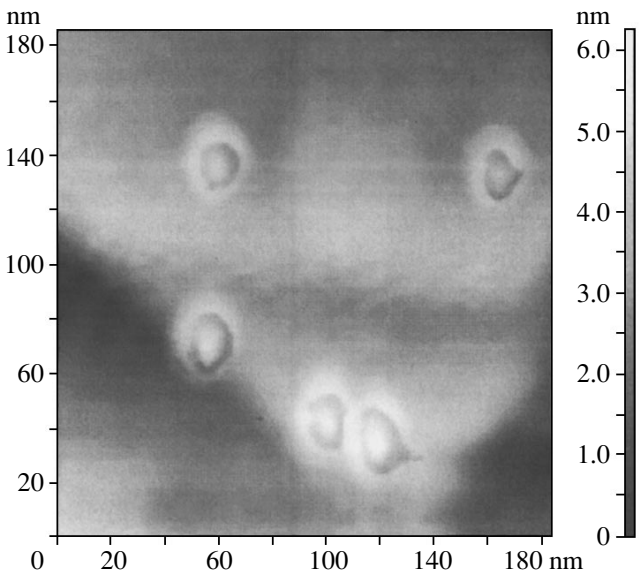

Fig. 1. AFM image of the sapphire surface irradiated by 710-MeV Bi ions. Image size, 180 × 180 nm.

3. RESULTS AND DISCUSSION

As demonstrated in the AFM studies, irradiation by bismuth ions with energies of 710, 557, and 269 MeV produces single defects on the surface of sapphire single crystals, whereas at ion energies of 151 MeV and less, no changes were observed on the surface. The density of the observed defects is in agreement with the ion fluence of 10^{10} ion/cm^2 to within experimental accuracy, ±10%. It was established that the shape of the defects depends qualitatively on the ion ionization energy losses near the surface and, to a lesser extent, on the crystallographic sample orientation, although it should be noted that the most pronounced surface changes were observed on **m**-oriented samples.

The defects observed on the surface of the **m**-oriented sample irradiated by 710-MeV bismuth ions [$(dE/dx)_{ion}$ = 41 keV/nm] represent hillocks with a diameter of about 15 nm at the base and an average height of 2 nm surrounded by an outer ridge about 1 nm high and about 27 nm in diameter (Figs. 1, 2a). The defects produced by 557-MeV ions with approximately the same ionization losses (40 keV/nm) exhibit practically the same shape.

Ions of lower energy [269 MeV, $(dE/dx)_{ion}$ = 35 keV/nm] produce defects of another type, namely, hillocks about 1 nm high with an average base diameter of 22 nm, which feature a small depression at the center about 5 nm in diameter and approximately 0.7 nm deep (Fig. 2b).

The data presented in Figs. 1 and 2 and the dependence of the character of the observed damage on the ionization density permit one to unambiguously assign the formation of radiation defects on the surface of sapphire single crystals to inelastic energy losses of the bismuth ions. As follows from the table, while the ionization density falls off with decreasing ion energy, the elastic scattering losses increase. The nature of the structural distortions in dielectrics caused by the energy relaxation of excited electrons, more specifically, latent tracks, is treated using two main models, ion-explosion and thermal spikes, which are considered in detail in [7, 8]. In the former model, one assumes a heavy charged particle to produce, along its trajectory, a cylindrical zone of ionized atoms, which subsequently explodes as a result of Coulomb interaction among the ions to form an extended defect zone. In the thermal spike model, the formation of latent tracks is associated with a tem-

perature increase (in the volume surrounding the ion trajectory) above the melting point T_{melt}, followed by a phase transformation (amorphization or recrystallization) due to the rapidly cooling overheated region. In our opinion, the AFM measurements argue for the thermal mechanism of defect formation on the surface of α-Al_2O_3 crystals. It may be conjectured that within the interval $35 > (dE/dx)_{ion} > 27$ keV/nm, the temperature is already in excess of T_{melt}, such that the material melts and is subsequently expelled onto the sample surface because of the difference in volume between the liquid and crystalline phases. The shape of the melt surface is governed by the surface tension and the pressure of the melt column. If the surface tension is not strong enough to support the surface, a crater forms in the melt. These processes, shown schematically in Figs. 3a and 3b, take place in the adiabatic stage, i.e., when the heat cannot be removed from the place of its release. Craters can also form through atom evaporation from the central, most overheated part of the melt or as a result of surface rupture already in the cooling stage.

The topography of the defects observed to occur at ionization densities of 40–41 keV/nm gives one grounds to relate their origin to the formation of an amorphous phase with a density substantially lower than that of the crystal. This gives rise to a volume difference, which is assumed to favor expulsion of the excess volume onto the surface (Fig. 3c). This interpretation was invoked in some earlier studies (see, e.g., [4]) to account for the formation of hillocks on the surface of a fullerene-irradiated sapphire.

A comparative analysis of the experimental data obtained from AFM and transmission electron microscopy revealed a correlation between the transverse dimensions of the hillocks and of the latent tracks in the bulk of the material. According to [9], the diameter of a track is approximately equal to the Gaussian FWHM of the hillocks. Our estimates yield $D \approx 7$ nm for the diameter of the latent tracks in α-Al_2O_3 single crystals formed by bismuth ions of 570 and 710 MeV, which is close to 8.4 nm, the value obtained for the case of a fullerene-irradiated sapphire with an ionization density of 41.4 keV/nm [4].

The dissipation of the energy confined in a cylindrical volume with a radius of a few nanometers is known to entail generation of thermoelastic stresses, which may exceed the ultimate stress and should substantially affect the defect formation in the bulk and on the surface of the irradiated material [10, 11]. Let us estimate the level of the stresses which are created in the thermal spike zone produced by a single bismuth ion assuming a Gaussian distribution of thermal energy in the track:

$$\varepsilon(r) = [(dE/dx)/\pi R_C^2]\exp\left(-\frac{r^2}{R_C^2}\right), \qquad (1)$$

where R_C is the effective track radius. The time in which the ion kinetic energy is converted to the energy

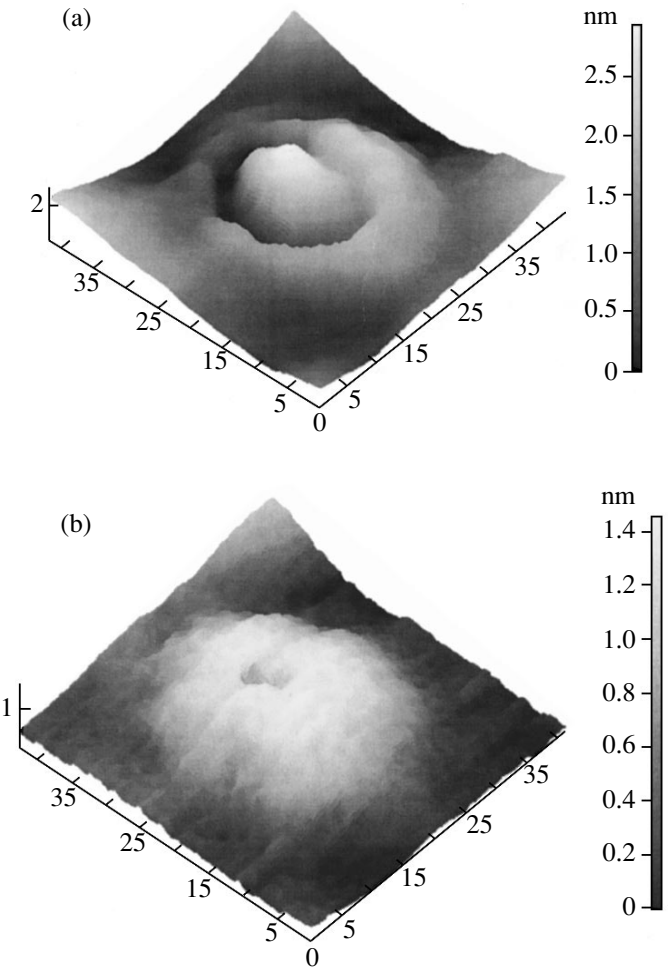

Fig. 2. Three-dimensional AFM image of surface defects produced by Bi ions with an energy equal to (a) 710 and (b) 269 MeV. Image size, 40×40 nm.

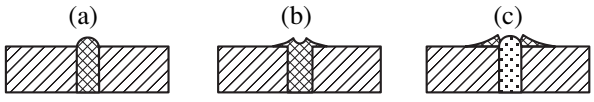

Fig. 3. Schematic of the formation of the observed surface defects produced by (a, b) local melting and (c) subsequent amorphization of the target material in the ion track.

of lattice thermal vibrations, 10^{-12}–10^{-13} s, does not exceed the characteristic time of action of the stress pulse, $2R_C/s \geq 10^{-12}$ s, where s is the sound velocity. One may therefore accept that the heat source acts instantaneously at time $t = 0$, i.e., that $\partial\varepsilon/\partial t = \varepsilon(r)\delta(t)$. Here, $\varepsilon(r, t)$ is the density of absorbed energy by time t and $\delta(t)$ is the Dirac delta function. We use for the calculation, the equations given in [10] for the stress tensor

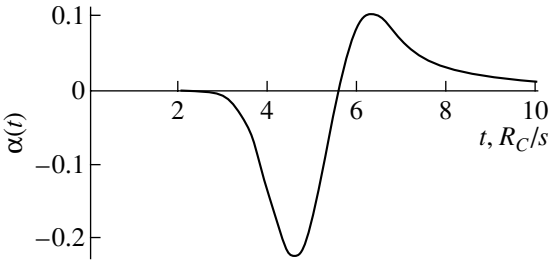

Fig. 4. Function $\alpha(t)$ plotted vs. time for $r = 5R_C$ (the shape of the radial component of the thermoelastic stress pulse).

components in the track of a charged particle. It can be shown that for $r > R_C$, the radial tensile stress is

$$\sigma_{rr} \approx \frac{\Gamma}{\pi^{3/2} R_C^2} \frac{dE}{dx} \alpha\left(\frac{r}{R_C}, \frac{st}{R_C}\right), \quad (2)$$

where Γ is the Grüneisen parameter and α is a function having the shape of a bipolar pulse which propagates with the sound velocity and decays with distance as $r^{-1/2}$. Figure 4 plots the dependence of α on time for $r = 5R_C$. One cannot exclude the possibility that the hillock shape displayed in Fig. 3b is the result of the action of a thermoelastic stress pulse.

Accepting $\Gamma = 1.4$, $(dE/dx)_{ion} = 35$ keV/nm, and $R_C = 3$ nm, we obtain 40 GPa for the maximum stress at a distance of 15 nm from the track axis. This value can be contrasted with the literature data on the macroscopic compressive strength for sapphire at 0.3–2.0 GPa [12]. At such thermoelastic stresses, the linear equations for the stress tensor components are most likely inapplicable; thus, they can be employed only for very rough estimates. Nevertheless, one can conclude that the thermoelastic stresses created at our ionization loss levels can contribute appreciably to the formation of radiation defects on the surface and to target lattice destruction even at distances far exceeding the size of the thermal spike region. Moreover, for $(dE/dx)_{ion} = 40$–41 keV/nm, one should take into account that the excited pulse is not purely thermoelastic, because it should contain a contribution associated with the change in the volume of the material, ΔV_q, connected with the phase transformation. As shown in [11], the acoustic pulse excited by particles stimulating a phase transition can exceed, by an order of magnitude or more, the values following from linear thermoacoustic theory.

Note that the assumption of the thermal energy distribution in a track being Gaussian is also a rough approximation. To more accurately estimate the profile of the thermal energy distribution in the lattice and the size of the region where melting and subsequent amorphization take place, one should consider the heat transfer processes involved in more detail. The standard thermal-spike model for metals considers the lattice heating to be a two-stage process, which consists of the thermalization of the released energy in the electron subsystem and the transfer of this energy to the lattice mediated by electron–phonon coupling. This is done by means of coupled nonlinear differential equations, whose parameters are the electron and lattice specific heats and heat conductivities, the electron–phonon coupling constant, and the energy transferred to the electron subsystem in a time substantially shorter than the characteristic thermalization time [8].

Because the mechanism of heat transport from electrons to the lattice in a dielectric differs from that in a metal, the parameters describing energy relaxation in the electron subsystem and energy transfer to the lattice cannot be determined in the way this is done for metals. While the heat transport by free electrons in metals occurs to a considerable extent through the replacement of the hot electrons in the excitation region by cold peripheral electrons, in insulators, there are no free electrons outside the excited region. A simplified thermal-spike model was proposed for insulators in [8, 12], in which all parameters of the electron subsystem are considered to be temperature-independent. The main parameter in this model is the electron mean free path $\lambda = \sqrt{D\tau}$, where D is the thermal diffusion coefficient of hot electrons and τ is the electron–phonon relaxation time. The latent track radius (the maximum distance from the axis of the track over which melting occurs) derived experimentally as a function of $(dE/dx)_{ion}$ offers the possibility of finding the electron mean free path. To determine the parameter λ, one has to quantify the threshold energy from which latent tracks start to form in sapphire. In accordance with the present study, this value is confined within the 27–35 keV/nm interval.

Thus, irradiation by bismuth ions with energies above 269 MeV produces radiation defects associated with inelastic energy losses on the surface of α-Al_2O_3 single crystals. The defect morphology depends on the level of ionization losses near the surface. For $(dE/dx)_{ion} = 40$–41 keV/nm, the defects are shaped as conical hillocks whose most probable origin is the formation, in the track region, of an amorphous phase with a density lower than that of the crystal lattice. The high thermoelastic stresses generated in the track region can also considerably affect defect formation.

ACKNOWLEDGMENTS

This study was supported by the Russian Foundation for Basic Research, project no. 00-02-16559.

REFERENCES

1. B. Canut, S. M. M. Ramos, P. Thevenard, *et al.*, Nucl. Instrum. Methods Phys. Res. B **80/81**, 1114 (1993).
2. B. Canut, A. Benyagoub, G. Marest, *et al.*, Phys. Rev. B **51** (18), 12194 (1995).
3. S. M. M. Ramos, N. Bonardi, and B. Canut, Phys. Rev. B **57** (1), 189 (1998).

4. S. M. M. Ramos, N. Bonardi, B. Canut, *et al.*, Nucl. Instrum. Methods Phys. Res. B **143**, 319 (1998).
5. D. L. Zagorski, V. A. Skuratov, A. E. Efimov, *et al.*, in *Abstracts of the 20th International Conference on Nuclear Tracks in Solids, Portoroz, Slovenia, 2000*, p. 113, Radiat. Meas. (in press).
6. V. A. Skuratov, A. Illes, Z. Illes, *et al.*, JINR Commun. (Dubna) **E13-99-161**, 8 (1999).
7. R. L. Fleisher, P. B. Price, and R. M. Walker, *Nuclear Tracks in Solids* (Univ. of California Press, Berkeley, 1975).
8. M. Toulemonde, C. Dufour, and E. Paumier, Phys. Rev. B **46** (22), 14362 (1992).
9. A. Audouard, R. Mamy, M. Toulemonde, *et al.*, Nucl. Instrum. Methods Phys. Res. B **146**, 217 (1998).
10. A. A. Davydov and A. I. Kalinichenko, At. Énerg. **53** (3), 186 (1982).
11. A. I. Kalinichenko and V. T. Lazurik, in *Radiation Acoustics*, Ed. by L. M. Lyamshev (Nauka, Moscow, 1987), p. 27.
12. A. Meftah, F. Brisard, J. M. Constantini, *et al.*, Phys. Rev. B **49** (18), 12457 (1994).

Translated by G. Skrebtsov

Physics of the Solid State, Vol. 44, No. 1, 2002, pp. 176–180. Translated from Fizika Tverdogo Tela, Vol. 44, No. 1, 2002, pp. 170–174.

FULLERENES AND ATOMIC CLUSTERS

Excitation and Ionization of Sodium Clusters by a Strong Electromagnetic Field

L. I. Kurkina

Institute of Thermophysics, Siberian Division, Russian Academy of Sciences, pr. Akademika Lavrent'eva 1, Novosibirsk, 630090 Russia

Novosibirsk State University, ul. Pirogova 2, Novosibirsk, 630090 Russia

e-mail: kurkina@itp.nsc.ru

Received April 5, 2001

Abstract—This paper reports on a study of the excitation and ionization of small sodium clusters by femtosecond light pulses with a maximum intensity of 5×10^{12}–1×10^{14} W/cm^2 and photon energy from 1 to 3 eV made in terms of the density functional theory and jellium model through direct numerical solution of the Kohn–Sham time-dependent equation. The dependence of the degree of ionization on the intensity, duration, and frequency of the light pulses, as well as on the cluster size, is studied. The efficiency of the processes is shown to be determined primarily by the field intensity rather than by the total pulse energy. © *2002 MAIK "Nauka/Interperiodica".*

1. INTRODUCTION

The photoexcitation of electrons is an important tool in the investigation of condensed media, including atomic clusters. The behavior of metallic clusters in weak external fields has been dealt with in a large number of theoretical and experimental publications (see, e.g., [1–10]). One of the most powerful approaches to the description of the interaction of atomic clusters with electromagnetic radiation is the nonstationary density functional theory [11]. This theory is applied to clusters in weak fields in a very efficient linearized version, which, when combined with the jellium model, provides the best fit to experimental data at the present time [1–6]. Recently, experiments on clusters in a field of short (femtosecond) high-intensity laser pulses, which induce strong electronic excitations in clusters, have been reported [12–14]. The response of clusters to a strong laser field is nonlinear and includes multiphoton ionization and fragmentation of the clusters. Therefore, the linear response theory and, hence, the linearized density functional method based on this theory can no longer be applied to the investigation of electron systems in strong fields. The general density functional formalism, however, does not use the perturbation theory and can be employed to study nonlinear effects. This work reports on a study of the ionization of Na_N clusters by strong femtosecond light pulses in the energy range from 1 to 3 eV, which is made through direct numerical solution of the one-dimensional Kohn–Sham time-dependent equation in the jellium model. We considered clusters with magic numbers of valence electrons $N = 8$, 20, and 40, which, in the jellium model, correspond to spheres with closed electronic shells. The dependence of the degree of ionization on the intensity, duration, and frequency of the light pulses, as well as on the cluster size, is studied. The change in the kinetic energy of the electrons left in the clusters, which results from interaction with the laser pulses, is calculated.

2. FORMALISM

Our study of electronic excitations in small metallic clusters initiated by a strong laser field is based on direct numerical solution of the time-dependent Schrödinger equation (here and henceforth, the atomic system of units is used, with $|e| = m = \hbar = 1$)

$$i\frac{\partial}{\partial t}\Psi_j(\mathbf{r}, t) = \left[-\frac{\nabla^2}{2} + V(\mathbf{r}, t)\right]\Psi_j(\mathbf{r}, t) \qquad (1)$$

for a jellium sphere in an external potential $V_{ext}(\mathbf{r}, t)$ created by an electromagnetic field. Within the electronic density-functional theory, the one-electron effective potential $V(\mathbf{r}, t)$ in Eq. (1) is written as

$$V(\mathbf{r}, t) = V_{ext}(\mathbf{r}, t) + \int\frac{n(\mathbf{r}', t) - n^+(\mathbf{r}')}{|\mathbf{r} - \mathbf{r}'|}d\mathbf{r}' + V_{xc}(\mathbf{r}, t) \qquad (2)$$

[in this case, Eq. (1) is the Kohn–Sham equation]. The electronic density of the jellium cluster $n(\mathbf{r}, t)$ is calculated using the one-electron wave functions of filled states:

$$n(\mathbf{r}, t) = \sum_j |\psi_j(\mathbf{r}, t)|^2.$$

The radial distribution $n^+(r)$ of the uniform positive jellium background of radius R is defined as

$$n^+(r) = \frac{3}{4\pi r_s^3}\Theta(R - r).$$

1063-7834/02/4401-0176$22.00

Here, r_s is the Wigner–Seitz electronic radius (for sodium, $r_s = 3.98a_0$, where a_0 is the Bohr radius), $\Theta(R - r)$ is the Heaviside unit function, and the radius of the jellium positive background R (considered to be the cluster radius) is connected to the number of valence electrons N in a cluster through the relation $R = N^{1/3}r_s$. The exchange-correlation potential $V_{xc}(\mathbf{r}, t)$ is defined by the time-independent local expression obtained by Vosko *et al.* [15].

If the cluster interacts with a light pulse polarized linearly along the z axis, then, within the dipole approximation, the external potential can be written in the form

$$V_{ext}(\mathbf{r}, t) = zE(t)\cos\omega t.$$

The electric field $E(t)$ is approximated by a Gaussian function.

To retain spherical symmetry of the problem, we transfer to spherical coordinates. To do this, we accept $z = r\cos\theta$ (where θ is the angle between the position vector $\mathbf{r}$ of the electron and the electric field vector $\mathbf{E}$ of the electromagnetic wave) and average $V_{ext}(\mathbf{r}, t)$ over the angular coordinates. The result is

$$V_{ext}(r, t) = \frac{2r}{\pi}E(t)\cos\omega t. \quad (3)$$

It should be pointed out that the use of a spherically symmetric model limits our consideration to single-particle excitations by separating them from the dipole surface plasma oscillations, which also take part in the absorption of electromagnetic radiation by clusters [10–12, 16]. A similar spherical approximation was successfully employed recently in [17] to describe the multiple ionization of sodium clusters by a strong electromagnetic field in the Thomas–Fermi model.

Equation (1), with the potential given by Eqs. (2) and (3), reduces to a one-dimensional (with respect to spatial coordinates, i.e., radial) time-dependent Kohn–Sham equation, which was solved using the method proposed in [18] with a time step of 2.5×10^{-18} s. The initial state was calculated by self-consistently solving the ground-state density-functional problem for a spherical jellium cluster [19]. The solution of Eq. (1) permits one to study electronic emission from metal clusters acted upon by strong light pulses. The emission was estimated from the decrease in the number of valence electrons in a spherical box of radius $R_{box} = 1.5R$, whose center coincides with that of the cluster:

$$N_{esc}(t) = 4\pi\int_0^{R_{box}}[n(r, 0) - n(r, t)]r^2 dr.$$

The excitation of electrons to higher bound states should also manifest itself in the N_{esc} spectra, provided that these states lie partially beyond R_{box}.

3. RESULTS

The formalism described in the preceding section was used to study the ionization of small sodium jellium-like clusters by light pulses with lengths at half-maximum T = 10, 20, 40, 100, and 200 fs (their full length was 25, 50, 100, 250, and 500 fs, respectively; we will understand the quantity T to be the pulse length in what follows), maximum intensity $I_0 = 5 \times 10^{12}$–1×10^{14} W/cm^2, and photon energy ω varied from 1 to 3 eV in 0.05-eV steps. Figure 1 shows the $N_{esc}(t)$ dependences for the case of interaction of a Na_8 cluster with 40-fs pulses of maximum intensity 2.5×10^{13} W/cm^2 and with various photon energies. To characterize the result of the cluster interaction with the light pulse on the whole, the $N_{esc}(t)$ functions were averaged over the last one-third of the pulse (in this region, their average values reach saturation). The averaged values are denoted by $\langle N_{esc}\rangle$. Figure 2 presents $\langle N_{esc}\rangle$ functions for jellium clusters Na_8, Na_{20}, and Na_{40} placed in a field of light pulses of the same intensity but with different durations (curves *1*, *2*), or the same length for different intensities (curves *1*, *5*), or the same energy for different lengths and intensities (curves *2*–*6*). As expected, an increase in the pulse length for the same intensity, or in the pulse intensity for the same pulse length, produces an increase in the electron emission [compare curves *1* and *2* in Fig. 2 (T = 20 and 200 fs) for $I_0 = 5 \times 10^{12}$ W/cm^2, as well as curves *1* and *5* for 20-fs pulses

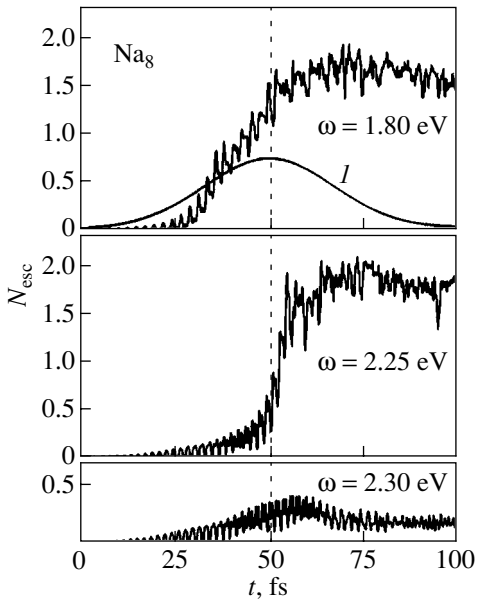

Fig. 1. Time evolution of the number of electrons N_{esc} emitted from a Na_8 cluster in interaction with a 40-fs light pulse (the figure specified is full length at half-maximum; the total length is 100 fs) of maximum intensity 2.5×10^{13} W/cm^2 and with photon energies of 1.80, 2.25, and 2.30 eV. Curve *1* is the pulse envelope (in arbitrary units).

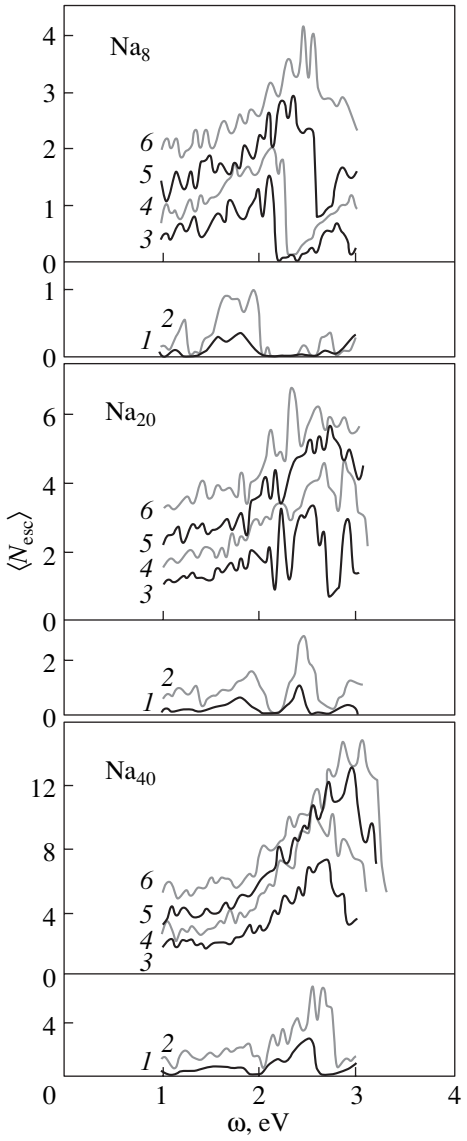

Fig. 2. Spectral dependence of the number of electrons $\langle N_{esc}\rangle$ that escaped from Na_8, Na_{20}, and Na_{40} clusters as a result of interaction with laser pulses of different maximum intensities I_0 (in units of 10^{12} W/cm^2) and durations T (fs) equal to (*1*) 5 and 20, (*2*) 5 and 200, (*3*) 10 and 100, (*4*) 25 and 40, (*5*) 50 and 20, and (*6*) 100 and 10, respectively. Pulses (*2*–*6*) are of the same energy.

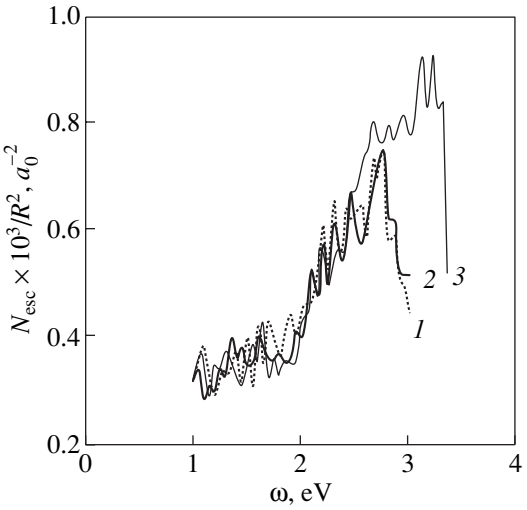

Fig. 3. Spectral dependence of the number of electrons $\langle N_{esc}\rangle$ that escaped from (*1*) Na_8, (*2*) Na_{20}, and (*3*) Na_{40} clusters acted upon by a 20-fs laser pulse with a maximum intensity 10^{14} W/cm^2. The values of $\langle N_{esc}\rangle$ are normalized to the squared cluster radius.

with intensities at a maximum of $I_0 = 5 \times 10^{12}$ and 5×10^{13} W/cm^2, respectively]. Note that the dependence of $\langle N_{esc}\rangle$ on the pulse intensity is stronger than that on the pulse length. A comparison of the results obtained for pulses with the same energy but different intensities and lengths shows that the number of emitted electrons grows with increasing intensity even if the pulse length has been reduced accordingly. The ionization also increases with increasing cluster size. The $\langle N_{esc}\rangle$ spectra obtained for different clusters but normalized to the squared cluster radius coincide very closely at photon energies below 2 eV, while in the interval from 2 to 3 eV, the maximum values of $\langle N_{esc}\rangle/R^2$ for the clusters become increasingly similar, although the size dependence (associated with specific features of the electronic energy structure in clusters of different size) is retained (Fig. 3).

We consider the variation of the $\langle N_{esc}\rangle$ spectra as a function of the cluster size and laser pulse intensity and length in more detail. The $\langle N_{esc}\rangle$ spectra obtained for the lowest of the laser pulse intensities studied ($I_0 = 5 \times 10^{12}$ W/cm^2) reflect the electronic structure of the cluster ground state and, therefore, are most likely associated with resonant one-photon absorption. For instance, for the Na_8 jellium cluster (electron configuration $1s^21p^6$), the increase in $\langle N_{esc}\rangle$ in the energy range below 2 eV could be due to electron transitions from the $1p$ shell to the more highly lying $1d$ and $2s$ discrete levels (the energies of these transitions, derived from a cluster ground-state calculation using the density-functional method, are 1.21 and 1.90 eV, respectively). The one-photon ionization threshold of the $1p$ shell is 3.23 eV. Between 2 and 3 eV, the $\langle N_{esc}\rangle$ spectrum is close to zero because of the absence of allowed electronic transitions (recall that the approach used here disregards surface plasma oscillations, whose energy lies exactly in this region). Transitions between discrete bound levels from the outer filled shells also take place in the jellium clusters Na_{20} ($1s^21p^61d^{10}2s^2$) and Na_{40} ($1s^21p^61d^{10}2s^21f^{14}2p^6$) below 2 eV (the stationary density-functional theory yields, for a zero external field, the following values for Na_{20}: $2s \longrightarrow 2p$: 1.19 eV, $1d \longrightarrow 1f$: 1.13 eV, $1d \longrightarrow 2p$: 1.80 eV; and for Na_{40}: $2p \longrightarrow 3s$: 1.21 eV, $1f \longrightarrow 2d$: 1.74 eV). The one-pho-

ton ionization thresholds are about 2.7 eV for both clusters. For $I_0 = 5 \times 10^{12}$ W/cm^2, the maxima in the $\langle N_{esc} \rangle$ spectra lie slightly below these values; this may be due to the clusters becoming polarized by the external electric field, a factor that increases the energy of the one-electron states while affecting the level separation only weakly [20]. As the laser pulse intensity increases, the main peaks in the $\langle N_{esc} \rangle$ spectra grow in amplitude, become broader and more complex in shape, and shift toward higher energies (this displacement is particularly pronounced in the Na_8 spectra). The broadening and shift of the main maxima is connected primarily with the onset of over-barrier ionization, upon which resonant absorption is superposed. (As follows from our calculations of the effective potential $V(\mathbf{r}, t)$, the conditions favoring over-barrier electron escape out of clusters become realized in the cases considered (Fig. 2) at intensities of $I_0 \geq 1 \times 10^{13}$ W/cm^2.) The over-barrier cluster ionization in an alternating field occurs stepwise (within the time intervals near the pulse maximum, where $\cos\omega t$ in $V_{ext}(r, t)$ assumes values close to –1). In the course of cluster interaction with a pulse, over-barrier ionization sets in before resonant ionization and results in a lowering of the one-electron energy levels in the cluster and an increase in level separation; therefore, resonant absorption occurring at higher energies than this can be expected in the case of an unperturbed energy spectrum. We will illustrate this process using Fig. 4. In the frequency range under consideration, over-barrier ionization depends on the radiation frequency only weakly. Therefore, in the course of cluster interaction with pulses of the same intensity and length but having different photon energies, the level shift caused by over-barrier ionization occurs in approximately the same way from the E_j^0 position (in the absence of an external perturbation) to E_j^T (at the pulse maximum). If the photon energy lies in the range E_j^0 to E_j^T, resonant excitation and/or ionization will take place as soon as the photon energy becomes equal to the energy of the bound–bound or bound–free electron transition. In this case, the higher the photon energy, the later the resonance will occur. Figure 1 shows the time dependences $N_{esc}(t)$ for an Na_8 cluster interacting with a 40-fs laser pulse with photon energies of 1.80, 2.25, and 2.30 eV. In the first case, $\langle N_{esc} \rangle$ = 1.523; in the second, 1.803; and in the third, 0.169. As seen from Fig. 1, the sharp increase in $\langle N_{esc} \rangle$ at a photon energy of 1.80 eV occurs earlier than that at ω = 2.25 eV. In both cases, the electron escape from the cluster is associated with the ionization decay of the 1p electron excitation to outer electron shells. For ω = 2.30 eV, no resonance is observed, because the energy levels in the cluster do not have time to drop to the required position in the over-barrier ionization. The higher the radiation intensity, the more intense the over-barrier ionization. As a consequence, the one-electron

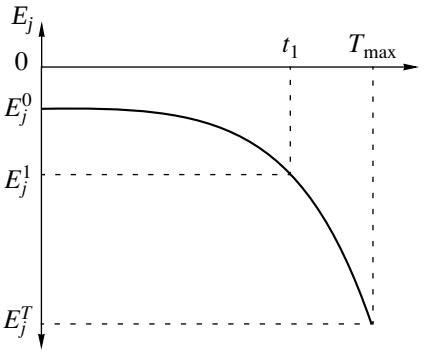

Fig. 4. Schematic illustrating the change in position of a one-electron energy level E_j in the jellium cluster induced through over-barrier ionization by a light pulse reaching its maximum intensity at time T_{max}.

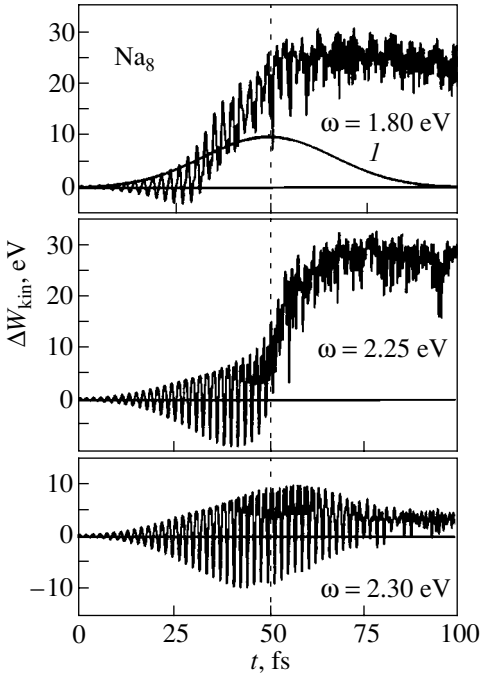

Fig. 5. Time evolution of the change in kinetic energy ΔW_{kin} of the electrons left in an Na_8 cluster acted upon by a 40-fs pulse with a maximum intensity 2.5×10^{13} W/cm^2 and photon energies of 1.80, 2.25, and 2.30 eV. Curve *1* is the pulse envelope (in arbitrary units).

levels drop and the resonant maxima in the $\langle N_{esc} \rangle$ spectra broaden and shift toward higher energies (Fig. 2). As the pulse intensity increases, the spectra become more complex, which may be due to the enhancement of multiphoton absorption.

As already mentioned, the effect of the pulse duration on the cluster ionization spectrum is weaker than that of the field intensity. As is evident from Fig. 2 (curves *1* and *2* for pulses with an equal intensity of $I_0 = 5 \times 10^{12}$ W/cm^2 and T = 20 and 200 fs, respectively), an

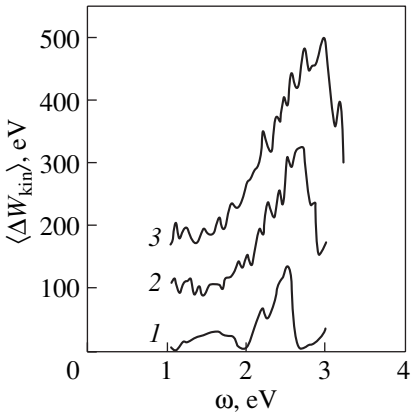

Fig. 6. Spectral dependence of the change in the kinetic energy $\langle \Delta W_{kin} \rangle$ of the electrons left in an Na_{40} cluster acted upon by laser pulses of different maximum intensities I_0 (in units of 10^{12} W/cm^2) and lengths T (fs) equal to (*1*) 5 and 20, (*2*) 10 and 100, and (*3*) 50 and 20, respectively. Pulses (*2*) and (*3*) have the same energy.

increase in the pulse duration for the same maximum intensity primarily influences the resonant (one- and multiphoton) absorption by enhancing the resonant maxima. In stronger fields, a change in the pulse duration also affects the fine structure of the $\langle N_{esc} \rangle$ spectra.

Figure 5 shows the variation of the kinetic energy $\Delta W_{kin}(t)$ of the electrons left in a Na_8 cluster in interaction with laser pulses, which have the same parameters as those in Fig. 1 for $N_{esc}(t)$. $\Delta W_{kin}(t)$ was calculated as the difference between the kinetic energy of the electrons remaining inside a spherical box of radius R_{box} at a given time t and that of electrons in an unperturbed cluster at $t = 0$. One clearly sees that the $N_{esc}(t)$ and $\Delta W_{kin}(t)$ curves behave in a correlated manner. Note the strong oscillations in $\Delta W_{kin}(t)$ during the cluster–pulse interaction, which, in the absence of resonant absorption (in Fig. 5, $\omega = 2.30$ eV), damp by the end of the pulse without changing the kinetic energy of the cluster electrons markedly.

To analyze the variation in the kinetic energy of electrons in a cluster in the course of interaction with a laser pulse on the whole, we averaged $\Delta W_{kin}(t)$ over the last one-third of the pulse (as in the case of $\langle N_{esc} \rangle$). The calculation showed that the structure of the averaged $\langle \Delta W_{kin} \rangle$ spectra (Fig. 6) reproduces that of the corresponding $\langle N_{esc} \rangle$ spectra. As expected, the energy is pumped into a cluster most efficiently in resonant one-photon absorption. However, the dependence of $\langle \Delta W_{kin} \rangle$ on cluster size is stronger than that of $\langle N_{esc} \rangle$; for photon energies below 2 eV, $\langle N_{esc} \rangle$ is, on the average, proportional to the squared cluster radius, whereas $\langle \Delta W_{kin} \rangle$ is proportional to the fourth power of the cluster radius (above 2 eV, this relation is more complex, which is connected with specific features of the electron energy spectrum in clusters of different size).

Thus, our studies of cluster interaction with strong laser pulses show that, at high pulse intensities, one-particle mechanisms of the absorption of electromagnetic radiation may give rise to multiple ionization and heating of metallic clusters. The efficiency of this process is dominated by the field intensity rather than by the total pulse energy.

ACKNOWLEDGMENTS

This study was supported by the Russian Foundation for Basic Research, project nos. 00-03-33043 and 99-15-96028.

REFERENCES

1. W. Ekardt, Phys. Rev. Lett. **52** (21), 1925 (1984).
2. W. Ekardt, Phys. Rev. B **31** (10), 6360 (1985).
3. M. J. Puska, R. M. Nieminen, and M. Manninen, Phys. Rev. B **31** (6), 3486 (1985).
4. D. E. Beck, Phys. Rev. B **35** (14), 7325 (1987).
5. A. Rubio, L. C. Balbas, and J. A. Alonso, Phys. Rev. B **45** (23), 13657 (1992).
6. L. I. Kurkina and O. V. Farberovich, Phys. Rev. B **54** (20), 14791 (1996).
7. K. Selby, M. Vollmer, J. Masui, *et al.*, Phys. Rev. B **40** (8), 5417 (1989).
8. K. Selby, V. Kresin, J. Masui, *et al.*, Phys. Rev. B **43** (6), 4565 (1991).
9. W. A. de Heer, Rev. Mod. Phys. **65** (3), 611 (1993).
10. M. Brack, Rev. Mod. Phys. **65** (3), 677 (1993).
11. E. K. U. Gross and W. Kohn, Adv. Quantum Chem. **21** (1), 255 (1990).
12. T. Ditmire, T. Donnelly, A. M. Rubenchik, *et al.*, Phys. Rev. A **53** (5), 3379 (1996).
13. R. Schlipper, R. Kusche, B. von Issendorf, and H. Haberland, Phys. Rev. Lett. **80** (6), 1194 (1998).
14. L. Köller, M. Schumacher, J. Köhn, *et al.*, Phys. Rev. Lett. **82** (19), 3783 (1999).
15. S. H. Vosko, L. Wilk, and M. Nusair, Can. J. Phys. **58** (8), 1200 (1980).
16. C. F. Ullrich, P.-G. Reinhard, and E. Suraud, Eur. Phys. J. D **9** (1–4), 407 (1999).
17. M. B. Smirnov and V. P. Kraĭnov, Zh. Éksp. Teor. Fiz. **115** (6), 2014 (1999) [JETP **88**, 1102 (1999)].
18. S. E. Koonin, *Computational Physics* (Benjamin, Manlo Park, 1986; Mir, Moscow, 1992).
19. L. I. Kurkina, Fiz. Tverd. Tela (St. Petersburg) **43** (4), 759 (2001) [Phys. Solid State **43**, 792 (2001)].
20. L. I. Kurkina and O. V. Farberovich, Z. Phys. D **37** (4), 359 (1996).

Translated by G. Skrebtsov

Physics of the Solid State, Vol. 44, No. 1, 2002, pp. 181–185. Translated from Fizika Tverdogo Tela, Vol. 44, No. 1, 2002, pp. 175–179.

FULLERENES AND ATOMIC CLUSTERS

Phonon Propagation through Photonic Crystals—Media with Spatially Modulated Acoustic Properties

V. N. Bogomolov*, L. S. Parfen'eva*, I. A. Smirnov*, H. Misiorek, and A. Jzowski****

**Ioffe Physicotechnical Institute, Russian Academy of Sciences, St. Petersburg, Politekhnicheskaya ul. 26, 194021 Russia*

e-mail: Igor.Smirnov@pop.ioffe.rssi.ru

***Institute of Low-Temperature and Structural Research, Polish Academy of Sciences, 50-950 Wroclaw, Poland*

Received June 7, 2001

Abstract—The thermal conductivity κ of photonic crystals differing in degree of optical homogeneity (single crystals of synthetic opals) was measured in the 4.2–300 K temperature range. The thermal conductivity revealed, in addition to the conventional decrease in comparison with solid amorphous SiO_2 characteristic of porous solids, a noticeable decrease for $T < 20$ K, the range wherein the phonon wavelength in amorphous SiO_2 approaches the diameters of the contact areas between the opal spheres. This effect is enhanced in the case of phonon propagation along the SiO_2 sphere chains (six directions in the cubic opal lattice). The propagation of light waves (photons) through a medium with spatially modulated optical properties (photonic crystals) is presently well studied. The propagation of acoustic waves through a medium with spatially modulated acoustic properties (phononic crystals) may also reveal specific effects, which are discussed in this paper; among them are, e.g., the ballistic mode of phonon propagation and waveguide effects. © *2002 MAIK "Nauka/Interperiodica".*

1. INTRODUCTION

The propagation of light through a medium with a spatially modulated refractive index (opals as photonic crystals) was discussed earlier [1]. That work was paralleled by a study of the propagation of phonons (thermal conductivity) through these media, because phonons can also produce coherent effects in such regular systems (and related composites). This paper presents experimental data indicating that phonon propagation in opals with spatially modulated acoustic properties exhibit features that permit one to consider them to be "phononic crystals," which also manifest some specific effects in thermal conductivity when the phonon wavelength approaches the modulation scale of the medium.

Opals possess a peculiar fractal-type crystalline structure [2, 3]. They are made up of closely packed spheres of amorphous SiO_2. The diameters of the spheres usually range from 2000 to 2500 Å (first-order spheres). These spheres contain an array of smaller closely packed spheres 300–400 Å in size (second-order spheres), which, in turn, are formed of closely packed particles about 100 Å in diameter (third-order spheres).

The closely packed sphere lattice contains voids of the octahedral and tetrahedral types interconnected by horn-shaped channels. Depending on the sphere size, the voids can also be classed under the first, second, and third orders. Filling the first-order voids with various substances produces new lattices (replicas). The voids contribute to the total volume porosity of the opal, which can be estimated theoretically as 59%. In practice, however, the real total porosity of the opal is 46% [4, 5]. This results from partial sintering of the second- and third-order SiO_2 spheres.

The first-order amorphous SiO_2 spheres make up a closely packed regular fcc lattice with a period of ~3000–4000 Å and with sphere contacts shaped as diaphragms where their diameters cross.

Thus, opal can be considered to be an amorphous medium (amorphous first-order SiO_2 spheres) with a regular spatial modulation of its properties (a regular array of amorphous SiO_2 spheres forming a closely packed cubic lattice).

2. RESULTS AND DISCUSSION

This paper reports on measurement of the thermal conductivity κ of single-crystal synthetic opal made on several samples in the 4.2–300 K and 4.2–100 K temperature ranges.[1] The κ was measured using a technique similar to that described in [8]. Opal is an insulator. Thus, the experimental values of $\kappa(T)$ are related to the thermal conductivity of the crystal lattice. The technique used to prepare opal single crystals was described briefly in [6]. X-ray diffraction measurements showed the opal samples studied to be purely amorphous. No traces of a crystalline phase were revealed. The parameter of the cubic lattice formed through the first-order

[1] The thermal conductivity of opals was studied by us earlier [5–7].

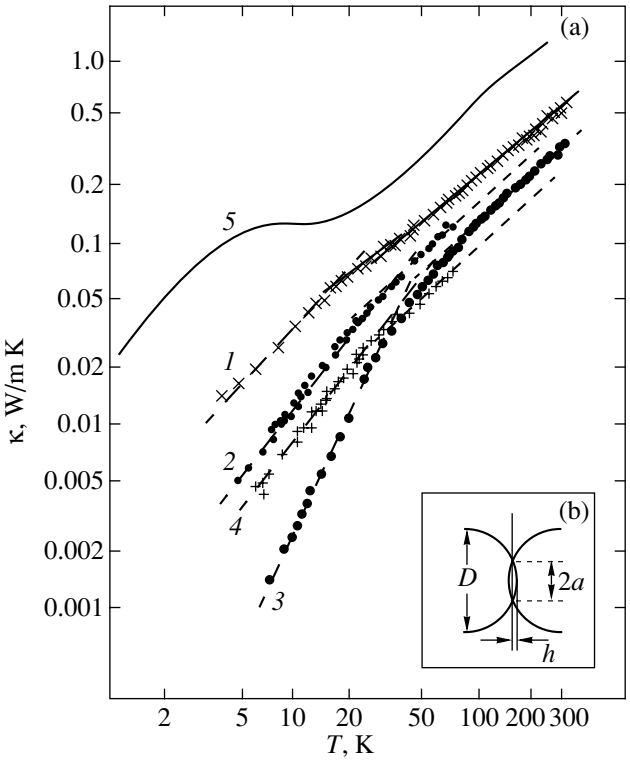

Fig. 1. (a) Temperature dependence of the thermal conductivity of amorphous SiO_2 (curve *5*) [12, 13] and synthetic opal single crystals (curves *1–4*); (*1*) through (*4*) are the opal sample numbers. (b) Schematic of two adjacent first-order amorphous SiO_2 spheres in the opal lattice. *D* is the sphere diameter, 2*a* is the diameter of the contact region formed by intersecting spheres, and *h* is the depth of the overlap of adjacent spheres in their contact.

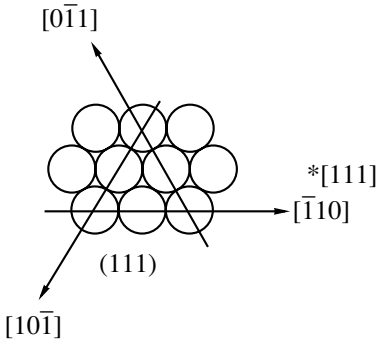

Fig. 2. Schematic of the (111) plane in a closely packed opal sphere array. [0$\bar{1}$1], [$\bar{1}$10], and [10$\bar{1}$] are the directions along the chains of first-order amorphous SiO_2 spheres. The asterisk specifies the [111] axis (directed perpendicular to the plane of the figure).

amorphous SiO_2 spheres was determined by optical structural analysis [5, 9]. The lattice parameter is comparable to the wavelength of visible light, which acted in this case as a counterpart of the x-rays used in x-ray diffractometry.

The degree of structural perfection of the opal single crystals studied was judged both from optical structural measurements and (visually) from the presence or absence of diffuse light scattering, as well as from the easiness with which the single crystals could be cleaved along the (100) plane.

The thermal conductivity of opals should decrease compared to bulk amorphous SiO_2 because of the porosity of the former. The opals considered in this work were prepared using the same technology, and their porosities were found to be similar. Therefore, based on the standard theory of thermal conductivity, including the effect of the porosity of a material on κ [10, 11], the samples studied should not have exhibited any difference in thermal conductivity to be referred to amorphous SiO_2. However, this conjecture has no experimental support. Moreover, the measurements (Fig. 1) produced a result which may seem at first glance paradoxical, namely, the thermal conductivity of the opals decreased with increasing degree of perfection of the crystals, which, as determined from the optical and structural studies, increased from sample 1 to sample 4 (Fig. 1).

Therefore, to explain the experimental data obtained, a model other than that of [10, 11] for the behavior of the thermal conductivity of the opal had to be invoked, which is a porous medium with a regular structure.

The propagation of heat flux through the opal at the contacts between the first-order amorphous spheres gives rise to contact thermal resistance similar to the contact electrical resistance *r*:

$$2r = (\rho/4a_0) \times 2, \qquad (1)$$

where ρ is the electrical resistivity and $2a_0$ is the contact diameter.

When the contact area is small (in the limit approaching a point), the opal thermal conductivity at high temperatures will be dominated by this contact thermal resistance (a purely geometric factor).

Thus, the more perfect the opal crystal structure (when the contacts between all the spheres are the same and approach a point type), the larger the part played by the contact thermal resistance between spheres and the smaller the crystal thermal conductivity (in the $a \longrightarrow 0$ limit, $\kappa \longrightarrow 0$, with a weak dependence on the opal density).

The samples of the opals studied by us were cut from (111)-oriented plates (Fig. 2). All the samples, except sample no. 3, had an arbitrary crystallographic orientation. Sample *3* was cut close to the [$\bar{1}$10] direction, so that when it was used in thermal conductivity measurements, the heat flux propagated along the chains of the first-order amorphous SiO_2 spheres. For $T > 20$ K, the κ increases at temperatures close to the $\kappa \sim T$ law in all the samples studied. For $T < 20$ K, the κ behaves differently. The thermal conductivity

decreases with decreasing temperature as T^n but with different values of n for different samples, namely, n = 1.1 for sample *1*, 1.3 for samples *2* and *4*, and 2.3 for sample *3*.

An analysis of the behavior of κ in opals of different degrees of perfection and arbitrary orientation will be presented elsewhere. We will consider here only the results obtained on sample *3*.

Optical structural analysis yielded 2350 Å for the size of the first-order amorphous SiO_2 spheres and 3300 Å for the fcc lattice parameter.

Opal single crystals provide an illustration of porous media which, due to their density being spatially modulated in a regular manner, lend themselves to correct geometric description. Using simple geometric relations and experimental data for κ of bulk amorphous SiO_2 obtained at 300 K [12, 13] and of opal sample no. *3*, we calculated, for the latter, the depth h of crossing of adjacent SiO_2 spheres in opal and the contact radius a of these spheres (Fig. 1b). The values of h and a were found to be ~1 and ~45 Å, respectively.

Thus, first-order amorphous SiO_2 spheres in opal are in contact through sufficiently small "contact transparency windows" representing diaphragms $2a$ in diameter.

The values of h and a were calculated from the easily derivable relations

$$2a = 2\sqrt{h(D-h)}, \tag{2}$$

$$R_1/R_2 \sim 8a/D, \tag{3}$$

where D is the diameter of a first-order opal amorphous sphere and R_1 and R_2 are the opal thermal resistances for $h = h_1$ and $h = h_2$, respectively. Equations (2) and (3) are valid for $h < D/12$ and $2a < D/\sqrt{3}$.

One may thus draw the conclusion that a new phonon scattering mechanism not operative in continuous amorphous SiO_2 exists in this case.

We consider the relation obtained for κ of opal sample *3* in more detail. The value of its thermal conductivity is matched with that of bulk amorphous SiO_2 (Fig. 3a). We denote the difference between these values as Δκ. In this way, we exclude the simple geometrical factors that result in a decrease in the opal thermal conductivity, namely, the thermal resistance of the contacts between the amorphous spheres of the opal and its porosity. Next, we raise the values of κ of the opal by an amount Δκ throughout the temperature range studied (Fig. 3a). As seen from Fig. 3a, the κ of the opal coincides with the κ of continuous amorphous SiO_2 in the temperature range 300–50 K. The only difference is observed for $T < 50$ K, where the κ of the opal scales with decreasing temperature as $\sim T^{2.3}$.

The observed effect can originate from phonon scattering from the diaphragms, which are the contact transparency windows of the opal. For $T \sim 20$ K, the phonon mean free path l in bulk amorphous quartz is

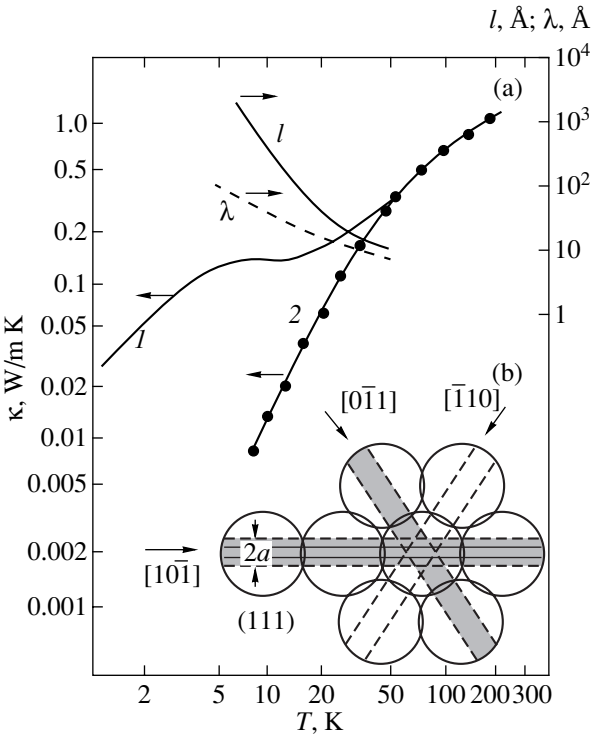

Fig. 3. (a) Temperature dependences (left-hand scale) of κ of amorphous quartz (curve *1*) [12, 13] and of the thermal conductivity of sample *3* reduced to 300 K (curve *2*) and (right-hand scale) of the phonon mean free path l and dominant phonon wavelength λ in bulk amorphous quartz [12]. (b) Schematic of opal sphere chains [in the (111) plane]. The arrows indicate possible phonon propagation paths in the opal crystal along the amorphous SiO_2 chains.

~40 Å and the dominant wavelength is ~20 Å [12] (Fig. 3a), which is close to the radius of the amorphous-sphere contact region, with the result that the contact transparency regions start to place a constraint on the mean free path of long-wavelength phonons and l becomes constant and temperature-independent within the temperature range of interest here. The thermal conductivity is related to the specific heat C, the sound velocity v, and the phonon mean free path through

$$\kappa = 1/3Cvl. \tag{4}$$

As a rule, v depends on temperature only weakly in solids (v = const). If l and v are constant, then

$$\kappa(T) \sim C(T). \tag{5}$$

As evident from Fig. 4, Eq. (4) is satisfied fairly well for the opal sample in the 5–20 K temperature interval of interest; indeed, $\kappa \sim T^{2.3}$ and $C \sim T^{2.5}$.

For the above model (which is an analog of the model of a thin rod at whose boundaries long-wavelength phonons are scattered) to become realized, the contact transparency windows must be arranged regularly along the heat flux propagation direction and be

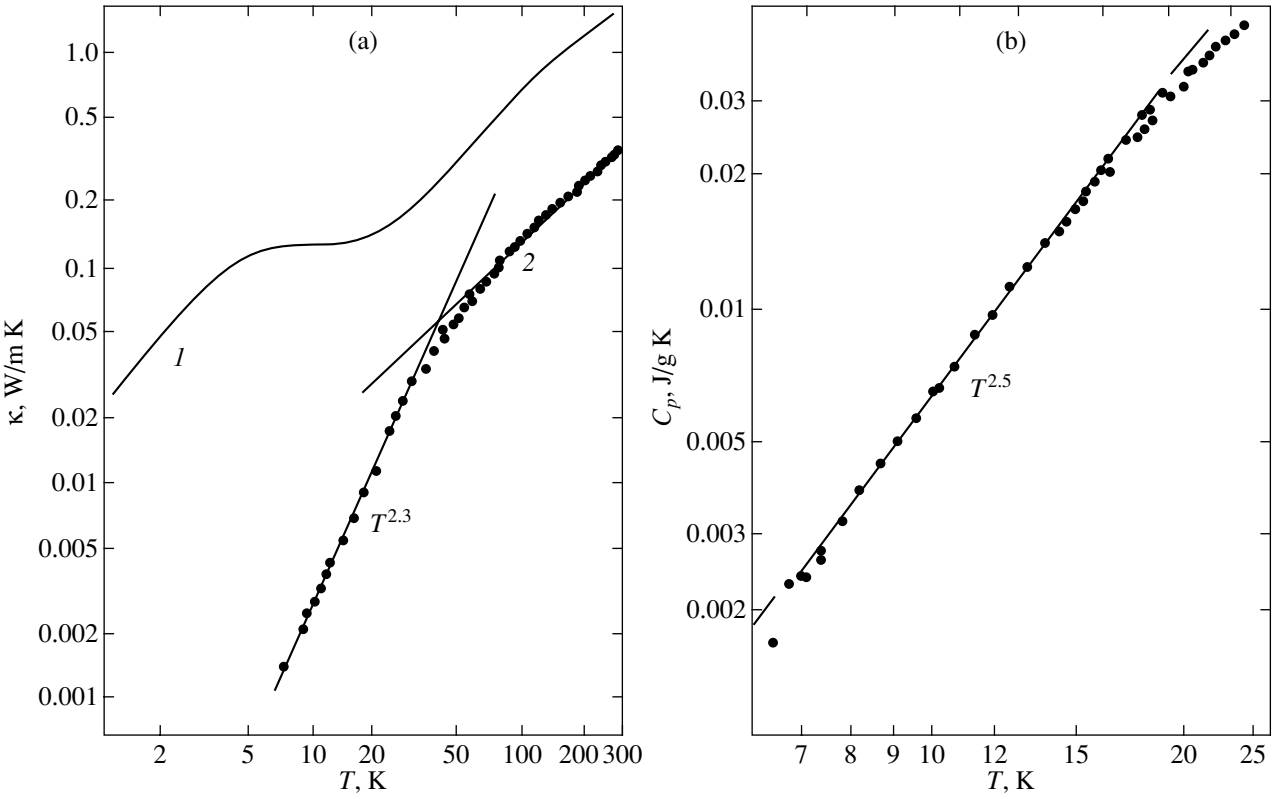

Fig. 4. (a) Temperature dependence of the thermal conductivity of amorphous quartz (curve *1*) [12, 13] and of a single-crystal opal sample *3* (curve *2*). (b) Temperature dependence of the thermal conductivity of opal sample *3* taken from [14].

close to one another; these conditions exactly apply to sample *3*. In Fig. 3b, the dashed lines connecting the opal contact transparency windows, which scatter the phonons, illustrate the thin rod model. At sufficiently low temperatures, the phonons can propagate along the opal channels in the ballistic mode (Fig. 3b).

Propagation of phonons along a modulated nanochannel would undoubtedly require a comprehensive theoretical analysis. A similar problem is also relevant to the case of phonon propagation through replica lattices, i.e., substances that fill the void sublattices in opals; this was studied by us earlier in [15, 16]. In this case, the junctions connecting the structural lattice elements resemble cut horns rather than diaphragms [2].

We do not exclude the possibility of applying other models to the interpretation of the results obtained.

For example, it appears only natural to use the analogy of acoustic and dielectric waveguides as applied to opal-based systems at sufficiently low temperatures. According to [17], the number of electromagnetic modes N fitting a circular dielectric waveguide depends on the reduced waveguide diameter $\tilde{d}$ as

$$N = \tilde{d}^{1.84} \sim (2a'/\lambda)^{1.84}. \quad (6)$$

Here, a' is the waveguide radius and λ is the wavelength of the electromagnetic wave in the waveguide

$$\lambda = \frac{\lambda_0}{\sqrt{c_1^{-2} - c_2^{-2}}}, \quad (7)$$

where λ_0 is the wavelength in vacuum and c_1 and c_2 are the velocities of light in the waveguide and the surrounding medium, respectively. Since the thermal conductivity is proportional to the number of phonons (i.e., to the number of modes), one may assume that $\kappa \sim N$.

Because the λ of phonons in amorphous quartz scales in the temperature range of interest (4–30 K) as $\lambda \sim 1/T$, the thermal conductivity, according to Eq. (6), should vary as $\kappa \sim T^{1.84}$, which is close to the temperature dependence of κ obtained by us experimentally (Fig. 4a).

As already stated, other models can also be applied to the interpretation of the results obtained.

3. CONCLUSIONS

Thus, one may draw the following conclusions.

A model taking into account phonon scattering from the contact transparency windows of opal has been employed to explain the results obtained. At sufficiently low temperatures, the opal is also considered to be a

three-dimensional array of acoustic waveguides in which phonons can propagate ballistically along the chains of amorphous SiO_2 spheres (Fig. 3b).

In the latter model, each site of the opal lattice (an amorphous SiO_2 sphere) is the crossing point of six independent acoustic channels (Fig. 3b), which, in principle, can also be used to exert an acoustic action on any opal lattice site to produce filters, delay lines, and other nanoacoustic devices. By placing a nanodevice that is sensitive to the acoustic wave amplitude at each site, one can obtain a three-dimensional array of transducers controlled by coherent phonon fluxes (Fig. 3b).

In the case where the phonon wavelength becomes comparable not to $2a$ but to the SiO_2 sphere diameter D, the vibrational spectrum of such a lattice of heavy clusters will be shifted toward low frequencies, with its position changing by approximately $\sqrt{(2a)^2/D^3} \sim 10^3$ times compared to that of amorphous SiO_2 and falling into the radio frequency range (10^9–10^{10} Hz for $T < 4$ K). In this case, the condition $\lambda \sim D$ is similar to that for the realization of photonic crystals, thus justifying, in a certain sense, the concept of phononic crystals.

A number of problems concerning nanoacoustics have remained uncovered and will be considered in subsequent publications. Among these are the effect of waveguide properties on the behavior of κ of asbestos, a model material with fibers ~100–200 Å in diameter; the photonic properties of opals transmitting radiation with a wavelength $\lambda \sim 100$ Å (because of the existence of channels of this size in opals); and so on.

ACKNOWLEDGMENTS

The authors are indebted to N.F. Kartenko for the x-ray structural characterization of the opal samples and to A.V. Prokof'ev for the optical analysis of the sample structure.

This work was carried out in the framework of a bilateral agreement between the Russian and Polish Academies of Science and was supported by the Russian Foundation for Basic Research (project no. 00-02-16883) and the Polish Academy of Sciences (project no. 2 PO3B 127-19 KBN).

REFERENCES

1. V. N. Bogomolov, D. A. Kurdyukov, A. V. Prokof'ev, and S. M. Samoĭlovich, Pis'ma Zh. Éksp. Teor. Fiz. **63**, 49 (1996) [JETP Lett. **63**, 56 (1996)].
2. V. N. Bogomolov and T. M. Pavlova, Fiz. Tekh. Poluprovodn. (St. Petersburg) **29** (2), 826 (1995) [Semiconductors **29**, 428 (1995)].
3. V. G. Balakirev, V. N. Bogomolov, V. V. Zhuravlev, *et al.*, Kristallografiya **38** (3), 111 (1993) [Crystallogr. Rep. **38**, 348 (1993)].
4. V. V. Ratnikov, Fiz. Tverd. Tela (St. Petersburg) **39** (5), 956 (1997) [Phys. Solid State **39**, 856 (1997)].
5. V. N. Bogomolov, D. A. Kurdyukov, L. S. Parfen'eva, *et al.*, Fiz. Tverd. Tela (St. Petersburg) **39** (2), 392 (1997) [Phys. Solid State **39**, 341 (1997)].
6. V. N. Bogomolov, L. S. Parfen'eva, A. V. Prokof'ev, *et al.*, Fiz. Tverd. Tela (St. Petersburg) **37** (11), 3411 (1995) [Phys. Solid State **37**, 1874 (1995)].
7. V. N. Bogomolov, I. A. Smirnov, N. V. Sharenkova, and G. Bruls, Fiz. Tverd. Tela (St. Petersburg) **43** (1), 186 (2001) [Phys. Solid State **43**, 194 (2001)].
8. A. Jezowski, J. Mucha, and G. Pompe, J. Phys. D **20**, 1500 (1987).
9. V. N. Bogomolov, A. V. Prokof'ev, and A. I. Shelykh, Fiz. Tverd. Tela (St. Petersburg) **40** (4), 648 (1998) [Phys. Solid State **40**, 594 (1998)].
10. G. N. Dul'nev and Yu. P. Zarichnyak, *Heat Conductivity of Mixtures and Composite Materials* (Énergiya, Leningrad, 1974).
11. E. Ya. Litovskiĭ, Izv. Akad. Nauk SSSR, Neorg. Mater. **16** (3), 559 (1980).
12. R. C. Zeller and R. O. Pohl, Phys. Rev. B **4** (6), 2029 (1971).
13. R. B. Stephens, Phys. Rev. B **8** (6), 2896 (1973).
14. V. N. Bogomolov, L. S. Parfen'eva, I. A. Smirnov, *et al.*, Fiz. Tverd. Tela (St. Petersburg) **43** (1), 182 (2001) [Phys. Solid State **43**, 190 (2001)].
15. L. I. Arutyunyan, V. N. Bogomolov, N. F. Kartenko, *et al.*, Fiz. Tverd. Tela (St. Petersburg) **39** (3), 586 (1997) [Phys. Solid State **39**, 510 (1997)].
16. V. N. Bogomolov, N. F. Kartenko, D. A. Kurdyukov, *et al.*, Fiz. Tverd. Tela (St. Petersburg) **41** (2), 348 (1999) [Phys. Solid State **41**, 318 (1999)].
17. V. F. Vzyatyshev, *Dielectric Waveguides* (Sov. Radio, Moscow, 1970), p. 213.

Translated by G. Skrebtsov

Physics of the Solid State, Vol. 44, No. 1, 2002, pp. 186–194. Translated from Fizika Tverdogo Tela, Vol. 44, No. 1, 2002, pp. 180–187.

FULLERENES AND ATOMIC CLUSTERS

Molecular Dynamics Study of Orientational Melting and Thermodynamic Properties of $C_{60}@C_{240}$ Nanoparticles

Yu. E. Lozovik and A. M. Popov

Institute of Spectroscopy, Russian Academy of Sciences, Troitsk, Moscow oblast, 142092 Russia

e-mail: lozovik@isan.troitsk.ru

Received February 26, 2001

Abstract—The barriers to relative shell rotation and other energy characteristics of $C_{60}@C_{240}$ two-shell carbon nanoparticles ("onions") with outer shells of different shapes are calculated. The disturbance of the orientational order in the mutual arrangement of shells with an increase in temperature (orientational melting) is studied by the molecular dynamics method. The intershell orientational diffusion is represented by the Arrhenius relationship, and the Arrhenius parameters are calculated numerically. A definition is proposed for the temperature of short-range order disturbance in systems that undergo melting without structural change. The calculated temperature of orientational melting of the $C_{60}@C_{240}$ nanoparticle is approximately equal to 60 K. © *2002 MAIK "Nauka/Interperiodica".*

1. INTRODUCTION

Over the last decade, after the discovery of fullerenes [1] and the development of the method of their preparation in macroscopic amounts [2], considerable interest has been expressed by researchers in other carbon nanostructures, specifically in nanoparticles that have a shell structure and can be produced in an arc discharge [3, 4]. The structure and energetics of these nanoparticles have been investigated in a number of works [5–13]. However, to date, the thermodynamic properties of these objects have not been adequately studied.

The melting of a cluster can differ essentially from phase transitions in macroscopic systems [14–20]. In particular, the melting of a cluster with a shell structure can be represented as a hierarchy of transitions with several stages in the destruction of the order of particle arrangement. For example, for two-dimensional clusters in an external confining potential with Coulomb [14–16], screened Coulomb [18], logarithmic [19], and dipole [20] interactions between particles, the disturbance of the order in the mutual arrangement of neighboring shells precedes the breakdown of the order in the particle arrangement inside the shell. This phenomenon, which involves relative reorientations of shells and, at an increasing temperature, their relative rotation, is referred to as the orientational melting of a cluster. Investigation into the relative rotation of shells in nanoparticles is of great interest in nanomechanics. In particular, Porto *et al.* [21] proposed a technique for transferring energy to a shell consisting only of three particles in such a way as to induce directed shell rotation.

The van der Waals interaction between atoms of neighboring shells in a carbon nanoparticle is considerably weaker than the chemical interaction between atoms inside the shell. It is quite probable that these objects undergo orientational melting [5]. Possible orientational melting was also considered for a long two-shell nanotube [22] and single-shell nanotube ropes [23].

In the present work, we investigated the orientational melting in a $C_{60}@C_{240}$ carbon nanoparticle composed of two shells, namely, C_{60} and C_{240} fullerenes with the I_h symmetry. The energy characteristics of the studied nanoparticle (such as the interaction and strain energies for shells and the barriers to their relative rotation) were determined at zero temperature. The thermodynamic properties of the nanoparticle in the course of orientational rotation were investigated using the molecular dynamics technique. A definition was proposed for the temperature of complete orientational melting of a nanoparticle. This temperature was calculated.

2. NUMERICAL CALCULATION AND SIMULATION TECHNIQUES

Our choice of the nanoparticle shells (C_{60} and C_{240} fullerenes with the I_h symmetry) as the subject of investigation was made for the following reasons. First, the examination of transmission electron microscope images of nanoparticles revealed that the diameter of the inner shell can be close to the diameter of the C_{60} fullerene [24, 25]. Second, fullerenes whose size is smaller than that of C_{60} are absent among the fullerenes extracted from fullerene-containing soot with benzene, toluene, and other solvents (see, for example, [26, 27]). This fact was explained under the assumption that fullerene atoms shared by two adjacent pentagons can form chemical bonds with neighboring fullerenes and

1063-7834/02/4401-0186$22.00 © 2002 MAIK "Nauka/Interperiodica"

other clusters and molecules involved in the soot [28, 29]. These chemical bonds between neighboring fullerenes are observed, for example, in C_{36} fullerene crystals [30]. Fullerene C_{60} with the I_h symmetry is the smallest fullerene whose structure contains no adjacent pentagons. Thus, we believe that the C_{60} fullerene with the I_h symmetry is the smallest inner shell for which chemical bonds with the outer shell are, most probably, absent (this is the necessary condition for relative rotation of shells). Fullerene C_{240} with the I_h symmetry was chosen as the outer shell of the nanoparticle. In this case, the theoretical distance between the shells agrees with the experimental distance determined by Ugarte [25]. Moreover, the binding energy of the C_{240} fullerene with the I_h symmetry is higher than that of C_{240} fullerenes of the other structure [7].

The lengths of single and double bonds in the C_{60} fullerene were taken equal to 1.455 and 1.391 Å, respectively [31]. We considered five different shapes of the second C_{240} shell with the I_h symmetry. Shapes *B*, *C*, *D*, and *E* were obtained from first-principles calculations of the binding energy minima for the C_{240} fullerene with the I_h symmetry by optimizing seven independent geometric parameters [5, 8, 9]. Shapes *B* and *D* correspond to the global and local binding energy minima of the C_{240} shell [8] and are similar to a sphere and a truncated icosahedron, respectively. Shapes *C* and *E* are similar to each other and are intermediate between the *B* and *D* shapes. The former (*C* and *E*) shapes correspond to the sole binding energy minima determined by Yoshida and Osawa [5] and Scuceria [9]. All atoms of the C_{240} shell with shape *A* are arranged on a sphere. This shape was obtained by optimizing three independent geometric parameters [8].

The van der Waals interaction between atoms of the neighboring shells can be described by the Lennard-Jones potential $U = 4\varepsilon[(\sigma/r)^{12} - (\sigma/r)^6]$ with parameters $\varepsilon = 28$ K and $\sigma = 3.4$ Å. These parameters were used by Cheng and Klein [32] to simulate a solid C_{60} fullerene. The atomic interaction inside the C_{60} and C_{240} shells can be represented by the Born potential:

$$U = \frac{\alpha - \beta}{2} \sum_{i,j=1}^{60} \left(\frac{(\mathbf{u}_i - \mathbf{u}_j)\mathbf{r}_{ij}}{|\mathbf{r}_{ij}|} \right)^2 + \frac{\beta}{2} \sum_{i,j=1}^{60} (\mathbf{u}_i - \mathbf{u}_j)^2,$$

where $\mathbf{u}_i$ and $\mathbf{u}_j$ are the atomic displacements from equilibrium positions at zero temperature and $\mathbf{r}_{ij}$ are the interatomic distances. The parameters of the potential $\alpha = 1.14 \times 10^6$ dyn/cm and $\beta = 1.24 \times 10^5$ dyn/cm were taken from Jiang *et al.* [33], who used the Born potential to calculate the spectrum of the internal vibrations of the C_{60} fullerene. It is evident that the Born potential adequately describes the interaction only in the vicinity of the potential well bottom. However, the use of the simple Born potential in this work is justified, because the system is studied at temperatures that are tens times less than the temperature of bond breaking in fullerenes.

The orientational melting of $C_{60}@C_{240}$ nanoparticles whose second shells have a *D* shape was investigated by the molecular dynamics technique. The molecular dynamics simulation was performed within a microcanonical ensemble. The equations of motion were integrated using a step-by-step scheme with a time step $t = 6.1 \times 10^{-16}$ s. This corresponds to approximately 100 steps per period of atomic vibrations inside the shell. At the initial instant of time, the velocities of atoms in the outer graphitic layer were specified with a Maxwell distribution in a random manner and the atomic deviations from equilibrium positions were assigned to a Gaussian distribution in such a way that the kinetic energy was approximately equal to the internal energy of the shell according to the virial theorem for harmonic potential. The system was equilibrated for 300–500 ps, which corresponds to approximately 30 periods of rotational vibrations of the shells. In this time interval, the root-mean-square fluctuations of the total energy and temperature decayed and reached steady-state values. Then, the properties of the system were analyzed for 100 ps. The root-mean-square fluctuations of the total energy were less than 0.3% of the kinetic energy, and the root-mean-square fluctuations of temperature were less than 1.3%. The time it took for the angular velocities of the shells to change their directions was long as compared to the time reachable in the given numerical experiment. Therefore, all the physical quantities at each temperature involved were obtained by averaging over 34–46 numerical experiments with different random directions and magnitudes of angular velocities of the shells in accordance with the distribution of these velocities at the given temperature.

3. RESULTS AND DISCUSSION

3.1. Energy characteristics of nanoparticles. The global and local minima of the potential energy (including the intershell interaction and shell strain energies) for $C_{60}@C_{240}$ nanoparticles were determined by optimizing three angles of mutual orientation of the shells and the interatomic bond lengths inside the shell. (The intershell interaction energy minima and the barriers to rotation of the shells without regard for their strain were calculated for several shapes of the second shell in our earlier work [34].) The angles α_z, α_y, and α_x of successive rotations of the first shell about the *OZ*, *OY*, and *OX* axes of the coordinate system were used as the angles of mutual orientation of the shells. Figure 1 displays the initial shell orientation from which the α_z, α_y, and α_x angles were reckoned. The centers of both shells coincide with the origin of the coordinate system. Owing to the high symmetry I_h of the shells, the number of the equivalent global or local potential energy minima of the nanoparticle is equal to 60. These equivalent minima are attributed to different mutual shell orientations.

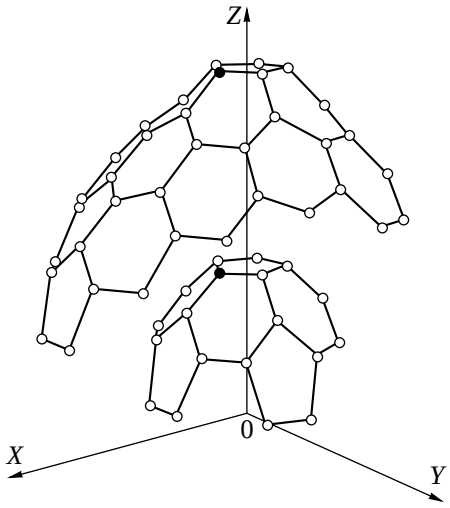

Fig. 1. Fragments of two shells (the second shell has the *D* shape) with the initial orientation. *OX*, *OY*, and *OZ* are the axes of the coordinate system. One of the fivefold axes of both shells coincides with the *OZ* axis. In each shell, one atom (closed circles) nearest to the *OZ* axis is located in the *OXZ* plane: this fixes the orientation of shells with respect to the *OX* and *OY* axes.

Table 1 lists the intershell interaction energies and the orientation angles that correspond to the global and local potential energy minima of a nanoparticle with a particular mutual shell orientation.

The intershell interaction energies calculated in this work are insignificantly less than those determined for the studied nanoparticle within the framework of the other models of van der Waals interaction (16.9 [10], 18.57 [11], and 20.3 meV/atom [10]) and are approximately three times less than the estimate obtained for graphite [35]. Note that, contrary to the assumption made by Lu and Yang [11], the energy of interaction between spherical shells is not maximum.

Table 1. Intershell interaction energies E and the angles α_z, α_y, and α_x for the global and local potential energy minima of the nanoparticle with a particular mutual shell orientation

Shape	E, meV/atom	α_z, rad	α_y, rad	α_x, rad
A	15.034	0.0819	0.1452	0.0540
A	15.033	0.2495	0.8128	−0.0081
A	15.032	0.6283	0.4634	0.0
B	15.124	0.6283	0.4634	0.0
B	15.101	0.0	0.0	0.0
C	15.180	0.0	0.0	0.0
C	15.098	0.6283	0.4634	0.0
D	13.819	0.0	0.0	0.0
D	13.777	0.6283	0.4634	0.0
E	15.166	0.0	0.0	0.0
E	15.061	0.6283	0.4634	0.0

According to our calculations, the mutual shell orientation angles that correspond to the potential energy minima of the nanoparticle are determined by the shape of the second shell. For the *C*, *D*, and *E* shapes similar to the shape of a truncated icosahedron, the mutual orientation of shells with aligned symmetry axes corresponds to the global potential energy minimum of the nanoparticle. Selected global minima of the potential energy are shown in Fig. 2a. In the case of a nearly spherical shape *B*, this mutual orientation corresponds only to the local minimum of the potential energy (Fig. 2b). For spherical shape *A*, the mutual shell orientation with the aligned symmetry axes is inconsistent with all minima of the potential energy. It is of interest that the differences ΔE_{loc} between the potential energies of nanoparticles at global and local minima are several orders of magnitude less than the potential energy itself and (as is the case with the angles of mutual shell orientation) are determined by the shape of the second shell (Table 2). It is this small difference that is responsible for the orientational melting at low temperatures. Table 2 presents the geometric parameters of the second shell, which determine the ΔE_{loc} differences. These parameters are as follows: (1) the difference $l = h - r_{min}$ (where $h = \langle R_{i2}\rangle - \langle R_{i1}\rangle$ is the mean distance between the shells, R_{i1} and R_{i2} are the distances from the nanoparticle center to atoms of the first and second shells, and r_{min} is the intershell distance corresponding to the minimum of the interatomic potential) and (2) the mean deviation of the second shell from spherical shape, $\langle \Delta R_{i2}\rangle = \langle |R_{i2} - \langle R_{i2}\rangle|\rangle$.

The differences ΔE_{loc} are especially small for nanoparticles with a small value of $\langle \Delta R_{i2}\rangle$, i.e., when the second shell is nearly spherical or spherical (the *A* and *B* shapes). Moreover, among nanoparticles with second shells similar in shape to a truncated icosahedron (the *C*, *D*, and *E* shapes), the difference between the global and local minima for the *D* shape is several times smaller. This fact can be explained as follows. The l value for the nanoparticle with the second shell of the *D* shape is several times smaller than those for the nanoparticles with the second shells of the *C* and *E* shapes; i.e., the distance between the shells in the nanoparticle with the second shell of the *D* shape is several times closer to the value corresponding to the interparticle potential bottom. Consequently, in this particle, a smaller number of the distances d_{12} between atoms of different shells falls in the interatomic potential range characterized by a steeper dependence of the interaction energy on the distance. Therefore, the change in the d_{12} distances upon shell rotation more weakly affects the change in the intershell interaction energy and leads to a smaller difference between the interaction energies for different mutual shell orientations.

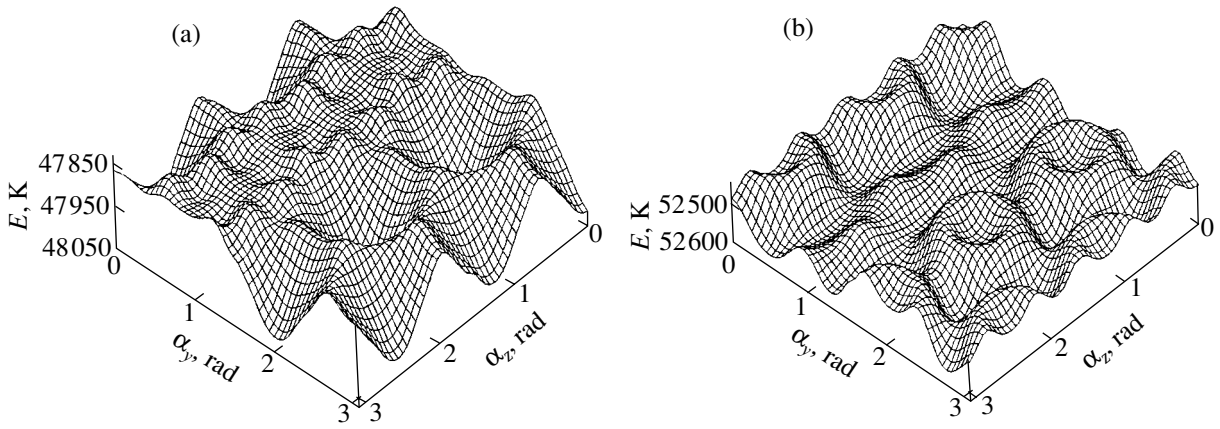

Fig. 2. Dependences of the intershell interaction energy E on the angles of mutual shell orientation for different shapes of the second shell: (a) D and (b) B. α_z and α_y are the angles of successive rotations of the first shell from the initial orientation about the OZ and OY axes of the coordinate system. The angle of rotation about the OX axis is taken equal to zero.

The shell strain energies averaged over three angles of the mutual shell orientation are given in Table 2. The effect of the shell strain on the barriers to relative shell rotation at zero temperature was analyzed in terms of the barriers B_5 to the relative rotation of shells about a fivefold axis as an example. (This rotation began from the mutual orientation of the shells with the aligned symmetry axes.) A comparison of the B_5 barriers calculated with and without inclusion of the shell strain demonstrates that the inclusion of the shell strain leads to a change in the B_5 barriers by less than 1% for all five shapes of the second shell. For this reason, we disregarded the shell strain in the calculation of the barriers to relative shell rotation at zero temperature. (The interatomic bond lengths and bond angles in the shells were fixed during their rotation.) Note that the reverse is true, for example, in a cluster with a logarithmic interparticle interaction [19]. In this case, the interactions between particles in the same and neighboring shells are identical and the inclusion of the shell strain is necessary for adequate calculation of the barriers to shell rotation. When calculating the barriers to relative shell rotation, the symmetry centers of the shells were fixed at the same point, because the displacement of shells with respect to each other only increases the potential energy of the nanoparticle.

The energy barriers to relative rotation of the shells were calculated for the mutual shell orientations corresponding to the global potential energy minima of the nanoparticle (Table 1). The surprising thing is that the rotation barriers are only several times higher than the barriers ΔE_a in the dependence of the energy of interaction between one atom of the second shell and all atoms of the first shell on the shell rotation angle. For example, the barrier to rotation about the fivefold axis for the nanoparticle with the second shell of shape D is equal to 158.8 K. On the other hand, the maximum barrier among the ΔE_a barriers for different atoms of the second shell for this rotation is 21.6 K. A detailed analysis demonstrates that the maxima of the ΔE_a barriers for different atoms are observed at different angles of shell rotation. As a result, the dependence of the intershell interaction energy on the rotation angle is considerably smoothed (Fig. 3). This leads to a substantial decrease in the effective barrier to shell rotation. The barriers to

Table 2. Characteristics of nanoparticles at zero temperature: geometric parameters l and $\langle \Delta R_{i2} \rangle$; differences ΔE_{loc} between the global and local minima of the total energy for the nanoparticle; the minimum $B_{\min}$ and average $B_{\text{av}} \pm \Delta B_{\text{av}}$ barriers to relative shell rotation (the B_{av} barriers are obtained by averaging over the rotation axis directions, and ΔB_{av} is the variance of this barrier); and the mean strain energies $E_{s1} \pm \Delta E_{s1}$ and $E_{s2} \pm \Delta E_{s2}$ for the first and second shells, respectively (the E_{s1} and E_{s2} energies are obtained by averaging over three angles of the relative shell orientation and ΔE_{s1} and ΔE_{s2} are the variances of these energies)

Shape	l, Å	$\langle R_{i2} \rangle$, Å	ΔE_{loc}, K	$B_{\min}$, K	$B_{\text{av}} \pm \Delta B_{\text{av}}$, K	$E_{s1} \pm \Delta E_{s1}$, K	$E_{s2} \pm \Delta E_{s2}$, K
A	−0.245	0.0	3.2, 5.5	19.0	20.5 ± 0.8	2.09 ± 0.02	34.56 ± 0.12
B	−0.258	0.057	76.7	82.9	122.1 ± 12.1	1.62 ± 0.07	29.98 ± 0.50
C	−0.289	0.152	287.4	349.3	363.1 ± 8.8	2.17 ± 0.26	18.19 ± 0.42
D	−0.119	0.244	144.4	160.3	177.3 ± 9.6	3.75 ± 0.20	34.40 ± 0.55
E	−0.299	0.147	368.3	441.2	459.9 ± 12.9	4.58 ± 0.44	13.78 ± 0.38

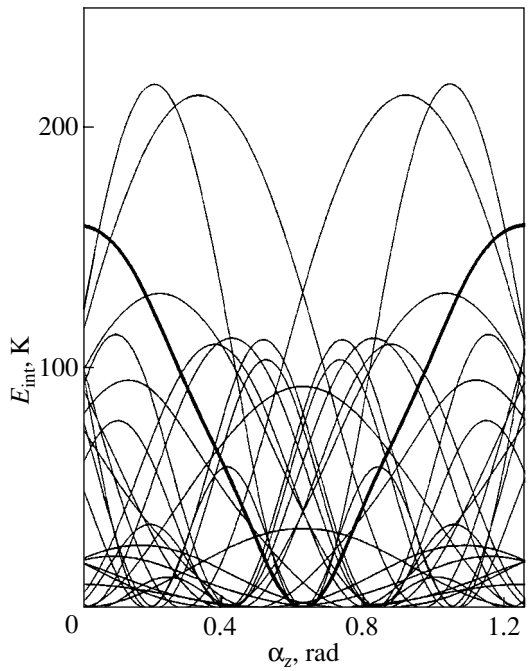

Fig. 3. Dependences of the energy of interaction between the first nanoparticle shell and groups of atoms of the second shell of shape *D* on the angle α_z of rotation of the first shell from the initial orientation about the *OZ* axis. Each group of atoms involves all the atoms characterized by the same dependence of the energy E_a of interaction between an individual atom and the first shell on the rotation angle. The thin lines correspond to 25 groups of atoms (23 groups of 10 atoms each and 2 groups of 5 atoms each) with different dependences of the energy E_a on the rotation angle. The thick line represents the dependence of the total energy of interaction between the nanoparticle shells on the rotation angle α_z. All the energies are measured from their minima.

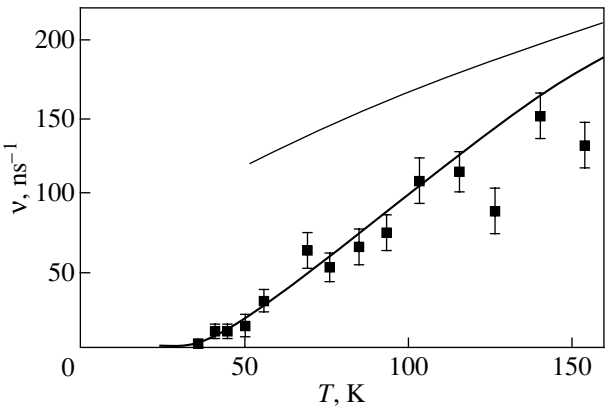

Fig. 4. Temperature dependences of the shell reorientation frequency ν. Points are the results of simulation. The thick line is the interpolation according to the Arrhenius formula (1) at temperatures $kT \ll B_{\text{eff}}$. The thin line represents the estimates obtained from relationship (2) at $kT \gg B_{\text{re}}$.

relative shell rotation are also governed by the shape of the second shell. Similarly to the behavior of the difference between the global and local potential energy minima of the nanoparticle (see above), the rotation barriers decrease at $\langle R_{i2} \rangle \longrightarrow 0$ and $h \longrightarrow r_{\min}$. Note that the calculation for the second shell of spherical shape results in an appreciable underestimation of the rotation barriers.

Thus, our calculations demonstrated that the barriers to relative shell rotation are very sensitive to the shape of the second shell. As a result, the barriers calculated using different shapes (taken from [5, 8, 9]) of the second shell in the nanoparticle vary over a wide range (from 80 to 500 K). However, the barrier to relative rotation of shells about the fivefold axis in the $C_{60}@C_{240}$ nanoparticle with the second shell of shape *E*, which was calculated in our work with due regard for the shell strain, is only 12% less than the barrier obtained from quantum-chemical calculations for the same direction of the rotation axis and shape of the second shell [5]. Therefore, in our calculations, the van der Waals interaction between the shells is adequately described by the simple Lennard-Jones potential.

3.2. Simulation of orientational melting. By using the molecular dynamics method, we obtained the temperature dependences of the following quantities: the total energy for the nanoparticle, the shell reorientation frequency, the angular velocity autocorrelation functions of shells, the spectrum of rotational vibrations of shells (librons), the distribution of the Eulerian angles of mutual shell orientation, and the real barriers in the intershell interaction energy at the instant of reorientation.

The temperature dependence of the total energy was used to calculate the heat capacity of the nanoparticle. In the temperature range 30–150 K, the difference between the heat capacity per degree of freedom and a similar heat capacity for a system of harmonic oscillators appears to be less than 2%. This is less than the computational error, which does not exceed 5%. Only three degrees of freedom are associated with the mutual orientation of shells. Therefore, as could be expected, features in the temperature dependence of the heat capacity for the nanoparticle are absent and the orientational melting of the two-shell carbon nanoparticle has a crossover character.

The numerically simulated temperature dependence of the shell reorientation frequency ν is plotted in Fig. 4. The hopping orientational diffusion of shells proceeds in the temperature range $kT \ll B_{\text{eff}}$ (where B_{eff} is the effective energy barrier to shell reorientation). In this temperature range (30–150 K), we interpolated the shell reorientation frequency ν by using the Arrhenius formula (thick line in Fig. 4):

$$\nu = \Omega_0 \exp\left(-\frac{B_{\text{eff}}}{kT}\right), \qquad (1)$$

where Ω_0 is the preexponential factor. The least-squares fitting gives the following Arrhenius parameters: B_{eff} = 167 ± 22 K and Ω_0 = 540 ± 180 ns^{-1}. The use of a narrower temperature range (T = 30–75 K) for the interpolation only slightly affects the calculated parameters B_{eff} and Ω_0. It is of interest that the B_{eff} effective barrier obtained in the numerical experiment is in agreement (within the limits of error) with the minimum (B_{min}) and average (B_{av}) barriers to relative shell rotation at zero temperature. This allows one to use the barriers B_{min} and B_{av} as the effective barrier in estimating the orientational melting temperature of carbon nanoparticles and nanotubes.

The reorientation frequency ν ceases to increase exponentially at temperatures of 100–150 K, which indicates the onset of the relative shell rotation (shell rotations in this temperature range were observed in approximately 30% of the numerical experiments). It can be demonstrated that the reorientation frequency ν in the case of free shell rotation (at temperatures $kT \gg B_{eff}$) can be estimated from the relationship

$$\nu = \frac{n}{2\pi}\sqrt{\frac{3kT(I_1 + I_2)}{I_1 I_2}}, \qquad (2)$$

where n is the mean number of reorientations over the period of the relative shell rotation ($n \approx 5$) and I_1 and I_2 are the moments of inertia of the first and second shells, respectively. The temperature dependence of the shell reorientation frequency ν calculated from relationship (2) is shown by the thin line in Fig. 4 (the moments of inertia of unstrained shells were used in the calculations).

The considerable smoothing of the distributions of the Eulerian angles of mutual shell orientation (Fig. 5) and the disappearance of maxima in the angular velocity autocorrelation functions of the shells (Fig. 6) and in the libron spectrum (Fig. 7) confirm the assumption that the shell rotation determines the thermodynamic properties of the nanoparticle at temperatures above 140 K.

The experimental values of the barrier B_{re} in the intershell interaction energy were obtained by averaging over all the observed reorientations (approximately 30–70 reorientations at temperatures in the range from 40 to 55 K and 200–600 reorientations at temperatures in the range from 70 to 150 K). The temperature dependence of the B_{re} barrier is displayed in Fig. 8. In the temperature range 30–100 K (characterized by the hopping orientational diffusion of shells), the B_{re} barriers reasonably agree with the minimum barrier B_{min} to shell rotation (Table 2) and the effective barrier B_{eff} in the Arrhenius formula. At 100–150 K, when the shells begin to rotate freely, the real barriers increase by ΔB_{re}, which becomes equal to about 50 K at a temperature of 154 K. This increment exceeds the variance ΔB_{av} (10 K) of the barrier to shell rotation at zero temperature (Table 2). Consequently, it is impossible to explain the increment ΔB_{re} in the barriers in terms of the fact that, as the temperature increases, the barrier can be overcome not only in its deepest point. Hence, we believe that the increment ΔB_{re} in the real barriers with an increase in the temperature results from the shell strain. The effect of the shell strain on the B_{re} barriers is also

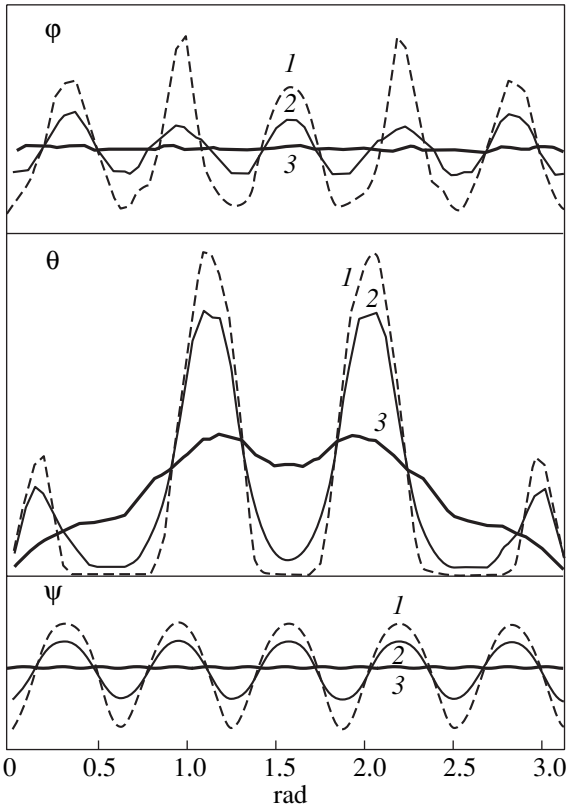

Fig. 5. Distributions of Eulerian angles of the mutual shell orientation at temperatures T = (*1*) 21, (*2*) 36, and (*3*) 140 K. θ, ψ, and φ are the polar angle and azimuths of the mutual shell orientation.

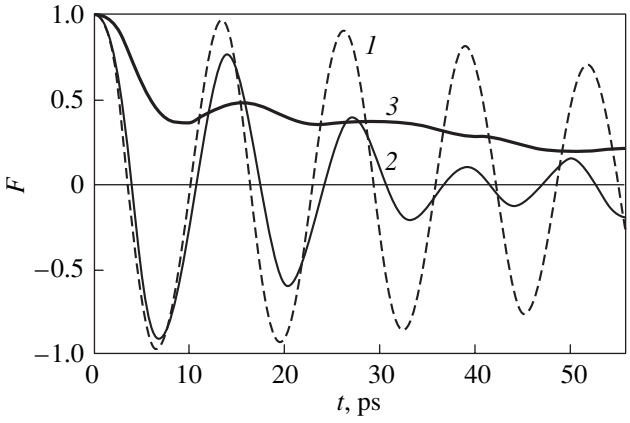

Fig. 6. Angular velocity autocorrelation functions F of the first shell at temperatures T = (*1*) 21, (*2*) 36, and (*3*) 140 K.

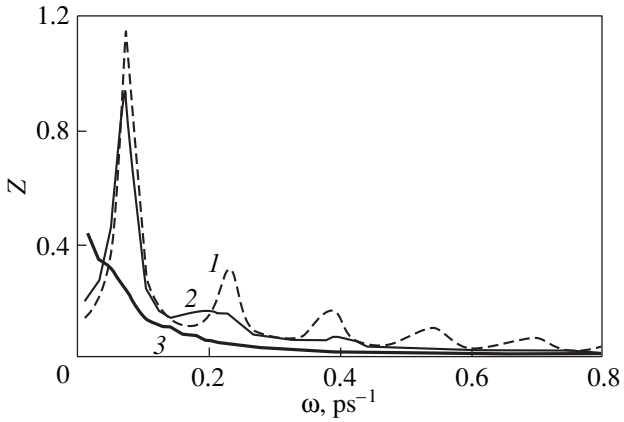

Fig. 7. Libron spectra Z at temperatures T = (*1*) 21, (*2*) 36, and (*3*) 140 K.

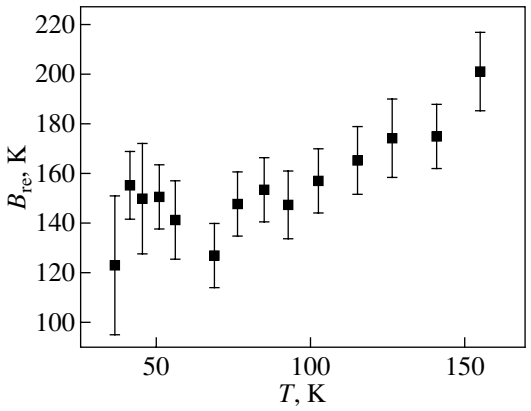

Fig. 8. Temperature dependence of the barrier B_{re} in the intershell interaction energy.

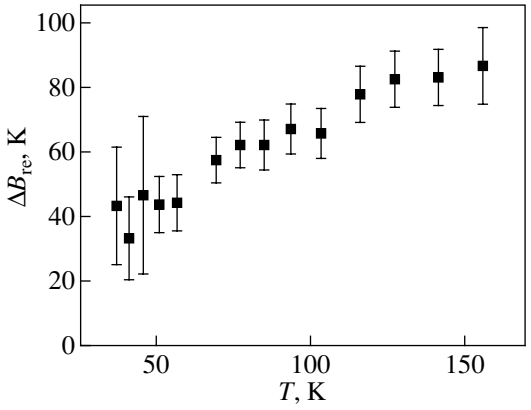

Fig. 9. Temperature dependence of the variance ΔB_{re} of the barrier in the intershell interaction energy.

indicated by an increase in the variance ΔB_{re} of the barriers with an increase in the temperature (Fig. 9). Note that the shell strain energy is three orders of magnitude larger than the increase in the B_{re} barriers due to the shell strain. (The shell strain energies E_s determined in the numerical experiment are consistent with the virial theorem for a harmonic system $E_s = kT(3N - 6)/2$, where N is the number of atoms in the shell.)

As a rule, the phenomena associated with the disturbance of order in systems with a finite number of particles take place in a certain temperature range. This presents problems in attempts to define the temperature of order disturbance in these systems (see, for example, [36] and references therein). During melting of the majority of clusters (as during melting of a macroscopic system), as the temperature increases, the cluster structure undergoes a change and, in addition to the ground state, other potential energy minima are filled in the system. In a number of cases, the system upon melting fluctuates between different states separated by barriers: the solid state corresponding to the ground state of the system and the liquid state with a structure corresponding to other potential energy minima. Jellinek *et al.* [37] proposed to characterize this system in the course of melting by the quantity $K = \gamma_l/\gamma_s$, where γ_l and γ_s are the probabilities of the system occurring in the liquid and solid states, respectively. In this case, the temperature at which the system spends equal time in each of the two states, i.e., at which $K = 1$, can be considered the melting temperature.

In our system (the $C_{60}@C_{240}$ nanoparticle), the shell reorientations upon orientational melting are transitions between the states corresponding to the equivalent minima of the potential energy. Therefore, the orientational melting of this nanoparticle does not lead to a change in its structure. In order to characterize the "degree of melting" of the systems in which the order disturbance is accompanied by the appearance of diffusion without structural changes, we propose to use the quantity $K_m = \nu_t/\omega_t$, where ν_t is the frequency of transitions between the equivalent potential energy minima and ω_t is the frequency of vibrations at which particle motion provides the transition. In our opinion, the temperature of the order disturbance in the systems under consideration can be defined as the temperature T_c at which $K_m = 1$ (i.e., one-half the relevant vibrations are attended by the transition to the equivalent minimum). It should be noted that the proposed definition (unlike the above definition for systems with transitions between nonequivalent minima) adequately describes the temperature of the short-range order disturbance and has no parallels with phase transitions in macroscopic systems.

For the $C_{60}@C_{240}$ nanoparticle, the quantity $K_r = \nu/\omega$ (where ν is the shell reorientation frequency and ω is the frequency of rotational vibrations of the shells) characterizes its orientational melting. The equality $K_r = 1$ implies that, in half the cases, the relative rotational vibration of shells starts in a particular minimum (in the dependence of the total energy of the nanoparticle on the mutual shell orientation angles) and is com-

pleted by the transition to the neighboring minimum rather than by the return to the initial minimum. The orientational melting temperature T_c (K_r = 1) numerically simulated for the $C_{60}@C_{240}$ nanoparticle with a second shell of shape *D* is equal to ≃60 K (the frequency of rotational vibrations of shells was determined from the maximum in the libron spectrum).

According to the calculations carried out in the present work, the barriers to relative shell rotation are very sensitive to the shell shape. Consequently, the possibility of the orientational melting occurring in multiple-shell carbon nanoparticles is determined by their shape. The nanoparticles formed in the arc discharge, as a rule, have a faceted shape [3, 4]. However, their shape becomes almost spherical under electron bombardment [25, 35, 38]. This should lead to a decrease in the barriers to relative shell rotation and, hence, in the orientational melting temperature. Different theoretical works predict faceted [7, 10] and spherical [11, 13] shapes of multiple-shell nanoparticles and also the transformation from a faceted to a spherical shape of shells containing more than 3500 atoms [39]. Furthermore, according to the calculations performed by Maiti *et al.* [10, 12], faceted nanoparticles can transform into spherical nanoparticles with an increase in the temperature. In this case, the barriers to relative shell rotation can decrease with an increase in the temperature due to a change in the shell shape. The orientational melting temperature determined for the $C_{60}@C_{240}$ nanoparticle, $T_c \simeq 60$ K, is more than one order of magnitude smaller than the destruction temperature of the shells. Hence, we assume that the orientational melting can also proceed in carbon nanoparticles and short nanotubes comprised of several shells [40].

The carbon nanoparticles with a shell structure are not unique examples of nanoparticles with different types of interactions between atoms in the same and neighboring shells. For example, a two-shell nanoparticle composed of MoS_2 was obtained by Srolovita *et al.* [13]. We believe that orientational melting can also occur in nanoparticles consisting of this and other similar materials (MX_2, where *M* = Mo or W and *X* = S or Se) with a layered structure.

The orientational melting of nanoparticles with a shell structure can be revealed from the experimental temperature dependence of the linewidth in the IR and Raman spectra. Actually, the rotational diffusion of shells should result in the Arrhenius contribution to the relevant linewidths (as in plastic crystals [41]). These investigations also make it possible to estimate the reorientation barrier. Moreover, the orientational melting can lead to the narrowing of NMR lines.

ACKNOWLEDGMENTS

This work was supported by the Russian Foundation for Basic Research, the Russian Research Program "Fullerenes and Atomic Clusters," and the International Scientific and Technical Program "Physics of Solid-State Nanostructures."

REFERENCES

1. H. W. Kroto, J. R. Heath, S. C. O'Brien, *et al.*, Nature **318** (6042), 162 (1985).
2. W. Kratschmer, L. D. Lamb, K. Fostiroupolos, and D. R. Huffman, Nature **347** (6291), 354 (1990).
3. S. Iijima, J. Cryst. Growth **50**, 675 (1980).
4. D. Ugarte, Chem. Phys. Lett. **198** (6), 596 (1992).
5. M. Yoshida and E. Osawa, Fullerene Sci. Technol. **1** (1), 54 (1993).
6. D. Tomanek, W. Zhang, and E. Krastev, Phys. Rev. B **48** (20), 15461 (1993).
7. A. Maiti, C. J. Brabec, and J. Bernhole, Phys. Rev. Lett. **70** (20), 3023 (1993).
8. D. York, J. P. Lu, and W. Yang, Phys. Rev. B **49** (12), 8526 (1994).
9. G. E. Scuceria, Chem. Phys. Lett. **243** (3–4), 193 (1995).
10. A. Maiti, C. J. Brabec, and J. Bernhole, Mod. Phys. Lett. B **7** (29–30), 1883 (1993).
11. J. P. Lu and W. Yang, Phys. Rev. B **49** (16), 11421 (1994).
12. A. Maiti, C. J. Brabec, and J. Bernhole, Chem. Phys. Lett. **219** (5–6), 473 (1994).
13. D. J. Srolovita, S. A. Safran, M. Homyonfer, and R. Tenne, Phys. Rev. Lett. **74** (10), 1779 (1995).
14. Yu. E. Lozovik, Usp. Fiz. Nauk **153** (2), 356 (1987) [Sov. Phys. Usp. **30**, 912 (1987)].
15. Yu. E. Lozovik and V. A. Mandelshtam, Phys. Lett. A **145** (5), 269 (1990).
16. Yu. E. Lozovik and E. A. Rakoch, Phys. Lett. A **240** (6), 311 (1998).
17. V. M. Bedanov and F. M. Peeters, Phys. Rev. B **49** (4), 2667 (1994).
18. G. E. Astrakharchik, A. I. Belousov, and Yu. E. Lozovik, Phys. Lett. B **258** (2–3), 123 (1999).
19. Yu. E. Lozovik and E. A. Rakoch, Phys. Rev. B **57** (2), 1214 (1998).
20. Yu. E. Lozovik and E. A. Rakoch, Phys. Lett. A **235** (1), 55 (1997).
21. M. Porto, M. Urbakh, and J. Klafter, Phys. Rev. Lett. **84** (26), 6058 (2000).
22. Y. K. Kwon and D. Tomanek, Phys. Rev. B **58** (24), R16001 (1998).
23. Y. K. Kwon and D. Tomanek, Phys. Rev. Lett. **84** (7), 1483 (2000).
24. S. Iijima, J. Phys. Chem. **91** (13), 3466 (1987).
25. D. Ugarte, Nature **359** (6397), 707 (1992).
26. D. H. Parker, P. Wurz, K. Chatterrjee, *et al.*, J. Am. Chem. Soc. **113**, 7499 (1991).
27. Y. Chai, T. Guo, C. Jin, *et al.*, J. Phys. Chem. **95** (20), 7564 (1991).
28. Yu. E. Lozovik and A. M. Popov, Phys. Low-Dimens. Struct. **6**, 33 (1994).
29. Yu. E. Lozovik and A. M. Popov, Usp. Fiz. Nauk **167** (7), 751 (1997) [Phys. Usp. **40**, 717 (1997)].

30. C. Pishoti, J. Yarger, and A. Zetti, Nature **395** (6704), 771 (1998).
31. W. I. F. David, R. M. Ibberson, J. C. Matthewman, *et al.*, Nature **353** (6340), 147 (1991).
32. A. Cheng and M. L. Klein, J. Phys. Chem. **95** (18), 6750 (1991).
33. Q. Jiang, H. Xia, Z. Zhang, and D. Tian, Chem. Phys. Lett. **191** (1–2), 197 (1991).
34. Yu. E. Lozovik and A. M. Popov, Phys. Low-Dimens. Struct. **8–9**, 63 (1997).
35. D. Ugarte, Europhys. Lett. **22** (1), 45 (1993).
36. P. Borrmann, O. Mülken, and J. Harting, Phys. Rev. Lett. **84** (16), 3511 (2000).
37. J. Jellinek, T. L. Beck, and R. S. Berry, J. Chem. Phys. **84** (5), 2783 (1986).
38. D. Ugarte, Chem. Phys. Lett. **207** (4–6), 473 (1993).
39. A. Pérez-Garrido, Phys. Rev. B **62** (11), 6979 (2000).
40. Yu. E. Lozovik, Phys. Low-Dimens. Struct. (2002) (in press).
41. G. N. Zhizhin, Yu. E. Lozovik, M. A. Moskalova, and A. Usmanov, Dokl. Akad. Nauk SSSR **190** (1–3), 301 (1970) [Sov. Phys. Dokl. **15**, 36 (1970)].

Translated by O. Borovik-Romanova

Physics of the Solid State, Vol. 44, No. 1, 2002, pp. 195–198. Translated from Fizika Tverdogo Tela, Vol. 44, No. 1, 2002, pp. 188–191.

FULLERENES AND ATOMIC CLUSTERS

Relaxation Contribution to Shear Moduli of the Low-Temperature Phase of Solid C_{60}

N. P. Kobelev

Institute of Solid-State Physics, Russian Academy of Sciences, Chernogolovka, Moscow oblast, 142432 Russia
e-mail: kobelev@issp.ac.ru

Received May 7, 2001

Abstract—The relaxation contribution of the molecular reorientation in an elastic field of an acoustic wave to the effective shear moduli is calculated in the framework of the phenomenological two-level model of orientational states in the low-temperature phase of solid C_{60}. The polarity of the rotation axis of C_{60} molecules and the possible existence of orientational domains in the structure of the low-temperature phase are taken into consideration. The estimates obtained are compared with the available experimental data. © *2002 MAIK "Nauka/Interperiodica".*

1. INTRODUCTION

It is known [1–4] that, upon cooling of solid C_{60}, an orientational phase transition from the face-centered cubic phase to the simple cubic phase with the $Pa\bar{3}$ symmetry occurs in the range of T_c = 260 K. However, C_{60} molecules partially retain their orientational mobility [5]: in the low-temperature phase, C_{60} molecules can rotate about the [111]-type axes of the crystal so that, for all four molecules in the unit cell, the directions of these axes differ from one another. The rotation of C_{60} molecules brings about a change in their mutual orientation and, consequently, a change in the molecular interaction energy; in this case, the intermolecular energy exhibits two minima depending on the rotation angle, namely, the absolute energy minimum (the so-called pentagonal orientation) and the relative minimum (the hexagonal orientation) [6–8]. This situation has been described in the framework of the phenomenological model of double-well orientational potential [6, 9–11], according to which a molecule can reside in two energy states that differ from each other by approximately 10 meV [6, 10, 12] and are separated by a potential barrier of approximately 0.3 eV [5, 10, 12–14]. (In principle, the orientational motion of molecules has a cooperative character; however, recent estimates [15] demonstrated that the activation volume involved in an elementary act of a transition from one energy state to another is approximately equal to the crystal volume per C_{60} molecule, which confirms the validity of the phenomenological single-particle (single-molecule) model used in the case under investigation.) A considerable amount of C_{60} molecules (~40%) at temperatures close to the orientational phase transition point can occur in the excited state due to thermal motion. As is known, external actions upset the equilibrium of a system. In the case when an acoustic wave propagates in the material, the disturbance of the equilibrium gives rise to an additional inelastic strain and additional relaxation contribution to the effective elastic moduli [11, 15–18]. The available experimental data on the temperature dependences of the elastic properties of solid C_{60} suggest the relaxation contribution to the effective elastic moduli [15–20]. Moreover, the estimates made for the activation parameters of the relaxation process are in agreement with the results obtained using other techniques [5, 10, 12–14, 21]. It should be noted that theoretical calculations (see, for example, [11]) have predicted a similar relaxation contribution only in the case of elastic vibrations of the longitudinal type that are accompanied by dilatation of the crystal. However, the recent investigation [15] experimentally revealed an additional relaxation contribution to the effective shear moduli. As will be shown below, the inclusion of specific structural features of the C_{60} low-temperature solid phase in the theoretical treatment also leads to the relaxation contribution of the molecular reorientation to the effective shear moduli.

2. THEORETICAL ANALYSIS

2.1. A C_{60} molecule should possess a polar rotation axis in a simple cubic lattice, as predicted by theoretical calculations [22]. In general, this is predetermined by the crystal symmetry ($Pa\bar{3}$) and stems from the fact that the {110} crystal planes passing through the rotation axis of a molecule are not planes of symmetry for this molecule (according to recent estimates [8, 23], the deviation of the symmetry planes of the molecule from the {110} planes ranges from 2° to 6°). The crystal symmetry is also responsible for the structural isomorphism of the phase under investigation [24]. In this case, the coexistence of isomorphic structures through the formation of domains is energetically more favor-

able than that in the form of a homogeneous solution. Therefore, it can be assumed that the real structure of the C_{60} low-temperature phase involves orientational domains of the isomorphic type. This assumption is supported by the experimental data available in the literature [9, 25].

The characteristic size of domains is determined by the energy of domain boundaries and the conditions of formation of the structure during the orientational phase transition. These conditions are taken to be such that individual domains are large enough to contain a statistically significant number of molecules and the total volume of domain boundaries is considerably smaller than the crystal volume. It is also assumed that the crystal is sufficiently perfect so as to disregard the lattice disturbance brought about by undissociated and partial dislocations and other defects. Under these conditions, the direction and sign of polarity of the rotation axis of a particular molecule remain unchanged upon translation through the lattice spacing within a particular domain. To every molecule of a particular domain there corresponds an axial vector $\mathbf{S}^\alpha$ (α = 1, 2, 3, 4), which is collinear with respect to the rotation axis of this molecule. For example, if one of the structural variants is represented by the set of vectors (1, 1, 1), (1, $\bar{1}$, $\bar{1}$), ($\bar{1}$, $\bar{1}$, 1), and ($\bar{1}$, 1, $\bar{1}$) [24], the other (isomorphic) variant will be described by the set of vectors ($\bar{1}$, $\bar{1}$, $\bar{1}$), (1, 1, $\bar{1}$), (1, $\bar{1}$, 1), and ($\bar{1}$, 1, 1). Therefore, all the molecules involved in a particular domain can be divided into four subsystems depending on the direction of vectors $\mathbf{S}^\alpha$. At temperatures far from T_c, these subsystems are statistically independent of one another, because the direction and sign of the rotation axis remain unchanged and the transition of a particular molecule from one subsystem to another becomes impossible. On the other hand, these subsystems are statistically equivalent to one another when external actions are absent. Hence, it follows that the number N_e^α of excited orientational states in the α subsystem is determined from the formula $N_e^\alpha = N_e/4$ (where N_e is the number of excited states of the domain) and the total number N^α of orientational states in the α subsystem is expressed as $N^\alpha = N/4$ (where N is the total number of orientational states of the domain). By analogy with the theoretical treatment made by Natsik and Podol'skiĭ [11], we write the following kinetic equation for N_e^α in terms of the phenomenological model of double-well orientational potential:

$$\frac{\partial N_e^\alpha}{\partial t} = -\frac{N_e^\alpha}{\tau_0}\exp\left(-\frac{U_h}{kT}\right) + \frac{(N/4 - N_e^\alpha)}{\tau_0}\exp\left(-\frac{U_p}{kT}\right), \quad (1)$$

where $U_h = E_0 - \Delta U/2$, $U_p = E_0 + \Delta U/2$, E_0 is the activation energy, ΔU is the difference between the energy levels of the ground and excited states, and τ_0 is the characteristic time of relaxation. Note that such a simple kinetic equation can be written only at a low density of excited states, when the interaction between these states can be ignored. Otherwise, the activation parameters will depend on the excitation density, which, in turn, should lead to the appearance of the spectra of the activation energies, relaxation times, etc. Therefore, at a high density of excited states, the quantities E_0, ΔU, and τ_0 in relationship (1) (as well as the deformation potentials considered below) should be treated as effective integrated quantities, which, in general, depend on the temperature.

For convenience, we change over to the relative density of excited states $n^\alpha = N_e^\alpha/N^\alpha$. It is easily seen that $n = N_e/N = (\sum_\alpha n^\alpha)/4$ and the relative equilibrium density of excited states without external actions can be written as $n_0^\alpha = n_0 = 1/(1 + \exp(\Delta U/kT))$. Let us introduce now, as was done by Natsik and Podol'skiĭ [11], additional terms for the potential barriers U_h and U_p, which are related to small elastic strains of the crystal lattice; that is,

$$U_{p,h}^\alpha(\varepsilon) = U_{p,h} - V_{p,h}^{(1)}\delta_{ij}\varepsilon_{ij} - V_{p,h}^{(2)}S_i^\alpha S_j^\alpha\varepsilon_{ij}. \quad (2)$$

Here, summation over α is absent and $V_{p,h}^{(1)}$ and $V_{p,h}^{(2)}$ are constants expressed in terms of energy. The first additional term in expression (2) is similar to the component related to the elastic strain of a cubic crystal, which was introduced in [11]. The second additional term in expression (2) arises from the fact that the symmetry of the molecular environment in the α subsystem is determined by the vector $\mathbf{S}^\alpha$. Consequently, the kinetic equation for n^α in the approximation linear in the strain ε can be represented in the form

$$\tau\frac{\partial n^\alpha}{\partial t} + (n^\alpha - n_0) = n_0(1-n_0)(\Delta V_1\delta_{ij}\varepsilon_{ij} + \Delta V_2 S_i^\alpha S_j^\alpha\varepsilon_{ij})/(kT), \quad (3)$$

where $\Delta V_1 = V_p^{(1)} - V_h^{(1)}$, $\Delta V_2 = V_p^{(2)} - V_h^{(2)}$, and $\tau = \tau_0\sqrt{n_0(1-n_0)}\exp(E_0/kT)$.

2.2. Now, we analyze the effect of orientational excitations of the crystal on its elastic characteristics in the same manner as was described in [11]. Small strains ε_{ij} bring about small deviations of the density of orientational excited states from equilibrium values: $\nu^\alpha = n^\alpha - n_0$, which, in turn, leads to a change in the density of free energy F. The change in the free energy density in a particular domain at a given temperature can be

determined accurate to the second-order in ε and ν from the expression

$$F = F_0 - a\sum_{\alpha}\nu^{\alpha}(\Delta V_1\delta_{ij}\varepsilon_{ij} + \Delta V_2 S_i^{\alpha}S_j^{\alpha}\varepsilon_{ij}) + b\sum_{\alpha}(\nu^{\alpha})^2 + c\sum_{\alpha,\beta}\nu^{\alpha}\nu^{\beta} + 1/2C_{ijkl}\varepsilon_{ij}\varepsilon_{kl}, \quad (4)$$

where F_0 is the equilibrium density of the free energy and a, b, and c are the temperature-dependent coefficients. For simplicity, the additional terms related to the possible temperature change are omitted from expression (4), because our prime interest here is in the effect of orientational excitations on the propagation of shear vibrations that are not accompanied by dilatation and thermoelastic effects [26]. For longitudinal modes of acoustic vibrations, this expression corresponds to an isothermal approximation. The thermoelastic effect on the propagation of longitudinal acoustic vibrations in fullerite was thoroughly considered in [11].

By using the thermodynamic definition of the elastic stress tensor ($\sigma_{ij} = |\partial F/\partial\varepsilon_{ij}|_{T,\nu}$) and relationship (4), we obtain the following expression for σ, ε, and ν:

$$\sigma_{ij} = C_{ijkl}\varepsilon_{kl} - a\sum_{\alpha}\nu^{\alpha}(\Delta V_1\delta_{ij} + \Delta V_2 S_i^{\alpha}S_j^{\alpha}). \quad (5)$$

We seek a solution to this equation combined with the equation

$$\tau\dot{\nu}^{\alpha} + \nu^{\alpha} = n_0(1-n_0) \times (\Delta V_1\delta_{ij}\varepsilon_{ij} + \Delta V_2 S_i^{\alpha}S_j^{\alpha}\varepsilon_{ij})/(kT) \quad (6)$$

(which describes the relaxation of orientational excitations) in the form of an expansion in the harmonics $\exp(i\omega t)$. As a result, the complex elastic moduli are represented in the form

$$\tilde{C}_{ijkl}(\omega) = C_{ijkl} - \frac{an_0(1-n_0)}{kT(1+i\omega\tau)} + \left[4(\Delta V_1)^2\delta_{ij}\delta_{kl}\Delta V_1\Delta V_2\sum_{\alpha}(\delta_{ij}S_k^{\alpha}S_l^{\alpha} + \delta_{kl}S_i^{\alpha}S_j^{\alpha}) + (\Delta V_2)^2\sum_{\alpha}S_i^{\alpha}S_j^{\alpha}S_k^{\alpha}S_l^{\alpha}\right]. \quad (7)$$

It can easily be shown that, upon substituting either of the two sets of vectors $\mathbf{S}^{\alpha}$ into relationship (7) and performing subsequent summation, the second term in the square brackets reduces to the expression $8\Delta V_1\Delta V_2\delta_{ij}\delta_{kl}$ and the third term transforms to $4(\Delta V_2)^2(\delta_{ij}\delta_{kl} + \delta_{ik}\delta_{jl} + \delta_{il}\delta_{jk})$. This implies that the elastic properties of a crystal at any volume ratio between its isomorphic structures can be described by the same expression

$$\tilde{C}_{ijkl}(\omega) = C_{ijkl} - \frac{4an_0(1-n_0)}{kT(1+i\omega\tau)} \times [(\Delta V_1 + \Delta V_2)^2\delta_{ij}\delta_{kl} + (\Delta V_2)^2(\delta_{ik}\delta_{jl} + \delta_{il}\delta_{jk})]. \quad (8)$$

In actual fact, the initial conditions used in solving this problem are redundant. For example, expression (8) was derived without resorting to the condition for polarity of the rotation axis of a particular molecule. Moreover, analysis of relationships (7) and (8) shows that the condition for the existence of a statistically significant number of molecules in an individual domain is not a necessary condition. In the case when the crystal involves microdomains, statistical averaging can be performed over each of the possible $\mathbf{S}^{\alpha}$ states of the crystal, which results in the same relationship (8). It is necessary that the volume of defect regions (domain boundaries) be considerably smaller than the crystal volume, whereas the lifetime of microdomains must be substantially longer than the time of orientational relaxation τ and the time of measurement.

2.3. Let us now use relationship (8) in order to write the real parts of the effective elastic constants C_{11}, C_{12}, and C_{44} for fullerite:

$$C_{11}(\omega) = C_{11}^{(\infty)} - \frac{4an_0(1-n_0)}{kT(1+(\omega\tau)^2)}(\Delta V_1 + \Delta V_2)^2, \quad (9)$$

$$C_{12}(\omega) = C_{12}^{(\infty)} - \frac{4an_0(1-n_0)}{kT(1+(\omega\tau)^2)}(\Delta V_1 + \Delta V_2)^2, \quad (10)$$

$$C_{44}(\omega) = C_{44}^{(\infty)} - \frac{4an_0(1-n_0)}{kT(1+(\omega\tau)^2)}(\Delta V_2)^2. \quad (11)$$

Expressions (9) and (10) are similar (to within the designations used) to those derived earlier in [11] (see also [15]). From relationship (11), it follows that the orientational mobility of C_{60} molecules in the fullerite cubic lattice should also make a relaxation contribution to the elastic modulus C_{44}. The magnitude of this contribution is determined by the difference ΔV_2 between the deformation potentials $V_p^{(2)}$ and $V_h^{(2)}$. At the same time, it is clearly seen from expressions (9) and (10) that the relaxation component is absent in the shear modulus $C' = (C_{11} - C_{12})/2$. This is in excellent agreement with the experimental results obtained in the recent study [15], which experimentally revealed the relaxation contribution to the elastic modulus C_{44} and the absence of this contribution (to within the measurement error) to the shear modulus C'. The experimental relaxation contributions found in [15] for different elastic moduli can be used to estimate the difference ΔV_2. As was noted in [15], the quantity $V_{\Delta} = \Delta V_1 + \Delta V_2 \approx -0.8$ eV can be determined from the data obtained in [27]. As follows from relationships (9)–(11),

$(\Delta V_2)^2/(V_\Delta)^2 = A_G/A_K$, where A_G and A_K are the relaxation contributions to the shear modulus C_{44} and the bulk modulus $K = (C_{11} + 2C_{12})/3$, respectively. Consequently, substitution of the experimental data taken from [15] yields $|\Delta V_2| \approx 0.45$ eV.

ACKNOWLEDGMENTS

This work was supported by the State Scientific and Technical Program "Topical Directions in the Physics of Condensed Matter: Fullerenes and Atomic Clusters," complex project no. 2.

REFERENCES

1. P. A. Heiney, J. E. Fischer, A. R. McGhie, *et al.*, Phys. Rev. Lett. **66**, 2911 (1991).
2. R. Sachidanandam and A. B. Harris, Phys. Rev. Lett. **67**, 1467 (1991).
3. W. I. F. David, R. M. Ibberson, J. C. Matthewman, *et al.*, Nature **353**, 147 (1991).
4. S. Liu, Y. Lu, M. M. Kappes, and J. A. Ibers, Science **254**, 408 (1991).
5. R. Tycko, R. C. Haddon, G. Dabbagh, *et al.*, J. Phys. Chem. **95**, 518 (1991).
6. W. I. F. David, R. M. Ibberson, and T. Matsuo, Proc. R. Soc. London, Ser. A **442**, 129 (1993).
7. S. Savin, A. B. Harris, and T. Yildirim, Phys. Rev. B **55**, 14182 (1997).
8. K.-P. Bohnen and R. Heid, Phys. Rev. Lett. **83**, 1167 (1999).
9. W. I. F. David, R. M. Ibberson, T. J. S. Dennis, *et al.*, Europhys. Lett. **18**, 219 (1992); **18**, 735 (1992).
10. R. C. Yu, N. Tea, M. V. Salamon, *et al.*, Phys. Rev. Lett. **68**, 2050 (1992).
11. V. D. Natsik and A. V. Podol'skiĭ, Fiz. Nizk. Temp. **24**, 689 (1998) [Low Temp. Phys. **24**, 523 (1998)].
12. F. Gugenberg, R. Heid, C. Meingast, *et al.*, Phys. Rev. Lett. **69**, 3774 (1992).
13. T. Matsuo, H. Suga, W. I. F. David, *et al.*, Solid State Commun. **83**, 711 (1992).
14. R. D. Johnson, C. S. Yannoni, H. C. Dorn, *et al.*, Science **255**, 1235 (1992).
15. N. P. Kobelev, R. K. Nikolaev, N. S. Sidorov, and Ya. M. Soĭfer, Fiz. Tverd. Tela (St. Petersburg) **43** (12), 2262 (2001) [Phys. Solid State **43**, 82 (2001)].
16. X. D. Shi, A. R. Kortan, J. M. Williams, *et al.*, Phys. Rev. Lett. **68**, 827 (1992).
17. W. Shranz, A. Fuith, P. Dolinar, *et al.*, Phys. Rev. Lett. **71**, 1561 (1992).
18. N. P. Kobelev, A. P. Moravskiĭ, Ya. M. Soĭfer, *et al.*, Fiz. Tverd. Tela (St. Petersburg) **36**, 2732 (1994) [Phys. Solid State **36**, 1491 (1994)].
19. S. Hoen, N. G. Chopra, R. Mostovoy, *et al.*, Phys. Rev. B **46**, 12737 (1992).
20. Ya. M. Soifer and N. P. Kobelev, Mol. Mater. **7**, 267 (1996).
21. G. B. Alers, B. Golding, A. R. Kortan, *et al.*, Science **257**, 511 (1992).
22. E. Burgos, E. Halas, and H. Bonadeo, Phys. Rev. B **49**, 15544 (1994).
23. O. Blaschko, G. Krexner, Ch. Maier, and R. Karavatzki, Phys. Rev. B **56**, 2288 (1997).
24. A. V. Harris and R. Sachidanandam, Phys. Rev. B **46**, 4944 (1992).
25. H.-B. Bürgi, E. Blanc, D. Schwarzenbach, *et al.*, Angew. Chem. **104**, 667 (1992).
26. W. Nowacki, *Theory of Elasticity* (PWN, Warsaw, 1970; Mir, Moscow, 1975), translated from Polish.
27. W. I. F. David and R. M. Ibberson, J. Phys.: Condens. Matter **5**, 7923 (1993).

Translated by O. Borovik-Romanova

Physics of the Solid State, Vol. 44, No. 1, 2002, pp. 22–29. Translated from Fizika Tverdogo Tela, Vol. 44, No. 1, 2002, pp. 22–28.

METALS AND SUPERCONDUCTORS

Two-Dimensional Mesoscopic Vortex Clusters in a Superconducting Ring: Shell Structure and Melting

Yu. E. Lozovik, E. A. Rakoch, and S. Yu. Volkov

Institute of Spectroscopy, Russian Academy of Sciences, Troitsk, Moscow oblast, 142092 Russia

e-mail: lozovik@isan.msk.su

Received February 26, 2001; in final form, April 16, 2001

Abstract—The structure and phase transitions in the mesoscopic system of vortices in a quasi-two-dimensional superconducting ring are investigated. The shell structure of the mesoscopic system of vortices is studied, and its variation with the number of vortices and the parameters of the superconducting ring is analyzed. Two mechanisms of formation of new shells in vortex clusters with an increasing number of vortices in an increasing magnetic field are discovered: the generation of a new shell in a cluster and the splitting of the internal shell into two shells. The melting of vortex clusters and their thermodynamic parameters are analyzed using the Monte Carlo method. It is found that the melting of shell-type clusters occurs in two stages, orientation melting taking place at the lower temperature (during which nearly crystalline adjacent shells start rotating relative to each other) and blurring of the vortex structure occurring at the higher temperature. The shells obtained by splitting upon an increase in the number of vortices do not participate in orientational melting. The two-stage form of melting is associated with the smaller height of potential barriers being surmounted during the rotation of shells relative to one another as compared to the barrier for vortices jumping from one shell to another. *© 2002 MAIK "Nauka/Interperiodica".*

1. INTRODUCTION

A magnetic field $H > H_{c1}$ penetrates a type II superconductor in the form of Abrikosov vortices, which form a perfect triangular lattice in the low-temperature region (in the absence of pinning centers) [1]. As the temperature increases, this lattice can melt and the liquid phase can be formed from vortices, which has indeed been observed for high-temperature superconductors (see review [2]).

The behavior of vortices in mesoscopic superconducting structures is of considerable interest in connection with their possible application as an elemental base in memory devices.

Real type II superconductors contain pinning centers associated with defects and impurities. Superconducting properties, such as the critical current, depend to a considerable extent on the behavior of vortices near such centers. For large distances between pinning centers, a group of vortices near a defect can be regarded as a vortex cluster. Artificial superconducting structures with a profiled surface, apertures, etc. are also of considerable interest from the theoretical point of view and for their practical usefulness [3, 4]. It can be expected that, among other things, the critical current in such structures might increase considerably owing to pinning.

In the light of what has been said above, the simulation of a system of vortices in such a structure is of considerable interest. As the first step, we can analyze the structure and melting of vortex clusters in a mesoscopic superconducting ring (this forms the basis of the present work). It was found that mesoscopic vortex clusters in superconducting rings possess some properties analogous to the properties of vortex clusters in superconducting islands [5, 6].

In Section 2, we describe the physical model under investigation. The numerical methods used by us are discussed in Section 3. In Section 4, the configurations of vortex clusters in global and local potential-energy minima are studied in terms of their dependence on the geometrical parameters of the ring and on the number of vortices. The results of an analysis of melting in vortex clusters in a ring are presented in Section 5. In Section 6, the potential barriers for the relative rotation of shells and for the hopping of particles between shells are investigated.

2. PHYSICAL MODEL

Let us consider an island of a type II superconductor in the form of a ring in a transverse magnetic field. If the island thickness d in a certain temperature range is smaller than the coherence length $\xi(T)$ of the superconductor, the island can be regarded as two-dimensional in regards to its superconducting properties. The magnetic field penetrates into the system in the form of two-dimensional (2D) vortices. We will take the interaction potential between two 2D vortices in the form (see [7]) $U(r) = -q^2\ln(r/a)$, $a \ll r \ll \lambda_\perp$; and $U(r) = q^2\lambda_\perp/r + \text{const}$, $r \gg \lambda_\perp$, where q is the charge, proportional to the density of the superfluid component; r is the separation

1063-7834/02/4401-0022$22.00 © 2002 MAIK "Nauka/Interperiodica"

between vortices; a is the radius of a vortex core, $a \sim \xi(T)$; $\lambda_\perp = \lambda^2/d$ is the depth of penetration of a transverse magnetic field in the 2D superconductor; and λ is the London penetration depth of the magnetic field into a 3D superconductor. For example, for films of thickness $d \simeq 100$ Å and for $\lambda \simeq 2000$ Å, we have $\lambda_\perp \simeq 4$ μm.

We assume that the size of a superconducting island satisfies the relation $\xi \ll R_{\max} - R_{\min} \ll \lambda_\perp$. In this case, vortices in a superconducting ring can be regarded as point particles which repel one another in accordance with a logarithmic law. In this model, the stabilization of the vortex concentration in superconductors in an external magnetic field is taken into account by introducing an effective external confinement potential $U_{\text{ext}} = \alpha(\mathbf{r} - \mathbf{r}_0)^2$ (the parameter $\mathbf{r}_0$ is chosen in the annular region of the ring) corresponding to a homogeneous compensating background with a charge density $\rho_{\text{ext}} = 2\alpha$. The variation of the effective interaction near the boundary of the superconducting system can be taken into account through the introduction of image forces; however, image forces for vortices do not change the properties of a cluster qualitatively; rather, they affect its quantitative characteristics only slightly (see [5, 8]). For this reason, these forces will be disregarded here.

Thus, we arrive at a model of a 2D cluster consisting of N classical particles (N = 1–50) with a logarithmic law $U(r_{ij}) = q^2 \ln(r_{ij}/a)$ of repulsion between the particles confined by the external potential $U_{\text{ext}}(r_i) = \alpha(\mathbf{r}_i - \mathbf{r}_0)^2$.

After scaling the transformations $r \longrightarrow (\alpha^{1/2}/q)r$, $T \longrightarrow (k_B/q^2)T$, and $U \longrightarrow (1/q^2)U$, the potential energy assumes the form

$$U = -\sum_{i>j} \ln r_{ij} + \sum_i (\mathbf{r}_i - \mathbf{r}_0)^2 \qquad (1)$$

to within the constant $C_N^2 \ln(q/\alpha^{1/2}a)$. It can be proved that (see [5, 6]) the properties of clusters under investigation do not change qualitatively even in the case of a slight anisotropy of $U_{\text{ext}}(r)$.

3. NUMERICAL METHODS

In order to find equilibrium configurations of the particles, we used the following two approaches: the annealing method and the gradient descent method. In order to analyze the dependence of physical quantities on the temperature and melting of a cluster, we used the Monte Carlo method with a modified Metropolis algorithm [5, 6]. The following quantities were calculated:

(1) Total potential energy U_{pot}.

(2) Heat capacity

$$C = \frac{\langle U_{\text{pot}}^2 \rangle - \langle U_{\text{pot}} \rangle^2}{T}. \qquad (2)$$

(3) Radial mean square displacements (RMSD), both the total displacement and the displacement of each shell separately:

$$U_R = \frac{1}{N_R} \sum_{i=1}^{N_R} \frac{\langle \mathbf{r}_i^2 \rangle - \langle \mathbf{r}_i \rangle^2}{a^2}, \qquad (3)$$

where N_R is the number of particles in a cluster or in a shell; averaging $\langle \ldots \rangle$ was carried out over various Monte Carlo configurations.

(4) Angular mean square displacements (AMSD) relative to the nearest neighbor particles in the same shell:

$$U_{\varphi_1} = \frac{1}{N_R} \sum_{i=1}^{N_R} \frac{\langle \varphi_i - \varphi_{i_1} \rangle - \langle \varphi_i - \varphi_{i_1} \rangle^2}{\varphi_0^2}; \qquad (4)$$

and AMSD relative to the particles of the nearest neighbor shell:

$$U_{\varphi_2} = \frac{1}{N_{R_1} N_{R_2}} \sum_{i=1}^{N_{R_1}} \sum_{i_2=1}^{N_{R_2}} \frac{\langle (\varphi_i - \varphi_{i_2})^2 \rangle - \langle \varphi_i - \varphi_{i_2} \rangle^2}{\varphi_0 \varphi_{0_2}}, \qquad (5)$$

where i_1 and i_2 correspond to the nearest neighbor particle from the same shell and to a particle from the neighboring shell, respectively, and $\varphi_0 = 2\pi/N_R$ is the mean angular distance between adjacent particles for a given shell.

(5) The radial distribution function for particles in a cluster,

$$g_r = \sum_{i=1}^{N} \langle \delta(\mathbf{r}_i - \mathbf{r}_0) \rangle, \qquad (6)$$

where r_i are the radial coordinates of particles in the cluster.

(6) Angular correlation function for two shells,

$$g_{\Delta\varphi} = \sum_{i=1}^{N_1} \sum_{i=1}^{N_2} \langle \delta(\varphi_i - \varphi_j - \varphi_0) \rangle, \qquad (7)$$

where φ_i and φ_j are the angular coordinates of particles from two neighboring shells of a cluster and N_1 and N_2 are the numbers of particles in each of the two shells.

(7) The parameter of mutual orientational order of shells s_1 and s_2,

$$g_{s_1 s_2} = \langle \mathrm{Re}(\Psi_{s_1} \Psi_{s_2}) \rangle, \qquad (8)$$

where $\Psi_l = 1/N_l \sum_{i=1}^{N_l} \exp(iN_l \varphi_{il})$ is the angular order parameter of the lth shell and N_l is the number of particles in the lth shell. In the case of orientational melting, the parameter of mutual orientational order of the shells must vanish.

The potential barriers for relative rotation of the shells and for particles jumping between shells were

analyzed taking into account relaxation, i.e., by tuning particles to the corresponding changes in configuration. Otherwise, the theory gives nonrealistic (exaggerated) values of the potential barriers.

4. EQUILIBRIUM CONFIGURATIONS OF CLUSTERS

We determined global potential-energy minima for two-dimentional clusters of vortices in a ring-shaped confining potential with numbers of vortices $N = 1, \ldots, 50$ for various values of the radial parameter r_0 of the confining potential. It turned out that vortex clusters in the ring have a shell structure at low temperatures and for small numbers of particles (Fig. 1).

A shell in a cluster is defined as a convex polygon formed by the maximum possible number of particles (containing the previous shell in its interior), which satisfies the following condition: the maximum distance from a particle in the given shell to the center of the system must be smaller than the minimum distance from particles of the neighboring outer shell to the center of the system.

The potential energy of the system and the potential energy per particle (specific potential energy) decrease according to a quadratic and a linear law, respectively, upon an increase in the number of particles. This result can be obtained from the model of vortices uniformly smeared over the ring. The charge density of the island in this case is given by

$$\rho = \frac{qN}{\pi(R_{\max}^2 - R_{\min}^2)}. \quad (9)$$

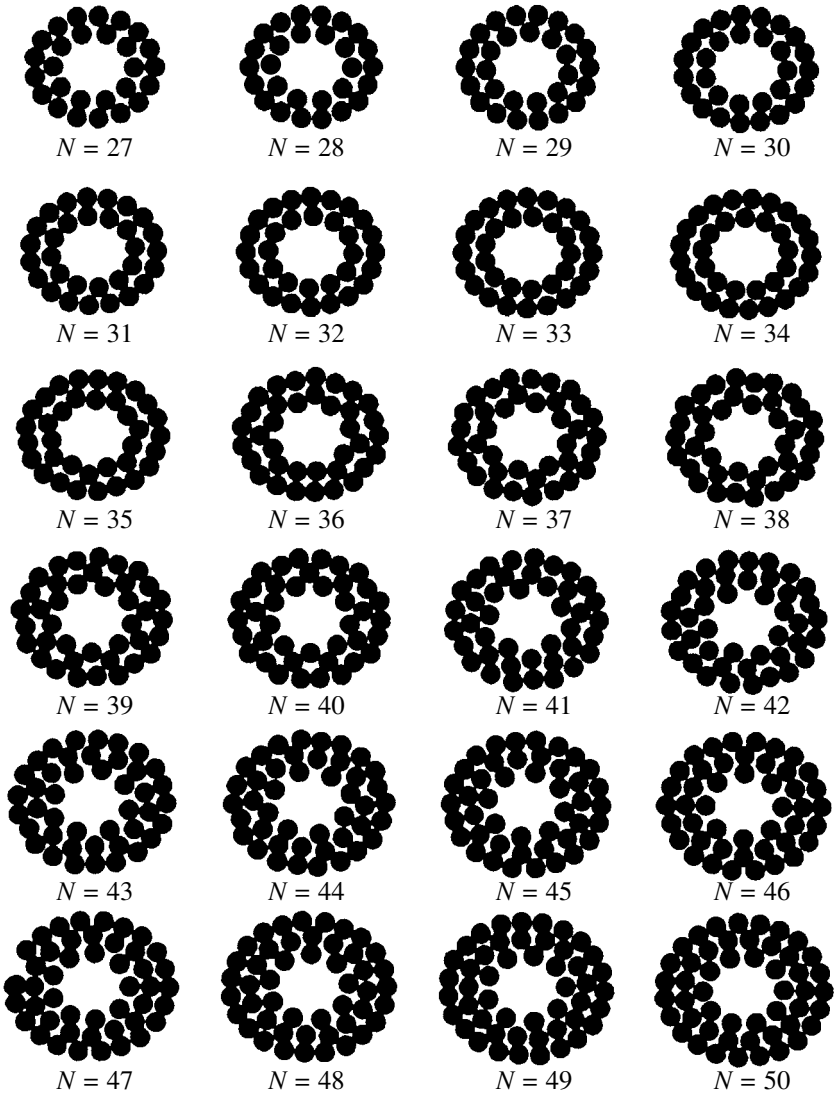

Fig. 1. Configurations of vortex clusters in a ring depending on the number of particles.

Table 1. Shell structure and the potential energy of vortex clusters in a ring

N	$N_1, N_2, \ldots, r_0 = 0.5$	$U_{pot}, r_0 = 0.5$	$N_1, N_2, \ldots, r_0 = 2$	$U_{pot}, r_0 = 2$
8	8	-1.179805×10^1	8	-3.222613×10^1
9	1, 8	-1.607791×10^1	9	-4.124632×10^1
12	3, 9	-3.457878×10^1	12	-7.548147×10^1
13	3, 10	-4.269991×10^1	13	-8.936393×10^1
14	4, 10	-5.187863×10^1	14	-1.045188×10^2
15	4, 11	-6.210678×10^1	8, 7	-1.209840×10^2
23	8, 15	-1.855514×10^2	8, 15	-3.046596×10^2
24	1, 8, 15	-2.065622×10^2	8, 16	-3.342975×10^2
34	5, 11, 18	-4.922492×10^2	13, 21	-7.165943×10^2
35	5, 12, 18	-5.286966×10^2	7, 7, 21	-7.636627×10^2
38	6, 13, 19	-6.470145×10^2	8, 8, 22	-9.150325×10^2
43	8, 14, 21	-8.748539×10^2	8, 14, 21	-1.201622×10^3
44	1, 7, 15, 21	-9.251369×10^2	8, 14, 22	-1.264181×10^3

Here, q is the charge of a vortex and R_{max} and R_{min} are the outer and inner radii of the ring island, respectively. The potential energy of such a cluster is $U = -\text{const}SN^2$, where S is the area of the ring island independent of N; in other words, the potential energy of the cluster is proportional to N^2 and the specific potential energy is proportional to N.

Table 1 gives examples of equilibrium configurations and their energies for vortex clusters in a ring-shaped confining potential with the radial parameters $r_0 = 0.5$ and 2.

Clusters with ring and circular confining potentials are characterized by different mechanisms of formation of new shells. When a new shell is formed in a circular cluster, one particle appears first at the center of symmetry of the cluster and then the numbers of particles in all shells increase monotonically. In the case of a ring-shaped cluster with $r_0 = 2$, the formation of a new shell begins with the splitting of the inner shell into two shells with approximately equal numbers of particles and a further increase of particles in number leads to a monotonic increase in the numbers of particles in the shells. In this process, some particles from the inner shell come close to the neighboring shell and a structural transformation of the inner shells takes place for a certain critical number of particles: the numbers of particles in two inner shells change jumpwise, after which a monotonic increase in the number of particles takes place in all the shells until the next splitting of the inner shell occurs. Thus, the formation of new shells in a ring cluster with a large radial parameter occurs in two stages. In the intermediate case of a cluster in a ring with $r_0 = 0.5$, the formation of a new shell occurs in one stage as in a circular cluster. In this case, the formation of a new shell in the cluster also begins with the emergence of a particle, but, first, the particle is displaced from the symmetry center of the cluster and, second, this configuration is not stable: an increase in the number of particles by unity leads to the formation of an inner shell consisting of two particles, in contrast to a cluster in a circle.

In order to determine the structural changes in clusters upon an increase in the number of particles, we analyzed the mean distance $\bar{a}$ between nearest neighbor particles, the inner and outer radii R_{min} and R_{max} of the cluster, the cluster area S, and the numbers of particles N_l in the shells as functions of the number of particles in the cluster. Here, $\bar{a} = \sqrt{\pi}(R_{ext} - R_{int})/\sqrt{N}$, where R_{ext} and R_{int} are the radial coordinates of the particles located at the maximum and minimum distances from the cluster center, respectively: $R_{max} = R_{ext} + \bar{a}/2$, $R_{min} = R_{int} - \bar{a}/2$, $S = \pi(R_{max} - R_{min})^2$ (Figs. 2a, 2b).

The mean distance $\bar{a}$ between particles decreases abruptly during the formation of new shells and experiences small jumps in the course of a structural transformation of inner shells. In the absence of structural rearrangements, the value of $\bar{a}$ decreases monotonically with increasing N if a cluster has only one shell and increases monotonically for a cluster consisting of two or more shells. The values of R_{max}, R_{min}, and S also experience drops and jumps during the formation of new shells and in the course of structural rearrangements of inner shells.

It is also interesting to trace the changes in the structure of clusters with the same N but with different values of parameter r_0. These changes were analyzed for clusters with $N = 12$, 24, and 38. It was found that for a given N, the change in parameter r_0 gives rise to the same structural transformations as for clusters with dif-

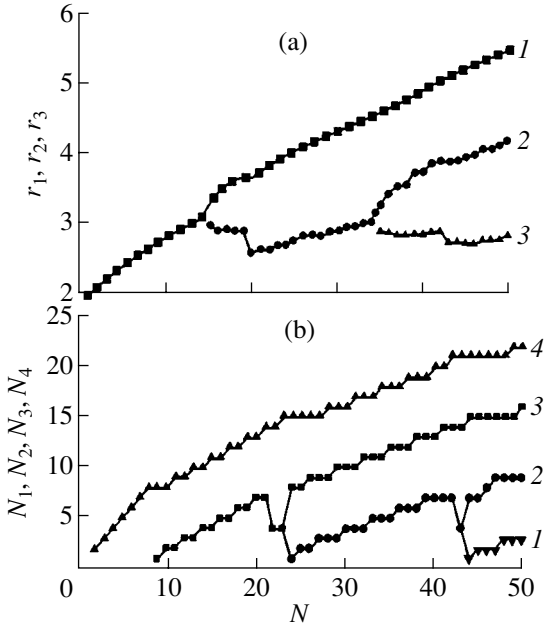

Fig. 2. Dependence of (a) mean radii of shells and (b) the number of particles in shells on the number of particles in a cluster. The figures correspond to the shell numbers. Parameter r_0 is equal to (a) 2.0 and (b) 0.5.

ferent values of N for a given r_0. With increasing r_0, the inner shells are first rearranged and then two shells are combined into one. The numbers of particles in the shells at intermediate stages between structural transformations change insignificantly. For example, in a cluster with $N = 12$, an increase in r_0 leads to the chain of configurations (3, 9), (2, 10), (6, 6), and (12); in a cluster with $N = 24$, an increase in r_0 gives the configurations (2, 8, 14), (1, 8, 15), (9, 15), (8, 16), (6, 6, 12), (12, 12), and (24); while in a cluster with $N = 38$, the following configurations alternate: (6, 13, 19), (8, 10, 20), (8, 8, 22), (15, 23), (16, 22), (19, 19), and (38). The potential energy decreases monotonically upon an increase in r_0.

Table 2. Potential barriers and melting temperatures for vortex clusters

N	r_0	U_{rot}	U_{jump}	T_{c_1}	T_{c_2}
12	0.5	1.7×10^{-2}	6.5×10^{-2}	4.0×10^{-3}	1.5×10^{-3}
17	0.5	1×10^{-9}	5×10^{-2}	4.5×10^{-3}	5.0×10^{-8}
27	0.5	5×10^{-3}	3.1×10^{-2}	4.0×10^{-3}	8.0×10^{-4}
16	2.0	6×10^{-2}	1×10^{-2}	3.3×10^{-3}	–
21	2.0	6.5×10^{-2}	7×10^{-2}	2.7×10^{-3}	2.3×10^{-3}
22	2.0	7×10^{-3}	9×10^{-2}	2.5×10^{-3}	8.0×10^{-5}

Note: U_{rot} is the potential barrier to relative rotation and U_{jump} is the potential barrier to particle jumps between shells.

We also analyzed the dependences of $\bar{a}$, R_{max}, R_{min}, and S on r_0 for $N = 12$, 24, and 38. The mean distances $\bar{a}$ between particles undergo jumps upon an increase in r_0 for structural transitions associated with a decrease in the number of shells. Moreover, the value of $\bar{a}$ decreases abruptly during structural transitions associated with rearrangement of the inner shells. In the absence of structural transitions, the value of $\bar{a}$ decreases monotonically for clusters consisting of two or more shells and increases monotonically for clusters with only one shell. In fact, parameter r_0 is a function of the inner and outer radii for a given number of vortices. However, it is easier to study the inverse dependence, viz., the formal dependence of r_1 and r_2 on r_0. The inner radius of a cluster increases on the whole as a function of parameter r_0, experiencing small jumps in the course of rearrangements of inner shells and small drops when two shells merge into one (the number of shells decreases). The outer radius of a cluster increases monotonically with parameter r_0, undergoing jumps in the case of coalescence of two shells.

5. MELTING AND PHASE TRANSITIONS

In order to study the melting of vortex clusters in a ring, we determined the temperature dependences of the quantities described in Section 3 for several clusters (Table 2). The following regularities were revealed. In all clusters with $r_0 = 0.5$, as well as in clusters with $r_0 = 2$, in which the inner shells have strongly different numbers of particles, melting occurs in two stages as in the case of clusters in a circle. For example, complete (radial) melting of clusters takes place at T_{c_1}, while the specific orientational melting typical of clusters with a shell structure occurs at a temperature T_{c_2}, which is considerably lower than T_{c_1}. The shells in a cluster, preserving their crystalline nature, start rotating relative to one another. The ratio T_{c_1}/T_{c_2} of temperatures of complete and orientational melting for magic clusters (with a multiple number of particles in the shells) is much smaller than that for other clusters. On the whole, an increase in the number of particles in the shells leads to an increase in the orientational melting temperature and to a decrease in T_{c_1}/T_{c_2}. In clusters with $r_0 = 2$ with inner shells obtained through the splitting of a cluster shell with a smaller number of particles (i.e., with approximately equal numbers of particles in two inner shells), orientational melting of the inner shells does not take place at all (Table 2).

The melting of vortex clusters in a ring is considered for clusters with $N = 12$, 17, and 27 with $r_0 = 0.5$ and for clusters with $N = 16$, 21, 22, and 38 with $r_0 = 2$ (Table 2).

Complete melting in the clusters is demonstrated most visually through the temperature dependences of

the RMSD. Figure 3 shows a jump in the RMSD (for a cluster with $N = 27$ and $r_0 = 0.5$) at the complete-melting temperature T_{c_1} (Table 2). The sharp peaks in the function $g(r)$ that correspond to the shells (see Section 3) and are observed for $T > T_{c_1}$ are blurred and merge into one at $T < T_{c_1}$.

The orientational melting of vortex clusters in a ring can be observed with the help of the temperature dependences of the AMSD, the RMSD, the angular correlation function of particles from two shells, and the order parameter $g_{s_1 s_2}$. It is shown for clusters with $N = 21$, 22, and 38 and $r_0 = 2$ and with $N = 12$ and 27 for $r_0 = 0.5$ that the AMSD as a function of T displays a sharp kink (only for the two outer shells in the case of $N = 38$) at $T = T_{c_2}$ (Fig. 4 and Table 2). The RMSD also experiences small jumps at $T = T_{c_2}$. The angular correlation function $g_{\Delta\varphi}$ has zero values in some ranges for $T < T_{c_2}$, the ranges vanishing for $T > T_{c_2}$. Consequently, for $T > T_{c_2}$, the particles in adjacent shells can be separated from one another by arbitrary angular intervals, while for $T < T_{c_2}$ they can only be within definite intervals of angular separations. The order parameter $g_{s_1 s_2}$ decreases abruptly at the orientational melting point (Fig. 5 for a cluster with $N = 12$ and $r_0 = 0.5$) and then fluctuates about its zero value.

The potential energy increases linearly with temperature up to the point of complete melting, after which it starts increasing at a higher rate near the melting point and fluctuates strongly (Fig. 6). The heat capacity also starts fluctuating vigorously. This is due to the fact that at temperatures higher than the complete melting point, a cluster can exist (with different probabilities) in configurations corresponding to different local minima (dynamic coexistence).

6. POTENTIAL BARRIERS TO SHELL ROTATIONS AND TO JUMPING OF A PARTICLE FROM ONE SHELL TO ANOTHER

The method described in Section 3 was used by us to determine the rotational potential barrier U_{rot} and the potential barrier U_{jump} to the jumping of a particle from one shell to another in clusters with various values of N and r_0 (Table 2 and Fig. 7). As expected, the potential barriers to the relative rotation of shells are lower than the potential barriers to particles jumping between shells only for those pairs of shells in clusters that melt orientationally relative to each other. The ratio $U_{\text{rot}}/U_{\text{jump}}$ of the potential barriers coincides in order of magnitude with the ratio of the temperature corresponding to orientational melting for the relevant shells and the complete-melting temperature of the cluster. For shells with equal numbers of particles (appearing as

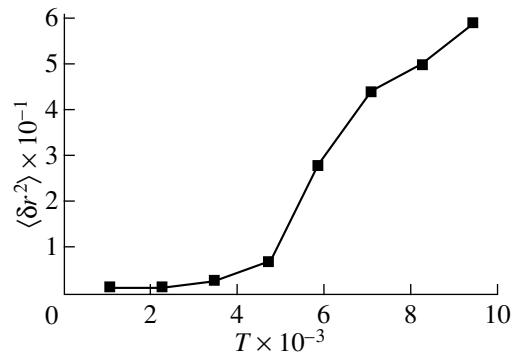

Fig. 3. Temperature dependence of the radial mean square displacement for a cluster with $N = 27$, $r_0 = 0.5$. The rapid growth of this parameter corresponds to complete melting of the vortex cluster.

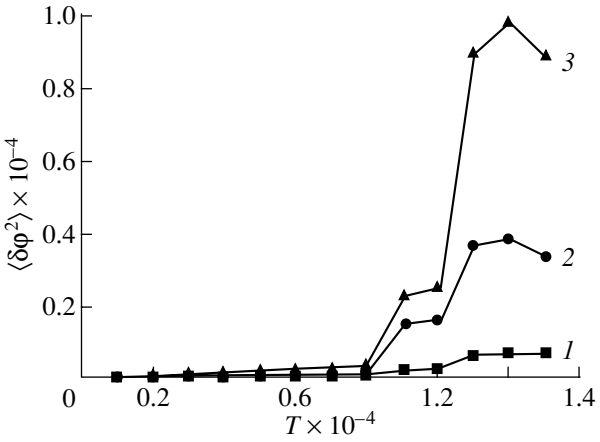

Fig. 4. Temperature dependence of the angular mean square displacement for a cluster with $N = 22$, $r_0 = 2$: (*1*) the intrashell AMSD of the outer shell, (*2*) the intrashell AMSD of the inner shell, and (*3*) the AMSD of the inner shell relative to the outer shell.

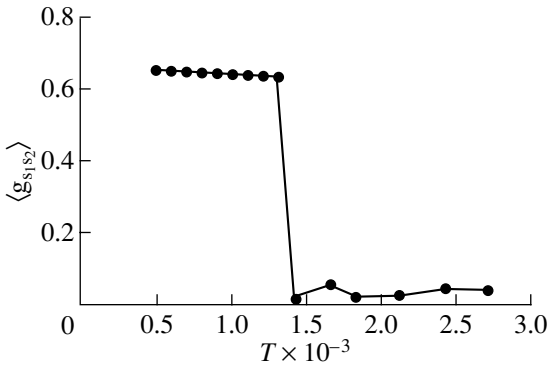

Fig. 5. Temperature dependence of the order parameter $g_{s_1 s_2}$ of a cluster with $N = 12$, $r_0 = 0.5$.

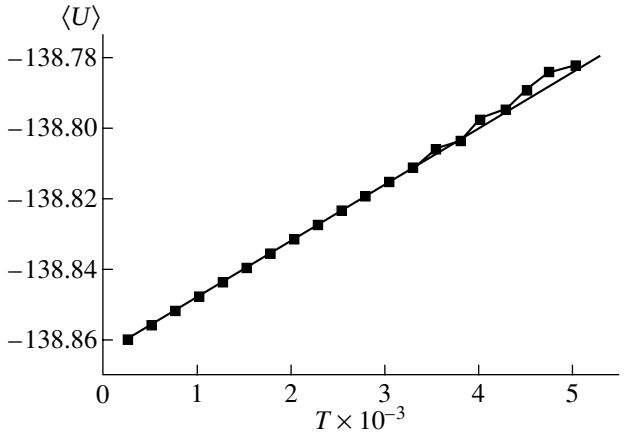

Fig. 6. Temperature dependence of the mean potential energy $\langle U \rangle$ of a cluster with $N = 16$, $r_0 = 2$.

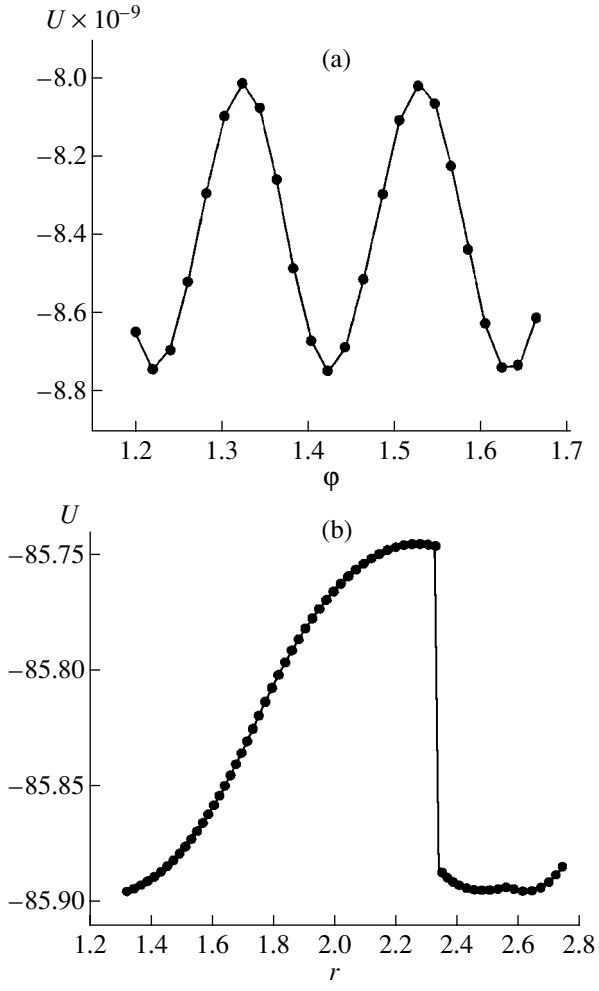

Fig. 7. Dependence of the total potential energy of a vortex cluster with $N = 17$, $r_0 = 0.5$ on (a) the relative angular position of the shells and (b) the coordinate of a particle upon its displacement from one shell to another. Dependence (a) gives the potential barrier to relative rotation of the shells, while dependence (b) gives the potential barrier to a particle jump between the shells.

a result of splitting), orientational melting does not take place in view of the large height of the rotational barrier for these shells. In the case of relative rotation of such shells, the angular coordinates of particles of the outer shell simultaneously assume the same values as the angular coordinates of the corresponding particles of the inner shell. For this reason, the separations between the corresponding particles in these shells simultaneously assume minimum values and the radial separation between these shells is small (and hence, the potential barrier is very high). In other words, a large value of the barrier is connected with the commensurability of shells; a small value, with their incommensurability.

7. CONCLUSIONS

The results obtained in the present work can be formulated as follows.

(1) It is shown that two-dimensional mesoscopic vortex clusters in a superconducting ring have a shell structure at low temperatures. The possible configurations of the system are determined at the local and global minima of the potential energy. Two mechanisms of formation of new shells upon a change in the number of vortices caused by an increase in the magnetic field and in parameter r_0 have been discovered: (a) a new vortex shell is formed in a cluster and (b) the inner shell of a cluster splits into two shells with an equal number of particles, which is followed by further structural rearrangement of the inner shells formed. The latter mechanism is typical of particles in the ring-shaped potential and prevails upon an increase in r_0.

(2) The temperature dependences of potential energy, heat capacity, and mean square (radial and angular) displacements and the function of radial and angular distributions of particles are analyzed in detail. The melting of the system is studied thereby. It is shown that melting in mesoscopic clusters occurs in two stages: orientational melting (from the frozen phase to the state with rotational reorientation of crystalline shells relative to one another), occurring at lower temperatures, is followed by a transition with disturbance of the radial order. The reason behind the orientational melting lies in the smallness of the potential barrier to relative rotation of the shells (associated with the incommensurability of adjacent shells) as compared to the barrier to particle jumping from one shell to another. Orientational melting is not observed for inner shells that are formed as a result of splitting and contain an equal number of particles.

The ratio of temperatures corresponding to orientational and complete radial melting is found to be equal, in order of magnitude, to the ratio of the barriers to relative rotation of the shells and to a jump in a vortex from one shell to another.

ACKNOWLEDGMENTS

This work was supported by the Russian Foundation for Basic Research and INTAS, project no. 99-02-16654-a.

REFERENCES

1. A. A. Abrikosov, Zh. Éksp. Teor. Fiz. **32**, 1442 (1957) [Sov. Phys. JETP **5**, 1174 (1957)].
2. G. Blatter, M. V. Feigel'man, V. B. Geshkenbein, *et al.*, Rev. Mod. Phys. **66** (4), 1125 (1994).
3. V. V. Molshchalkov, V. Bruyndoncx, L. van Look, J. van Bael, and Y. Bruynserade, *Handbook of Nanostructured Materials and Nanotechnology*, Ed. by H. S. Halwa (Academic, New York, 1999), Vol. 3.
4. A. K. Geim, I. V. Grigorieva, S. V. Dubonos, *et al.*, Nature **390**, 259 (1997).
5. Yu. E. Lozovik and E. A. Rakoch, Pis'ma Zh. Éksp. Teor. Fiz. **65**, 268 (1997) [JETP Lett. **65**, 282 (1997)]; Yu. E. Lozovik and E. A. Rakoch, Phys. Rev. B **57** (2), 1214 (1998).
6. Yu. E. Lozovik and V. A. Mandelshtam, Phys. Lett. A **145**, 269 (1990); F. M. Peeters, V. A. Schweigert, and V. M. Bedanov, Physica B (Amsterdam) **212**, 237 (1995); Yu. E. Lozovik and E. A. Rakoch, Phys. Lett. A **235**, 55 (1997).
7. Y. Pearl, Appl. Phys. Lett. **5**, 65 (1964).
8. L. J. Campbell and R. M. Ziff, Phys. Rev. B **20** (5), 1886 (1979).

Translated by N. Wadhwa

Physics of the Solid State, Vol. 44, No. 1, 2002, pp. 30–33. Translated from Fizika Tverdogo Tela, Vol. 44, No. 1, 2002, pp. 29–32.

METALS AND SUPERCONDUCTORS

Field and Temperature Dependences of the Specific Heat of the $La_{1.85}Sr_{0.15}CuO_4$ Superconductor

G. Kh. Panova, A. A. Shikov, M. N. Khlopkin, and N. A. Chernoplekov

Russian Research Centre Kurchatov Institute, pl. Kurchatova 1, Moscow, 123182 Russia

e-mail: khlopkin@isssph.kiae.ru

Received May 31, 2001

Abstract—This paper reports on the temperature and field dependences of the specific heat of high-quality $La_{1.85}Sr_{0.15}CuO_4$ single crystals carried out at low temperatures in magnetic fields of up to 8 T for two magnetic field orientations, namely, along the [100] and [110] crystallographic axes. The field dependence of the electronic density of states (DOS) was found to be anisotropic for different magnetic field orientations in the *a*–*b* plane, with the electronic density being the lowest along the *a* axis (for $H \parallel [100]$) and maximum for the field inclined at 45° to the *a* axis (for $H \parallel [110]$). Electronic specific heat in a magnetic field was observed to depend linearly on temperature T and nonlinearly on the magnetic field H: $C_{DOS} = bTH^{1/2}$. In a zero field, the electronic specific heat grows quadratically with temperature as $C_{DOS} = \alpha T^2$. Estimation of the maximum superconducting gap width from the experimentally determined values of the α coefficient of T^2 and of the electronic DOS in the normal state yields $\Delta_0 = 300$ K. The observed features indicate that $La_{1.85}Sr_{0.15}CuO_4$ is a superconductor with *d* symmetry of the order parameter. © *2002 MAIK "Nauka/Interperiodica".*

1. INTRODUCTION

Considerable attention has been focused in recent years on investigation of the symmetry of the order parameter in HTSCs by measuring the specific heat in magnetic fields, because in this way, one can determine the electronic density of states (DOS), which can be readily compared with various theoretical predictions. Since specific heat is a volume thermodynamic characteristic of matter, such measurements are a convenient approach to studying the mechanism of superconductivity.

The theory of superconductors with *d* symmetry of the order parameter suggests that the *d* and *s* components of the superconducting gap have different spatial distributions. Therefore, the electronic density of states and, particularly, its dependence on the magnetic field differ for *d*- and *s*-electron pairing; hence, specific-heat measurements performed in a magnetic field can contribute substantially to our understanding of the nature of pairing. Such measurements also yield the densities of electronic states, which are essential in making comparisons with model calculations of the quasiparticle excitation spectrum.

The low-temperature behavior of the thermodynamic properties depends on the energy density of states in the excitation spectrum of the superconductor near the Fermi level. The vanishing of the superconducting gap in some sections of the Fermi surface affects the energy spectrum strongly, which gives rise to temperature anomalies in the thermodynamic properties of the superconductor in both the superconducting (Meissner) and mixed (Shubnikov) states. Theory [1–5] predicts that the specific heat of a superconductor with *d* symmetry of the order parameter will have three characteristic features in the low-temperature region: (i) In a zero field, the electronic specific heat depends quadratically on temperature. (ii) In a magnetic field and in the mixed state, the electronic specific heat scales as $C \sim bTH^{1/2}$. (iii) The specific heat exhibits a nontrivial fourth-order anisotropy for a magnetic field oriented in the *a*–*b* plane.

The first two features have been observed experimentally in a number of laboratories [6–10], primarily on polycrystalline samples of $La_{1.85}Sr_{0.15}CuO_4$ and $YBa_2Cu_3O_7$. Single crystals of $YBa_2Cu_3O_7$ were studied in differently oriented magnetic fields [11–13]. The effect of magnetic field on the specific heat was found to be trivially anisotropic, depending on the field orientation relative to the Cu–O plane in fields parallel and perpendicular to the *c* axis. Those studies, however, did not reveal any nontrivial anisotropy, within experimental accuracy, in the *a*–*b* plane.

The present work was aimed at studying the temperature and field dependences of the electronic component of the specific heat on bulk high-quality $La_{1.85}Sr_{0.15}CuO_4$ single-crystal samples, as well as the nontrivial anisotropy in the electronic density of states for different magnetic field orientations in the *a*–*b* plane. Preliminary results of these studies were published in [14–17].

1063-7834/02/4401-0030$22.00

2. SAMPLE PREPARATION AND CHARACTERISTICS

The studies were performed on a high-quality bulk $La_{1.85}Sr_{0.15}CuO_4$ single crystal grown by crucibleless zone melting under radiative heating. Room temperature x-ray diffraction analysis showed the sample to have a tetragonal structure ($F4/mmm$) with the lattice parameters $a = b = 3.773(1)$ Å and $c = 13.233(2)$ Å.

The superconducting transition temperature T_c and the transition width ΔT_c were derived from the magnetic susceptibility and electrical resistivity (T_c = 39.2 K, ΔT_c = 0.5 K) and from the specific heat (T_c = 38 K, ΔT_c = 2 K). The temperature dependence of the specific heat exhibited a distinct jump corresponding to a superconducting transition; the magnitude of the jump was $\Delta C/T = 10$ mJ mol^{-1} K^2. The specific heat of the sample was measured using the adiabatic method with pulsed heating. The measurement error was 2% in the 1.5- to 4-K interval, 1% in the 4- to 10-K interval, and 0.2–0.5% from 10 to 50 K.

The specific heat was studied for two magnetic field orientations in the *a*–*b* plane, namely, along the *a* axis (in the [100] direction) and at 45° to the *a* axis (along [110]). We estimated the total error of determination of the orientation and sample adjustment with respect to the field as not exceeding 5′.

3. EXPERIMENTAL RESULTS

The specific-heat measurements on the $La_{1.85}Sr_{0.15}CuO_4$ single-crystal sample were carried out at low temperatures and in magnetic fields of 0, 2, 4, 6, and 8 T oriented in two directions, along the [100] and [110] axes. Figures 1–3 display series of the $C(T, H)$ dependences measured in the two magnetic field directions.

The experimental data obtained were analyzed as a sum of contributions, with each depending differently on the temperature and magnetic field.

Since, in a zero field, there is a line along which the energy gap vanishes, the electronic contribution to the low-temperature specific heat due to the electronic DOS at the Fermi level $C_{DOS}(T, 0)$ is proportional to the temperature squared:

$$C(T, 0) = C_{bkgd}(T) + C_{DOS}(T, 0)$$
$$= \gamma^*(0)T + \beta T^3 + \alpha T^2,$$

where $C_{bkgd}(T)$ includes a contribution that is linear in temperature, $\gamma^*(0)T$, whose nature remains unclear, and the phonon contribution βT^3.

In accordance with theory, we analyzed $C(T, H)$ under the assumption that the αT^2 term vanishes in a magnetic field and that $C_{bkgd}(T)$ is field-independent. Then, in a magnetic field, we have

$$C(T, H) = C_{bkgd}(T) + C_{DOS}(T, H).$$

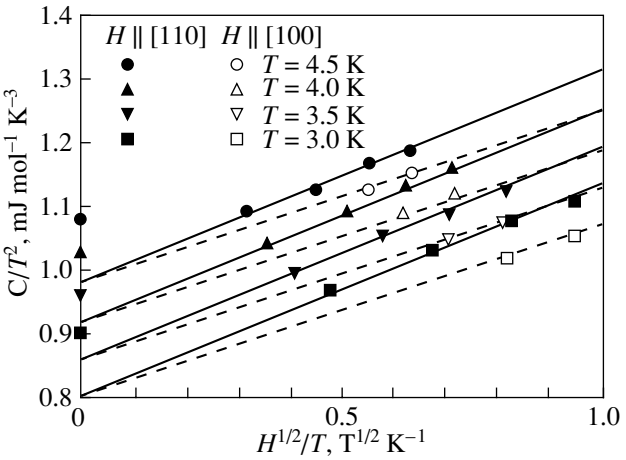

Fig. 1. Specific heat $C(T, H)$ of an $La_{1.85}Sr_{0.15}CuO_4$ sample in magnetic fields H = 0, 2, 4, 6, and 8 T plotted as $C(T, H)/T^2$ vs. $H^{1/2}/T$ for four fixed values of temperature and two magnetic field orientations along the [100] and [110] axes. The straight lines are least squares fits of the experimental points measured at 0, 2, 4, 6, and 8 T.

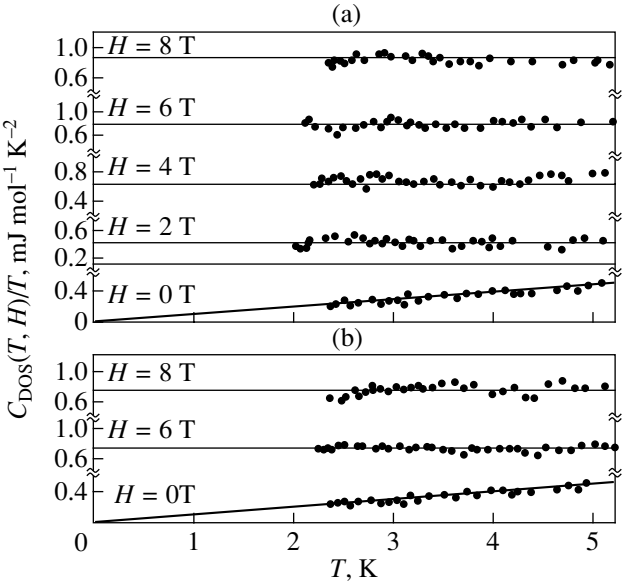

Fig. 2. Temperature dependence of C_{DOS}/T measured in magnetic fields of 0, 2, 4, 6, and 8 T for two magnetic field orientations: (a) along the [110] and (b) [100] axes.

To separate the contributions to specific heat that have dependences of the form $C_{DOS}(T, H) = \alpha T^2$ for $H = 0$ and $C_{DOS}(T, H) = bTH^{1/2}$ in a magnetic field, as predicted by theory, one can conveniently present the results as a series of $C(T, H)/T^2$ vs. $H^{1/2}/T$ relations plotted for several fixed temperatures. In such a representation, a relation of type $C(T, H) = C_{bkgd}(T) + bTH^{1/2}$ will be a straight line, whose slope is the coefficient b and whose vertical intercept yields a value of $C_{bkgd}(T)/T^2$ at

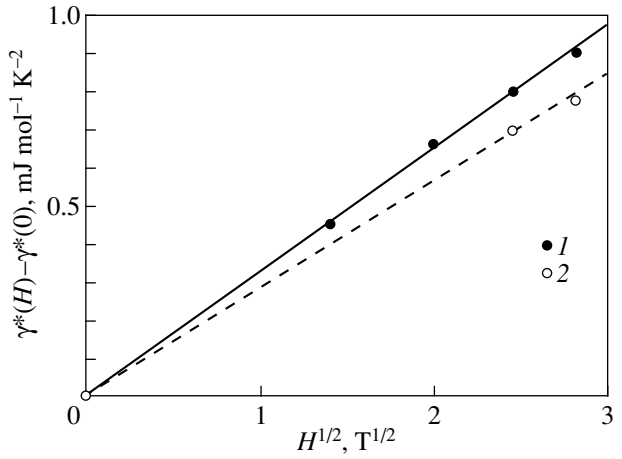

Fig. 3. Magnetic field dependence of the quantity $\Delta\gamma(H) = \gamma^*(H) - \gamma^*(0)$ plotted vs. $H^{1/2}$ for two magnetic field orientations, (*1*) along the [110] and (*2*) [100] axes. The straight lines are least squares fits corresponding to the relation $\Delta\gamma(H) = bH^{1/2}$.

the given temperature. One readily sees, however, that this relation does not persist to a zero field; indeed, the experimental points measured in a zero field lie above the straight line drawn through the points obtained with a magnetic field present. This may be due to the fact that at low magnetic fields, an additional contribution to the specific heat appears, which vanishes when a magnetic field is applied. The magnitude of this contribution is equal to the difference between the specific heat measured experimentally in a zero field and its value extrapolated to a zero field.

Figure 1 presents experimental data obtained for four fixed temperatures (3, 3.5, 4, and 4.5 K) in magnetic fields of 0, 2, 4, 6, and 8 T plotted in the C/T^2 vs. $H^{1.2}/T$ form for two magnetic field orientations ($H \parallel [100]$ and $H \parallel [110]$). The data obtained at each fixed temperature, except those measured at $H = 0$, are seen to lie on parallel straight lines having a slope dependent on the magnetic field orientation. The solid lines drawn on the data corresponding to the $H \parallel [110]$ orientation yield a slope $b_{[110]} = 0.34$ mJ mol^{-1} K^{-2} T$^{-1/2}$, and the dashed lines corresponding to the $H \parallel [100]$ case lie at a slope $b_{[100]} = 0.27$ mJ mol^{-1} K^{-2} T$^{-1/2}$.

The difference between the specific heat C/T^2 measured experimentally in a zero field and that extrapolated to a zero field is approximately constant for different temperatures and magnetic field orientations. The value of the α coefficient of the quadratic term derived from this difference is $\alpha = 0.1$ mJ mol^{-1} K^{-3}. This calculational scheme, which takes into account the quadratic term in the specific heat, permits one first to separate $C_{bkgd}(T)$ and then to determine the electronic specific heat $C_{DOS}(T, H) = C(T, H) - C_{bkgd}(T)$.

We analyzed the temperature dependence of the C_{bkgd} term obtained in the standard manner, $C_{bkgd}(T) = \gamma^*(0)T + \beta T^3$, and determined the coefficients of the linear and cubic contributions to the specific heat: $\gamma^*(0) = 0.65$ mJ mol^{-1} K^{-2} and $\beta = 0.189$ mJ mol^{-1} K^{-4}. This value of β corresponds to a Debye temperature of $\Theta_D = 419$ K.

Figure 2 plots the $C_{DOS}(T, H)/T$ relation as a function of temperature for two magnetic field directions, along the [100] and [110] axes. In a zero field, the experimental data fall on a straight line which passes through the origin, corresponding to $C_{DOS}(T, H) \sim T^2$. In a magnetic field, the experimental points fall on horizontal straight lines, corresponding to a linear temperature dependence of the specific heat, $C_{DOS}(T, H) \sim T$. As the magnetic field increases, the $C_{DOS}(T, H)/T$ plots shift toward larger values without changing their slope.

Figure 3 plots the quantity $\Delta\gamma(H) = \gamma^*(H) - \gamma^*(0)$ vs. $H^{1/2}$ for two magnetic field orientations, along the [100] and [110] axes. The specific heat is seen to increase with magnetic field, this effect being smaller for the field oriented along the *a* axis (for $H \parallel [100]$) than at 45° to this axis. The straight lines obtained using least squares fitting describe the experimental data well and provide supportive evidence for the quantity $\gamma^*(H) - \gamma^*(0)$ scaling nonlinearly as $bH^{1/2}$. The values of the slope *b* depend on the magnetic field orientation ($b_{[100]} = 0.28$ mJ mol^{-1} K^{-2} T$^{-1/2}$ and $b_{[110]} = 0.33$ mJ mol^{-1} K^{-2} T$^{-1/2}$) and are close in magnitude to the results displayed in Fig. 1. This means that the $C_{DOS}(T, H)$ contribution of the electronic DOS to the specific heat of $La_{1.85}Sr_{0.15}CuO_4$ has been determined to within acceptable accuracy.

A comparison of these values shows that the anisotropy in the electronic DOS for different magnetic field orientations, $[\gamma^*(H) - \gamma^*(0)_{[110]}]/[\gamma^*(H) - \gamma^*(0)_{[100]}]$, is 20%.

The electronic DOS anisotropy in the *a*–*b* plane observed by us can be assigned to that of the energy gap whose minimum lies along the [110] direction.

The energy gap in a two-dimensional $d_{x^2-y^2}$ superconductor can be written as $\Delta(k) = \Delta_0\cos(2\varphi)$, where φ is the angle characterizing the direction of the quasimomentum relative to the crystallographic axes. Assuming the Fermi surface to be cylindrical, the energy DOS of quasiparticles can be found by integrating over all values of the angle φ:

$$N(E) = \frac{N_0}{2\pi}\int_0^{2\pi} d\varphi \mathrm{Re}\left[\frac{E}{\sqrt{E^2 - \Delta_0^2\cos^2(2\varphi)}}\right],$$

where N_0 is the energy DOS at the Fermi level in the normal state. The electronic specific heat C_{DOS} in a zero field is related, for $T \ll T_c$, to the maximum width of the gap through the expression [6]

$$C_{DOS} = 3.28\gamma_n T^2/\Delta_0 = \alpha T^2,$$

where Δ_0 is the maximum energy gap in units of temperature.

Taking the estimate of the electronic specific-heat coefficient of $La_{1.85}Sr_{0.15}CuO_4$ in the normal state, γ_n = 9 mJ mol^{-1} K^{-2} [14], and our value of the coefficient α = 0.1 mJ mol^{-1} K^{-3}, we come to Δ_0 = 300 K as an estimate of the maximum energy gap at the Fermi level. For a dimensionless ratio of the energy gap width to the critical temperature, we obtain $2\Delta_0/T_c$ = 16, which implies strong coupling in the superconductor under study. Our estimate of $2\Delta_0/T_c$ is substantially larger than the value derived from the experimentally measured specific heat [6] and inelastic neutron scattering [18] and Raman scattering data [19], which may be due to the high quality of the single-crystal sample employed by us.

Low-energy Raman spectra of an $La_{1.83}Sr_{0.17}CuO_4$ single crystal were measured both above and below T_c. Redistribution of the Raman scattering intensity as a result of the opening of the superconducting gap was observed. An analysis of the Raman scattering intensity as a function of photon polarization showed that the gap is anisotropic and has zeros along the [±1, ±1] directions and maxima along [0, ±1]and [±1, 0], which indicates $d_{x^2-y^2}$ symmetry of the superconducting order parameter.

Our results on the electronic DOS anisotropy support the information obtained in Raman scattering experiments and give one grounds to assume that the energy gap on the Fermi surface is anisotropic and has zero lines on it.

ACKNOWLEDGMENTS

The authors are indebted to D.A. Shulyatev for preparation of the single-crystal $La_{1.85}Sr_{0.15}CuO_4$ samples.

This study was supported by the Scientific Council on the HTSC problem and by the State R & D program "Topical Problems in Condensed Matter Physics: Superconductivity," grant no. 96039.

REFERENCES

1. G. E. Volovik, Phys. Lett. A **142**, 282 (1989).
2. G. E. Volovik, Pis'ma Zh. Éksp. Teor. Fiz. **58**, 457 (1993) [JETP Lett. **58**, 469 (1993)].
3. N. V. Kopnin and G. E. Volovik, Pis'ma Zh. Éksp. Teor. Fiz. **64**, 641 (1996) [JETP Lett. **64**, 690 (1996)].
4. G. E. Volovik, Pis'ma Zh. Éksp. Teor. Fiz. **65**, 465 (1997) [JETP Lett. **65**, 491 (1997)].
5. Yu. A. Izyumov, Usp. Fiz. Nauk **169**, 225 (1999).
6. N. Momono and M. Ido, Physica C (Amsterdam) **264**, 311 (1996).
7. S. J. Chen, C. F. Chang, H. L. Tsay, *et al.*, Phys. Rev. B **58**, R14753 (1998).
8. N. E. Phillips, D. Buffeteau, R. Calemczuk, *et al.*, J. Supercond. **12**, 105 (1999).
9. R. A. Fisher, N. E. Phillips, A. Schilling, *et al.*, Phys. Rev. B **61**, 1473 (2000).
10. D. A. Wright, J. P. Emerson, B. F. Woodfield, *et al.*, Phys. Rev. Lett. **82**, 1550 (1999).
11. K. A. Moler, D. J. Baar, J. S. Urbach, *et al.*, Phys. Rev. Lett. **73**, 4023 (1994).
12. K. A. Moler, D. L. Sisson, J. S. Urbach, *et al.*, Phys. Rev. B **55**, 3954 (1997).
13. Y. Wang, B. Revaz, A. Erb, and A. Junod, Phys. Rev. B **63**, 094508 (2001).
14. A. M. Balbashov, D. A. Shulyatev, G. Kh. Panova, *et al.*, Physica C (Amsterdam) **256**, 371 (1996).
15. M. N. Khlopkin, G. Kh. Panova, N. A. Chernoplekov, *et al.*, Zh. Éksp. Teor. Fiz. **112**, 1386 (1997) [JETP **85**, 755 (1997)].
16. M. N. Khlopkin, G. Kh. Panova, N. A. Chernoplekov, and A. A. Shikov, Pis'ma Zh. Éksp. Teor. Fiz. **66**, 683 (1997) [JETP Lett. **66**, 715 (1997)].
17. G. Kh. Panova, A. A. Shikov, M. N. Khlopkin, *et al.*, Physica C (Amsterdam) **334**, 25 (2000).
18. K. Yamada, S. Wakimoto, G. Shirane, *et al.*, Phys. Rev. Lett. **75**, 1626 (1995).
19. X. K. Chen, J. C. Irwin, H. J. Trodahl, *et al.*, Phys. Rev. Lett. **73**, 3290 (1994).

Translated by G. Skrebtsov

Physics of the Solid State, Vol. 44, No. 1, 2002, pp. 34–41. Translated from Fizika Tverdogo Tela, Vol. 44, No. 1, 2002, pp. 33–40.

SEMICONDUCTORS AND DIELECTRICS

Anharmonicity of Lattice Vibrations Induced by Charged Nickel Impurities in II–VI Semiconductors

V. I. Sokolov*, N. B. Gruzdev*, E. A. Shirokov*, and A. N. Kislov**

** Institute of Metal Physics, Ural Division, Russian Academy of Sciences, ul. S. Kovalevskoĭ 18, Yekaterinburg, 620219 Russia*

*** Ural State Technical University, ul. Mira 19, Yekaterinburg, 620002 Russia*

e-mail: visokolov@imp.uran.ru

Received December 19, 2000; in final form, May 29, 2001

Abstract—The lattice vibrations induced by nickel impurities with a negative charge relative to the lattice in ZnSe : Ni, ZnO : Ni, ZnS : Ni, and CdS : Ni semiconductors are investigated using very sensitive field-induced vibronic spectroscopy. This technique is based on the interaction of lattice vibrations with impurity excitons and the effect of an ac electric field on these excitons. The phonon replicas of the zero-phonon line (ZPL) of impurity excitons (including intense peaks of combination replicas up to the eighth order) in the experimental spectra of the system under investigation are observed for the first time. These spectra make it possible to analyze the interaction between different vibrations. The experimental results are interpreted in terms of model calculations of the vibrations in a lattice with a charged impurity center and vibrations in a monoatomic chain with a strong anharmonicity. It is demonstrated that charged impurity centers initiate new lattice vibrations, namely, extrinsic anharmonic modes with a considerable third- or fourth-order anharmonicity. © *2002 MAIK "Nauka/Interperiodica".*

1. INTRODUCTION

Lattice vibrations induced by impurities have been investigated over the last decades. As a rule, new lattice vibrations associated with changes in the mass or force constants upon the introduction of an isovalent (neutral with respect to the lattice) impurity into the crystal are observed using IR absorption or first-order Raman spectroscopy. Recently, primary attention has been focused on either light impurities (that initiate local vibrations whose frequencies are substantially higher than those of phonons in a perfect lattice) or heavy impurities responsible for noticeable peaks in the frequency range of acoustic phonons. New vibrations (both local and resonance) are primarily due to vibrations of an impurity center and have a harmonic nature.

Substitutional impurities with an excess charge relative to the lattice in semiconductors, as a rule, are 3*d* or 4*f* ions, because an excess charge can be localized on the impurity only at the expense of a change in the number of electrons in a partially filled *d* or *f* shell. The 3*d* impurity can possess a stationary excess charge in the presence of a compensating impurity. Photoionization of the 3*d* impurity brings about the detachment of a *d* electron or a *d* hole from the impurity under exposure to light and the formation of a nonstationary excess charge. Hereafter, the vibrations thus induced by a charged impurity will be referred to as photoinduced vibrations. The majority of 3*d* impurities in semiconductors are not very light or very heavy compared to atoms of the host lattice. Consequently, new vibrations are predominantly governed by the motion of lattice atoms surrounding the impurity. Since the nearest-neighbor ions in a Coulomb field of the charged center are displaced in opposite directions, it can be assumed that new vibrations in the vicinity of displaced equilibrium positions exhibit a considerable anharmonicity. This situation is of particular interest from the viewpoint of existing theoretical concepts concerning the initiation of localized vibrations in the model of a monoatomic chain, provided the anharmonicity is very strong [1–4].

Under exposure to light, the impurity undergoes a transition to a hydrogen-like excited state; i.e., it forms an impurity exciton. In this case, both donor and acceptor excitons can be formed [5]. The formation of an impurity exciton is attended by a change in the impurity charge. This initiates photoinduced lattice vibrations. The charge carrier in the Coulomb field of the impurity center is sufficiently far removed and virtually does not affect the lattice strain in the vicinity of the charged impurity. Hence, knowing the type of impurity exciton, it is possible to assign unambiguously the new lattice vibrations to a particular charge of the impurity center.

The absorption spectrum at the photoionization band edge of nickel contains a zero-phonon line (ZPL), which is attributed to an electron transition to the impurity exciton state, and a series of its phonon replicas associated with the interaction between the impurity exciton and photoinduced lattice vibrations. This series of phonon replicas overlaps with the absorption caused by the transition of a carrier from the impurity to the allowed band. For this reason, it is extremely difficult or

even impossible to identify the phonon replicas of the zero-phonon line of the impurity exciton from the absorption spectra. In the present work, we used a radically different approach to the identification of the photoinduced vibrations. This approach accounts for the strong effect of an ac electric field on the hydrogenlike component of the wave functions for vibronic states and the weak effect of an ac electric field on the background absorption. The sensitivity of the proposed technique of field-induced vibronic spectroscopy is substantially higher than that of traditional methods. This technique makes it possible to separate reliably the phonon replicas of the zero-phonon line and to characterize them in detail. It was found that these replicas can be represented by a series of overtones of the dominant mode with frequencies $n\Omega$ and a series of combination phonon replicas with frequencies $(n\Omega + \omega_i)$, which are superpositions of overtones of the dominant mode and satellite modes with frequencies ω_i [6, 7]. Our special interest here is in the combination phonon replicas, which provide valuable information on the interaction of impurity excitons with photoinduced lattice vibrations and the interaction of the dominant mode with satellite vibrations. In this work, we systematically investigated four II–VI : Ni compounds and performed a comparative analysis of their experimental spectra.

2. EXPERIMENTAL TECHNIQUE

The measurements of the electroabsorption spectra for impurity excitons were described in detail in review [5]. In order to obtain the spectra with a large number of phonon replicas of the zero-phonon line, it is necessary to use samples with a low concentration of nickel impurities. This makes it possible to measure reliably signals within the energy range of photoionization with photon energies for which the absorption noticeably increases compared to that at the photoionization band edge. For the purpose of optimizing the conditions of measuring the variable and constant components of the light intensity, the measurements were carried out for several samples of different thicknesses and impurity concentrations [5]. The electroabsorption second-harmonic amplitude spectra were recorded on a setup equipped with an MDR-3 monochromator. The resolution was equal to 1–2 meV depending on the spectral range. The lowest resolution was observed in the high-energy range of the electroabsorption spectrum, i.e., in the range of the strongest absorption of the material. The error in determining the second-harmonic amplitude α_2 in this spectral range was 20–30%, whereas the error in the low-energy spectral range was 3–5%. As a rule, the reproducibility of the spectra was checked using samples of different thicknesses.

3. EXPERIMENTAL SPECTRA

Figures 1–3 display the spectra of the electroabsorption second harmonic amplitude α_2 for ZnSe : Ni, ZnS : Ni, and CdS : Ni semiconductors. The spectrum for ZnO : Ni is reported in [6]. In order to demonstrate more clearly the advantages of field-induced vibronic spectroscopy, the excitation spectra of the intracenter luminescence of ZnSe : Ni [8] and ZnS : Ni [9] are also shown for comparison in Figs. 1 and 2. The spectra are divided into regions that correspond to the first-order processes (F-OP) and higher-order processes (M-OP). Arrows in the spectra indicate the positions of negative peaks. For all the studied crystals, the line attributed to the acceptor exciton shifts in response to the electric

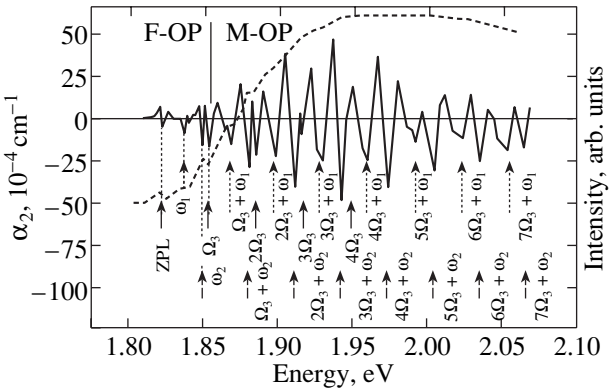

Fig. 1. Electroabsorption spectrum of ZnSe : Ni in the range of the acceptor exciton $[d^9h]$ (solid line). T = 4.2 K. The amplitude F_M of the ac electric field is 20 kV/cm. The dashed line represents the excitation spectrum of the $Ni^{+2}(d^8)$ intracenter photoluminescence [8]. Arrows indicate the positions of the zero-phonon line (ZPL) and its replicas at frequencies of the satellite modes ω_1 and ω_2, the dominant mode Ω_3, and their combinations $(n\Omega_3 + \omega_i)$. The electroabsorption and intracenter luminescence excitation spectra are divided into two regions that correspond to first-order processes (F-OP) and higher-order processes (M-OP).

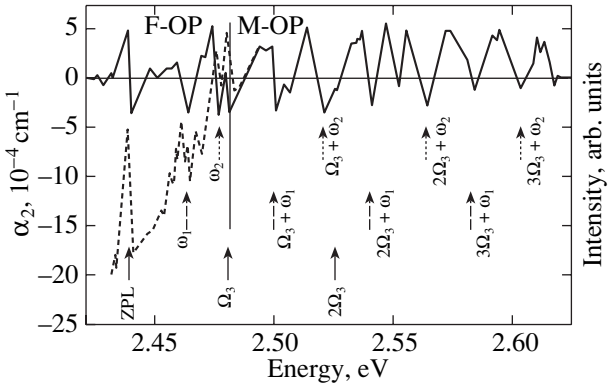

Fig. 2. Electroabsorption spectrum of ZnS : Ni in the range of the acceptor exciton $[d^9h]$ (solid line). T = 4.2 K. The amplitude F_M of the ac electric field is 25 kV/cm. The dashed line represents the excitation spectrum of the $Ni^{+2}(d^8)$ intracenter photoluminescence [9]. Arrows indicate the positions of the lines attributed to the dominant and satellite modes and their combinations.

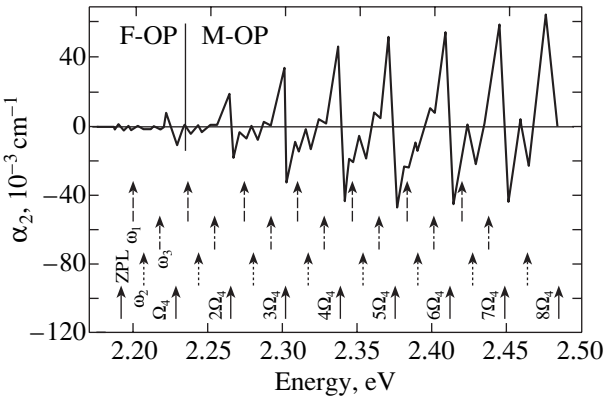

Fig. 3. Electroabsorption spectrum of CdS : Ni in the range of the acceptor exciton [d^9h] (solid line). T = 4.2 K. The amplitude F_M of the ac electric field is 30 kV/cm. The electric vector of the light wave is perpendicular to the optic axis. Arrows indicate the positions of the lines attributed to the dominant and satellite modes and their combinations.

field. As a result, the electroabsorption spectrum involves a structure of positive and negative peaks of identical intensity [5] and the point of passage through zero in this structure corresponds to the spectral line core in the absorption spectrum. If the lines in the absorption spectra are closely spaced, the structures in the electroabsorption spectrum overlap, which is especially pronounced in our spectra. Since, in this situation, the true energy positions of absorption bands are determined ambiguously, we indicate the locations of negative peaks whose energies are determined fairly exactly (to within the limits of spectral resolution).

It is clearly seen that all the spectra obtained are characterized by a common feature: the phonon replicas of the zero-phonon line are separated into several series in the region of higher-order processes. The peaks in each series are replicated at frequencies of the same mode. Let us consider, in greater detail, this pattern for the ZnSe : Ni semiconductor. The electroabsorption spectrum of ZnSe : Ni (Fig. 1) reflects the effect of the ac electric field on the zero-phonon line of the acceptor exciton [d^9h] and its phonon replicas. The interaction of the impurity exciton with first-order vibrations manifests itself in the first region of the electroabsorption spectrum, and the interactions of the impurity exciton with second-, third-, and higher-order vibrations are observed in the second region. The first region of the spectrum involves the zero-phonon line replicas at the frequencies ω_1 and ω_2 and the most intense structure at the frequency Ω_3. The region of multimode replicas contains the peaks $2\Omega_3$, $3\Omega_3$, and $4\Omega_3$ and more intense combination peaks ($n\Omega_3 + \omega_1$) and ($n\Omega_3 + \omega_2$). Therefore, all the peaks in the first-order region are replicated in the higher-order region at frequencies shifted by $n\Omega_3$. The most unexpected feature observed in the structure of phonon replicas is that the intensities of the ($n\Omega_3 + \omega_1$) and ($n\Omega_3 + \omega_2$) peaks of the combination replicas are considerably higher than those of the peaks attributed to the $n\Omega_3$ overtones of the dominant mode. Intense combination replicas are observed at $n > 4$, for which the $n\Omega_3$ peaks of the dominant mode are absent. This feature has defied explanation in the case when the vibrational process is considered within the harmonic approximation, because the intensities of the peaks of the combination phonon replicas should be proportional to the product of the intensities of peaks forming the combination replicas [10]. Consequently, the intensities of the ($n\Omega_3 + \omega_1$) combination peaks should be small because of the low intensity of the first-order peak at the frequency ω_1, whereas the peaks at $n > 4$ should be absent. However, the intensities of the combination peaks are substantially higher than those of the zero-phonon line and the maximum peaks of the dominant mode at $n = 2$. The number n of the last peak observed in the series of overtones of the dominant mode will be referred to as the critical number n_{cr}. As can be seen from the figures, the critical number n_{cr} has the following values: $n_{cr} = 2$ for ZnS : Ni, $n_{cr} = 4$ for ZnSe : Ni, and $n_{cr} = 8$ for CdS : Ni. According to [6], the critical number n_{cr} for ZnO : Ni is 6.

Let us now compare our electroabsorption spectra with the spectra of other systems that are characterized by the carrier localization and sufficiently intense phonon replicas of electron transitions. In particular, the line of the exciton bound to either a Zn vacancy or a Cu impurity substituting for Zn (the total energy of additional localization of the electron–hole pair is approximately equal to 20 meV) and a series of phonon replicas due to the interaction with longitudinal optical (LO) phonons were repeatedly observed for ZnSe. As is seen from Fig. 1 reported in [11], the spectrum involves four clear-cut LO replicas of the I_1^{DEEP} line. The intensity of these replicas is considerably less than that of the zero-phonon line and decreases rapidly with an increase in the replica number n. This indicates that the Huang–Rhys factor S, which characterizes the coupling of longitudinal optical lattice vibrations with a hydrogen-like electronic state, is appreciably less than unity. Note that, for this system, combined states of the ($n\omega_{LO} + \omega$) type were not found. Recently, Vavilov *et al.* [12] examined the cathodoluminescence spectrum of ZnSe and revealed the series $I_i^S - n\text{LO} = m\text{P1}$, where I_i^S is the line of an exciton bound to a zinc vacancy defect and mPl is a series of phonon replicas of the plasma type. However, the nLO and mPl series manifest themselves independently of each other and cannot be considered combination phonon replicas when each nLO replica of the zero-phonon line is accompanied only by a single Pl peak.

Another local system is an exciton bound to an O oxygen impurity in ZnTe : O [13]. The energy of additional localization of the electron–hole pair is approximately equal to 410 meV. In this case, the energy of the

strongly localized electron trapped by the local potential is equal to 350 meV and the energy of the hydrogen-like hole is 60 meV. The wave function of the electron is spatially localized and decays rapidly. This leads to a strong interaction of the localized exciton with lattice vibrations [14]. As a result, the luminescence and impurity absorption spectra exhibit intense phonon replicas that consist of a set of $n\Omega$ peaks and $(n\Omega + \omega_i)$ combination replicas (the Ω frequency is close to the frequency of the longitudinal optical phonons). It should be noted that the intensities of the combination replicas of the zero-phonon line in the luminescence spectrum do not exceed the intensity of the $n\Omega$ peaks. The absorption spectrum contains the background contribution due to the impurity–valence band transitions, which changes the intensity ratio of the $n\Omega$ and $(n\Omega + \omega_i)$ peaks. In this system, the S factor is approximately equal to 3. This value corresponds to the maximum intensity of the peaks at $n = 3$.

A molecular ion MnO_4^- in the lattice of KBr and RbBr alkali halide crystals [15, 16] is the most prominent example of a system of the local type. The vibrational frequencies of this ion are considerably higher than the maximum frequency of optical phonons in the aforementioned crystals. The phonon replicas of the $^1A_1$–$^1T_2$ electron transition in the absorption and photoluminescence spectra of KBr crystals involve a set of $n\nu_1$ and $(n\nu_1 + \nu_2)$ peaks. The intensity of the $n\nu_1$ overtones is described by the Poisson distribution $I_n \sim (e^{-S}S^n/n!)$. Here, the factor S is equal to two or three. However, the intensity of the $(n\nu_1 + \nu_2)$ combination (composite) modes is universally less than that of the $n\nu_1$ peaks. For these systems, there occurs no situation when, at $n > n_{cr}$, the composite modes are clearly observed but overtones of the dominant mode are absent.

Thus, the observed structure of the phonon replicas of the zero-phonon line for Ni impurity excitons differs from the spectra obtained earlier for the other systems in two aspects. First, for the ZnSe : Ni and ZnO : Ni crystals, the intensity of the combination peaks substantially exceeds the intensity of overtones of the dominant mode. Second, in the series of phonon replicas of the zero-phonon line for the ZnSe : Ni, ZnS : Ni, and ZnO : Ni crystals, there exists such a critical number n_{cr} that the $n\Omega$ overtones of the dominant mode and the $(n\Omega + \omega_i)$ combination peaks are observed at $n < n_{cr}$, whereas only the $(n\Omega + \omega_i)$ combination peaks arise at $n > n_{cr}$. These features are revealed only for impurity excitons in II–VI : Ni crystals.

4. DISCUSSION

Now, we consider the type of lattice vibrations interacting with an impurity exciton. The theoretical parameters of the vibrational spectrum and the frequencies of phonon replicas in the electroabsorption spectra of II–VI semiconductor crystals are listed in the table. It can be seen that, in a number of cases, the frequency Ω of the dominant mode is very close to the frequencies of longitudinal optical vibrations. Possibly, this was the reason why the peaks in the absorption and intracenter luminescence excitation spectra were assigned to longitudinal optical phonons [8, 9]. The impurity exciton can interact with phonons at the expense of the hydrogen-like carrier. However, in this case, the S factor must be less than unity. In our case, the structure of the phonon replicas is similar to that for systems with a considerable localization, because the carrier held by the local potential resides in the d shell. This gives rise to an excess charge, which, in turn, induces lattice strains and localized vibrations. It is these vibrations that interact with the impurity exciton through the d shell of the impurity center. The model calculations of these vibrations in ZnSe : Ni and ZnO : Ni were performed in our earlier works [21, 22].

First, we calculated the displacements of the nearest-neighbor ions to new equilibrium positions (lattice relaxation) after the change in the impurity charge. It was assumed that the radius of the impurity in the neutral state is close to the radius of the replaced atom and that displacements of the nearest neighbors with respect to the neutral impurity center are absent. This situation takes place for Ni^{+2} substituting for Zn^{2+} in II–VI compounds. Then, we calculated the vibrational spectrum of the lattice. According to [21], the lattice relaxation was calculated without regard for the hybridization of electrons in the d shell with the band states; i.e., the charge of the Ni^+ impurity ion (the d^9 configu-

Parameters of lattice vibrations and experimental frequencies of phonon replicas in the electroabsorption spectra of crystals (in THz)

Crystal	Gap	ω_M	LO	TO	Ω	ω_i			References
ZnSe	5.76–6.00	8.32	7.58	6.26	$\Omega_3 = 7.84$	$\omega_1 = 3.48$	$\omega_2 = 6.28$	–	[17, 20]
ZnO	8.25–11.58	17.00	17.22	11.40	$\Omega_4 = 17.65$	$\omega_1 = 3.63$	$\omega_2 = 10.63$*	$\omega_3 = 15.74$	[7, 18, 20]
ZnS	6.18–8.10	10.5	11.00	8.22	$\Omega_3 = 10.35$	$\omega_1 = 5.32$	$\omega_2 = 9.19$	–	[17, 20]
CdS	4.0–6.9	9.2	9.06	6.84	$\Omega_4 = 8.94$	$\omega_1 = 1.43$	$\omega_2 = 3.63$	$\omega_3 = 6.29$*	[19, 20]

* Experimental frequencies of vibrational modes in the gap between acoustic and optical vibrations calculated for crystals free of Ni impurities.

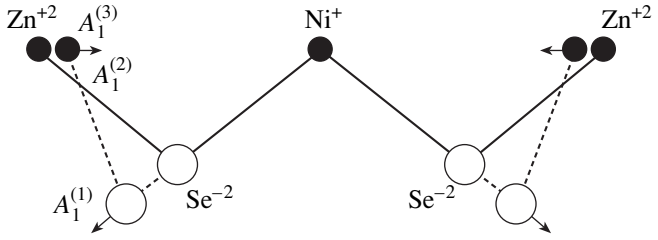

Fig. 4. Section of the $NiSe_4Zn_{12}$ cluster by the (110) plane. Positions of the Se^{2-} ions of the first coordination sphere and the Zn^{2+} ions of the second coordination sphere and the chemical bonds for the $Ni^{+2}(d^8)$ neutral impurity (solid lines) and the $Ni^{+}(d^9)$ impurity with an excess negative charge (dashed lines) are shown. Arrows indicate the ionic displacements corresponding to the totally symmetric vibrational modes A_1 of the T_d cluster.

ration) was taken precisely equal to –1. The results of the model calculations demonstrate that the ions of the first coordination sphere undergo the largest displacement. This displacement is equal to 0.24–0.25 Å; i.e., it comprises approximately 10% of the bond length. The ions of the second coordination sphere are displaced with respect to the initial equilibrium position by approximately 0.04 Å, which corresponds to approximately 1% of the distance to the impurity. The ions of other coordination spheres are displaced from equilibrium positions by a substantially smaller distance. The distortion of the cluster is shown in Fig. 4. The change in the distance between the Se^{-2} ions of the first coordination sphere and the Zn^{2+} ions of the second coordination sphere is equal to 0.1 Å; i.e., it comprises 4% of the bond length. For comparison, we note that the bond lengths in the majority of solids at melting temperatures increase by approximately 3% and that the hydrostatic compression of ZnSe crystals leads to a change in the lattice parameter by 4% at a pressure of approximately 100 kbar and to a transition between the phases with zinc blende and NaCl-type lattices at a pressure of 135 kbar [23]. These findings give grounds to believe that the photoionization of the impurity can result in a considerable lattice distortion in the vicinity of the charged impurity center. Within the model of a diatomic chain with a charged impurity, it is easy to demonstrate that the displacement of the Zn^{2+} (the second coordination sphere) and Se^{2-} (the first coordination sphere) ions leads to an asymmetric arrangement of these ions with respect to the nearest neighbors. In addition to changes in the distances between the atoms of the first and second coordination spheres, the lattice distortion is accompanied by a change in the distance between the neighboring ions of the same coordination sphere. In our case, the Zn^{2+} ions (the second coordination sphere) approach each other, whereas the distance between the Se^{2-} ions (the first coordination sphere) increases. This can be represented as a symmetric lattice distortion that is equivalent to a uniform contraction or elongation of a monoatomic chain.

The results of the vibrational mode calculations for ZnSe : Ni^{+} (d^9) and ZnO : Ni^{+} (d^9) are shown in Figs. 5 and 6, respectively. For ZnSe : Ni, a change in the charge $Ni^{+2} \longrightarrow Ni^{+}$ results in the appearance of peaks *1–4*. Peaks *1* and *2* in the acoustic spectral range are associated with the motion of Se^{2-} ions and correlate with the spectral structure at the frequency ω_1 in the experimental spectrum. Peak *3*, which is attributed to the motion of Zn^{2+} ions with the symmetries A_1 and E [the sum of the A_1(Zn) and E(Zn) modes], can be assigned to the satellite mode with the frequency ω_2. Peak *4* correlates with the Ω_3 dominant mode and arises from the vibrations of the Zn^{2+} ions with the A_1 symmetry. The model calculations for ZnO : Ni demonstrate that the dominant mode with the frequency Ω_4 corresponds to an E(O)-type peak in the optical range of the vibrational spectrum, whereas the ω_2 satellite mode giving rise to the most intense combination peaks is governed by the gap mode with the A_1(O) symmetry.

The results of model calculations and a certain similarity of the combination phonon replica structure in the electroabsorption spectra to the absorption spectra for systems with a strong localization [15, 16] indicate that vibrations induced by a change in the charge of the impurity center substantially differ from the vibrations observed in a perfect lattice. These differences are associated with the specific features of the lattice distortion, i.e., with symmetric and asymmetric changes in the positions of ions in the first and second coordination spheres with respect to the nearest neighbors. This is clearly seen from Fig. 4. The Se^{2-} ion (the first coordination sphere) is asymmetrically arranged relative to the Ni^{+} and Zn^{2+} (the second coordination sphere) ions, and the Zn^{2+} ion (the second coordination sphere) is asymmetrically located with respect to the Se^{2-} (the first coordination sphere) and Se^{2-} (the third coordination sphere) ions. (The ions of the third coordination sphere are not shown in Fig. 4.) This can give rise to a considerable cubic anharmonicity (K_3x^3) of the lattice vibrations induced by a charged impurity. It is because of this cubic anharmonicity that one of the modes becomes dominant. The reason for this is that, owing to the anharmonicity, this mode loses its energy to other vibrations. An increase in the replica number n occurs with an increase in the amplitude of the dominant mode and, correspondingly, in its anharmonicity, which results in an increase in the rate of energy transfer. At $n = n_{cr}$, the dominant mode completely loses the energy stored from light to other vibrations; hence, it is not observed in the spectrum for $n > n_{cr}$. Seemingly, the combination vibrations should also disappear, because two of the three satellite modes are only a very small fraction of the total number of the vibrations to which the dominant mode loses its energy. Therefore, it is reasonable to expect that the energy transferred to the sat-

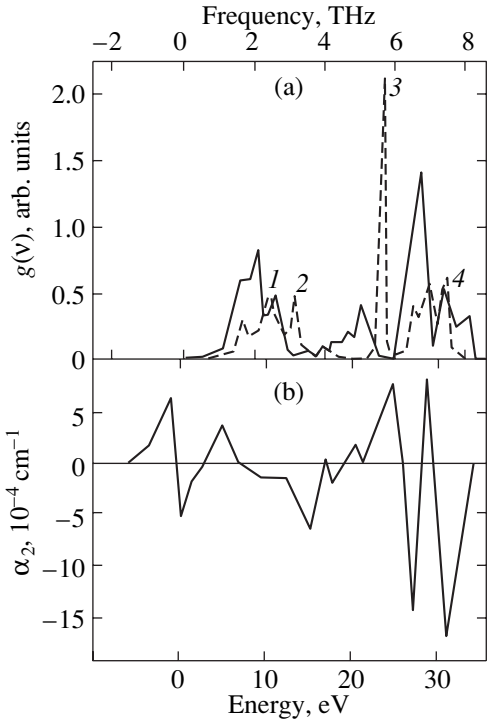

Fig. 5. Vibrational states of ZnSe. (a) The total density of vibrational states for a perfect crystal (solid line) [17] and the total projected density of the modes A_1, E, and T_2 for a crystal with Ni^+ ions (dashed line). Peaks *1* (A_1) and *2* (T_2) are attributed to motion of Se^{2-} ions (first coordination sphere), and peaks *3* (A_1, E) and *4* (A_1) are assigned to motion of Zn^{2+} ions (second coordination sphere). (b) Phonon replicas of the zero-phonon line of the $[d^9h]$ acceptor exciton in the region of first-order processes (F-OP).

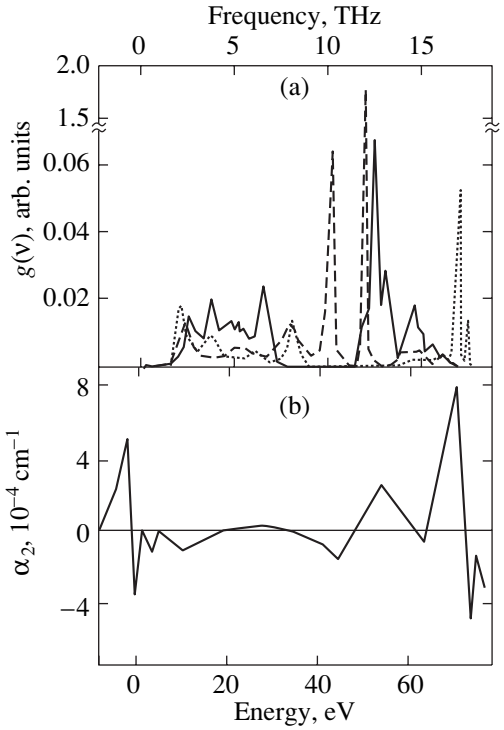

Fig. 6. Vibrational states of ZnO. (a) The total density of vibrational states for a perfect crystal (solid line) and the total projected density of the vibrational modes A_1 (dashed line) and E (doted line) for a NiO_4 cluster with an excess negative charge of the nickel impurity. (b) Phonon replicas of the zero-phonon line of the $[d^9h]$ acceptor exciton in the region of first-order processes (F-OP).

ellite modes should be insignificant. However, in actual fact, the intensity of combination peaks slowly decreases with an increase in the replica number n at $n > n_{cr}$. In our opinion, this can be explained in terms of the anharmonicity of the satellite modes. This anharmonicity differs in magnitude and character from the anharmonicity of the dominant mode, and the interaction between these modes is very unusual.

A comparison of the electroabsorption spectra for different materials indicates a difference between the intensities of the combination peaks and the peaks of the dominant mode in these spectra. For example, the intensity of the combination peaks for ZnSe : Ni is appreciably higher than that of the peaks of the dominant mode. At the same time, as the number n increases, the intensity of the combination peaks for CdS : Ni exceeds the intensity of the zero-phonon line but remains considerably less than the intensity of the peaks of the dominant mode. The difference between the intensities of combination replicas for different satellite modes in the same material is especially pronounced for ZnO : Ni, in which the sole mode ω_2 is observed at $n > n_{cr}$. This suggests a different interaction of the satellite modes with the dominant vibrations due to the difference in anharmonicity of the satellite modes.

At present, it is difficult to draw conclusions regarding the nature of the anharmonicity of satellite modes. We can only make certain assumptions based on recent theoretical results that prove the strong anharmonicity of satellite modes and experimental data on the anharmonicity of molecules and molecular defects in alkali chalcogenide crystals. The potential energy of a chain composed of identical atoms can be represented as $U(x) = K_2x^2 + K_2x^4$, where x is the displacement from an equilibrium position. In a perfect lattice, the fourth-order anharmonicity can induce specific vibrations whose frequency depends on the vibration amplitude and the ratio K_4/K_2 between the anharmonic and harmonic constants. The high-frequency localized mode (termed the discrete breather [4]) arises at $K_4 > 0$, whereas the anharmonic resonant mode appears at $K_4 < 0$. According to Takeno and Sievers [3], the anharmonic resonant mode is associated with the motion of only a single atom and the neighboring atoms are virtually at rest. Within the model of a monoatomic chain with

fourth-order anharmonicity and an impurity center, Kosevich and Kovalev [24] showed that the anharmonicity favors the excitation of quasi-localized vibrations of the impurity center. In our case, the dominant and satellite modes are initiated by the impurity. Hence, they can be referred to as extrinsic anharmonic modes or extrinsic breathers. The extrinsic anharmonic modes are induced by the motion of ions in the first and second coordination spheres when the distances between these ions and their neighbors in a cluster are symmetrically and asymmetrically distorted as a result of lattice strain. Therefore, it can be assumed that a noticeable fourth-order (K_4x^4) and third-order (K_3x^3) anharmonicity can appear in the expansion of the potential energy in terms of the displacement from the equilibrium position. It is quite possible that the different ratios of these contributions determine the specific features of the interaction between the satellite and dominant modes. For example, the Ω_3 dominant mode for the Ni acceptor exciton in ZnSe : Ni has the A_1 symmetry and can be associated with Zn^{2+} ion motion when the ions are displaced to new equilibrium positions in the asymmetrically distorted structure (Fig. 4). This mode should exhibit a considerable cubic anharmonicity (K_3x^3). The ω_2 satellite mode corresponds to the calculated peak *3* in the projected density of states (Fig. 5). The two modes A_1(Zn) and E(Zn) contribute to this peak. The A_1(Zn) mode is characterized by a cubic anharmonicity. The vibration with the E(Zn) symmetry is initiated by the interaction of all ions in the cluster, including the interaction between the Zn^{2+} and Zn^{2+} ions, which approach each other upon lattice distortion in the field of the negatively charged Ni^+ ion. This suggests that the fourth-order anharmonicity for the E(Zn) mode increases in the same manner as for the monoatomic chain upon its contraction. The A_1(Zn) and E(Zn) vibrations derive their energy from the dominant mode in different ways. The A_1(Zn) oscillator with cubic symmetry loses its energy upon the negative displacement x, because the anharmonic force $-K_3x^2$ and the harmonic force $-K_2x$ act in opposite directions. For the E(Zn) oscillator, the anharmonic force $-K_4x^3$ always coincides in direction with the harmonic force $-K_2x$. As a consequence, this oscillator accumulates the energy derived from the dominant mode. This manifests itself in an increase in the intensity of the peaks of the $(n\Omega_3 + \omega_2)$ combination replicas with an increase in the number n. The satellite mode with K_4x^4 anharmonicity resembles the anharmonic resonant mode studied in [3]. The sole difference lies in the fact that all ions of the $NiSe_4Zn_{12}$ cluster participate in the extrinsic anharmonic mode, whereas only the motion of a single atom of the chain contributes to the modes investigated by Takeno and Sievers [3]. Therefore, there are grounds to believe that the cluster distortion in the field of the negatively charged Ni^+ impurity brings about an increase in the fourth-order anharmonicity of the ω_2 satellite mode (as is the case with the monoatomic chain upon its uniform contraction) and in the cubic anharmonicity of the Ω_3 dominant mode. Since the constant K_3 for different materials can differ significantly, it can be expected that the rate of energy transfer to other vibrations in different materials will also be different. Moreover, several modes can exhibit a cross anharmonicity (in [25], the anharmonicity constants are designated as x_{ij}). Note that the x_{ij} constant describing the interaction of two modes, as a rule, is slightly larger than the anharmonicity constant x_{ii}. In the case when the anharmonicity constants x_{ij} and x_{ii} are small, there appear only dominant peaks and very low-intensity combination replicas. In this situation, the replicas do not exceed the dominant peaks and are absent at $n > n_{cr}$. It is this pattern that is observed in the absorption, luminescence, and Raman spectra of KBr : MnO_4 and RbBr : MnO_4 crystals and the electroabsorption spectrum of CdS : Ni. In the last case, the overall spectrum of phonon replicas remains unknown because of the proximity to the fundamental absorption edge, which makes correct interpretation of the experimental results complicated.

5. CONCLUSION

Thus, the experimental data and the results of model calculations allow us to make certain inferences concerning the nature of vibrations induced by charged impurity centers. First, the vibrations under investigation are associated primarily with the motion of lattice ions in the vicinity of an impurity center. These vibrations are characterized by either the gap modes or the quasi-localized modes whose frequencies only slightly exceed the maximum frequencies ω_M of optical vibrations. The contribution from the $Ni^+(d^9)$ impurity center to excitation of the dominant and satellite modes is insignificant. Second, the dominant and satellite modes exhibit a considerable anharmonicity. This justifies the term extrinsic anharmonic mode (extrinsic breather) introduced in this work. The satellite modes with fourth-order anharmonicity somewhat resemble the anharmonic resonant modes considered by Takeno and Sievers [3] for a monoatomic chain. The dominant and satellite extrinsic anharmonic modes induced by charged impurity centers in II–VI semiconductors and their interaction with each other and with impurity excitons call for further theoretical and experimental investigations. In our opinion, it is of particular interest to consider vibrations initiated by charged impurities in crystals with a substantial intrinsic anharmonicity (for example, BeSe and BeTe [26]). Third, the excitation of extrinsic anharmonic modes upon photoionization of impurity centers makes it possible to use very sensitive field-induced vibronic spectroscopy to identify new vibrations. The generation of charged centers during photoionization of impurities provides a way of transforming the light energy into the energy of crystal vibrations under conditions of considerable anharmo-

nicity. Moreover, elucidation of the nature and mechanisms responsible for photoinduced vibrations opens up ways to investigate the dynamics of formation of extrinsic breathers upon changes in the impurity charge with the use of short laser pulses, as in the case of the kinetics of chemical reactions [27].

ACKNOWLEDGMENTS

We are grateful to A.B. Borisov and K.A. Kikoin for their participation in discussions of the problem concerning the anharmonicity of lattice vibrations.

REFERENCES

1. A. S. Dolgov, Fiz. Tverd. Tela (Leningrad) **28** (6), 1641 (1986) [Sov. Phys. Solid State **28**, 907 (1986)].
2. A. J. Sievers and S. Takeno, Phys. Rev. Lett. **61** (8), 970 (1988).
3. S. Takeno and A. J. Sievers, Solid State Commun. **67** (11), 1023 (1988).
4. S. Flach and C. R. Willis, Phys. Rep. **295**, 181 (1998).
5. V. I. Sokolov, Fiz. Tekh. Poluprovodn. (St. Petersburg) **28** (4), 545 (1994) [Semiconductors **28**, 329 (1994)].
6. V. I. Sokolov, E. A. Shirokov, A. N. Kislov, and V. G. Mazurenko, Phys. Status Solidi B **221** (1), 553 (2000).
7. V. I. Sokolov, E. A. Shirokov, A. N. Kislov, and V. G. Mazurenko, J. Cryst. Growth **214–215** (4), 304 (2000).
8. S. G. Bishop, D. J. Robbins, and P. J. Dean, Solid State Commun. **33**, 119 (1980).
9. R. Heitz, A. Hoffmann, and I. Broser, Phys. Rev. B **48** (12), 8672 (1993).
10. K. K. Rebane, *The Elementary Theory of Vibrational Structure of the Spectra of Impurity Centers in Crystals* (Nauka, Moscow, 1968).
11. S. Satoh and K. Igaki, Jpn. J. Appl. Phys. **20** (10), 1889 (1981).
12. V. S. Vavilov, A. A. Klyukanov, K. D. Sushkevich, *et al.*, Fiz. Tverd. Tela (St. Petersburg) **41** (7), 1176 (1999) [Phys. Solid State **41**, 1070 (1999)].
13. D. G. Thomas, J. J. Hopfield, and C. J. Frosch, Phys. Rev. Lett. **15**, 857 (1965).
14. V. I. Sokolov and T. P. Surkova, Fiz. Tverd. Tela (Leningrad) **29** (10), 2938 (1987) [Sov. Phys. Solid State **29**, 1689 (1987)].
15. T. I. Maksimova and A. M. Mintairov, Fiz. Tverd. Tela (Leningrad) **27** (8), 2468 (1985) [Sov. Phys. Solid State **27**, 1477 (1985)].
16. T. I. Maksimova and A. M. Mintairov, Fiz. Tverd. Tela (Leningrad) **29** (5), 1422 (1987) [Sov. Phys. Solid State **29**, 813 (1987)].
17. K. Kunc, M. Balkanski, and M. A. Nusimovici, Phys. Status Solidi B **72**, 229 (1975).
18. S. V. Mel'nichuk, V. I. Sokolov, T. P. Surkova, and V. M. Chernov, Fiz. Tverd. Tela (Leningrad) **33** (11), 3247 (1991) [Sov. Phys. Solid State **33**, 1833 (1991)].
19. J. Camacho and A. Cantarero, Phys. Status Solidi B **215**, 181 (1999).
20. *Landolt–Börnstein: Numerical Data and Functional Relationships in Science and Technology*, Vol. 17: *Semiconductors: Physics of II–VI Compounds*, Ed. by O. Madelung (Springer-Verlag, Berlin, 1982).
21. A. N. Kislov, V. G. Mazurenko, V. I. Sokolov, and A. N. Varaksin, Fiz. Tverd. Tela (St. Petersburg) **39** (12), 2147 (1997) [Phys. Solid State **39**, 1921 (1997)].
22. A. N. Kislov, V. G. Mazurenko, V. I. Sokolov, and A. N. Varaksin, Fiz. Tverd. Tela (St. Petersburg) **41** (6), 986 (1999) [Phys. Solid State **41**, 897 (1999)].
23. S. Ves, K. Strössner, N. E. Christensen, *et al.*, Solid State Commun. **56**, 479 (1985).
24. A. M. Kosevich and A. S. Kovalev, Fiz. Nizk. Temp. **1** (12), 1544 (1975) [Sov. J. Low Temp. Phys. **1**, 742 (1975)].
25. A. A. Ovchinnikov and N. S. Érikhman, Usp. Fiz. Nauk **138** (2), 289 (1982) [Sov. Phys. Usp. **25**, 738 (1982)].
26. V. Wagner, J. J. Liang, R. Kruse, *et al.*, Phys. Status Solidi B **215** (1), 87 (1999).
27. M. Gruebele and A. Zewail, Phys. Today **43**, 24 (1990).

Translated by O. Borovik-Romanova

Physics of the Solid State, Vol. 44, No. 1, 2002, pp. 4–7. Translated from Fizika Tverdogo Tela, Vol. 44, No. 1, 2002, pp. 6–8.

Canonical Form of the Averaged Equations of Motion of a Charged Particle upon Superposition of an Electromagnetic Wave Field on a Weakly Inhomogeneous Magnetic Field

V. E. Tarasov, K. Sh. Khodzhaev, and A. G. Chirkov

St. Petersburg State Technical University, Politekhnicheskaya ul. 29, St. Petersburg, 195251 Russia

Received May 21, 2001

Abstract—The Hamiltonian function of a charged particle in a weakly inhomogeneous magnetic field perturbed by a plane wave is determined correct to terms of the order of the small parameter inclusive. The canonical motion equations averaged over the fast phase for motion in the vicinity of the resonance are derived.

The problem of motion of a charged particle in an electromagnetic wave field was treated earlier in [1–3]. In these works, the motion of a particle was investigated under the conditions when an electromagnetic wave field was superposed on a constant magnetic field. However, the methods used in [1–3] failed to analyze the equation of motion of a charged particle upon superposition of an electromagnetic wave field on a weakly inhomogeneous magnetic field. In our recent work [4], we obtained an expression for the Hamiltonian function that provides an adequate description of the aforementioned motion.

Similar problems are of considerable interest in astrophysics, plasma physics, and practical applications. In particular, the problem of controlled thermonuclear reactions can be reduced, in many cases, to the problem of confinement of charged particles in closed configurations. The properties of the simplest adiabatic traps were studied earlier. Resonance motions and nonadiabatic resonance methods of confinement can be analyzed after the sought equations have been deduced.

We consider the case when a field rapidly varying with time is induced by a plane elliptically polarized wave. The electric field of this wave can be represented in the form

$$\mathbf{E}_v = \mathbf{n}_1 E_1 \cos\left(\frac{\omega}{c}\mathbf{n}_3\mathbf{r} - \omega t\right) + \mathbf{n}_2 E_2 \sin\left(\frac{\omega}{c}\mathbf{n}_3\mathbf{r} - \omega t\right). \quad (1)$$

Here, E_1 = const, E_2 = const, and $\mathbf{n}_i$ (i = 1, 2, 3) are the unit vectors forming a right Cartesian trihedron. The scalar potential of the wave field is set equal to zero, and the vector potential can be taken in the form

$$\mathbf{A}_v = \frac{c}{\omega}\left[\mathbf{n}_1 E_1 \sin\left(\frac{\omega}{c}\mathbf{n}_3\mathbf{r} - \omega t\right) - \mathbf{n}_2 E_2 \cos\left(\frac{\omega}{c}\mathbf{n}_3\mathbf{r} - \omega t\right)\right]. \quad (2)$$

By analogy with the calculations performed in [4], we change over to dimensionless variables and write the expression for a dimensionless vector potential as equal to the dimensional potential divided by the product $[L][B]$, where the quantities in square brackets denote representative values of the corresponding variables. Let us assume that $[E]$ is the representative value of the electric wave amplitude. By introducing the same designations for the dimensional and dimensionless quantities, we obtain

$$\mathbf{A}_v = \frac{c[E]}{\omega[L][B]}\left[\mathbf{n}_1 E_1 \sin\left(\frac{\varepsilon_1}{\varepsilon}\mathbf{n}_3\mathbf{r} - \nu t\right) - \mathbf{n}_2 E_2 \cos\left(\frac{\varepsilon_1}{\varepsilon}\mathbf{n}_3\mathbf{r} - \nu t\right)\right]. \quad (3)$$

Here, $\varepsilon_1 = \omega[R_L]/c$, $\nu = \omega/[\omega_L]$, and $\varepsilon = [R_L]/L$ (the designations are similar to those used in [4]).

The parameter ε_1 can be rewritten in the form $\varepsilon_1 = (\omega/[\omega_L])([V]/c)$. In what follows, we will consider motions for which the values of ω and $[\omega_L]$ are of the same order of magnitude. Moreover, the motion is assumed from the outset to be nonrelativistic; hence, the ratio $[V]/c$ is a small quantity. Correspondingly, the parameter ε_1 is also small.

Let us now consider the relationship

$$\frac{c[E]}{\omega[L][B]} = \frac{c}{\omega[R_L]}\frac{R_L}{[L]}\frac{[E]}{[B]} = \frac{\varepsilon}{\varepsilon_1}\frac{[E]}{[B]}. \quad (4)$$

We restrict our consideration to the case when the parameters ε and ε_1 are of the same order of smallness. Furthermore, in order to remain within the framework of the perturbation theory, it is necessary that the ratio of the wave potential to the potential of the slowly varying magnetic field should be a small quantity. To accomplish this, the ratio $[E]/[B]$, which we designate as ε_2^2, should be small. The parameter ε_2 is assumed to be a small quantity of the same order of smallness as ε_1 and ε. For convenience, we introduce the following designations: $\varepsilon_1 = \mu_1\varepsilon$ and $\varepsilon_2^2/\varepsilon_1 = \mu\varepsilon$, where $\mu = \mu_1 = O(1)$.

The quantities $\mathbf{n}_1$, $\mathbf{n}_2$, $\mathbf{n}_3$, and $\mathbf{r}$ in expression (3) can be treated as standard functions of the magnetic field coordinates εq^1, εq^2, and εq^3 [4]. As a result, we have $\mathbf{A}_\nu = A_{\nu i}(\varepsilon q^1, \varepsilon q^2, \varepsilon q^3)\mathbf{r}_i$. Here,

$$\begin{aligned} A_{\nu i} = \mu\varepsilon^2\{&[\mathbf{n}_1\mathbf{r}_i E_1\sin(\mu_1\mathbf{n}_3\mathbf{r}) \\ &- \mathbf{n}_2\mathbf{r}_i E_2\cos(\mu_1\mathbf{n}_3\mathbf{r})]\cos\nu t \\ -[\mathbf{n}_1\mathbf{r}_i E_1\cos(\mu_3\mathbf{n}_3\mathbf{r}) &+ \mathbf{n}_2\mathbf{r}_i E_2\sin(\mu_i\mathbf{n}_3\mathbf{r})]\sin\nu t\}. \end{aligned} \quad (5)$$

The valence of the canonical transformation upon introducing the variables q_i and p^i is equal to $1/\varepsilon^2$ [4]. Therefore, the Hamiltonian function (see formula (2.3) in [4]) should be supplemented by the components of the total vector potential $A_{\nu i}$ [defined by Eq. (5)], which are divided by ε (hereafter, they are designated by the same symbols). In other words, relationship (2.3) derived in [4] should include the quantities $A_i + A_{\nu i}$ instead of A_i, where $A_{\nu i}$ are taken from relationship (5) but without the factor ε. As a result, the addition to the vector potential is of the order of $O(\varepsilon)$. We change over now, as was done in [4], to the variables J, φ, etc. Let us again calculate the Hamiltonian function accurate to within the terms of the order of ε. We can set $q^1 = q^2 = 0$ and $rq^3 = \varepsilon z$ in the εq^1, εq^2, and εq^3 functions involved in $A_{\nu i}$ (see [4]) and rewrite the total vector potential in the form

$$A_{\nu i} = \mu\varepsilon(F_{\nu i}\cos\nu t - G_{\nu i}\sin\nu t). \quad (6)$$

Next, we introduce the designations for the following functions of the argument εz:

$$\begin{aligned} F_{\nu i} &= \mathbf{n}_1\mathbf{r}_i E_1\sin(\mu_1\mathbf{n}_3\mathbf{r}) - \mathbf{n}_2\mathbf{r}_i E_2\cos(\mu_1\mathbf{n}_3\mathbf{r}), \\ G_{\nu i} &= \mathbf{n}_1\mathbf{r}_i E_1\sin(\mu_1\mathbf{n}_3\mathbf{r}) + \mathbf{n}_2\mathbf{r}_i E_2\sin(\mu_1\mathbf{n}_3\mathbf{r}). \end{aligned} \quad (7)$$

Consequently, the Hamiltonian function takes the form

$$H = H_0 + \varepsilon H_1 + \varepsilon H_\nu, \quad (8)$$

where the terms H_0 and H_1 were determined in [4], the addition εH_ν to the Hamiltonian function can be obtained from the sum $g^{ik}A_{\nu i}(P_{k0} - A_k)$, and the function H_ν has the form

$$\begin{aligned} H_\nu = \mu(&G_{\nu 4}\sqrt{2J}\sin\varphi\sin\nu t + F_{\nu 4}\sqrt{2J}\sin\varphi\cos\nu t \\ &+ G_{\nu 5}\sqrt{2J}\cos\varphi\sin\nu t + F_{\nu 5}\sqrt{2J}\cos\varphi\cos\nu t \\ &+ P_{11}F_{\nu 3}\cos\nu t - P_{11}G_{\nu 3}\sin\nu t). \end{aligned} \quad (9)$$

Here,

$$\begin{aligned} G_{\nu 4} &= -(\sqrt{\omega g^{11}})_0 G_{\nu 1} - (g^{12})_0 G_{\nu 2} + \left(g^{13}\sqrt{\frac{\omega}{g^{11}}}\right)_0 G_{\nu 3}, \\ F_{\nu 4} &= -(\sqrt{\omega g^{11}})_0 F_{\nu 1} + (g^{12})_0 F_{\nu 2} - \left(g^{13}\sqrt{\frac{\omega}{g^{11}}}\right)_0 F_{\nu 3}, \\ G_{\nu 5} &= -\omega_0 G_{\nu 2} - \left(\frac{\omega^2 g_{23}}{\sqrt{\omega g^{11}}}\right)_0 G_{\nu 3}, \\ F_{\nu 5} &= \omega_0 F_{\nu 2} + \left(\frac{\omega^2 g_{23}}{\sqrt{\omega g^{11}}}\right)_0 F_{\nu 3} \end{aligned} \quad (10)$$

are the aforementioned functions of the argument εz.

The system under consideration is a two-phase system; i.e. it is characterized by two fast phases, φ and $\nu = \nu t$. Hence, two cases of the motion become possible, namely, the resonance and nonresonance motions.

The nonresonance case embraces the motion in which the characteristic cyclotron frequency substantially differs from the wave frequency. The system with the Hamiltonian of the unperturbed problem has the integral of motion J (the action variable). The level set of this integral is a one-dimensional torus (a circle), because we are considering a single-frequency system. This torus is invariant by the phase flow of the unperturbed problem: each phase curve beginning at a point of this torus remains on it. Therefore, when analyzing the nonresonance motions in a perturbed system, we can use the averaging method (see [5]). In this case, the Hamilton equations can be averaged over both fast phases and no problems of small denominators arise. Furthermore, the terms of the equations of motion, which appear upon differentiation of the part of the Hamiltonian associated with the wave, vanish after averaging; hence, to a first approximation, the wave field does not affect the motion.

This circumstance is confirmed by the general theory. The following theorem holds (see, for example, [5]): the evolution of the variables J does not take place in a Hamiltonian system with n frequencies. This theory is a corollary of the more general Kolmogorov–Arnold–Moser theorem, which states (in the appendix to the problem under consideration) that, when the perturbation of the Hamiltonian function is small (and the Hamiltonian perturbation is also small), the invariant tori are only slightly deformed and do not disappear.

The fundamental effect exhibited in two-frequency systems is the passage through the resonance. In this case, the difference $(\omega - \nu)$ is a small quantity and $\delta = \varphi - \nu$ is a slow variable. Let us accept δ as a new variable in place of the variable φ. This is a canonical change of the variables, and the new Hamiltonian H' is related to the foregoing Hamiltonian by the expression $H' = H - \nu J$.

By using the results obtained in [4], we derive the following relationship:

$$\begin{aligned}
H'(J, \delta, x_L, y_L, p_{11}, \varepsilon z, \nu) &= (\omega - \nu)J + \frac{p_{11}^2}{2} \\
&+ \varepsilon[p_{11}^2(x_L F_1 + y_L F_2) + p_{11}F_3 + p_{11}(y_L^2 - J)F_4 \\
&+ p_{11}x_L y_L F_5 + y_L J F_6 + x_L J F_7 + (p_{11}^2 F_1 + p_{11}x_L F_9 \\
&+ p_{11}y_L F_8 + y_L^2 F_{10} + x_L y_L F_{11} + J F_{12})\sqrt{2J}(\cos\delta\sin\nu \\
&+ \sin\delta\cos\nu) + (p_{11}^2 F_2 + p_{11}y_L F_{13} + p_{11}x_L F_{14} + y_L^2 F_{15} \\
&+ x_L y_L F_{16} + J F_{17})\sqrt{2J}(\cos\delta\cos\nu - \sin\delta\sin\nu) \\
&+ p_{11}J F_{18}(\cos 2\delta\sin 2\nu + \sin 2\delta\cos 2\nu) \\
&+ p_{11}J F_{19}(\cos 2\delta\cos 2\nu - \sin 2\delta\sin 2\nu) \qquad (11) \\
&+ J\sqrt{2J}F_{20}(\cos 3\delta\sin 3\nu + \sin 3\delta\cos 3\nu) \\
&+ J\sqrt{2J}F_{21}(\cos 3\delta\cos 3\nu - \sin 3\delta\sin 3\nu)] \\
&+ \varepsilon\mu\Big[\frac{\sqrt{2J}}{2}G_{v4}(\cos\delta - \cos\delta\cos 2\nu + \sin\delta\sin 2\nu) \\
&+ \frac{\sqrt{2J}}{2}F_{v4}(\sin\delta + \cos\delta\sin 2\nu + \sin\delta\cos 2\nu) \\
&+ \frac{\sqrt{2J}}{2}G_{v5}(-\sin\delta + \cos\delta\sin 2\nu + \sin\delta\sin 2\nu) \\
&+ \frac{\sqrt{2J}}{2}F_{v5}(\cos\delta + \cos\delta\cos 2\nu - \sin\delta\sin 2\nu) \\
&+ p_{11}F_{v3}\cos\nu - p_{11}G_{v3}\sin\nu\Big].
\end{aligned}$$

In general, the application of the averaging method to two-frequency systems in resonance is not valid. However, an important feature of this case is that the perturbed system remains a Hamiltonian.

Recall that there is a theorem of the passage through resonances in two-frequency systems ([5], p. 146). As applied to the problem under investigation, this theorem can be reformulated as follows: if the rate of change in the frequency ratio ω/ν along the trajectory of the perturbed system is universally nonzero, the difference between $J(t)$ in the perturbed problem and $I(t)$ in the averaged problem remains small during the time $t \sim 1/\varepsilon$:

$$|J(t) - I(t)| \le c_1\sqrt{\varepsilon}, \quad 0 \le t \le \frac{1}{\varepsilon}. \qquad (12)$$

According to relationship (12), the passage through the resonance neighborhood results in a dispersion of the order of $\sqrt{\varepsilon}$.

In the case when the condition of the theorem is satisfied only on the trajectories of the averaged system, we obtain the estimate

$$|J(t) - I(t)| \le c_2\sqrt{\varepsilon}|\ln\varepsilon|, \quad 0 \le t \le \frac{1}{\varepsilon}. \qquad (13)$$

Thus, the question as to the justified applicability of the averaging method in the case of resonance (the validity of the Neĭshtadt theorem [6]) should be resolved specifically for each type of magnetic field.

Let us consider the Hamilton equations with the H' function. Instead of εz, we introduce the new variable λ through the relationship $\omega(\varepsilon z) - \nu = \sqrt{\varepsilon}\lambda$. It is assumed that ω and λ are close to $\lambda = O(1)$. As a result, we obtain a system of equations in a standard form with the parameter $\sqrt{\varepsilon}$. However, this system has the following feature: the right-hand sides of four out of the six equations are proportional to ε rather than to $\sqrt{\varepsilon}$. Certain interest arises here in the averaged equations of the second approximation with respect to $\sqrt{\varepsilon}$, i.e., the equations containing the terms proportional to ε.

After introducing the variable λ, the argument εz in the initial equations should be expressed in terms of λ. For this purpose, we should invert the dependence $\omega(\varepsilon z) = \nu + \sqrt{\varepsilon}\lambda$. As a result, we obtain

$$\varepsilon z = \Psi(\nu + \sqrt{\varepsilon}\lambda) \qquad (14)$$

or, to within the required accuracy,

$$\varepsilon z = \Psi(\nu) + \sqrt{\varepsilon}\lambda\Psi'(\nu) + \ldots . \qquad (15)$$

In order to achieve the required accuracy, it is sufficient to substitute the expression $\varepsilon z = \Psi(\nu)$ into all the equations, except for the equation containing $\varepsilon\dot{z}$; after this, the functions F_{v4}, G_{v4}, etc. become constant. The equation involving $\varepsilon\dot{z}$ is transformed as follows:

$$\varepsilon\dot{z} = \dot{\lambda}(\sqrt{\varepsilon}\Psi'(\nu) + \varepsilon\lambda\Psi''(\nu)).$$

Whence, it follows that

$$\dot{\lambda} = \frac{\sqrt{\varepsilon}}{\Psi'}p_{11} - \varepsilon\frac{\Psi''}{\Psi'^2}p_{11}\lambda. \qquad (16)$$

Generally speaking, in the second approximation, the expressions for the desired variables should have the following form: $J = I + \sqrt{\varepsilon}\,u_J(\nu, I, \Delta, \ldots)$, $\delta = \Delta +$

$\sqrt{\varepsilon}\,u_\delta(v, I, \Delta, \ldots)$, etc. Here, I and Δ are the evolution components and the functions u_y and u_δ depend on both v and these components.

However, owing to the specificity of the appearance of the terms proportional to $\sqrt{\varepsilon}$ in the equations, all the first corrections can be taken equal to zero. In this case, the desired variables should be equal [to within an accuracy of the order of $O(\varepsilon)$] to their evolution components. Therefore, in the representation of the averaged equations of the second approximation, they can be identified with one another. Consequently, we obtain the following system:

$$\dot{J} = \varepsilon\mu\frac{\sqrt{2J}}{2}[(G_{v4} + F_{v5})\sin\delta + (G_{v5} - F_{v4})\cos\delta],$$

$$\dot{x}_L = -\varepsilon(p_{11}^2 F_2 + 2p_{11}y_L F_4 + p_{11}x_L F_5 + JF_6),$$

$$\dot{p}_{11} = -\frac{\varepsilon}{\Psi'}J,$$

$$\dot{\delta} = \sqrt{\varepsilon}\lambda + \varepsilon(-p_{11}F_4 + y_L F_6 + x_L F_7) \qquad (17)$$

$$+ \frac{\varepsilon\mu}{2\sqrt{2J}}[(G_{v4} + F_{v5})\cos\delta + (F_{v4} - G_{v5})\sin\delta],$$

$$\dot{y}_L = \varepsilon(p_{11}^2 F_1 + p_{11}y_L F_5 + JF_7),$$

$$\dot{\lambda} = \frac{\sqrt{\varepsilon}}{\Psi'}p_{11} - \frac{\varepsilon\Psi''}{\Psi'^2}p_{11}\lambda.$$

Here, G_{v4}, F_{v4}, …, Ψ', and Ψ'' are constant.

REFERENCES

1. A. B. Kitsenko, I. M. Pankratov, and K. N. Stepanov, Zh. Éksp. Teor. Fiz. **66** (1), 166 (1974) [Sov. Phys. JETP **39**, 77 (1974)].
2. A. B. Kitsenko, I. M. Pankratov, and K. N. Stepanov, Zh. Éksp. Teor. Fiz. **67** (1), 1728 (1974) [Sov. Phys. JETP **40**, 860 (1975)].
3. A. J. Lichtenberg and M. A. Lieberman, *Regular and Stochastic Motion* (Springer-Verlag, New York, 1982; Mir, Moscow, 1984).
4. V. E. Tarasov, K. Sh. Khodzhaev, and A. G. Chirkov, Zh. Tekh. Fiz. **71** (1), 16 (2001) [Tech. Phys. **46**, 14 (2001)].
5. V. I. Arnol'd, *Supplementary Chapters of the Theory of Ordinary Differential Equations* (Nauka, Moscow, 1978).
6. A. I. Neĭshtadt, Dokl. Akad. Nauk SSSR **221**, 301 (1975) [Sov. Phys. Dokl. **20**, 189 (1975)].

Translated by O. Moskalev

Physics of the Solid State, Vol. 44, No. 1, 2002, pp. 42–47. Translated from Fizika Tverdogo Tela, Vol. 44, No. 1, 2002, pp. 41–46.

SEMICONDUCTORS AND DIELECTRICS

The Nernst–Ettingshausen, Seebeck, and Hall Effects in Sb_2Te_3 Single Crystals

M. K. Zhitinskaya*, S. A. Nemov*, and L. D. Ivanova**

**St. Petersburg State Technical University, ul. Politekhnicheskaya 29, St. Petersburg, 195251 Russia*

***Baĭkov Institute of Metallurgy and Materials Sciences, Russian Academy of Sciences, Leninskiĭ pr. 49, Moscow, 117911 Russia*

Received January 22, 2001; in final form, June 8, 2001

Abstract—This paper reports on measurement of the temperature dependences of the following transport coefficients: electrical conductivity in the σ_{11} cleavage plane, the Seebeck coefficients S_{11} and S_{33} (axis 3 is along the trigonal crystal axis), the Hall coefficients R_{123} and R_{321}, and the Nernst–Ettingshausen constant Q_{123}; all measurements were made on high-quality Czochralski-grown Sb_2Te_3 single crystals. The results obtained are analyzed in terms of phenomenological theory. It is shown that the main features of the experimental data, including the anisotropy of the Hall and Seebeck effects, can be explained within a two-band model with noticeably different anisotropy of the mobilities of holes of two types in the cleavage-plane and trigonal-axis directions. Estimates are made of the band-gap width ($\varepsilon_g \cong 0.3$ eV), as well as of the energy gap between the main and additional valence-band extrema ($\Delta\varepsilon_v \sim 0.1$ eV). © *2002 MAIK "Nauka/Interperiodica".*

1. INTRODUCTION

Antimony telluride is employed as a constituent of high-efficiency room-temperature thermoelectric materials, such as the $(Sb_{1-x}Bi_x)_2Te_3$ solid solutions. This accounts for its application potential and the intense interest expressed in it by researchers [1–5]. However, despite the wealth of literature data available, the character of its band structure remains a subject of debate.

Sb_2Te_3 is a narrow-band-gap semiconductor, belongs to the class of layered compounds, and is characterized by the presence of a large number of intrinsic acceptor-type defects, presumably antisite-type (the case where part of the excess antimony atoms occupy the tellurium sites, Sb_{Te} [3]). This compound has a high hole concentration ($p \sim 10^{20}$ cm^{-3}), which can be varied only within a narrow range; this factor complicates the study of the Sb_2Te_3 energy spectrum. As far as we know, satisfactory theoretical calculations of the Sb_2Te_3 band structure are lacking.

Some studies of the transport phenomena [6–10] treat experimental data in terms of a two-band model, whereas others (see, e.g., [4]) invoke a one-band nonparabolic model. However, no success has been made in explaining data on the transport phenomena as a whole and details of the band structure remain a subject of debate. Some features in the experimental data, such as the thermopower anisotropy, the crossing of the temperature dependences of the Hall tensor components, and the temperature dependence of the coefficient of the transverse Nernst–Ettingshausen effect (TNEE), have not been satisfactorily explained.

In this work, the scope of the transport phenomena studied is broadened. We studied the TNEE together with the Seebeck and Hall effects, as well as their anisotropy and temperature dependences. The investigation of the kinetic effects was carried out on more perfect single crystals. Furthermore, we attempted a somewhat different approach to the analysis of the results, more specifically, we made use of the phenomenological theory without invoking any specific assumptions on the band structure.

2. SAMPLES

Sb_2Te_3 single crystals were Czochralski grown using a unique technology developed at the Baĭkov Institute of Metallurgy and Materials Sciences, which makes use of a floating crucible to feed the growing crystal with liquid melt [1]. This method permits one to grow sufficiently large crystals in given crystallographic directions, including that parallel to the trigonal axis. The single crystals were 15–20 mm thick and had well-developed cleavage planes. The crystals had a perfect structure and high compositional homogeneity. The microdistribution of the carrier concentration was estimated from the local values of the Seebeck coefficient on the single-crystal surface. The scatter in the measurements did not exceed 2–3%. The experiment was performed on samples of three types, namely, stoichiometric samples and samples doped by Bi and Se isovalent impurities. The crystals were prepared from constituents (Te, Sb, Bi, Se) of semiconductor-grade purity with 99.9999 wt % of the main material. The

impurity content was determined through chemical analysis. All the crystals exhibited hole conductivity.

3. EXPERIMENT

On each sample, the following independent transport tensor components were measured: the Seebeck coefficients S_{11} and S_{33}, the Hall coefficients R_{123} and R_{321}, the Nernst–Ettingshausen constant Q_{123}, and electrical conductivity σ_{11}. Axis 3 in this notation coincides with the trigonal axis C_3 of the crystal. The subscripts on the coefficients indicate the following in the order they are given: the first subscript indicates the direction of the measured electric field; the second, the direction of the electric current or of the temperature gradient; and the third, the magnetic field direction. The Hall and Nernst–Ettingshausen effects were studied using techniques that permitted one to reduce to a minimum the effect of their parasitic nonisothermal components, which may make up a noticeable fraction of the measured effect in thermoelectric materials.

The measurements were carried out mainly in the 77–420 K temperature range (one of the samples, prepared using the metal–ceramic technique, was studied up to 650 K). In accordance with [11], the carrier concentration was derived from the larger component of the Hall tensor R_{321} at 77 K using the expression

$$p = (eR_{321})^{-1}. \quad (1)$$

4. RESULTS AND DISCUSSION

We note immediately that our results on the anisotropy and temperature dependences of the Hall and Seebeck coefficients and the electrical conductivity agree well with the data quoted in [12]. For this reason, we do not present all of them here. Main attention is focused, in this paper, on those transport coefficients that are less covered in the literature, namely, anisotropy in the Seebeck coefficient and the Nernst–Ettingshausen effect. As far as we know, this paper is the first publication to present experimental data on the Nernst–Ettingshausen effect in Sb_2Te_3 on this scope.

All the Sb_2Te_3 samples studied exhibited the following characteristic features in the temperature dependences of the transport coefficients:

(i) A negative sign of the Nernst–Ettingshausen coefficient Q_{123} throughout the temperature range covered. The temperature dependences of the Nernst mobility $|Q_{ijk}|e/k_0$ have a derivative $d|Q|/dT > 0$ and a maximum near $T \cong 400$ K (Fig. 1).

(ii) The Seebeck coefficient is isotropic (within the experimental accuracy) in the low-temperature region (near 100 K) and reveals, for $T \geq 140$ K, an anisotropy $\Delta S = S_{33} - S_{11}$ (Fig. 2) which grows with temperature.

(iii) The Hall tensor components R_{321} and R_{123} grow with temperature at different rates; this is accompanied by a decrease in the Hall coefficient anisotropy ($R_{321}/R_{123} \sim 1.3$ at 77 K) and a crossing of its components near 300 K (Fig. 3).

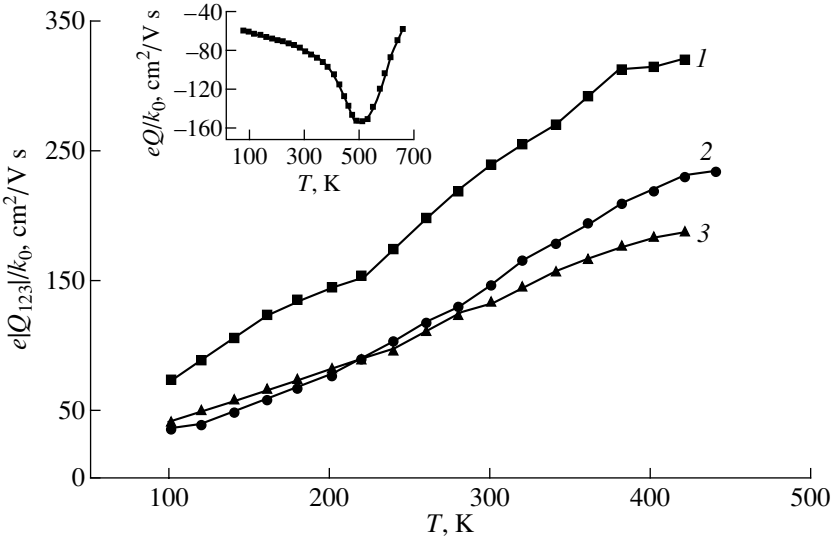

Fig. 1. Temperature dependences of one of the transverse Nernst–Ettingshausen tensor components, Q_{123} ($\nabla T \perp \mathbf{c} \perp \mathbf{B}$), obtained for single-crystal Sb_2Te_3 samples with different original hole concentrations p (10^{20} cm^{-3}): (*1*) 0.78, (*2*) 1.21, and (*3*) 1.36; **c** is the direction of the trigonal crystal axis C_3, ∇T is the direction of the temperature gradient, and **B** is the magnetic field direction. Inset shows the temperature dependence $Q(T)$ used for a polycrystalline pressed sample to determine the energy gap width ε_g from the temperature range above 500 K ($\varepsilon_g \cong 0.3$ eV).

4.1. The Nernst–Ettingshausen Effect

We start the discussion with the data on the Nernst–Ettingshausen effect. Figure 1 presents the temperature dependences of the Q_{123} coefficient of Sb_2Te_3 single crystals and the $Q(T)$ relation for a polycrystalline sample (inset). The small magnitude of the Hall coefficient ($R_{321} \sim 5 \times 10^{-2}$ cm^3/C) implies a high hole concentration in the samples studied; therefore, the hole gas should be considered degenerate. In this case, the one-band model yields, for the TNEE coefficient,

$$eQ_{123}k_0 = R_{123}\sigma_{11}\pi^2/3(r-1/2)(k_0T/\mu), \qquad (2)$$

where μ is the chemical potential, $R_{123}\sigma_{11}$ is the carrier Hall mobility, k_0 is the Boltzmann constant, and r is the exponent in the energy dependence of the relaxation time $\tau(\varepsilon) \sim \varepsilon^{r-1/2}$. The negative sign of Q_{123} indicates that the effective scattering parameter $r < 1/2$. Numerical estimates of r made using experimental data yield values close but not equal to zero ($r \approx 0.25$). This means that in the temperature region from 100 to 250 K, holes scatter through a mixed mechanism, which is dominated, however, by long-wavelength longitudinal acoustic lattice vibrations.

At high temperatures ($T > 500$ K), the contribution from the minority carriers to the transport phenomena becomes noticeable and grows rapidly with temperature. In the simplest case of a valence band consisting of only one subband, the Q_{123} coefficient in the region of mixed electron–hole conduction has the form

$$Q = \sigma_p/\sigma Q_p + \sigma_n/\sigma Q_n + Q_{np}, \qquad (3)$$

where Q_p is described by Eq. (2),

$$eQ_n/k_0 = R_{123}\sigma_{11}(r-1/2), \qquad (4)$$

$$\sigma = \sigma_n + \sigma_p, \qquad (5)$$

$$eQ_{np}/k_0 = \sigma_n\sigma_p/\sigma^2(S_p - S_n)(u_{pH} + u_{nH}), \qquad (6)$$

and u_{pH} and u_{nH} are the corresponding Hall mobilities of the holes and electrons. At the very beginning of mixed conductivity, where the concentration of the minority carriers (electrons in this case) is still low, i.e., for $\sigma_n \ll \sigma_p$, Eq. (6) assumes the form

$$\begin{aligned} eQ_{np}/k_0 &\sim \sigma_n/\sigma(S_p - S_n)(u_{pH} + u_{nH}) \\ &\sim n \sim \exp(-\varepsilon_g/k_0T) \end{aligned} \qquad (7)$$

(e_g is the band-gap width). The mixed term Q_{np} is always positive and proportional to the electron contribution to the conductivity, which, in turn, is proportional to the electron concentration n. As a result, the measured negative coefficient Q, according to Eqs. (3)–(7), passes through a minimum (inset to Fig. 1) and thereafter starts to decrease rapidly in absolute value and tends to sign reversal.

An analysis of the experimental data obtained at the onset of the intrinsic conductivity yielded an estimate of the thermal energy gap between the valence and conduction bands extrapolated to zero. It was found to be equal to $\varepsilon_g \cong 0.3$ eV, which is close to the band-gap width derived in [13] from optical absorption measurements.

As already mentioned, a characteristic feature of the experimental data obtained on all samples in the region $140 < T < 300$ K is the increase of Q in absolute value with a positive derivative $d|Q|/dT$. This behavior of the TNEE coefficient cannot be explained within the one-band model. It can be accounted for by the effect of an additional extremum lying deeper in energy than the main one. The energy gap was deduced from TNEE data using Eq. (A18) for the two-band model. In the temperature range where the carriers of the additional band just begin to contribute, the ratio of the hole concentration in the second band p_2 to the total hole concentration $p_0 = p_1 + p_2$ is $\nu = p_2/p_0 \ll 1$. In this case, using Eqs. (A3) and (A11), Eq. (A18) for $Q_{123}^{(1,2)}$ can be written in a form similar to Eq. (7):

$$\begin{aligned} Q_{123}^{(1,2)} &= [S_{11}^{(1)} - S_{11}^{(2)}][A_c^{(1)}u_a^{(1)} - A_c^{(2)}u_a^{(2)}]t_a^{(1)}t_a^{(2)} \\ &\sim p_2/p_0 \sim \exp(-\Delta\varepsilon_v/k_0T), \end{aligned}$$

where $\Delta\varepsilon_v$ is the energy gap between the valence bands. Experimental data on $Q_{123}^{(1,2)}$ yield $\Delta\varepsilon_v \sim 0.1$ eV for all samples. It should be pointed out that this value of the band-gap $\Delta\varepsilon_v$ is an order-of-magnitude estimate, because it does not include the contribution of interband hole scattering to the TNEE coefficient.

4.2. The Seebeck Coefficient

Antimony telluride is one of the few materials in which the Seebeck coefficient was experimentally observed to be anisotropic in the region of extrinsic conductivity. Its possible origin, namely, the participation of carriers of two types (holes) in the transport phenomena and the anisotropic mixed scattering mechanism, was treated in considerable detail in [14]. We believe that both factors play a substantial role, although in different degrees at different temperatures. If only one kind of hole is involved in the transport phenomena, the thermopower can become anisotropic only if several scattering mechanisms operate, with the relative contributions of these mechanisms being different in different directions. The most probable mechanism of scattering in Sb_2Te_3 is scattering from impurity ions and acoustic lattice vibrations. Scattering from impurity ions is anisotropic, and that from acoustic vibrations is largely isotropic. As the temperature is increased from 100 to 450 K, the contribution from the impurity anisotropic scattering decreases and that from the less anisotropic acoustic scattering of holes increases. In this case, if there is only one type of hole, the anisotropy of the Seebeck coefficient should decrease, which is at odds with experimental data. As

seen from Fig. 2, the anisotropy of the Seebeck coefficient grows with temperature. The growth of ΔS is the largest at $T \sim 250$ K (in the same temperature range, where the features in the temperature dependences of the TNEE associated with the participation of two types of holes were revealed).

The present paper suggests that the onset of anisotropy in the Seebeck coefficient ΔS originates from the involvement of holes of two types (heavy and light) in the transport phenomena, with different anisotropy in their mobilities. Assuming the partial thermopower coefficients for the light and heavy holes to be isotropic, the thermopower anisotropy in conduction involving holes of two types can be written as

$$\Delta S = S_{33} - S_{11} = (S^{(1)} - S^{(2)})\nu(b_c - b_a)/b_c b_a, \quad (8)$$

where $b_a = u_1^a/u_2^a$ and $b_c = u_1^c/u_2^c$ are the hole mobility ratios in the directions of the cleavage plane and perpendicular to it, respectively.

As follows from Eq. (8), for $\Delta S > 0$ (in agreement with the experiment), we have $b_a/b_c > 1$. This condition is met if the holes of the band characterized by a higher mobility possess a larger anisotropy. In particular, if the hole mobilities in the additional band (2) are higher than those in the main one (1), $b_a/b_c > 1$, the anisotropy of the hole mobilities in the main band (1) will be smaller than that in the additional one (2), because $b_a/b_c = (u_1^a/u_1^c)/(u_2^a/u_2^c)$.

The fact that the anisotropy of the Seebeck coefficient is associated with the generation of carriers (holes) of the second type permits one to use its temperature dependence to estimate the energy gap separating the main and additional extrema. In the temperature range where the holes of the second band just start to contribute to conduction, i.e., where $\nu = p_2/p_0 \ll 1$, Eq. (8) assumes the form

$$\Delta S \sim \nu \sim \exp(-\Delta\varepsilon_v/k_0 T).$$

Calculations yielded $\Delta\varepsilon_v \sim 0.1$ eV. Thus, experimental data obtained on the Nernst–Ettingshausen and Seebeck effects support a complex structure of the Sb_2Te_3 valence band with an energy gap $\Delta\varepsilon_v \sim 0.1$ eV.

4.3. The Hall Effect

The two-band model provides a natural explanation to the marked increase in the Hall coefficient, a phenomenon observed by us and known from the literature. Our estimates made using Eqs. (A16) show that the present model, which assumes a substantially different anisotropy in the mobility between holes of two types and is characterized by the parameters b_a and b_c, is also capable of accounting for the crossing of the temperature dependences of the two Hall tensor components (Fig. 3). The inset to Fig. 3 illustrates the overall behavior of the $R_{ijk}(T)$ components with temperature as

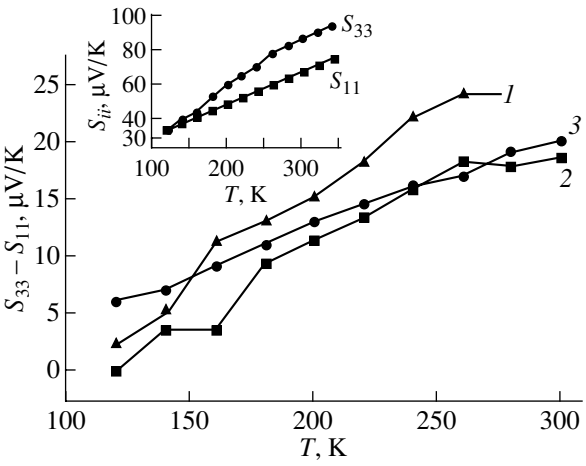

Fig. 2. Temperature dependences of the anisotropy in the Seebeck coefficient $\Delta S = S_{33} - S_{11}$ [$S_{11}(\nabla T \perp \mathbf{c})$ and $S_{33}(\nabla T \parallel \mathbf{c})$]. Inset shows the temperature dependences of both Seebeck tensor components for a sample with $p = 1.21 \times 10^{20}$ cm^{-3} (curve *2* in Fig. 1).

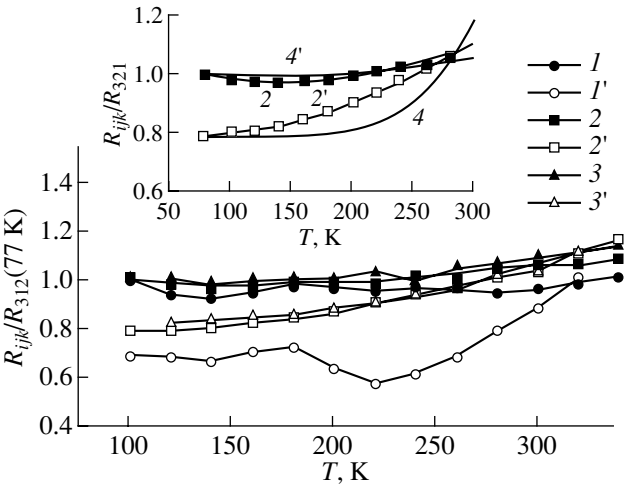

Fig. 3. Temperature dependences of the ratios of the Hall coefficient components (*1–3*) $R_{321}(\mathbf{j} \perp \mathbf{c} \perp \mathbf{B})$ and (*1'–3'*) $R_{123}(\mathbf{j} \perp \mathbf{c} \parallel \mathbf{B})$ to R_{321} obtained at 77 K on Sb_2Te_3 single crystals. The curve notation is the same as in Fig. 1. Inset: comparison of experimental temperature dependences of R_{ijk}/R_{321} for a sample with $p = 1.21 \times 10^{20}$ cm^{-3} (curves *2*, *2'*) with the theoretical values (curves *4*, *4'*) obtained in a two-band model with additional light holes using the parameters from [4].

obtained within the two-band model using the band structure parameters given in [4].

Thus, we have shown that the experimental data, as a whole, on the electrical conductivity and the Seebeck, Hall, and Nernst–Ettingshausen effects obtained within a broad temperature range (77–350 K) can be explained within the two-band model of the valence band, which involves holes of two types possessing substantially different mobility anisotropies along the trigonal axis

and the cleavage plane ($b_a/b_c > 1$). Evaluation of the energy gap between the main and additional valence-band extrema yielded $\Delta\varepsilon_v \sim 0.1$ eV.

APPENDIX

PHENOMENOLOGICAL THEORY

The papers we are aware of analyze the experimental results with expressions which, as a rule, assume a concrete band structure and a concrete carrier scattering mechanism in the compound under study. In using a phenomenological description of the transport effects, we invoked as few assumptions as possible.

A phenomenological description of the main transport coefficients was already made in [14], a publication to which we refer interested readers. Here, we are going to present only those relations necessary in our study.

In single crystals of rhombohedral symmetry, to which Sb_2Te_3 belongs, the σ_{ij}, S_{ij}, and R_{ijk} tensors have two independent components each and Q_{ijk} has three; the subscripts are presented here in the same order as in Section 2 of the text.

(1) Electrical Conductivity

Taking into account the anisotropy in the contributions of the carriers of the two valence bands (1 and 2), we can write

$$\sigma_a = \sigma_{11} = \sigma_{11}^{(1)} + \sigma_{11}^{(2)}, \tag{A1}$$

$$\sigma_c = \sigma_{33} = \sigma_{33}^{(1)} + \sigma_{33}^{(2)}. \tag{A2}$$

Here and henceforth, the trigonal axis of the crystal is denoted by 3 or *c*; the direction in the cleavage plane, as 1 and 2 or *a*.

The contribution to the conductivity has the following coefficients:

$$\begin{aligned} t_a^{(1)} &= \sigma_a^{(1)}[\sigma_a^{(1)} + \sigma_a^{(2)}], \quad t_a^{(2)} = \sigma_a^{(2)}/[\sigma_a^{(1)} + \sigma_a^{(2)}], \\ t_c^{(1)} &= \sigma_c^{(1)}[\sigma_c^{(1)} + \sigma_c^{(2)}], \quad t_c^{(2)} = \sigma_c^{(2)}/[\sigma_c^{(1)} + \sigma_c^{(2)}]. \end{aligned} \tag{A3}$$

With this notation, Eqs. (A1) and (A2) can be recast as

$$t_a^{(1)} + t_a^{(2)} = 1, \quad t_c^{(1)} + t_c^{(2)} = 1. \tag{A4}$$

(2) The Seebeck Coefficient

$$S_a = S_{11} = S_a^{(1)} t_a^{(1)} + S_a^{(2)} t_a^{(2)}, \tag{A5}$$

$$S_c = S_{33} = S_c^{(1)} t_c^{(1)} + S_c^{(2)} t_c^{(2)}. \tag{A6}$$

The anisotropy in the Seebeck coefficient is defined as $\Delta S = S_c - S_a$ and can be written as

$$\Delta S = S_c - S_a = [S^{(1)} - S^{(2)}][t_c^{(1)} - t_a^{(1)}]. \tag{A7}$$

Equation (A6) was derived assuming the partial Seebeck coefficients for carriers of bands 1 and 2 to be isotropic. Anisotropy is known not to appear in the one-band model; therefore, we assume the partial contributions from carriers in bands 1 and 2 to be isotropic:

$$S_a^{(1)} = S_c^{(1)}, \quad S_a^{(2)} = S_c^{(2)}.$$

(3) The Hall Effect

$$R_{123} = R_c = R_c^{(1)}[t_a^{(1)}]^2 + R_c^{(2)}[t_a^{(2)}]^2, \tag{A8}$$

$$R_{321} = R_a = R_a^{(1)}[t_c^{(1)}][t_a^{(1)}] + R_a^{(2)}[t_c^{(2)}][t_a^{(2)}]. \tag{A9}$$

(4) The Nernst–Ettingshausen Effect

$$Q_{123} = Q_{123}^{(1)}[t_a^{(1)}] + Q_{123}^{(2)}[t_a^{(2)}] + Q_{123}^{(1,2)},$$

where

$$Q_{213}^{(1,2)} = [S_{11}^{(1)} - S_{11}^{(2)}][R_{123}^{(1)}\sigma_a^{(1)} - R_{123}^{(2)}\sigma_a^{(2)}]t_a^{(1)}t_a^{(2)}. \tag{A10}$$

Using the earlier notation for ν, b_a, b_c, and p_0, we transform Eqs. (A3)–(A10) to

$$\begin{aligned} t_a^{(1)} &= (1-\nu)b_a/[(1-\nu)b_a + \nu], \\ t_a^{(2)} &= \nu/[(1-\nu)b_a + \nu], \\ t_c^{(1)} &= (1-\nu)b_c/[(1-\nu)b_c + \nu], \\ t_c^{(2)} &= \nu/[(1-\nu)b_c + \nu], \end{aligned} \tag{A11}$$

$$\begin{aligned} \sigma_a &= \sigma_a^{(1)} + \sigma_a^{(2)} = p_0 u_a^{(1)}[(1-\nu) + \nu/b_a], \\ \sigma_c &= \sigma_c^{(1)} + \sigma_c^{(2)} = p_0 u_c^{(1)}[(1-\nu) + \nu/b_c], \end{aligned} \tag{A12}$$

$$\begin{aligned} S_a &= S_a^{(1)}(1-\nu)b_a/[(1-\nu)b_a + \nu] \\ &\quad + S_a^{(2)}\nu/[(1-\nu)b_a + \nu], \\ S_c &= S_c^{(1)}(1-\nu)b_c/[(1-\nu)b_c + \nu] \\ &\quad + S_c^{(2)}\nu/[(1-\nu)b_c + \nu], \end{aligned} \tag{A13}$$

$$\begin{aligned} \Delta S &= S_c - S_a = [S^{(1)} - S^{(2)}]\nu(1-\nu) \\ &\times (b_c - b_a)/([(1-\nu)b_c + \nu][(1-\nu)b_a + \nu]). \end{aligned} \tag{A14}$$

(5) The Hall Coefficients

Consider Eqs. (A8) and (A9) and transform them by introducing an additional notation: $\chi_c = A_c^{(1)}/A_c^{(2)}$ and $\chi_a = A_a^{(1)}/A_a^{(2)}$, where χ_a and χ_c are the ratios of the structural Hall factors and $A_c^{(1)}$, $A_c^{(2)}$, $A_a^{(1)}$, and $A_a^{(2)}$ are the structural Hall factors for bands 1 and 2 for $H \parallel$

c (subscript c) and $H \perp \mathbf{c}$ (subscript a). Then, we obtain for bands 1 and 2,

$$\begin{aligned} R_c^{(1)} &= A_c^{(1)}/p_1 = A_c^{(1)}/[p_0(1-\nu)], \\ R_c^{(2)} &= A_c^{(2)}/p_2 = A_c^{(1)}/(p_0\nu\chi_c), \\ R_a^{(1)} &= A_a^{(1)}/[p_0(1-\nu)], \\ R_a^{(2)} &= A_a^{(1)}/(p_0\nu\chi_a). \end{aligned} \tag{A15}$$

The expressions for the Hall tensor components are

$$\begin{aligned} R_c &= R_{123} = [A_c^{(1)}/p_0] \\ &\times [(t_a^{(1)})^2/(1-\nu) + (t_a^{(2)})^2/\nu\chi_c], \\ R_a &= R_{321} = A_a^{(1)}/p_0 \\ &\times [t_c^{(1)}t_a^{(1)}/(1-\nu) + t_c^{(2)}t_a^{(2)}/\nu\chi_a] \end{aligned} \tag{A16}$$

or

$$\begin{aligned} R_c &= [A_c^{(1)}/p_0] \\ &\times [(1-\nu)b_a^2 + \nu/\chi_c]/[(1-\nu)b_a + \nu]^2, \\ R_a &= [A_a^{(1)}/p_0][(1-\nu)b_c b_a \\ &+ \nu/\chi_a]/\{[(1-\nu)b_c + \nu][(1-\nu)b_a + \nu]\}. \end{aligned} \tag{A17}$$

(6) The TNEE Coefficient Q_{123}

$$Q_{123} = Q_{123}^{(1)}[t_a^{(1)}] + Q_{123}^{(2)}[t_a^{(2)}] + Q_{123}^{(1,2)},$$

where

$$\begin{aligned} Q_{123}^{(1)} &= A_c^{(1)}u_a^{(1)}\pi^2/3(r-1/2)(1\mu^*), \quad \mu^* = \mu/k_0T, \\ Q_{123}^{(1,2)} &= [S_{11}^{(1)} - S_{11}^{(2)}][A_c^{(1)}u_a^{(1)} - A_c^{(2)}u_a^{(2)}]t_a^{(1)}t_a^{(2)}. \end{aligned} \tag{A18}$$

REFERENCES

1. G. Simon and W. Eichler, Phys. Status Solidi B **107**, 201 (1981).
2. J. Horak and P. Lostak, in *Transport in Verbindungshalbleitern 1990* (Martin-Luther-Universitat Halle-Wittenberg, Halle, 1990), p. 96.
3. J. Horak, P. Lostak, and M. Matyas, Phys. Status Solidi B **129**, 381 (1985).
4. M. Stordeur, Phys. Status Solidi B **124**, 439 (1984); Phys. Status Solidi B **124**, 799 (1984).
5. V. A. Kulbachinskii, S. A. Azou, J. Horak, and P. Lostak, in *Transport in Verbindungshalbleitern 1990* (Martin-Luther-Universitat Halle-Wittenberg, Halle, 1990), p. 170.
6. B. M. Gol'tsman, V. A. Kudinov, and I. A. Smirnov, *Semiconducting Materials Based on Bi_2Te_3* (Nauka, Moscow, 1972).
7. B. Ronlund, O. Beckman, and H. Levy, J. Phys. Chem. Solids **26**, 1281 (1965).
8. M. Stordeur and W. Heiliger, Phys. Status Solidi B **78**, K103 (1976).
9. I. A. Smirnov, A. A. Andreev, and V. A. Kutasov, Fiz. Tverd. Tela (Leningrad) **10** (6), 1782 (1968) [Sov. Phys. Solid State **10**, 1403 (1968)].
10. D. M. Bercha, Z. V. Pankevich, A. V. Savitskiĭ, and K. D. Tovstyuk, Fiz. Tverd. Tela (Leningrad) **7** (8), 2437 (1965) [Sov. Phys. Solid State **7**, 1968 (1965)].
11. W. Eichler and T. Krug, Phys. Status Solidi B **101**, K1 (1980).
12. G. Simon and W. Eichler, Phys. Status Solidi B **103**, 289 (1981).
13. H. T. Langhammer, M. Stordeur, H. Sobotta, and V. Riede, Phys. Status Solidi B **109**, 673 (1982).
14. *Film Thermoelements: Physics and Application*, Ed. by N. S. Lidorenko (Nauka, Moscow, 1985).

Translated by G. Skrebtsov

Physics of the Solid State, Vol. 44, No. 1, 2002, pp. 48–51. Translated from Fizika Tverdogo Tela, Vol. 44, No. 1, 2002, pp. 47–50.

SEMICONDUCTORS AND DIELECTRICS

The Excitonic Absorption Spectrum of Thin Ag_2ZnI_4 Films

O. N. Yunakova*, V. K. Miloslavskiĭ*, and E. N. Kovalenko**

**Kharkov National University, Kharkov, 61077 Ukraine*

***Scientific Center of Physics and Technology, Education Ministry and National Academy of Sciences of Ukraine, Kharkov, 61145 Ukraine*

Received January 22, 2001

Abstract—The electron absorption spectrum of thin films of the Ag_2ZnI_4 complex compound is studied at photon energies of 3–6 eV. It is established that the interband absorption edge corresponds to an allowed direct transitions across the energy gap E_g = 3.7 eV. A strong exciton band is adjacent to the absorption edge at E_{ex} = 3.625 eV (80 K); in the 80–390 K range, the temperature behavior of the half-width Γ of this band is determined by the exciton–phonon interaction typical of quasi-one-dimensional excitons. At $T \le 390$ K, a discontinuity in the slope of the $E_{ex}(T)$ and $\Gamma(T)$ dependences is observed. This discontinuity is associated with the generation of Frenkel defects and is accompanied by the transfer of Ag ions to the interstitial sites and vacancies of the crystal lattice of the compound. © *2002 MAIK "Nauka/Interperiodica".*

Among the AgI-based compounds with high ionic conductivity, the Ag_2ZnI_4 triple compound is the least studied. Controversial information on the phase diagrams and crystal structure of Ag_2ZnI_4 can be found in a few papers [1–4]. According to [2, 3], the Ag_2ZnI_4 complex compound exists in the $(ZnI_2)_x(AgI)_{1-x}$ system in a small interval of molar concentrations x near $x = 0.33$ and at temperatures up to 192°C. According to [1, 2], the compound has a hexagonal lattice with parameters $a = 0.439$ and $c = 0.73$ nm. However, as pointed out in [2], the parameters of the complete unit cell have not yet been determined because of the difficulties involved in x-ray diffraction measurements: at the parameters mentioned, the unit cell contains a half of the formula unit. At $T > 192$°C, the compound dissociates into ZnI_2 and αAgI. On the contrary, more recent data [4] indicate that Ag_2ZnI_4 is formed into two phases: a low-temperature orthorhombic phase with lattice parameters $a = 1.173$, $b = 1.334$, and $c = 0.73$ nm and a high-temperature phase which forms at $T >$ 265°C and exists in the narrow temperature range from 265 to 280°C. The temperature dependence of the conductivity suggests [2] that the transition of Ag_2ZnI_4 to a superionic state occurs at $T \approx 146$°C. This temperature coincides with the temperature of the phase transition from β-AgI to α-AgI, which allows one to conclude that the compound is partially decomposed at $T <$ 192°C.

Additional information on the phase composition and possible phase transitions comes from the electron spectra of the compounds. As far as we know, the electronic spectrum of Ag_2ZnI_4 has not yet been studied. Since the absorption coefficient in the intrinsic absorption band is large, thin films are the most appropriate samples for use in experimental study of the absorption spectrum. We investigated the absorption spectra of Ag_2ZnI_4 within the temperature range 80–440 K for energies from 3 to 6 eV. The results of this investigation are presented in this paper.

Ag_2ZnI_4 films 100-nm thick were fabricated through vacuum evaporation of a mixture of AgI and ZnI_2 powders in a given molar proportion onto quartz substrates heated to 100°C. Due to the hygroscopicity of the compound, the originally smooth and transparent films, being exposed to air and cooled, become highly diffused and are unsuitable for optical measurements. For this reason, the heated films were placed in a vacuum cryostat whose copper finger was preliminary heated to 70°C. After the cryostat had been evacuated and filled with liquid nitrogen, the films retained their initial transparency (in the visible region). The phase composition of the films was determined from the absorption spectra, which was made possible by the spectral positions of the narrow exciton bands in AgI, Ag_2ZnI_4, and ZnI_2 being essentially different (Fig. 1). At the molar concentration $x > 0.35$, an additional band appears in the spectrum of Ag_2ZnI_4 at 4.45 eV. This band is typical of ZnI_2 and is 0.77 eV from the low-frequency exciton band of the triple compound. At $x < 0.3$, additional absorption associated with excess AgI appears within the transparency range of Ag_2ZnI_4 at 3 eV. At a given thickness of the film, the most intensive exciton peak at $E = 3.625$ eV, corresponding to Ag_2ZnI_4, was observed at $x = 0.32$. Since the films were hygroscopic, their thickness was determined from the transmission spectrum in the transparency range using the method described in [5].

With increasing temperature, the exciton peak at 3.625 eV slightly broadens and shifts to the low-frequency range. Judging from the intensity of the peak in a thin film ($t = 110$ nm), the exciton band is adjacent to the edge of the region of direct allowed interband tran-

sitions. Separating the exciton band from this edge, we found $E_g \approx 3.7$ eV for the band-gap width of the compound (the estimate is made with respect to the inflection point in the vicinity of the edge). The absence of a noticeable temperature dependence in the optical-density spectrum at $E > E_g$ indicates that there are no exciton bands at higher frequencies. The continuous interband absorption spectrum has a broad peak at E = 5.55 eV. Supposing that this peak corresponds to transitions between the centers of the energy bands, we find the combined width of the conduction and valence bands adjacent to the band gap, $\Delta E = \Delta E_c + \Delta E_v = 2(E_m - E_g) = 3.7$ eV.

Comparison of the electronic spectra of the triple compounds derived from AgI is also of interest. At T = 80 K, the low-frequency exciton bands in compounds $RbAg_4I_5$, KAg_4I_5, $NH_4Ag_4I_5$, and Ag_2CdI_4 are at 3.35 [6, 7], 3.33 [6, 8], 3.33 [6], and 3.31 eV [9], respectively. The close excitation energies of the 1*s* excitons are indicative of a weak dependence of E_{ex} on the type of cations substituting for Ag ions. This fact suggests that the excitons are localized in the AgI sublattice of the compounds under consideration [7–9]. We suppose that, as is the case with AgI, the upper valence band in the triple compounds is formed by the 5*p* states of I atoms and 4*d* states of Ag atoms, while the lower conduction band is associated with 5*s* states of Ag atoms. In all the compounds, the edge of the continuous spectrum corresponds to allowed interband transitions. In the triple compounds, the high-frequency shift of the exciton bands with respect to the low-frequency band in AgI (E_{ex} = 2.3 eV) is mainly due to the increase in the number M of Ag atoms in the second coordination shell [7–9]. The tetrahedral ionic–covalent bond between Ag atoms and the I atoms surrounding them is typical of all these compounds. At the same time, the exciton band in Ag_2ZnI_4 is shifted to the high-frequency spectral range by 0.32 eV with respect to the band in the more closely related compound Ag_2CdI_4.

Since the electronegativities of the Zn and Cd atoms (1.6 and 1.7, according to Pauling and more recent data [10]) differ only slightly, it is unlikely that this shift is due to an increase in the ionicity of the chemical bond in Ag_2ZnI_4 as compared with Ag_2CdI_4. Probably, the difference in the spectral position of the exciton bands can be explained in terms of the difference in the structure of the crystal lattices of these two compounds. The Ag_2CdI_4 compound forms into an Ag_2HgI_4-type tetragonal lattice with the unit-cell parameters a = 0.635 and c = 1.27 nm [2]. Ag_2CdI_4 is characterized by a tetrahedral bond between the Ag and I ions and the coordination number M = 6; the volume per I atom is V_I = 0.064 nm^3. As was already mentioned, $AgZnI_4$ has a hexagonal lattice with half a molecule per unit cell and a volume per I atom of V_I = 0.61 nm^3 [1, 2]. At the same time, according to [4], the low-temperature phase of this compound has an orthorhombic lattice with four

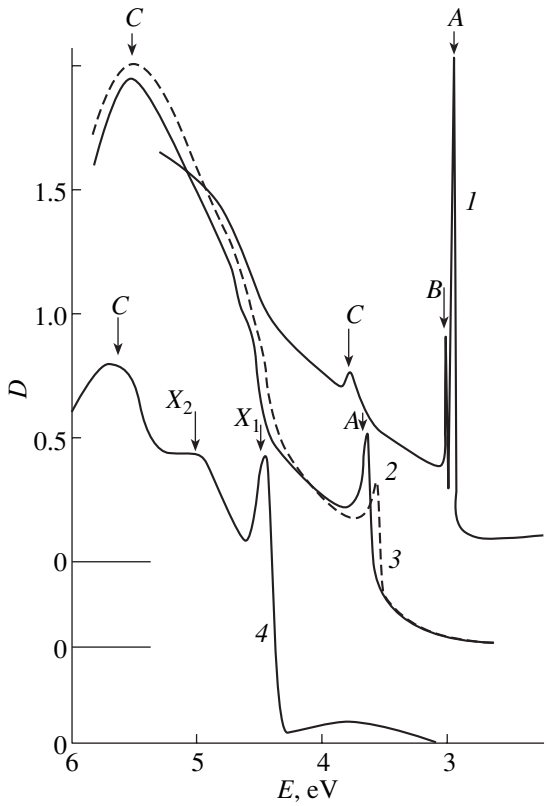

Fig. 1. Absorption spectra of thin films: (*1*) AgI at T = 90 K; (*2*, *3*) Ag_2ZnI_4 at T = 90 and 290 K, respectively; and (*4*) ZnI_2 at T = 90 K.

molecules per unit cell and V_I = 0.072 nm^3. These data lead to the conclusion that the parameters of a structural element of the unit cell of the orthorhombic lattice, rather than of the unit cell itself, were determined in [1, 2] using x-ray structural analysis.

In this connection, it makes sense to compare the electronic spectrum of Ag_2ZnI_4 with that of the $CsAg_2I_3$ triple compound, which also has an orthorhombic lattice with parameters a = 1.108 nm, b = 1.374 nm, and c = 0.623 nm [11] and four molecules per unit cell. As established in [11], $CsAg_2I_3$ is characterized by double chains consisting of AgI_4 tetrahedrons oriented along the c-axis of the crystal. It should be noted that the volume per I atom is V_I = 0.060 nm^3 in a double chain of $CsAg_2I_3$, while in the unit cell, this volume is 0.071 nm^3. These values of V_I are very close to the corresponding values of V_I for the structural element and the unit cell in Ag_2ZnI_4. The difference between the values of V_I indicates that the heteropolar bonds within the double chains and structural elements in $CsAg_2I_3$ and Ag_2ZnI_4 are stronger than the bonds between them. It was shown in [12] that the low-frequency absorption spectrum of $CsAg_2I_3$ is associated with excitons and electrons in the double chains and that the electronic

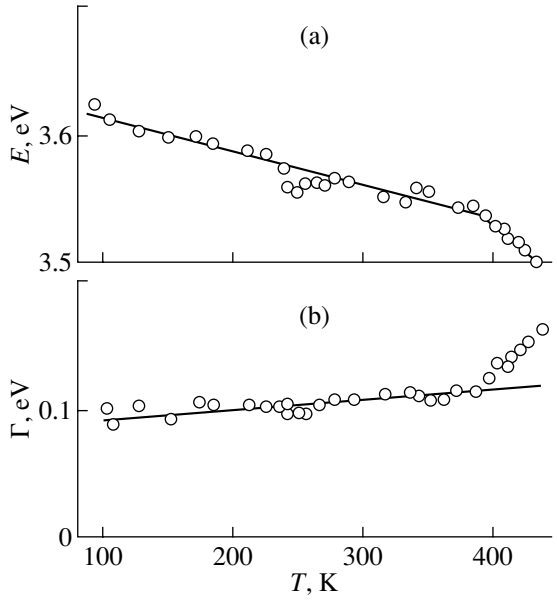

Fig. 2. Temperature dependence of (a) the spectral position $E_m(T)$ and (b) half-width $\Gamma(T)$ of the long-wavelength *A*-exciton band in Ag_2ZnI_4; the solid line is calculated under the assumption of a linear $\Gamma_{ex\text{-}ph}(T)$ dependence and the dots are the experimental values of $\Gamma(T)$.

energy bands in this compound are of quasi-one-dimensional character.

In $CsAg_2I_3$, the low-frequency exciton peak is at 3.73 eV, and its energy is close to E_{ex} = 3.625 eV in Ag_2ZnI_4. From the above discussion it is clear that the excitons and electronic excitations in Ag_2ZnI_4 are localized in the structural elements of the hexagonal symmetry oriented along the *c* axis of the orthorhombic lattice and that the energy bands of this compound are quasi-one-dimensional. It seems to be difficult to obtain more detailed information on the relation between the structure of the electronic spectrum of Ag_2ZnI_4 and its crystal structure, because there are no reliable data available on the structure of the crystal lattice of this compound.

The temperature dependence of the parameters of the low-frequency excitonic band in Ag_2ZnI_4 was studied in the temperature range 80–435 K, containing the temperature of the phase transition $\beta \longrightarrow \alpha$ in AgI (495 K). The excitonic band was approximated by a combined Gaussian and Lorentzian symmetric contour, and the parameters of the band (spectral position E_{ex}, half-width Γ, oscillator strength) were determined by the best fit between the experimental and calculated spectral dependences of the optical density in the long-wavelength tail of the band. The light interference in the thin layer was taken into account using the method described in [13]. At low temperatures, the excitonic bands are closely approximated by a Lorentzian. With increasing temperature, the Gaussian component increases, and the shape of the bands becomes Gaussian above room temperature. In the temperature range 80–390 K, a linear shift of the excitonic band to lower frequencies is observed with $dE_{ex}/dT = -2.8 \times 10^{-4}$ eV/K (Fig. 2a). The shift is of the same order of magnitude as in a number of AgI-based triple compounds and is indicative of exciton–phonon interaction. The exciton–phonon interaction is also manifested in a decrease in the oscillator strength and in the asymmetry of the excitonic band with increasing temperature *T* (Fig. 1). However, the half-width increases with growth in *T* only slightly (Fig. 2b). In the same temperature range, the half-width Γ grows from 0.1 to 0.115 eV. Data processing using the least squares method and the linear-law approximation yields $\Gamma(0) = 0.09 \pm 0.01$ eV and $d\Gamma/dT = (1.3 \pm 0.4) \times 10^{-4}$ eV/K. A possible cause of the weak dependence of Γ on *T* is the quasi-one-dimensional character of the excitons in this compound. For comparison, the half-width of the bands of three-dimensional excitons in Ag_2CdI_4 increases from 0.025 to 0.15 eV in the same temperature range [9]. The theory of exciton–phonon interaction developed for excitons of different dimensionality [14] predicts larger band widths at low *T* and weaker temperature growth in Γ for one-dimensional excitons as compared with three-dimensional ones under the same conditions (the energy of the interstitial exciton transfer, phonon frequency).

At $T \geq 390$ K, a noticeable shift of the exciton band to lower frequencies with $dE_{ex}/dT = -8.75 \times 10^{-4}$ eV/K is observed. This band shift is accompanied by a discontinuity in the slope of the $\Gamma(T)$ dependence, and the half-width increases from 0.115 to 0.165 eV in the narrow temperature interval 390–445 K. The changes in E_{ex} and Γ observed in this temperature range correlate well with the sharp increase in the ionic conductivity of the compound by three orders of magnitude. As in other AgI-containing compounds, we associate the changes in the temperature dependence of Γ at $T \geq 390$ K with the generation of Frenkel defects. The generation of Frenkel defects is accompanied by the appearance of random internal electric fields, leading to additional scattering of excitons [15]. Since the excitonic band has a Gaussian shape at $T \geq 390$ K, the total half-width of the band in this temperature range is

$$\Gamma = \sqrt{\Gamma_{ex\text{-}ph}^2 + \Gamma_F^2}, \quad (1)$$

where $\Gamma_{ex\text{-}ph}$ and Γ_F are the contributions of the exciton–phonon interaction and Frenkel defects to the half-width, respectively. The value of Γ_F and its temperature dependence can be estimated from the experimental values of Γ and the values of $\Gamma_{ex\text{-}ph}$ extrapolated to the given temperature range. Since Γ_F is proportional to the concentration of Frenkel defects n_F, whose temperature dependence is described by the Arrhenius law

$$n_F = Ae^{-u_F/kT}, \quad (2)$$

the linearized $\Gamma_F(T)$ dependence in the range 390–445 K gives the activation energy for Frenkel defects u_F = (0.31 ± 0.04) eV. This activation energy is almost two times smaller than the activation energy characterizing the temperature dependence of the ionic conductivity of Ag_2ZnI_4 (u_σ = 0.77 eV [2]). It should be noted that for superionic conductors, the activation energy determined from the $\Gamma_F(T)$ dependence is usually smaller than u_σ [8]. Probably, this difference is due to the fact that the motion of cations over the interstitial sites has been activated and, therefore, the temperature dependence $\sigma(T)$ includes the activation energy for cation migration over the lattice.

A sharp decrease in E_{ex} with increasing temperature is also typical of the classical conductor β-AgI at temperatures close to the temperature of the phase transition to α-AgI (T_c = 419 K) [16]. As is the case with Ag_2ZnI_4, the sharp decrease in E_{ex} is accompanied by a growth in the band half-width. At $T \geq T_c$, the saturation of E_{ex} and Γ occurs. However, in contrast to Ag_2ZnI_4, the band in AgI is shifted within a narrower temperature range (408–421 K) and the value of this shift is noticeably larger (ΔE_{ex} = 0.185 eV). Based on the aforesaid, one can conclude that the formation of Frenkel defects and the ionic conductivity in Ag_2ZnI_4 are determined by Ag ions occupying interstitial sites and vacancies that accompany the Zn^{2+} ions. Probably, partial disorder of the compound with precipitation of α-AgI occurs at $T \geq$ 419 K and is followed by complete decomposition of the compound into ZnI_2–α-AgI at 455 K [2]. The latter conclusion is in agreement with the phase diagrams and conductivity data presented in [2, 3].

In conclusion, it should be noted that the significant difference in the electronic absorption spectra and temperature dependences of the excitonic bands of the chemically similar compounds Ag_2CdI_4 and Ag_2ZnI_4 is due to the difference between their crystal lattices. It seems likely that the quasi-one-dimensional character of the low-frequency electronic excitations in Ag_2ZnI_4 is determined by the specific features of its lattice structure.

REFERENCES

1. P. Fourcroy, I. Rivet, and I. Flahaut, C. R. Acad. Sci., Ser. C **278** (19), 1189 (1974).
2. J. W. Brightwell, C. N. Buckley, G. Forton, *et al.*, J. Mater. Sci. Lett. **1** (10), 429 (1982).
3. J. W. Brightwell, C. N. Buckley, R. C. Hollyoak, and B. Ray, J. Mater. Sci. Lett. **3** (5), 443 (1984).
4. R. Blachnik and U. Stoter, Thermochim. Acta **145**, 93 (1984).
5. V. K. Miloslavskiĭ, A. I. Rybalka, and V. I. Shmandiĭ, Opt. Spektrosk. **48** (3), 619 (1980) [Opt. Spectrosc. **48**, 341 (1980)].
6. I. Kh. Akopyan, D. N. Gromov, A. V. Mishchenko, *et al.*, Fiz. Tverd. Tela (Leningrad) **26** (9), 2628 (1984) [Sov. Phys. Solid State **26**, 1593 (1984)].
7. V. K. Miloslavskiĭ, O. N. Yunakova, and Sun Tsya-Lin, Funkts. Mater. **1**, 438 (1994).
8. V. K. Miloslavskiĭ and Sun Tsya-Lin, Funkts. Mater. **2** (4), 438 (1995).
9. O. N. Yunakova, V. K. Miloslavskiĭ, and M. Zhavhlangiyn, Ukr. Fiz. Zh. **35** (10), 1502 (1990).
10. W. Gordy and W. J. Thomas, J. Chem. Phys. **24**, 439 (1956).
11. C. Brink, N. F. Binnenijk, and J. van de Linde, Acta Crystallogr. **7** (1), 176 (1954).
12. V. K. Miloslavskiĭ, Sun Tsya-Lin, and O. N. Yunakova, Opt. Spektrosk. **80** (4), 643 (1996) [Opt. Spectrosc. **80**, 577 (1996)].
13. V. K. Miloslavskiĭ, O. N. Yunakova, and Sun Tsya-Lin, Opt. Spektrosk. **78** (3), 436 (1995) [Opt. Spectrosc. **78**, 391 (1995)].
14. M. Schreiber and Y. Toyozawa, J. Phys. Soc. Jpn. **51** (5), 1528 (1982).
15. I. Kh. Akopyan, B. V. Bondarev, D. I. Gromov, *et al.*, Fiz. Tverd. Tela (Leningrad) **29** (8), 2263 (1987) [Sov. Phys. Solid State **29**, 1305 (1987)].
16. R. Galbadrakh, V. K. Miloslavskiĭ, and U. Mayer, Zh. Prikl. Spektrosk. **59** (1), 139 (1993).

Translated by A. Poushnov

Physics of the Solid State, Vol. 44, No. 1, 2002, pp. 52–57. Translated from Fizika Tverdogo Tela, Vol. 44, No. 1, 2002, pp. 51–56.

SEMICONDUCTORS AND DIELECTRICS

Electron Paramagnetic Resonance and Luminescence of Chromium in Calcium Germanate Crystals

O. N. Gorshkov, E. S. Demidov, S. A. Tyurin, A. B. Chigineva, and Yu. I. Chigirinskiĭ

Research Physicotechnical Institute, Nizhni Novgorod State University, pr. Gagarina 23/5, Nizhni Novgorod, 603600 Russia

e-mail: ett@phys.unn.runnet.ru

Received April 24, 2001

Abstract—The luminescence of $Ca_2GeO_4 : Cr^{4+}$ single crystals at wavelengths in the range of 1.3 μm upon excitation with a 1-μm semiconductor laser is investigated in the temperature range up to 573 K. At $T < 110$ K, the $Ca_2GeO_4 : Cr^{4+}$ crystals are characterized by the electron paramagnetic resonance, which is attributed to the Cr^{4+} ions substituted for Ge^{4+} ions. The components of the *g* tensor and its principal axes are determined. It is revealed that the Cr^{4+} impurity centers in calcium germanate affect the crystal symmetry to a lesser degree compared to Cr^{4+} ions in forsterite. The observed deviation of the temperature dependence of the electron paramagnetic resonance from the Curie law is explained by the transition to the excited state with a low activation energy, as is the case in impurity 3*d* ions in diamond-like semiconductors. The inference is made that the giant effective degeneracy multiplicity of the excited state is associated with the initiation of soft phonon modes in the crystal upon excitation of the defect. © *2002 MAIK "Nauka/Interperiodica".*

1. INTRODUCTION

Crystals of calcium germanate Ca_2GeO_4 doped with chromium are promising materials for use in near-IR laser technology. Calcium germanate compares favorably with its structural analog, namely, forsterite (Mg_2SiO_4): the close values of Cr and Ge ion radii (0.41 and 0.39 Å, respectively [1]) provide predominant dissolution of chromium in the charge state 4+ as an impurity substituting for germanium. Note that chromium in forsterite crystals can substitute for both magnesium in two different positions in the unit cell and silicon and can occur in three charge states (2+, 3+, and 4+) [1–4]. Moreover, the highly efficient photoluminescence band, which is assigned to the $^3T_2 \longrightarrow {}^3A_2$ transition of Cr^{4+} ions in calcium germanate, corresponds to the highest transparency of a glass fiber at a wavelength of approximately 1.3 μm, whereas this transition in forsterite is observed at approximately 1.1 μm. Petricevic *et al.* [1] succeeded in achieving a lasing efficiency of 10% in $Ca_2GeO_4 : Cr^{4+}$ crystals with the use of 0.8- to 1-μm semiconductor laser diode pumping.

It is known from optical spectroscopy that chromium ions in Ca_2GeO_4 predominantly occur in the charge state 4+, which, as was already mentioned, is explained by the close values of chromium and germanium ion radii. However, up to now, there has been no research done to determine the charge states of chromium in this material with the use of other techniques. In the present work, we undertook a combined investigation into the electron paramagnetic resonance and photoluminescence in $Ca_2GeO_4 : Cr^{4+}$ single crystals in the temperature range 55–600 K. As in [1], the photoluminescence due to intracenter transitions in the 3*d* shell of Cr^{4+} ions was observed at a wavelength $\lambda \approx 1.3$ μm up to a temperature of 573 K. In addition, we observed the electron paramagnetic resonance (EPR) spectrum with a fine structure and attributed this spectrum to the Cr^{4+} ions. The angular and temperature dependences of the electron paramagnetic resonance were examined. It was found that the Cr^{4+} centers can reside in excited states with anomalously high effective degeneracy multiplicities, which are similar to those observed earlier for impurity 3*d* ions of the iron group in diamond-like semiconductors [5, 6].

2. EXPERIMENTAL TECHNIQUE

The experiments were performed with single-crystal samples ($4 \times 4 \times 1.5$ mm in size) cut from Ca_2GeO_4 ingots, which were grown from the undoped melt and the melt containing approximately 0.5 wt % chromium oxide. The edges of rectangular samples were oriented parallel to the *a*, *b*, and *c* crystallographic axes of the crystal. The undoped crystals were transparent and colorless, whereas the doped crystals were transparent and deep green.

The EPR spectra were recorded on a spectrometer operating in the 3-cm band [7] at the frequency $\nu = 9.34 \times 10^9$ Hz. The magnetic field was calibrated against an MgO : Mn powder or a Fremi salt used as the reference sample [6]. The intensity was calibrated against a powdered silicon with a *g* factor of 2.0055. The sample to be studied was placed inside a Dewar glass vessel in the antinode of a magnetic field of a

TE_{103} rectangular cavity, and the reference sample was placed in the other antinode. The angular dependences of the electron paramagnetic resonance were measured in a cryostat cooled with liquid nitrogen [8]. The preliminary investigations showed that the boiling temperature of liquid nitrogen is too high to provide saturation of the concentration of Cr paramagnetic centers in the ground state. The temperature was reduced to 55 K through the evaporation of nitrogen during its evacuation. After completion of the evacuation, the sample was gradually heated. The temperature dependences of the EPR spectra were recorded using 30-s periodic scanning. The temperature was measured with a calibrated copper–constantan thermocouple fabricated from wires 0.05 mm in diameter. A thermocouple junction was cemented to the sample with a nitrolacquer. The error in temperature measurement did not exceed 3 K. The EPR absorption spectra and their first derivatives were recorded. The measurement conditions, even at the lowest temperatures, corresponded to insignificant microwave saturation of the EPR spectrum.

Tetravalent chromium in the Ca_2GeO_4(Cr) crystals was also determined from the photoluminescence spectra. The spectra were measured using a setup based on an MDR-23 spectrometer in the temperature range 77–600 K. The spectra were excited with a 2-W GaInPAs heterostructure injection semiconductor laser diode at a wavelength of 0.98 μm.

3. RESULTS AND DISCUSSION

In chromium-free Ca_2GeO_4 crystals, no luminescence is observed. At the same time, the crystals doped with chromium exhibit an intense luminescence in the wavelength range λ = 1.1–1.6 μm. The luminescence spectra of the Ca_2GeO_4 : Cr crystals at different temperatures are displayed in Figs. 1 and 2. It is seen from Fig. 1 that, at liquid-nitrogen temperatures, the photoluminescence spectrum of the studied crystals is similar to that observed in [1] and contains a line of the zero-phonon transition (according to the assignment made in [1]) and the lines attributed to the $^3T_2 \longrightarrow {}^3A_2$ phonon-assisted transitions, which are split by a nearly tetrahedral crystal field of the $3d^2$ shell of the Cr^{4+} ions. As the temperature increases to room temperature (Fig. 2, curve *1*), the luminescence spectrum flattens and becomes bell-shaped with a maximum at approximately 1.25 μm, as was observed in [1]. The small dip at a wavelength of approximately 1.38 μm is associated with the absorption of water molecules. The luminescence is also observed at temperatures higher than room temperature (Fig. 2, curves *2–4*). An increase in the temperature is accompanied by a shift of the luminescence maximum to 1.3 μm. At $T \sim 600$ K, the luminescence virtually disappears. Figure 3 shows the temperature dependence of the integrated intensity of luminescence in the wavelength range 1.1–1.6 μm. It can be seen that the luminescence decay slows down at $T \approx$ 350 K. The ratio of the luminescence intensities at temperatures of 77 and 293 K slightly exceeds the inverse ratio of these temperatures.

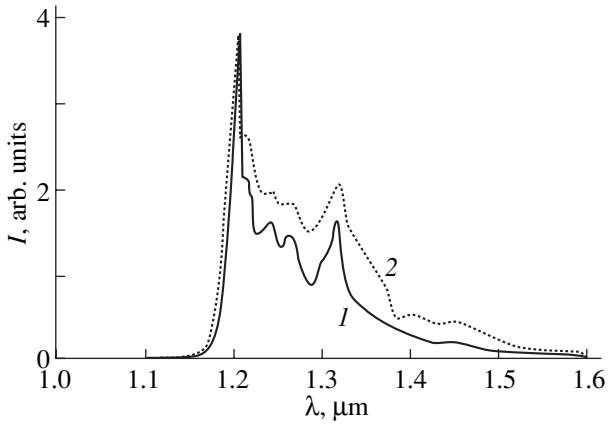

Fig. 1. Photoluminescence spectra of the Ca_2GeO_4 : Cr crystals at 77 K: (*1*) the spectrum taken from [1] and (*2*) the spectrum obtained in this work.

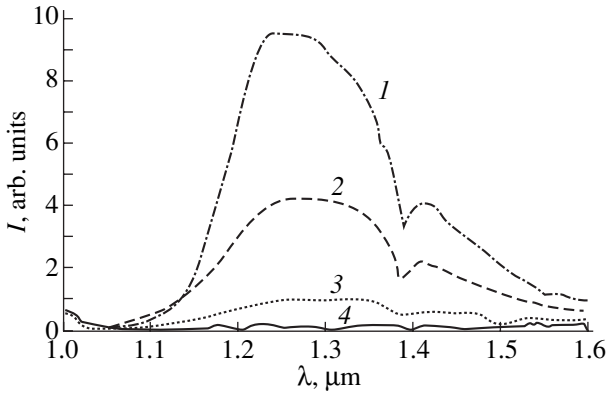

Fig. 2. Luminescence spectra of the Ca_2GeO_4 : Cr crystals at temperatures of (*1*) 293, (*2*) 373, (*3*) 473, and (*4*) 573 K.

Within the detection limits of the EPR spectrometer (about 5×10^9 spins/G), the paramagnetic resonance absorption is not observed in the undoped Ca_2GeO_4 crystals at $T \geq 55$ K in the magnetic field range from 0 to 7000 G. However, the chromium-doped crystals exhibit an EPR spectrum at $T < 110$ K. This spectrum involves two lines of a fine structure whose location is dependent on the crystal orientation. Identical temperature behavior of the fine structure lines suggests that these lines are attributed to the same paramagnetic center. In this case, the spectroscopic splitting factor g is equal (to the third decimal place) to the pure spin g factor of a free electron. This implies that the orbital angular momentum of the paramagnetic center is either equal to zero or frozen by the crystal field. The presence of two fine structure lines in the spectrum indicates that the paramagnetic center has the spin $S = 1$, which corresponds to a center with two electrons whose spins are

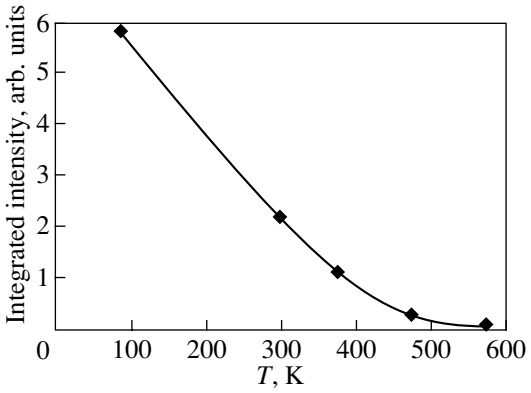

Fig. 3. Temperature dependence of the integrated intensity of luminescence in the wavelength range 1.1–1.6 μm for the Ca_2GeO_4 : Cr crystals.

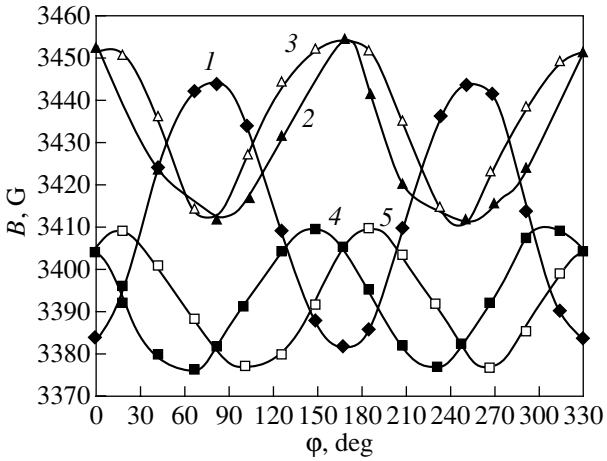

Fig. 4. Dependences of the location of the EPR lines on the angle of rotation φ of the crystal with respect to the magnetic induction vector in different crystal planes: (*1*) *bc*, (*2*, *3*) *ac*, and (*4*, *5*) *ab*. Two lines of the fine structure with different *g* factors are observed in the *ac* and *ab* planes.

parallel to each other. On this basis, by analogy with Cr^{4+} ions in forsterite [2], we can assume that the EPR spectrum observed for the Ca_2GeO_4 : Cr crystals is attributed to Cr^{4+} ions with a $3d^2$ shell in the $^3A_2(e^2)$ singlet state and two electrons at the *e* level split off by the crystal field.

In addition to the aforementioned two intense lines, the EPR spectrum contains a group of unresolved lines that overlap with these intense lines. The intensity of the unresolved lines is more than one order of magnitude less than that of the intense lines. It seems likely that the unresolved structure of the spectrum arises from the hyperfine interaction of ^{53}Cr isotopes with a nonzero nuclear spin (3/2) [9] and a content of 9.55% in a natural isotopic mixture. A decrease in the temperature leads to an increase in the asymmetry of the intense fine-structure lines. These findings can be explained by the specific features of spin-lattice relaxation and spin diffusion. However, the observed phenomenon and the hyperfine structure call for further investigation and will be discussed in a separate work.

The angular dependences of the location of the Cr^{4+} EPR lines at 80 K are depicted in Fig. 4. The components of the *g* tensor calculated from these dependences are as follows:

$$g = \begin{bmatrix} 1.9275 & 0 & 0 \\ 0 & 1.9528 & 0 \\ 0 & 0 & 1.9851 \end{bmatrix}. \quad (1)$$

The axes of this tensor with respect to the crystal axes are determined by the unit vectors

$$a_{1g} = \begin{bmatrix} 0.967 \\ -0.254 \\ -0.018 \end{bmatrix},$$
$$a_{2g} = \begin{bmatrix} 0.249 \\ 0.926 \\ 0.283 \end{bmatrix}, \quad a_{3g} = \begin{bmatrix} -0.055 \\ -0.278 \\ 0.959 \end{bmatrix}. \quad (2)$$

As can be seen from Fig. 4 and the components of tensor (1), the *g* factors have lesser values compared to the pure spin *g* factor of a free electron (2.0023), which is typical of paramagnetic chromium ions in crystals. The direction cosines (2) of the *g* tensor axes indicate that these axes deviate from the crystal axes by no more than 15°, whereas the corresponding deviation in chromium-containing forsterite may be as much as 43° [3]. This means that the smaller difference between the Cr^{4+} and Ge^{4+} ion radii in Ca_2GeO_4, as compared to that between the Cr^{4+} and Si^{4+} ion radii in forsterite, leads to a weaker distortion of the tetrahedral symmetry and the crystal lattice in the vicinity of chromium impurity ions in calcium germanate. Most likely, the weaker distortions can also be explained by the fact that the germanium ion has the 3*d* shell, which is absent in the silicon ion; i.e., the radial electron density distributions in chromium and germanium ions more closely resemble each other. It is seen from Fig. 4 that the fine structure lines virtually do not split upon rotation of the crystal in the *bc* plane, i.e., when the rotation axis coincides with the crystal axis *a*, which is parallel to the threefold axis C_3 in Ca_2GeO_4 crystals with a forsterite-like structure.

Figure 5 displays the temperature dependences (corrected for the Curie law) of the intensity *Y* of the Cr^{4+} EPR absorption line and the intensity *Y'* of its first derivative for a magnetic field oriented in the *bc* plane of the crystal in such a manner that a single line has the highest intensity. Both dependences exhibit a similar behavior; i.e., the shape of the EPR line remains invariant as the temperature increases. Numerical analysis shows that the spectrum has a nearly Gaussian shape.

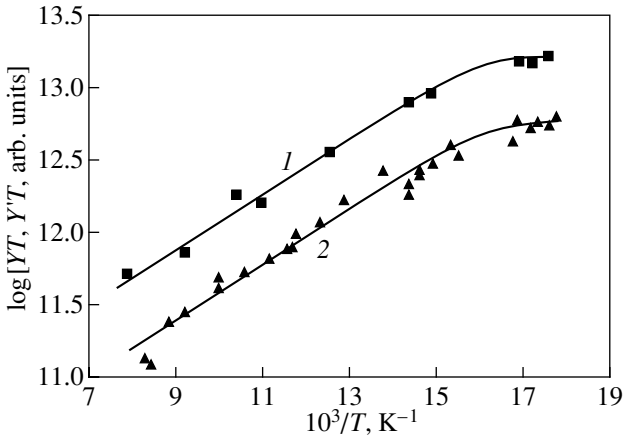

Fig. 5. Temperature dependences (corrected for the Curie law) of (*1*) the intensity Y of the Cr^{4+} EPR absorption line and (*2*) the intensity Y' of its first derivative for the $Ca_2GeO_4 : Cr^{4+}$ crystal.

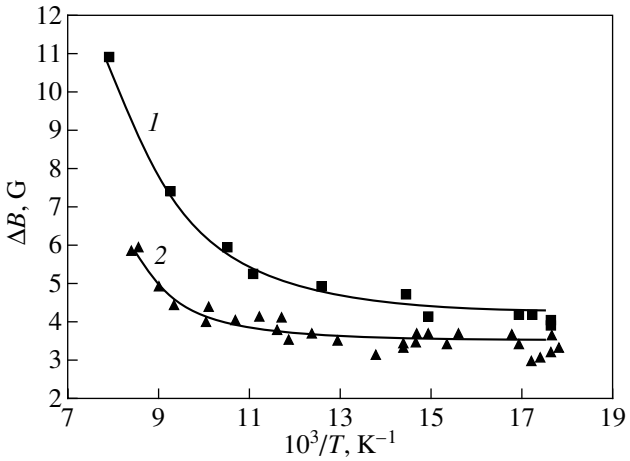

Fig. 6. Temperature dependences of (*1*) the half-height line width $\Delta B_{1/2}$ of the EPR absorption spectrum and (*2*) the peak-to-peak derivative width ΔB_{pp} of the Cr^{4+} EPR spectrum for the $Ca_2GeO_4 : Cr^{4+}$ crystal.

The temperature dependences of the EPR linewidth are plotted in Fig. 6. These dependences, as well as the fine and hyperfine structures of the spectrum, will be analyzed after more precise and detailed measurements in a separate work. Here, it is worth noting that the broadening of spectral lines without changes in their shape is a rare case. As a rule, pure spin-lattice relaxation results in Lorentzian broadening of the EPR lines [10].

The temperature dependence of the concentration of visible Cr^{4+} EPR centers is shown in Fig. 7. The invariability of the EPR line shape simplified the construction of this dependence from the data presented in Figs. 5 and 6. It can be seen that the dependence does not obey the Curie law. This manifests itself in a decrease in the number of centers in the ground state with an increase in the temperature. Demidov *et al.* [5, 6] observed a similar phenomenon for impurity 3*d* ions of the iron group in diamond-like semiconductors. Cooling of the sample upon nitrogen evacuation ensured saturation of the concentration N of chromium centers at low temperatures. The saturation corresponded to the total concentration of Cr^{4+} centers $N_0 \approx 1.3 \times 10^{16}$ cm^{-3}. This is a relatively low concentration at which electron exchange between chromium centers is highly improbable. As in [5, 6], we attribute the deviation from the Curie law to the transition of the defects to excited states.

The experimental points plotted in Fig. 7 fit the theoretical curve fairly well. This dependence corresponds to the transition to an excited energy level and can be represented by the relationship

$$N(Cr^{4+}) = N_0(Cr^{4+})[1 + g_{10}\exp(-E_{10}/kT)]^{-1}, \quad (3)$$

where $g_{10} = 550$ is the degeneracy multiplicity of the excited state with respect to the ground state and $E_{10} =$ 0.03 eV is the excitation energy. The spin–orbit splitting is of no significance for the $^3A_2$ singlet state of the Cr^{4+} ion, especially as the parameter of this splitting is estimated as $\lambda \ll E_{10}$. For the band gap $E_g > 3.5$ eV in Ca_2GeO_4 (the undoped crystals are colorless and transparent in visible light), it is unlikely that the impurity Cr 3*d* level is close to the allowed band edges of the crystal to a hundredth of an electron-volt. The resistivity of the chromium-doped crystals at room temperature is substantially higher than 10^{12} Ω cm. To put it differently, a decrease in the concentration N with an increase in the temperature T cannot be caused by the recharging of centers through electron exchange with the allowed bands of the crystal. The excitation is also unrelated to

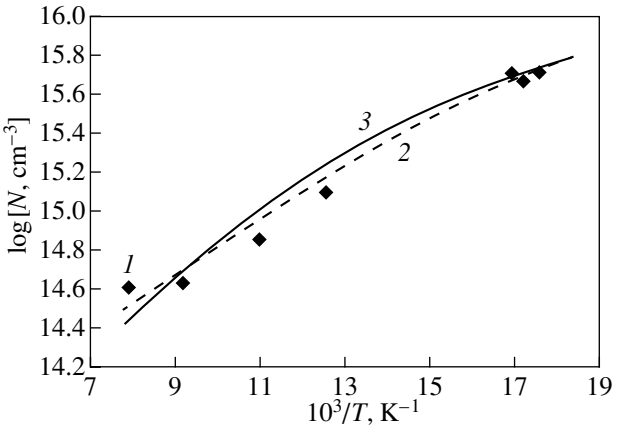

Fig. 7. Temperature dependence of the concentration of Cr^{4+} paramagnetic centers in the ground state in the $Ca_2GeO_4 : Cr^{4+}$ crystal: (*1*) experimental data, (*2*) calculation according to formula (3) (dashed line), and (*3*) calculation according to formula (6) (solid line).

the inner electron transition in the 3*d* shell. According to the Tanabe–Sugano diagrams [9], the nearest energy state $^3T_2$ of the $3d^2$ shell is separated from the ground state by the crystal field energy $\Delta \approx 1$ eV, which is characteristic of ionic compounds and is appreciably higher than E_{10}. All these factors, taken together, suggest that, as in the case of 3*d* ions in semiconductor crystals, the above transition to the excited state can be considered one of the two possible electron transitions to the Kohn–Luttinger localized *s* state [11],

$$3d^2(e^2, t_2^0) \longrightarrow 3d^1(e^1, t_2^0)s_n^1, \quad (4)$$

$$3d^2(e^2, t_2^0) \longrightarrow 3d^3(e^2, t_2^1)s_p^1, \quad (5)$$

which results in the formation of either the hydrogen-like donor state s_n^1 (split off from the conduction band of Ca_2GeO_4) with a single-electron occupation [variant (4)] or the acceptor state s_p^1 (split off from the valence band of Ca_2GeO_4) with a single-hole occupation [variant (5)]. Here, we are dealing with the high-spin approximation; i.e., it is assumed that the Hund rule is fulfilled.

It is difficult to decide between these variants of the excitonic excitation of the center with the formation of an electron [variant (4)] or a hole [variant (5)] which is more delocalized than that in the 3*d* shell. Upon substitution of the 3*d* ion for the trivalent or tetravalent atom in covalent elemental Group IV semiconductors or compounds III–V with a high degree of covalence, the 3*d* ion exhibits an acceptor behavior. If the same is also true for the more ionic compound Ca_2GeO_4, variant (5) is more probable. In order to increase the fraction of laser-active neutral Cr^{4+} centers substituted for germanium, calcium germanate crystals should be additionally doped with nontransition elements whose valence is less by unity than that of the matrix elements and whose ionic radius is close to the radius of the matrix ions; i.e., these elements should be acceptor impurities with the smallest possible size and a low activation energy. As a result, the Fermi level shifts toward the valence band and the fraction of Cr^{4+} centers increases. In particular, the role of these impurity ions can be played by either Na^+ or Al^{3+} substituted for Ca^{2+} or Ge^{4+}, respectively. Another possibility consists in creating an oxygen nonstoichiometry. The observed Cr^{4+} concentration $N_0 = 1.3 \times 10^{16}$ cm^{-3} (Fig. 7) is substantially less than the predicted concentration of dissolved chromium (approximately 10^{20} cm^{-3}), provided that all chromium oxides (0.5 wt %) in the melt pass into the Cr(Ge) solid solution upon the growth of the Ca_2GeO_4 crystals. In other words, the Fermi level is located well above the chromium recharging level in the band gap of the crystal.

As in the case of 3*d* ions in semiconductors, the excited states are characterized by the giant degeneracy multiplicity $g_{10} = 550$, which has defied explanation in the framework of the conventional pure electronic model. On the left-hand sides of schemes (4) and (5), we have the multiplicity of electron degeneracy $g_{e0} = 3$ in accordance with the spin triplet. On the right-hand sides of these schemes, there appears a doubling [scheme (4)] or tripling [scheme (5)] factor owing to the orbital degeneracy of the *e* or t_2 states. Consequently, the multiplicity $g_{e10} = g_{e1}/g_{e0}$ should be equal to two or three. As for 3*d* ions in semiconductors, the high value of g_{10} can be explained by the change in the phonon spectrum of the crystal upon excitation of the defect. This is attended by the initiation of soft phonon resonant modes due to the decrease in the force constants of the crystal in the vicinity of the defect upon transition to the orbitally degenerate state according to variant (4) or variant (5) [12]. In this case, the concentration of Cr^{4+} centers in the ground state can be determined by the expression

$$N(Cr^{4+}) = N_0(Cr^{4+})[1 + \alpha_{10}T^3\exp(-E_{10}/kT)]^{-1}. \quad (6)$$

The best fitting of the calculated curve $N(T)$ to the experimental data (Fig. 7) gives $\alpha_{10} = 5 \times 10^{-5}$ K and $E_{10} = 0.01$ eV. According to [12], when the phonon resonance frequency ω_p is considerably less than the Debye frequency ω_D, we can write the following relationship:

$$\alpha_{10} \approx \frac{g_{e1}}{g_{e0}}\left(\frac{k}{\hbar\omega_p}\right)^3. \quad (7)$$

From this relationship, under the assumption that the Debye temperature for calcium germanate, as for germanium, is approximately equal to 300 K, we obtain the following parameters for variant (5) with $g_{e10} = 3$: $\hbar\omega_p \approx 3.4 \times 10^{-3}$ eV and $\omega_p \approx 0.1\omega_D$.

Since the ground and excited states in variant (5) are energetically close to each other, we can assume that the majority of the Cr^{4+} centers at low temperatures reside in the $3d^3(e^2, t_2)s_p^1$ state (characterized by the electron paramagnetic resonance) due to lattice strains in the crystal. The strains have a stronger effect on the more delocalized Kohn–Luttinger states and result in a decrease in their energy as compared to the ground state [on the left-hand side of scheme (5)]. This is the second reason for the large difference between the predicted concentration of the Cr^{4+} centers and their concentration determined from the EPR data. For the luminescence, the ground and excited states in variant (5) are almost energetically indistinguishable; however, the excited state is more favorable owing to the large statistical weight and the higher probability of dipole phononless transitions.

4. CONCLUSIONS

Thus, the luminescence of Ca_2GeO_4 : Cr crystals at wavelengths in the range of 1.3 μm (which is of partic-

ular importance in laser optical fiber technology) upon excitation with a 1-μm semiconductor heterolaser is observed in the temperature range up to 573 K. The luminescence decay occurs rather slowly with an increase in the temperature and becomes still slower at 350 K. It was found for the first time that these crystals exhibit electron paramagnetic resonance at temperatures up to 110 K. The EPR spectrum was attributed to the Cr^{4+} ions substituted for the Ge^{4+} ions. The *g* tensor of the spectroscopic splitting was determined. The small deviation of the *g* tensor axes from the crystallographic axes indicates a smaller distortion of the point and translational symmetry in the vicinity of Cr^{4+} ions in the studied crystals as compared to that in forsterite.

The temperature dependence of the Cr^{4+} EPR spectrum for the calcium germanate crystals was analyzed. It was revealed that the Cr^{4+} ions can reside in the excited state with a low activation energy and a giant degeneracy multiplicity. A similar state was observed earlier in impurity 3*d* ions of the iron group in diamond-like semiconductors. As for these semiconductors, the giant degeneracy multiplicity can be explained in terms of soft quasi-local phonon resonant modes initiated in the crystal upon excitation of the defect. By analogy with the free 3*d* ions or atoms characterized by energy competition between the 3*d* and 4*s* states, we assumed that the Cr^{4+} impurity ions experience a similar competition between the 3*d* states and more delocalized states, which are conventionally denoted as the Kohn–Luttinger *s* states. The latter states can be treated as being "genetically" formed from the 4*s* and 4*p* states of the free ion [13, 14]. It seems likely that the competition between the energies of the 3*d* and *s* states of impurity 3*d* ions is a commonly occurring phenomenon, because it is observed in narrow-gap semiconductor crystals and a nearly wide-gap ionic Ca_2GeO_4 crystal.

The observed features of the states of electrons localized on Cr^{4+} impurity ions can be useful in determining the oscillator strengths of photoinduced electronic transitions and the conditions of existence for laser-efficient *d* centers. For the purpose of improving the laser efficiency of the $Ca_2GeO_4 : Cr^{4+}$ crystals, it is necessary to increase the fraction of chromium impurity ions in the charge state 4+. From this standpoint, it is of interest to investigate how the shift of the Fermi level toward the valence band due to either additional doping with Na and Al acceptor impurities or oxygen nonstoichiometry can affect the fraction of Cr^{4+} ions.

ACKNOWLEDGMENTS

We are grateful to Yu.V. Paskhin for his assistance in measuring the angular dependences of the electron paramagnetic resonance.

REFERENCES

1. V. Petricevic, A. B. Bykov, J. M. Evans, and R. R. Alfano, Opt. Lett. **21**, 1750 (1996).
2. W. Jia, H. Liu, S. Jaffe, and W. M. Yen, Phys. Rev. B **43** (7), 5234 (1991).
3. K. R. Hoffman, J. Casas-Gonzales, S. M. Jacobson, and W. M. Yen, Phys. Rev. B **44** (22), 12589 (1991).
4. G. S. Shakurov, V. F. Tarasov, and A. N. Gavrilenko, Fiz. Tverd. Tela (St. Petersburg) **37** (2), 499 (1995) [Phys. Solid State **37**, 270 (1995)].
5. E. S. Demidov, A. A. Ezhevskiĭ, and V. V. Karzanov, Fiz. Tekh. Poluprovodn. (Leningrad) **17** (4), 661 (1983) [Sov. Phys. Semicond. **17**, 412 (1983)].
6. E. S. Demidov and A. A. Ezhevskiĭ, Fiz. Tekh. Poluprovodn. (Leningrad) **19** (9), 1629 (1985) [Sov. Phys. Semicond. **19**, 1003 (1985)].
7. E. S. Demidov, Author's Abstract of Doctoral Dissertation (NNGU, Nizhni Novgorod, 1994).
8. E. S. Demidov and A. A. Ezhevskiĭ, Zavod. Lab. **47** (11), 42 (1981).
9. A. Abragam and B. Bleaney, *Electron Paramagnetic Resonance of Transition Ions* (Clarendon, Oxford, 1970; Mir, Moscow, 1973), Vol. 1.
10. L. A. Sorin, M. V. Vlasova, and V. D. Lavadovskiĭ, *Introduction to the Radiospectroscopy of Paramagnetic Single Crystals* (Naukova Dumka, Kiev, 1969).
11. E. S. Demidov, Fiz. Tverd. Tela (St. Petersburg) **34** (1), 37 (1992) [Sov. Phys. Solid State **34**, 18 (1992)].
12. E. S. Demidov, Fiz. Tverd. Tela (Leningrad) **27** (6), 1896 (1985) [Sov. Phys. Solid State **27**, 1140 (1985)].
13. E. S. Demidov and V. A. Uskov, Fiz. Tverd. Tela (Leningrad) **16** (3), 963 (1974) [Sov. Phys. Solid State **16**, 624 (1974)].
14. E. S. Demidov and V. A. Uskov, Fiz. Tekh. Poluprovodn. (Leningrad) **8** (8), 1607 (1974) [Sov. Phys. Semicond. **8**, 1043 (1974)].

Translated by O. Borovik-Romanova

Physics of the Solid State, Vol. 44, No. 1, 2002, pp. 58–63. Translated from Fizika Tverdogo Tela, Vol. 44, No. 1, 2002, pp. 57–61.

SEMICONDUCTORS AND DIELECTRICS

Effect of a DC External Field on the Photorefractive-Response Dynamics in Crystals with Double-Donor Centers and Shallow Traps

A. M. Plesovskikh and S. M. Shandarov

Tomsk State University of Control Systems and Radio Engineering, Tomsk, 634050 Russia

e-mail: shand@stack.ru

Received May 18, 2001

Abstract—This paper presents a theoretical analysis of the dynamics of space-charge field formation in a photorefractive crystal with double-donor centers and shallow traps. The evolution of the photorefractive-grating recording processes in the absence of an external electric field, the relaxation of the grating in the presence of a reference beam, and its subsequent development under application of an external field are considered. © *2002 MAIK "Nauka/Interperiodica".*

1. INTRODUCTION

Photorefractive crystals are promising materials for use in the processing of optical information and storage of holographic images [1]. The processes initiated in a crystal by light can be described using various band transfer models. The process of space charge formation is traditionally considered in terms of a model including photoactive donor centers of one type and nonphotoactive compensating acceptors [2]. A two-center model taking into account an additional shallow trap level was proposed to explain the phenomenon of photoinduced absorption observed experimentally in sillenite and $BaTiO_3$ crystals [3]. In 1995, a "trivalent" model was introduced [4] in which one donor center can reside in three different charge states. This model permitted one to successfully describe photoinduced absorption and photoconductivity in $KNbO_3$: Fe and KTN : Fe crystals [4–7]. A model involving both trivalent centers and shallow traps was proposed in [8] to interpret the experimentally observed dynamics of photoinduced absorption in undoped $Bi_{12}TiO_{20}$.

This paper presents a theoretical analysis of the photorefractive response made in the frame of the latter model. It is shown that the effects of nonmonotonic dynamics of diffraction efficiency observed earlier [9–12] and of latent-image development [13] can be accounted for by the interaction of the charge gratings formed on singly and doubly ionized donors and shallow traps.

2. THEORETICAL MODEL

Figure 1 presents an energy level diagram of the model in question [8]. In this model, deep donors D can reside in three charge states (0, +1, +2) and there is a trap S which can be in the 0 and –1 states. The model assumes the absence of doubly ionized donor centers D_{2+} and of filled shallow traps S_- in the dark. The S_- level can become empty as a result of thermal carrier excitation into the conduction band. Light ionizes the D, D_+, and S_- centers by exciting electrons into the conduction band, where the electrons move through diffusion or drift until they recombine at the D_+, D_{2+}, and S_0 defects.

These processes can be described mathematically by the following coupled equations:

$$\frac{\partial N_D^{1+}}{\partial t} = S_D I(N_D - N_D^{1+} - N_D^{2+}) - \gamma_1 n N_D^{1+} + \gamma_2 n N_D^{2+} - S_1 I N_D^{1+}, \quad (1)$$

$$\frac{\partial N_D^{2+}}{\partial t} = S_1 I N_D^{1+} - \gamma_2 n N_D^{2+}, \quad (2)$$

$$\frac{\partial M}{\partial t} = -(S_T I + \beta)M + \gamma_T n(M_T - M), \quad (3)$$

$$\frac{\partial}{\partial t}(N_D^{1+} + 2N_D^{2+} - M - n) + \frac{1}{e}\nabla(e\mu nE + \mu k_B T \nabla_n) = 0, \quad (4)$$

$$\partial \mathbf{E} = -\frac{e}{\varepsilon}(n - N_D^{1+} - 2N_D^{2+} + N_A + M), \quad (5)$$

where N_D, M_T, and N_A are the total concentrations of the donors, shallow traps, and acceptors, respectively; N_D^{1+}, N_D^{2+}, M, and n are the concentrations of the singly and doubly ionized donors, filled shallow traps, and electrons, respectively; S_D, S_1, S_T and γ_1, γ_2, γ_T are the photoionization cross sections and recombination constants for the neutral (subscript D), singly (1) and doubly (2) ionized donors, and shallow traps (T); β is the

shallow-trap thermal excitation coefficient; μ is the electron mobility; k_B is the Boltzmann constant; T is the temperature; e is the elementary electric charge; and ε is the static dielectric constant of the crystal.

Consider the space-charge field produced in the interference of two, reference and signal, light beams with intensities I_R and I_S, respectively. The intensity distribution in the crystal can be written as

$$I = I_0[1 + m\cos(Kz)], \tag{6}$$

where $I_0 = I_R + I_S$ is the average intensity, $m = 2\sqrt{I_R I_S}/I_0$ is the modulation depth of the interference pattern, $|\mathbf{K}| = K = 2\pi/\Lambda$ is the magnitude of the grating vector, and Λ is the grating spatial period. The grating vector $\mathbf{K} = K\mathbf{z}_0$ and the externally applied field $\mathbf{E}_0 = E_0\mathbf{z}_0$ are assumed to be aligned with the z axis of the reference frame. In the low contrast approximation ($m \ll 1$) of the interference pattern forming the photorefractive grating, the coupled equations (1)–(5) can be linearized by expanding the unknown functions $N_D^{1+}(z, t)$, $N_D^{2+}(z, t)$, $M(z, t)$, $n(z, t)$, and $E(z, t)$ in a Fourier series. The equations describing the dynamics of the zeroth and first spatial Fourier components of the charge gratings in the crystal can be written as

$$\frac{dN_0^{2+}}{dt} = S_1 I_0 N_0^{1+} - \gamma_2 n_0 N_0^{2+}, \tag{7}$$

$$\frac{dM_0}{dt} = -(S_T I_0 + \beta)M_0 + \gamma_T n_0 (M_T - M_0), \tag{8}$$

$$N_0^{1+} = N_A + M_0 - 2N_0^{2+}, \tag{9}$$

$$n_0 = \frac{S_D I_0 (N_D - N_0^{1+} - N_0^{2+}) + S_1 I_0 N_0^{1+} + (S_T I_0 + \beta)M_0}{\gamma_1 N_0^{1+} + \gamma_T (M_T - M_0) + \gamma_2 N_0^{2+}}, \tag{10}$$

$$\frac{dN_1^{1+}}{dt} = mI_0[S_D(N_D - N_0^{1+} - N_0^{2+}) - S_1 N_0^{1+}] - [(S_D + S_1)I_0 + \gamma_1 n_0]N_1^{1+} - (S_D I_0 - \gamma_2 n_0)N_1^{2+} - (\gamma_1 N_0^{1+} - \gamma_2 N_0^{2+})n_1, \tag{11}$$

$$\frac{dN_1^{2+}}{dt} = mI_0 S_1 N_0^{1+} + S_1 I_0 N_1^{1+} - \gamma_2 n_0 N_1^{2+} - \gamma_2 N_0^{2+} n_1, \tag{12}$$

$$\frac{dM_1}{dt} = -mI_0 S_T M_0 - [(S_T I_0 + \beta) + \gamma_T n_0]M_1 + \gamma_T (M_T - M_0)n_1, \tag{13}$$

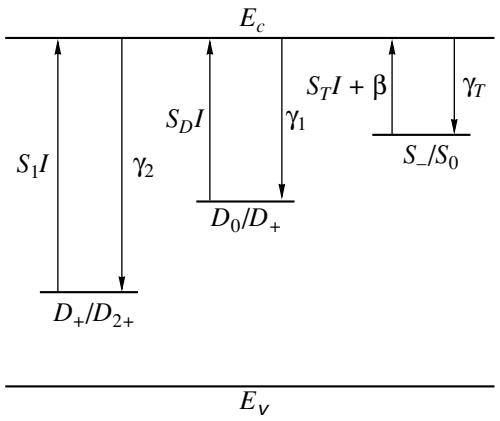

Fig. 1. Energy level diagram in the band gap of a crystal with deep donor centers that can reside in three charge states (D_0, D_+, D_{2+}) and with shallow traps (S_0 and S_-). The arrows identify possible transitions in the photoexcitation, thermal generation, and recombination of carriers.

$$n_1 = \left\{ mI_0[S_D(N_D - N_0^{1+} - N_0^{2+}) + S_1 N_0^{1+} + S_T M_0] - \left[(S_D - S_1)I_0 + \gamma_1 n_0 - \frac{1}{\tau_d}\right]N_1^{1+} - \left(S_D I_0 + \gamma_2 n_0 - 2\frac{1}{\tau_d}\right)N_1^{2+} + \left(S_T I_0 + \beta + \gamma_T n_0 - \frac{1}{\tau_d}\right)M_1 \right\} \times \{K^2 \mu k_B T/e - iK\mu E_0 + \gamma_1 N_0^{1+} + \gamma_2 N_0^{2+} + \gamma_T (M_T - M_0)\}^{-1}, \tag{14}$$

where $\tau_{di} = \varepsilon/\mu e n_0$ is the dielectric relaxation time. These equations were derived under the assumption of a low light intensity I_0 (conditions where the electron concentration n satisfies the inequalities $N \ll N_D$, $n \ll M$, and $N \ll N_A$) and in the adiabatic approximation, where $\partial n/\partial t = 0$. The coupled equations (7)–(10) for the zeroth Fourier components form a closed system, which does not contain amplitudes of the first spatial harmonics and of the applied external field. To determine the first Fourier components N_1^{1+}, N_1^{2+}, M_1, and n_1 from Eqs. (11)–(14), one has to find a solution to the above system. Our method of numerical analysis of these systems enabled us to vary the diffraction grating period Λ; the duration of the hologram writing, storage, and development processes; and the amplitude of the applied external dc electric field E_0. It also permitted us to turn the pump (I_R) and signal (I_S) light beams, their

The material parameters of photorefractive crystals with the double-donor centers and shallow traps used in the calculations

Material parameter	Parameter values for various shallow-trap concentrations		
	[8]	this work	
M_T, m^{-3}	10^{25}	10^{24}	10^{23}
M_D, m^{-3}	10^{25}	10^{25}	10^{25}
N_A, m^{-3}	10^{22}	2.5×10^{22}	4×10^{22}
S_D, m^2/J	4.9×10^{-6}	2×10^{-7}	1.5×10^{-7}
S_T, m^2/J	10^{-4}	32.5×10^{-4}	30.5×10^{-4}
S_1, m^2/J	2.5×10^{-6}	2×10^{-6}	3×10^{-6}
γ_1, m^3/s	3.5×10^{-17}	0.8×10^{-17}	0.8×10^{-17}
γ_T, m^3/s	2.6×10^{-17}	6×10^{-17}	2.2×10^{-15}
γ_2, m^3/s	4.9×10^{-18}	1.2×10^{-18}	5×10^{-19}
β, s^{-1}	5.5×10^{-5}	5.5×10^{-4}	5.5×10^{-4}

mutual coherence, and the external electric field E_0 on and off at arbitrary instants of time. Using Eq. (5) and the calculated amplitudes of the first charge-grating harmonics, one can derive the amplitude of the space-charge field in the crystal in the form

$$E_1(t) = -i\frac{e}{\varepsilon K} \times [N_1^{1+}(t) + 2N_1^{2+}(t) - M_1(t) - n_1(t)]. \quad (15)$$

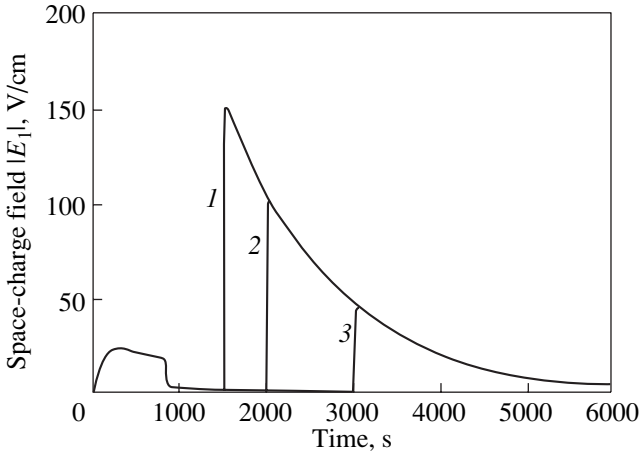

Fig. 2. Evolution of the space-charge field of a photorefractive grating with a period $\Lambda = 10$ μm after crystal illumination by a mutually coherent signal and pump beams with a total intensity $I_0 = 10$ mW/cm^2 at time $t_c = 0$, turn-on of mutual coherence at $t_i = 800$ s, and application of an external dc electric field $E_0 = 17.5$ kV/cm at time t_e equal to (*1*) 1500, (*2*) 2000, and (*3*) 3000 s.

3. RESULTS OF THE CALCULATIONS AND DISCUSSION

To calculate the relations describing the dynamics of the photorefractive response, one can use the values of material parameters presented in [8]. To determine these parameters, the theoretical relations characterizing the evolution of photoinduced absorption during sample illumination and relaxation of this absorption in the dark were fitted to the experimental data available for the $Bi_{12}TiO_{20}$ crystal. We also found other sets of parameter values, which fit the variation of the absorption coefficient with time under crystal illumination presented in [8] well. The material parameters used in our subsequent numerical calculations are listed in the table. The carrier mobility was assumed equal to $\mu = 2 \times 10^{-6}$ m^2/V s.

It was assumed that before illumination by the signal and pump beams at time $t = 0$, the crystal was in the dark. This corresponds to the initial conditions $N_0^{1+}(0) = N_A$, $N_0^{2+}(0) = 0$, and $M_0(0) = 0$, which were used by us in the numerical integration of the coupled equations (7)–(10). The charge gratings started to form after the mutual beam coherence was switched on at time $t_c \geq 0$.

Figures 2–5 display typical time dependences characterizing the dynamics of variation of the space-charge field of a photorefractive grating with a period $\Lambda = 10$ μm and contrast $m = 0.1$ produced under different conditions by beams with a total intensity $I_0 = 10$ mW/cm^2 in a crystal with the parameters taken from [8]. If the mutual beam coherence is switched on simultaneously with crystal illumination ($t_0 = t_c = 0$, Figs. 2–4 and curve *1* in Fig. 5), the space charge field formed by diffusion evolves nonmonotonically. In the case where the coherence is switched on later, e.g., at $t_c = 2000$ s (curve *2* in Fig. 5), the grating field grows faster in the initial stage. Then, the field continues to increase slowly, until the coherence is turned off at $t_i = 2800$ s. The nonmonotonic pattern of the field evolution can be accounted for by the fact that, in the first case, the charge gratings form in essentially nonstationary conditions. In the initial stage, the average concentrations of the centers N_0^{1+}, N_0^{2+}, and M_0 and of the electrons n_0 (Fig. 6) undergo strong changes, while for $t > 2000$ s, these concentrations practically reach a steady-state level. The faster growth of the grating amplitude in the second case is due to the higher electron concentration in the conduction band. Note that the nonstationary photoconductivity observed in our case in the initial stage of crystal illumination was indicated to be the reason for the nonmonotonic pattern of the space-charge field dynamics in [14, 15].

Two characteristic regions can be seen in the evolution of the space-charge field amplitude observed after the mutual beam coherence is turned off at time t_i (Figs. 2–5). In the first stage of the grating erasure, the

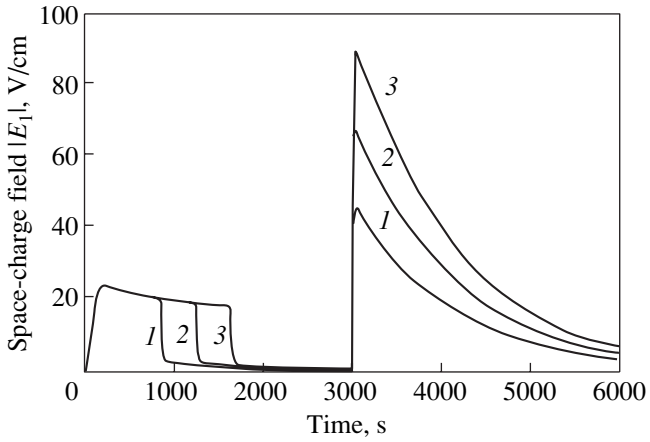

Fig. 3. Same as in Fig. 2 but for $t_c = 0$, $t_e = 3000$ s, and t_i equal to (*1*) 800, (*2*) 1200, and (*3*) 1600 s.

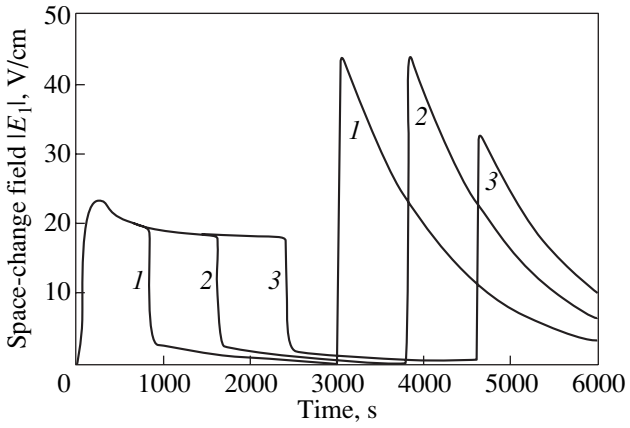

Fig. 4. Same as in Fig. 2 but for (*1*) $t_c = 0$, $t_i = 800$ s, $t_e = 3000$ s; (*2*) $t_c = 0$, $t_i = 1600$ s, $t_e = 3800$ s; and (*3*) $t_c = 0$, $t_i = 2400$ s, $t_e = 4600$ s.

amplitude drops rapidly in a time comparable to $\tau_d \approx 15$ s. Dielectric relaxation sharply reduces the difference between the charge-grating amplitudes $[N_1^{1+} + 2N_1^{2+} - M_1]$. However, as follows from Fig. 7, the amplitudes themselves decrease insignificantly in this time. Thereafter, one observes a slow space-charge field falloff, whose rate is governed by the charge-grating relaxation (cf. Figs. 2–5 with Fig. 7).

Applying a dc electric field to the crystal at a time $t_e > t_i$ does not change the dynamics of the charge-grating amplitude relaxation (Fig. 7). However, after application of an external field, the space-charge field amplitude increases with a time constant close to the dielectric relaxation time τ_d (Figs. 2–5). The grating field amplitude at the maximum depends on the time of mutual beam coherence turn-on and off (t_c and t_i, respectively), as well as on the time of the field application t_e. For the conditions of the formation, erasure, and development of the grating presented in Figs. 2–5, its amplitude always exceeds the initial value associated with the diffusion mechanism of charge separation. This behavior of the space charge field is connected with the fact that the relative positions of the charge gratings formed by the singly and doubly ionized donors and shallow traps are changed under the action of the applied voltage. This is evident from Fig. 8, which illustrates the dynamics of displacement of gratings with amplitudes N_1^{1+}, N_1^{2+}, and M_1 along the z coordinate relative to their initial positions after the application of an external field. The grating displacement is caused primarily by the conduction-current nonuniformity, which is due to the crystal conducting properties being spatially modulated. As follows from Eq. (14), the first spatial harmonic of the electron concentration in the conduction band is also nonzero in the absence of nonuniform illumination, i.e., for $m = 0$. In the model used here, the spatial nonuniformity of con-

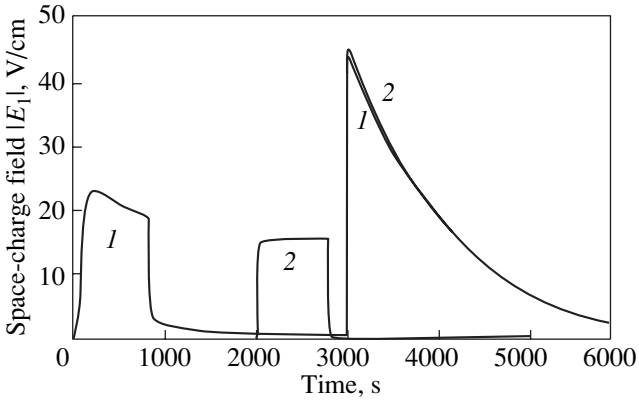

Fig. 5. Same as in Fig. 2 but for $t_e = 3000$ s and (*1*) $t_c = 0$, $t_i = 800$ s and (*2*) $t_c = 2000$ s, $t_i = 2800$ s.

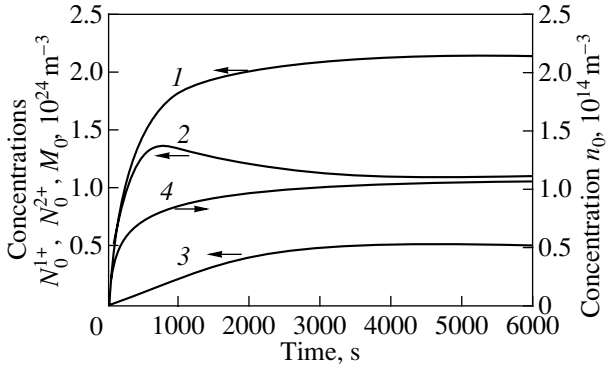

Fig. 6. Evolution of the average concentrations of (*1*) shallow traps $M_0(t)$, (*2*) singly ionized donors $N_0^{1+}(t)$, (*3*) doubly ionized donors $N_0^{2+}(t)$, and (*4*) electrons $n_0(t)$ following crystal illumination by a signal and pump beams with a total intensity $I_0 = 10$ mW/cm^2.

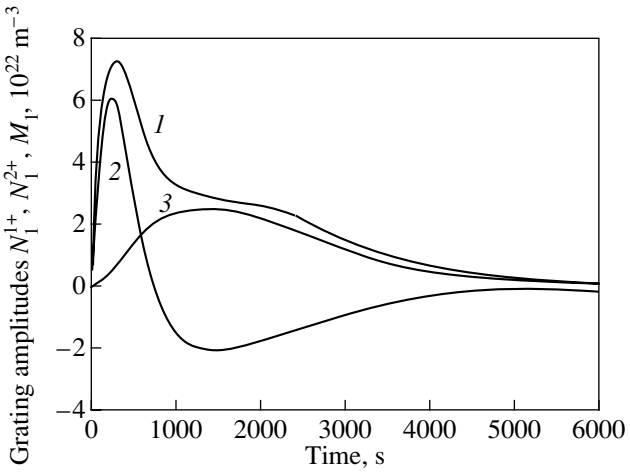

Fig. 7. Evolution of the amplitudes of the charge gratings forming on (*1*) shallow traps $M_1(t)$, (*2*) singly ionized donors $N_1^{1+}(t)$, and (*3*) doubly ionized donors $N_1^{2+}(t)$. The crystal is illuminated by a mutually coherent signal and pump beams with a total intensity $I_0 = 10$ mW/cm^2 at time $t_c = 0$ and with the mutual coherence turned off at time $t_i = 2400$ s. The application of a dc electric field $E_0 = 17.5$ kV/cm at time $t_e = 4600$ s does not affect the charge-grating amplitudes markedly.

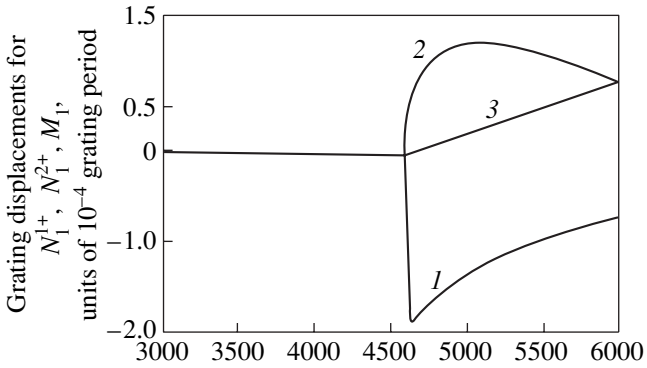

Fig. 8. Time dependences of the spatial displacements of charge gratings formed on (*1*) shallow traps and (*2*) singly and (*3*) doubly ionized donors along the *z* axis relative to their original positions. The dc electric field $E_0 = 17.5$ kV/cm is applied at time $t_e = 4600$ s. The conditions of grating formation are the same as for the dependences displayed in Fig. 7. The ordinates are in units of a 10^{-4} grating period.

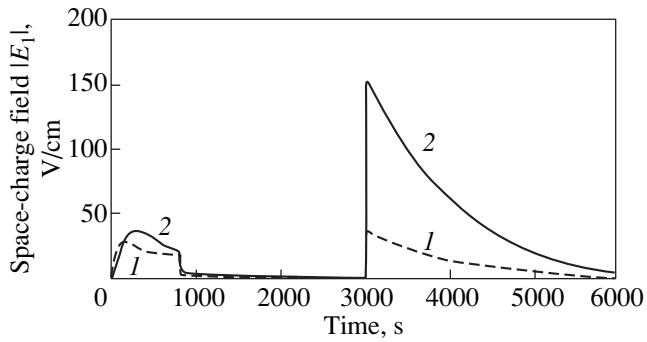

Fig. 9. Same as for curve *3* in Fig. 2 but for M_T equal to (*1*) 10^{24} and (*2*) 10^{23} m^{-3}.

ductivity is connected with the modulation of crystal parameters such as the absorption coefficient and the carrier lifetime. This interpretation of our results agrees qualitatively with the approach to describing the processes observed in a $Be_{12}SiO_{20}$ crystal in the course of photorefractive-grating recording in an alternating field, of grating storage with no field applied but with a reference beam present, and of development after field removal [15]. It is assumed here that optical information in a crystal can persist in the form of a photosensitivity grating, which has a long relaxation time even under uniform illumination. The photosensitivity grating is related in [15] to the spatial modulation of crystal parameters such as the light absorption coefficient, the carrier lifetime or mobility, and the quantum yield.

On reaching the maximum level, the space-charge field falls off with a time constant close to the charge-grating decay rate (cf. Figs. 2–5 with Fig. 7 for $t > t_e$). The results displayed in Figs. 2–8 relate to a crystal with a very high shallow-trap concentration ($M_T = 10^{25}$ m^{-3}). The evolution of the growth of photoinduced absorption observed experimentally in a $Bi_{12}TiO_{20}$ crystal after sample illumination [8] can also be described for lower concentrations, for instance, for $M_T = 10^{23}$ m^{-3}, but for substantially larger values of the photoionization cross section ($S_T = 3.05 \times 10^{-3}$ m^3/J) and of the two-particle recombination coefficient ($\gamma_T = 2.2 \times 10^{-15}$ m^3/s) than in the case of crystals with a high shallow-trap concentration (table). The time dependences of the space charge field in crystals with concentration $M_T = 10^{24}$ (curve *1*) and 10^{23} m^{-3} (curve *2*) are presented in Fig. 9 for the same conditions as curve *3* in Fig. 2. Note that the processes of recording, erasure, and development of gratings in crystals with the parameters used here do not differ. However, in a crystal with a lower shallow-trap concentration, relaxation under uniform illumination proceeds more slowly.

Thus, we have demonstrated the possibility of describing the processes of development of holographic gratings in photorefractive crystals in terms of the band transfer model, which includes singly and doubly ionized donors and shallow trap centers.

REFERENCES

1. M. P. Petrov, S. I. Stepanov, and A. V. Khomenko, *Photorefractive Crystals in Coherent Optics* (St. Petersburg, 1992).
2. N. V. Kukhtarev, V. B. Markov, S. G. Odulov, *et al.*, Ferroelectrics **22**, 949 (1979).
3. G. A. Brost, R. A. Motes, and J. R. Rotge, J. Opt. Soc. Am. B **5**, 1879 (1988).
4. K. Buse and E. Krätzig, Appl. Phys. B **B61**, 27 (1995).
5. K. Buse, S. Loheide, D. Sabbert, and E. Krätzig, J. Opt. Soc. Am. B **13**, 2644 (1996).
6. K. Buse, Appl. Phys. B **B64**, 391 (1997).

7. K. Buse, Appl. Phys. B **B64**, 273 (1997).
8. O. V. Kobozev, S. M. Shandarov, A. A. Kamshilin, and V. V. Prokofiev, J. Opt. A **1**, 442 (1999).
9. A. A. Kamshilin and M. P. Petrov, Fiz. Tverd. Tela (Leningrad) **23** (10), 3110 (1981) [Sov. Phys. Solid State **23**, 1811 (1981)].
10. S. G. Odoulov, K. V. Shcherbin, and A. N. Shumelyuk, J. Opt. Soc. Am. B **11**, 1780 (1994).
11. M. Miteva and L. Nicolova, Opt. Commun. **67**, 192 (1988).
12. S. Zhivkova and M. Miteva, Opt. Commun. **86**, 449 (1991).
13. M. P. Petrov, M. G. Shmelin, N. O. Shalaevskiĭ, *et al.*, Zh. Tekh. Fiz. **55** (6), 2247 (1985) [Sov. Phys. Tech. Phys. **30**, 1331 (1985)].
14. A. I. Grachev, Fiz. Tverd. Tela (St. Petersburg) **41** (6), 1012 (1999) [Phys. Solid State **41**, 922 (1999)].
15. A. I. Grachev, A. A. Kamshilin, O. V. Kobozev, and V. V. Prokofiev, in *Abstracts of the International Scientific Conference "Optics of Crystals" (OC-2000), Mozyr, 2000*, p. 17.

Translated by G. Skrebtsov

Physics of the Solid State, Vol. 44, No. 1, 2002, pp. 64–67. Translated from Fizika Tverdogo Tela, Vol. 44, No. 1, 2002, pp. 62–65.

SEMICONDUCTORS AND DIELECTRICS

Structural Characteristics and Physical Properties of Manganese-Intercalated Titanium Diselenide

V. G. Pleshchev, A. N. Titov, and N. V. Baranov

Ural State University, pr. Lenina 51, Yekaterinburg, 620083 Russia

e-mail: Valery.Pleshov@usu.ru

Received June 1, 2001

Abstract—This paper reports on an experimental study of the concentration and temperature dependences of the structural parameters, as well as of the electrical and magnetic properties, of manganese-intercalated titanium diselenide. The effect of manganese on the properties of the compounds produced by its intercalation between Se–Ti–Se layers is shown to differ strongly in character from those of other guest 3*d* elements. The results obtained are interpreted with account taken of the specific features of the manganese electronic structure.

1. INTRODUCTION

Intercalated compounds based on titanium dichalcogenides, which have a CdI_2-type hexagonal structure, attract a significant portion of the interest focused on the study of the physical properties of low-dimensional compounds. The host matrices used for intercalation, namely, TiS_2, $TiSe_2$, and $TiTe_2$, have a layered atomic structure and form weakly coupled TiX_2 structural blocks. The interlayer distance between these blocks increases as one goes from TiS_2 to $TiTe_2$ [1], thus changing the degree of two-dimensionality of the crystal lattice and the anisotropy of the physical properties. Depending on their concentration, the embedded (intercalated) atoms can form ordered chains and layers sandwiched between these blocks. Compounds with transition elements employed as intercalant atoms are of particular interest. Because 3*d* elements have magnetic moments, they can be used to obtain layered materials with magnetic layers on the atomic scale. Investigation of such compounds based on TiS_2 [2, 3] and $TiSe_2$ [4–8] has revealed a variety of magnetic states, including magnetically ordered states. Studies of the intercalation of titanium diselenide by various 3*d* elements have brought some general features in the variation of structural parameters and physical properties to light and revealed the part played by the electronic structure of these elements in the formation of the physical properties of such materials [5, 7]. In this series, the compounds containing manganese as an intercalant have thus far remained practically unstudied, even though manganese differs noticeably in its electronic characteristics from other iron-group elements.

This paper is the first integrated investigation into the structural characteristics and magnetic and electrical properties of titanium diselenide intercalated by manganese over a broad concentration range.

2. EXPERIMENT

Mn_xTiSe_2 samples ($0 < x \leq 0.5$) were synthesized in solid-phase reactions in evacuated quartz ampoules. The starting materials were titanium iodide, OSCh-grade selenium, and 99.98%-pure metallic manganese. $TiSe_2$ was prepared in the first stage to serve subsequently as the host material for intercalation, and, in the second stage, the samples of the Mn_xTiSe_2 system under study were fabricated. After each stage, the material was pressed into pellets and subjected to homogenization annealing at a temperature of 900°C for 150 h.

Phase analysis using x-ray diffraction and determination of the unit-cell parameters were carried out on a DRON-3M diffractometer. The samples were found to be single-phase and uniform in composition. The electrical conductivity was studied using the standard four-probe technique on sintered cylindrical samples 4 mm in diameter and 16 mm long. The thermopower was measured at a constant temperature gradient of 10 K over the sample length.

The magnetic susceptibility measurements were performed using the Faraday method on an automatically compensated magnetic balance.

The structural characteristics were studied at room temperature; the physical properties, in the 80- to 300-K interval.

3. EXPERIMENTAL RESULTS AND THEIR DISCUSSION

As follows from Fig. 1, which displays the concentration dependence of the unit-cell parameter *c* of the Mn_xTiSe_2 samples, the incorporation of manganese atoms between the Se–Ti–Se blocks loosens the crystal structure along the hexagonal axis. This is in marked contrast to the behavior of similar M_xTiSe_2 systems,

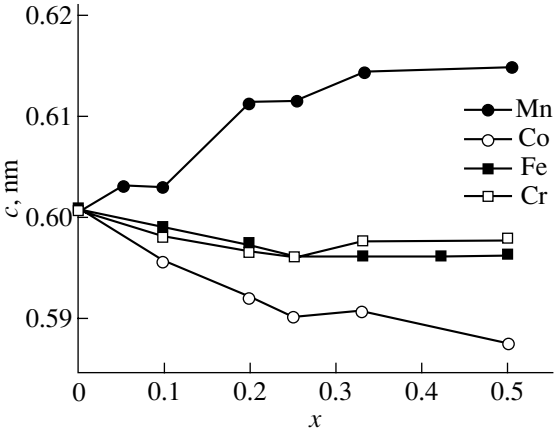

Fig. 1. Concentration dependences of the lattice parameter c of the M_xTiSe_2 compounds (M = Cr, Fe, Mn, Co).

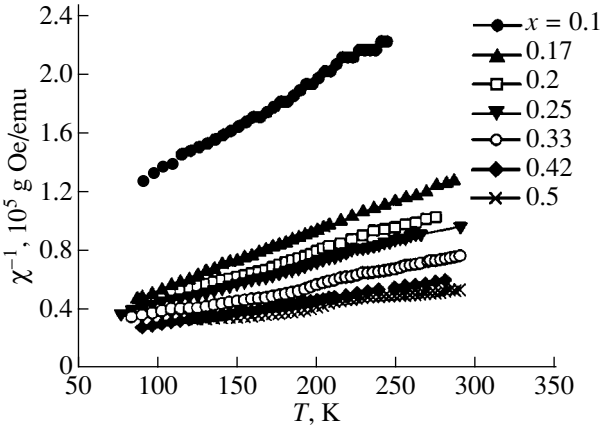

Fig. 2. Temperature dependences of the inverse magnetic susceptibility of Mn_xTiSe_2 compounds with different manganese contents.

where other 3*d* metals are used as guest intercalant atoms. Figure 1 also illustrates the $c(x)$ dependences obtained for M_xTiSe_2 (M = Cr, Co, Fe) reported in [7]. The lattice compression along the *c* axis resulting from the incorporation of these atoms into the van der Waals gap was assigned to the formation of covalent bonds between the *d* metal intercalants and the Se–Ti–Se layers. Moreover, the observed correlation between the effective magnetic moment of the intercalant atom and the parameter *c* suggest that the *d* electrons of the intercalant are involved in the formation of such bonds [7].

As for the parameter *a*, its variation with increasing intercalant concentration turned out to have the same character for all the studied systems intercalated by 3*d* elements. The parameter *a* was found to increase monotonically with *x*. This suggests that the difference in the behavior between the crystal structure of Mn_xTiSe_2 and similar systems with other 3*d* intercalants with increasing intercalant concentration is due to the specific features of the electronic structure of manganese; this structure possesses a half-filled 3*d* shell, and, hence, its 3*d* electron density distribution is spherically symmetric. The latter is apparently the main factor that, in our case, places a constraint on the possibility of formation of additional covalent bonds between the Se–Ti–Se layers and, as a result, does not bring about a decrease in their separation, unlike in other M_xTiSe_2 systems, where the intercalant atoms have a 3*d* electron shell filled to less (Cr) or more (Fe, Co) than one half.

As should be expected, intercalation of manganese atoms into the $TiSe_2$ host, possessing Pauli paramagnetism [9], gives rise to a considerable rise in the magnetic susceptibility of the compounds and affects its behavior with temperature. The temperature dependence of the inverse susceptibility χ^{-1} for the Mn_xTiSe_2 compounds is displayed in Fig. 2 and can be satisfactorily fitted by a relation for a Curie–Weiss paramagnet supplemented with a temperature-independent contribution:

$$\chi(T) = \chi_0 + \frac{C}{T - \Theta_p}. \quad (1)$$

Fitting the experimental $\chi(T)$ data to this relation yielded the values of χ_0. The effective magnetic moment of Mn in the Mn_xTiSe_2 compounds calculated using these values was found to be somewhat smaller than the value (Fig. 3) typical of the high-spin state of a free Mn^{2+} ion ($\mu_{eff} = 5.92\mu_B$). In our opinion, this point, as well as the nonmonotonic character of the concentration dependence of μ_{eff} in the compounds studied, suggests the possibility of partial *d*-electron delocalization, depending on the intercalant concentration. This delocalization may give rise to the formation of hybrid bound states, as was demonstrated in [10] for titanium disulfide-based materials used to interpret the results obtained in a study on intercalated titanium diselenides [5, 7]. Because no correlation is observed to exist

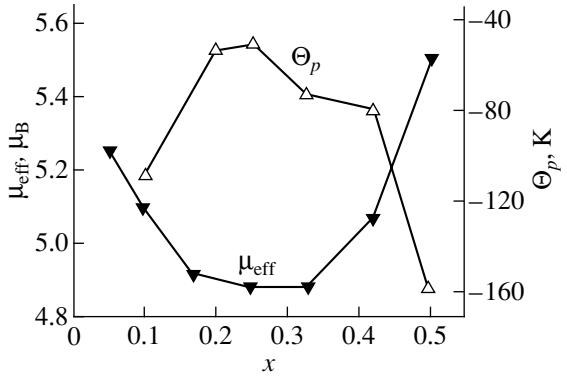

Fig. 3. Effective magnetic moment of manganese μ_{eff} and the paramagnetic Curie temperature Θ_p plotted vs. manganese content in Mn_xTiSe_2.

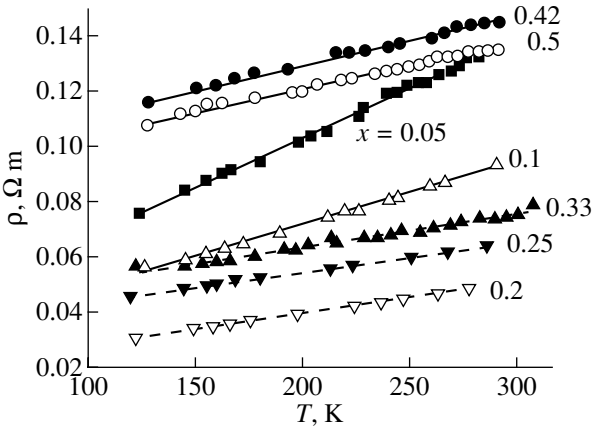

Fig. 4. Temperature dependences of the electrical resistivity of the Mn_xTiSe_2 compounds.

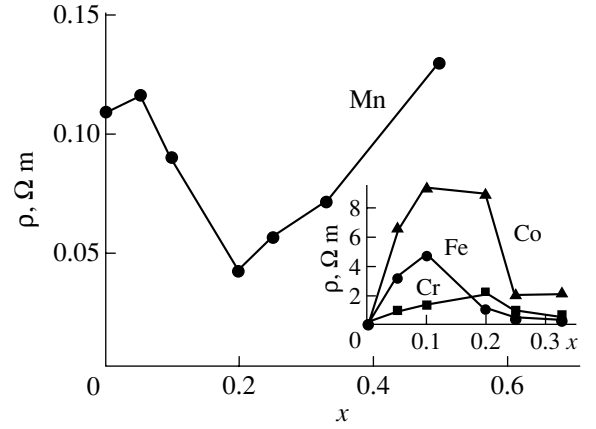

Fig. 5. Electrical resistivity of Mn_xTiSe_2 samples vs. manganese content at T = 273 K. Inset: concentration dependences of the electrical resistivity of titanium diselenide intercalated by chromium, iron, and cobalt.

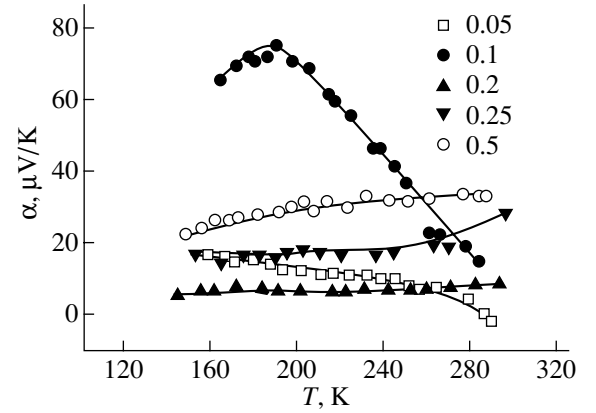

Fig. 6. Temperature dependences of the Seebeck coefficient for different manganese contents in Mn_xTiSe_2.

between the concentration dependences $\mu_{eff}(x)$ and $c(x)$, the decrease in μ_{eff} in the initial stages of manganese intercalation cannot be the result of formation of covalent bonds with the $TiSe_2$ layers, as is the case with intercalation by iron, chromium, and cobalt. As already mentioned, the reason for this apparently lies in the specific features of the manganese electronic structure.

For all the compounds studied, the paramagnetic Curie temperatures were found to be negative (Fig. 3), which indicates the coupling between the localized manganese magnetic moments to be a predominantly antiferromagnetic exchange. Taking into account the available data on M_xTiSe_2 compounds intercalated by other 3*d* metals [4, 7], it may be conjectured that the Mn_xTiSe_2 system also resides at low temperatures in a variety of magnetic states, from spin glass states at low manganese concentrations to magnetically ordered states in the high-concentration region. Note the nonmonotonic concentration dependence of the Curie paramagnetic temperature of the compounds under study. Assuming that the exchange coupling between the localized manganese moments is indirect and mediated by the conduction electrons, the nonmonotonic $\Theta_p(x)$ relation could reflect the changes in the electronic band structure of the compounds that occur with increasing intercalant concentration.

The temperature-independent contribution χ_0 in Eq. (1), which includes the diamagnetic contribution of filled electronic shells and the itinerant-electron paramagnetism (the Pauli paramagnetism), is positive and grows with increasing manganese content. Such a relation can be associated only with a change in the density of electronic states, because the diamagnetic component is determined primarily by the filled $TiSe_2$ electronic shells and cannot vary noticeably.

In addition to the investigation of the magnetic properties, we measured the electrical resistivity ρ and thermopower of all the samples prepared. In all compositions, the electrical resistivity was observed to grow linearly with increasing temperature (Fig. 4), a feature characteristic of the metallic state and suggesting a predominantly phonon carrier scattering mechanism. Figure 5 demonstrates the variation in the electrical resistivity of the Mn_xTiSe_2 compounds, measured at 273 K, with increasing manganese content. Also shown for comparison are similar dependences obtained for compounds intercalated by other *d* metals [7]. We readily see that the incorporation of iron, cobalt, and chromium results in a decrease in the electrical conductivity compared with that of $TiSe_2$ ($\sigma \cong 10\ \Omega^{-1}\ cm^{-1}$) [11], whereas intercalation with manganese produces the opposite effect. A characteristic feature here is the correlation between the concentration dependences of the electrical resistivity and of the effective magnetic moment, which suggests that the delocalized manganese *d* electrons take part in conduction. The temperature dependences of the Seebeck coefficient were also

found to be different for samples with different manganese concentrations (Fig. 6). For the $x = 0.05$ and 0.1 compositions, the Seebeck coefficient, while being positive at low temperatures, decreases in absolute value and even reverses its sign. For the other samples, the Seebeck coefficient retains its positive sign and grows with increasing temperature.

The above data as a whole demonstrate that at low manganese concentrations, for which its solution in titanium diselenide may be considered dilute, the simultaneous decrease in μ_{eff} and ρ can be due to the increasing contribution to charge transfer from the *s* and *d* electrons donated to the host lattice by the manganese atoms. In this stage of intercalation, the behavior of the transport characteristics can be described in terms of the rigid-band model. That both the holes and electrons are involved in the conduction is argued for by the above-mentioned character of the temperature dependence of the Seebeck coefficient at low manganese concentrations. For concentrations $x > 0.2$, ρ increases, despite the formally increasing carrier concentration; this may be a consequence of a qualitative change in the electron energy spectrum of the crystal, which brings about noticeable *d*-electron localization in a narrow impurity band. This conclusion is independently buttressed by the increase in the effective magnetic moments and the behavior of the Seebeck coefficient in this manganese concentration region, as well as by the growth in χ_0, which signals an increase in the density of states at the Fermi level.

4. CONCLUSIONS

Thus, our studies show that the specific features in the electronic structure of manganese atoms, which are characterized by spherical symmetry of the 3*d*-electron density distributions, zero orbital magnetic moment, and no spin–orbit coupling, play a major role in the formation of the physical properties of this class of quasi-two-dimensional materials. The intercalation of titanium diselenide with manganese substantially changes the behavior of the structural characteristics and physical properties of the host compared with the effect produced by other 3*d* elements. One may also draw the conclusion that the incorporation of various 3*d* elements brings about both a decrease (in the case of Co, Cr, Fe) and an increase (for Mn) in the degree of two-dimensionality of the crystal lattice.

ACKNOWLEDGMENTS

This study was supported by the US Civilian Research and Development Foundation, grant no. REC-005.

REFERENCES

1. T. Hibma, *Intercalation Chemistry* (Academic, London, 1982), p. 285.
2. M. Inoue, H. P. Hughes, and A. D. Yoffe, Adv. Phys. **38**, 565 (1989).
3. M. Koyano, M. Suezava, H. Watanabe, and M. Inoue, J. Phys. Soc. Jpn. **63**, 1114 (1994).
4. G. Calvarin, J. Calvarin, M. Buhannic, *et al.*, Rev. Phys. Appl. **22** (10), 1131 (1987).
5. Yu. Tazuke and T. Takeyarma, J. Phys. Soc. Jpn. **66** (3), 827 (1997).
6. V. G. Pleshchev, A. N. Titov, and A. V. Kuranov, Fiz. Tverd. Tela (St. Petersburg) **39** (9), 1618 (1997) [Phys. Solid State **39**, 1442 (1997)].
7. A. V. Kuranov, V. G. Pleshchev, A. N. Titov, *et al.*, Fiz. Tverd. Tela (St. Petersburg) **42** (11), 2029 (2000) [Phys. Solid State **42**, 2089 (2000)].
8. V. G. Pleshov, N. V. Baranov, A. N. Titov, *et al.*, in *Abstracts of the Euro-Asian Symposium "Trends in Magnetism," Yekaterinburg, Russia, 2001*, p. 362.
9. P. Klipshtein and R. Friend, J. Phys. C **17**, 2713 (1984).
10. T. Yamasaki, N. Suzuki, and K. Motizuki, J. Phys. C **20**, 395 (1987).
11. J. A. Wilson, Phys. Status Solidi B **86** (11), 11 (1978).

Translated by G. Skrebtsov

Physics of the Solid State, Vol. 44, No. 1, 2002, pp. 68–74. Translated from Fizika Tverdogo Tela, Vol. 44, No. 1, 2002, pp. 66–71.

DEFECTS, DISLOCATIONS, AND PHYSICS OF STRENGTH

Surface Segregation of ZrC from a Carbide Solid Solution

S. V. Rempel and A. I. Gusev

Institute of Solid-State Chemistry, Ural Division, Russian Academy of Sciences, ul. Pervomaĭskaya 91, Yekaterinburg, 620219 Russia

e-mail: gusev@ihim.uran.ru

Received April 28, 2001

Abstract—The surface segregation of zirconium carbide from carbide solid solutions is investigated. The spontaneous surface segregation of ZrC grains from solid solutions in the pseudobinary ZrC–NbC system is revealed for the first time. It is demonstrated that the ZrC precipitation is associated with the decomposition of the carbide homogeneous solid solutions $Zr_{1-x}Nb_xC \equiv (ZrC)_{1-x}(NbC)_x$. The boundaries of the latent solid-phase decomposition region formed at $T < 1200$ K are determined for the solid solutions formed by ZrC_y and $NbC_{y'}$ carbides with different nonstoichiometry. The experimental and theoretical estimates obtained for the segregation energy of ZrC are equal to –50 and –31 kJ mol^{-1}, respectively. © *2002 MAIK "Nauka/Interperiodica".*

1. INTRODUCTION

This paper reports on the results of investigations into the surface segregation of zirconium carbide from $(ZrC)_{1-x}(NbC)_x$ solid solutions. This phenomenon was not observed earlier in carbide solid solutions.

According to the experimental results obtained in [1–3], zirconium and niobium carbides with a cubic structure form a continuous series of solid solutions in the Zr–Nb–C system at temperatures of 1973, 1773, and 1273 K. Unfortunately, experimental data on the phase equilibria in the Zr–Nb–C or ZrC_y–$NbC_{y'}$ system at temperatures below 1273 K are not available in the literature. However, the recent investigation [4] revealed that, at $T < 1300$ K, the disorder–order transformations occur in the carbon sublattice of nonstoichiometric carbides with the formation of different ordered phases. In addition to the ordering in the carbon sublattice, the formation of short-range order and transformations of the ordering or decomposition type can proceed in the metal sublattice of $M^{(I)}C_y$–$M^{(II)}C_{y'}$ carbide solid solutions [5]. In particular, theoretical estimates [6] indicate that, under equilibrium conditions, an extended region of a decomposition can be observed in the ZrC–NbC system at $T < 800$ K.

2. SAMPLE PREPARATION AND EXPERIMENTAL TECHNIQUE

For the purpose of revealing the solid-phase decomposition, we studied the $(ZrC)_{1-x}(NbC)_x$ solid solutions in the range $0.001 \le (1 - x) \le 0.05$. The solid solutions were synthesized by solid-phase vacuum sintering from NbC and ZrC carbides (at a maximum sintering temperature of 2500 K) or from Nb, Zr, and C (at a maximum sintering temperature of 2300 K). The content of the main elements and impurities in the initial compounds was determined using chemical and spectral analyses. The initial compounds contained the following impurities (wt %): 10^{-2}–10^{-3} Ti, 10^{-3} Hf, 2×10^{-3} Al, and 3×10^{-3} Si in metallic zirconium; 5×10^{-3} Fe, 4×10^{-3} Si, 2×10^{-3} Al, 3×10^{-4} Ni, <0.01 Ta, <0.01 N, and 0.05 O in metallic niobium; 0.28 S and less than 1% volatile impurities in carbon (carbon black); 10^{-3} V, 10^{-3} Ni, 10^{-4} Mg, 10^{-2} Fe, 10^{-3}–10^{-4} Zr, 10^{-2} Ti, 0.32 O, and 0.06 N in $NbC_{0.95}$ niobium carbide; and 10^{-3} Hf, 10^{-2} Ti, 10^{-3} Fe, 0.28 O, and 0.08 N in $ZrC_{0.96}$ zirconium carbide.

All the synthesized solid solutions have a single-phase composition and a cubic structure of the *B*1 type. The lattice parameter $a_{B1} = 0.44670 \pm 0.00002$ coincides, to within the limits of measurement error, with the lattice parameter of niobium carbide of a nearly stoichiometric composition [6]. Cylindrical samples (15 mm in diameter and 10–15 mm in height) of the solid solutions synthesized were annealed at a temperature of 2300 K under vacuum at a residual pressure of 10^{-3} Pa for 1 h. After annealing, the samples were cooled first rapidly (at a mean rate of 200 K min^{-1}) to 1300 K and then slowly to 600 K. The total time of cooling was 3 h. The x-ray diffraction patterns were recorded on a Siemens D-500 automated diffractometer in the Bragg–Brentano geometry. The recording was performed in the stepped scan mode with a 2θ step of 0.025° in the range $2\theta = 10°$–$158°$. The exposure time at each point was 12 s. The x-ray diffraction patterns taken from the surface regions of the $(ZrC)_{1-x}(NbC)_x$ $(1 - x \le 0.02)$ solid solutions prepared from niobium and zirconium carbides and subjected to annealing demonstrate that, apart from the lines assigned to the niobium-containing phase with the lattice parameter $a_{B1} = 0.44655$ nm, there appear intense lines attributed to another phase. The former phase predominantly con-

tains niobium carbide and is close in composition to the initial solid solution. The latter phase has a $B1$ cubic structure with the lattice parameter a_{B1} = 0.4698 nm, which is very close to the lattice parameter of the zirconium carbide $ZrC_{0.93–0.98}$ (0.4699 nm) [4]. Judging from the change in the lattice parameter of the niobium-containing phase after annealing and the lattice parameter of the new phase, the initial solid solution contains ~99 mol % NbC and ~1 mol % ZrC. As can be clearly seen in the cross sections of the annealed samples, a very dense layer 0.1–0.2 mm thick is formed on the free surface. This layer is brighter than the bulk of the sample. The x-ray diffraction patterns of the surface regions of the annealed samples, which were synthesized from Nb, Zr, and C, exhibit only the lines assigned to a phase with the parameter a_{B1} = 0.46986 nm, whereas the diffraction reflections from the main (niobium-containing) phase are absent (Fig. 1). Analysis revealed that the surface region contains traces (less than 1 mol %) of the $(ZrC)_{1-x}(NbC)_x$ solid solutions at a high ZrC content and a low NbC content. This is indicated by a nearly constant intensity against the background in a narrow range of angles to the right of the lines attributed to zirconium carbide (see the inset in Fig. 1). The lattice parameter of these solid solutions changes from 0.4698 to 0.4670 nm, which corresponds to variations in the niobium carbide content x in the range from 0.004 to 0.120.

The electron microscopic examination of the annealed samples of the $(ZrC)_{1-x}(NbC)_x$ solid solutions synthesized from niobium and zirconium carbides revealed the presence of well-faceted precipitates (covering as much as 50% of the surface area) of the second phase on the surface of the sample (Fig. 2). The size of precipitates falls in the range 3–10 μm (the size of particular grains is as large as 20 μm), and the size of the main-phase grains is approximately equal to 1 μm. For the most part, the precipitated particles have the form of trihedra or hexahedra, which is characteristic of the (111) section of cubic crystals. The observed morphology can be explained by the fact that the growth of cubic crystals predominantly occurs along the (111) planes with the highest reticular density. The microhardness H_V of the precipitated crystals is equal to 26.0 ± 1.5 GPa and considerably exceeds the microhardness of the bulk region of the sample: $H_V \approx$ 17–19 GPa. The surface of the annealed samples of the $(ZrC)_{1-x}(NbC)_x$ solid solutions prepared from Zr, Nb, and C is completely covered with grains of the precipitated phase and contains no traces of the main phase.

The chemical composition of the precipitated phase was determined using a JFXA-733 Superprob x-ray microanalyzer. A backscattered electron image of the surface was obtained. The scanning over the surface with recording of the characteristic radiation revealed that the sample matrix contains niobium, whereas the precipitated grains of the new phase contain zirconium and are almost free of niobium (Fig. 3). The semiquantitative elemental analysis was performed on an ÉMAL-2 laser energy–mass analyzer. Figure 4 displays the mass spectra of the surface regions of the annealed samples of the $(ZrC)_{1-x}(NbC)_x$ solid solutions synthesized from Zr, Nb, and C. For comparison, the mass spectra of the bulk regions of the same samples are also shown in this figure. The mass analysis of the bulk region of the samples (i.e., the main phase) confirmed that this phase contains niobium, carbon, and a small amount of zirconium. At the same time, zirconium and carbon are the basic components of the compound evaporated from the surface completely covered with grains of the precipitated phase. The niobium content on the surface is no more than 0.5 at. %. Similar mass spectra were observed for individual grains of the phase precipitated on the surface of the annealed solid solutions, which were synthesized from niobium and zirconium carbides.

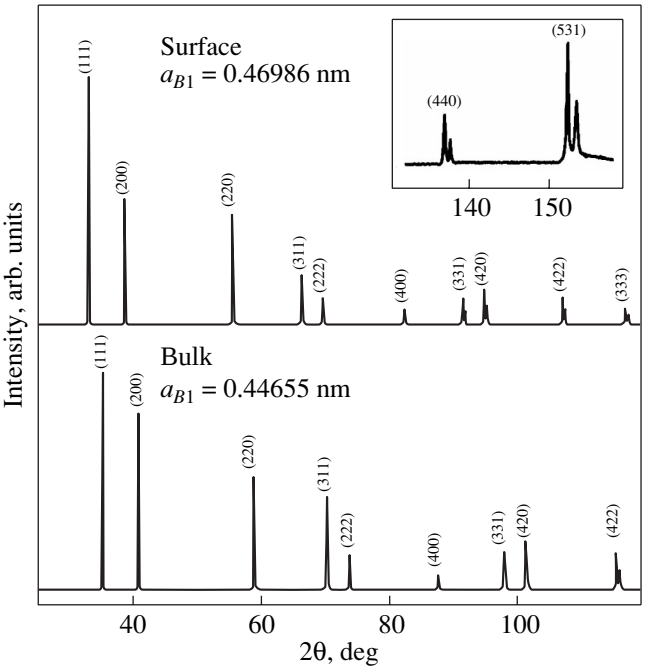

Fig. 1. X-ray diffraction patterns of the bulk and surface regions of the annealed sample of the $(ZrC)_{0.02}(NbC)_{0.98}$ solid solution. The main niobium-containing phase (the initial solid solution with the cubic lattice parameter a_{B1} = 0.44655 nm) is identified in the bulk. The surface region contains the cubic phase with the lattice parameter a_{B1} = 0.46986 nm, which corresponds to zirconium carbide, and traces (less than 1 mol %) of the $(ZrC)_{1-x}(NbC)_x$ solid solutions at a high ZrC content and a low NbC content (x progressively increases from 0.004 to 0.120). This is indicated by a nearly constant intensity against the background in a narrow range of angles to the right of the lines attributed to zirconium carbide (see the inset).

The precipitation of the second phase (zirconium carbide grains) on the surface of the sample can be due to either the decomposition of solid solutions or their initial inhomogeneity. In order to exclude the inhomo-

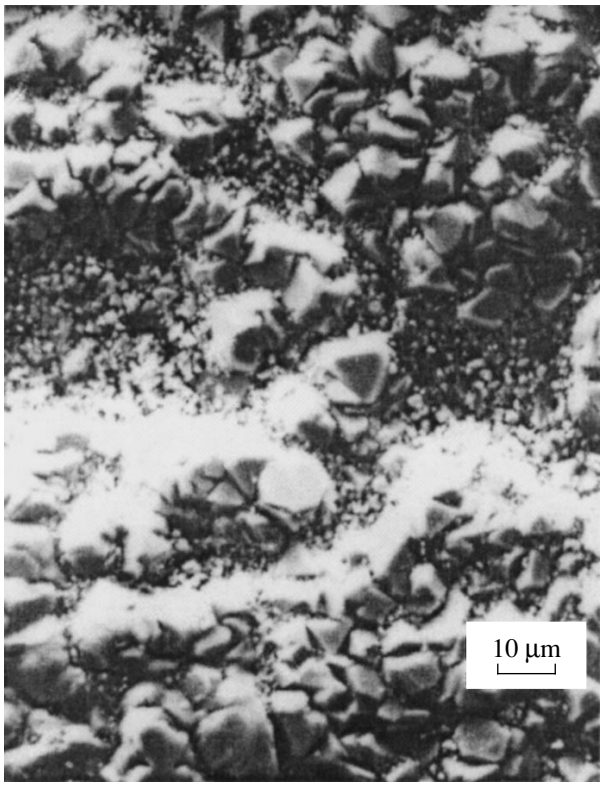

Fig. 2. Electron micrograph of the surface of the annealed sample of the $(ZrC)_{1-x}(NbC)_x$ $(1 - x \le 0.02)$ solid solution with precipitated zirconium carbide single crystals 3–10 μm in size (the size of particular zirconium carbide grains is as large as 20 μm).

geneity as a possible cause of the formation of the new phase, the degree of homogeneity of the initial solid solutions was determined using x-ray diffraction.

Recall that an inhomogeneity as a structural defect can be considered a fluctuation of the concentration c in the volume V of a solid solution [7]. In a crystal, the concentration fluctuations at points $\mathbf{r}$ are described by the continuous fluctuation distribution function $\delta c(\mathbf{r})$, which can be expanded into the Fourier series $\delta c(\mathbf{r}) = \sum_{\mathbf{k}} c_{\mathbf{k}} \exp(-i\mathbf{kr})$, where $c_{\mathbf{k}} = (1/V)\int \delta c(\mathbf{r}) \exp(i\mathbf{kr}) dV$ and $\mathbf{k}$ is the fluctuation wave vector. Since the fluctuations reduce only to the redistribution of the concentration among different crystal regions without changes in the concentration, we have $\int \delta c(\mathbf{r}) dV = 0$. The concentration fluctuations in the crystal give rise to inhomogeneities, which, in turn, bring about static atomic displacements and broadening of reflections in diffraction experiments. If the composition of the $Zr_{1-x_0}Nb_{x_0}C$ solid solution is specified as $x_0 \pm \Delta x$, the degree of inhomogeneity Δx for the solid solution can be determined from the broadening of the diffraction reflections.

Since the grain size in the initial solid solutions $Zr_{1-x}Nb_xC$ is approximately equal to 1 μm, the broadening of diffraction reflections due to small sizes (less than 100 nm) of the grains is absent. The structural investigation demonstrated that the Cu$K\alpha_{1,2}$ doublets

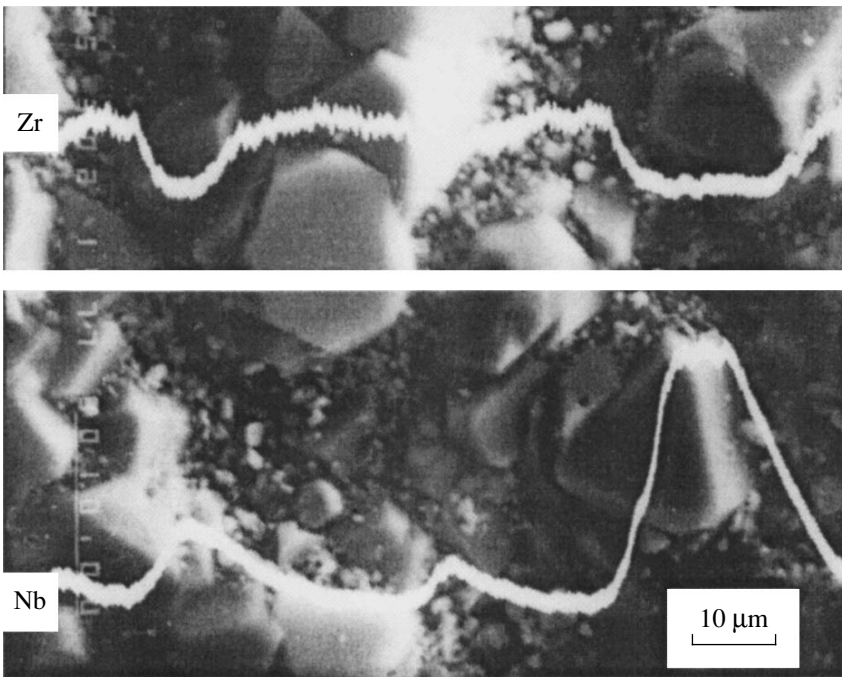

Fig. 3. Distributions of the intensity of Zr and Nb secondary electrons upon scanning of the surface of the annealed sample of the $(ZrC)_{0.02}(NbC)_{0.98}$ solid solution along the white horizontal line. Maxima in the distributions of Zr and Nb secondary electrons correspond to precipitated zirconium carbide grains and the main niobium-containing phase (the matrix solid solution at a NbC content close to 100%), respectively.

are split already beginning at the $(111)_{B1}$ line, i.e., at the smallest 2θ angles. This suggests a high homogeneity of the solid solutions. The inhomogeneity Δx, which was determined from the broadening of the $(222)\alpha_1$, $(400)\alpha_1$, and $(331)\alpha_1$ reflections, is approximately equal to 0.003. Consequently, the degree of homogeneity $(1 - \Delta x)$ for the initial solid solutions $Zr_{1-x}Nb_xC$ is estimated at ~0.997; i.e., it is close to unity. Therefore, the initial solid solutions are homogeneous and the formation of the second phase after annealing can be associated only with the decomposition of the solid solutions rather than with their inhomogeneity.

3. THE SOLID-PHASE DECOMPOSITION REGION

In order to determine the solid-phase decomposition region in the phase diagram of the ZrC_y–$NbC_{y'}$ pseudobinary system, we calculated the phase equilibria in this system at temperatures below 1300 K. The lower and upper boundaries of the continuous series of solid solutions are the $ZrC_{1.0}$–$NbC_{1.0}$ and $ZrC_{0.60}$–$NbC_{0.70}$ pseudobinary sections in the phase diagram, respectively. The calculations were performed in the framework of the subregular solution model [6]. Note that the thermodynamic calculations can prove the possibility of decomposing the solid solutions but do not allow one to judge the mechanism of this process.

According to our calculations, the ZrC_y and NbC_y carbides at any carbon content within the homogeneity regions of the cubic phase form a continuous series of solid solutions at $T > 1200$ K. However, at lower temperatures, there exists a latent solid-state decomposition region in this system (Fig. 5). As the carbon content decreases, the maximum decomposition temperature T_d^{max} of the solid solution increases from T_d^{max} = 843 K for the $ZrC_{1.0}$–$NbC_{1.0}$ section to T_d^{max} = 1210 K for the $ZrC_{0.60}$–$NbC_{0.70}$ section (at a $NbC_{0.70}$ content of 57.2 mol %). The observed asymmetry of the decomposition region and shift of its vertex in the ZrC_y–NbC_y pseudobinary sections toward the NbC_y niobium carbide (66.8 mol % NbC_y at y = 1.00 and 53.6 mol % NbC_y at y = 0.70) indicates that, at temperatures $T < T_d$, the solubility of ZrC_y in niobium carbide is several times less than that of NbC_y in zirconium carbide.

Thus, the results of x-ray microanalysis, laser mass analysis, electron microscopy, and x-ray diffraction unambiguously indicate that zirconium carbide grains precipitate on the surface of the carbide solid solution. The thermodynamic calculation confirmed that a latent low-temperature decomposition region of solid solutions exists in the ZrC_y–$NbC_{y'}$ system.

However, analysis showed that the bulk region of the samples has a single-phase composition. This enables us to make certain assumptions about the mechanism of decomposition of the $(ZrC)_{1-x}(NbC)_x$ solid solutions at a low zirconium carbide content.

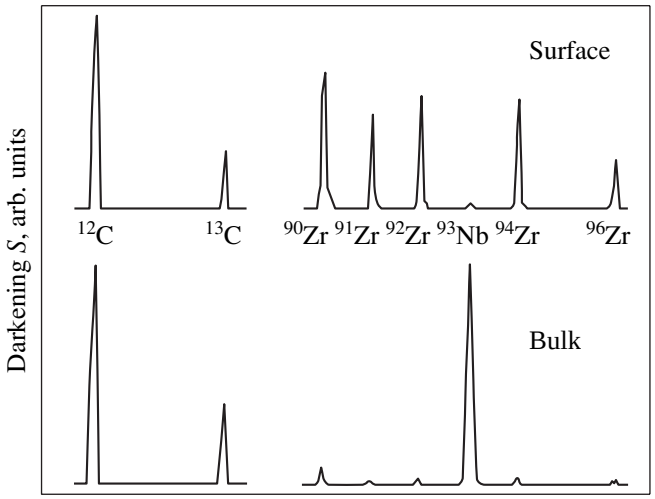

Fig. 4. Mass spectra of the precipitated surface phase and the bulk region (main phase) of the annealed samples of the $(ZrC)_{0.02}(NbC)_{0.98}$ solid solution. The optical density is determined from the relationship $S_i \sim \log c_i$, where c_i is the concentration of the ith element (isotope) in at. %.

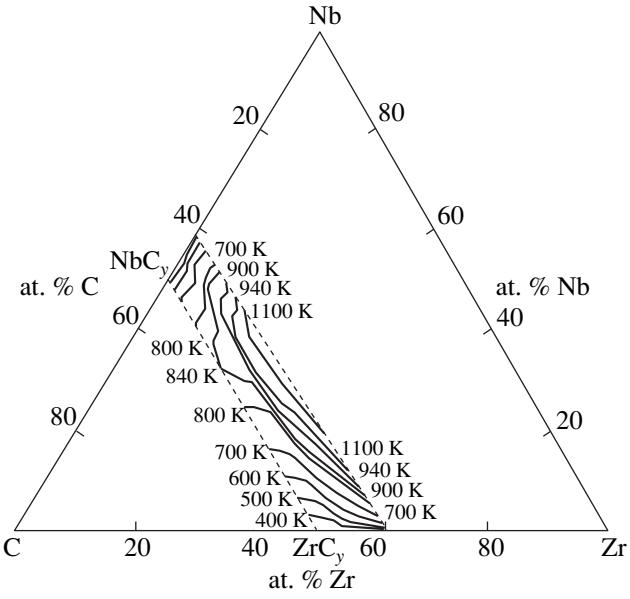

Fig. 5. Projections of the isothermal surface sections of the latent decomposition region of the $Zr_{1-x}Nb_xC_y$ solid solutions onto the ternary Zr–Nb–C phase diagram.

The diffusion decomposition of solid solutions can occur through two mechanisms [8]. The first mechanism is the spinodal decomposition proceeding throughout the bulk of the solution. In this case, nuclei of a new phase are not formed and the free energy of the

system decreases continuously (without a jump). The second mechanism is the fluctuation nucleation of phases and their subsequent growth. Spinodal decomposition is not realized most likely due to the low temperatures at which the diffusion mobility of atoms in the crystal is too small to provide spatial separation of the niobium and zirconium phases (i.e., the phases with a predominant content of niobium and zirconium carbides, respectively). In the case of fluctuation nucleation, the growth of new-phase grains in the surface layer is facilitated as a result of the favorable effect of the interfacial energy [8]. Therefore, the formation of the zirconium phase becomes possible even at a relatively low temperature.

At sufficiently high temperatures, the surface of the solid-phase system can be enriched in a component with a higher partial vapor pressure as the result of sublimation (evaporation). However, the precipitation of the ZrC carbide in the ZrC_y–$NbC_{y'}$ system is observed at low temperatures ($T < 1000$ K), whereas the evaporation of the ZrC and NbC carbides cannot be experimentally detected already at $T < 1800$ K, because the evaporation rate V_{ev} tends to zero. Furthermore, for the ZrC and NbC carbides at $T \le 2073$K, the partial pressure of zirconium is less than that of niobium [6].

The surface of the solid-phase system can be enriched in the light component owing to gravity separation (emersion). However, the isotopic composition of zirconium in the precipitated zirconium carbide coincides with the conventional isotopic composition of zirconium; i.e., no enrichment in the light isotopes ^{91}Zr and ^{92}Zr occurs and the content of the heaviest isotope ^{96}Zr does not decrease. This suggests that the gravity separation does not lead to the precipitation of ZrC on the free surface of the $(ZrC)_{1-x}(NbC)_x$ solid solutions.

4. SEGREGATION

The segregation of the second phase becomes possible when its content exceeds the solubility limit. The calculations of the immiscibility region boundaries (Fig. 5) demonstrated that the $(ZrC)_{1-x}(NbC)_x$ solid solutions with $(1 - x) \ge 0.01$ at $T < 700$ K are supersaturated with ZrC. Consequently, in the $(ZrC)_{1-x}(NbC)_x$ solid solutions containing ~1 mol % ZrC or more, the necessary condition of segregation is met at $T < 700$ K. The sufficient conditions of surface segregation depend on the segregation energy and diffusion.

In the regular solution approximation, the models of an equilibrium state of the solid solution surface [9–11] suggest that the bulk and surface phases coexist in a solid under equilibrium conditions. Let us consider an *A*–*B* system in which *A* is the solute and *B* is the solvent. As applied to our system ZrC_y–$NbC_{y'}$, the niobium carbide is the solvent and the zirconium carbide is the solute; i.e., $A \equiv ZrC_y$ and $B \equiv NbC_{y'}$. For the *A*–*B* system, the atomic concentration x_{A-s} of the solute in the surface phase can be represented in the form

$$x_{A-s} = x_{B-s}(x_{A-b}/x_{B-b})\exp(-\Delta H_{seg}/k_B T), \qquad (1)$$

where x_{A-b} and x_{B-b} are the atomic concentrations of the solute and solvent in the bulk phase, respectively; $x_{B-s} = 1 - x_{A-s}$; and ΔH_{seg} is the segregation energy of the solute *A*. The segregation energy is equal to the change in the energy of the system when an atom (molecule) of the *A* component of the bulk phase replaces an atom (molecule) of the *B* component in the surface phase. By substituting $x_{ZrC-s} \approx 0.985$, $x_{ZrC-b} \approx 0.013$, and $T = 700$ K into formula (1), we obtain the surface segregation energy of ZrC: $\Delta H_{seg,\ exp} \approx -50$ kJ mol^{-1}.

According to [10, 11], the segregation energy ΔH_{seg} includes the interfacial energy ΔH_{int}, the energy of pair interatomic interactions ΔH_{bin}, and the strain energy ΔH_{str}; i.e., $\Delta H_{seg} = \Delta H_{int} + \Delta H_{bin} + \Delta H_{str}$.

The interfacial energy characterizes the thermodynamic potential responsible for the transfer of components with a lower specific surface energy to the surface and can be represented as

$$\Delta H_{int} = (\gamma_A - \gamma_B)s_B N_A, \qquad (2)$$

where γ_A and γ_B are the specific (per unit area) interfacial energies of solute *A* and solvent *B*, respectively; $s_B = (M/\rho N_A)^{2/3}$ is the surface area per solvent molecule; *M* is the molecular mass of the solvent; and ρ is the density of the solvent. For the ZrC–NbC system at $T = 1773$ K, we have $\gamma_A \equiv \gamma_{ZrC} = 2.13$ J m^{-2} and $\gamma_B \equiv \gamma_{NbC} = 2.60$ J m^{-2} [12], and s_B is equal to 0.0793 nm^2 for $NbC_{1.0}$. Therefore, the ΔH_{int} energy in the ZrC–NbC system is approximately equal to –22.4 kJ mol^{-1}. This value of ΔH_{int} is merely a rough estimate, because the accuracy of determining the γ energies for carbides is rather low (±30–40%).

The contribution from the energy of pair interatomic interactions in the case of solid solutions can be represented as $\Delta H_{bin} = -G_s^e/(z x_{A-b} x_{B-b})$, where G_s^e is the excess energy of mixing of the solid solution and *z* is the coordination number of the lattice in which the substitutional solid solution is formed. For the solid phase, we can write the relationship $G_s^e = x_A x_B B_s$, where B_s is the interchange energy [6]. It follows that $\Delta H_{bin} = -B_s/z$. In the ZrC_y–$NbC_{y'}$ solid solutions with a face-centered cubic metal sublattice, the coordination number *z* is equal to 6 and the calculated interchange energy B_s in the solid phase is approximately –15 kJ mol^{-1}. As a result, we obtain the energy of pair interatomic interactions $\Delta H_{bin} \approx -2.5$ kJ mol^{-1}.

The solute strain energy ΔH_{str} is associated with the difference in sizes of the substituted atoms in the solid

solution and can be expressed in terms of elastic moduli in the form [11, 13]

$$\Delta H_{str} = -24\pi N_A \times [K_A G_B R_A R_B (R_A - R_B)^2]/(4G_B R_B + 3K_A R_A), \quad (3)$$

where K_A is the bulk modulus of the solute, G_B is the shear modulus of the solvent, and R_A and R_B are the effective atomic (ionic) radii of the substituted atoms of the solute and solvent, respectively. The effective ionic radii of Nb^{5+} and Zr^{4+} for the coordination number z = 6 are as follows: R_{Nb} = 0.064 nm and R_{Zr} = 0.072 nm; the elastic moduli for NbC and ZrC are $G_{NbC} = 2.20 \times 10^{11}$ Pa and $K_{ZrC} = 2.28 \times 10^{11}$ Pa. By substituting these values of R, G, and K into formula (3), we calculated the strain energy ΔH_{str} for the ZrC_y–$NbC_{y'}$ solid solutions: $\Delta H_{str} \approx -6.4$ kJ mol^{-1}.

The theoretical energy ΔH_{seg} of segregation of zirconium carbide from the ZrC_y–$NbC_{y'}$ solid solution with inclusion of the calculated contributions ΔH_{int}, ΔH_{bin}, and ΔH_{str} is approximately equal to –31.3 kJ mol^{-1}. This value substantially differs from the experimental estimate $\Delta H_{seg,\,exp} \approx -50$ kJ mol^{-1}. The underestimated (in magnitude) theoretical energy ΔH_{seg} can be explained by an approximate estimate of the interfacial energy ΔH_{int}, which makes the largest contribution to the segregation energy ΔH_{seg}.

Let us now consider the effect of the other factors on the segregation. In the case when the new phase precipitates on the surface and $\alpha \equiv x_{A-s}/x_{A-b} \gg 1$, the solution to the diffusion equation has the following form [14]:

$$x_{A-s}(t) = x_{A-s}\{1 - \exp(Dt/\alpha^2 d^2)\mathrm{erfc}[(Dt/\alpha^2 d^2)^{1/2}]\}, \quad (4)$$

where $x_{A-s}(t)$ and x_{A-s} are the contents of compound A on the surface at the instant t and after attaining the equilibrium, respectively; D is the diffusion coefficient of solute A at the temperature T; d is the thickness of the surface layer of the new phase; and α = const is the maximum coefficient of the surface enrichment with solute A at $t \longrightarrow \infty$. The function

$$\mathrm{erfc}(x) = 1 - \mathrm{erf}(x) = \frac{2}{\sqrt{\pi}}\int_x^\infty \exp(-x^2)dx$$

is the complementary probability integral: $\mathrm{erfc}(x) \longrightarrow 0$ at $x \longrightarrow \infty$.

The evaporation from the free surface at the rate $V_{ev} = Edx_{A-b}(t)/(\alpha^2 d)$ leads to a decrease in the segregant concentration $x_{A-s}(t)$, which, in this case, is determined by the relationship [14]

$$x_{A-s}(t) = \frac{x_{A-s}}{E+1}\{\exp(-EDt/\alpha^2 d^2) - \exp(Dt/\alpha^2 d^2) \times \mathrm{erfc}[(Dt/\alpha^2 d^2)^{1/2}] - (E\pi)^{1/2} \times \exp(-EDt/\alpha^2 d^2)[1 - \exp(EDt/\alpha^2 d^2)^{1/2}] \times \mathrm{erfc}[-(EDt/\alpha^2 d^2)^{1/2}]\}. \quad (5)$$

At $E \longrightarrow 0$ (i.e., in the absence of evaporation), relationship (5) reduces to formula (4). With due regard for expression (1), formula (4) takes the form

$$x_{A-s}(t) = x_{B-s}(x_{A-b}/x_{B-b})\exp(-\Delta H_{seg}/k_B T) \times \{1 - \exp(Dt/\alpha^2 d^2)\mathrm{erfc}[(Dt/\alpha^2 d^2)^{1/2}]\}. \quad (6)$$

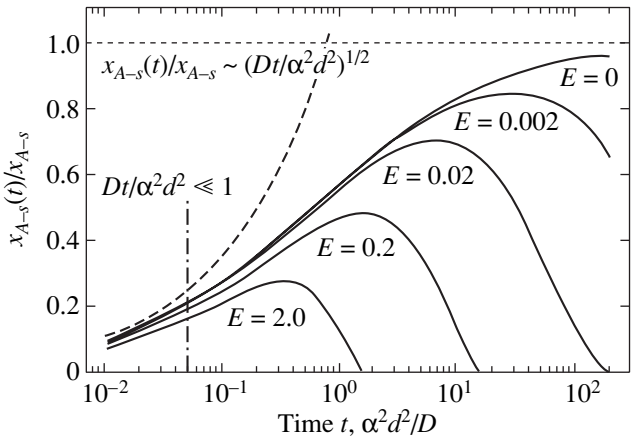

Fig. 6. Calculated dependences of the relative surface content $x_{A-s}(t)/x_{A-s}$ of the segregant on the time t and on the evaporation rate according to formula (5). The evaporation rate is proportional to the dimensionless parameter E, and the time is expressed in conventional units of $\alpha^2 d^2/D$. The equilibrium content of the segregant is determined from the formula $x_{A-s} = x_{B-s}(x_{A-b}/x_{B-b})\exp(-\Delta H_{seg}/k_B T)$ and depends only on the solid solution composition and temperature. In the absence of evaporation (E = 0) and at $t \longrightarrow \infty$, the ratio $x_{A-s}(t)/x_{A-s}$ asymptotically tends to unity. The dashed line shows the time dependence of $x_{A-s}(t)/x_{A-s}$ calculated by formula (7), which is applicable in the range of short times at $Dt/\alpha^2 d^2 \ll 1$.

Figure 6 shows the dependences of the relative surface content $x_{A-s}(t)/x_{A-s}$ of the segregant on the time t, which is expressed in conventional units of $\alpha^2 d^2/D$. At $t \longrightarrow \infty$ and E = 0 (in the absence of evaporation), the segregant content asymptotically tends to the equilibrium content $x_{A-s} = x_{B-s}(x_{A-b}/x_{B-b})\exp(-\Delta H_{seg}/k_B T)$. The evaporation brings about a decrease in the surface concentration of the segregant. However, the evaporation rate V_{ev} of zirconium carbide at $T < 1600$ K tends to zero [6]. Therefore, the time dependence of the ZrC segrega-

tion on the surface of the $(ZrC)_{1-x}(NbC)_x$ solid solutions can be described by function (6).

If $Dt/\alpha^2d^2 \ll 1$, we can write the relationship

$$\exp(Dt/\alpha^2d^2)\mathrm{erfc}[(Dt/\alpha^2d^2)^{1/2}] = 1 - (2/\pi^{1/2})(Dt/\alpha^2d^2)^{1/2}.$$

Hence, expression (5) at $E = 0$ takes a simpler form,

$$x_{A-s}(t) = x_{A-s}(2/\pi^{1/2})(Dt/\alpha^2d^2)^{1/2}. \quad (7)$$

As can be seen from Fig. 6, formula (7) adequately describes the dependence of $x_{A-s}(t)/x_{A-s}$ on t only in the range $0 < t < 0.05\alpha^2d^2/D$.

The equilibrium content x_{A-s} of the segregant in the surface region depends only on the solid solution composition and the segregation energy. According to the estimates made from formula (6), in the $(ZrC)_{0.01}(NbC)_{0.99}$ solid solution at temperatures of 700–500 K and the segregation energy $\Delta H_{seg} = -31.3$ kJ mol^{-1}, the equilibrium (at $t \longrightarrow \infty$) concentration x_{ZrC-s} of zirconium carbide in the surface phase lies in the range from ~0.80 to ~0.98. This is in good agreement with the experimental value, which is no less than 0.97.

ACKNOWLEDGMENTS

This work was supported by the Russian Foundation for Basic Research, project no. 01-03-96510.

REFERENCES

1. P. Stecher, F. Benesovsky, A. Neckel, and H. Nowotny, Monatsch. Chem. **95** (6), 1630 (1964).
2. T. F. Fedorov, N. M. Popova, and Yu. I. Gladyshevskiĭ, Izv. Akad. Nauk SSSR, Met., No. 3, 158 (1965) [Russ. Metall., No. 3, 72 (1965)].
3. T. F. Fedorov and Yu. I. Gladyshevskiĭ, Poroshk. Metall., No. 1, 37 (1965) [Sov. Powder Metall. Met. Ceram., No. 1, 27 (1965)].
4. A. I. Gusev, Usp. Fiz. Nauk **170** (1), 3 (2000) [Phys. Usp. **43**, 1 (2000)].
5. A. I. Gusev and A. A. Rempel, *Structural Phase Transitions in Nonstoichiometric Compounds* (Nauka, Moscow, 1988).
6. A. I. Gusev, *Physical Chemistry of Nonstoichiometric Refractory Compounds* (Nauka, Moscow, 1991).
7. A. A. Rempel and A. I. Gusev, Fiz. Tverd. Tela (St. Petersburg) **42** (7), 1243 (2000) [Phys. Solid State **42**, 1280 (2000)].
8. V. V. Slezov and V. V. Sagalovich, Usp. Fiz. Nauk **151** (1), 67 (1987) [Sov. Phys. Usp. **30**, 23 (1987)].
9. R. Defay, I. Prigogine, A. Bellemans, and D. H. Everett, *Surface Tension and Adsorption* (Wiley, New York, 1966), p. 158.
10. P. Wynblatt and R. C. Ku, Surf. Sci. **65** (2), 511 (1977).
11. R. C. McCune and P. Wynblatt, J. Am. Ceram. Soc. **66** (2), 111 (1983).
12. R. Warren, J. Mater. Sci. **15** (10), 2489 (1980).
13. J. Friedel, Adv. Phys. **3** (12), 446 (1954).
14. C. Lea and M. P. Seah, Philos. Mag. **35** (1), 213 (1977).

Translated by O. Borovik-Romanova

Physics of the Solid State, Vol. 44, No. 1, 2002, pp. 75–81. Translated from Fizika Tverdogo Tela, Vol. 44, No. 1, 2002, pp. 72–77.

DEFECTS, DISLOCATIONS, AND PHYSICS OF STRENGTH

Dynamic Recovery and Stress Relaxation Kinetics in Crystals at Low and High Homologous Temperatures

S. V. Lubenets

Verkin Institute for Low Temperature Physics and Engineering, National Academy of Sciences of Ukraine, Kharkov, 61103, Ukraine

e-mail: lubenets@ilt.kharkov.ua

Received May 15, 2001

Abstract—Experiments on stress relaxation revealed that, in NaCl crystals with a surface layer damaged by grinding, plastic flow at a low homologous temperature $T/T_M = 0.28$ (T_M is the melting point) and with total deformation far from stage III on the work-hardening curve occurs with a noticeable contribution from dynamic recovery processes, which is typical of higher temperatures. The kinetics of relaxation of effective and long-range stresses is studied. The results are compared with the behavior of unground NaCl crystals at the same temperature, as well as with the behavior of polycrystalline In–4.3 at. % Cd samples deformed at $T/T_M = 0.7$, for which the dynamic recovery is complete and is manifested not only in experiments on relaxation but also in the shape of the deformation curves. © *2002 MAIK "Nauka/Interperiodica".*

1. INTRODUCTION

Plastic flow of crystals is accompanied by a continuous change in the density of structural defects. Their accumulation is manifested in a form of work hardening that requires an increase in the mechanical stress for continuation of the deformation. However, work hardening in the general case is always accompanied by work softening (dynamic recovery) due to the instability of the defect structure and to a tendency of the system towards the minimum of the internal energy associated with defects. The resultant density of defects is determined by the balance between the number of defects formed as a result of deformation and the number of defects "quitting" through annihilation or the formation of lower energy structures during dynamic recovery.

Although work hardening and work softening are mainly caused by the interactions between dislocations, these two effects differ in essence, because the former is athermal, while the latter is thermally activated to a considerable extent [1]. The simultaneous realization of opposite tendencies (work hardening and softening) occurring in a dislocation subsystem determines the peculiarities of plastic flow of crystals. Their relative contributions to the deformation dynamics and kinetics depend on many factors, such as the strain, density of defects, and the rate and temperature of deformation. For large densities of dislocations and point defects, the probability of their annihilation and redistribution increases, while a decrease in the rate of deformation and an increase in its temperature activate these processes. Athermal work hardening in single crystals is typical of the first two stages on the stress–strain curve, while dynamic recovery effects are enhanced as the system approaches stage III and dominate in this stage of deformation [1, 2].

When dynamic recovery becomes significant, the plastic flow of crystals acquires a number of specific features: (1) the work-hardening rate becomes a function of temperature, (2) the Cottrell–Stokes law and the Arrhenius equation associated with it are violated, and (3) the stress dependence of the strain-rate sensitivity of the flow stress changes (the Haasen graph becomes nonlinear) [1]. These features can be observed most clearly at stage III, where the effective work-hardening rate $\theta \equiv d\sigma/d\varepsilon$ (σ and ε are the normal stress and strain) decreases with increasing strain; at high temperatures, θ assumes negative values almost immediately after the elastic segment of deformation [3].

However, a more reliable and simpler indicator of the initial stages of dynamic recovery is the relaxation curves of deforming stresses [4], even at a distance from stage III of deformation and at low temperatures (see below). In the present work, it is established that an analysis of the curves describing a transition to a steady flow upon repeated loading also provides a useful deformation concerning recovery processes. To our knowledge, this final stage of experiments on relaxation has been disregarded by researchers. The significance of the stress relaxation method in studying qualitative and quantitative features of plastic deformation under dynamic-recovery conditions is demonstrated in the present work for NaCl single crystals at $T = 300$ K. Room temperature can be regarded as a low temperature for NaCl (the homologous temperature of the experiment is $T/T_M = 0.28$), and the processes of deformation-defect annealing are strongly retarded. For the sake of comparison, some experiments were made on

1063-7834/02/4401-0075$22.00

polycrystals of an In–4.3 at. % Cd alloy (henceforth referred to as In–Cd), because the temperature T = 300 K is high in this case ($T/T_M = 0.7$) and the annealing of structural defects must be activated completely. The results obtained for pure In single crystals (which are not given here) are virtually the same as those obtained for an In–Cd alloy.

2. EXPERIMENTAL TECHNIQUE

The crystals of NaCl were grown from a raw material intended for optical single crystals. Samples $8 \times 8 \times 24$ mm in size were cut along the cleavage planes from a large block preliminarily annealed at a temperature of $(3/4)T_M$ and were not subjected to additional annealing (NaCl samples). For some samples, the lateral faces were ground using abrasive paper with an abrasive grain size of 200 μm (NaCl* samples).

Samples of the In–Cd alloy were prepared from an ingot by rolling, cutting, and forging to a size of $3 \times 3 \times 9$ mm [5]. After this mechanical treatment, the samples were annealed in air at temperature $(4/5)T_M$ for 8 h. The grain size was 1.5–2 mm.

The samples under investigation were deformed at room temperature through compression on a MRK-1 test machine (designed at the Institute for Low Temperature Physics and Engineering, National Academy of Sciences of Ukraine) with the rate of change in the sample length $\dot{y} = 1.52 \times 10^{-3}$ mm/s. The strain diagrams were recorded simultaneously on a KSP-4 recorder in the load–time coordinates $P(t)$ and on an N-307 recorder in the load–length change coordinates $P(y)$. The experiments on stress relaxation included the following three stages: (1) sample loading to a preset strain at a constant compression rate, (2) stress relaxation proper on a given time interval under arrested tierod of the testing machine, and (3) repeated loading at the previous rate. This procedure was repeated many times with increasing strain. The recorded curves were processed graphically in order to plot the normal stress vs. normal compressive-strain curves $\sigma(\varepsilon)$, the stress vs. time curves $\sigma(t)$, and the stress vs. stress-rate curves $\sigma(\dot{\sigma})$.

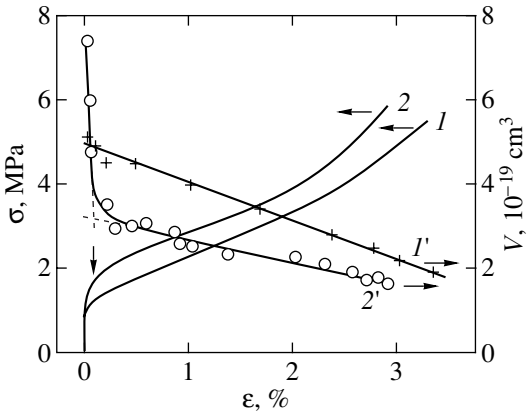

Fig. 1. Stress–strain diagrams (*1*, *2*) and the strain dependence of the activation volume V (*1*', *2*') for NaCl (*1*, *1*') and NaCl* (*2*, *2*') samples; σ and ε are normal stress and strain, respectively.

3. EXPERIMENTAL RESULTS AND DISCUSSION

3.1. Strain Diagrams

The stress–strain curves $\sigma(\varepsilon)$ for NaCl and NaCl* samples in the region $\varepsilon \lesssim 3\%$ are shown in Fig. 1. The qualitative difference between these curves is insignificant. The effective work-hardening rate virtually remains unchanged in the strain range from 0.3 to 2% (stage I): $\theta = d\sigma/d\varepsilon \simeq 100$ MPa or $d\tau/d\gamma \simeq \mu/600$ (τ and γ are the shear stress and shear strain, respectively, and μ is the shear modulus in the (110)[110] slip system). During the transition to stage II following the strain range 2–2.5%, the value of θ increases smoothly.

The main difference between the stress–strain curves were observed at the initial stage of plastic flow near the yield stress. A gradual transition from the elastic region to deformation at a constant work-hardening rate (from micro- to macroplastic flow) of an NaCl* sample complicates the procedure of determining the yield stress. According to [6–8], the value of yield stress can be determined to sufficient accuracy from the strain dependence of the activation volume $V(\varepsilon)$. Figure 1 shows such dependences. The activation volume was determined from the initial region of the stress-relaxation curves: $V = kT(\Delta \ln|\dot{\tau}|/\Delta\tau)$ ($\dot{\tau}$ is the rate of variation of the shear stress). It can be seen that the $V(\varepsilon)$ dependence for an NaCl* sample can be clearly split into two regions. The range of small deformations, in which the activation volume decreases sharply upon an increase in strain, corresponds to microplasticity associated with the movement of a small number of fast dislocations, while the second region of slow variation of the activation volume corresponds to macroplasticity associated with a large-scale multiplication of dislocations. The intersection of two segments of the $V(\varepsilon)$ dependence indicates the strain corresponding to the beginning of the macroscopic flow and, hence, the yield stress (vertical arrow in Fig. 1). The activation volume of an NaCl sample decreases linearly with increasing strain without any features in the transition region occupying a small strain range on the whole. The higher values of the activation volume of this sample as compared to that of the NaCl* sample are due to the lower density of dislocations [9, 10].

The yield stress for an NaCl* sample with a damaged surface layer, which creates serious obstacles for the emergence of dislocations from the bulk, is almost 70% higher than the yield stress for the NaCl sample. The origin of this effect was discussed in [9–11]. It will be proved later that slip under a constraint is manifested not only in a general increase in the yield stress and

deforming stress but also in a considerable change in the stress relaxation kinetics over the entire strain range.

The stress–strain curves $\sigma(\varepsilon)$ for In–Cd polycrystalline samples basically differ from those presented in Fig. 1. The effective work-hardening rate in the given case decreases with increasing strain, as expected for a plastic flow at a high homologous temperature. Dynamic-recovery processes are detected best of all in experiments on stress relaxation. The relaxation depth may reach 50% or more of the stress σ_{0R} corresponding to the onset of relaxation, and the process of stress relaxation proceeds very slowly. After repeated loading, the transition from elastic deformation to plastic flow begins at stresses σ_{ER}, which are much smaller than σ_{0R}, and the deformation continues with a smaller work-hardening rate as compared to the initial value.

It should be noted that two completely different types of deformation are realized in NaCl crystals and In–Cd alloys. In the former case, the deformation is a strictly crystallographic slip in the matrix, while in the latter case, one observes a superposition of slip and twinning in the matrix and a slip over grain boundaries, with macroscopic rotation of grains relative to one another and the formation of a relief at the sample faces. However, it turns out that stress relaxation in the NaCl* crystal and in the In–Cd alloy is qualitatively identical to the visual features of softening in the course of relaxation. The existence of a large number of channels for the relaxation of internal stresses in the latter case obviously affects the quantitative parameters of the dynamic-recovery process.

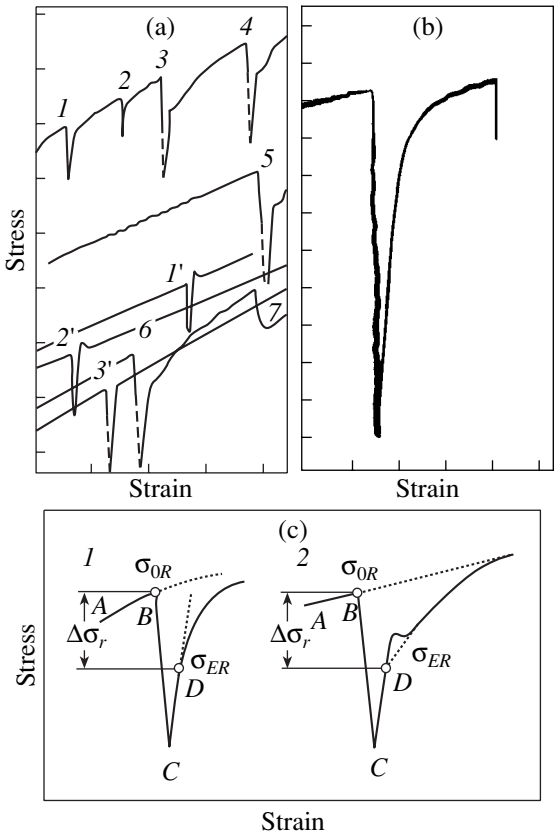

Fig. 2. Segments of stress–strain diagrams with stress relaxation recording: (a) NaCl samples [(*1*' ⟶ *3*') correspond to increasing strain] and NaCl* samples [(*1* ⟶ *6*) correspond to increasing strain for different durations of stress relaxation; (*7*) is the jump in the strain rate ensured by the machine, $\dot{y} \longrightarrow 0.1\dot{y}$]; (b) In–Cd polycrystal; and (c) the diagram explaining the change in work softening during stress relaxation in IN–Cd (*1*) and in NaCl* (*2*).

3.2. Stress Relaxation

Figure 2 shows segments of stress–strain diagrams for NaCl and NaCl* samples (Fig. 2a) and for an In–Cd alloy sample (Fig. 2b) with recording of the stress relaxation (curves *1–6* for NaCl*, *1*'–*3*' for NaCl) and with a change in the strain rate $\dot{y} \longrightarrow 0.1\dot{y}$ (curve *7* for NaCl*). NaCl crystals exhibit a sharp yield point after relaxation, which indicates that dynamic strain ageing (DSA) occurs in the course of stress relaxation. Although the crystals were grown from fairly pure raw materials, the impurity concentration was nevertheless sufficient for the pinning of mobile dislocations. The starting stress for these crystals, when subjected to repeated loading, increases, and the subsequent motion of dislocations occurs in the previous prerelaxation mode. DSA was studied by us in detail for crystals of In-based alloys [12–14].

A peculiar feature of the stress relaxation diagrams for a NaCl* sample is that a sharp yield point (curve *3* in Fig. 2a) or a yield plateau (*4*, *5* in Fig. 2a) after relaxation is observed for stresses lower than the stress σ_{0R} corresponding to the onset of relaxation. A transition to the plastic flow mode with a steady-state work-hardening rate under repeated loading takes a finite time, which (or the corresponding deformation) increases upon an increase in the total strain of the sample (cf. curves *3*, *6* in Fig. 2a). It should be noted that the strain-rate sensitivity of the deforming stress in NaCl and NaCl* samples remains positive over the entire $\sigma(\varepsilon)$ curve (*7* in Fig. 2a).

The above singularity of deformation after relaxation indicates that, in the course of stress relaxation in a NaCl* sample, two processes occur against the background of conventional work hardening; one of these processes (DSA) leads to hardening and to the emergence of a yield plateau or a sharp yield point, while the other process (dynamic recovery) leads to work softening. In spite of the fact that the experiments were made at a low homologous temperature $T/T_M = 0.28$, the conditions obviously facilitated the effective impurity–dislocation (strengthening) interaction (DSA) and the realization of the interaction between dislocations, resulting in a decrease in the internal stresses. Dynamic recovery in a NaCl* crystal is obviously realized owing to high dislocation densities (especially in the surface

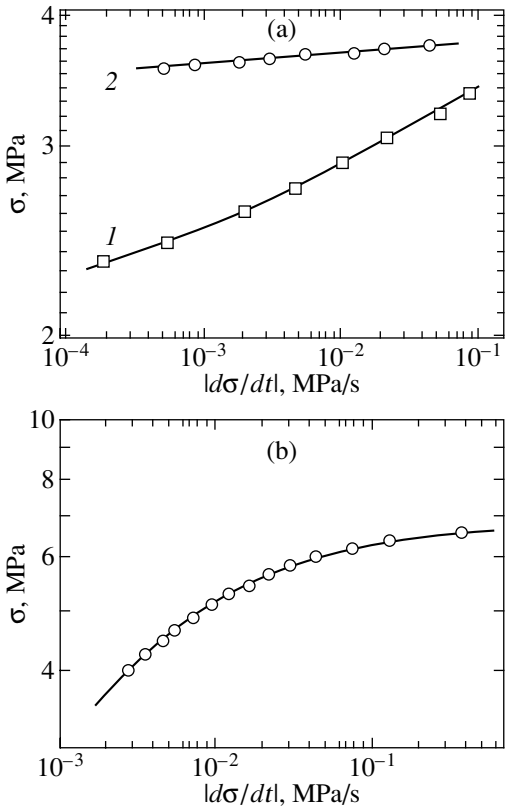

Fig. 3. Relaxation curves in the $\log\sigma$–$\log|d\sigma/dt|$ coordinates obtained (a) for NaCl (*1*) and NaCl* (*2*) samples under a strain $\varepsilon \simeq 2\%$ and (b) for an In–Cd sample for strain $\varepsilon = 3.3\%$.

layers) in the case of a small total strain of the sample [9, 10].

It is not surprising that in the course of stress relaxation, an In–Cd sample clearly displays softening (due to a high value of the homologous temperature $T/T_M = 0.7$). In this case, there are no conditions for the formation of stable impurity atmospheres at dislocations and dynamic-recovery processes, stimulated by thermal activation in the dislocation subsystem, occur in pure form. The dislocation structure that is formed under active deformation may be partially modified either due to a high temperature (as in the In–Cd alloy) or as a result of a high density of dislocations (as in the NaCl* sample).

Naturally, strengthening and softening must be manifested not only after relaxation but also in the kinetics of stress relaxation.

Stress relaxation curves for NaCl crystals with a strain $\varepsilon \simeq 2\%$ (stage I on the $\sigma(\varepsilon)$ curves in Fig. 1) and for In–Cd polycrystals with a strain $\varepsilon \simeq 3.3\%$ are presented in Fig. 3 in a $\log\sigma$–$\log|\dot\sigma|$ coordinates. These coordinates were not chosen accidentally. Hart [15, 16] (see also review [17]) used the results of experiments on stress relaxation carried out under special conditions to obtain information on $\sigma(t)$ with a high degree of accuracy even at strain rates of $\sim 10^{-9}$ s^{-1} and proposed a systematic description of the behavior of a number of deformed structurally stable metals and alloys in terms of directly measurable quantities σ and $\dot\sigma$. Later, similar experiments were made on alkali halide crystals [18]. It follows from those experiments and from the phenomenological theory developed by Hart [15, 16] that the relaxation curves in these coordinates have considerably different curvatures depending on the deformation temperature (or strain rate), which is due to different mechanisms controlling the plastic flow. In the low-temperature (LT) region, purely dislocation mechanisms (slip of dislocations) dominate, while in the high-temperature (HT) region, diffusion–dislocation processes come into play and start to dominate. The LT curves $\log\sigma$ vs. $\log\dot\varepsilon$ ($\dot\varepsilon \sim |\dot\sigma|$) are such that the derivative $\nu = (\partial\log\sigma/\partial\log\dot\varepsilon)|_{T,\varepsilon}$ (strain rate sensitivity) increases with stress (or with strain rate), while for HT curves, this derivative increases upon a decrease in σ (or $\dot\varepsilon$). In the intermediate region, where both mechanisms operate, the $\log\sigma$ vs. $\log\dot\varepsilon$ curves may have a varying curvature or be linear.

It should be emphasized that such a form of stress relaxation curves was predicted for conditions when plastic deformation and, accordingly, the change in the structure are negligibly small during relaxation. Nabarro [17] paid attention to the fact that the HT region is favorable to the dynamic-recovery process when the relaxation deformation cannot be treated as small and the structure as invariable. The involvement of dynamic recovery leads to an increase in the strain-rate sensitivity ν (especially at the slow-relaxation stage).

The above-mentioned features of the $\log\sigma$–$\log|d\sigma/dt|$ curves ($d\sigma/dt \equiv \dot\sigma$) can be seen in Fig. 3: the NaCl sample exhibits a behavior typical for the LT region (curve *1* in Fig. 3a), sample NaCl* exhibits an intermediate behavior (curve *2* in Fig. 3a), and the In–Cd sample displays a typical HT behavior (Fig. 3b); in the latter two cases, the observed behavior is due to a strong dynamic-recovery effect. It was found in [18] that NaCl (and NaF) crystals are characterized by an intermediate behavior when the $\log\sigma$ vs. $\log\dot\varepsilon$ relaxation curves are close to straight lines. In contrast to our experiments on the NaCl* sample, relaxation was not accompanied by a change in the dislocation structure; this is in complete accordance with the Hart model [15, 16].

Experiments on stress relaxation make it possible not only to detect dynamic recovery reliably during deformation but also to determine the characteristics of

strain hardening and softening. We use the stress relaxation equation obtained in [19],

$$\Delta\sigma = \frac{kT}{V}\frac{1}{1+\theta_h/M} \times \ln\left[\frac{\dot{\varepsilon}_0(1+\theta_h/M)}{r/M}\left(\exp\frac{rV}{kT}t-1\right)+1\right]. \quad (1)$$

Here, $\Delta\sigma = \sigma_{0R} - \sigma(t)$, where the first term is the stress corresponding to the onset of relaxation, the second is the current stress, and $\dot{\varepsilon}_0$ is the plastic strain rate at the beginning of relaxation at point *B* on the diagram in Fig. 2c. The value of $\dot{\varepsilon}_0$ was calculated from the active-deformation region, as well as from the $\log|\dot{\sigma}|$–σ relaxation curve. The value of *M* corresponds to the rigidity of the machine–sample system, which was determined experimentally from the slope of the curve in the elastic region of repeated sample loading after relaxation (segment *CD* in Fig. 2c). This equation was derived in [19] under the assumption that not only the effective stress σ^*, but also the long-range stress σ_μ, changes during relaxation under dynamic-recovery conditions and

$$d\sigma_\mu = \theta_h d\varepsilon - r dt. \quad (2)$$

Here, $\theta_h = (\partial\sigma_\mu/\partial\varepsilon)_T$ is the work-hardening rate and $r = -(\partial\sigma_\mu/\partial t)_{\varepsilon, T} > 0$ is the recovery rate. In this case, the effective work-hardening rate, determined from the stress–strain curve at a given temperature *T* and plastic strain rate $\dot{\varepsilon}_0$, is given by

$$\theta = \left.\frac{\partial\sigma}{\partial\varepsilon}\right|_{\varepsilon, T} = \theta_h - \frac{r}{\dot{\varepsilon}_0} \quad (3)$$

and, hence, $\theta < \theta_h$.

Expression (1) is transformed into the conventional relaxation equation for small *r*, when dynamic recovery does not play any significant role, and at small times. The latter means that, using the initial segment on the relaxation curve, one can determine the activation volume that characterizes the process of plastic deformation even under dynamic-recovery conditions. The subsequent kinetics of stress relaxation is determined to a considerable extent by the kinetics of work softening, i.e., by the change in the dislocation structure (and, accordingly, by the long-range internal stresses).

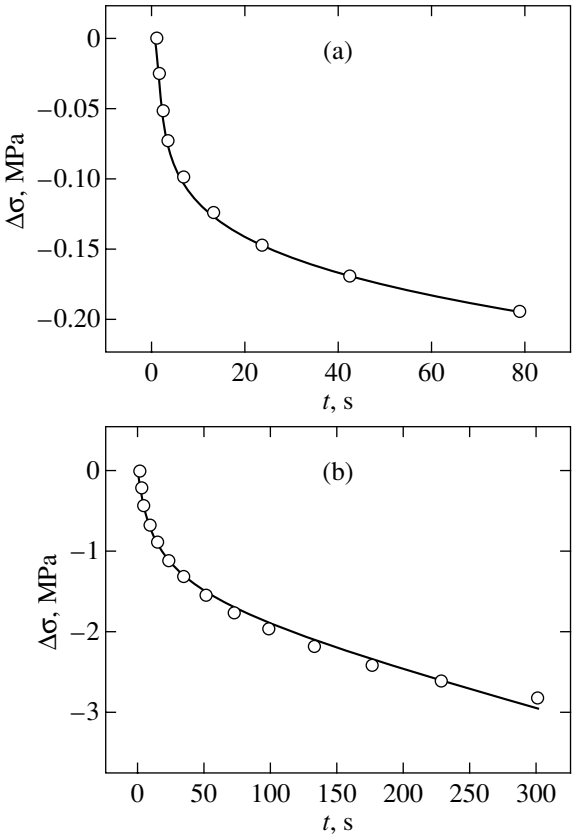

Fig. 4. Relaxation curves $\sigma(t)$ obtained (a) for NaCl* samples for a strain $\varepsilon \simeq 2\%$ and (b) for an In–Cd sample for strain $\varepsilon = 3.3\%$. Solid curves correspond to fitting of experimental points to Eq. (1). The fitting parameters are given in the table.

Figure 4 shows the stress relaxation curves for an NaCl* sample (Fig. 4a, the relaxation duration is 80 s) and for an In–Cd sample (Fig. 4b, the relaxation duration is 300 s). Solid curves correspond to Eq. (1). The values of the parameters involved in Eq. (1) are given in the table. In the case of tensile deformation of whiskers of pure iron at room temperature and a shear strain of 9.39%, it was found that $r = 3 \times 10^{-3}$ MPa/s [19], which is comparable with the value obtained for the In–Cd sample. In the NaCl* sample, dynamic recovery is much less significant because of the lower homologous temperature and the value of *r*, in this case, is approximately 20 times smaller than that for the In–Cd alloy.

Values of the parameters of Eq. (1) for an NaCl* crystal and an In–Cd sample

Sample	*M*, MPa	$\dot{\varepsilon}_0$, s^{-1}	*V*, cm^3	θ_h, MPa	*r*, MPa/s
NaCl*	1.6×10^3	5.6×10^{-5}	2.16×10^{-19}	102	2×10^{-4}
In–Cd	2.23×10^3	1.63×10^{-4}	1.1×10^{-20}	70	4.7×10^{-3}

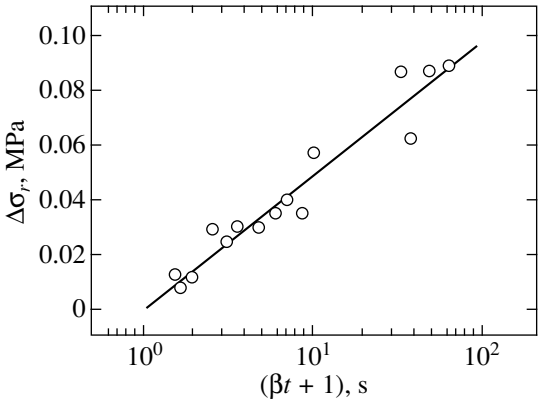

Fig. 5. Dependence of work hardening during stress relaxation on the duration of the relaxation in the NaCl* sample.

A comparison of the effective rates of work hardening determined from the stress–strain curve and calculated using Eq. (3) shows good agreement between them (100 and 98.4 MPa for NaCl* and 38 and 41 MPa for In–Cd).

It should be noted that the values of parameters obtained in this work that characterize work hardening and dynamic recovery can be treated as rough estimates, because while processing stress-relaxation curves, we disregarded the DSA, which was clearly manifested in the NaCl* sample. This effect was not detected explicitly in the In–Cd sample but apparently plays a certain role. Probably, the deviation of the fitting curve from the experimental points for long relaxation times ($t \gtrsim 300$ s) is associated with the strengthening effect of DSA: real relaxation proceeds slightly more rapidly than theoretical relaxation (Fig. 4b) due to the pinning (even if weak) of mobile dislocations by impurity atoms.

The dynamic-recovery kinetics (i.e., the change in internal long-range stresses) was studied by measuring the dependence of $\Delta\sigma_r(t) = \sigma_{0R} - \sigma_{ER}$ on the relaxation time, where σ_{0R} is the stress corresponding to the beginning of relaxation and σ_{ER} is the stress at which the stress–strain curve begins to deviate from the elastic dependence during repeated loading after stress relaxation. This is shown schematically in Fig. 2c. Figure 5 shows that the results of measurements of the work softening $\Delta\sigma_r(t)$ within stage I on the $\sigma(\varepsilon)$ curve for the NaCl* sample are correctly described by the function

$$\Delta\sigma_r(t) = \alpha\log(\beta t + 1). \quad (4)$$

A similar dependence was obtained for description of the dependence of the effective stress on the relaxation time [20, 21]. Parameters α and β in formula (4) were determined using the standard computer procedure of fitting the proposed function to the experimental data: $\alpha = 4.8 \times 10^{-2}$ MPa and $\beta = 0.1$ s^{-1}. Since dynamic recovery is controlled by thermally activated mechanisms, we can determine the activation volume as one of the parameters of these mechanisms according to the formula $V_r = kT/\alpha'$ ($\alpha' = 0.5 \times 2.3\alpha$, where the factor 0.5 transforms normal stresses to shear stresses). A calculation based on this formula gives a value of $V_r = 7.5 \times 10^{-20}$ cm^3, which is smaller by a factor of 2–4 than the values of V measured from the initial segments of the stress relaxation curves $(2.88–1.56) \times 10^{-19}$ cm^3. According to [20, 21], we have $\alpha\beta = M\dot{\varepsilon}_0$. Substituting the values of the parameters of formula (4) into the formula gives $\alpha\beta = 4.8 \times 10^{-3}$ MPa/s, while $M\dot{\varepsilon}_0 = 9 \times 10^{-2}$ MPa/s, in accordance with the data presented in the table. It is apparently premature to comment on the difference between the values of the quantities characterizing the kinetics of effective and long-range stresses, because more detailed studies are required in this field.

The kinetics of work softening in the In–Cd sample was studied less comprehensively, but the results and conclusions do not differ qualitatively from those for the NaCl* crystal.

ACKNOWLEDGMENTS

The author is sincerely grateful to V.D. Natsik and L.S. Fomenko for useful discussions and critical remarks.

This work was partially supported by the Swiss National Science Foundation, grant no. 7UKPJ048645.

REFERENCES

1. H. Mecking and U. F. Kocks, Acta Metall. **29**, 1865 (1981).
2. A. D. Rollet and U. F. Kocks, in *Solid State Phenomena. Dislocations 93*, Ed. by J. Rabier, A. George, Y. Bréchet, and K. Kubin (Scites Publ., Switzerland, 1994), Vols. 35–36, p. 1.
3. H. Heinrich, V. Abächerli, D. J. Wilkins, and G. Kostorz, in *Proceedings of the XIII MRS Symposium on High-Temperature Ordered Intermetallic Alloys*, Ed. by E. P. George, M. J. Mills, and M. Yamaguchi (Materials Research Society, Warrendale, 1999); Mater. Res. Soc. Symp. Proc. **552**, KK4.1 (1999).
4. M. Bartsch, U. Messerschmidt, B. Baufeld, *et al.*, in *Abstracts of the European Research Conference on Plasticity of Materials, 1998*, p. 58.
5. S. V. Lubenets, V. D. Natsik, P. P. Pal-Val, *et al.*, Mater. Sci. Eng. A **256**, 1 (1998).
6. B. Escaig, J. Phys. (Paris) **35**, 7 (1974).
7. J.-L. Farvaque, J. Crampon, J.-C. Dunkhan, and B. Escaig, Phys. Status Solidi **14**, 623 (1972).
8. P. Spätig, J. Bonneville, and J.-L. Martin, Mater. Sci. Eng. A **167**, 73 (1993).
9. S. V. Lubenets and L. S. Fomenko, Fiz. Tverd. Tela (Leningrad) **31** (10), 290 (1989) [Sov. Phys. Solid State **31**, 1822 (1989)].

10. S. V. Lubenets and L. S. Fomenko, Cryst. Res. Technol. **24**, K189 (1989).
11. S. V. Lubenets and L. S. Fomenko, Fiz. Tverd. Tela (Leningrad) **32**, 3144 (1990) [Sov. Phys. Solid State **32**, 1825 (1990)].
12. S. V. Lubenets and L. S. Fomenko, Fiz. Met. Metalloved. **61**, 971 (1986).
13. S. V. Lubenets and L. S. Fomenko, Fiz. Met. Metalloved. **62**, 377 (1986).
14. L. S. Fomenko, Fiz. Nizk. Temp. **26**, 1245 (2000) [Low Temp. Phys. **26**, 923 (2000)].
15. E. W. Hart, Acta Metall. **18**, 599 (1970).
16. E. W. Hart, Trans. ASME, Ser. H **98**, 193 (1976).
17. F. R. N. Nabarro, Acta Metall. **37**, 521 (1989).
18. I. Lerner, S.-W. Chiang, and D. L. Kohlstedt, Acta Metall. **27**, 1187 (1979).
19. P. Groh and R. Conte, Acta Metall. **19**, 895 (1971).
20. P. Feltham, J. Inst. Met. **89**, 210 (1961).
21. G. A. Sargent, Acta Metall. **13**, 663 (1965).

Translated by N. Wadhwa

Physics of the Solid State, Vol. 44, No. 1, 2002, pp. 8–15. Translated from Fizika Tverdogo Tela, Vol. 44, No. 1, 2002, pp. 9–16.

METALS AND SUPERCONDUCTORS

Electron and Electron–Phonon Effects in the Quasi-Two-Dimensional Molecular Conductor θ-$(BETS)_4HgBr_4(C_6H_5Cl)$: Optical Studies at 300–15 K

R. M. Vlasova*, N. V. Drichko*, B. V. Petrov*, V. N. Semkin*, E. I. Zhilyaeva, O. A. Bogdanova**, R. N. Lyubovskaya**, and A. Graja*****

**Ioffe Physicotechnical Institute, Russian Academy of Sciences, Politekhnicheskaya ul. 26, St. Petersburg, 194021 Russia*

e-mail: Rema.Vlasova@pop.ioffe.rssi.ru

***Institute of Problems in Chemical Physics, Russian Academy of Sciences, Chernogolovka, Moscow oblast, 142432 Russia*

****Institute of Molecular Physics, Polish Academy of Sciences, Poznan, 60-179 Poland*

Received May 11, 2001

Abstract—This paper reports on a study of the polarized reflectance and optical conductivity spectra of the quasi-two-dimensional molecular conductor θ-$(BETS)_4HgBr_4(C_6H_5Cl)$ within the 700–6500-cm^{-1} region at 300–15 K and within the 9000–40 000 cm^{-1} region at 300 K performed along two principal directions in the crystal plane parallel to the conducting layers of the BETS molecules. The IR spectra obtained at 300 K follow a close-to-Drude behavior, with strong broad features (1200–1400 cm^{-1}) due to electron–vibrational (vibronic) coupling (VC) superposed on the high Drude background. As the temperature is lowered in the range 180–80 K, in the spectra there appears a Lorentz term with $\omega_t = 2900$ cm^{-1}, as well as three additional VC-induced bands in the 800–1180-cm^{-1} region, which disappear as the temperature is decreased further. The results obtained indicate the existence of unstable structural distortions along the two principal directions in the crystal, which are accompanied by the formation of a commensurate charge-density wave. © *2002 MAIK "Nauka/Interperiodica".*

1. INTRODUCTION

Radical-ion salts based on BEDT–TSeF (abbreviated to BETS)[1] exhibit the highest stability of the metallic state over a broad temperature range among the organic quasi-two-dimensional conductors based on the BEDT–TTF molecule[2] and its derivatives (see, e.g., [1–4]). This molecule is obtained by substituting Se for the four S atoms in the central part of the BEDT–TTF molecule. The large radius of the Se atom compared to that of the S atom ensures a stronger two-dimensional molecular-orbital overlap in the conducting BETS layers in crystals, which brings about a larger width of the bands [3]. A series of BETS-based organic conductors with the general formula λ-$BETS_2MX_4$ (M = Ga, Fe; X = Cl, Br) was recently synthesized [5]; their properties vary within a broad range depending on the actual M and X elements and reveal a number of new phenomena, namely, superconductivity (λ-$BETS_2GaBr_xCl_{4-x}$), giant magnetoresistance, and ferromagnetic and antiferromagnetic phases (λ-$BETS_2FeCl_4$), which accounts for the additional interest in these compounds.

We report here on a study of polarized reflectance spectra of θ-$(BETS)_4HgBr_4(C_6H_5Cl)$ single crystals performed in the 700–6500-cm^{-1} spectral region at temperatures ranging from 300 to 15 K and in the 9000–40000-cm^{-1} region at 300 K in investigating, by optical means, the features of the metallic state and of vibronic coupling in this organic conductor, as well as the metal–semiconductor–metal transition, which was observed to occur in a study [3] of the electrical properties of this compound. We are aware of only one communication on the investigation of the optical properties of BETS-based salts [4], which presents optical spectra of κ-$(BETS)_2FeCl_2$, as well as IR and Raman spectra of molecular BETS ($BETS^0$) that will be used in the interpretation of our results.

2. EXPERIMENT

The θ-$(BETS)_4HgBr_4(C_6H_5Cl)$ crystals were prepared through electrochemical oxidation of the BETS molecule [1], a method described in considerable detail in [3], which also reports on the crystal structure, electronic structure calculations, and measurements of the electrical conductivity and Shubnikov–de Haas oscillations.

[1] BEDT–TSeF stands for bis(ethylenedithio)tetraselenefulvalene.

[2] BEDT–TTF stands for bis(ethylenedithio)tetrathiofulvalene.

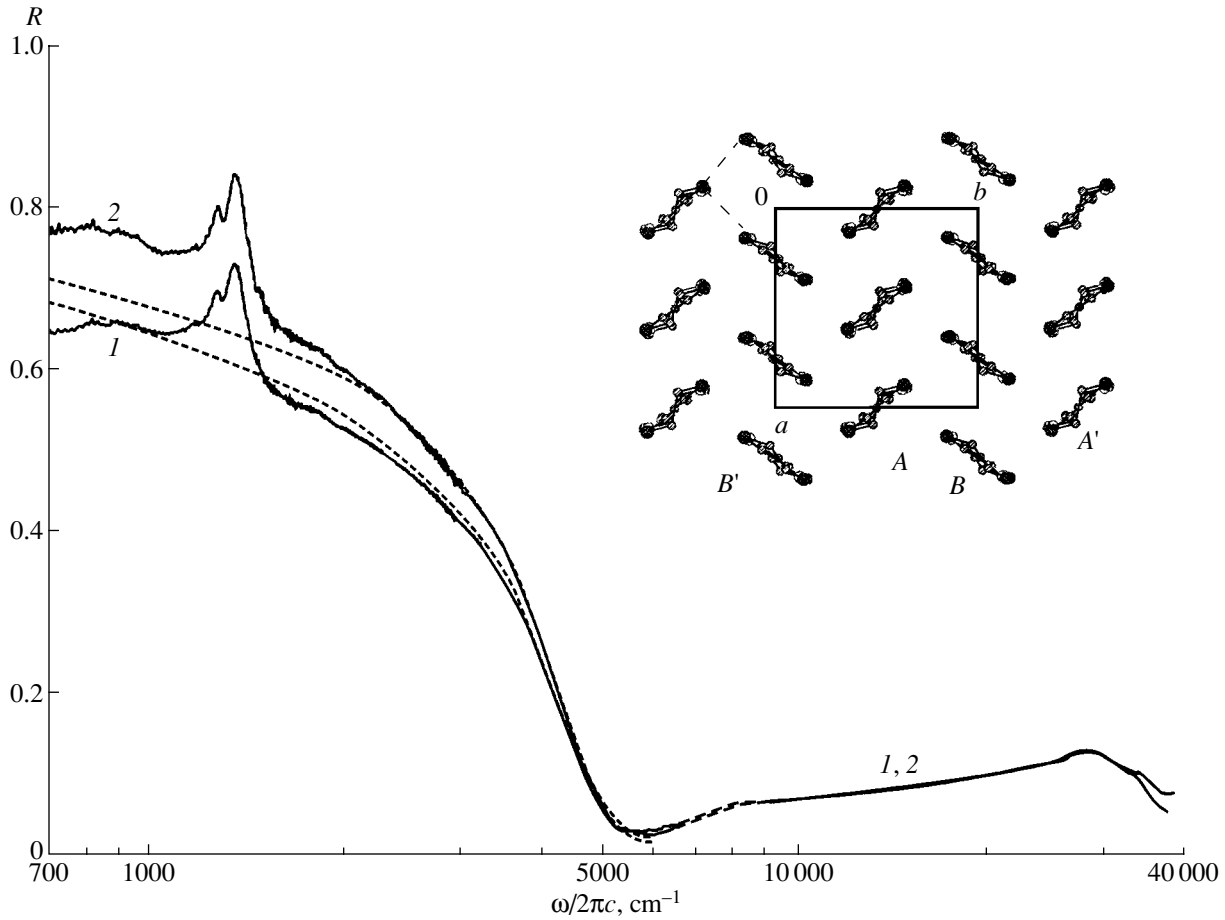

Fig. 1. Polarized reflectance spectra of the θ-$(BETS)_4HgBr_4(C_6H_5Cl)$ crystal obtained in the (*1*) **E** ∥ *a* and (*2*) **E** ∥ *b* polarizations; solid lines are experiment and dotted lines are calculations with the Drude model (the reflectance *R* in the region not covered in the experiment, 6500–9000 cm^{-1}, is indicated by dashed lines). Inset: projection of the crystal structure on the (001) plane.

The crystals are black, well-faceted, rectangular platelets ~1 × 1 × 0.3 mm in size with smooth specular surfaces. Their main crystallographic characteristics can be summarized as follows: tetragonal system, space group $I4_1/a$, $Z = 4$, $a = 9.9774(2)$ Å, $c = 75.73(1)$ Å, $V = 7190(4)$ $Å^3$, $M = 713.7$, and $d = 2.64$ g cm^{-3}. The radical cation bears a formal charge of +0.5 ($BETS^{0.5+}$). The crystals have a layered structure. The $BETS^{0.5+}$ radical-cation layers (shown in the inset to Fig. 1), parallel to the (001) plane, alternate with layers of the $(HgBr_4)^{2-}$ anions along the *c* axis. In the conducting layer along the [100] direction, the radical cations form two different alternating *A* and *B* stacks characteristic of the θ phase. The angle between the central planes of the molecules making up the *A* and *B* stacks is 73.9°. The distance between the central planes of the molecules in the *A* stack is 3.52(3) Å and that in stack *B* is 3.82(4) Å. The molecules in stack *B* are in a zigzag arrangement, with neighboring molecules displaced with respect to one another along the long axis of the BETS molecule by 2.5 Å. Note that while there are no shortened intermolecular distances along the stacks, the separations between the S and Se atoms of neighboring molecules in the layer sandwiched between the stacks are shorter (3.55–3.52 Å). The molecules of the solvent C_6H_5Cl make up a strongly disordered anion layer [1, 3].

According to the calculations made in the tight-binding approximation [3], the electronic band structure of the θ-$(BETS)_4HgBr_4(C_6H_5Cl)$ crystal consists of four partially overlapping bands derived from the top filled BETS molecular orbitals, of which the two lower ones are fully filled and the two upper bands are filled only partially, in accordance with the fact that there are four $BETS^{0.5+}$ cations in a unit cell. The Fermi surface calculated for the tetragonal unit cell consists of two hole and two electronic pockets.

Polarized reflectance spectra $R(\omega)$ were measured under normal light incidence on the largest area (001) crystal face in the 700–6500 cm^{-1} region at temperatures ranging from 300 to 15 K and only at room temperature in the 9000–40 000 cm^{-1} region. By varying the crystal orientation in the light wave field, we showed the anisotropy of the $R(\omega)$ spectra in the 700–6500 cm^{-1} region to be the largest in the polarizations

where the electric vector **E** is aligned with the *a* and *b* crystallographic axes.

The reflectance spectra in the 700–6500 cm^{-1} region were measured with a Perkin–Elmer 1725X Fourier spectrometer equipped with a microscope with a liquid-nitrogen-cooled MTC detector and a golden-wire polarizer. The light spot diameter was 100 μm; the resolution, 4 cm^{-1}. Measurements in the 300–15 K range were performed in an Oxford continuous-helium-flow cryostat. The spectra were obtained both under cooling and under heating of the crystal. We estimate the error of temperature measurement on the sample as 10 K. In the 9000–40 000 cm^{-1} region, the spectra were measured on a double-beam microspectroreflectometer developed by the State Optical Institute, with a beam diameter of 25 μm, a resolution of 60 cm^{-1}, and a Glan–Thompson prism used as a polarizer. The quality and position of the surface under study relative to the microscope axis and the crystal orientation in the light wave field were monitored by observing the pattern seen in the exit pupil of the instruments. The absolute value of the reflectance *R* was determined relative to an aluminum mirror and an SiC crystal.

The optical conductivity spectra $\sigma(\omega)$ were derived from the corresponding reflectance spectra using the Kramers–Kronig relations. The reflectance was extrapolated to the 0–700 cm^{-1} region with the use of the Hagen–Rubens relation, $R(\omega) = 1 - \alpha\omega^{1/2}$, and to frequencies above 40 000 cm^{-1} using the standard relation $R(\omega) \sim (\omega_0/\omega)^d$, where $d = 2$ for $\omega < 2 \times 10^6$ cm^{-1} and $d = 4$ for higher frequencies. The extrapolation to the region not covered in the measurements (6500–9000 cm^{-1}) was carried out using spectra of the $(BEDT–TTF)_4Hg_{2.89}Br_8$ superconductor investigated in this region in [6].

3. RESULTS

Figure 1 presents $R(\omega)$ room-temperature spectra of crystalline θ-$(BETS)_4HgBr_4(C_6H_5Cl)$ obtained from the (001) face in the **E** || *a* and **E** || *b* polarizations in the 700–40 000 cm^{-1} spectral region. We readily see that the IR spectra have a metallic, close-to-Drude character in both polarizations and, hence, are due to quasi-free carriers in the partially filled electronic and hole bands. The spectra exhibit a slight anisotropy. We believe that the largest reflectance corresponds to the **E** || *b* polarization, because, as already mentioned, the intermolecular distances in the direction parallel to *b* (i.e., perpendicular to the direction of the BETS molecule stacks) were found to be shorter [3]; in other words, the extent of molecular orbital overlap is the largest in this direction. Earlier, we observed a similar anisotropy in $R(\omega)$ in the $(BEDO–TTF)_5[CsHg(SCN)_4]_2$ conductor [7]. In the 3500–5000 cm^{-1} region, the spectra exhibit a plasma reflectance edge with a deep minimum at 5500 cm^{-1}. Measurements made in both polarizations in the region of intramolecular BETS vibrations [4] reveal strong and broad vibrational features against an intense Drude reflectance background that peak at 1353 and 1270 cm^{-1} for **E** || *a* and at 1350 and 1274 cm^{-1} for **E** || *b*.

In the high-frequency region, 9000–40 000 cm^{-1}, the spectra of both polarizations almost coincide; near 30 000 cm^{-1}, one can see a broad band, which we assigned to an intramolecular electronic transition in the BETS molecule polarized along its long axis.

The reflectance spectra in the 700–6500 cm^{-1} region were measured in the 300–15 K interval in steps of 20–15 K. To avoid superposition, Figs. 2 and 3 present only the $R(\omega)$ spectra observed at 300, 250, 200, 100, and 15 K obtained in the **E** || *a* and **E** || *b* polarizations, respectively. As seen from the **E** || *a* spectra in Fig. 2, as the temperature *T* decreases from 300 to 250 K, the reflectance due to quasi-free carriers increases slightly (by 5%), while the spectrum as a whole retains its Drude-like character. Decreasing *T* from 250 to 200 K virtually does not involve an increase in *R*, with the 250- and 200-K spectra nearly coinciding. As *T* is lowered further to 180 K, the spectra exhibit qualitative changes, which become most pronounced at 100 K; namely, *R* grows more rapidly in the 3000–4500 cm^{-1} interval to form a shoulder in the spectrum at 3500 cm^{-1}. The spectrum retains this shape down to 80 K. Below 80 K, these features in $R(\omega)$ disappear, so that within the 60–15-K interval, $R(\omega)$ again recovers its Drude pattern and the spectrum obtained at 15 K almost coincides with the 300-K spectrum [inset (a) to Figs. 2, 3, where the spectra measured at 300, 100, and 15 K are shown without translation along the *R* axis]. The temperature-induced changes in $R(\omega)$ are also observed in the **E** || *b* polarization (Fig. 3), although in a somewhat less pronounced form. The spectra obtained at 15 and 300 K also almost coincide.

The spectra measured in the 180–80 K interval reveal qualitative changes in the region of intramolecular vibrations (700–1600 cm^{-1}). As evident from Figs. 2 and 3, the $R(\omega)$ spectrum obtained at 100 K in the **E** || *a* polarization has new bands at 1180 and 1124 cm^{-1} and a weak band at 820 cm^{-1} which do not rise above the background at higher temperatures [in inset (b), the new bands are identified by arrows]. When observed in the **E** || *b* polarization, new bands appear at 1183 and 1122 cm^{-1} and a weak band appears at 960 cm^{-1}. The 1350 cm^{-1} band splits into a doublet that peaks at 1379 and 1350 cm^{-1}; in the **E** || *a* polarization, the corresponding feature does not split. This difference may be due to the BETS molecules being stacked differently along the *a* and *b* axes (inset to Fig. 1). All these new features in the $R(\omega)$ spectra observed in the 180–80 K interval disappear below 80 K.

The optical-conductivity spectra $\sigma(\omega)$ derived for the temperatures 300, 250, 200, 100, and 15 K are displayed in Figs. 4a and 4b for **E** || *a* and **E** || *b*, respectively. At 300 K, in full accordance with the metallic

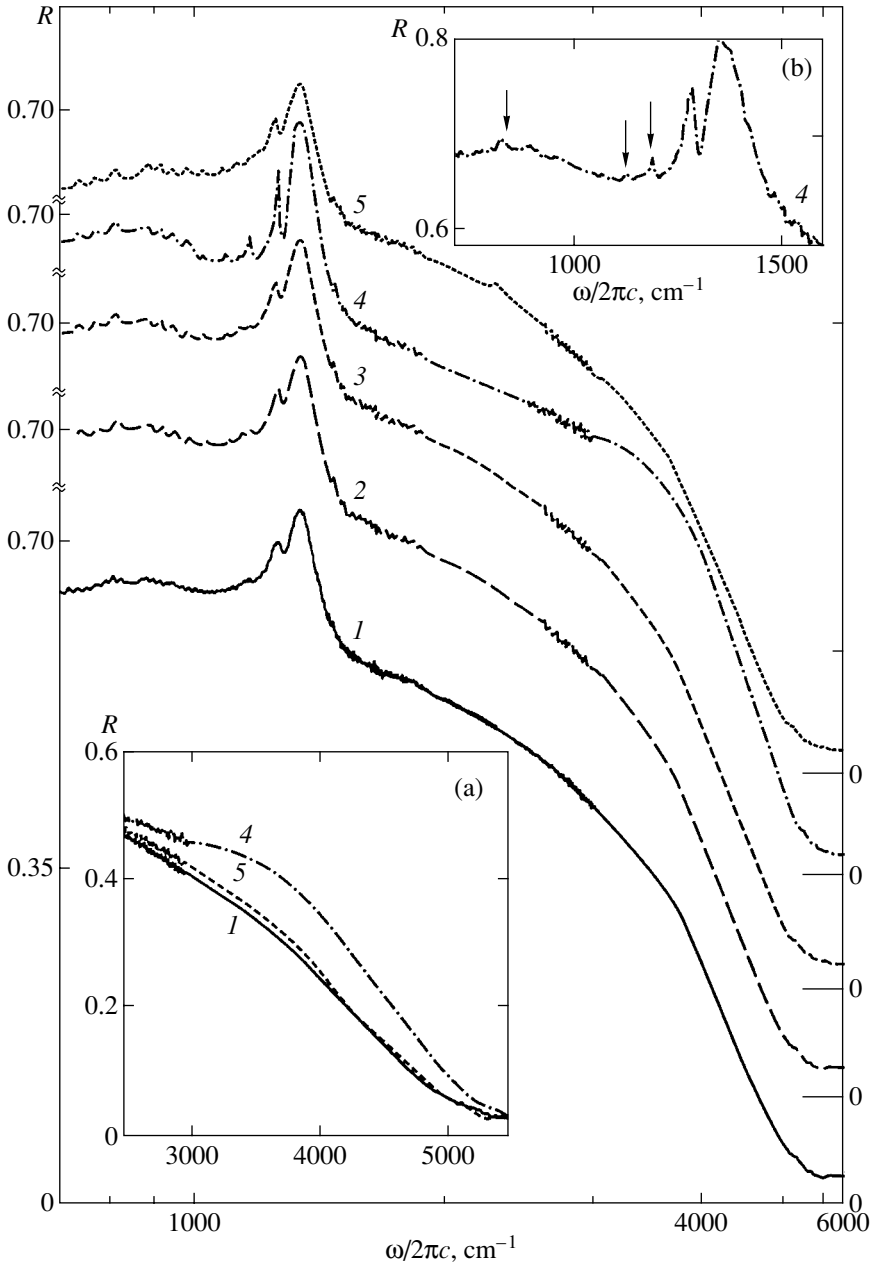

Fig. 2. Reflectance spectra of the θ-$(BETS)_4HgBr_4(C_6H_5Cl)$ crystal for **E** ∥ *a* obtained at *T* equal to (*1*) 300, (*2*) 250, (*3*) 200, (*4*) 100, and (*5*) 15 K. Insets: (a) reflectance spectra (2500–5500 cm^{-1}) without displacement of the zero at *T* equal to (*1*) 300, (*4*) 100, and (*5*) 15 K; and (b) reflectance spectrum (700–1600 cm^{-1}) measured at (*4*) *T* = 100 K.

type of $R(\omega)$, σ exhibits the largest values in both polarizations in the low-frequency region 700–1200 cm^{-1}. At 1600–6500 cm^{-1}, σ decreases smoothly with increasing frequency. Against this metallic background, the $\sigma(\omega)$ spectra exhibit deep dips near the BETS intramolecular vibration frequencies (1388 and 1283 cm^{-1} for **E** ∥ *a*, and at 1374 and 1276 cm^{-1} for **E** ∥ *b*), with their positions shifted slightly relative to those of the maxima of the corresponding vibrational features in the reflectance spectrum. As seen from Fig. 4, the spectra obtained in the **E** ∥ *a* polarization at 300, 250, 200, and 15 K are very similar, with a noticeable hump [corresponding to the shoulder in the $R(\omega)$ spectrum] appearing at 100 K in the 2000–3500 cm^{-1} interval. The $\sigma(\omega)$ spectra measured in the **E** ∥ *b* polarization at 300 and 15 K also almost coincide. At 100 K, σ is seen to decrease markedly at low frequencies (700–1200 cm^{-1}) compared to the values obtained at 300, 250, 200, and 15 K. The changes in the vibrational features observed to occur in

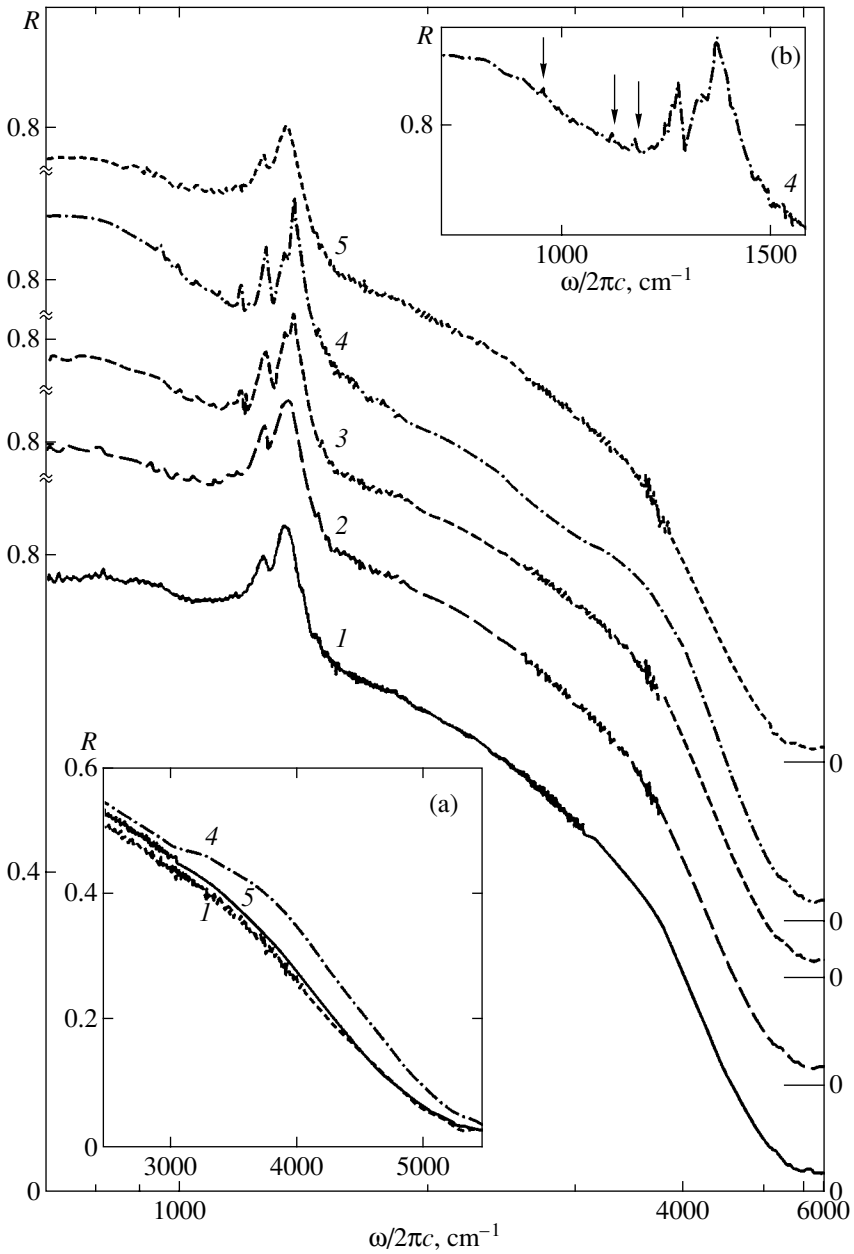

Fig. 3. Reflectance spectra of the θ-$(BETS)_4HgBr_4(C_6H_5Cl)$ crystal for **E** || *b* obtained at *T* equal to (*1*) 300, (*2*) 250, (*3*) 200, (*4*) 100, and (*5*) 15 K. Insets: (a) reflectance spectra (2500–5500 cm^{-1}) shown without displacement of the zero at *T* equal to (*1*) 300, (*4*) 100, and (*5*) 15 K; and (b) reflectance spectrum (700–1600 cm^{-1}) measured at (*4*) *T* = 100 K.

the $R(\omega)$ spectra at 180–80 K are also manifest in the optical conductivity spectra.

4. DISCUSSION OF RESULTS

4.1. Electronic Phenomena

The $R(\omega)$ and $\sigma(\omega)$ spectra obtained in the 1600–6500 cm^{-1} region at the above temperatures and presented in Figs. 1–4 were described by us in terms of the Drude–Lorentz phenomenological theory using the following expression for the principal components of the complex dielectric permittivity tensor:

$$\varepsilon(\omega) = \varepsilon_\infty - \frac{\omega_p^2}{\omega(\omega + i\Gamma)} + \frac{\omega_L^2}{\omega_t^2 - \omega^2 - i\gamma\omega}, \qquad (1)$$

where ε_∞ is the high-frequency dielectric permittivity of the lattice; ω_p and Γ are the plasma frequency and the quasi-free carrier optical-relaxation parameter, respectively; and ω_L, ω_t, and γ are the longitudinal and transverse frequencies and the relaxation parameter of the

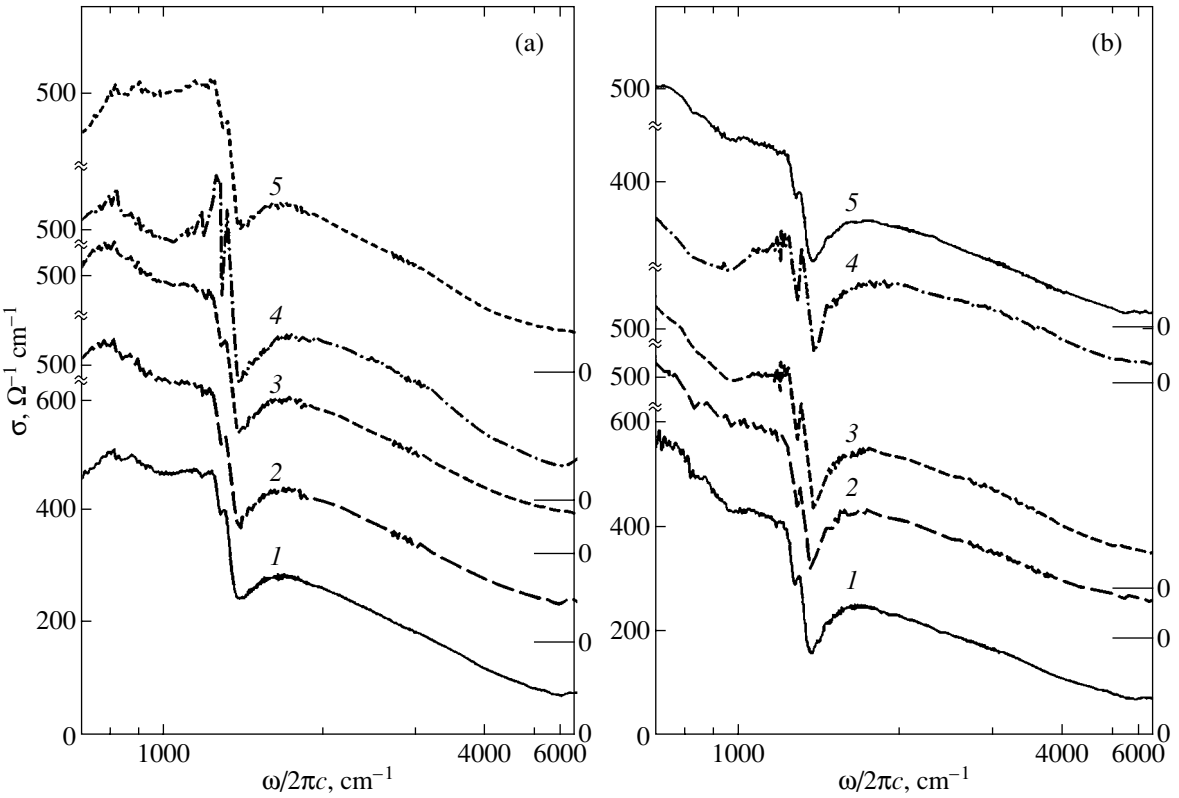

Fig. 4. Optical conductivity spectra of the θ-(BETS)$_4$HgBr$_4$(C_6H_5Cl) crystal obtained at T equal to (*1*) 300, (*2*) 250, (*3*) 200, (*4*) 100, and (*5*) 15 K. (a) **E** || *a* and (b) **E** || *b*.

Lorentz oscillator describing bound electrons, respectively.

The $R(\omega)$ and $\sigma(\omega)$ relations were calculated from the relations

$$R = \left[\frac{\sqrt{\varepsilon(\omega)}-1}{\sqrt{\varepsilon(\omega)}+1}\right]^2, \quad (2)$$

$$4\pi\sigma(\omega) = \omega \mathrm{Im}\varepsilon(\omega). \quad (3)$$

Fitting these relations to the experimental spectra showed that the spectra measured at 300, 250, 200, and 15 K in the 1600–6500 cm^{-1} region are well described by the first two terms in Eq. (1), i.e., the Drude expression, and, hence, can be associated in this region with quasi-free carriers. The $R(\omega)$ relations calculated for the **E** || *a* and **E** || *b* polarizations are presented in Fig. 1 for comparison. The table lists the corresponding fitting parameters for the temperatures used. As seen from the table, ε_∞ and ω_p are temperature-independent. The relaxation parameter Γ decreases only slightly when the temperature is lowered to 200 K, which corresponds to a small increase in R. Further cooling to 15 K virtually does not affect Γ. This behavior of Γ suggests that the optical relaxation apparently involves some structural defects rather than thermal vibrations. These defects could be associated, for instance, with the random potential in the crystal structure created by the C_6H_5Cl solvent molecules, which, as mentioned above, are distributed in a strongly disordered manner in the anion layer.

It should also be noted that the interband transitions, which can take place at 300 K for the band structure calculated in [3] and which are usually observed in the *k* phase of BEDT–TTF-based molecular conductors

Parameters of the Drude and Drude–Lorentz models obtained by fitting calculated $R(\omega)$ and $\sigma(\omega)$ spectra to the experimental data

T, K	ε_∞	ω_p, cm^{-1}	Γ, cm^{-1}	ω_L, cm^{-1}	ω_t, cm^{-1}	γ, cm^{-1}
E || *a*						
300	2.9	4820	2170			
200	2.9	4870	1970			
100	2.9	4800	1880	1400	2900	1500
15	2.9	4850	2200			
E || *b*						
300	2.9	4850	1900			
200	2.9	4850	1700			
100	2.9	4810	1780	800	2900	1600
15	2.9	4860	2050			

[8, 9], are not seen in the optical spectra of θ-$(BETS)_4HgBr_4(C_6H_5Cl)$. The Drude character of the spectrum taken at 300–180 and 60–15 K indicates only the existence of intraband transitions in the upper electronic and hole bands.

θ-$(BETS)_4HgBr_4(C_6H_5Cl)$ crystals grown together with our sample and investigated in [3] exhibited changes in the pattern of the temperature dependences of the dc resistivity $\rho_{dc}(T)$ from the metallic to semiconducting and back to the metallic type of conduction with decreasing temperature in the 245–240 K interval; these changes were reproduced in repeated heating and cooling runs with a noticeable hysteresis and were interpreted as a metal–semiconductor–metal phase transition [3]. In our optical measurements performed in this temperature range, the reflectance stopped increasing with decreasing temperature, so that the $R(\omega)$ spectra obtained at 250, 245, 240, and 200 K almost coincide.

At temperatures from 180 to 80 K, the spectra reveal qualitative changes and are no longer described by the Drude expression, so that one should fit them with inclusion of the third Lorentzian term in Eq. (1), whose fitting parameters for 100 K are given in the table. The appearance of the Lorentzian term in the fitting expressions for $R(\omega)$ and $\sigma(\omega)$ can be considered to be a continuation of the metal–semiconductor–metal phase transition reported in [3], which makes interband optical transitions possible; however, this does not involve any noticeable changes near the Fermi level.

The appearance of new bands in the vibrational spectrum in the same temperature range (180–80 K) observed by us is an indication of the onset of a periodic structural distortion along the stacks of BETS molecules with decreasing temperature, as was shown earlier [10, 11] to occur in TTF- and TMTSF-based quasi-one-dimensional compounds (dimerization of the molecules is the most probable process). Unstable dimerization of BETS molecules in the 180–80 K interval accounts for the interband transitions in the $R(\omega)$ and $\sigma(\omega)$ spectra. The periodic structural distortions along the BETS stacks initiated by a decrease in temperature also indicate the formation of a commensurate charge-density wave in the crystals [10, 11]. These changes in the spectra may also be treated as a manifestation of two groups of carriers: quasi-free carriers and those partially localized on the $(BETS)_2^{1+}$ dimers created. Note also that the independence of the Γ parameter from temperature below 200 K may also be associated with relaxation on the structural lattice distortions formed.

We used the values of ω_p for 300 K given in the table to estimate the full band width from the relation obtained for the one-dimensional case in the tight-binding approximation [12, 13],

$$\omega_p^2 = \frac{16\pi t d^2 e^2 \sin\left(\frac{\pi\rho}{2}\right)}{\varepsilon_0 h^2 V_m}, \qquad (4)$$

assuming it to hold for each of the principal directions chosen. Here, t is the transfer integral, V_m is the volume per molecule, and ρ is the number of carriers on a molecule. Using the crystallographic data presented in Section 2 to determine the parameters entering into Eq. (4), we obtained the following values for the band width $4t$: $4t(\| a) = 0.85$ eV and $4t(\| b) = 0.92$ eV. These band widths are close to the values reported in [13] for the $(BEDO–TTF)_2ReO_4(H_2O)$ organic superconductor, namely, 0.77 eV and 0.80 eV for the directions ($\| c$) and ($\perp c$), respectively.

4.2. Vibrational Features

The above-mentioned broad and strong vibrational features, more specifically, the maxima in the $R(\omega)$ spectra and the dips in the $\sigma(\omega)$ spectra, attest to a resonant interaction of the electron–hole system with BETS intramolecular vibrations (IMV), which is a characteristic property of most molecular conductors, including those based on the BEDT–TTF molecule and its derivatives (see, e.g., [6, 8, 9, 14–18]). This interaction was detected earlier to exist in TCNQ salts and was identified with Fano resonance [19, 20]. As a result of vibronic coupling (VC), the optically inactive, fully symmetric (A_g) IMVs manifest themselves in optical spectra. We made a tentative assignment of the vibrational features in the spectra displayed in Figs. 1–4 using the results of [4] and the data presented in [9, 17, 21]. The broad strong bands observed in $R(\omega)$ at 1353 ($\| a$) and 1350 cm^{-1} ($\| b$) and the corresponding dips in the $\sigma(\omega)$ spectra at 1388 ($\| a$) and 1374 cm^{-1} ($\| b$) are due to the interaction of carriers with the stretching vibrations of the central bond and the C=C bonds in the rings $\nu_3(A_g)$ of $BETS^0$ (1493 cm^{-1}). As known from studies of BEDT–TTF salts, the low-frequency shift of this feature is determined by the shift of this frequency caused by molecule ionization and by the shift due to the VC (see, e.g., [9, 17]). The correctness of this assignment is also buttressed by the fact that the BETS molecule does not have optically active vibrations in the 1350–1390 cm^{-1} interval. The maxima in $R(\omega)$ seen at 1270 ($\| a$) and 1274 cm^{-1} ($\| b$) and the corresponding dips in $\sigma(\omega)$ are due to carrier interaction with the C–C bond stretch vibrations in the ethylene groups $\nu_5(A_g)$ of $BETS^0$ (1282 cm^{-1}).

It was shown in [10, 11] that the additional bands caused by periodic structural distortions in the conducting stacks in the TTF and TMTSF salts that are observed at low temperatures also originate from carrier interaction with some of the A_g vibrations of these

molecules. The new bands observed by us at 1180 and 1124 cm^{-1} (|| *a*) and 1183 and 1122 cm^{-1} (|| *b*), which appear in the spectra at 180–80 K, lie close to the bands seen in the BETS^0 Raman spectra at 1173 (B_{2g}) and 1124 cm^{-1} (B_{1g}) [4]. We cannot, however, assign them to the B_g symmetry, because such vibrations usually do not couple to the electronic system. The new band at 1180/1183 cm^{-1} belongs, most likely, to the $\nu_7(A_g)$ vibration mode (1195 cm^{-1}, bending vibrations of the C–C–H bonds), which is observed in the Raman spectra of BEDT–TTF salts and was obtained by calculating the D_2 symmetry of this molecule [21]. We believe that the band at 1124/1122 cm^{-1} should be assigned to the $\nu_{67}(B_{3u})$ vibration mode (1152 cm^{-1}, out-of-plane vibrations of the C–H bonds; see calculations in [22]), which, in accordance with the data in [23], can interact with electrons. The weak bands seen at 960 (|| *b*) and 820 cm^{-1} (|| *a*) can be assigned to the $\nu_9(A_g)$ mode (917 cm^{-1}, C–C bond stretching vibrations) and the $\nu_{10}(A_g)$ mode (C–Se bond stretching vibrations). The 820 cm^{-1} band is shifted toward low frequencies relative to the C–S bond stretching vibration mode (876 cm^{-1} [21]).

Thus, the appearance of the Lorentz term in the $R(\omega)$ and $\sigma(\omega)$ metallic spectra (1600–6500 cm^{-1}) of the θ-$(BETS)_4HgBr_4(C_6H_5Cl)$ quasi-two-dimensional conductor cooled to 180–80 K, which is accompanied by the formation of new bands in the vibrational spectrum (700–1600 cm^{-1}), is evidence of periodic structural distortions along the BETS stacks and the formation of a commensurate charge-density wave.

ACKNOWLEDGMENTS

The authors are indebted to N.F. Kartenko and A.S. Kolosova for their assistance in the orientation of the crystal and its x-ray characterization.

This study was supported by the Russian Foundation for Basic Research, project nos. 98-02-18303 and 01-03-33009.

REFERENCES

1. T. Naito, A. Miyamoto, H. Kobayashi, *et al.*, Chem. Lett., No. 11, 1945 (1991).
2. A. Kobayashi, R. Kato, T. Naito, and H. Kobayashi, Synth. Met. **55–57**, 2078 (1993).
3. R. B. Lyubovskii, S. I. Pesotskii, S. V. Konovalikhin, *et al.*, Synth. Met. (2001) (in press).
4. I. Olejniczak, A. Graja, N. D. Kushch, *et al.*, J. Phys. I **6**, 1631 (1996).
5. H. Kobayashi, H. Akutsu, H. Tanaka, *et al.*, Synth. Met. **102**, 1654 (1999).
6. R. M. Vlasova, S. Ya. Priev, V. N. Semkin, *et al.*, Synth. Met. **48**, 129 (1992).
7. N. Drichko, R. M. Vlasova, V. N. Semkin, *et al.*, Synth. Met. **120** (1–3), 879 (2001).
8. J. E. Eldridge, K. Kornelsen, H. H. Wang, *et al.*, Solid State Commun. **79** (7), 583 (1991).
9. O. O. Drozdova, V. N. Semkin, R. M. Vlasova, *et al.*, Synth. Met. **64**, 17 (1994).
10. R. Bozio and C. Pecile, J. Phys. C **13** (33–34), 6205 (1980).
11. R. Bozio, C. Pecile, K. Bechgard, *et al.*, Solid State Commun. **41** (12), 905 (1982).
12. C. S. Jacobsen, J. Phys. C **19**, 5643 (1986).
13. W. Sommer, J. Moldenhauer, D. Schweizer, *et al.*, Synth. Met. **68**, 133 (1995).
14. M. G. Kaplunov, E. B. Yagubskii, L. P. Rosenberg, and Yu. G. Borodko, Phys. Status Solidi A **89**, 509 (1985).
15. C. S. Jacobsen, D. B. Tanner, J. M. Williams, *et al.*, Phys. Rev. B **35** (18), 9605 (1987).
16. K. Kornelsen, J. E. Eldridge, C. C. Homes, *et al.*, Solid State Commun. **72** (5), 475 (1989).
17. J. E. Eldridge, Y. Xie, H. H. Wang, *et al.*, Spectrochim. Acta A **52**, 45 (1996).
18. R. M. Vlasova, O. O. Drozdova, V. N. Semkin, *et al.*, Fiz. Tverd. Tela (St. Petersburg) **41** (5), 897 (1999) [Phys. Solid State **41**, 814 (1999)].
19. M. V. Belousov, A. M. Vaĭnrub, and R. M. Vlasova, Fiz. Tverd. Tela (St. Petersburg) **18** (9), 2637 (1976) [Sov. Phys. Solid State **18**, 1538 (1976)].
20. M. J. Rice, Phys. Rev. Lett. **37** (1), 36 (1976).
21. M. Meneghetti, R. Bozio, and C. Pecile, J. Phys. (Paris) **47**, 1377 (1986).
22. M. E. Kozlov, K. I. Pokhodnia, and A. A. Yurchenko, Spectrochim. Acta A **45** (4), 437 (1989).
23. V. M. Yartsev and C. S. Jacobsen, Phys. Status Solidi B **145**, K149 (1988).

Translated by G. Skrebtsov

Physics of the Solid State, Vol. 44, No. 1, 2002, pp. 82–87. Translated from Fizika Tverdogo Tela, Vol. 44, No. 1, 2002, pp. 78–82.

DEFECTS, DISLOCATIONS, AND PHYSICS OF STRENGTH

Effect of Impact Loading in the β Phase of a Cu–Al–Ni Single-Crystal Alloy on Its Elastic and Inelastic Characteristics Measured at a Frequency of 5 MHz

N. P. Kobelev*, Ya. M. Soĭfer*, A. F. Gurov*, S. P. Nikanorov, A. B. Sinani**, R. de Batist***, and J. van Humbeeck******

** Institute of Solid-State Physics, Russian Academy of Sciences, Chernogolovka, Moscow oblast, 142432 Russia*

*** Ioffe Physicotechnical Institute, Russian Academy of Sciences, Politekhnicheskaya ul. 26, St. Petersburg, 194021 Russia*

**** University of Antwerpen (RUCA), Institute of Material Science, Antwerpen, B-2020 Belgium*

***** Katholieke Universiteit Leuven, Department MTM, Heverlee, B-3001 Belgium*

e-mail: soifer@issp.ac.ru

Received May 16, 2001

Abstract—The internal friction and velocity of ultrasonic waves in the β phase of Cu–Al–Ni single crystals are measured at a frequency of 5 MHz in the temperature range 190–300 K, including the range of thermoelastic martensite transformation. The effect of impact loading (5 GPa) on the elastic and dissipative characteristics of the samples is investigated. The results obtained are discussed within the framework of existing theoretical concepts on the martensite transformation mechanisms responsible for the acoustic characteristics of a material.

1. INTRODUCTION

The anomalies observed in elastic properties and internal friction due to martensite transformations have attracted the particular attention of researchers, because elucidation of the mechanism of this process is of considerable (both theoretical and practical) interest. The martensite-type transformation in copper-based alloys with the so-called shape memory effect is especially important from the technological standpoint. According to Gonzalez-Comas *et al.* [1], copper-based alloys exhibit anomalies in their dynamic lattice properties upon martensite transformations. Specifically, copper-based alloys are characterized by the low-lying transverse acoustic phonon branch, which corresponds to a low value of the elastic modulus $C' = (C_{11} - C_{12})/2$. These quantities become more consistent as the phase transition point is approached. Manosa *et al.* [2] measured the elastic constants and their temperature dependences for Cu–Al–Ni alloys of different compositions and demonstrated that the elastic properties of these alloys behave as those of other copper-based martensite alloys. No anomalies were observed in the behavior of the elastic moduli C_{11} and C_{44}: they increased with a decrease in the temperature. However, it was found that the elastic modulus C' decreased with a decrease in the temperature. In other words, the material became more subject to shear in the (110) plane along the ⟨110⟩ direction. This behavior is typical of all alloys that undergo martensite transformation. It remains unclear how external factors affect the mechanism responsible for the martensite transformation.

The aim of the present work was to investigate the effect of impact loading in the austenite phase on the thermoelastic martensite transformation by measuring the elastic moduli and internal friction at high frequencies. Our earlier measurements [3] were performed with Cu–Al–Ni samples in the martensite state under impact loading at 5.3 GPa for 2 μs and revealed considerable changes in the elastic and inelastic characteristics of the material. Similar variations in the elastic properties can be expected to occur under impact loading of the samples in the austenite phase. However, a situation involving an austenite phase might appear more intricate compared to that with a martensite phase. The Cu–Al–Ni alloy samples subjected to impact loading with a load amplitude up to 5.3 GPa undergo a reversible $\beta \longrightarrow \gamma'$ thermoelastic martensite transformation. Since the applied load obviously exceeds the yield stress for γ'-martensite, the plastic deformation of the sample can occur in the martensite phase. The question now arises as to whether the memory effect of this deformation is observed after the reversible martensite transformation.

1063-7834/02/4401-0082$22.00 © 2002 MAIK "Nauka/Interperiodica"

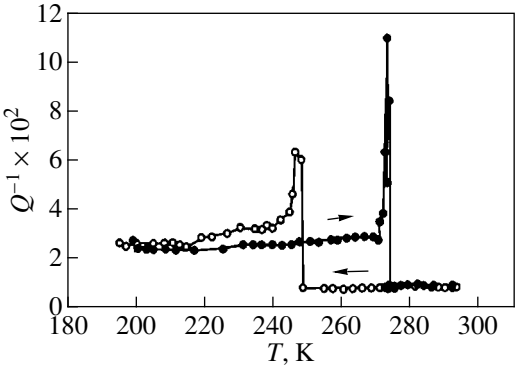

Fig. 1. Temperature dependence of the internal friction in the initial Cu–Al–Ni crystal upon cooling (open circles) and heating (closed circles) at a rate of 1 K/min.

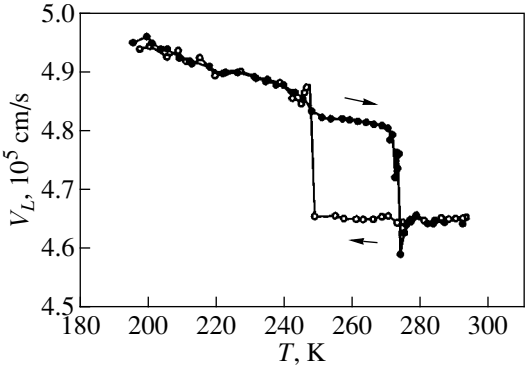

Fig. 2. Temperature dependence of the longitudinal velocity of sound in the initial Cu–Al–Ni crystal upon cooling (open circles) and heating (closed circles) at a rate of 1 K/min.

2. EXPERIMENTAL TECHNIQUE

Measurements were performed with single crystals of the Cu–Al–Ni alloy (81.9 wt % Cu, 14.1 wt % Al, and 4.0 wt % Ni) in the austenite phase. According to the data obtained from differential scanning calorimetry (DSC), the temperatures of thermoelastic transformations are as follows: M_s = 246 K, M_f = 230 K, A_s = 275 K, and A_f = 300 K. The samples were prepared in the form of cylinders (~3 mm long and 5 mm in diameter) cut out from a single-crystal cylindrical bar. The flat surfaces of the samples were mechanically ground and chemically polished to a parallelism of approximately 1 μm/cm. The structure of the samples was determined using x-ray diffraction. The deviation of the growing axis of the single crystal (the cylinder axis) from the [100] direction was approximately equal to 5°. Impact loading was performed along the cylindrical axis of the samples (i.e., along the [100] direction) in the same manner as was described earlier in [3, 4]. The internal friction and the longitudinal velocity of sound were measured using the pulse echo technique (at room temperature) and high-frequency resonance [5, 6] at a frequency of 5 MHz along the cylindrical axis of the samples. In our experiments, we used a liquid adhesive (monoethylsiloxane, $[-C_2H_3Si(H)O-]_n$, n = 9–14) with a freezing temperature of approximately 150 K, unlike the solid adhesive applied in [2], in order to cement the piezoelectric transducers to the sample and to provide acoustic contact. This is important because solid adhesives decompose below the temperature of martensite transformation [2] owing to the emergence of the surface relief associated with the formation of martensite domains, thus depressing the acoustic signal. The liquid adhesive made it possible to perform measurements in the temperature range from 150 to 300 K, including the range of martensite transformation.

The linear thermal expansion measurements (TMA) of the same samples were performed on a PC SERIES TMA7 instrument in the temperature range 100–350 K.

3. RESULTS AND DISCUSSION

The temperature dependences of the amplitude-independent internal friction Q^{-1} and the longitudinal acoustic wave velocity V_L measured at a frequency of 5 MHz and temperature dependences of the linear expansion of the samples prior to and after impact loading at 0.75 and 5 GPa are shown in Figs. 1–9. The table presents the characteristic temperatures of thermoelas-

Characteristic temperatures of thermoelastic transformation in the Cu–Al–Ni crystal prior to and after impact loading from the DSC and TMA data and measurements of the internal friction and velocity of sound

T_c	DSC	TMA			V_L			Q^{-1}		
	initial state	initial state	0.75 GPa	5 GPa	initial state	0.75 GPa	5 GPa	initial state	0.75 GPa	5 GPa
M_s, K	246	223	215	220	249	243	245	249	242	245
M_f, K	230	215	210	213	245	239	244	243	240	240
A_s, K	275	282	278	280	272	268	273	270	267	270
A_f, K	300	292	292	292	280	280	280	275	273	275

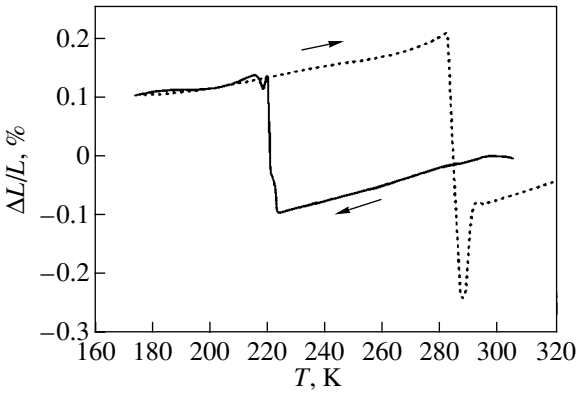

Fig. 3. Temperature dependence of the linear expansion in the initial Cu–Al–Ni crystal upon cooling (solid line) and heating (dashed line) at a rate of 12 K/min.

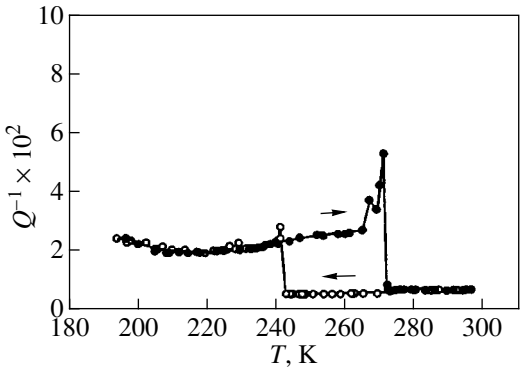

Fig. 4. Temperature dependence of the internal friction in the Cu–Al–Ni sample upon cooling (open circles) and heating (closed circles) at a rate of 1 K/min after impact loading (0.75 GPa).

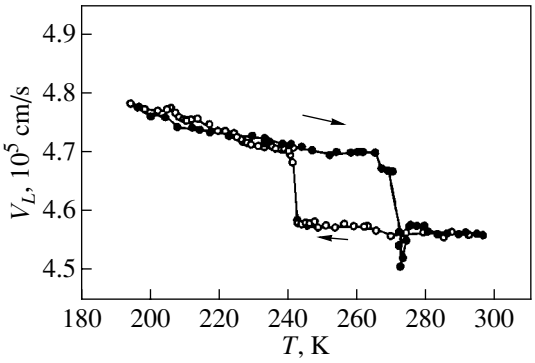

Fig. 5. Temperature dependence of the longitudinal velocity of sound in the Cu–Al–Ni sample upon cooling (open circles) and heating (closed circles) at a rate of 1 K/min after impact loading (0.75 GPa).

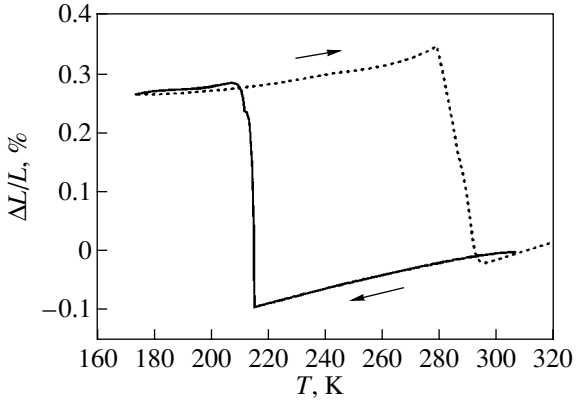

Fig. 6. Temperature dependence of the linear expansion in the Cu–Al–Ni sample upon cooling (solid line) and heating (dashed line) at a rate of 12 K/min after impact loading (0.75 GPa).

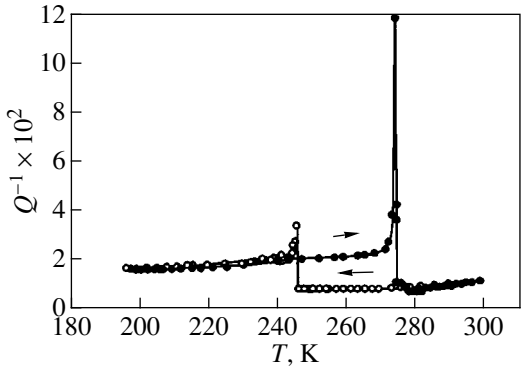

Fig. 7. Temperature dependence of the internal friction in the Cu–Al–Ni sample upon cooling (open circles) and heating (closed circles) at a rate of 1 K/min after impact loading (5 GPa).

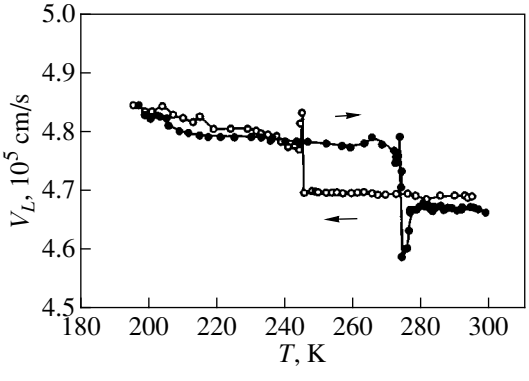

Fig. 8. Temperature dependence of the longitudinal velocity of sound in the Cu–Al–Ni sample upon cooling (open circles) and heating (closed circles) at a rate of 1 K/min after impact loading (5 GPa).

tic transformation in the Cu–Al–Ni crystal, which were obtained from DSC and TMA data and measurements of the internal friction and the velocity of sound.

The basic characteristics of the studied materials are as follows.

(1) In the initial state, the dependences $V_L(T)$ and $Q^{-1}(T)$ exhibit abrupt changes in the temperature range of the martensite transformation. (a) The longitudinal velocity of sound V_L (Fig. 2) drastically increases upon cooling in the course of the martensite transformation. As the temperature decreases, the velocity of sound V_L slightly decreases in the range 1–3 K below the M_s temperature and then smoothly increases. Upon heating, the velocity of sound V_L sharply decreases at the martensite transformation temperature and then rapidly increases. (b) The quantity dV/dT for the austenite phase is appreciably less than that for the martensite phase. (c) The dependence $Q^{-1}(T)$ (Fig. 1) shows very narrow peaks at the M_s and A_s temperatures. It should be noted that the internal friction in the austenite phase is less than that in the martensite phase over the entire temperature range covered, except for the internal friction at the M_s and A_s temperatures.

(2) As follows from the DSC data and measurements of the internal friction $Q^{-1}(T)$ and the velocity of sound $V_L(T)$, the temperatures of the onset of the austenite–martensite and martensite–austenite transformations almost coincide with each other, whereas the temperatures of the completion of these processes differ significantly. (The lower temperature of the austenite–martensite transformation, which was determined from TMA measurements, has a methodical origin and stems from the very high cooling and heating rates used in dilatometric measurements of the cylindrical samples.)

(3) Impact loading virtually does not affect the transformation temperatures and the shape of peaks in the $Q^{-1}(T)$ curve. However, the difference ΔV_L between the longitudinal velocities of sound in martensite and austenite phases considerably decreases with an increase in the load amplitude.

(4) The temperature dependences of $\Delta L/L(T)$ (Figs. 3, 6, 9) demonstrate a noticeable increase in $\Delta L/L$ upon martensite transformation after impact loading.

According to [7–9], materials in which two phases can coexist in the course of the phase transition in a certain temperature range are characterized by three main contributions to the total internal friction:

$$Q_{\text{tot}}^{-1} = Q_{\text{tr}}^{-1} + Q_{\text{pt}}^{-1} + Q_{\text{int}}^{-1}. \quad (1)$$

Here, Q_{int}^{-1} is the sum of contributions from each of the phases to the internal friction, which substantially depends on the defect structure of the material (interfaces, dislocations, point defects, boundaries of grains and clusters, their density and mobility, etc.); Q_{pt}^{-1} is

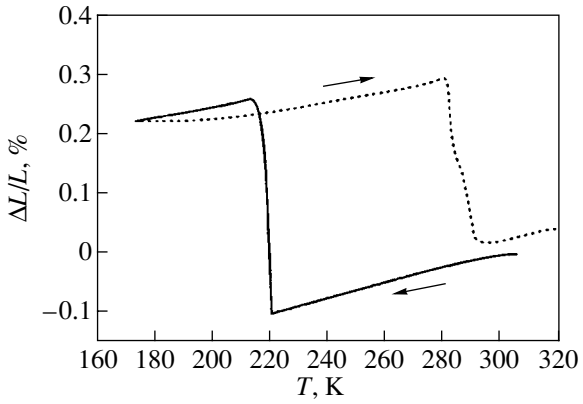

Fig. 9. Temperature dependence of the linear expansion in the Cu–Al–Ni sample upon cooling (solid line) and heating (dashed line) at a rate of 12 K/min after impact loading (5 GPa).

determined by the mechanism of the phase transformation and does not depend on the transformation rate; and Q_{tr}^{-1} is the transition component of the total internal friction Q_{tot}^{-1}, which exists only during heating or cooling, i.e., at $(dT/dt) \neq 0$. This quantity is determined by external factors, such as the cooling and heating rates and the amplitude and frequency of applied oscillating stresses. The transition component Q_{tr}^{-1} is governed by the transformation kinetics and is proportional to the rate of bulk transformation in a unit time. Since the Q_{tr}^{-1} quantity is inversely proportional to the frequency, its value should be very small at megahertz frequencies; hence, the contribution of Q_{pt}^{-1} to the internal friction dominates in the temperature range of the phase transformation. Until presently, there has been no universally accepted quantitative theory of acoustic wave attenuation in the vicinity of critical points (and, in particular, at temperatures of thermoelastic martensite transformation). The first attempts to explain the nature of the internal friction (independent of dT/dt) were made by Dejonghe *et al.* [7] and Koshimizu [10]. The strong attenuation of acoustic waves in the martensite phase was explained in terms of the displacement of interfaces without refinement of any microscopic mechanisms and without regard for anisotropy. A microscopic model accounting for the dislocation mechanism was proposed by Mercier and Melton [11]. They considered the effect of anisotropy on the elastic energy of dislocation and proved that the dislocation-assisted attenuation is proportional to the dislocation density, frequency, and the fourth power of the dislocation loop length and is inversely proportional to the elastic modulus $C' = (C_{11} - C_{12})/2$. Under the assumption that the anisotropy reaches a maximum in the course of the phase transition, Mercier and Melton [11] predicted the maximum internal friction at these tem-

peratures. Koshimizu [10] proposed another model of acoustic wave attenuation within the framework of the Landau model for first-order phase transitions [12]. The inclusion of the relaxation-type attenuation leads to a jump in the internal friction Q^{-1} and in the relaxed modulus at the transition temperature. Van Humbeeck [9] also considered a number of models based on the mechanism of stress-induced motion of coherent interfaces, including the interphase, intervariant, and twin boundaries. Thus, although there is no universally accepted quantitative theory of acoustic wave attenuation, the concepts formulated in the aforementioned works can be used for qualitative description of the elastic and dissipative properties of materials in the temperature range of martensite transformation.

As can be seen from Figs. 1, 4, and 7, the temperature dependences of the internal friction exhibit very narrow peaks. This is in qualitative agreement with the proportionality of the internal friction Q^{-1} to the quantity $1/(T_c - T)$ [12–14], where T_c is the critical temperature. In the case when the internal friction Q^{-1} is determined by the reversible displacement of the martensite–austenite interface or by the occurrence of partial dislocations, there should arise a modulus defect; i.e., the longitudinal velocity of sound V_L should decrease. At the same time, the structural transformation observed upon the austenite–martensite transition brings about an increase in V_L (or a decrease in V_L upon the martensite–austenite transition). Therefore, the behavior of $V_L(T)$ is controlled by at least two opposite processes. An increase in the longitudinal velocity of sound upon the martensite transition in the cooling cycle indicates that the contribution associated with the structural transformation is dominant. However, the temperature dependence of the longitudinal velocity of sound exhibits an interesting feature: a decrease (dip) in the velocity $V_L(T)$ below the temperature of the austenite–martensite transition and a similar decrease immediately above the temperature of the martensite–austenite transition. In both cases, the observed decrease in $V_L(T)$ upon the martensite transformation can be attributed to the formation of mobile defects (dislocations, interfaces, etc.), which give rise to the modulus defect. It should be noted that we measured the longitudinal velocity of sound along the ⟨100⟩ direction of the crystal. Manosa *et al.* [2] demonstrated that the Cu–Al–Ni crystals possess a strong anisotropy and that the longitudinal velocity of sound along the ⟨100⟩ direction is the minimum longitudinal velocity in the austenite phase. Therefore, the observed decrease (dip) in $V_L(T)$ upon the martensite–austenite transition can be associated only with an additional contribution from the inelastic strain to the effective elastic modulus and not with a change in the crystallographic orientation.

Note once again that the acoustic measurements were performed at temperatures above the freezing point of the liquid adhesive; hence, the influence of acoustic contact on the results obtained was insignificant.

Let us now discuss the background level of internal friction in the austenite and martensite phases. In our opinion, the background level of the internal friction is most likely governed by the scattering of acoustic waves from different-type structural (bulk and surface) defects rather than by acoustic absorption. The sound attenuation due to scattering of acoustic waves does not depend, to a first approximation, on the temperature but is determined by the amount of defects, their geometric sizes, and the wavelength. Although the studied samples in the austenite phase were single crystals, x-ray investigations revealed double reflections. This suggests the occurrence of twins that can give rise to acoustic scattering at megahertz frequencies.

4. CONCLUSION

The effect of impact loading appeared to be less significant than considered before. It can be assumed that the effect of impact loading primarily manifests itself in the formation of an additional crystal texture upon thermoelastic martensite transformation (selection of structural variants): the larger the number of favorably oriented variants, the weaker the scattering of acoustic waves and, correspondingly, the weaker the sound attenuation. The preferred orientation of structural variants can be such that the jumps in the acoustic velocity and $\Delta L/L$ will change upon thermoelastic martensite transformation. The verification of this assumption calls for measurements of the orientation dependences of the attenuation and the velocity of sound.

ACKNOWLEDGMENTS

This work was supported by the International Association of Assistance for the promotion of co-operation with scientists from the New Independent States of the former Soviet Union, project INTAS no. 96-2142.

Ya.M. Soĭfer and N.P. Kobelev acknowledge the partial support of the Russian Foundation for Basic Research, project no. 00-02-16461.

REFERENCES

1. A. Gonzalez-Comas, L. Manosa, A. Planes, and M. Morin, Phys. Rev. B **59**, 249 (1999).
2. L. Manosa, M. Jurado, A. Planes, *et al.*, Phys. Rev. B **49**, 9969 (1994).
3. Yu. Emel'yanov, S. Golyandin, N. Kobelev, *et al.*, J. Alloys Compd. **310**, 324 (2000).
4. N. A. Zlatin, S. M. Mochalov, G. S. Pugachev, and A. M. Baragov, Zh. Tekh. Fiz. **45**, 681 (1975) [Sov. Phys. Tech. Phys. **20**, 428 (1975)].

5. N. P. Kobelev and Ya. M. Soĭfer, Fiz. Tverd. Tela (Leningrad) **21**, 1362 (1979) [Sov. Phys. Solid State **21**, 787 (1979)].
6. N. P. Kobelev, R. K. Nikolaev, Ya. M. Soĭfer, and S. S. Khasanov, Fiz. Tverd. Tela (St. Petersburg) **40**, 173 (1998) [Phys. Solid State **40**, 154 (1998)].
7. W. Dejonghe, R. de Batist, and L. Delaey, Scr. Metall. **10**, 1125 (1976).
8. J.-E. Bidouh, R. Schaller, and W. Benoit, Acta Metall. **37**, 809 (1989).
9. J. van Humbeeck, J. Phys. IV **6**, C8–371 (1996).
10. S. Koshimizu, Ph. D. Thesis (Lausanne EPFL, 1981).
11. O. Mercier and K. N. Melton, Scr. Metall. **10**, 1075 (1976).
12. L. D. Landau and I. M. Khalatnikov, Dokl. Akad. Nauk SSSR **96**, 469 (1954).
13. I. A. Yakovlev and T. S. Velichkina, Usp. Fiz. Nauk **7**, 411 (1957).
14. C. W. Garland, in *Physical Acoustics: Principles and Methods* (Academic, New York, 1970), Vol. 7.

Translated by O. Borovik-Romanova

Physics of the Solid State, Vol. 44, No. 1, 2002, pp. 88–91. Translated from Fizika Tverdogo Tela, Vol. 44, No. 1, 2002, pp. 83–86.

MAGNETISM AND FERROELECTRICITY

Multiple Structure of Two-Pulse Nuclear Spin Echo in Cobalt Films

V. N. Berzhanskiĭ*, S. V. Kapel'nitskiĭ, V. S. Pokatilov***, and S. N. Polulyakh***

** Tavriya National University, Simferopol, 95007 Ukraine*
e-mail: roton@tnu.crimea.ua
*** Russian Research Centre Kurchatov Institute, pl. Kurchatova 1, Moscow, 123182 Russia*
e-mail: kapelnitsky@imp.kiae.ru
**** Moscow State Institute of Radio Engineering, Electronics, and Automation (Technical University), pr. Vernadskogo 78, Moscow, 117454 Russia*

Received January 26, 2001

Abstract—The conditions for the formation of two-pulse echo signals from ^{59}Co nuclei in thin magnetic films at $T = 4.2$ K are investigated. In the framework of the existing mechanisms, numerical simulation of the conditions for the formation of extra 3τ and 4τ echo signals (τ is the time delay between pulses) is carried out. It is shown that the multiple structure of the echo from ^{59}Co nuclei at $T = 4.2$ K is due to a mechanism in which an additional hyperfine magnetic field proportional to nuclear magnetization is acting on the nuclear spin system.

1. INTRODUCTION

The method of nuclear spin echo has been widely used in NMR study of magnetically ordered substances [1]. The echo is formed by applying two ac magnetic field pulses separated by a time interval τ to the sample. At the instant $t = 2\tau$, the nuclear spin system forms the main echo signal. In some cases, a multiple structure of the echo may be formed, which is manifested in the emergence of extra echo signals at instants proportional to τ in addition to the main echo 2τ.

At the present time, three different reasons for the formation of a multiple echo structure in magnetically ordered substances are known: (i) a very high pulse repetition frequency in sequences as compared to the spin–lattice relaxation rate [2], (ii) multiquantum effects in NMR of quadrupole nuclei [3–6], and (iii) dynamic effects associated with magnetic hyperfine interactions [1, 7].

In thin magnetic Co and Co–Fe films, a multiple echo-signal structure from ^{59}Co nuclei was observed experimentally in [8]. Echo signals were formed at instants $t = 2\tau$, 3τ, and 4τ. An analysis of the dependences of the amplitudes of echo signals on the time interval τ in the temperature range from 4.2 to 300 K led the authors of [3] to the conclusion that a multiple structure is formed as a result of strong nonlinearity of the nuclear spin system, as well as due to quadrupole effects.

The present work aims at studying the conditions for the formation of the multiple structure of the echo from ^{59}Co nuclei in cobalt films at 4.2 K.

2. EXPERIMENT

The experiments were performed on thin magnetic Co-based films used earlier in [9]. Echo signals were observed in a zero external magnetic field at 4.2 K on a pulsed NMR spectrometer in the frequency range 150–320 MHz. Two additional echoes at 3τ and 4τ were observed in the experiments apart from the main echo at 2τ.

Figure 1 shows the NMR spectra of ^{59}Co nuclei determined from the dependence of the amplitudes of the main and extra echo signals on the frequency of the ac magnetic field of exciting pulses. Each spectrum is normalized to the peak amplitude of the 2τ echo signal. The spectrum of the 2τ echo reflects the multiphase composition of the samples under investigation. The low-frequency ($\nu < 218$–220 MHz) component of the spectrum corresponds to the fcc phase, while the high-frequency spectrum component corresponds to the hcp phase [9]. It follows from the results presented in Fig. 1 that the spectral peaks of extra echo signals are observed at frequencies corresponding to both phases of cobalt. The intensity of extra echo signals at the frequencies of the hcp phase is higher than that at the frequencies of the fcc phase.

In order to analyze the mechanisms of formation of extra echo signals, we studied the dependences of echo amplitudes on the magnitude of the ac magnetic field ω_1 for the same duration of two exciting pulses: $t_1 = t_2 = 1$ μs (Fig. 2). Each dependence in Fig. 2 is normalized to the peak amplitude of the 2τ echo. The main feature of the observed dependences is that the magnitude of the ac field corresponding to the first peak of the echo signal amplitude decreases with increasing time of

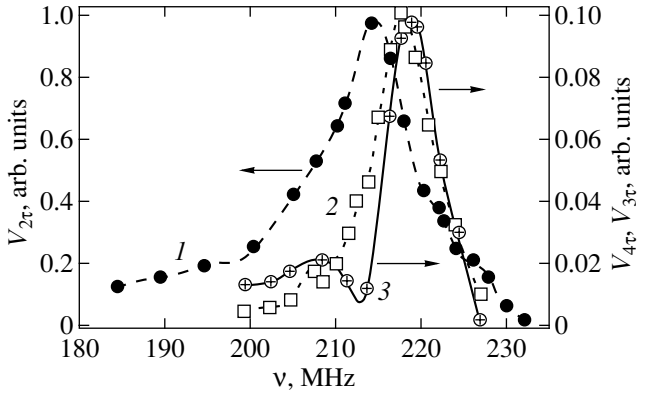

Fig. 1. NMR spectra of ^{59}Co nuclei in a cobalt film at T = 4.2 K: 2τ echo spectrum (*1*), 3τ echo spectrum (*2*), and 4τ echo spectrum (*3*).

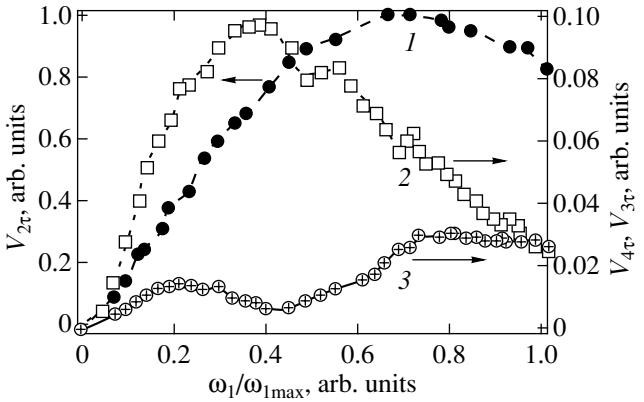

Fig. 2. Dependences of the amplitudes of the main ($V_{2\tau}$) and extra ($V_{3\tau}$ and $V_{4\tau}$) echo signals on the magnitude of the ac magnetic field at T = 4.2 K: 2τ echo (*1*), 3τ echo (*2*), and 4τ echo (*3*).

echo formation. The amplitudes of the ac magnetic field used in our experiments do not lead to additional broadening of the spectra, which indicates that the value of ω_1 does not exceed the NMR spectral width.

3. DISCUSSION

The first of the above mechanisms of echo formation was excluded experimentally by choosing a pulse repetition rate that was considerably higher than the spin–lattice relaxation rate [9].

In the second mechanism, the number of extra echo signals and the moments of their formation depend, to a considerable extent, on the type of inhomogeneous broadening of the spectral line [4]. For a quadrupole nucleus with spin $I = 7/2$, the multiquantum 3τ echo can be formed in two cases. In the first case, the inhomogeneity of the quadrupole constant is considerably higher than the inhomogeneity of the magnetic field. In this case, echo signals with 1.5τ, $\frac{7}{3}\tau$, 2.5τ, $\frac{8}{3}\tau$, 3.5τ, 4τ, 6τ, and 7τ must be observed in addition to the 2τ and 3τ signals. Numerical calculations of the dependences of the echo amplitudes on the magnitude of the ac magnetic field, which were carried out in accordance with the algorithm discussed in [6], revealed that the intensities of extra echo signals are of the same order of magnitude under identical excitation conditions. However, out of all possible extra signals, only the 4τ echo signals were observed experimentally; all other signals were absent. The absence of extra echo signals that could be formed before the 4τ signal cannot be due to relaxation damping.

In the case when magnetic inhomogeneous broadening dominates, the theoretically predicted echo signals must appear at instants multiple to τ: 2τ, 3τ,…, 8τ. Generally speaking, the absence of echo signals at instants larger than 4τ can be explained in terms of relaxation damping. However, the results of numerical calculations proved that, in all cases, the value of ω_1 corresponding to the first peak in the amplitude of the response is higher for extra echo signals than for the main echo. Thus, the experimentally observed features of the formation of a multiple echo structure do not match with the theoretical predictions, which indicates that the multiple quantum echo mechanism is inapplicable to the interpretation of the experimental results.

Moreover, numerical simulation of the multiple quantum echo revealed that the peak of the amplitude of an extra echo signal is observed for values of ω_1 that are comparable to the quadrupole splitting ω_q of the NMR spectrum. The value of ω_q for the hcp phase differs from zero in view of the symmetry of this phase. Thus, it can be assumed that in the case of NMR of ^{59}Co, we are dealing with a selective excitation of the spectral line $\omega_1 < \omega_q$. In this case, the classical equations of motion of the magnetization can be used for qualitative analysis of the behavior of the nuclear spin system. The difference between the classical and quantum-mechanical approaches lies in that the angles of rotation (defined as the product of the field amplitude ω_1 and the pulse duration) that ensure the maximum value of the echo signal amplitude for a quadrupole nucleus and for classical magnetization are different [5, 6]. Classical equations of motion are also applicable in the case when quadrupole splitting is absent, as, for example, is the case with NMR of ^{59}Co nuclei in the hcp phase.

The classical equations of motion for the isochromatic group of nuclear spins

$$\frac{d\mathbf{m}}{dt} = [\mathbf{m}\boldsymbol{\omega}] \qquad (1)$$

describe the precession of magnetization **m** around the field **ω** (measured in frequency units). At low tempera-

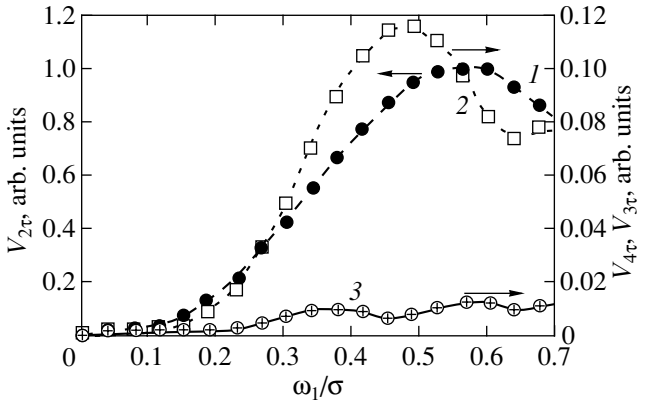

Fig. 3. Calculated dependences of the amplitudes of echo signals on the magnitude of the ac magnetic field for $\eta/\sigma = 0.125$ and $t_1 = t_2 = 4\pi/3\sigma$: 2τ echo (*1*), 3τ echo (*2*), and 4τ echo (*3*).

tures, hyperfine magnetic interactions lead to the emergence of a field [1, 7]

$$\omega_{x,y} = \eta\mu_{x,y}, \qquad (2)$$

where $\mu_{x,y} = \int_{-\infty}^{\infty} g(\omega) m_{x,y} d\omega$ is the integrated transverse magnetization, $g(\omega)$ is a function describing inhomogeneous broadening of the NMR spectral line, and η is a parameter determined by the magnetic susceptibility and the intensity of hyperfine magnetic interactions.

In the numerical simulation of a two-pulse response of a inhomogeneous broadened nuclear spin system, the time interval corresponding to the observation of the system was divided into time intervals of duration Δt. During the time Δt, the field was assumed to be unchanged and the magnitude of the hyperfine field in Eq. (2) was determined from the integrated nuclear magnetization at the beginning of this interval. It was taken into account that, during the action of pulses, the external ac field ω_1 was present along with the field given by Eq. (2). Equations (1) were solved under the assumption that during the time interval Δt, the magnetization of an isochromatic group of nuclear spins with detuning $\Delta\omega$ rotates through an angle $\alpha = \Delta t((\omega_1 + \eta\mu_x)^2 + \eta^2\mu_y^2 + \Delta\omega^2)^{1/2}$ about the effective magnetic field in the rotating system of coordinates [1, 2].

It was found as a result of numerical calculations that along with the main echo 2τ, extra echo signals appear at instants that are multiples of τ. The mechanism of the formation of these signals can be described as follows: owing to field (2), the echo signal plays the role of an exciting pulse. It is interesting to note that if we use in Eq. (2) the intrinsic transverse magnetization for each isochromatic group of spins instead of the integrated nuclear magnetization $\mu_{x,y}$ [1], no extra echo signals appear in the calculations. Moreover, an increase in parameter η in this case leads to suppression of the main echo.

By way of example, Fig. 3 shows the dependence of the amplitudes of the main and extra echo signals calculated using a Gaussian function with dispersion $\sigma = 1$ for $g(\omega)$. Each dependence in Fig. 3 is normalized to the peak of the amplitude of the 2τ echo. It follows from the results presented in Fig. 3 that, in the case under consideration, the first peak of the extra echo amplitude can arise for ac field amplitudes that are smaller than that corresponding to the first peak in the 2τ echo amplitude. The excitation amplitude corresponding to the first echo peak decreases with increasing time of the echo formation. In addition, the calculated amplitudes of extra echo signals (Fig 3), as well as the experimental amplitudes, are an order of magnitude lower than the amplitude of the main echo signal.

The magnitude of the field (2) responsible for the formation of the multiple echo structure is directly proportional to the nuclear magnetization. In the case of two-phase Co films, the hcp phase dominates [9] and, hence, its nuclear magnetization is greater in magnitude than that of the fcc phase. This explains the larger values of extra echo amplitudes at the NMR frequencies of the hcc phase as compared to those corresponding to the fcc phase (Fig. 1).

The main difference between the experimental (Fig. 2) and theoretical (Fig. 3) results is that an increase in the amplitude of the ac magnetic field leads to more rapid changes in the amplitude of experimental echo signals as compared to the theoretical values. This is due to the fact that, for the same duration of exciting pulses, the peak value of the amplitude of echo signals from quadrupole nuclei is attained for ac magnetic field amplitudes smaller than in the case of classical magnetization [5]. Furthermore, the samples under investigation are characterized by a high inhomogeneity of the NMR amplification factor, which was disregarded in our calculations and serves as an additional cause of the discrepancy between the experimental and theoretical dependences.

Thus, for the third mechanism, we observe good qualitative agreement between the theoretical and experimental results. A more detailed analysis requires a solution to the quantum-mechanical equations of motion for magnetization instead of the classical equations (1) and inclusion of the inhomogeneity of the NMR amplification factor [9]. In addition, the real function of the line shape $g(\omega)$ must be used rather than the model Gaussian function and the attenuation of the echo signal amplitude upon an increase in the delay time between pulses must be taken into account. All this involves considerable expenditures of computer time, which makes these calculations unrealistic.

Thus, a comparison of the results obtained using the available mechanisms with the experimental results reveals that preference should be given to the mechanism based on hyperfine dynamic interactions for the

formation of multiple echo structures for ^{59}Co nuclei in thin magnetic films at 4.2 K. Electric quadrupole interactions are apparently responsible for the emergence of extra oscillations in the dependences of echo amplitudes on the magnitude of the ac magnetic field, as well as for the fact that the experimentally observed echo amplitude increases with the ac magnetic field amplitude more rapidly than the theoretical dependence.

REFERENCES

1. M. I. Kurkin and E. A. Turov, *NMR in Magnetically Ordered Materials and Its Applications* (Nauka, Moscow, 1990).
2. A. Abragam, *The Principles of Nuclear Magnetism* (Clarendon, Oxford, 1961; Inostrannaya Literatura, Moscow, 1963).
3. G. N. Abelyashev, V. N. Berzhanskiĭ, N. A. Sergeev, and Yu. V. Fedotov, Zh. Éksp. Teor. Fiz. **94** (1), 227 (1988) [Sov. Phys. JETP **67**, 127 (1988)].
4. V. I. Tsifrinovich, Zh. Éksp. Teor. Fiz. **94** (7), 208 (1988) [Sov. Phys. JETP **67**, 1413 (1988)].
5. P. P. Man, Phys. Rev. B **52**, 9418 (1955).
6. S. N. Polulyakh, N. A. Sergeev, and A. A. Shemyakov, Fiz. Tverd. Tela (St. Petersburg) **42**, 1628 (2000) [Phys. Solid State **42**, 1675 (2000)].
7. A. S. Borovik-Romanov, Yu. M. Bun'kov, B. S. Dumesh, *et al.*, Usp. Fiz. Nauk **142**, 537 (1984) [Sov. Phys. Usp. **27**, 235 (1984)].
8. V. O. Golub, V. V. Kotov, A. N. Pogorelyĭ, and Yu. A. Podelets, Fiz. Tverd. Tela (Leningrad) **31** (11), 48 (1989) [Sov. Phys. Solid State **31**, 1864 (1989)].
9. V. S. Pokatilov, S. V. Kapel'nitskiĭ, and V. N. Karazeev, Fiz. Tverd. Tela (Leningrad) **32**, 1982 (1990) [Sov. Phys. Solid State **32**, 1155 (1990)].

Translated by N. Wadhwa

Physics of the Solid State, Vol. 44, No. 1, 2002, pp. 92–97. Translated from Fizika Tverdogo Tela, Vol. 44, No. 1, 2002, pp. 87–92.

MAGNETISM AND FERROELECTRICITY

Specific Features of Photo- and Electrical Conduction in Manganese Germanium Garnets

S. L. Gnatchenko*, I. I. Davidenko, N. A. Davidenko**, and J. M. Devin*****

** Physicotechnical Institute of Low Temperatures, National Academy of Sciences of Ukraine, Kharkov, 61164 Ukraine*

*** Shevchenko National University, Vladimirskaya ul. 64, Kiev, 01033 Ukraine*

**** LMMM, CNRS Laboratory, Meudon, France*

Received November 4, 2000; in final form, March 13, 2001

Abstract—The specific features of photo- and electrical conduction in manganese germanium garnet crystals are investigated in the temperature range 4.2–370 K for the first time. Under exposure of samples with ohmic contacts to visible light, the photocurrent in these samples is observed only at high temperatures. The characteristic times of the photocurrent rise differ from those of photocurrent relaxation after the light is switched off. The inference is made that the photo- and electrical conduction is determined by the electrical recharging of manganese ions. The generation and transport of charge carriers are controlled by centers with electrical inhomogeneities and shallow attachment levels. © *2002 MAIK "Nauka/Interperiodica"*.

1. INTRODUCTION

Earlier, it was found that the optical and magnetic properties of manganese germanium garnets change under exposure to visible light. The exposure of these crystals to linearly polarized light brings about changes in the linear birefringence [1] and linear dichroism [2], affects the magnetization reversal of sublattices in the antiferromagnetic state [3], and induces a phase transition from an antiferromagnetic state to a metamagnetic state [4]. Moreover, illumination of manganese germanium garnets leads to a change in the optical absorption coefficient [5, 6]. This effect does not depend on polarization and can be observed upon exposure of crystals to linearly and circularly polarized light, as well as to unpolarized light. The photoinduced effects observed in manganese germanium garnets can be used in optical recording, specifically for holographic writing of amplitude and phase gratings [7]. In this respect, manganese germanium garnets hold considerable promise as materials for active elements used in data recording, storage, and processing devices.

As a rule, the mechanisms responsible for induction and relaxation of photoinduced effects are associated with charge transfer between manganese ions of different valences in the garnet crystal lattice [1–8]. The processes of photoinduction are brought about by charge-transfer optical transitions. The charge transfer in the course of relaxation of photoinduced effects is due to thermal activation. At present, reliable data on photo- and electrical conduction in manganese germanium garnets are unavailable. However, this information can provide a better insight into the nature and mechanisms of photoinduced effects observed in these crystals. The purpose of the present work was to investigate the photo- and electrical conductivity in manganese germanium garnet crystals in the temperature range 4.2–370 K. Manganese germanium garnets of different compositions were chosen as the objects of investigation, because the photoinduced effects in these crystals should be sensitive to chemical impurities introduced into the crystal lattice.

2. SAMPLE PREPARATION AND EXPERIMENTAL TECHNIQUE

Photo- and electrical conduction was studied in manganese germanium garnet samples with surface electrical contacts. This made it possible to elucidate how the chemical composition of manganese germanium garnets affects the bulk and surface electrical properties.

The samples to be studied were as follows. Sample no. 1 was a single-crystal wafer of the $Ca_2Ga_{2-x}Mn_xGe_3O_{12}$ (x = 0.002) composition with a cubic lattice (~0.1% of the Ga ions are replaced by Mn ions) and the (100) crystallographic orientation, sample no. 2 was the $Ca_3Mn_2^{3+}Ge_3O_{12}$ single crystal with a tetragonal structure, sample no. 3 was the Na^+-doped $Ca_3Mn_2^{3+}Ge_3O_{12}$ single crystal with a tetragonal structure, and sample no. 4 was the $(CdCa)_3Mn_2^{3+}Ge_3O_{12}$ single crystal with a cubic structure (the Cd/Ca ratio in the batch was equal to 10).

For photoelectric measurements, two conducting contacts (silver paste) were applied to the ground surfaces of the samples. The gap between the contacts on each sample was equal to 0.5–0.7 mm, and the length of the contacts along this gap was 4–6 mm.

In the samples thus prepared, the thermostimulated current (TSC) was measured in the temperature range 4.2–370 K. In addition, we measured the dark current i_d and photocurrent i_{ph} as functions of the dc voltage U applied across the contacts on the sample surface, temperature T, the intensity I and wavelength λ of light used for irradiation of the samples, and the angle between the plane of polarization of the incident light and the crystallographic axes in the surface region of the sample.

The thermostimulated currents were investigated using a helium cryostat with optical windows and automatic control and regulation of temperature. The measurements were performed upon heating of the samples at a rate of 0.1 K/s. The surface electrical contacts were shorted out prior to cooling. Then, the sample was cooled to the temperature $T = 5$ K and exposed to light for the time $t = 5$ min. After the light was switched off, a dc voltage was applied across the electrical contacts. After relaxation of the transient currents for a time determined by the sample capacitance and reaching a steady-state potential between the electrical contacts, the sample was linearly heated and the thermostimulated current i_{TSC} passing between the electrical contacts was measured. The measurements of the current were performed using an electrometer. The sample was connected to the electrometer input as a photoresistor. The lower detection limit of the measuring setup was 2×10^{-12} A.

The dependences of the currents i_d and i_{ph} on T, U, I, and λ in the ranges $T = 285$–370 K, $U = 10$–600 V, and $\lambda = 380$–1000 nm were measured in a photoresistance mode using a storage oscilloscope. The samples placed in a thermostat with optical windows were exposed to light of mercury, and incandescent lamps (with the use of a condenser, glass light filters, and polarizers) and a helium–neon laser ($\lambda = 633$ nm). The light intensity could be changed with neutral light filters by a factor of 84. The angle of polarization of the incident light was changed by rotating the sample about the axis of the light beam. Moreover, after performing a cycle of measurements, the electrical contacts were removed from the sample surface and then again applied to the same surface so that the angle formed by the gap (between the contacts) and the crystallographic axes of the sample differed from that used in the preceding measurements. The cycle of measurements was repeated with the aim of analyzing the influence of the orientation of an external electric field on the effects under investigation. After the measurements, the results obtained were compared.

3. RESULTS

Examination of the thermostimulated current revealed that, for sample nos. 2–4, thermoactivated conduction currents in the temperature range 5–245 K were not observed even in samples irradiated with light.

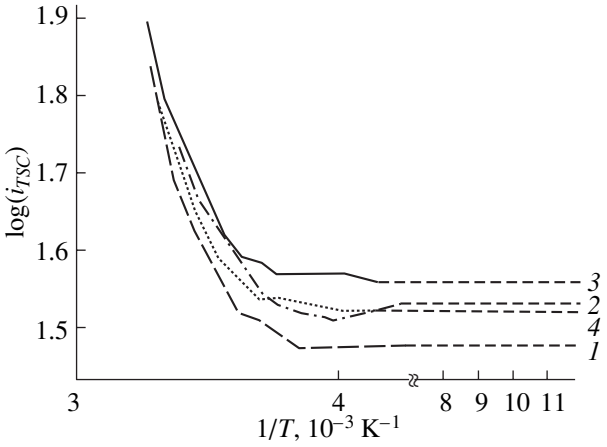

Fig. 1. Temperature dependences of the thermostimulated current for sample no. 2 (*1*) before preliminary irradiation and after preliminary irradiation with light at different temperatures T_{irr}: (*2*) 5, (*3*) 15, and (*4*) 150 K. The voltage across the electrical contacts is 90 V.

At $T = 250$–305 K, an increase in temperature leads to an increase in the i_{TSC} current. However, within the limits of experimental error, the i_{TSC} current does not depend on the irradiation of the sample at lower temperatures. Figure 1 displays the dependences of $\log(i_{TSC})$ on $1/T$ for sample no. 2 at $U = 90$ V prior to illumination at low temperatures (curve *1*) and after irradiation with light at temperatures $T_{irr} = 5$, 15, and 150 K (curves *2–4*, respectively). As is seen from Fig. 1, the i_{TSC} current does not increase at low temperatures and all the curves at $T > 250$ K are similar to each other and can be interpolated by a straight line. The activation energy W_{at} calculated from the slope of this straight line for the thermostimulated current i_{TSC} is close to $W_{at} = 0.52 \pm 0.02$ eV. Therefore, the temperature dependence of the i_{TSC} current at $T > 250$ K can be described by the exponential function

$$i_{TSC} \sim \exp(-W_{at}/kT), \qquad (1)$$

where k is the Boltzmann constant and W_{at} is the activation energy of the thermostimulated current i_{TSC}.

It should be mentioned that our experiments failed to reveal an increase in the i_{TSC} current in sample no. 1 with an increase in the temperature. Furthermore, in this sample, unlike the other samples under investigation, the dark current and photocurrent appeared to be small (beyond the detection limit of our measuring instruments).

The dependences of the i_d current on the applied voltage U at temperature $T = 293$ K for sample nos. 2 (curve *1'*), 3 (curve *2'*), and 4 (curve *3'*) are plotted in the log–log coordinates in Fig. 2. These dependences can also be interpolated by straight lines. The slopes m' of these straight lines for sample nos. 2, 3, and 4 are equal (to within ±5%) to 1.11, 1.14, and 1.0, respectively. The

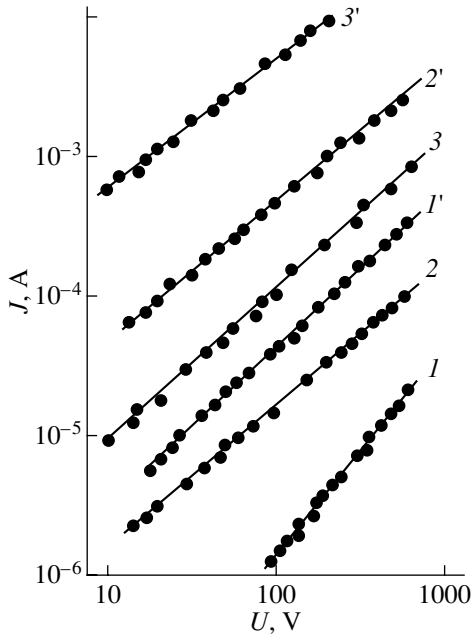

Fig. 2. Dependences of (*1–3*) the photocurrent and (*1'–3'*) the dark current on the applied voltage for sample nos. (*1*, *1'*) 2, (*2*, *2'*) 3, and (*3*, *3'*) 4. The wavelength λ of exciting light is equal to 633 nm. T = 293 K.

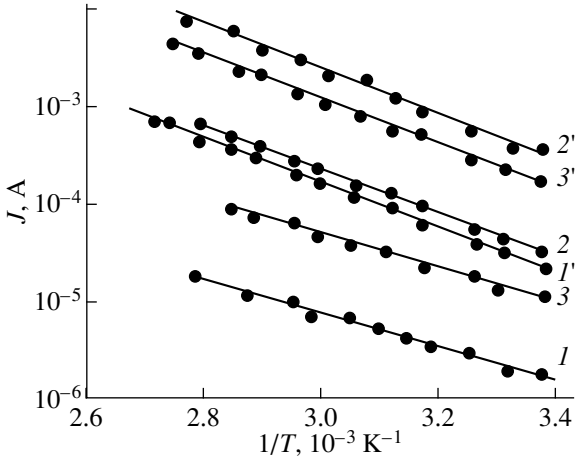

Fig. 3. Temperature dependences of (*1–3*) the photocurrent and (*1'–3'*) the dark current for sample nos. (*1*, *1'*) 2, (*2*, *2'*) 3, and (*3*, *3'*) 4. The wavelength λ of exciting light is equal to 633 nm. U = 110 V.

results obtained allow us to approximate the dependences of the i_d current on the U voltage by the following function:

$$i_d \sim U^{m'}. \quad (2)$$

Figure 3 shows the dependences of $\log(i_d)$ on $1/T$ for sample nos. 2–4. The curves can be interpolated by straight lines. The activation energy W_{at} of the dark current can be determined from the slopes of these straight lines. The dependences themselves can be represented in the analytical form

$$i_d \sim \exp(-W_{at}/kT). \quad (3)$$

The dependences of the activation energy W_{at} on the dc voltage U for sample nos. 2 (curve *1'*), 3 (curve *2'*), and 4 (curve *3'*) are depicted in Fig. 4. As is seen from this figure, the activation energy W_{at} only slightly depends on the voltage U and the highest energy W_{at} = 0.52 ± 0.005 eV is observed for sample no. 2.

For sample nos. 2–4 at an applied voltage, the electric current passing through the sample increases under exposure to visible light and decreases after the cessation of illumination. The observed rise and relaxation of the electric current (kinetics of the photocurrent i_{ph}) are long-term processes. The times of photocurrent rise and photocurrent relaxation in different samples differ from each other (to a lesser extent for sample no. 2 and to a greater extent for sample nos. 3 and 4). Note that, after the light is switched off, the photocurrent in sample nos. 3 and 4 regains its initial value more slowly. Figure 5 shows the normalized dependences of the i_{ph} current on the time t after switching the light on for sample nos. 2 (curve *1*) and 3 (curve *2*). The vertical arrow indicates the instant of time of switching the light off. The photocurrent kinetics in the studied samples does not depend on the dc voltage U and the intensity and wavelength of visible light but is sensitive to temperature. The temperature dependence of the photocurrent rise time constant τ_{ph} for sample no. 2 is plotted in the Arrhenius coordinates in Fig. 6. The time constant was determined from the slope of the initial linear portion in the time dependence of the i_{ph} current (Fig. 5, curve *1*). It can be seen from Fig. 6 that τ_{ph} decreases with an increase in the temperature. By using the results of these measurements, we calculated the activation energy of photocurrent rise: W_τ = 0.13 ± 0.03 eV. The temperature dependence of the photocurrent rise time can be represented by the relationship

$$\tau_{ph} \sim \exp(W_\tau/kT). \quad (4)$$

Upon irradiation of the studied samples with light at a wavelength λ < 450 nm, no photocurrent was found. In the visible light range, the i_{ph} current at constant values of U and t is directly proportional to the light intensity I and does not depend on further illumination at wavelengths λ < 450 nm or λ > 1000 nm, the angle of polarization of the incident light, and the direction of the applied electric field with respect to the crystallographic axes on the surface of the sample. However, the photocurrent substantially depends on the dc voltage U and temperature.

The dependences of the i_{ph} current on the voltage U at T = 293 K within 10 s after the onset of irradiation with laser light at λ = 633 nm for sample nos. 2 (curve *1*), 3 (curve *2*), and 4 (curve *3*) are plotted in the log–log coordinates in Fig. 2. These dependences can be inter-

polated by straight lines whose slopes m for sample nos. 2, 3, and 4 are equal (to within 5%) to 1.45, 1.1, and 1.0, respectively. The dependences of the i_{ph} current on the voltage U are represented by a relationship similar to expression (2), that is,

$$i_{ph} \sim U^m. \quad (5)$$

The slopes m and m' for sample nos. 3 and 4 are close to each other and only slightly differ from unity. For sample no. 2, the values of m and m' differ considerably. It is worth noting that the ratios i_{ph}/i_d for sample nos. 2 $[(5.6 \pm 0.2) \times 10^{-2}]$, 3 $[(1.5 \pm 0.3) \times 10^{-2}]$, and 4 $[(2.6 \pm 0.2) \times 10^{-2}]$ also differ substantially.

The dependences of $\log(i_{ph})$ on $1/T$ for sample nos. 2–4 are depicted in Fig. 3. These dependences can be interpolated by straight lines. The activation energy $W_{a\,ph}$ of the photocurrent can be determined from the slopes of these straight lines. The temperature dependence of i_{ph} can be represented by a relationship similar to formula (3), that is,

$$i_{ph} \sim \exp(-W_{a\,ph}/kT). \quad (6)$$

Figure 4 displays the dependences of the activation energy $W_{a\,ph}$ on the voltage U for sample nos. 2 (curve *1*), 3 (curve *2*), and 4 (curve *3*). It can be seen from Fig. 4 that the activation energy $W_{a\,ph}$ does not depend on the dc voltage U. This energy is less than the activation energy of the dark current. For sample nos. 2–4, the activation energies $W_{a\,ph}$ are equal to 0.41 ± 0.01, 0.38 ± 0.01, and 0.47 ± 0.01 eV, respectively.

4. DISCUSSION

As follows from the measurements under the above conditions, the electrical conduction and photoconduction do not occur in sample no. 1 but are observed in samples nos. 2–4. Therefore, we can assume that these effects are associated with the formation of an ordered structure of Mn^{3+} ions in the samples. The overlap of the outer electron shells of these ions provides a way of transferring mobile charge carriers.

In the general case, the dark current and photocurrent can be determined from the following expressions [9]:

$$i_d \sim q n_d \mu_d E, \quad (7)$$

$$i_{ph} \sim q n_{ph} \mu_{ph} E, \quad (8)$$

where q is the elementary charge; n_d and μ_d are the concentration and mobility of equilibrium charge carriers, respectively; n_{ph} and μ_{ph} are the concentration and mobility of nonequilibrium charge carriers, respectively; and E is the electric field strength. The concentration of charge carriers and their transfer are determined by both the possibility of escaping from photogeneration centers and the possibility of transitions occurring between neighboring lattice sites.

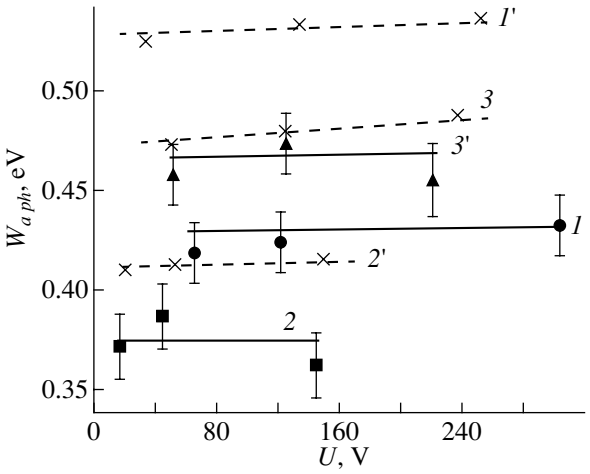

Fig. 4. Dependences of the activation energy of (*1*–*3*) photoconduction and (*1'*–*3'*) electrical conduction on the applied voltage for (*1*, *1'*) $Ca_3Mn_2^{3+}Ge_3O_{12}$, (*2*, *2'*) $(Cd,Ca)_3Mn_2^{3+}Ge_3O_{12}$, and (*3*, *3'*) $Ca_3Mn_2^{3+}Ge_3O_{12} : Na^+$ samples.

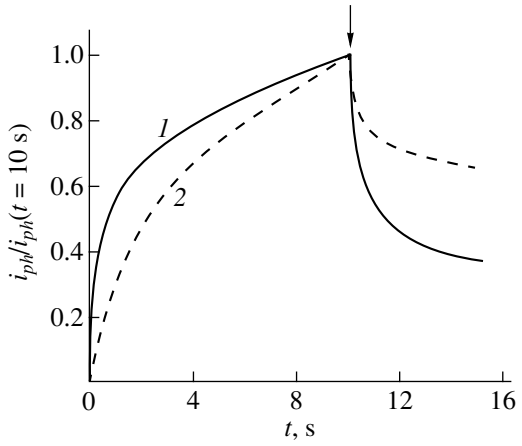

Fig. 5. Photocurrent kinetics in sample nos. (*1*) 2 and (*2*) 3.

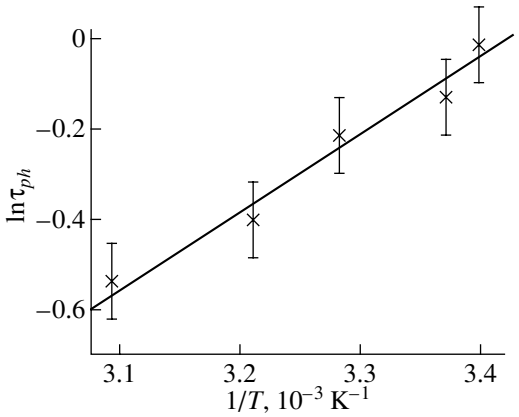

Fig. 6. Temperature dependence of the photocurrent rise time constant for sample no. 2 ($Ca_3Mn_2^{3+}Ge_3O_{12}$).

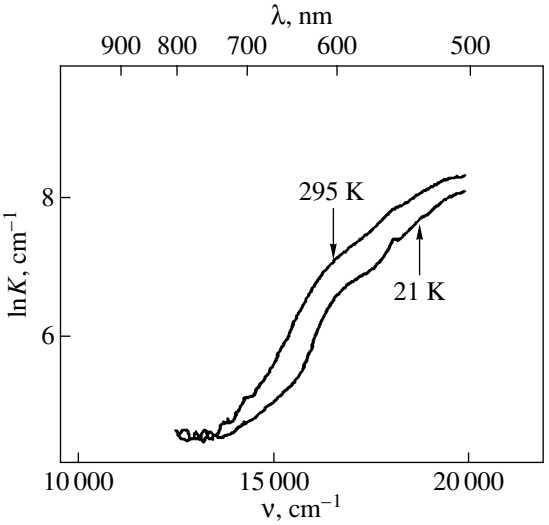

Fig. 7. Optical absorption spectra of sample no. 2 ($Ca_3Mn_2^{3+}Ge_3O_{12}$) at different temperatures.

In order to determine the type (intrinsic or extrinsic) of photoconductivity in the visible spectral range, we analyzed the effect of temperature on the long-wavelength absorption edge of the samples under consideration. As an illustration, Fig. 7 shows the spectra of the absorption coefficient K for sample no. 2 at different temperatures. As the temperature increases, the energy location of the absorption edge remains unchanged and the magnitude of the absorption coefficient increases. According to the available data [10–12], the drastic increase in absorption at an energy of approximately 2 eV in concentrated manganese germanium garnets is most likely caused by the ^5E_g–$^5T_{2g}$ transition in the Mn^{3+} ions. The maximum of this absorption is observed near 500 nm. It is known that the maximum of absorption of Mn^{4+} ions due to the transition between the $^4A_2$ and $^4T_2$ states is located at a wavelength of approximately 520 nm [13–16]. However, the concentration of Mn^{4+} ions in concentrated garnets is rather small and their contribution to the absorption is insignificant. Consequently, it can be assumed that the photoconductivity in the visible spectral range is governed by the excitation of Mn^{3+} ions.

Therefore, the optical, electrical, and photophysical properties of the studied crystals in the visible spectral range are determined by the presence of manganese ions and the specific features of their distribution in the crystal structure. The results obtained indicate that the manganese germanium garnets under investigation can be considered inhomogeneous semiconductors [17] and their photophysical properties can be associated with inhomogeneities of crystal sublattices. This assumption is confirmed by the experimental results: when changing over from sample no. 2 to sample nos. 3 and 4, the kinetics of photocurrent rise slows down and, after the cessation of irradiation, the kinetics of photocurrent relaxation becomes slower and the residual conductivity is observed (Fig. 5). This implies that charge carriers can be separated by electric fields of inhomogeneities and the charge transfer is controlled by retrapping processes. In the temperature range $T >$ 250 K, these processes have an activation nature. Since the dark current and photocurrent do not depend both on the direction of the applied electric field with respect to the crystallographic axes of the sample and on the light polarization, it is assumed that the charge carrier drift proceeds through retrapping into shallow attachment levels. The activation energy of carrier escape from these levels is close to $W_\tau = 0.13 \pm 0.03$ eV. In the low-temperature range, the deep trapping of charge carriers is a more efficient process as compared to the transfer of charge carriers over large distances and their drift. These deep traps are located in spatial regions in the vicinity of electrical inhomogeneities. The above assumption is also supported by the fact that the photoinduced linear birefringence [1] and photoinduced changes in the absorption coefficient [3] of manganese germanium garnets are observed at low temperatures.

5. CONCLUSIONS

Thus, the experimental data obtained and their analysis allowed us to make the following inferences.

(1) In manganese germanium garnets, the photo- and electrical conductivity in the visible light range is determined by the concentration and location of Mn^{3+} ions in the crystal lattice. It is the excitation of these ions that is responsible for the internal photoelectric effect.

(2) The specific feature of the photogeneration and charge carrier transfer in manganese germanium garnets is that these processes are controlled by electrical inhomogeneities in their crystal structure.

(3) At low temperatures, the inhomogeneity regions can involve, in addition to Mn^{3+} ions, an Mn^{4+} ion formed through the capture of an electron by an acceptor. The electrical recharging of manganese ions can occur with an increase in temperature and under exposure to light. As the temperature increases, the hole trapped in the inhomogeneity region can leave this region and then the valence electron occupying its position can be involved in conduction due to the interaction with phonons.

(4) The drift of nonequilibrium carriers is governed by shallow attachment levels with the W_τ energy and inhomogeneity regions with the $W_{a\,ph}$ energy. The concentration of inhomogeneities and the changes in the charge carrier potential in the vicinity of inhomogeneities depend on the chemical composition of the samples and the crystal lattice type. This manifests itself in the difference between the electrical characteristics of different manganese germanium garnet samples.

ACKNOWLEDGMENTS

This work was supported in part by the International Association of Assistance for the promotion of co-operation with scientists from the New Independent States of the former Soviet Union, project no. 97-0366.

REFERENCES

1. S. L. Gnatchenko, V. V. Eremenko, S. V. Sofroneev, and N. F. Kharchenko, Pis'ma Zh. Éksp. Teor. Fiz. **38** (4), 198 (1983) [Sov. Tech. Phys. Lett. **38**, 233 (1983)].
2. V. V. Eremenko, S. L. Gnatchenko, I. S. Kachur, *et al.*, Fiz. Nizk. Temp. **27** (1), 30 (2001) [Low Temp. Phys. **27**, 22 (2001)].
3. N. F. Kharchenko and V. A. Bedarev, Fiz. Nizk. Temp. **19**, 72 (1993) [Low Temp. Phys. **19**, 52 (1993)].
4. V. A. Bedarev, V. I. Gapon, and S. L. Gnatchenko, Fiz. Nizk. Temp. **25** (1), 38 (1999) [Low Temp. Phys. **25**, 28 (1999)].
5. V. A. Bedarev, S. L. Gnatchenko, R. A. Rupp, and B. Sugg, Fiz. Nizk. Temp. **24** (3), 281 (1998) [Low Temp. Phys. **24**, 212 (1998)].
6. V. V. Eremenko, S. L. Gnatchenko, I. S. Kachur, *et al.*, Phys. Rev. B **61** (16), 10670 (2000).
7. B. Sugg, S. L. Gnatchenko, and R. A. Rupp, J. Opt. Soc. Am. **13** (11), 2662 (1996).
8. S. L. Gnatchenko, V. A. Bedarev, V. V. Eremenko, *et al.*, OSA Trends Opt. Photonics Ser. **27**, 123 (1999).
9. S. M. Ryvkin, *Photoelectric Effects in Semiconductors* (Fizmatgiz, Leningrad, 1963; Consultants Bureau, New York, 1964).
10. D. T. Sviridov, R. K. Sviridova, and Yu. F. Smirnov, *Optical Spectra of Transition Metal Ions in Crystals* (Nauka, Moscow, 1976).
11. S. Kuck, S. Hurling, K. Peterman, and G. Huber, Phys. Rev. B **57** (4), 2203 (1998).
12. M. A. Noginov, G. B. Loutts, and M. Warren, J. Opt. Soc. Am. B **16** (3), 475 (1999).
13. A. E. Nosenko, A. P. Abramov, L. V. Kostyk, *et al.*, Opt. Spektrosk. **61** (5), 1037 (1986) [Opt. Spectrosc. **61**, 648 (1986)].
14. L. A. Riseberg and M. J. Weber, Solid State Commun. **9** (11), 791 (1971).
15. A. Brenier, A. Suchocki, C. Pedrini, *et al.*, Phys. Rev. B **46** (6), 3219 (1992).
16. M. A. Noginov and G. B. Loutts, J. Opt. Soc. Am. B **16** (1), 3 (1999).
17. M. K. Sheĭkman and A. Ya. Shik, Fiz. Tekh. Poluprovodn. (Leningrad) **10** (2), 209 (1976) [Sov. Phys. Semicond. **10**, 128 (1976)].

Translated by O. Borovik-Romanova

Physics of the Solid State, Vol. 44, No. 1, 2002, pp. 98–101. Translated from Fizika Tverdogo Tela, Vol. 44, No. 1, 2002, pp. 93–96.

MAGNETISM AND FERROELECTRICITY

Domain Walls in Magnetic Multilayers with a Biquadratic Exchange

V. V. Kostyuchenko

Institute of Microelectronics and Informatics, Russian Academy of Sciences, Universitetskaya ul. 21, Yaroslavl, 150007 Russia

Received December 13, 2000; in final form, April 10, 2001

Abstract—The structure of domain walls in magnetic multilayers is investigated taking into account the uniaxial anisotropy and biquadratic exchange between the layers. Analytical solutions are derived for different types of domain wall structures. The majority of the solutions obtained have no analogs in conventional magnetic materials. The thickness and the energy density per unit area are calculated for the domain walls under investigation. The range of parameters that correspond to more energetically favorable structures of domain walls is established. © *2002 MAIK "Nauka/Interperiodica".*

1. At present, the properties of magnetic multilayer structures are under extensive investigation. New materials with magnetic multilayer structures have aroused great interest owing to their unusual physical properties and wide prospects of practical application in memory devices.

Investigations into the phase transitions and the processes of magnetization reversal induced in magnetic superlattices under the action of an external magnetic field are being carried out particularly intensively (see, for example, [1] and references therein). Theoretical studies of phase transitions [2–9] have shown that these materials are characterized by a much greater number of phase transitions as compared to conventional magnetic materials (see, for example, [10]). It was found that the domain walls normal to the plane of layers in magnetic superlattices substantially affect the magnetization reversal in these materials [11–13]; this can lead, in particular, to changes in their resistive characteristics. Furthermore, the domain wall structure in itself can affect the electrical and physical properties of magnetic multilayers. Numerical calculations performed by Labrune and Milat [14] demonstrated that the domain walls in magnetic superlattices possess a number of unusual properties (asymmetry of the domain wall, deviation of the magnetization from the plane of layers, etc.) and could prove a very interesting object of investigation. It was also shown [15] that the symmetric domain walls in magnetic multilayers can be relatively unstable. Morozov and Sigov [16] explained the occurrence of domain walls in multilayers in terms of step-type inhomogeneities at the interface between the magnetic and nonmagnetic layers. However, the existence of domain walls between regions with a noncollinear orientation of magnetization in adjacent layers [11–13] was not interpreted. Moreover, experimental observations of magnetization reversal in magnetic multilayers through the nucleation and growth of domains of the other phase [11–13, 17] also contradict the aforementioned model.

The foregoing shows that the domain walls in magnetic superlattices have not been adequately investigated theoretically. In particular, no consideration is given to the structure of domain walls in the case of noncollinear orientation of the magnetization in adjacent layers, even though such domain walls have been observed experimentally. In the present work, the structure of domain walls in magnetic multilayers is investigated taking into account the biquadratic exchange interaction between the layers for both collinear and noncollinear orientation of the magnetization in adjacent layers. The only case considered is when the magnetization is identical in all the magnetic layers. The situation when the magnetization have different values in the magnetic layers, which is of particular interest, will be considered in a separate publication.

2. The domain wall structure is considered in the two-sublattice approximation; i.e., it is assumed that $\mathbf{M}_1$ and $\mathbf{M}_2$ are the magnetizations in all odd and even layers, respectively ($|\mathbf{M}_1| = |\mathbf{M}_2|$). This approximation holds for a large number of layers [18] and breaks down only in the case of surface spin-flop transition [19]. It should be noted that magnetic multilayer structures are characterized by a greater number of domain wall types as compared to conventional magnets (see, for example, [20]). We assume the thickness of each magnetic layer (d) to be smaller than that of the domain wall in the bulk sample ($d \ll \Delta$). Let the z axis be directed along the normal to the plane of the layers. In this case, the dependence of the magnetization on the z coordinate inside each layer can be ignored. Within this approximation, the problem of calculating the dependence of the magnetization $\mathbf{M}(x, y, z, t)$ on three spatial coordinates and time is reduced to the problem of calculating the dependences of two quantities, $\mathbf{M}_1(x, y)$ and

1063-7834/02/4401-0098$22.00

$\mathbf{M}_2(x, y)$, on only two spatial coordinates and time ($\mathbf{M}_i$ is the magnetization in the ith magnetic layer).

For a domain wall in a two-layer magnetic structure, we write the variational principle in the following form:

$$\delta\int F_S dS = 0. \tag{1}$$

It is appropriate to express the energy density F_S in terms of angular variables θ_i and φ_i, which determine the orientation of the magnetization in the ith magnetic layer. The polar angles θ_i are reckoned from the z axis, and the azimuthal angles φ_i are measured from the x axis in the xy plane.

The energy density F_S in angular variables θ_i and φ_i takes the form

$$\begin{aligned} F_S = &\sum_{i=1}^{2}\left\{\frac{1}{2}K\sin^2\theta_i\sin^2\varphi_i + 2\pi M^2\cos^2\theta_i\right. \\ &\left. + \frac{1}{2}A[(\nabla\theta_i)^2 + \sin^2\theta_i(\nabla\varphi_i)^2]\right\} \\ &+ \frac{1}{2}J_1(\cos\theta_1\cos\theta_2 + \sin\theta_1\sin\theta_2\cos(\varphi_1-\varphi_2)) \\ &+ \frac{1}{2}J_2(\cos\theta_1\cos\theta_2 + \sin\theta_1\sin\theta_2\cos(\varphi_1-\varphi_2))^2, \end{aligned} \tag{2}$$

where γ is the gyromagnetic ratio, M is the saturation magnetization in the ferromagnetic layer, H is the external magnetic field directed along the x axis, K is the uniaxial anisotropy constant, A is the inhomogeneous exchange constant, and J_1 and J_2 are the constants of the Heisenberg and biquadratic exchange between the magnetic layers, respectively. Relationship (2) is obtained from the Lagrangian density for a single-sublattice ferromagnet with inclusion of the exchange interaction between the magnetic layers.

Since the demagnetization energy inhibits the deviation of the magnetization from the plane of the layers, we can assume that $\theta_i = \text{const} = \pi/2$. In this case, it is convenient to introduce the variables φ and ψ:

$$\begin{cases}\varphi_1 = \varphi + \psi \\ \varphi_2 = -\varphi + \psi,\end{cases} \quad \begin{cases}\varphi_1 - \varphi_2 = 2\varphi \\ \varphi_1 + \varphi_2 = 2\psi.\end{cases} \tag{3}$$

Consequently, the functional F_S can be rewritten as

$$\begin{aligned} F_S = &K[\sin^2\varphi + \sin^2\psi\cos 2\varphi] + A[(\nabla\varphi)^2 + (\nabla\psi)^2] \\ &+ \frac{1}{2}J_1\cos 2\varphi + \frac{1}{2}J_2\cos^2 2\varphi \end{aligned} \tag{4}$$

and equations used to describe the domain wall structure take the form

$$K\sin 2\psi\cos 2\varphi = 2A\nabla^2\psi, \tag{5a}$$

$$K\sin 2\varphi\cos 2\psi - J_1\sin 2\varphi - J_2\sin 4\varphi = 2A\nabla^2\varphi. \tag{5b}$$

For definiteness, we assume that the domain wall plane is perpendicular to the z axis. In the case of a planar domain wall, the system of equations (5) has the first integral

$$\begin{aligned} &K[\sin^2\varphi + \sin^2\psi\cos 2\varphi] + \frac{1}{2}J_1\cos 2\varphi \\ &+ \frac{1}{2}J_2\cos 2\varphi + \text{const} = A[(\varphi')^2 + (\psi')^2]. \end{aligned} \tag{6}$$

This allows us to find analytical solutions to this system of equations.

In order to determine unambiguously the domain wall structure, it is necessary to complement the system of equations (5) with the boundary conditions. The boundary conditions can be determined from the condition of stability of the homogeneous state. The minimum condition of the functional for the homogeneous state can be met with the following four phases depending on the magnitudes of the Heisenberg and biquadratic exchange interactions between the layers (see, for example, [7]): the ferromagnetic and antiferromagnetic phases, the angular phase with the magnetization vectors in adjacent layers that are symmetrically oriented with respect to the easy axis, and the angular phase with the magnetization vectors in adjacent layers that are symmetrically oriented with respect to the hard axis.

3. At $J_1 < 0$ and $K > J_1 > 2J_2$, the minimum energy corresponds to the ferromagnetic phase. In this case, two types of domain walls become possible, namely, types 1*a* and 1*b* (Fig. 1). The rotation of magnetization in adjacent layers occurs in the same direction for type 1*a* and in opposite directions for type 1*b*. The boundary conditions for the type 1*a* domain walls have the form

$$\begin{aligned} &\varphi = \text{const} = 0, \\ &\psi(-\infty) = 0, \quad \psi(+\infty) = \pi, \quad \psi'(\pm\infty) = 0. \end{aligned} \tag{7}$$

The solution to the system of equations (4) with the boundary conditions (7) takes the form

$$\psi = 2\arctan\exp(x/\Delta_0), \tag{8}$$

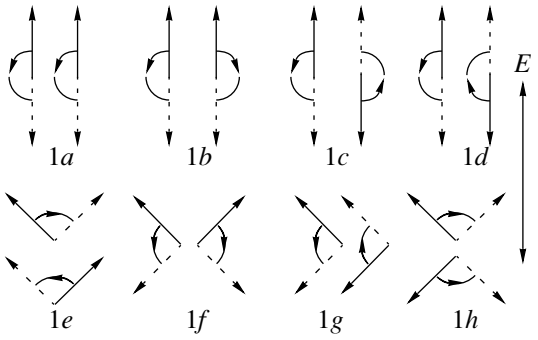

Fig. 1. The sense of rotation of the magnetization vector in adjacent layers for different types of domain walls. *E* is the easy axis.

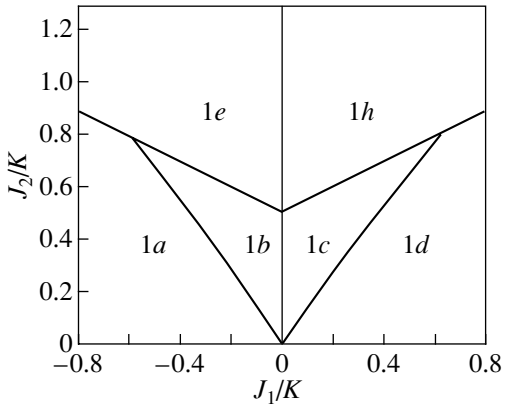

Fig. 2. The regions of parameters corresponding to the minimum energy for different types of domain walls shown in Fig. 1.

where $\Delta_0 = \sqrt{A/K}$. For domain walls 1*b*, the boundary conditions are represented as

$$\psi = \text{const} = 0,$$
$$\varphi(-\infty) = 0, \quad \varphi(+\infty) = \pi, \quad \varphi'(\pm\infty) = 0. \tag{9}$$

These conditions are satisfied with the solution

$$\varphi = \arccos\left[\frac{-\tanh(x\sqrt{1-q_f}/\Delta_f)}{\sqrt{1-q_f/\cosh^2(x\sqrt{1-q_f}/\Delta_f)}}\right], \tag{10}$$

where $\Delta_f = \sqrt{A/(K-J_1)}$ and $q_f = 2J_2/(K-J_1)$.

4. The calculated wall energies per unit area for different types of domain walls are presented in the table. If the magnitude of the exchange interaction between the layers is large [$|J_1| > (16/\pi^2 - 1)K$], the energy of the domain wall 1*a* is higher than that of the domain wall 1*b*. For $|J_1| < (16/\pi^2 - 1)K$, the lower energy can be observed for either the type 1*a* or the type 1*b* domain wall, depending on the magnitude of the biquadratic exchange interaction. The regions of parameters corresponding to different types of domain walls are shown in Fig. 2.

Calculated energies per unit area for different types of domain walls shown in Fig. 1

1*a*	$4\sqrt{AK}$
1*b*	$2\sqrt{A(K-J_1)}\left(\sqrt{1-q_f} + \frac{1}{\sqrt{q_f}}\arcsin\sqrt{q_f}\right)$
1*c*	$4\sqrt{AK}$
1*d*	$2\sqrt{A(K-J_1)}\left(\sqrt{1-q_a} + \frac{1}{\sqrt{q_a}}\arcsin\sqrt{q_a}\right)$
1*e*	$2\sqrt{2AJ_2}(\sin 2\varphi_I + 2\varphi_I\cos 2\varphi_I)$
1*f*	$2\sqrt{2AJ_2}(\sin 2\varphi_I + (\pi - 2\varphi_I)\cos 2\varphi_I)$
1*g*	$2\sqrt{2AJ_2}((\pi - 2\varphi_{II})\cos 2\varphi_{II} - \sin 2\varphi_{II})$
1*h*	$2\sqrt{2AJ_2}(2\varphi_{II}\cos 2\varphi_{II} - \sin 2\varphi_{II})$

5. In the case when the antiferromagnetic phase is more energetically favorable ($K + J_1 > 2J_2$, $J_1 > 0$), there can also exist two types of domain walls that differ in the sense of rotation of the magnetization in adjacent layers, namely, types 1*c* and 1*d* (Figs. 1*c*, 1*d*). The boundary conditions for domain walls 1*c* are given by

$$\varphi = \text{const} = \pi/2,$$
$$\psi(-\infty) = -\pi/2, \quad \psi(+\infty) = \pi/2, \quad \psi'(\pm\infty) = 0. \tag{11}$$

The solution to the system of equations (5) with the boundary equations (11) has the form

$$\psi = 2\arctan\exp(x/\Delta_0). \tag{12}$$

For domain walls 1*d*, the boundary equations are represented as

$$\psi = \text{const} = \pi/2,$$
$$\varphi(-\infty) = -\pi/2, \quad \varphi(+\infty) = \pi/2, \quad \varphi'(\pm\infty) = 0. \tag{13}$$

These conditions are satisfied with the following solution to the system of equations (5):

$$\varphi = \arcsin\left[\frac{\tanh(x\sqrt{1-q_a}/\Delta_a)}{\sqrt{1-q_a/\cosh^2(x\sqrt{1-q_a}/\Delta_a)}}\right], \tag{14}$$

where $\Delta_a = \sqrt{A/(K+J_1)}$ and $q_a = 2J_2/(K+J_1)$.

As in the case of the ferromagnetic phase when the magnitude of the Heisenberg exchange interaction between the layers is small [$|J_1| < (16/\pi^2 - 1)K$], the energy of the domain wall 1*d* with opposite directions of the magnetization vectors in adjacent layers can be less than that of the domain wall 1*c*. The region of parameters J_1 and J_2, which corresponds to this situation, is displayed in Fig. 2.

6. For $J_1 < 0$ and $K < J_1 + 2J_2$, the minimum energy corresponds to the angular phase with symmetric orientation of the magnetization vectors in adjacent layers with respect to the easy axis. The possible types of domain walls for this case are represented in Figs. 1*e* and 1*f*. The boundary conditions for domain walls 1*e* have the following form:

$$\psi = \text{const} = 0,$$
$$\varphi(-\infty) = -\varphi_I, \quad \varphi(+\infty) = \varphi_I, \quad \varphi'(\pm\infty) = 0. \tag{15}$$

The solution to the system of equations (5), which satisfies these boundary conditions, is given by the formula

$$\varphi = \arctan[\tan\varphi_I \tanh(x\sin 2\varphi_I/\Delta_1)], \tag{16}$$

where $\Delta_1 = \sqrt{2A/J_2}$ and $\varphi_I = \frac{1}{2}\arccos\frac{K-J_1}{2J_2}$.

For domain walls 1*f*, the boundary conditions are given by

$$\varphi(-\infty) = \varphi_I, \quad \varphi(+\infty) = \pi - \varphi_I, \quad \varphi'(\pm\infty) = 0. \tag{17}$$

In this case, we obtain the following solutions to the system of equations (5):

$$\psi = \text{const} = 0,$$
$$\varphi = \operatorname{arccot}[\cot\varphi_I \tanh(x \sin 2\varphi_I/\Delta_1)]. \quad (18)$$

The energy of the domain wall 1*e* is less than that of domain wall 1*f*, because the energy of the biquadratic exchange interaction is identical for both types of domain walls, whereas the energy of anisotropy and the energy of the Heisenberg exchange interaction for domain wall 1*e* are less than those for the domain wall 1*f*.

7. For $J_1 > 0$ and $K + J_1 < 2J_2$, the minimum energy corresponds to the angular phase with symmetric orientation of the magnetization in adjacent layers with respect to the hard axis. The possible types of domain wall structures for this case are shown in Figs. 1*g* and 1*h*. The boundary conditions for domain walls 1*g* have the form

$$\psi = \text{const} = \pi/2, \quad \varphi(-\infty) = \varphi_{II} - \pi/2,$$
$$\varphi(+\infty) = \pi/2 - \varphi_{II}, \quad \varphi'(\pm\infty) = 0, \quad (19)$$

where $\varphi_{II} = \frac{1}{2}\arccos\frac{K + J_1}{2J_2}$. The solution to the system of equations (5), which satisfies the boundary conditions (19), is represented by the formula

$$\varphi = \arctan[\cot\varphi_{II} \tanh(x \sin 2\varphi_{II}/\Delta_2)]. \quad (20)$$

Similarly, the boundary conditions for domain walls 1*h* have the form

$$\psi = \text{const} = \pi/2, \quad \varphi(-\infty) = \pi/2 - \varphi_{II},$$
$$\varphi(+\infty) = \pi/2 + \varphi_{II}, \quad \varphi'(\pm\infty) = 0. \quad (21)$$

The solution satisfying these conditions is given by

$$\varphi = \operatorname{arccot}[\tan\varphi_{II} \tanh(x \sin 2\varphi_{II}/\Delta_1)]. \quad (22)$$

As in the preceding case, the energy of the domain wall 1*h* is always less than that of the domain wall 1*g*, because the energy of the Heisenberg exchange interaction and the energy of anisotropy for the former structure are also less than those for the latter structure.

8. Thus, the structure of domain walls in magnetic superstructures is investigated. Eight exact solutions are obtained for different types of domain walls. The sense of rotation of the magnetization vectors in adjacent layers is represented in Fig. 1. The domain wall structures 1*b* and 1*d*–1*h* have no analogs in conventional magnetic materials. Domain walls of types 1*f* and 1*g* are universally characterized by a higher energy compared to that of domain walls of types 1*e* and 1*h*, respectively. However, it should be noted that the inclusion of the magnetostatic energy can change this ratio.

ACKNOWLEDGMENTS

The author is grateful to A.K. Zvezdin for numerous valuable remarks.

This work was supported by the International Scientific and Technical Program, project no. 02.04.5.2.

REFERENCES

1. I. K. Schuller, S. Kim, and C. Leiton, J. Magn. Magn. Mater. **200** (1–3), 571 (1999).
2. A. K. Zvezdin and S. N. Utochkin, Pis'ma Zh. Éksp. Teor. Fiz. **57** (7), 424 (1993) [JETP Lett. **57**, 439 (1993)].
3. S. N. Utochkin and A. K. Zvezdin, J. Magn. Magn. Mater. **140–144**, 787 (1995).
4. A. K. Zvezdin and S. N. Utochkin, Pis'ma Zh. Éksp. Teor. Fiz. **57** (7), 418 (1993) [JETP Lett. **57**, 433 (1993)].
5. R. W. Wang and D. L. Mills, Phys. Rev. B **50** (6), 3931 (1994).
6. N. S. Almeida and D. L. Mills, Phys. Rev. B **52** (18), 13504 (1995).
7. A. K. Zvezdin and V. V. Kostyuchenko, Fiz. Tverd. Tela (St. Petersburg) **41** (3), 461 (1999) [Phys. Solid State **41**, 413 (1999)].
8. V. V. Kostyuchenko and A. K. Zvezdin, J. Magn. Magn. Mater. **176** (1), 155 (1997).
9. V. V. Kostyuchenko and A. K. Zvezdin, Phys. Rev. B **57** (10), 5951 (1998).
10. A. K. Zvezdin, in *Handbook of Magnetic Materials*, Ed. by K. H. J. Buschow (Elsevier, Amsterdam, 1995), Vol. 9, p. 405.
11. V. I. Nikitenko, L. M. Dedukh, V. S. Gornakov, *et al.*, IEEE Trans. Magn. **33** (5), 3661 (1997).
12. V. I. Nikitenko, V. S. Gornakov, L. M. Dedukh, *et al.*, Phys. Rev. B **57** (14), R8111 (1998).
13. V. I. Nikitenko, V. S. Gornakov, L. M. Dedukh, *et al.*, J. Appl. Phys. **83** (11), 6828 (1998).
14. M. Labrune and J. Milat, J. Magn. Magn. Mater. **151** (1–2), 231 (1995).
15. A. K. Zvezdin and V. V. Kostyuchenko, Zh. Éksp. Teor. Fiz. **116** [4(10)], 1365 (1999) [JETP **89**, 734 (1999)].
16. A. I. Morozov and A. S. Sigov, Pis'ma Zh. Éksp. Teor. Fiz. **61** (11), 893 (1995) [JETP Lett. **61**, 911 (1995)].
17. S. G. E. te Velthuis, J. S. Jiang, and G. P. Felcher, Appl. Phys. Lett. **77** (14), 2222 (2000).
18. A. K. Zvezdin and V. V. Kostyuchenko, Fiz. Tverd. Tela (St. Petersburg) **39** (1), 178 (1997) [Phys. Solid State **39**, 155 (1997)].
19. R. W. Wang, D. L. Mills, E. E. Fullerton, *et al.*, Phys. Rev. Lett. **72** (6), 920 (1994).
20. K. P. Belov, A. K. Zvezdin, A. M. Kadomtseva, and R. Z. Levitin, *Orientational Transitions in Rare-Earth Magnets* (Nauka, Moscow, 1979).

Translated by O. Moskalev